WOFEX 2015

proceedings of the 13th annual workshop

Faculty of Electrical Engineering and Computer Science,
VŠB – Technical University of Ostrava

ISBN 978-80-248-3787-1

WOFEX 2015

http://wofex.vsb.cz/2015/

13th annual workshop,
Ostrava, 8th September 2015
Proceedings of papers

Organized by

VŠB – Technical University of Ostrava
Faculty of Electrical Engineering and Computer Science

WOFEX 2015

© Michal Krátký, Jiří Dvorský, Pavel Moravec, editors

ISBN 978-80-248-3787-1

This work is subject to copyright. All rights reserved. Reproduction or publication of this material, even partial, is allowed only with the editors' permission.

Page count:	719
Impression:	200
Edition:	1st
First published:	2015

This proceedings was typeset by pdfLaTeX.

Published by Faculty of Electrical Engineering and Computer Science, VŠB – Technical University of Ostrava

Preface

The workshop WOFEX 2015 (PhD workshop of Faculty of Electrical Engineering and Computer Science) was held on September 8th September 2015 at the VŠB – Technical University of Ostrava. The workshop offers an opportunity for students to meet and share their research experiences, to discover commonalities in research and studentship, and to foster a collaborative environment for joint problem solving. PhD students are encouraged to attend in order to ensure a broad, unconfined discussion. In that view, this workshop is intended for students and researchers of this faculty offering opportunities to meet new colleagues.

This book of proceedings includes 117 papers of faculty PhD students and 2 papers of external authors. The proceedings of WOFEX 2015 are also available at WOFEX Web site http://wofex.vsb.cz/2015/. I would like to thank the authors and the Organizing Committee from Department of Computer Science, namely Jiří Dvorský and Pavel Moravec, for their arduous editing work.

September 2015

Michal Krátký
Program Committee Chair
WOFEX 2015

Organization

Program Committee

Chair:

Michal Krátký (VŠB – Technical University of Ostrava)

Members:

Pavel Brandštetter (VŠB – Technical University of Ostrava)
Radim Briš (VŠB – Technical University of Ostrava)
Zdeněk Dostál (VŠB – Technical University of Ostrava)
Petr Chlebiš (VŠB – Technical University of Ostrava)
Stanislav Rusek (VŠB – Technical University of Ostrava)
Václav Snášel (VŠB – Technical University of Ostrava)
Vladimír Vašinek (VŠB – Technical University of Ostrava)

Organizing Committee

Jiří Dvorský (VŠB – Technical University of Ostrava)
Pavel Moravec (VŠB – Technical University of Ostrava)
Hana Dluhošová (VŠB – Technical University of Ostrava)

Workshop Location:

Campus of VŠB – Technical University of Ostrava
17. listopadu 15, 708 33 Ostrava–Poruba, Czech Republic
8th September 2015

http://wofex.vsb.cz/2015/

Table of Contents

Study Programme P2649 Electrical Engineering

Electrical Power Engineering (3907V001)

Daylight Statistical Evaluation of Dimmable Interior Lighting System Consumption 1
Petr Bos, Jan Šumpich, Tomáš Novák, and Karel Sokanský

Localization of Current Fields in the Vicinity of a Railway Platform 6
Jiří Cigánek

Geomagnetic Storms Effects on Power Transformers 12
Jan Fulneček

Statistical Evaluation of Measured Values from Photovoltaic Plant Using LabVIEW Software 18
Martin Gruss and Daniel Minařík

New Results of the Restoration Methodology in 2015 24
Vít Houdek

Analysis of Measuring the Thermal Part of the Biogas Plant 30
Jiří Janša

Application of Electron Spin Precession for Electric Power Generation . . . 36
Martin Koutný and Radomír Goňo

Application for Facilitating the Selection of Water Turbine and Generator Protection Design of Small Hydro Power Plant 43
Martin Kral and Radomir Gono

Active Charging Stations for Electric Cars 49
Oliver Marcincin

The Input Analysis of Parameters Energetic Technologies in Technological Centre ENET in Ostrava 55
Tomáš Mozdřeň

Evaluation of Electric Power Supply from Photovoltaic Plant in ENET Center 61
Michal Ney

The Basic Rules for Zebra Crossing Lighting 67
Tomáš Novák, Richard Baleja, and Karel Sokanský

Analysis of Data Measured on Co-generation Units in Biogas Station 72
Ladislav Novosád

Evaluating Traction Currents at Electric Traction Stations 78
Jiří Plaček

Measurement on the biogas plant Hodoňovice 84
Michal Špaček

Electrical Machines, Apparatus and Drives (2642V004)

Simulation of Sliding Mode Observer in Speed Control Structure of Induction Motor Drive 90
Chau Si Thien Dong

Controlled Systems with Electrical Drives Identification Using Genetic Algorithms 96
Jiri Hajovsky

Design and Simulation of Electric Traction Drive for 4WD Vehicles 102
Tomas Mrovec and Petr Chlebis

The Enlarged Linear d-q Model of Induction Motor with the Iron Loss ... 108
Jan Otýpka

Implementation of Luenberger Observer to Sensorless Vector Control Structure of Induction Motor Drive 114
Ondřej Petrtýl

Optimization of the Rotor Part of a Interior Permanent Magnet Synchronous Generator 120
Ladislav Slíva

Control Methods of Induction Motor Drives 127
Thinh Cong Tran, Chau Si Thien Dong, Hau Huu Vo

MRAS Techniques for Sensorless Control of Induction Motor With Using Artificial Neural Network 133
Tomáš Verner

Simulation of MRAS Observer in Direct Torque Control Structure of Induction Motor Drive 139
Hau Huu Vo

Electronics (2612V015)

Coupling of DC sources 145
Katerina Baresova

The Properties of Bidirectional Coupling Converter with Galvanic Insulation 151
Martin Borski

The investigation of reverse impacts of a six pulse controlled rectifier to a power supply 157
Jiří Špička

Application of Modern Active Structures in Signal Generators 163
Radek Šulák

Automotive Communication Buses and Their Analysis 169
Jiří Takáč

Technical Cybernetics (2612V045)

Accumulation system of electric vehicle 175
Kristýna Friedrischková, David Vala, and Bohumil Horák

Fuzzy Clusterization of Obese Patients 181
Jakub Hlavica, Michal Prauzek, and Marketa Michalikova

Corpus callosum tilt estimation algorithm for imaging systems 187
Radek Hrabuška and Niranjana Sampathila

Implementation and Comparison of Algorithms for Discreet Fourier Transform 193
Michal Kelnar

Exergaming Rehabilitation System for 3D Motion Analysis of Wobble Board 199
Jana Krohova and Maros Smondrk

Articular Cartilage Chondromalacia Detection Based on Soft Thresholding Segmentation Approach 204
Jan Kubicek

Simulation of technological process using .NET for control system design . 210
Martin Mikolajek

Electrical Impedance Tomography Image reconstruction with RBF Neural Network 216
Marketa Michalikova

Application for Evaluation of Biological Signals 222
Agáta Mročková, Martin Pieš, and Miroslav Pokorný

Controlling of Non-Stationary Systems Based on Fuzzy-Logic Approaches 228
Jana Nowaková and Miroslav Pokorný

Multi-source energy unit for family house 234
Vít Otevřel, Zdeněk Slanina, and Bohumil Horák

Multichannel Photoplethysmography; Possibility How to Noninvasively Determine State of Cardiovascular System 240
Lukas Peter

Classification of Actual Fetal State Determination using Random Forests . 246
Tomas Peterek, Maros Smondrk and Jana Krohova

Magnetometer with protection against detection by electronic countermeasure 250
David Vala

Study Programme P1807 Computer Science, Communication Technology and Applied Mathematics

Computer Science (1801V001)

Microsoft Azure Machine Learning and market prediction, performance . . 256
Marian Bielik

Data Classiffication using Evolutionary Algorithms 261
Petr Buček

Analysis and Implementation of the Active Demand Side Management in the Off-grid System 266
Tomas Burianek

Moodle logs analysing web application 272
Michal Čerbák

Software Process Resource Modeling based on UPMM 277
Jan Czopik, Jakub Stolfa, Svatopluk Stolfa, and Ivo Vondrák

A New Photogrammetric Tool for the Automatic Detection and Segmentation of Circular Objects in Low-quality Images 283
Karolína Feberová

High Performance Computing Framework for Uncertainty Modelling in a Flood Monitoring System 289
Martin Golasowski

Analysis of Medical Images, Using Active Contours Optimized by Self-Organizing Migration Algorithm 295
Jakub Hendrych and Radim Kunčický

Geodesic Distance and k-max Geodesic Distance in Image Segmentation . 301
Michael Holuša

Detection of Corners in LIDAR Data via Neural Network 307
Branislav Holý

The Radio Direction Finding with Advantage of the Software Defined Radio 313
Josef Hrabal

Differential Evolution based Cluster Forest Algorithm 319
Jan Janoušek

Replacing Pseudo-inverse in the Extreme Learning Machine Algorithm to Improve Algorithm Speed on GPU 326
Tomáš Ježowicz

Comparison of variable neighborhood search algorithm and particle swarm algorithm using travelling salesman problem optimization task ... 332
Adam Kašpar

Analytic programming on CPU and GPU 337
Lumír Kojecký

Parallelization of Cellular Automaton using Kaira 343
Lukáš Kroczek

Cost Estimations in XML Queries 348
Petr Lukáš

Improvements of Formal Veriffication in Kaira 354
Ondřej Meca

A survey of semantic database benchmarking 360
Roman Meca

Identity of users publishing on the Internet and their research area 365
Adam Ondrejka

Universal B-tree 370
Jakub Ondruš

Efficient data routing system ForceB – Webinar 376
Martin Prokeš

Differential Evolution Dynamics Analysis by Complex Networks 382
Lenka Skanderova and Tomas Fabian

Techniques of Czech Language Lossless Text Compression 388
Jiri Sevcik

Introduction to Integration of the Process Mining to the Knowledge Framework for Software Processes 394
Jakub Stolfa

Machine-Learning Supportive Methods for Software Effort Estimation ... 400
Radoslav Štrba

Memory Optimized Pheromone Structure for Max-Min Ant Systems 406
Martin Šurkovský

Parallelization of k-NN Problem on GPU to Speed up the Fruchterman-Reingold Graph Layout Algorithm 412
Vojtěch Uher

Feature Preprocessing Methods For Machine Learning Algorithms 418
Tomas Vantuch

Advances in Context Transformations 424
Michal Vašinek

Evolution Algorithms and Cryptography Based on Chaotic Systems 430
Filip Zatloukal

Computational and Applied Mathematics (1103V036)

Path Integral Monte Carlo Methods 436
Rajko Ćosić

Advances in fluid flow in porous medium 442
Martin Hasal

Risk of postoperative complications after surgeries: Laparoscopic versus open surgery 448
Pavel Jahoda, Radim Briš, Michal Běloch, and Lubomír Martínek

Reconstruction of the human bones from CT images and their visualization 454
Milan Jaroš

Towards parallel FEM data generation for PermonFLLOP FETI implementation 460
Pavla Jirůtková and Alexandros Markopoulos

Optimization Techniques for Finding Approximations of Perfect Difference Sets 466
Michal Kravčenko

Optimization Out-degree in Planar and Simple Graphs 472
Matěj Krbeček, Michal Kravčenko, and Adam Silber

Boundary Element Based Vertex Solver for Polygonal Subdomains 478
Lukáš Malý

Acceleration of the boundary element method 484
Michal Merta

Use of the ALNS Algorithm for Solving the Probabilistic Time-Dependent Vehicle Routing Problem 490
Tomáš Režnar

Short-term electricity spot prices prediction using Neural Networks and hybrid ARIMA-NN model 498
Robert Skopal

Probabilistic Time-Dependent Travel Time Computation using Monte Carlo Simulation 504
Radek Tomis

Parallel Inverse Modelling in Rainfall-Runoff Simulations 510
Radim Vavřík

Boundary element based evaluation of homogenized coefficients in conductivity 516
Jan Zapletal

Communication Technology (2601V018)

Different Metods of Optical Fibers for Use in Interferometric Arrangements 522
Jakub Cubik

Research of Ageing of Attenuation Parameters of Optical Coupler 528
Lukas Bednarek

Deformation measurement with Bragg gratings and analysis of multiplexing techniques for quasi-distributed measurement 534
Marcel Fajkus

Software Tool for Prediction and Implementation of QoS in IP Based Networks 540
Jaroslav Frnda

Determination of Empirical Equations for the FSO with Respect to Meteorological Measurements 546
Lukas Hajek

Research of Ageing of Optical Fibers and Development of Optical Sensor . 553
Tomáš Hlavinka

Effective planning and analysis of Huawei and Cisco routers for MPLS network design using fast reroute protection 559
Martin Hlozak and Jaroslav Zdralek

Measurement of masonry moisture with distributed temperature system . 565
David Hrubý

Measurement of attenuation of PDMS fiber 570
Jan Jargus

Temperature measurement inside metallic cables using distributed temperature system 576
Jakub Jaros

Study of the incidence of external influences on various types of optical connections 582
Tomáš Kajnar

Software Design of LEDs for Visible Light Communication 588
Andrej Liner

Calculation of the final key length for quantum key distribution using BB84 and B92 Protocol 594
Miralem Mehic and Miroslav Voznak

Convergence of OpenBTS and OpenIMS projects 600
Martin Mikulec and Miroslav Voznak

Fiber optic Mach-Zehnder interferometer with FBG for movement analysis 606
Jan Nedoma

Big analytics tools on cloud 612
Lukáš Orčík and Miroslav Voznak

Concrete Deflection Measurement Using Fiber Optic Distributed Strain System 616
Martin Papes

Stress Detection from Human Speech 620
Pavol Partila, Jaromir Tovarek, and Miroslav Voznak

The Influence of Radiation Burden on Ageing Effects of Optical Fiber Coupler 626
Frantisek Perecar

Hybrid WDM/TDM Topology Using the Fabry-Perot Laser 632
Radek Poboril

Improvements of neural network SIP attack classifier 638
Jakub Šafařík

Impact of IPsec Network Security on Video Quality 642
Lukáš Ševčík and Miroslav Vozňák

Exploratory Analysis of Measurements Real-time Applications in Virtualized Environment 648
Jiri Slachta and Miroslav Voznak

Railway Wireless Barrage State 654
Martin Tomis

Impact of classification methods for speech stress recognition accuracy ... 660
Jaromir Tovarek and Miroslav Voznak

Design and Creation of Czech Speech Emotional Database 666
Dominik Uhrin and Miroslav Voznak

Simulation of Modulation Formats for FSO with Respect to Measurements of the Influence of Atmospheric Phenomena 673
Ales Vanderka

Current progress in research of optical fibers ageing 679
Petr Závodný

Optoelectronic sensoric elements made from polydimethylsiloxane 684
Ondřej Zbořil

External Authors

Computer Application for Identification of the Geometry of Overhead Power Line Conductors 689
Michał Krawiec

Measurement of Partial Discharges with the Use of a High Voltage Testing System, Where PDS100 Analyser Was Used for Detection 694
Ireneusz Urbaniec

Author Index

Daylight Statistical Evaluation of Dimmable Interior Lighting System Consumption

Petr Bos, Jan Šumpich, Tomáš Novák, and Karel Sokanský

Department of Electrical Power Engineering, FEECS,
VŠB – Technical University of Ostrava, 17. listopadu 15, 708 33 Ostrava – Poruba
petr.bos@vsb.cz

Abstract. From the power engineers point of view, at the present time, the necessity to predict the consumption of lighting systems becomes more and more urgent at the time of the project phase. The reason is to compare the projects from different investors and especially to compare the projects with regulated (dimmed) lighting systems (these are regulated at a constant level of illumination) with the projects of unregulated lighting. In that case, the designer has to be able to determine the payback of regulated lighting system in comparison with classic unregulated lighting systems.

The calculating is determined by the LENI (Lighting Energy Numeric Indicator), according to EN 15193, which is based upon the analytical estimate of potential savings calculated on the base of empirically derived coefficients for standardized rooms, standardized operations, etc. However, this model is not based on real specific situations. Therefore, the team of VSB-TU Ostrava developed a predictive model, which is based on the daylight dynamics in specific lighting conditions. The long-term measurements were carried out to verify whether the model´s results correspond to the real facts.

Keywords: regulated lighting systems, daylight, constant level of illumination, predictive model, energy savings.

© M. Krátký, J. Dvorský, P. Moravec (Eds.): WOFEX 2015, pp. 1–5.
VŠB – Technical University of Ostrava, FEECS, 2015, ISBN 978-80-248-3787-1.

1 Introduction

The proposed prediction model uses an artificial interior lighting system which can be dimmed to a constant illuminance level and deals with the contribution of daylight entering the space through windows and skylights. This developed model gives transparent and unambiguous evidence of the economic benefit of using lighting systems that reduce the intensity of light emitted by them depending on the amount of daylight entering the rooms that are being illuminated.

2 Proposal of the prediction model

Diffuse illumination is being increasingly used in the interior lighting systems, a combination of daylight with artificial light. The technical level of the current lighting systems enables the regulation of the luminous flux in lighting control systems at a constant level of illumination due to the artificial lighting dimming systems of each lamp. Using daylight in these lighting systems can save a considerable part of electricity.

Based on the technical design of the interior lighting system and cyclic calculations of the dimming levels for light lines, or even for the individual lights, the dimming development patterns are obtained for the light lines or individual lights.

The dimming figures are converted to electric power enabling the power used for the lighting system to be calculated depending on the uniformly overcast sky in any given time.

The base for dynamic modeling of daylight is uniformly overcast sky, as it is mentioned above. Due to that the influence of windows positions towards the cardinal points can be eliminated. In the calculation we do not consider only the uniformly overcast sky, but also the influence of the Sun declination that is changing throughout the days and year. The external intensity of illumination varies not only during the day, but also during the whole year. Value of illuminance is also dependent on the time and the clock angle of the Sun, on the Solar elevation and on the diffuse illuminance. [4]

3 Verification of the prediction model

The artificial lighting system for our examined room must be designed to enable the power savings to be calculated. Calculations must be performed according to the norm EN 12464-1. Room is equipped with three ceiling-mounted ZC T5 228/12LOS ZK, 2x28W/840 luminaires.

Tested room is located on the 2nd (above-ground) floor of the detached house at the VSB – Technical University of Ostrava. The shading of surrounding buildings and trees were included in the calculation. The area of the room is 3975 mm x 3372 mm, and its height is 2100 mm. The shorter wall accommodates two windows which are 120 mm apart: the first window is 900 mm x 1000 mm area, at a height of 810 mm above the floor and 500 mm from the wall, and the second window is also 900 mm x 1000 mm area, at a height of 810 mm above the floor and 1520 mm from the wall. [3]

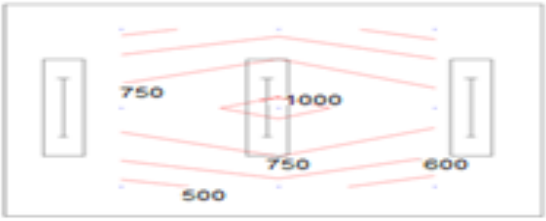

Fig. 1. Artificial lighting system calculation of the tested room

4 Prediction model application

Once the time dependences of the illuminance from daylight are known for the space treated, a cycle of dimming calculations for the parts of the lighting systems can be launched based on the requirement that meet the minimum regulatory illuminance levels in the area.

4.1 Electrical energy consumption of lighting system

Electrical energy consumption of the lighting system depends on the lighting intensity of the room, whose values depend on the outdoor diffuse illuminance that determines the level of power demand of the lighting system which we need to achieve the required level of illumination.

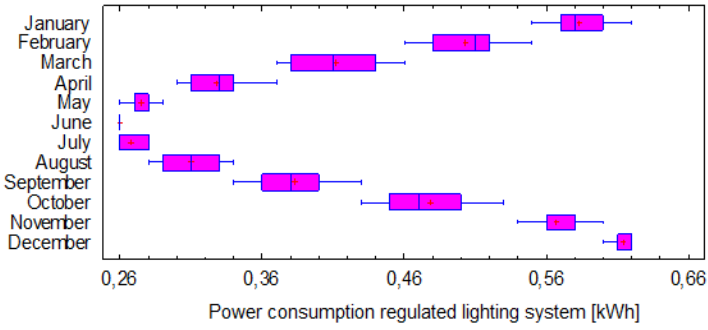

Fig. 2. Power consumption of regulated lighting system in tested room

Figure 2: You can see that it is necessary to increase or reduce the energy consumptions according to individual months of a year in the tested room. Levels of consumption are influenced by intensity of cloudiness and daylight. Every month, the minimum rates of electrical consumption were measured at the time of smallest cloudiness and, in the contrary, the highest consumption was measured at the time of high level cloudiness.

In case of unregulated lighting system there is a constant level of electrical consumption of 1.34 kWh. In case of regulated lighting system there is the highest consumption in winter time, it is 0.62 kWh, and the lowest level of consumption in summer months, it is 0.26 kWh. In comparison to the unregulated lighting system there is very significant energy savings.

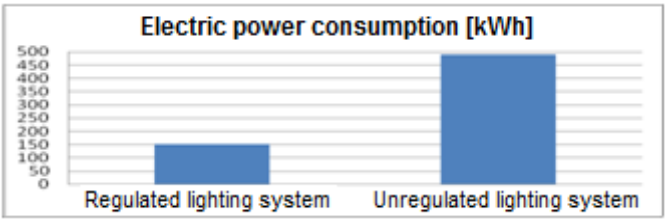

Fig. 3. Electric power consumption

Figure 3: The importance of regulation of lighting systems in tested room is evident in this diagram. The regulation is able to save up to 69 % electric energy in our case.

5 Conclusion

This article describes the application of the predictive model of the lighting system using natural daylight. From the statistical point of view it is determined that the regulation of lighting systems can save up to 69 % of electric energy. Total consumption of unregulated lighting system is 489 kWh / year, and on the other hand, the consumption of regulated lighting system is 151 kWh / year only.

The total yearly consumption of the artificial lighting system in tested room corresponds with the predictive model.

The measured values are influenced by the intensity level of daylight and cloud cover. Every day of a year the minimum consumption was measured on a clear day, while the highest consumption was at time of high level of cloudiness.

The intensity of artificial light significantly fluctuates during the day because of changing level of daylight during winter and autumn months. That is why it is necessary to regulate the intensity of artificial lighting during the day in winter time. On the contrary it is possible to keep approximate stable value of the artificial lighting in summer months due to constant daylight conditions. Therefore we are able to regulate lighting systems and achieve the desired illuminance values, reducing the power and consumption of artificial lighting and significantly increase energy savings.

6 Acknowledgment

This article was prepared with the support of the project "Transmission of control signals in lighting systems" SP2015/182, by institution of VSB-TU Ostrava.

7 References

1. S. Darula, and al., ”Osvětlování světlovody,” Grada Publishing 2009, ISBN 978-80-247-2459-1.
2. P. Rybar, and al., “Denní osvětlení a oslunění budov,” ERA 2001.ISBN 80-86517-33-0.
3. ČSN EN 12464-1 Světlo a osvětlení – Osvětlení pracovních prostorů – Část 1: Vnitřní pracovní prostory.
4. T. Novak, J. Vanus, J. Sumpich, J. Koziorek, K. Sokansky, and R. Hrbac, "Possibility to Achieve the Energy Savings by the Light Control in Smart Home," Proceedings of the 7th International Scientific Symposium on Electrical Power Engineering, pp. 260-263, 2013.
5. J. Sumpich, T. Novak, and K. Sokansky, “Příklady úspor vzniklých využitím denního osvětlení,” Kurz osvětlovací techniky XXX, DLOUHÉ STRÁNĚ, Loučná nad Desnou, 2013, s. 316-319, ISBN 978-80-248-3174-9.
6. J. Sumpich, K. Sokansky, T. Novak, and Z. Carbol, “Stanovení denní osvětlenosti pod rovnoměrně zatženou oblohou za účelem snížení energetické náročnosti v budovách,” In: Světlo 2011, VŠB-TU Ostrava, 2011, s. 207-209. ISBN: 978-80-248-2480-2.
7. P. Janiga, R. Dubnicka, A. Rusnak, and D. Gasparovsky, “Automated system of the measurement of electric parameters of luminaires and light sources at chosen operational conditions,” Proceedings of the 2014 15th International Scientific Conference on Electric Power Engineering, IEEE, 2014, s. 675-678. DOI: 10.1109/EPE.2014.6839517.
8. J. Sumpich, K. Sokansky, T. Novak, and Z. Carbol, “Potenciál úspor elektrické energie spotřebované soustavami sdruženého osvětlení s využitím denního světla,” Electric power engineering, Brno, 2012, s.1165-1168. ISBN 978-80-214-4514-7.
9. J. Skoda, and P. Baxant, “Control of Lighting Systems Using Compact Systems,” BRNO UNIV TECHNOLOGY, 2010, pp. 797-798. ISBN 978-80-214-4094-4.
10. D. Gasparovsky, A. Smola, and P. Janiga, “Assessment of lighting systems for energy certification of buildings,” PRZEGLAD ELEKTROTECHNICZNY, Volume: 84, Issue: 8, Pages: 29-33, 2008, ISSN: 0033-2097.

Localization of Current Fields in the Vicinity of a Railway Platform

Jiří Cigánek

Department of Electrical Engineering, FEECS,
VŠB – Technical University of Ostrava, 17. listopadu 15, 708 33 Ostrava – Poruba
jiri.ciganek.fei@vsb.cz

Abstract: The article deals with an examination of current fields in the vicinity of a railway platform of the SUDOP type. It compares a fault-free state in which the rail is connected with a gabion through a lightning arrester and a case in which there occurs a breakdown of the lightning arrester. The solution is reached with the use of the Comsol Multiphysics program, which solves partial differential equations by means of the finite element method.

Keywords: Electric railways, platform; current density; rail; gabion

1 Introduction

The occurrence of the so-called stray currents represents a major problem in the vicinity of a railway track. Stray current is a current which passes from a rail during the crossing of a railway vehicle into the earth and returns back to the power supply station. These currents disrupt concrete foundations in the vicinity of the railway substructure. Station platforms are some of the places through which these currents pass. This contribution deals with an examination of these fields in the railway platform of the SUDOP type. It compares a fault-free state in which a rail is connected with a gabion through a lightning arrester by means of a conductor and a case in which there occurs a breakdown of the lightning arrester. In this case there therefore occurs a significant voltage surge in the gabion and thus also passage of stray currents.

The term "platform" refers to a part of the railway substructure (a transport area and a pathway) intended for boarding or alighting of passengers and for handling of minor consignments. A gabion or a gabion structure is an element of a cube or cuboid shape made of a hexagonal steel wire mesh, welded steel nets or possibly high-strength polymer geogrids filled with natural aggregate, quarried rock, earth, recycled material, etc.

© M. Krátký, J. Dvorský, P. Moravec (Eds.): WOFEX 2015, pp. 6–11.
VŠB – Technical University of Ostrava, FEECS, 2015, ISBN 978-80-248-3787-1.

2 Mathematical Model

The basic field quantity describing current fields is a current density vector ***J***. It is a differential quantity and it therefore determines the quantity of the current flowing through the elementary area for every place of the solved space. The current density J depends on the resistivity ρ, or rather on the conductivity σ according to the differential form of the Ohm's law.

$$\boldsymbol{J} = \sigma.\boldsymbol{E} \tag{1}$$

In every place where it is possible to determine the intensity of the electric field ***E*** and where the conductivity is known, it is also possible to determine the current density vector. Its direction in the isotropic medium is the same as the direction of the vector of the electric field intensity.

The way to determine the current density vector is more complicated in the anisotropic medium where conductivity is in the form of a tensor. In most cases a tensor has only diagonal components, this means there are various conductivities in the direction of various coordinates, but the intensity of the electric field in the direction of one coordinate will not affect the current density in the direction of another coordinate, i.e. for example

$$J_x = \sigma_{xx}.E_x, \quad J_y = \sigma_{yy}.E_y, \quad J_z = \sigma_{zz}.E_z, \tag{2}$$

The differential form of the Ohm's law is then

$$J = \sigma.E = \sigma.(-\operatorname{grad}\varphi) \tag{3}$$

where

$$\sigma = \begin{bmatrix} \sigma_{ii} & 0 & 0 \\ 0 & \sigma_{jj} & 0 \\ 0 & 0 & \sigma_{kk} \end{bmatrix} \tag{4}$$

Electromagnetic problems associated with solving current fields in a railway superstructure and a substructure work generally with a resulting current, or current density, which is connected with intensity, or potential. Forced quantities are potentials or the primary (forced) intensity of the electric field ***E***v. The primary intensity determines the distribution of charges and currents and it is used for specifying this distribution. For the purposes of an analysis it is possible to accept that the primary intensity determines the secondary distribution of charges and currents and thus the secondary intensity ***E***sec, i.e.:

$$\nabla \times \boldsymbol{E} = -\partial B/\partial t \tag{5}$$

$$\nabla.\boldsymbol{D} = \rho_c \tag{6}$$

$$\nabla \times \boldsymbol{H} = \boldsymbol{J} \tag{7}$$

$$\nabla.\boldsymbol{B} = 0 \tag{8}$$

where the symbol ρ_c does not stand for resistivity, but for the volume density of the total charge. Similarly to the intensity ***E***, the current density ***J*** has also two components, i.e. forced

current density J_v and eddy current density $\sigma.E$. Material relationships must be added to these equations on the boundary

$$D = \varepsilon.E, \quad B = \mu.H, \quad J = \sigma.E \tag{9}$$

A dynamic solution of Maxwell's equations includes also the influence of eddy currents and it is advisable to use here a continuous vector potential

$$\nabla \xi \boldsymbol{A} = \boldsymbol{B} \tag{10}$$

$$\nabla \xi \boldsymbol{H} = \vartheta\varpi + \sigma E = \vartheta\varpi - \sigma.\partial A/\partial\tau \tag{11}$$

therefore $$\nabla \xi (\nabla \xi A) = \mu(\vartheta\varpi - \sigma.\partial A/\partial\tau) \tag{12}$$

It is often advisable to perform the solution of direct-current fields for the scalar potential of the electric field. The advantage of using the scalar potential for large ground fields resides in the replacement of the vector field E, which is given by 3 components, with only a single scalar variable. The boundary value problem is therefore described with one scalar variable φ and after its solution all components of the electric field intensity and subsequently also all components of the current density are obtained. The potential has an important role in connection with converting a spatial model into a circuit model described by a node voltage method.

The Laplace's equation in the Cartesian system applies to the scalar electric potential in homogeneous environments without sources:

$$\nabla^2\varphi = \frac{\partial^2\varphi}{\partial x^2} + \frac{\partial^2\varphi}{\partial y^2} + \frac{\partial^2\varphi}{\partial z^2} = 0 \tag{13}$$

The duality of the stationary current field with the electrostatic or magnetostatic field was used in modelling 3D direct-current fields of the railway electrification system.

3 Creating a Model

The Comsol Multiphysics program was chosen for the solution; this program makes it possible to use the finite element method to solve physical problems described by partial differential equations. These problems are generally solved on the basis of environment definitions which are described by partial differential equations and on boundary conditions entered in points, on edges or surfaces of a given model. The results can be obtained in several steps.

A. Geometric Layout

The first step is to choose and draw a geometric form of the solution. Its layout is shown in Fig. 1.

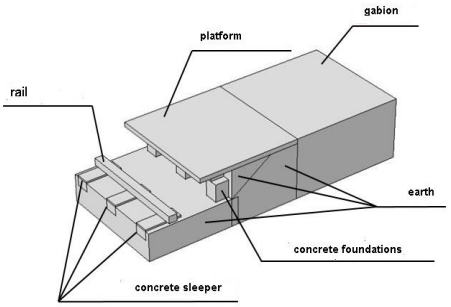

Fig. 1. A geometric layout of the model

The geometric layout is subject to several simplifications. The rail was drawn as a rectangle whose height and width correspond to the actual dimensions of a rail. A further simplification was made on the gabion. Although it is normally a mesh of wires, as was stated above, in the model it was simplified because it was modelled as a full surface. This simplification was necessary because of entering material properties. Other components and their dimensions correspond to the reality.

Two models were made for the purposes of the calculation; the first model corresponds to the fault-free state, where the rail is connected with the gabion through a lightning arrester. The model was prepared in a way that the rail is not connected with the gabion. The second case represents a situation in which there is a breakdown of the lightning arrester and the rail in the model is connected with the gabion by means of an insulated steel conductor.

B. Defining the Parameters

The material parameters were defined by means of the electric conductivity σ and the relative permeability μ_r. These are the primary parameters for calculating the model.

The conductor connecting the rail with the gabion was defined by means of the relative permeability $\mu_r = 4\,000$ and the electric conductivity $\sigma = 1.12e7$ S/m. The insulation of the conductor was defined by $\mu_r = 1$ and $\sigma = 1e\text{-}12$ S/m. The material properties of the rail were defined by means of the measured BH characteristics. Table values of $\mu_r = 1$ and electric conductivity $\sigma = 10$ S/m were assigned to the concrete sleepers under the rail, the concrete footings under the platform and the platform itself. The gabion was defined with the values of relative permeability $\mu_r = 1$ and $\sigma = 4.1e6$ S/m.

The most difficult task was to define various types of earth. It is problematic to determine precisely the material properties of earth because its precise composition is unknown. The resistivity of earth depends on its composition; in the case of soil it can range between $\rho = 10^{-1} \div 10^2\ \Omega$m; resistivity of clay is $\rho = 10 \div 10^2\ \Omega$m and resistivity of sand is $\rho = 10^2 \div 10^5\ \Omega$m. A gravel subgrade will also have higher resistivity – in the range of $\rho = 10^2 \div 10^5\ \Omega$m. The Comsol program requires entering of data by means of electric conductivity; resistivity was therefore converted to conductivity. In the present case the values for the earth were selected in the following way: compacted antifreeze material $\mu_r = 1$, $\sigma = 0.1$ S/m, hard surface $\mu_r = 1$, $\sigma = 0.001$ S/m.

C. Entering the Conditions

The conditions were entered in the following way: the condition of the electric potential $\varphi = 1\,000$ V was set for the upper surface of the rail. The electric potential value is the highest presumed value which can occur on the rail. The condition of a zero electric potential $\varphi = 0$ V was entered on the bottom side of the model. Other external boundaries were assigned the condition of electric insulation $\boldsymbol{n} \times \boldsymbol{J} = 0$.

D. Covering the Model with a Network

After the boundary conditions have been set, the model is prepared for generating a network in whose nodes the needed partial differential equations were calculated. The parameters for dividing the network can be set manually on the individual volumes, surfaces or lines. Furthermore, it is also possible to set the density of the network. The denser the network is, the more nodal points there are and the higher the number of the partial differential equations is. However, the calculation becomes more difficult at the same time. In our case a fine division corresponding to the number of approx. 750 000 nodal points was sufficient. As Figure 2 shows, the program makes the network intuitively denser in the smaller areas.

A stationary linear solver was used for the solution.

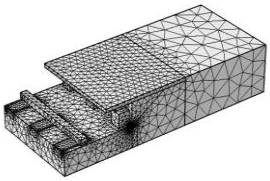

Fig. 2. The model covered with a network

E. Simulation Results

As was already stated above, the results are calculated in two models.

First, the model which simulates a fault-free state will be considered. This means the state in which the rail is connected with the gabion through the lightning arrester.

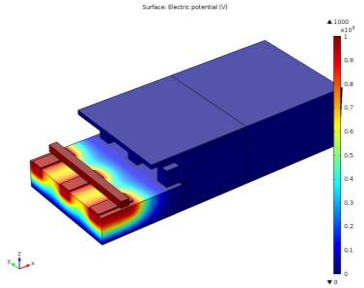

Fig. 3. Distribution of the electric potential, a fault-free state

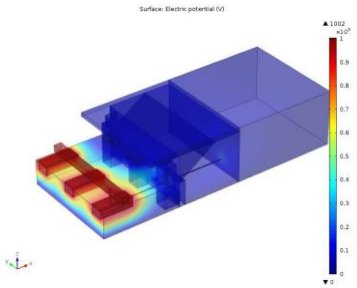

Fig. 4. Distribution of the electric potential, a faulty state

The maximum value of the electric potential is again 1,000 V in the rail. (Fig. 4) The other values, however, are now significantly higher than in the case of the fault-free state. In the platform the value of the electric potential is approx. 40 V. In the concrete foundations the potential reaches the values of approx. 60 V and the value of the electric potential in the gabion is about 20 V.

The maximum value of the current density is again present in the rail. In the concrete foundations, in the part which is under the level of the ground, the current density is dependent on the

proximity of the conductor which passes between the second and third concrete foundations. Its value is, therefore, in the range from approx. 500 A/m^2, in the case of the most distant concrete foundation, up to 2 000 A/m^2, which is the value in the third concrete foundation. In the level above the ground the current density reaches values from 100 A/m^2 to 450 A/m^2. The current density value in the platform is the highest in the places between the second and the third concrete foundations; there the value is 145 A/m^2. In contrast to the fault-free state the current density in the gabion also increases, to the value of approx. 1.5 A/m^2.

4 Conclusion

The aim was to prove if current density and consequently a stray current pass through concrete foundations. And if yes, what values they reach. This simulation was calculated with the maximum value of the electric potential on the rail, for example, during the passage of a train. The resulting values give an idea about the distribution of the current density and therefore about the passage of the current inside the concrete foundations and also in the earth under the platform. The simulated results confirm the supposition that the higher the value of the electric potential is, the higher the value of the normal current density is.

As the models given above show, a stray current passes from the rail to the concrete sleeper and enters the earth. Then it passes through the vertical concrete foundations. A part of the current flows directly in the earth, while another part of the current flows through the surface of the platform and the gabion into the earth.

In the case of a fault-free state the current density values are very low and in some parts even negligible. However, despite this fact the current density value in the concrete foundations under the surface of the ground is approximately 150 A/m^2. This certainly does not have a positive effect on the ageing of the concrete and there may occur degradation of the concrete in these places. Nevertheless, a much worse case occurs if there is a breakdown of the lightning arrester. In comparison with the fault-free state the current density values are very high in this case. The current density value in the platform increases by about 5 times. If the worst case is considered, the current density value in the concrete foundations increases by approximately 13 times, which represents a really very high value.

As can be seen, this fact has an adverse effect on the concrete sleepers under the rail and also on the concrete foundations of the platform. One of the possible consequences of these stray currents is that their occurrence may cause degradation of the concrete and subsequently its cracking.

The illustrative figure above shows how a stray current disrupts the concrete foundations in the vicinity of the railway substructure.

5 Bibliography

[1] J. Paleček, Selected Chapters from Electrical Engineering Problems in Transportation Engineering university textbook, VŠB-TU Ostrava 1996

[2] L. Ivánek, Models and Transfer Parameters for Propagation of Reverse Currents in Electric Traction post-doctoral thesis, Ostrava 1998

[3] ČSN EN 50122-2 Railway applications – Fixed installations - Part 2: Protective provisions against the effects of stray currents caused by DC traction systems as amended

[4] Promotion material from the company Humusoft

Geomagnetic Storms Effects on Power Transformers

Jan Fulneček

Department of Electrical Power Engineering, FEECS,
VŠB – Technical University of Ostrava, 17. listopadu 15, 708 33 Ostrava – Poruba
jan.fulnecek@vsb.cz

Abstract. This thesis deals with geomagnetic storms effects on power transmission lines. In the first part, basic principle of space weather and its influence on the geomagnetic field is explained. The second part describes a situation of geomagnetic induced currents in the Czech Republic. The third part describes a model of a transformer, created in ATP software, and its verification.

Keywords: Space Weather, Geomagnetic Induced Currents, Power Transformer, EMTP ATP, DST

1 Space weather and geomagnetic induced currents

The Sun emits a flow of particles called the solar wind. The solar wind interacts with the Earth's magnetic field and causes its variations in time. Flux lines of the magnetic field near the Earth's surface oscillate in a rhythm of the Sun activity. A frequency of these oscillations is very low, below 1 Hz (1).

There are several possible ways of describing the magnetic field activity, one of the most common is using a DST index. In its basic principle, DST represents a time derivation of a horizontal magnetic field intensity BH.

$$DST = \frac{dB_H}{dt} \tag{1}$$

In fact, the DST calculation is much more complicated. Data from several ground observatories must be taken into account for the reference field calculation (2).

1.1 Effects on power grids

Because of a TN - C system, each phase of the transmission line acts as a conductive loop. According to Faraday's law, current is induced during magnetic field changes. This is called geomagnetic induced current (GIC).

© M. Krátký, J. Dvorský, P. Moravec (Eds.): WOFEX 2015, pp. 12–17.
VŠB – Technical University of Ostrava, FEECS, 2015, ISBN 978-80-248-3787-1.

$$\oint_l \vec{E} \cdot d\vec{l} = -\frac{d}{dt} \cdot \int_S \vec{B} \cdot d\vec{S}$$

$$I_{GIC} = \frac{d\vec{B} \cdot \vec{S}}{dt \cdot R} \qquad (2)$$

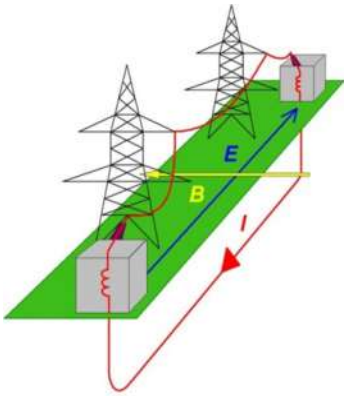

Fig. 1. Power line as a conductive loop

A frequency of the induced current is low, so it behaves like a direct current - easily passes through a transformer winding. A DC bias in the grid leads to a half cycle saturation of transformer's magnetic core (3).

2 Situation in the Czech Republic

Despite the density of electric power lines in our country, the Czech Republic seems to be unaffected by this phenomenon. There might be several reasons for this:

- The Earth's magnetic field poles, where the magnetic disturbances are most significant, are far away (North pole around 4500 km)
- The soil conductivity reaches high values on most of the territory in our country (4)
- The Czech transmission lines are not extremely long

The transmission power lines in the Czech Republic are operated by the ČEPS company. Since 2006, monthly company reports are available from (5). These reports were used to create a database containing transmission power lines faults between 2006 and 2014. It contains 401 faults, but 129 of them cannot be related with the solar activity (faults caused by human factor or mechanical conditions). This is why only 272 of them were used for regression.

Each single fault was associated with its DST value for further regression. The DST index database is available online from (6). The observed time period is situated in the end of the 23rd and the start of the 24th solar cycle. These are usually relatively quiet part of the cycles (7), so no strong geomagnetic storm was registered.

Table 1. Duration of geomagnetic stroms

DST value	Storm classification	Summary duration (h)
-50 nT to -100 nT	Weak	1102
-100 nT to -250 nT	Moderate	79
< -250 nT	Strong	0

Unfortunately, eight years is very short time to consider any consequences of the solar activity. At this time, the most suitable regression model of this database reaches an R squared value only 13,3%, so it cannot be trusted.

3 GIC effects on power transformers

The half cycle saturation, caused by GIC, has several negative effects on power transformers. The harmonic distortion is increased. The work point in a nonlinear part of a magnetization curve causes a sine wave distortion (3). The core loss and the magnetic stray flux is increased. To cover the loss, reactive power consumption is increased. This leads to additional voltage drops on a power line. The magnetic flux encloses inside transformer's tank and other construction elements instead in a core (3).

3.1 ATP model of transformer

There are several ways of model a transformer in ATP software. For this purpose, a saturable model was used. It is a model of a shell type single phase transformer with two windings, which takes core saturation into account.

Table 2. Transformer's parameters

I_0 (A)	ΔP_0 (W)	u_k (V)	ΔP_K (W)	n_p	n_s	P (W)	U_p (V)	I_p (A)	U_s (V)	I_s (A)
0,13	6,4	20	39,8	450	225	440	220	2	110	4

Where P is output power, U_p primary voltage, I_p primary current, U_s secondary voltage, I_s secondary current, I_0 is excitation current, ΔP_0 excitation losses, u_K short circuit voltage, ΔP_K short circuit losses, n_p number of primary turns, n_s number of secondary turns

3.2 Parameters estimation

Calculation of input parameters is described in an ATP manual (8)

Table 3. Input parametrs

F_0 (Wb)	R_{MAG} (Ω)	R_P (Ω)	L_P (mH)	R_S (Ω)	L_S (mH)
0,0025	7563	19,9	6,3	5	1,6

Where F_0 is magnetic flux, R_{MAG} resistance of magnetic branch, R_P leakage resistance of primary winding, R_S leakage resistance of secondary winding, L_P leakage inductance of primary winding, L_S leakage inductance of secondary winding.

To express a nonlinearity of the transformer, the voltage/current curve was entered into the model.

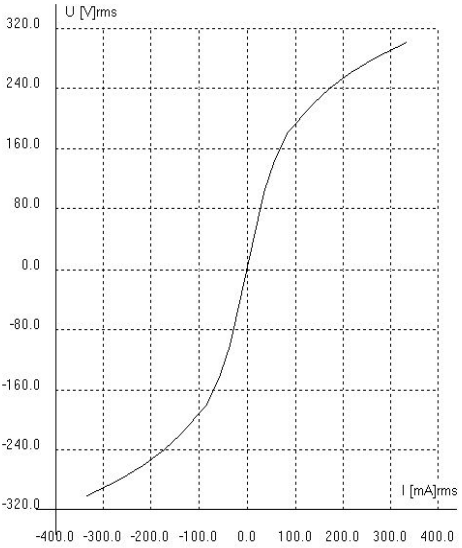

Fig. 2. Voltage – current characteristics

3.3 Model verification

For the model verification several measurements were done to compare the real transformer with its ATP model. This model is accurate if there is no DC offset present.

An AC power source with a DC offset was created to saturate the transformer. The AC source (regulated transformer) is connected through a condensator, which protects the source against the DC offset. The DC source is connected through a diode, which protects the source against negative half waves of the AC source (it could damage it). The nonlinearity of the diode is not considered in the model, only its initiation vol-

tage. Voltage drops on three resistors were measured with an oscilloscope for calculations of currents. The transformer was in a no-load configuration.

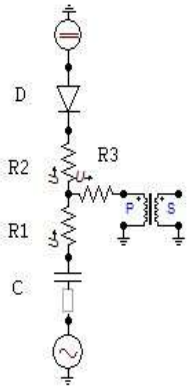

Fig. 3. Circuit diagram for model verification

Table 4. Circuit configuration

R_1 (Ω)	R_2 (Ω)	R_3 (Ω)	C (μF)	U_D (V)	U_{AC} (V)	U_{DC} (V)
100	100	50	46,5	0,6	130	3

During the presence of the DC offset, there is a significant difference between simulated and measured values of the current flowing through the transformer primary winding. Measured values are higher than simulated ones.

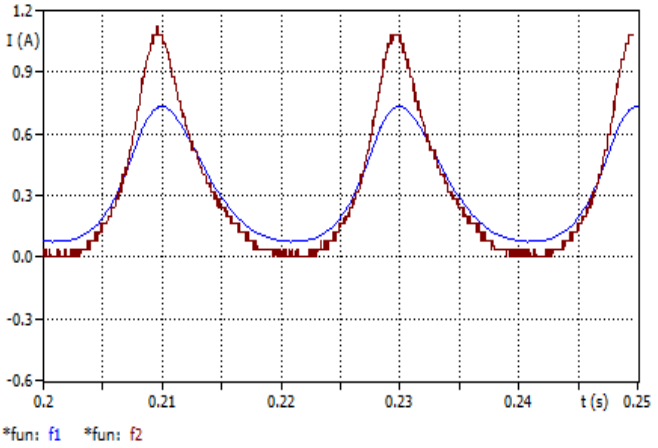

Fig. 4. Measured (red) and simulated (blue) values with the DC offset

This difference is probably caused by eddy currents inside construction elements of the transformer. As mentioned before, the magnetic stray flux is increased during the half cycle saturation. The eddy currents are induced into conductive objects in the space surrounding the transformer, acting as transformer's load.

To compensate this effect, a non-linear load should be connected into the secondary winding of the model. The calculation of such impedance is complicated and cannot be done without magnetic stray flux simulations. Another disadvantage is that the secondary winding is lost for any other purposes.

4 Conclusion

The geomagnetic storms have not caused any serious troubles in the Czech Republic yet. For proper research several power lines in our country should be equipped with direct current loggers and magnetometers. Even after that, it will be very difficult to get any credible data due to irregularity of this phenomenon.

The ATP software does not include any transformer model, which considers the eddy currents inside the construction elements. This might be a problem for oil transformer models especially, where the eddy currents in the tank are significant. The only way to compensate these currents in a model is to add a non-linear impedance as transformer's load.

5 Publications

Space Weather Effects on Power Grids. In: Proceedings of the 2015 17th International Scientific Conference on Electric Power Engineering (EPE).

6 Reference

1. D. MCMORROW. Impacts of Severe Space Weather on the Electric Grid. In: *Federation Of American Scientists* [online]. 2011 [cit. 2014-11-10]. Aviable from: https://fas.org/irp/agency/dod/jason/spaceweather.pdf
2. UNIVERSITY OF KYOTO. *World data center for geomagnetism* [online]. 2015 [cit. 2015-07-09]. Available from : http://wdc.kugi.kyoto-u.ac.jp/dstdir/dst2/onDstindex.html
3. V. BOTHMER, A. DAGALIS. *Space weather: physics and effects*. 2nd ed. Berlin Heidelberg: Springer Business Media, 2007. ISBN 978-364-2174-155.
4. Czech Geological Survey. *Zhodnocení účinků Goteborského protokolu na acidifikované a eutrofizované vody a půdy* [online]. [cit. 2015-01-18]. Available from: http://www.geology.cz/project666400/uvod/vysledky_potoky_vzorky/vysledky_potoky_vodivost
5. ČEPS. *Měsíční hodocení provozu PS* [online]. 2015 [cit. 2015-07-09]. Available from : https://www.ceps.cz/CZE/Cinnosti/Dispecerske_rizeni/Hodnoceni_provozu/Mesicni_hodnoceni_provozu/Stranky/default.aspx
6. UNIVERSITY OF KYOTO. *World data center for geomagnetism* [online]. 2015 [cit. 2015-07-09]. Available from : http://wdc.kugi.kyoto-u.ac.jp/dstae/index.html
7. M. ANDERSON. *Astronomica: galaxie, planety, hvězdy, mapy souhvězdí, výzkum vesmíru*. Editor F Watson. Prague: Slovart, 2009, 576 s. ISBN 978-80-7391-256-7.
8. *ATP Rulebook*. 1992 [cit. 2015-08-01].

Statistical Evaluation of Measured Values from Photovoltaic Plant Using LabVIEW Software

Martin Gruss and Daniel Minařík

Department of Electrical Power Engineering, FEECS,
VŠB – Technical University of Ostrava, 17. listopadu 15, 708 33 Ostrava – Poruba
martin.gruss@vsb.cz

Abstract. This paper deals with statistical evaluation of measured values from photovoltaic plant. Input data contains voltage, current, power and frequency values measured in a real photovoltaic plant situated in the Technological Centre Ostrava. For data processing, program was created in LabVIEW. First, the input data used for the graphic representation of measured values during the observed period. Next, statistical evaluation of measured values using standard static methods, as the plot histograms, box diagrams, calculation of probability and descriptive statistics, was performed.

Keywords: LabVIEW, statistical evaluation, block diagram, histogram

1 Introduction

LabVIEW is a highly productive graphical development environment for creating custom applications that interact with real-world data or signals in fields such as science and engineering. LabVIEW contains libraries of functions and development tools designed specifically for data capturing and control equipment. Programs, created in LabVIEW are called Virtual instruments (VIs), because their appearance and function resemble real instruments. VIs consist of an interactive user interface, data diagram and icons/connections. User interface (Front panel) includes knobs, buttons, graphs and other control and indicator elements. Subsequently, the data diagram representing the source code is drawn. Program does not run sequentially, the calculation is controlled by data flow. Block starts calculation at the time when the data are on all inputs, after processing sends the results to all outputs. Processes of each block thus run in parallel.

2 Exploratory analysis of measured values

This part of data processing is called exploratory (descriptive) statistics and is the first step to reveal information hidden in a large number of variables and their variants. Histograms of individual variables were created from measured values, identified

© M. Krátký, J. Dvorský, P. Moravec (Eds.): WOFEX 2015, pp. 18–23.
VŠB – Technical University of Ostrava, FEECS, 2015, ISBN 978-80-248-3787-1.

their basic statistical characteristics. (mean value, median, mode, standard deviation, variance, kurtosis, skewness, lower extreme, upper extreme and lower and upper quartile) and also created box plots.

The mean value is defined as the sum of all values of the random variable, divided by their quantity. Mode is defined as the most numerous variant variables. Median divides a data file so that half (50%) values are smaller than the median, and half (50%) values larger (or equal). Lower quartile divides the data file so that 25% of the values are smaller than the quartile and the rest, ie. 75% larger (or equal to). Upper quartile divides data file so that 75% of the values are smaller than the quartile and the rest, ie. 25% larger (or equal to). Variance, Skewness and Kurtosis belong among the so-called rates of variability of file, which determinate, how much the values differ from the average. Variance or even mean-square deviation expresses variability of distribution of file random variables around its mean value. Skewness measures the direction and degree of symmetry (or asymmetry) of distribution of variable. Positive value (or right-sided skewness) means, that average is greater than the median, which means that most of the values in the file has lower values than the average. If the skewness is equal to zero, it means that the distribution is symmetrical and therefore the average and median of the file are equal to each other. Kurtosis expresses the density of values around its average.

3 Statistical analysis functions in LabVIEW

NI LabVIEW software includes an extensive probability and statistics library where we can perform probability, descriptive statistics, analysis of variance, and interpolation functions. LabVIEW provides many virtual instruments (VI) for several types of statistical analyses, such as mean, median, mode and standard deviation. These numerical statistics involve straightforward computation, making them the basis for traditional statistical analysis. LabVIEW also has a powerful means of displaying data. For example, you can use LabVIEW to construct run sequence plots, scatter plots, boxplots, histograms and normal probability plots.

There are no specific VIs for calculating the Kurtosis and skewness, but you can easily calculate both using the following equation for the moment about the mean:

$$\sigma_x^m = \frac{1}{n}\sum_{i=0}^{n-1}\left(x_i - x\right)^{-m} \tag{1}$$

where, n is the number of elements in X and x-bar is the mean of X.

The Kurtosis is defined as a measure of peakedness and corresponds to the fourth-order (4th) moment. The skewness is defined as a measure of symmetry and corresponds to the third-order (3rd) moment. A box plot consists of rectangles and lines and shows the median of the data, the upper and lower quartiles, and any data points that possibly are outside values. The rectangle represents where the center 50% of the data points lie. The horizontal line in the center rectangle represents the median of the

data set. The long vertical lines are called whiskers. Whiskers have a length of 1.5 times the inner quartile spread, which is the difference between the upper quartile and the lower quartile. The upper and lower quartiles of the data set determine the size and location of this box. An X indicates a potential outlier, which is outside the range of the whiskers.

4 Statistical evaluation of measured values using LabVIEW software

Measuring of the input values to the program LabVIEW was carried out on photovoltaic system, which is installed on the roof of the technological center. The measured values were obtained from the period of 1.6.2015 to 14.6.2015. Data were recorded in six minutes intervals during all measurement time. Statistical analysis was performed on the section wits 30 panels with power of 210 Wp. Total range of input data is 2228 lines. On Fig. 1 is created application for evaluation of statistic analysis of measured data from photovoltaic power station.

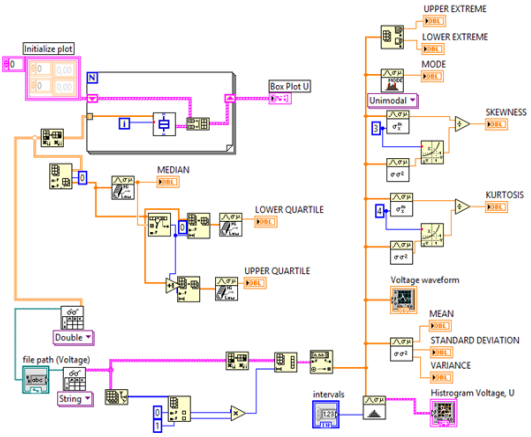

Fig. 1. Block diagram from LabVIEW environment for evaluation of static analysis

The first step is to retrieve the measured values via block Read From Spreadsheet File.vi, which reads from text file in format suitable for importing into a spreadsheet. Data are data type String with which you can not make calculations and so it is necessary to change the data type. To convert a string to data type „double" with which all computational blocks work, we will use block „Fract/Exp String To Number". On the input of block „String" we will bring chain and on the output of number we will receive measured value in numerical form, with which we can perform calculations. Data type, however, are 2-D array, therefore we will use block Transpose 2D a Index Array Function. Transpose 2D rearranges the elements of 2D array such that 2D array[i,j] becomes transposed array[j,i]. Returns the element or subarray of n-dimension array at index. On a pallet Mathematics Vis are located blocks Probability and Statis-

tics. Probability and Statistics VIs are used to perform probability, descriptive statistics, analysis of variance, and interpolation functions. Here are blocks for plotting of histograms and calculation of basic statistical characteristics, see Fig. 2.

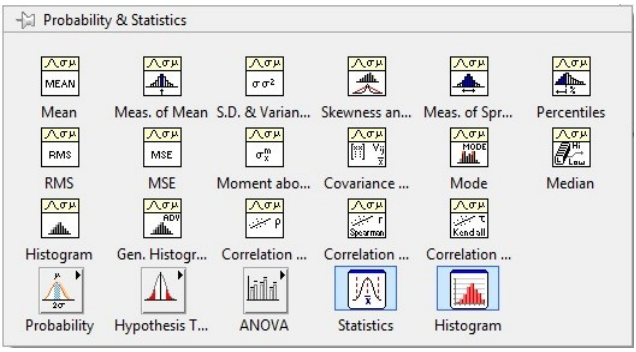

Fig. 2. Probability and Statistics VIs in LabVIEW

Following graphs show voltage, current, frequency and power waveform on AC side of converters. The waveforms of voltage and frequency show that converter connected to supply network must continually adapt to changing conditions. Photovoltaic power plant operates on the principle of direct conversion of sunlight into electrical energy. Variation of active power in solar power station is caused by change intensity of solar radiation. The intensity of solar radiation varies during the day and during the seasons. An important factor that affects the power of solar power station, is rotation of solar cells, the influence of cloudiness, panels pollution by dust or shading caused by snow. These sources provide low shot-circuit resistance.

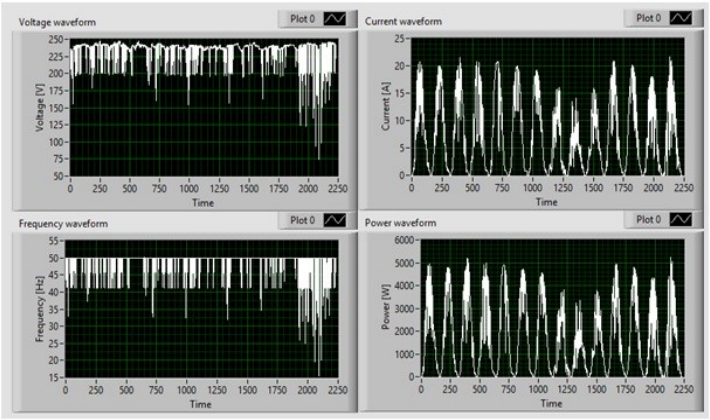

Fig. 3. Waveforms for voltage, current, frequency and power generated using application in LabVIEW

Histogram gives us quick visual information about selective distribution of frequency, see Fig. 3. For creation of histogram it is needed to divide measured values into the

appropriate intervals. There are many ways how to determinate there intervals. One of the alternatives in called Sturges rule.

$$k = 1 + 3{,}322 \cdot \log(n) = 1 + 3{,}322 \cdot \log(2228) = 12{,}12 \tag{2}$$

where n is total number of samples

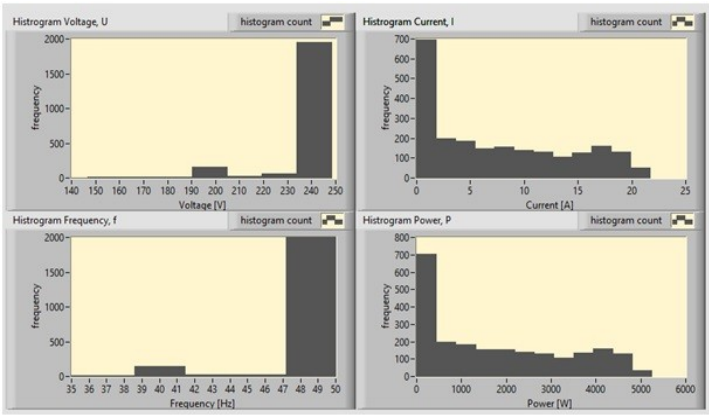

Fig. 4. Histograms of measured values

It is clearly seen that for the voltage is most frequent value of 240V. The average value of 2228 samples is 234,8V. The histogram of frequency shows instability of network frequency 50 Hz. The lowest value reacher 15,6 Hz, while modus is 49,87 Hz. From measured values of voltage, current, frequency and electrical power were determined statistical characteristics using Statistical Analysis Functions in LabVIEW, see Table 1.

Table 1. Results from LabVIEW

Statistical characteristics	Voltage [V]	Current [A]	Frequency [Hz]	Power [W]
Mean value	234,82	7,45	48,93	1775,27
Median	239,00	5,89	49,97	1400,50
Mode	240,17	0,11	49,87	26,24
Standard deviation	15,62	6,56	3,32	1570,63
Variance	243,83	43,01	10,99	2466889,5
Kurtosis	20,61	-1,13	20,32	-1,14
Skewness	-3,92	0,50	-4,00	0,50
Lower quartile	233,00	1,16	49,95	269,00
Upper quartile	239,00	5,89	49,97	1400,50

Kurtosis of current and power is negative, their distribution is therefore in all cases flat. Skewness of voltage and frequency is also negative, thus prevail values larger than average, Skewness of current and power is however positive, thus here prevail values lower than average. In all cases, the condition of normality of data is not met. In order for data to be considered as normal, Kurtosis and Skewness must be near zero. In this case we are dealing with unknown distribution of probability. In Fig. 5 for voltage and frequency obvious outlying observation. This outlying observation might be due to measurement error or any defect.

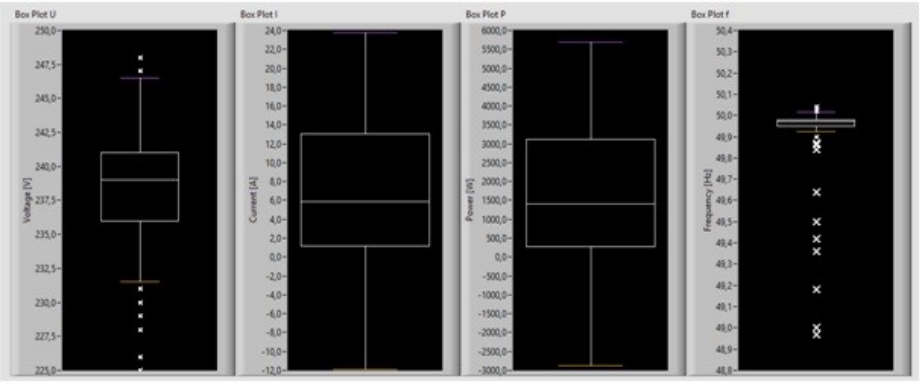

Fig. 5. Box graphs describing voltage, current, power and frequency balance

5 Conclusion

The result of test is that half of measured data, median of current and voltage, has a values lower than 5,89A and 1400,5W. We can conclude, that Skewness of data is positively slanted because average value is greater than median (absolute majority of the data is less than 7,45A and 1775,3W). Since the average values for current and power are greater than median and median is greater than modus, there is asymmetry of examined values. Negative Kurtosis of current and power indicates that the distribution is more even and the density curve is flatter. The frequency histogram shows instability of mains frequency of 50Hz. The lowest value reached 15,6Hz. These outages of photovoltaic power plant can be caused due to environmental influences or operation and maintenance.

References

[1] ŽÍDEK, J. *Grafické programování ve vývojovém prostředí LabVIEW*. Ostrava: VŠB-TUO, 2002.

[2] BRIŠ, R., LITSCHMANNOVÁ, M., *Statistics I*. subject syllabus 2004

[3] NATIONAL INSTRUMENTS CORPORATION, [online], [cit. 2015-08-04]. Available online at http://www.ni.com/

New Results of the Restoration Methodology in 2015

Vít Houdek

Department of Electrical Power Engineering, FEECS,
VŠB – Technical University of Ostrava, 17. listopadu 15, 708 33 Ostrava – Poruba
vit.houdek@centrum.cz

Abstract. This paper focuses on restoration methodology for 110 kV power lines. The methodology is based on reliability centered maintenance. The methodology uses distributed power, effect of failure and database of faults to determine technical condition and importance of line. This input data is typically collected in the operation of the distribution network. Functional application is used to determine the results and analysis. The paper shows new results for 2015.

Keywords: Power line, RCM, reliability, technical condition, importance of line, restoration priority

1 Introduction

Maintenance of equipment in distribution networks ensures safe and reliable supply of electric power. Hence, maintenance is an important part of the distribution network operation. Performance of maintenance actions is controlled by the Preventive Maintenance Guide (ŘPÚ). Preventive maintenance refers to maintenance within set time intervals for each piece of equipment within the distribution network. The Preventive Maintenance Guide stipulates deadlines, procedures and rules obeyed by the distribution network operator.

The modern trend is outlined by the Reliability Centered Maintenance (RCM). The Reliability Centered Maintenance is the type of maintenance dependent on the technical condition and importance of the particular equipment. Time intervals of the RCM are therefore different even for the same equipment. The RCM helps optimise and improve the effectiveness of maintenance within the distribution network. The input data represents a vital part of the Reliability Centered Maintenance. The data can be obtained from operation of the distribution network and it forms a part of regular details of network operation nowadays.

Another option to utilize the principle of RCM is to create a restoration scheme for the particular equipment within the distribution network. This scheme applies to operation of the particular equipment, not the service life period. This is the principle of methodology for restoration of the 110 kV power line. The methodology makes use of essential data collected in operation of distribution networks and defines the overall order of maintenance sections for the restoration scheme purposes.

© M. Krátký, J. Dvorský, P. Moravec (Eds.): WOFEX 2015, pp. 24–29.
VŠB – Technical University of Ostrava, FEECS, 2015, ISBN 978-80-248-3787-1.

2 Restoration methodology for 110 kV power lines

The power line Restoration Scheme represents an outcome from this methodology. The power line Restoration Scheme comprises an orderly list of maintenance sections depending on the restoration priority *PO*. The restoration priority can be calculated using the formula (1). The restoration priority is a relative value between 0 and 100 %. The higher the restoration priority value the higher the rank of the particular section in the list should be. Frankly speaking, the higher the value of *PO*, the sooner the maintenance should be performed.

$$PO = (100 - TS)\cdot(1 - k_{\mathrm{TSDV}}) + DV\cdot k_{\mathrm{TSDV}} \quad (1)$$

Looking at the formula (1), *TS* refers to the technical condition of the maintenance section, *DV* refers to the specific power line importance. The k_{TSDV} coefficient serves for division of the technical condition *TS* and the power line importance *DV* to produce the resultant priority value. If the coefficient equals 0.5, the resultant value shall be split between *TS* and *DV* evenly. If the value is below 0.5, priority will be given to the technical condition and vice versa.

2.1 Technical condition

Employment of methodology requires details of technical condition of each maintenance section. The 110 kV power line Database of Faults has proven itself as the most convenient tool to determine the technical condition. The most important data are priority of fault, quantity.

The priority of fault defines the maximum deadline for remedy. The fault priority then describes the severity of particular fault that occurs. That is the reason to use this value for evaluation of technical condition of maintenance section. Designation of priority is expressed both words as well as a (numeric) code. There are currently four different types of faults: 1-Urgent, 3-Month, 4-Year, 5-Control at ŘPÚ.

The quantity value serves a specifying parameter to determine the technical condition. It does not refer the total number of faults within a single maintenance section, yet rather the total number of fault of particular type detected during a single check. The number of defective insulators can be an example.

The worst problem with the quantity item is that some values are quoted in meters, while the other would be defined in pieces. A unit of quantity depends on the object (exported from the database), where the fault developed. Any fault on the grounding line or a line will be always defined as the length of the affected sections in meters. Any other parts of the 110 kV power line (supporting point, bracket) are recorded defined as the number of pieces of the specific equipment. This problem is addressed by means of classification. There are three categories in total.

Determination of the technical condition *TS* requires details of fault per specific maintenance section depending on the fault priority and the quantity category. The technical condition is determined in two steps. The first step deals with establishment

of the technical condition points BTS. Technical condition points can be calculated using the formula (2):

$$BTS = \sum VP_x \cdot \sum (p_{M1x} + k_2 \cdot p_{M2x} + k_3 \cdot p_{M3x}) \quad (2)$$

where VP_x refers to the weight of the particular priority. The variable p_{M1x} refers to the number of fault per quantity category 1 and the particular priority x, p_{M2x} and p_{M3x} refer to numbers for higher quantity categories. Coefficients k_2 and k_3 increase the *BTS* with respect to a higher quantity category.
The second step comprises determination of the technical condition TS using the technical condition points BTS. This process is performed using the Table 1.

Table 1. BTS limits

BTS limits						
50	100	150	250	350	500	>500
Technical condition *TS*						
95%	80%	70%	60%	50%	40%	30%

2.2 Importance of line

Power line importance DV has two input parameters. One of them is the distributed energy through the power line in a year. The other one is the effect of failure. Unlike the technical condition TS, the power line importance DV is determined for the entire power line.
The value of distributed power is obtained from measurements recorded during operation of the distribution network. Determination of importance does not require the exact value of distributed power, a reference value can be used instead. That is why each 110 kV power line is assigned with the relevant category, similar to the technical condition points (Table 2). The interval threshold limit per category is then defined by values of limits applicable to the distributed energy plotted in the table.

Table 2. Distributed power categorization

Energy (GWh)	50	100	200	300	400	>400
Category	1	2	3	4	5	6

The effect of power line failure is another input parameter of the power line importance. The effect of failure is a general indication of steps required within the power line in case of failure. It may be described as a certain method of power line backup. Backup schemes are in place for operation of the distribution network to cater for outage of individual power lines. These also define the consequence of power line

outage. The results of outage recorded therefore indicate the backup methods for distribution network operation. There are seven different types of effects:

- 1 – " No effect"– no manipulation necessary,
- 2 – Back-up by 110 kV line of approx. the same length,
- 3 – Back-up by 110 kV line of approx. the same length with limited power,
- 4 – Back-up by a longer 110 kV line,
- 5 – Back-up by a longer 110 kV line - limited power,
- 6 – Back-up by MV line,
- 7 – Back-up by MV line – limited power.

The effect of failure 1 is basically a hot backup, i.e. a backup without the need for any handling within the distribution network. Other backup types always require handling operations. Back-ups marked "limited power" are not able to transmit full power, as before an outage.
The power line importance matrix (Table 3) is employed for determination of power line importance. Both input parameters - the distributed power and effect of failure - are placed in categories. That is why the power line importance can be determined using the matrix.

Table 3. Matrix of importance

MATRIX Importance of line		Distributed power					
		1	2	3	4	5	6
Effect of failure	1	0%	2%	3%	5%	6%	8%
	2	3%	5%	8%	11%	14%	16%
	3	9%	14%	18%	23%	28%	36%
	4	5%	7%	10%	13%	16%	20%
	5	15%	21%	27%	36%	42%	48%
	6	12%	15%	18%	22%	26%	34%
	7	19%	26%	32%	41%	51%	60%

3 Results of restoration methodology

The purpose of development and tune-up of the restoration methodology for 110 kV power line was served by the data sourced from one distribution area in the Czech Republic. Determination of the technical condition is made according to the Database of Faults for the period from August 2009 until the end of the year 2014. Those are records of failures for 66 months of operation. There are 3 312 entries in total (Table 4). Older records were omitted with respect to the development of the whole database system. The database development is still in progress.
The distributed energy has been calculated using the data from the year 2010. There are 168 power lines within the distribution area. The change of infrastructure resulted

in modification of the relevant category of distributed power. The same distribution area was covered a list of power lines with effect of. The list was altered with respect to changes in the distribution network infrastructure.

Table 4. Count of faults per priority

Priority	1-Urgent	3-Month	4-Year	5-Control at ŘPÚ
Count	174	212	2365	561

The calculation itself was also preceded by a statistical evaluation of essential input parameters. Table 4 shows an example of the count of faults depending on the priority of fault. This is an evident indication that most faults need to be removed within a year. There are also signs of gradual changes in the fault evaluation methodology.
Another evaluation may concern the count of power lines depending on the effect of failure (Table 5). The table clearly shows the category 1 effect of failure for more than a half of power lines. Power reductions due to power line outage will occur at two power lines only.

Table 5. Count of power lines per effect of failure

Effect of Failure	Count (-)	Count (%)
1	94	56%
2	51	30%
3	1	1%
4	12	7%
5	1	1%
6	9	5%
7	0	0%

The results obtained by calculation helps us set the order of individual maintenance sections. As there is more data about technical condition available, the *TS* can be considered more informative, that is the reason for its slight preference. The distribution coefficient for determination of the restoration scheme k_{TSDV} has been set to 0.4. The Table 6 shows outcome of distribution for three coefficients k_{TSDV} for comparison purposes. The resultant best restoration priority value is 6.8 %, the worst one is 56.4 %.
The coefficient k_{TSDV} serves for better distribution into the individual groups monitored. The group highlighted in green (restoration priority value up to 15%) marks sections that do not require restoration. The group between 16 and 30 % (yellow) comprises sections that should be rather monitored during regular inspections. The red band marks sections that require restoration. That shall apply primarily to the last part (47 sections) of the red band, the restoration of maintenance sections should be launched here as soon as possible, and the restoration priority exceeds 50 %. Most of these sections were identified with a greater number of even serious faults.

Table 6. Results of the restoration priority distribution

Restoration Priority	Coefficient k_{TSDV}		
	0,4	0,5	0,6
5%	0	0	0
10%	61	36	36
15%	16	60	60
20%	48	52	53
30%	67	86	105
40%	69	56	49
> 50%	47	18	5

4 Conclusion

The first part of this paper describes the actual version for restoration methodology for the 110 kV power line. The main advantages of this methodology include simplicity, the option to utilize the existing measurements and records within the distribution network. There is no need to implement any new measurements or records.
The total of restoration priority values calculated then equaled to 308. These results were used to develop the restoration scheme for the specific distribution area. The Table 6 shows numbers of individual maintenance sections ordered by restoration priority values. The maintenance sections can be generally divided into 3 groups: Status OK, Vigilance and Restoration. These groups are highlighted in green, yellow and red in the table.
ACKNOWLEDGEMENTS
Work was partially supported by SGS grant VŠB-TU Ostrava No. SP2015/192.
The results of the thesis are published in:

- conference CIRED 2014, Tábor, ISBN 978-80-905014-3-0
- conference EPE 2015, Dlouhé Stráně, ISBN 978-1-4673-6787-5

5 References

1. M. Kolcun, J. Szkutnik: The methodology for optimization of energy distribution network, Journal of Electrical Engineering. ISSN 1582-4594.
2. M. Abbasghorbani, H.R. Mashhadi, Y.Damchi: Reliability-centred maintenance for circuit breakers in transmission networks, IET Generation, Transmission & Distribution. ISSN 1751-8695
3. V. Houdek, S. Rusek, R. Goňo: Stages of development of 110 kV power lines restoration method. EPE 2014. ISBN 978-1-4799-3806-3.

Analysis of Measuring the Thermal Part of the Biogas Plant

Jiří Janša

Department of Electrical Power Engineering, FEECS,
VŠB – Technical University of Ostrava, 17. listopadu 15, 708 33 Ostrava – Poruba
jiri.jansa.st@vsb.cz

Abstract. This article deals with the evaluation of measurement to a specific biogas plant. The introduction describes itself biogas plant at which the measurement was carried out, which is discussed in more detail next section. Heat readings are performed on heated buildings. We only know the amount of recovered heat, but not produced. Therefore, measurement has been performed the flow of heating water quantity to CHP. From the calculated approximate value of thermal energy produced. It was also used a known ratio between heat and electricity cogeneration unit and a known amount of electricity produced. It was then evaluated the amount of heat produced and utilized in different months. This article is part of a long-term comprehensive research of biogas plants.

Keywords: biogas plant, biogas, thermal part, measurement, cogeneration, cogeneraion units

© M. Krátký, J. Dvorský, P. Moravec (Eds.): WOFEX 2015, pp. 30–35.
VŠB – Technical University of Ostrava, FEECS, 2015, ISBN 978-80-248-3787-1.

1 Introduction

The biogas station (BGS) in which the measurement was carried out in the territory of the Moravian-Silesian Region. BGS lies within an agricultural enterprise engaged in pig and processes mainly corn silage and pig manure. The main reason for this location was a source of pig manure, which serves as a source of fluids for use wet fermentation technology. One other reason this location was the possibility of using waste heat for heating the adjacent stables, office buildings, and in the summer in a newly built afterharvest line used to dry corn. The biogas plant has an installed electric capacity in the amount of 1,090 kW and 1,080 kW thermal output. The conversion of biogas into electricity is assured by four cogeneration units. Three identical diesel unit with an output of 250 kWe and is ignition unit with an output of 340 kWe.

2 Flow measurement of heating system

In March this year was the measurement of heat flow to the BGS. Measured amount of heat which is needed both for heating the fermenter and dofermenter. Another com-Trebic thermal energy unit to adjust the quality of biogas, which is used mainly to dehumidification, therefore decreasing humidity controlled biogas. The device is first biogas is cooled to a temperature at which water vapor contained condense and are removed via the separator. The advantage of this procedure is that when dehumidification is also part of the biogas is removed some impurities. Another point of measurement was to determine the flow of the heating medium in heat pipe, which is used to heat the entire complex BPS. This caliduct provides for heating and hot water for the office building, workshop, hall and of course pigpens. From the heat pipeline it is also in the autumn taken heat for drying corn grain technology within harvest lines, but during the measurement was not used, as took place in the spring. Last and integral part of the measurement was then on individual outputs of CHP into chillers that transmit the unused heat to the environment.

Figure 1. Measurement gauges connected to measure consumption of heat flowing into the biogas processing plant

During measurement, BGS worked at full installed electric capacity ie. 1090kW. The measurements were used in these two gauges - thermocouple type "K" attached compensating cable for universal measuring instrument Ahlborn ALMEMO 2690 to determine the surface temperature measured pipe outlet and return. The second device was then ultrasonic clamp-on flow meter YOKOGAWA type US300PM with BPHG0196 type of sensor that measured the flow of heat transfer media in the distribution of heat. Clamp-on ultrasonic flowmeter has been set for each parameter measured according to duct pipes (outer diameter, wall thickness, roughness, material pipe), a heat transfer medium and medium temperature determined by calculating the heat transmission based on the measured surface temperature of the tube (measured thermocouple type " K '). They were also deducted the value of individual consumption of biogas CHP from stationary gas flow.

From the measurements we obtained drain flow mass flow rates of heat transfer media. With the help of thermocouple temperature we measured outlet and return, specific heat capacity, we have identified and searched by the type of flowing medium and the measured temperature using the software Engineering Equation Solver. These data were used to calculate the heat output, which transported the individual pipes.

Since flows into biogas CHP were on different terms than those given standard, were recalculated based on the temperature and pressure at the gas so. Normal conditions, a temperature of 0 ° C and a pressure of 101 325 Pa. Energy inputs in biogas supplied to CHP units were calculated based on recalculated flow of biogas to normal conditions and the calorific value of biogas determined by analyzing the chemical composition of biogas. Analysis of the chemical composition of biogas in the past had processed biogas plant operator. On the basis of power of biogas entering the CHP and power generation at the generator CHP was determined electrical efficiency CHP.

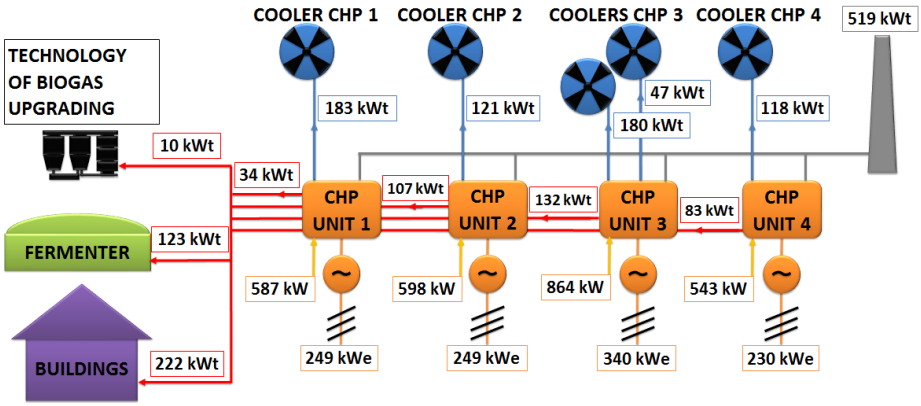

Figure 2. Review diagram of energy flows within BGS [1]

3 Thermal heat utilization

On the individual buildings hold regular monthly readings of heat consumed, we used to evaluate the amount of recovered heat. The heat is used to heat the entire agricultural complex. Namely, to heat office buildings (AB) building workshops (UOS), which is used to repair and preparation of agricultural equipment, and buildings used for agricultural production associated trailers. In these buildings, heat is used mainly in the winter months. By contrast, the large-scale pig farrowing (VKP), heat is used all year round as there used not only for heating but also for domestic hot water (DHW), which is widely used especially for sows with piglets, when designed capacity is 700 sows. To make better use of waste heat from biogas in the period of reduced heat consumption ie. The summer season was in 2014 built a large-scale post-drying type LAW SBC 9L with capacity up to 23 tons of wheat per hour. This dryer was first used in autumn 2014 for drying of grain corn.

As shown in the graph in FIG. 5, the heat is logically used in the winter months, when used for heating. In the summer, heat is used mainly for the needs of farrowing pigs and of course for their own consumption BPS. It is used only about 8% of the heat energy from biogas installed capacity of 1016 kW. In winter it is used up to 3.5 times more heat, ie. About 28%. The graphs show that the construction of grain dryers was a good choice because in two months last fall (October, November) consumes about 1.5 times the amount of heat energy than the entire remaining area BGS.

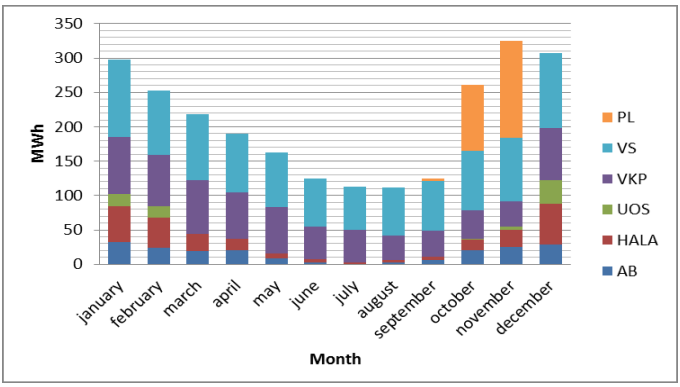

Figure 3. Individual monthly consumption figures for heat consuming devices in year 2014

The graph also shows that BPS needs for its operation a considerable amount of heat is used for heating the fermenter operating temperature. Fermenters operating temperature must be maintained because of the permanent environment for microorganisms producing biogas. Normally, the operating time ranges from 38-42 ° C. This need varies according to the outside temperature. Own heat consumption for fermenters is normally not measured and therefore it was necessary to calculate. We proceeded from the known outdoor temperature at the time of measurement of heat flow BPS. From the temperature differential between the inside and outside temperature fermentrou we determined the amount of thermal energy required for heating the fermenter by one degree Celsius. From the statistical data of the Czech Hydrometeorological [2] Constitution were detected an average monthly temperatures in the Region. Because digesters must be heated continuously over the year can determine individual monthly consumption for heating fermenters using dennostupňové methods. The number of heating days corresponding to the number of days in the respective month, the temperature inside the digester is constant throughout the year, such as external temperature appropriate considering the average outdoor temperature.

Heat consumption is in the range 7-15% of the total heat energy produced when the lower value corresponds to the summer months and higher after the winter months. It follows that the installed thermal power 1016 kW can realistically be used only about 850 kW in winter and 940 kW in the summer months. Currently, it is used about 21% of the total annual amount of thermal energy, of which about 43% self-consumption BPS, thus the share of recovered heat for other purposes is 12%, which is true legislative requirement for guaranteed purchase price for electricity use at least 10% of the heat valid for units running in the period from 1. 1. 2012 to 31. 12. 2012, when it was put into operation last cogeneration unit.

4 Conclusion

Measurements made at a specific BGS were detected energy flow and a predetermined quantity of unused heat. There was also found its own technological consump-

tion of heat the biogas plant, which serves primarily for heating fermenters and dofermentoru to operating temperature, to a lesser extent, to adjust the quality of biogas. Internal consumption is approximately 1082 MWh / year. This coverage is, of course, depends on the outside temperature throughout the year.

Thanks to the subsidy policy of the Czech Republic in supporting the development of biogas most biogas stations in the Czech Republic utilizes thermal energy to a limited extent, mainly for self-consumption (heating fermenters etc.), Respectively. 10% for heating which was later condition to qualify for a subsidy. BGS in question is not an exception and uses only 21% of the total possible amount of heat energy. This represents a huge share of thermal energy which is uselessly discharged to the environment until 9277 MWh / year. When the 500 BGS in the Czech Republic and the installed total output of 392.25 MW represents the unused heat energy to 272 GWh / year [3]. This energy from renewable sources, which input material into BGS undoubtedly is, could be used to reduce the need for fossil fuels and mitigate negative consequences on the environment by burning fossil fuels accompanies.

The main reasons why the heat from the biogas plant is not used to a greater extent, include:

• Subsidies economical operation independent of sale (usage) heat.

• Problematic use by placing the BPS in rural areas, distances-tion from densely populated areas or industrial companies, where there is sufficient demand for year-round thermal energy.

BPS particularity is stable year-round heat. Year-round stable heat energy usually only guarantee the technological processes in the industry.

To further increase the percentage of utilization of heat energy possible are essentially four PRI-outputs:

• can build up heat pipeline from the BGS to the point of consumption (village, town)

• build a gas pipeline from the place of production of biogas (from BPS) and move the location of CHP to the point of consumption of thermal energy (boiler settlements)

• construction of new consumers of thermal energy near the BPS (dryers toils-va, crops, etc.)

• installation of the conversion of heat to electricity in BPS (ORC sys-themes, etc.).

References

[1] J. Janša, J. Janša, “Heat Flow Measurement Report from BGS Loděnice,” Ostrava, VŠB-TUO, 2015-03-25.

[2] Czech Hydro Meteorogical Institute, “Územní teploty v roce 2014,” [online], Praha, ©2007-2015,[cit.2015-03-27]. Available from: http://portal.chmi.cz/portal/dt?action=content&provider=JSPTabContainer&menu=JSPTabContainer/P4_Historicka_data/P4_1_Pocasi/P4_1_4_Uzemni_teploty&nc=1&portal_lang=cs#PP_Uzemni_teploty

[3] National technology platform for biogas, “Statistiky výroby bioplynu” [online], České Budějovice, ©2013-2015, [cit.2015-04-03]. Avaible from: http://www.czba.cz/statistiky-vyroby-bioplynu.html

Application of Electron Spin Precession for Electric Power Generation

Martin Koutný and Radomír Goňo

Department of Electrical Power Engineering, FEECS,
VŠB – Technical University of Ostrava, 17. listopadu 15, 708 33 Ostrava – Poruba
{martin.koutny.st3, radomir.gono}@vsb.cz

Abstract. This paper focuses on the theoretical background and operational testing of the device described in a patent published in 1984 by Kalfaian Meguer Vartan. The name of the patent is Method and Means for Producing Perpetual Motion with High Power registered under code GB 2 130 431 [1].

The author presents the static energy of electron caused by electron spin interacting with magnetic fields of permanent magnets. In this new state the electron is a source of electromagnetic radiation, which can be converted into electric power.

Keywords: electron, electron spin, precession, vacuum, permanent magnet, electric power generation

1 Introduction

Ever since the dawn of time, a source of energy such as fire has been used to benefit people. People started to derive benefit from potential energy of water and kinetic energy of wind as useful alternative sources of energy. Many inventors began searching for a perpetuum mobile, a machine capable of perpetual motion. It seems that laws of physics do not allow this to happen. However, we can find a lot of movement inside matter. For example, magnetism is a macroscopic evidence of electron movement. According to the author of the patent GB2 130 431, the proposed device uses mutual interaction between the magnetic field of permanent magnets and electron spin in electron gas in vacuum to generate electric power.

© M. Krátký, J. Dvorský, P. Moravec (Eds.): WOFEX 2015, pp. 36–42.
VŠB – Technical University of Ostrava, FEECS, 2015, ISBN 978-80-248-3787-1.

2 Theoretical background

2.1 Electron spin

An electron placed in a magnetic field (B) interacts with the field due to the electron spin magnetic moment (μ) called spin. The spins are oriented along the magnetic field as a result of the relative position of B and μ. The magnetic moment of electron spin can be expressed as equation (1). [3]

$$\mu = g_s \mu_B M_s \qquad (1)$$

where g_S is g-factor (g_S=2.00232 for free electron), μ_B is the Bohr magneton (μ_B=9.2732 $\cdot 10^{-24}$ Am^2) and M_S is the magnetic quantum number (M_S= ±1/2)

A free electron with energy E in a homogeneous magnetic field takes one of the energy levels:

$$E_2 = E \quad \frac{1}{2} g_s \mu_B B \qquad (2)$$

$$E_2 = E + \frac{1}{2} g_s \mu_B B \qquad (3)$$

2.2 Electron motion in vacuum

Electron motion in electric and magnetic field is affected by the Lorentz force, which can be expressed as equation (4)

$$F_L = -e(E + v \times B) \qquad (4)$$

where the electron charge v stands for speed, E for electric field intensity and B for magnetic induction. For our purpose we considered only the stationary, homogeneous and parallel field. The vectors B and E have the same direction and the same magnitude of vector in the observed space. The equation (4) can be divided into 6 basic model situations shown in Fig. 1.

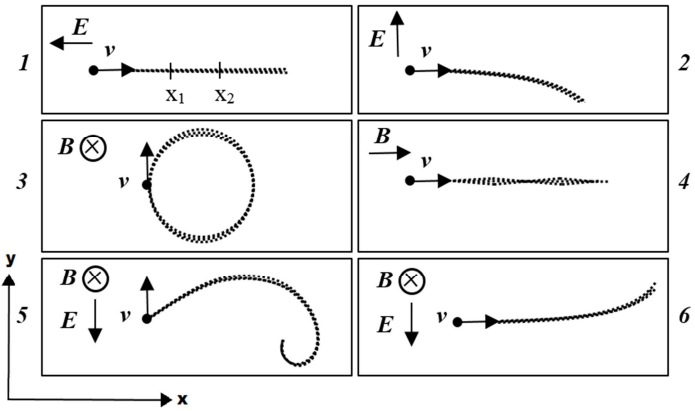

Fig. 1. Movement of a cathode ray in electric and magnetic field

In the case of this article the formulation of the Lorentz force comprises a combination of some of the situations in Fig. 1. When the electrostatic field is switched off, the electron acceleration stops. The Lorentz force equation for situation 4 in Fig. 1 is expressed as equation (2)

$$F_L = B \cdot v \cdot \sin 0 = 0 \qquad (5)$$

The electrons in the magnetic field aren't actuated by force except when the magnetic field is changing. [2]

3 Principle of operation of the device

The principle of the device is described in Fig. 2 – 4. The electron is represented by a rotating permanent magnet in the shape of a spinning top T with the south pole on the top and the north pole on the bottom, shown as B in Fig. 2a. The permanent magnet M1 in Fig. 2b attracts the south pole of the spinning top and deflects the vertical axis. It will wobble in a gyroscopic motion, such as the one shown in Fig.2c. The faster the top spins, the faster the wobbling motion will be. This motion can be described by the Larmor precession frequency.

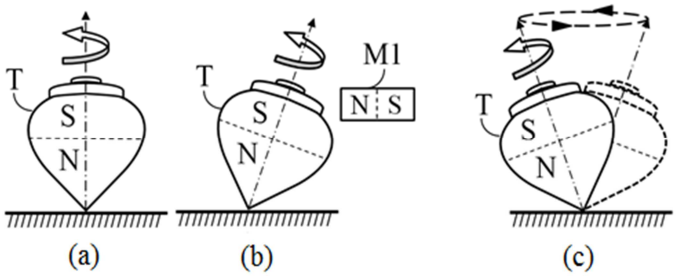

Fig. 2. a-c The spinning top describing the device principle [1]

The same wobbling motion can be reached by placing magnet M2 above the spinning top as shown in Fig. 3a. Because of the same polarization of the spinning top and the M2 magnet will cause the same gyroscopic effect depicted in Fig. 2c.

The spinning top is replaced with an electron, which is then aligned with magnetic lines in the center of the M4 magnet in Fig. 3a. In the same picture, the M3 magnet is placed next to the M4 magnet. Now the south pole of M3 interacts with the south pole of the electron and the result of this configuration is a wobbling gyroscopic motion, same as in Fig.3a.

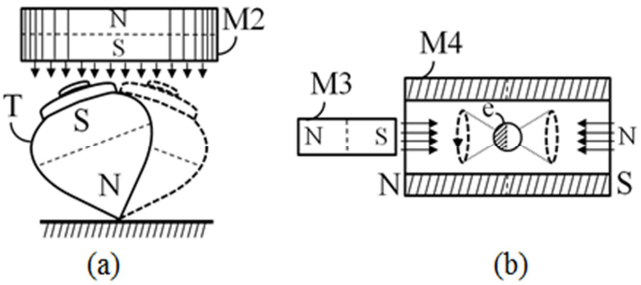

Fig. 3. a-b The spinning top and the electron in a wobbling gyroscopic motion [1]

The principle described above is applied to a device shown in Fig 4. The purpose of this device is conversion of the electromagnetic radiation of an electron into electrical energy by means of induction in an induction coil (L1). The Electrons are emitted from an electron gun (1) through an anode (2) towards another anode (3). These electrons are captured in the magnetic field of magnet M11 permanently even if the electrostatic field between the anodes and the cathode is switched off. The vacuum chamber C is properly shaped with respect to magnet M10. [1]

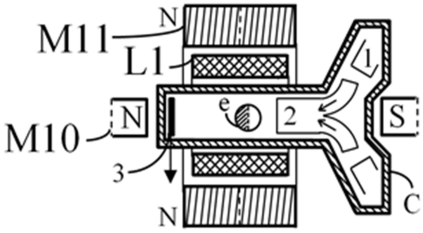

Fig. 4. The sectional side view of the structure of the device [1]

4 Design of the device

The constructed device is shown in Fig. 5. The blue hose connects the glass vacuum chamber with a vacuum pump.

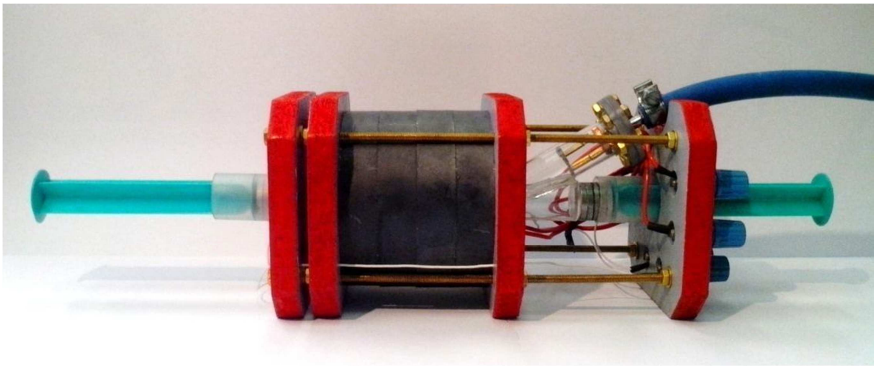

Fig. 5. The sectional side view of the structure of the device

Four red wooden boards bonded by brass rods serves as a solid basis. The cylindrical magnet M11 in Fig 4 is composed of four cylindrical ferrite magnets. Neodymium magnets M10 are held in modified syringes on both sides of the vacuum chamber.

4.1 The vacuum chamber and the electron gun

A high level of vacuum is required in the vacuum chamber. We need to reduce residual gas. Low pressure of the gas required for our chamber is about 10^{-4} Pa.

In Fig. 6 the vacuum chamber and the electron gun are made of glass tubes and joined together using epoxy glue. The air was vacuumed out through the output of the electron gun. There is a hose insert protruding out of the electron gun. The cathode of the electron gun used to produce free electrons by thermo-emission is made of Kanthal wire 0.2 mm wide. The production of the electron gas depends on temperature (a value of the current) and electric field intensity. The electron gun has two anodes. The first anode is made of copper lamination and is placed at the end of the vacuum chamber. The second anode is made of copper ring and is placed at the end of electron gun.

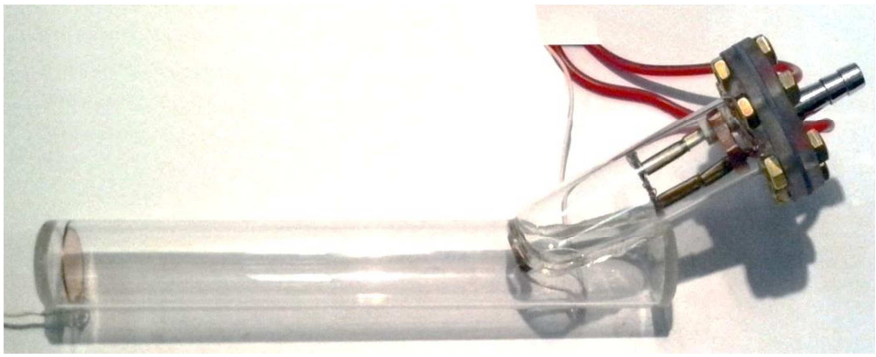

Fig. 6. The vacuum chamber and the electron gun

4.2 Output induction coil

The output induction coil shown in Fig. 7 is situated in the center of the cylindrical magnet M11 and on the vacuum chamber used to generate power output. The coil has 1,665 turns.

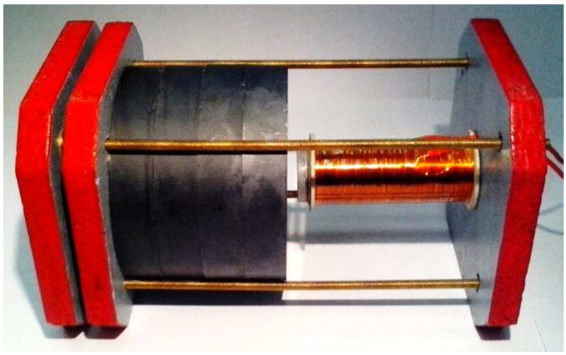

Fig. 7. The induction coil is situated on the horizontal axis of the cylindrical ferrite magnet

5 Measuring the electric power output

The value of flux density of the permanent magnets M10 is about 1.2 T. By changing the position of the neodymium magnets M10, the shape of the resulting magnetic field can be modified and the optimal power output could be fine-tuned. An oscilloscope used to measure output voltage has a frequency range up to 200 MHz but no electric output voltage was measured.

6 Conclusion

Although the polarization and position of the M10 magnets were changed, no electric voltage at the output was registered by the oscilloscope. No output power of the device can be caused by many deficiencies in the design.

6.1 Design deficiencies of the constructed prototype

1. The comparatively low underpressure was reached by means a rotary-oil vacuum pump. We were able to get a vacuum of about 10^{-1} Pa. However, the vacuum of about 10^{-4} Pa is necessary for our purpose.
2. The vacuum chamber and the electron gun are joined using by low-temperature resistance epoxy. The glow is in the class F temperature (155 °C). There is a risk of epoxy melt.
3. Maximum working temperature of the Kanthal wire is about 1,400 °C. The Kanthal has low electron emissivity at this temperature.

Arguably, a higher technical precision of the vacuum is needed to achieve measurable results. There is Czech Republic-based electron tubes producing company (Tesla electrontubes), which could produce a vacuum tube for this purpose.

References

[1] Tuks. [online]. 2015 [cit. 2015-08-09]. http://www.tuks.nl/pdf/Patents/UfoHowto/Method%20and%20means%20for%20producing%20perpetual%20motion%20with%20high%20power%20-%20GB2130431A.pdf

[2] L. Kavan, Metodyelektronovéspektroskopie. 1. vyd. Praha: Academia, 1986, 141 s.

[3] J. Schraml, Dvourozměrná NMR spektroskopie. 1. vyd. Praha: Academia, 1987, 130 s. Pokrokychemie.

[4] R. Kirmse, ESR [Elektronenspinresonanz] - Spektroskopie: Anwendungen in der Chemie. Berlin: AkademieVerlag, 1985, 188 s. WissenschaftlicheTaschenbücher.

Application for Facilitating the Selection of Water Turbine and Generator Protection Design of Small Hydro Power Plant

Martin Kral and Radomir Gono

Department of Electrical Power Engineering, FEECS,
VŠB – Technical University of Ostrava, 17. listopadu 15, 708 33 Ostrava – Poruba
{martin.kral.st3, radomir.gono}@vsb.cz

Abstract. This paper deals with a description of the created application in Microsoft Office Excel, this application has the task to facilitate the selection of appropriate water turbine for small hydro power plant, and also determine appropriate protections for generator of the small hydro power plant.

Keywords: small hydro power plant, protections, water turbine

1 Introduction

Although a small hydro power plant (SHP) is with respect to a small installed power production plants to smaller sources in the energy system, question of correctly designed system protect should not be an underestimated. Each generator is connected to the power grid must be equipped with electrical protections. Electrical protection protects against damage to the machine, it protects even the power grid before the negative effects of generator in cases of failure the regulators or the circuits of automatics.

The cases of the recent past shows that even "small" hydro power plants with asynchronous generator can cause, for example, in the conditions of operation of the island due to the "disease control" of its terminal voltage and frequency of the annoying damage to equipment purchasers of electric energy. Electrical protections of small sources then acquire great significance.

2 The Theoretical Part

2.1 Basic Parameters of Hydro Energy

If we want to effectively utilize water energy of a certain section of the water flow rate, we must suitably place in this site momentum and flow rate. Under the concept

This research was partially supported by the SGS grant from VSB - Technical University of Ostrava (No. SP2015/192) and by the project LO1404: Sustainable development of ENET Centre.

© M. Krátký, J. Dvorský, P. Moravec (Eds.): WOFEX 2015, pp. 43–48.
VŠB – Technical University of Ostrava, FEECS, 2015, ISBN 978-80-248-3787-1.

of momentum we understand the difference in the levels of water in the tank above the plant and in the runoff below it. The flow rate is the amount of water flowing of the specific profile of the flow rate in one second.

The water flowing from the upper reservoir to the lower tank performs work. Then is the used gradient of hydro power plant H [m] and flow rate of water turbine Q $[m^3 \cdot s^{-1}]$, then theoretical output power is:

$$P = \rho \cdot g \cdot Q \cdot H \quad [W] \qquad (1)$$

where: ρ - the specific weight of water $[1000\ kg \cdot m^{-3}]$
g - acceleration due to gravity $[9{,}81\ m \cdot s^{-2}]$

or

$$P = 9{,}81 \cdot Q \cdot H \quad [kW] \qquad (2)$$

The actual power and energy of water resources will be less, because losses arise the conversion of the hydraulic energy into mechanical energy in the turbine and mechanical energy into electric energy in generator. For the necessary output power estimates are used the formulas for small hydro power plants:

$$P = (5\ to\ 7) \cdot Q \cdot H \quad [kW] \qquad (3)$$

The basic variables for the calculation of the output power and production of electric energy from the water sources are: flow rate, gradient and the effectiveness of the hydro-alternator, i.e. a water turbine or water wheel and the electric generator. Alternatively, we can write the gradient of water tank, such as the specific energy:

$$Y = g \cdot H \quad [J \cdot kg^{-1}] \qquad (4)$$

2.2 Protection of Generators of SHP

Each generator which is connected to the power grid must be equipped with electrical protections. Electrical protection protects against damage to the machine itself, but also the power grid before the negative effects of generator in cases of failure of the regulators or the circuits of automatics.

Ways to protect the generators in small hydro power plants are determined by a number of aspects. In the design of the system of protections, must be determined if is a SHP with asynchronous generator, synchronous generator, what are the nominal values of the device, as is done by the outlet of the power – whether working generator directly into the system nn, or the output power is escorted into the system nn with the help of transformer. Part of the operation of an asynchronous generator is the need compensation, and therefore is necessary to consider the protection of the compensation switchboards against overload.

Individual protection SHP generators:

- over-current protection
- voltage protection

- frequency protection
- power protection
- ground protection
- load unbalance protection

Protection SHP according to ČSN 33 3051.

Technical standard ČSN 33 3051 "Protection of electric machines and distribution equipment" (effective from 1992) defines the general principles for the design of protection and their proper function and for the output power of the electrical machine specifies the used protection.

According to this technical standards must protect electrical machinery and distribution equipment to carry out the following activities.

- quickly and reliably determine the failure or limit exceeded the normal operation of the protected equipment
- shut them down in time, which must be determined so as to avoid the risk of damage or limit their scope to the machine or equipment and to ensure the protection of persons
- to reduce the risk of fire due to the thermal effects of short-circuit current
- ensure that the disorder spread to other elements of the power grid and do not endanger the operation and the power of the consumer

The definition of technical standards ČSN 33 3051 for nominal output power of different hydro-alternators.

- asynchronous hydro-alternators to power rating 2.5 MVA
- synchronous hydro-alternators to power rating 1.0 MVA
- synchronous hydro-alternators to power rating from 1.0 MVA to 2.5 MVA
- synchronous hydro-alternators to power rating from 2.5 MVA to 5.0 MVA
- synchronous hydro-alternators to power rating from 5.0 MVA to 10.0 MVA

Protection SHP according to the rules of the operators.

The necessary electrical protection SHP are also defined the rules of the distribution system operators to the site it built SHP. For example, the directive "rules for parallel operation with network resource distribution system operator (current as of June 2010)" governing ČEZ distribution, and "rules for parallel operation with network resource distribution system operator (current as of November 2011)", which is governed by the E.ON distribution, the above named rules define the requirements on the protected production (SHP).

3 The Practical Part

The goal was to create an application in Microsoft Office Excel to which can be entered the basic parameters to generate useful information concerning the small hydro power plants.

3.1 Description of the Application

This application makes it easy to select the appropriate water turbine design of small hydro power plants (SHP). After you enter the expected flow rate and specific energy SHP (sheet: Input data, protections from ČSN), the application displays a point of ideal selection in a regional chart using individual turbines (sheet: Area diagram of use). Calculates the expected output power of the generator, respectively, due to the known value of the generator power recommend to protection according to ČSN 33 3051 (sheet: Input data, protections from ČSN) and the rules of the operators (ČEZ, E.ON), see sheet: "Protection from operators". To preview graphic is the inclusion of projected water turbines according to the output power (sheet: Dividing SHP from output power).

The whole Excel is divided into multiple sheets, each sheet I described below.

Input data, protection from ČSN 33 3051.

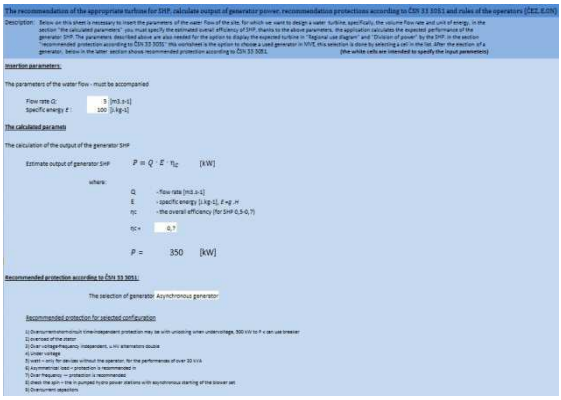
The recommendation of the appropriate turbine for SHP, calculate output of generator power, recommendation protections according to ČSN 33 3051 and rules of the operators (ČEZ, E.ON)

Description: Below on this sheet is necessary to insert the parameters of the water flow of the site, for which we want to design a water turbine, specifically, the volume flow rate and unit of energy, in the section "the calculated parameters" you must specify the estimated overall efficiency of SHP, thanks to the above parameters, the application calculates the expected performance of the generator SHP. The parameters described above are also needed for the option to display the expected turbine in "Regional use diagram" and "Division of power" by the SHP. In the section "recommended protection according to ČSN 33 3051" this worksheet is the option to choose a used generator in NVE, this selection is done by selecting a cell in the list. After the erection of a generator, below in the latter section shows recommended protection according to ČSN 33 3051. (the white cells are intended to specify the input parameters)

Insertion parameters:

The parameters of the water flow - must be accompanied

Flow rate Q: 5 [m3.s-1]
Specific energy E: 100 [J.kg-1]

The calculated params

The calculation of the output of the generator SHP

Estimate output of generator SHP $P = Q \cdot E \cdot \eta_C$ [kW]

where:

Q - flow rate [m3.s-1]
E - specific energy [J.kg-1], E.wp..w
ηc - the overall efficiency (for SHP 0,5-0,7)

ηc = 0,7

P = 350 [kW]

Recommended protection according to ČSN 33 3051:

The selection of generator Asynchronous generator

Recommended protection for selected configuration

1) Overcurrent short-circuit time-independent protection may be with unlocking when undervoltage, 500 kW to P + can use breaker
2) overload of the motor
3) Over-voltage-frequency, independent, u HV alternators double
4) Under voltage
5) watt – only for decides without the operator, for the performances of over 30 kVA
6) Asymmetrical load – protection is recommended in
7) Over frequency – protection is recommended.
8) check the spin – line in pumped hydro power stations with asynchronous starting of the blower set
9) Overcurrent-stepless

Fig. 1. Sheet of Input data, protection from ČSN 33 3051

This sheet is divided into multiple sections: pasted the parameters, calculated parameters and featured the protection according to ČSN 33 3051.

On this sheet are inserted the important parameters for the calculation, among them the flow rate, specific energy, the overall estimated efficiency of small hydro power stations and the type of generator, which are to be recommended for protection.

There are also some calculations and results. The main results are the power output of small hydro power plants, more precisely the output power of the generator and the list of recommended protections from ČSN 33 3051.

Protection from operators point of view.

This Excel sheet describes the most important requirements for protection of generators of small hydro power plants according to the distribution system operator, the operators are ČEZ distribution and E.ON distribution. At the end of the parties are listed the values for the settings of the individual protections from both operators.

Area diagram of use.

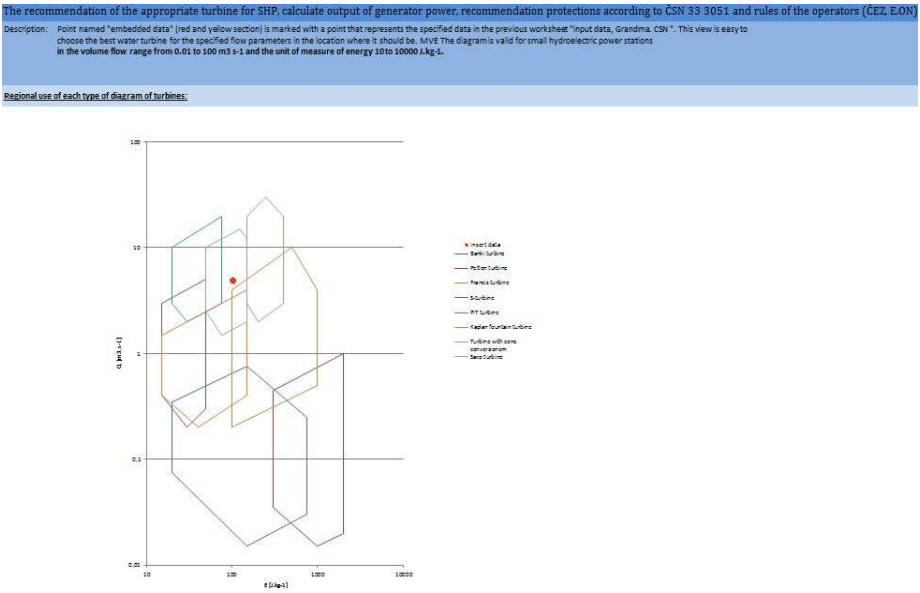

Fig. 2. Area diagram of use

Point named "embedded data" (red/ yellow point) is marked with a point that represents the specified data in the previous worksheet "Input data, protection from ČSN 33 3051". This view is easy to choose the best water turbine for the specified parameters in the location where it should be SHP. The diagram is valid for small hydro power plant in the flow rate from 0.01 to 100 $m^3 \cdot s^{-1}$ and the unit of specific energy 10 to 10000 $J \cdot kg^{-1}$.

Dividing SHP from output power point of view.

Point named "embedded data" (red/ yellow point) is marked with a point that represents the specified data in the previous worksheet " Input data, protection from ČSN 33 3051". This Division is evident classification of water turbines, which matches the specified parameters. You can specify whether it is a small, medium or large hydro power plant, SHP is further division: home, micro, small and industrial small hydro power plant. You can specify the size of the gradient: low pressure, medium pressure

and high pressure. Diagonal lines indicate the output power of hydro power plant. The diagram is valid for hydro power plant in the flow rate from 0.1 to 1000 $m^3 \cdot s^{-1}$ and the unit of specific energy 10 to 10000 $J \cdot kg^{-1}$. The view is optimized for the calculation of the total efficiency $\eta_C = 0.7$.

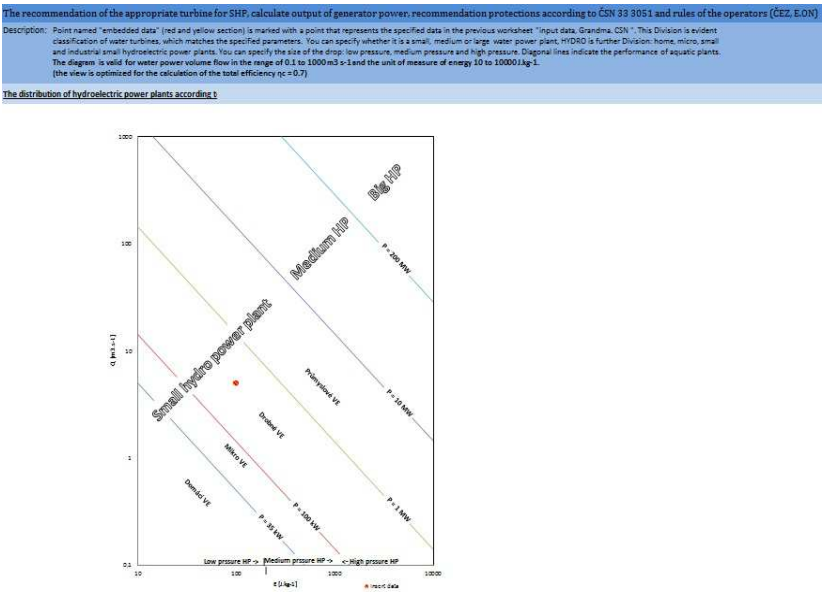

Fig. 3. Dividing SHP from output power

4 Conclusion

In this paper there are, included the basic theories which have been used to build an application, it is about the basics of the parameters of hydro energy and the protection of the generator small hydro power plants. In the practical part the application is described that was created in Microsoft Office Excel, which displays many useful values for example, the expected output power of small hydro power plants. According to this performance, the application displays the recommended protection. There are also shown the basic rules of distribution system operators (ČEZ, E.ON) with values that are necessary for setting up protections. This application has also facilitated a selection of water turbine for small hydro power plants. The last point is the diagram of the distribution according to the output power SHP, due that it is easy to classify small hydro power plant, to the unit of energy, output power, flow rate, and use.

Acknowledgment

The presented research was supervised by doc. Ing. Radomir Gono, Ph.D. from Department of Electrical power engineering, VSB - TU Ostrava, Czech republic.

Active Charging Stations for Electric Cars

Oliver Marcincin

Department of Electrical Power Engineering, FEECS,
VŠB – Technical University of Ostrava, 17. listopadu 15, 708 33 Ostrava – Poruba
oliver.marcincin.st@vsb.cz

Abstract. This paper deals with charging stations for electric cars containing accumulation of electrical energy support. Usually these charging stations are called active charging stations and are parts of modern electrical grids known as "Smart Grids" or "Micro Grids". This paper also contains a brief summary of current knowledge about structure and service of electricity distribution networks, and analysis of electric car industry growth and its potential impact on electrical network.

Keywords: Electric network; active charging station; accumulation of electrical energy; electric car; charging station

1 Introduction

Electromobility is currently perhaps the most commonly discussed term of automotive technology. Low number of vehicles operated in the Czech Republic is corresponding to the low density of charging stations, most of which are operated amateur way. In case of expansion of electric vehicles will also increase the demands on the construction of an adequate network of charging stations.

For these purposes seems to be very advantageous to combine the emerging system of infrastructure charging stations with renewable power sources, such as the energy produced by the sun with the possibilities of accumulation and its subsequent delivery to the uniform charging infrastructure [3].

2 Connecting of Charging Stations for Electric Cars to the Distribution Network

If the number of electric vehicles operators will increase, it will be necessary to build sufficiently dense network of charging stations, to ensure not only the range of electric cars in its area of operation, but also to allow occasional crossing for medium distances up to about 300 km [2]. This requires the deployment of charging stations along major roads within a maximum of 50-60 km.

© M. Krátký, J. Dvorský, P. Moravec (Eds.): WOFEX 2015, pp. 49–54.
VŠB – Technical University of Ostrava, FEECS, 2015, ISBN 978-80-248-3787-1.

2.1 Estimation of the Needed Electrical Energy Amount for Charging Vehicles

The amount of electric power consumption can be estimated on the based expected performance structure of the vehicle and their fail safe distances. The energy needed for an average range 120 km of electric vehicles in three distinctive categories gives us Tab. 1. The three basic categories of electric vehicles, which are characterized by different engine power, were chosen for analysis [3]. Category "A" - a small urban vehicle with traction engine power about 10 kW, category "B" - standard vehicle lower middle class with performance of traction engine about 30 kW and category "C" - a higher class with performance of traction engine about 80 kW. Range is in all three categories averaged 120 km. The energy required for operation of the vehicle was determined simplified calculation based on basic physical equations for calculating the energy performance of engine vehicles (Table I.).

Table 1. Energy and Sampling Intensity in Terms of Charging Electric Vehicles in Selected Categories for a Single Driving cycle

Category of vehicle	**Stored energy of the vehicle (range 120 km)**	**Charging current**		
		t = 8 hours	***t = 4 hours***	***t = 0.5 hour***
A	13.3 kWh ($W_{ak(A)}$)	5.1 A	10.2 A	81.6 A
B	30.0 kWh ($W_{ak(B)}$)	10.2 A	20.4 A	163.2 A
C	41.1 kWh ($W_{ak(C)}$)	14.2 A	28.4 A	227.2 A

Charging current is calculated for the stored energy and the expected nominal voltage of 350 V battery, for three different charging times. These times have been set for probable modes:

- t = 8 hours - long-term (e.g. night) charging electric vehicles by low current at full capacity battery,
- t = 4 hours - charging electric vehicles during the day (e.g. a vehicle parked during working hours around lunch breaks or business meetings),
- t = 0.5 hours - so-called fast charging as during a long journey stops.

2.2 Estimation of the Needed Electrical Amount to Charge the Vehicles in the Region of Ostrava

The basic premise solutions and designing active networks of charging stations is to create conditions for adequate consumption of electrical energy in repetitive cycles, which can be linked to the cycles of the daily load diagram distribution network.

The second prerequisite for successful application of active power stations in the area is its positive effect on the network. The solution must be open enough to allow even the use of non-traditional and renewable energy sources [5].

Table 2. The Expected Number of Electric Vehicles in the Ostrava Region in the Period 2015 – 2020

Category of vehicles	Number of vehicles (%)	Number of vehicles (pc)
A	70	17 500 (N_A)
B	25	6 250 (N_B)
C	5	1 250 (N_C)

On the basis of this distribution can be calculated energy stored in vehicles for daily cruising range of 120 km, which would correspond to daily charging cycle.

Stored energy in all vehicles:

$$\begin{aligned} W_{ak(celk)} &= N_{(A)} \cdot W_{ak(A)} + N_{(B)} \cdot W_{ak(B)} + N_{(C)} \cdot W_{ak(C)} = \\ &= 17500 \cdot 13300 + 6250 \cdot 30000 + 1250 \cdot 41100 = \\ &= 471.6\,(MWh) \end{aligned} \tag{1}$$

It can be assumed that the actual status of distribution network in the Ostrava region, in terms of its design and possible sources, would not be enough to cover the requirements of electromobility in a certain period of time (increase output by about 42 MW). The solution shows the necessity of using active charging stations.

3 Concept of Charging Stations for Electric Cars with Minimal Impact on the Supply Network

The concept of charging stations must ensure that the energy required for charging electric cars is available regardless of network options, such as at the time of decommissioning the vehicle and its charging even during peak sampling network.

Another key requirement for active charging station is the suppression of reverse effects on different semiconductor chargers. A possible structure of such network shows Fig. 1.

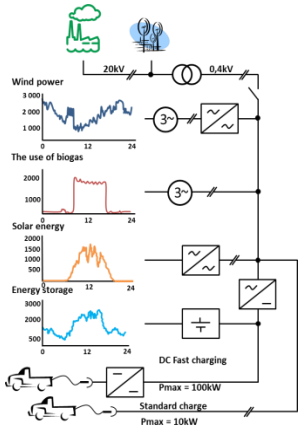

Fig. 1. The integration of active charging station into the structure with the accumulation of renewable sources [1]

A distinctive feature is to use multiple sources of energy, which significantly reduce the particular peak load distribution networks. Typically is utilization of non-traditional and renewable resources in the temporal distribution of energy to the grid. Energy storage in the charging station also creates stabilizing element for network. Involvement of active charging stations, in addition, to its stabilizing function to perform a variety of additional features:

- minimizing the consumption of reactive power from the network and the conditions EMC as network traffic and RF interference,
- achieve the highest energy conversion efficiency for all types of converters,
- remote control of charging modes by dispatching (e.g., discontinue charging vehicles from the network and go to the charging of the battery charging station).

3.1 The Basic Structure of the Active Charging Station

For a conventional vehicle charging typically uses its own charger connected directly to the AC grid. Charging power usually does not exceed 10-15 kW. The problems with increased of power draw in the 3rd and 5th harmonic are caused by this simple method of charging with the concept of switching power supply in the electric charger. This concept does not allow for the fast charging.

The process allows fast charging the vehicle's battery in time less than 1 hour, which is a charging current of up to several times larger than the current amp-hour capacity battery. A basic comparing size of these currents is performed in the Table I.

Block diagram of the active charging station with AC output is shown in Fig. 2.

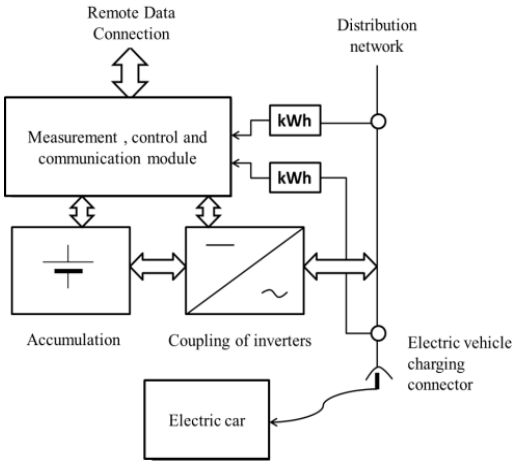

Fig. 2. The structure of the charging station for electric vehicles

The concept of charging station uses the parallel connection of storage to the power supply charging socket. The basic power blocks are bidirectional invertor, which allows bidirectional power flow between the network and the battery. The whole system

is controlled by a unit of measurement, control and communication. The power section of active charging station must, therefore, satisfy the following requirements:

- high dynamic management of operating conditions,
- four-quadrant operation relative to the grid,
- active filtering reverse effects of electric chargers,
- high efficiency of conversion of electrical energy.

This solution enables to cover needs of the electric charging power at a time when the network failure by drawing power from the auxiliary battery of active charging station. This solution allows control of inverter, which suppress the negative feedback effects of electric vehicle charging on the power grid as the basic harmonic, reactive power supply and in the higher order harmonics. The advantage of the solution is that in the case of energy shortage, in the auxiliary accumulator station, can only operate as a so-called parallel active filter.

4 Daily Load Balance of Active Charging Station

The impact on daily load diagram by small charging stations with one to three charging sockets is minimal. Therefore, it doesn't make sense to deal with it. Battery of active charging station has its justification only with regard to the possibility of charging efficient vehicles and doesn't overload the power network.

During the operation of electric vehicles in their vast majority can be expected their operation during daylight hours. This operation allows basic charge at night. For example electric energy is reduced overnight rates directly from a garage by the private socket.

We assume that the vehicles in larger cities will be charged from public charging stations overnight. In focus to daily load diagram, it makes sense to think primarily about impact active charging stations with more sockets and with greater energy stored in the battery.

The basic requirement is balancing of electric energy consumption from the network on the mean value power of daily load diagram. If we use to the accumulation all possible energy, it will ensure that the network will be loaded at night to medium power, resulting in more efficient use of the network. However, it doesn't suppress the extent of peak demand, because they are made from other appliances. The important thing is that, if during the day electric vehicles need additional charge, they can be charged in a network of charging stations from the energy stored in the battery charging stations. This won’t contribute to further increase the demand of daily peak.

For an overall proposal power cables is appropriate to determine the values of equivalent powers for morning and evening accumulation, which correspond to a constant (equable) flow of energy throughout accumulation.

If the active charging station is interconnected with a photovoltaic power station, the peak of supply energy from solar panels is equalized by the battery of station. This contributes to more efficiency of the charging station, but also to suppress the negative impacts of photovoltaic on network stability.

With respect to the power network, at night is irrelevant if is charged the electric vehicle or the battery of charging station. The main priority is charging an electric vehicle when is connected. In the remaining time can be charged battery of charging station. If is sufficiently proposed electric connection of charging station, they may be charged together. In the case that the charging station is a part of Smart Grids or Micro Grids, should be available remote control by dispatching center or control system of network.

5 Conclusion

The paper deals with active charging stations for electric vehicles in the event of mass deployment. This type of charging stations is not yet used by us, so there isn't experience with the operation and impact on the power grid.

The purpose is to create such an active station, which is in equilibrium with the opportunities and needs of daily load diagram at the site. Therefore, the whole calculation is based on the needs for continuous cycling of energy in one day.

The solution shows the necessity of using active charging stations suitable with geographical distribution. Such as location with high density in cities or in areas that are likely to be implemented in infrastructure between the larger sites.

This work was partially supported by SGS grant VŠB-TU Ostrava No. SP2015/192.

References

1. R. Benger, R. Heyne, A. Haubrock, and H.P. Beck, "Sustainable Fast Charging Stations for Electric Vehicles," in 5 th, International Renewable Energy Storage Conference (IRES 2010), Berlin, Germany.
2. E. Chlebišová, J. Kyzeková, and H. Svobodová, "Marketing Study of the Electric Vehicles' Diffusion," in 11th International Scientific Conference on Electric Power Engineering 2010, Brno, Czech Republic, pp. 807-811, 2010, ISBN 978-80-214-4094-4.
3. H. Barešová, "Vliv nabíjecích stanic elektromobilů na elektrickou síť," DP VŠB-TU Ostrava 2011, Ostrava, Czech Republic.
4. J. Koždoň, "Rychlonabíjecí stanice pro elektromobily," in Hybrid [online]. 12/5 2010.[cit: 2015-02-02] available on internet <http://www.hybrid.cz/clanky/rychlonabijeci-stanice-pro-elektromobily>
5. The Ministry of the Interior of the Czech Republic, "Motor Vehicle Register," in MVCR [online]. 18/7 2012.[cit: 2015-02-02] available on internet <http: http://www.mvcr.cz/clanek/centralni-registr-vozidel-865510.aspx?q=Y2hudW09NQ%3d%3d

The Input Analysis of Parameters Energetic Technologies in Technological Centre ENET in Ostrava

Tomáš Mozdřeň

Department of Electrical Power Engineering, FEECS,
VŠB – Technical University of Ostrava, 17. listopadu 15, 708 33 Ostrava – Poruba
tomas.mozdren.st1@vsb.cz

Abstract This paper deals with a description and partial analysis of energy production units and their implementation in the laboratories of ENET technological centre in Ostrava -Vitkovice. The paper refers to individual types of conventional and non-traditional sources of electric power that are connected to the technological centre distribution grid, together with analysis of their topological configuration, with a presentation showing division of individual power sources into logical technological groups with definition of either nominal or estimated operating parameters. The data summarised in this paper will serve mainly as input material to design a dynamic model, for modelling of transients and short-circuit ratios mainly on non-traditional energy sources, as well as full energetic systems already implemented. That is why the paper also addresses an introduction of concept and expected software products for future creation of the model.

Keyword non-traditional energy sources; renewable sources; hydrogen technologies; accumulation of energy; modelling.

1 Introduction

The current demand for sources of electric power keeps rising and the existing deposits of fossil fuels are unfortunately exhaustible. This is the reason for accelerated efforts towards search and application of new renewable energy sources for humankind. The reasons mentioned above then supported evolution of the ENET project dealing with research on utilisation and application options covering non-traditional sources of energy in the laboratory of the technological centre in Ostrava - Vitkovice ("TCO") since the year 2010. The technological centre ENET in Ostrava has been adapted to the project needs and it is located in formerly abandoned industrial premises in the municipality of Vitkovice. The ENET project lays emphasis on energetic utilisation and processing of alternate fuels transformed into heat and electric power. Further objectives of the research include utilisation and practical verification of accumulation of electric power supplied from either the distribution grid or power generating units installed within the TCO. The main components of the TCO energy system comprise a co-generation unit, a high-capacity power storage system, a photovoltaic system and an energy accumulation system based on hydrogen technologies.

© M. Krátký, J. Dvorský, P. Moravec (Eds.): WOFEX 2015, pp. 55–60.
VŠB – Technical University of Ostrava, FEECS, 2015, ISBN 978-80-248-3787-1.

2 Connection and Topology of TCO

The simplified electric diagram of the technological centre in Ostrava is illustrated by the Fig. 1. Individual energy sources have been divided and drawn into technological blocks for legibility purposes.

The primary supply of power to TCO and the power outlet from the centre are ensured in terms of connection to the local distribution system. The backbone source of electric output from TCO is the co-generation unit with an asynchronous generator with the power output of 100 kW cooperating with a gas piston combustion engine. This unit is supplied with gas fuel from the processing thermal cracker with typical continuous supply of 250-450 kg of the fuel material per hour (depending on its composition). The topology of electric power distribution system of TCO comprises the main AC bus with the option to connect onto the backup AC bus. The whole distribution system at the centre has been designed and built as fully subsistent with potential opportunity to switch into island operation mode with 3x230/400 V and with the optional power supply to the adjacent industrial buildings. Installation of various accumulation systems forms a vital part of the whole TCO. This accumulation is ensured with various types of batteries that are always linked to the main direct-current bus DC 400V. The bus enables distribution of electric power into the individual parts and components of the system using converters. The links between direct-current buses and the standard network buses are made of power semi-conductor inverters combined with coupling transformers and chokers TR1+TL1 and TR2+TL2 to enable two-way transfer of power between buses. If the centre is disconnected from the grid supply and its internal accumulation capacity has been fully depleted, it is still fitted with a diesel generator to ensure stable supply of power and safe shutdown of all technologies, especially the thermal cracker.

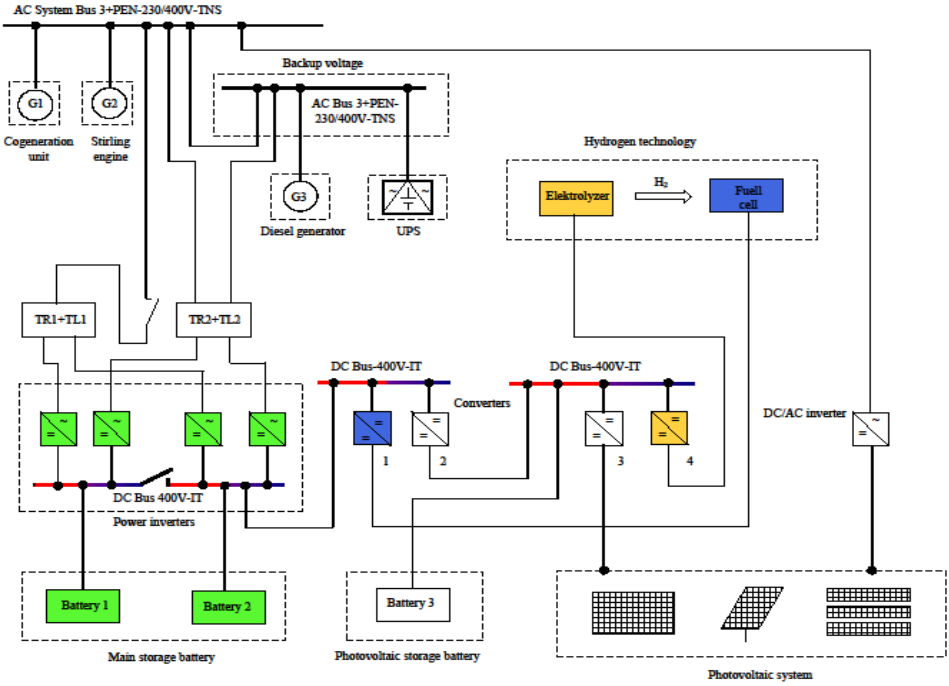

Figure 1 Connection of TCO

3 Non-Traditional Sources at the Technological Centre

Major non-traditional sources of electric power used in laboratories of the technological centre in Ostrava to be reflected in the dynamic model to enable research of transients, besides other, include the following:

3.1 Co-generation unit

Co-generation is combined generation of electric power and heat. The technology helps achieve better utilisation of energy when burning fuel or other primary sources available in power engineering or transport applications. Operation of a turbine motor generates great volume of waste heat representing the heat loss in the process of power generation and transformation. The co-generation process used within TCO makes use of the waste heat to warm up domestic hot water (DHW), for heating or other similar purposes. That helps achieve an approximately high calorific efficiency with respect to the energy content fuel efficiency. The technological centre is fitted with the co-generation unit rated for 100 kW that is supplied from the thermal cracker burning the pyrolyzed gas. Power output from the co-generation unit depends on the input material subject to testing in the thermal cracker. The co-generation unit is designed as a combustion engine linked to an asynchronous generator considered in the model design.

Figure 2 Co-generation unit

Table 1 CHP generator parameters

Generator			
Cover	IP23	Voltage	400 V
Frequency	50 Hz	Phase	3
R.P.M	1500	Conn.	D
Full load	23.9 V/ 2.97A	Cont.	125 kVA
At no load	0.83 A	BR	100 kW
Th. Class	H/H	40ϕC	180 A

3.2 Stirling engine

The Stirling engine, installed as a non-traditional source of energy, is a hot-air or even heat-gas engine working with an external source of heat [3]. That means the heat source is located outside its cylinder. The range of such external sources could comprise various primary sources as coal, petroleum fraction, biomass, solar energy, etc. The Stirling engine installed in the technological centre of the PCU35 solar/gas type model with the electric

power output of 10 kW_e and the heat output of 25 kW_{th}, it works with combustion of a mixture comprising pyrolyzed and natural gas or even pure natural gas only. The Stirling engine is designed for being driven by its asynchronous mechanism connected to the grid.

Figure 3 Stirling engine

Table 2 Stirling and asynchronous parameters

Stirling		**Asynchronous engine**	
Type	PCU35-GAS	Phase	3
Cover	IP45	Power	11 kW
Frequency	50Hz	Cos. φ	0.85
Voltage	230/400 V	Voltage	Y 690 V D 400 V
Gas	LPG, Natural gas, Pyrolyzed gas	Current	Y 12.1 A D 21 A
Electric/ Heat power	2-10 kW / 9-25 kW	R.P.M	1470

3.3 Storage batteries

Suggestion to store power in batteries is that allow connection to the alternating grid rated 3x400 V via reversible power converters. The accumulator room is virtually split into two sections provided with two battery banks functioning separately. Both battery bank supply the electric power at level 400 V.

The first section comprises five battery blocks at side of the accumulator room. Each block is formed by 40 lead blocks connected in series. The voltage per block is 80 V with the capacity of 930 Ah. These main batteries stand for the major power storage capacity of the centre and they also define the basic reference voltage level for direct-current buses in TCO that are linked by means of converters.

The second section comprises 100 batteries of LiFeYPO4 type connected in series on each side, with the capacity of 100 Ah. These batteries are used for storage of surplus power output form photovoltaic panels and used as energy "buffers" for electrolysis to cover output fluctuation of power supply to electrolysers. The accumulator room suffers from low efficiency of the charging cycle due to restriction of the charging current.

Figure 4 Battery room and main storage battery

3.4 Photovoltaic cells

The photovoltaic system is installed on roof of the technological centre and it is formed by three sections, each made of different panel types. Polycrystalline photovoltaic panels represent the first type of components installed in static configuration on the inclined roof of the centre. This section includes 60 panels with the nominal output of 210 Wp per unit. Positioning polycrystalline photovoltaic panels, the so-called "trackers", represent another type of components used and benefiting from the most convenient alignment with the sun. This section comprises 18 panels with the nominal output of 230 Wp per unit. The third type is represented by amorphous (non-crystalline) photovoltaic bands installed on the horizontal roof of the technological centre. The third section includes 10 panels with the nominal output of 576 Wp per unit. The electric power generated by individual panels is channelled into batteries using electrolysis as "buffers" or stored. The total power output from photovoltaic panels is approximately 22.5 kWp. However, these sources suffer from output fluctuations caused by weather changes. They also provide low short-circuit capacity.

Figure 5 Different Types of Photovoltaic cells

3.5 Hydrogen Laboratory

Hydrogen technologies utilise storage of power based on the hydrogen gas closed circuit principle. Hydrogen technologies ensure conversion of electric power into hydrogen gas inside the TCO; the electric power is therefore transformed into chemical power by means of water electrolysis using electrolyser units with polymer membranes [4]. Hydrogen gas is then stored in pressure contains to be used for reverse production of electric power if needed. Electric power is generated from hydrogen in laboratories of hydrogen technologies on low-temperature fuel cells with polymer membrane.

Figure 6 Laboratory of Hydrogen in Technologies

The hydrogen storage system has been designed for operation of four electrolyzer units with the hydrogen production capacity of approx. 1 Nm3/h of hydrogen gas each. Five fuel cell modules generate up to 50 kW. The hydrogen system has been designed for planned operation in power generating mode twice a week for 4 hours per session and for continuous operation in electrolysis mode. To ensure proper functioning of the hydrogen technology, the fuel cells, electrolysis and other operating functions the system design had to rely on details of the gas lines, large storage space for hydrogen, inspections and measurement, coolant and electrolyte lines with the safety air-conditioning of the laboratory as the last but not the least aspect.

4 Conclusion

The contribution contains description of energy units located in the Technological Centre Ostrava and established within the ENET project. The first part describes laboratory in block schema. The second part of contribution describes installation of individual sources and their connection to the distribution grid with the necessary technical specifications and pictures made right in the TCO. These sources include the co-generation unit, the accumulator room, the photovoltaic system, the Stirling engine and hydrogen technologies. Some sources still require some completion work on cable lines and other components.

Acknowledgements

Work was partially supported by SGS grant VŠB-TU Ostrava No. SP2015/192 and No. SP2015/73. This paper was also supported by the project New Creative Teams in Priorities of Scientific Research, reg. No. CZ.1.07/2.3.00/30.0055 and by the project LO1404: Sustainable development of ENET Centre.

The results of the thesis are published in:

- Conference EPE 2015, Dlouhe Strane, Czech Republic, ISBN 978-1-4673-6787-5
- Magazine ENERGETIKA 6/66/2015, ISSN 0375-8842

References

[1] D. Minarik, S. Rusek and R. Gono, “Implementation of accumulation technologies of electric energy to hybrid energy system”, – project, In Electric Power Engineering 2012, ISBN 978 - 80 - 214 - 4514 - 7

[2] M. Uher, “Optimization of network operation with renewable resources with the use of a dynamic model”, Dissertation thesis, Ostrava, 2014.

[3] J. Blaha, “Stirling Engine”, Diploma thesis, Brno, 2008

[4] M. Hlousek, “Application of hydrogen fuel cell”, Nová Paka, 2012

[5] Pas Daisy off-line v. 4.42 Bizon, “User manual”, 2013, [cit. 2014-10-2]. Avalaible at WWW: < http://www.daisy.cz>

[6] EMTP-ATP, “About ATP”, 2015, [cit. 2015-20-2]. Avalaible at WWW: <http://www.emtp.org/>

[7] TCO, “Information and technical documention”

Evaluation of Electric Power Supply from Photovoltaic Plant in ENET Center

Michal Ney

Department of Electrical Power Engineering, FEECS,
VŠB – Technical University of Ostrava, 17. listopadu 15, 708 33 Ostrava – Poruba
michal.ney.st@vsb.cz

Abstract. This paper deals with evaluation of electric power supply from photovoltaic plant in ENET center, specifically with voltage, current, active power, power factor and frequency characteristics.

Keywords photovoltaic plant; DC/AC inverter; voltage; frequency; power factor

1 Introduction

Technological center ENET uses photovoltaic plant installed on its roof as an electric power supply primarily for electrolytic cells in hydrogen technology lab. This photovoltaic plant consists of three sections of photovoltaic panels with the total nominal power of 22.5 kW. The first section consists of 60 polycrystalline panels Trina Solar TSM PC05 with the nominal power of 210 W. The second section consists of 18 polycrystalline panels EcoDuoAUO PM220P00 (see Fig. 1) with the nominal power of 230 W. The third section consists of 10 amorphous panels Fatrasol Model 576 with the nominal power of 576 W. Photovoltaic panels are connected via four DC/AC inverters Ingecon Sun (see Fig. 2) to AC single-phase grid with nominal voltage of 230 V/ 50 Hz. This paper analyses data from the third section inverter (voltage, current, active power, power factor and frequency values) recorded during one day (14.6.2015) operation of the photovoltaic plant.

© M. Krátký, J. Dvorský, P. Moravec (Eds.): WOFEX 2015, pp. 61–66.
VŠB – Technical University of Ostrava, FEECS, 2015, ISBN 978-80-248-3787-1.

Fig. 1. Photovoltaic panels of the second section

Fig. 2. DC/AC inverters

2 Input data

Input data are downloaded from inverter control system in Excel file. This file contains 61 lines of values of DC voltage of photovoltaic panels output (U_{DC}), inverter internal DC bus voltage ($U_{DC\text{-}BUS}$), AC phase voltage (U_{AC}), DC current (I_{DC}), AC current (I_{AC}), AC active power (P_{AC}), power factor (cos φ) and frequency (f). Values

are recorded in 15 minute intervals from 5:00 to 20:00. Table below represents first 10 lines sample of the input data file.

Time	U_{DC} [V]	U_{DC-BUS} [V]	U_{AC} [V]	I_{DC} [A]	I_{AC} [A]	P_{AC} [W]	cos φ [-]	f [Hz]
5:00	240	248	237	0	0	0	1	48,51
5:15	272	348	241	0	0	0	1	49,97
5:30	268	338	209	0,03	0,14	10	0,92	39,48
5:45	254	320	219	0,09	0,27	23	0,832	43,12
6:00	245	324	238	0,1	0,37	24	0,711	50
6:15	246	323	238	0,14	0,35	34	0,812	49,99
6:30	262	320	205	0,13	0,29	32	0,857	38,95
6:45	259	323	226	0,56	0,76	136	0,868	46,46
7:00	282	326	218	1,22	1,45	322	0,965	43,54
7:15	263	326	237	3,01	3,18	741	0,994	49,99

All recorded values are represented graphically below.

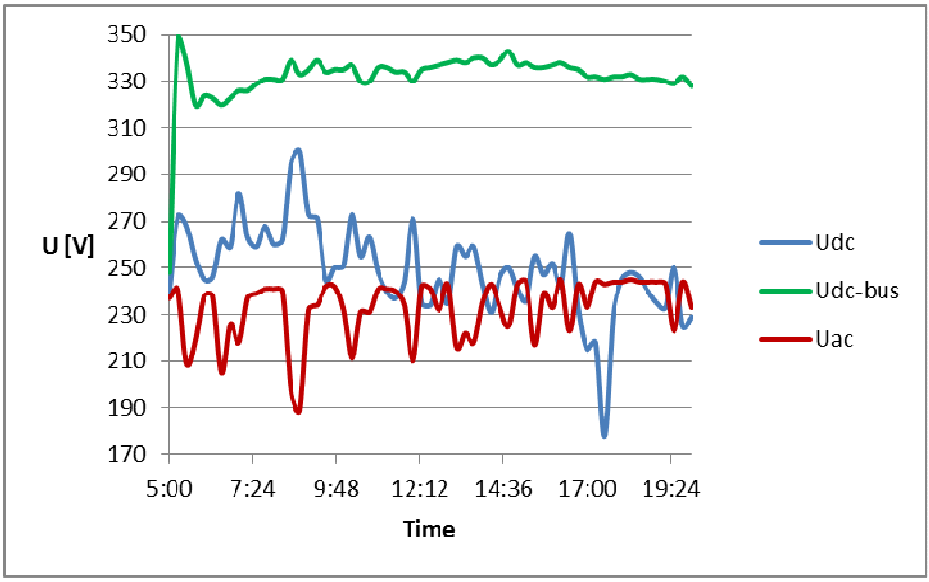

Fig. 3. Voltage graph

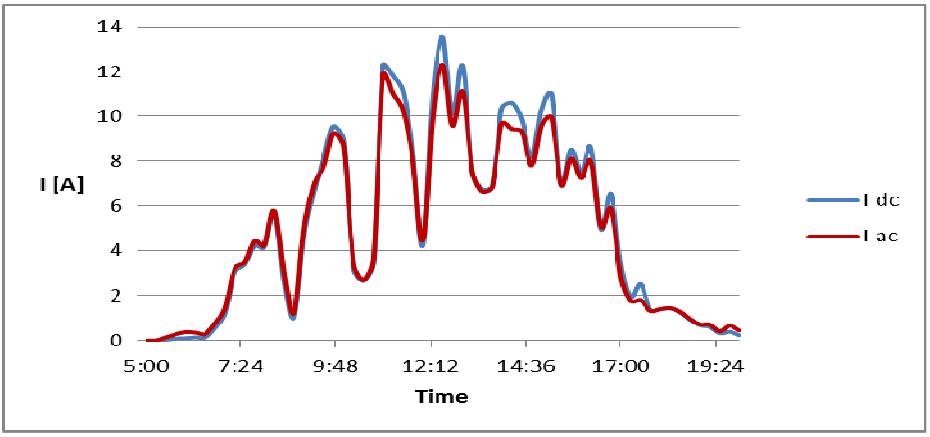

Fig. 4. Current graph

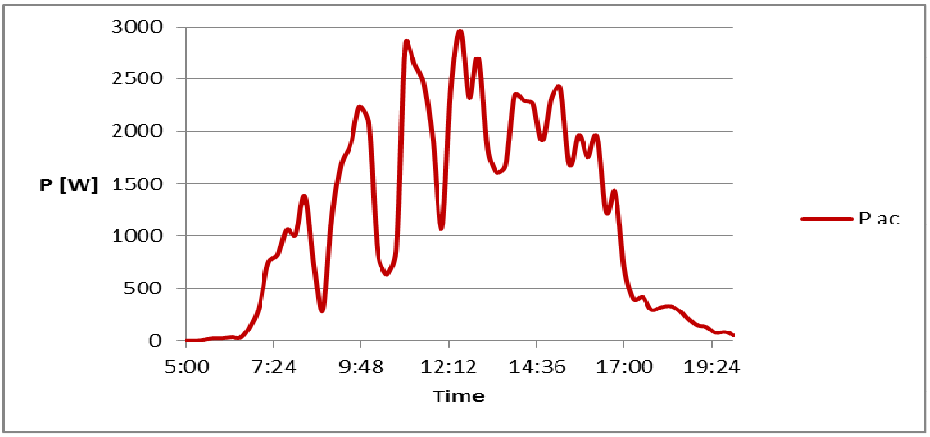

Fig. 5. Active power graph

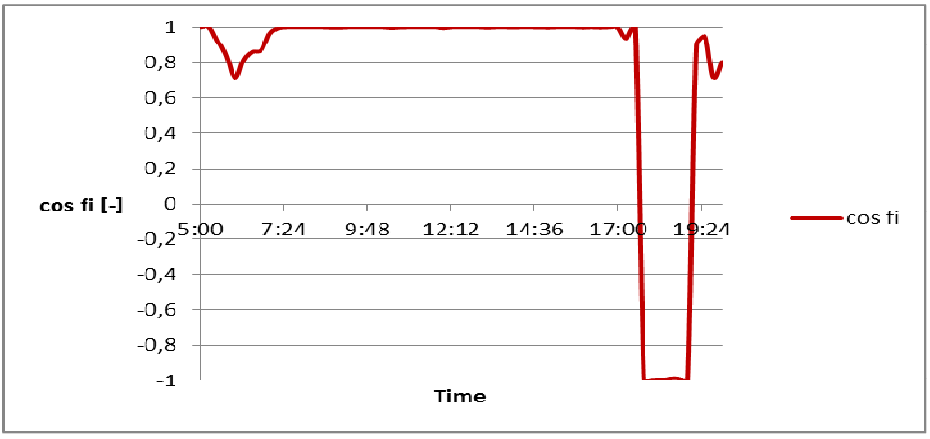

Fig. 6. Power factor graph

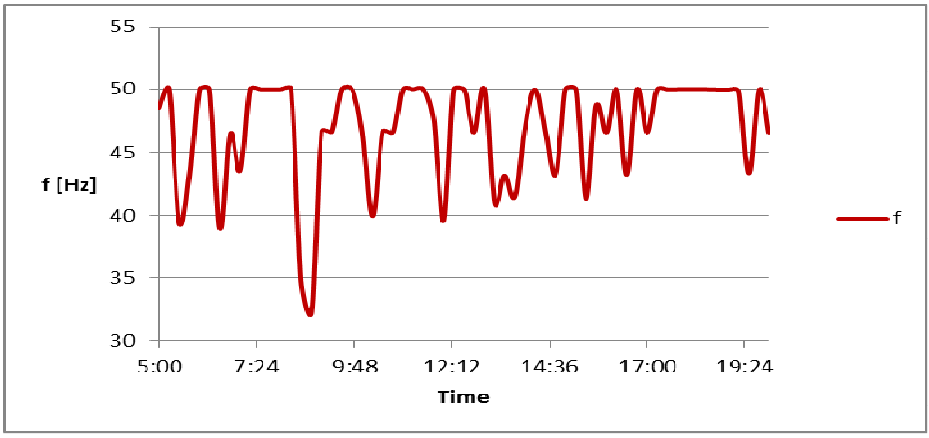

Fig. 7. Frequency graph

3 Data evaluation

DC voltage of photovoltaic panels output is varying from 178 to 300 V, inverter internal DC bus voltage is varying from 248 to 348 V and AC phase voltage is varying from 189 to 245 V. Standard ČSN EN 50160 allows voltage fluctuation ±10% U_n [1], which means allowed voltage range from 207 to 253 V. So values recorded at 6:30 (205 V), 8:30 (197 V) and 8:45 (189 V) are incompatible with this standard. DC current is varying from 0 to 13.56 A, AC current is varying from 0 to 12.32 A and AC active power is varying from 0 to 2967 W. The maximum values are recorded at 12:30. Power factor is varying from 0.711 to 1 in positive (inductive) range and from 0.986 to 0.998 in negative (capacitive) range. Minimum required power factor is 0.95, so values recorded from 5:30 to 6:45 (0.711 – 0.92), at 17:15 (0.938), at 19:15 (0.9) and from 19:45 to 20:00 (0.716 – 0.801) are incompatible with this requirement. Frequency is varying from 32.22 to 50.02 Hz. Transmission system code allows frequency fluctuation ±0.2 Hz [2], which means allowed frequency range from 49.8 to 50.2 Hz. There are many values during data recording, which are incompatible with this requirement and there's question if this values are real (in this case frequency protection must disconnect plant from grid) or if they're only measurement errors probably caused by default on Shannon theorem.

4 Conclusion

Due to above mentioned divergences between measured and required values of AC voltage, power factor and frequency, there's suitable use of an external network analyser for acquiring of more exact values and their comparison with data from inverter control system.

Acknowledgement

This work was supported by SGS grant VŠB – TU Ostrava No. SP2015/192 and by the project LO1404: Sustainable development of ENET Centre.

References

[1] ČSN EN 50160 Charakteristiky napětí elektrické energie dodávané z veřejných distribučních sítí
[2] ČEPS, a.s., Kodex přenosové soustavy, Část II. Podpůrné služby

The Basic Rules for Zebra Crossing Lighting

Tomáš Novák, Richard Baleja, and Karel Sokanský

Department of Electrical Engineering, FEECS,
VŠB – Technical University of Ostrava, 17. listopadu 15, 708 33 Ostrava – Poruba
tomas.novak@vsb.cz

Abstract. Zebra crossings are one of the most dangerous places in the road, so it is important to pay close attention to their suggestion. At present, the greatest emphasis is mainly on the lighting, which is not always realized in accordance with applicable rules and regulations. Lighting system for zebra crossings must meet the new requirements of the Ministry of Transport of Czech Republic. The paper describes criteria for solution of illumination of pedestrians on zebra crossings. Unfortunately many of zebra crossings lighting systems do not lit a pedestrian. Pedestrians see perfectly where they are stepping, but they are not seen by drivers. It is necessary to illuminate the pedestrian on the zebra crossing not only the zebra crossing itself. As a part of the article we will present well- and badly-realized zebra crossing lighting systems and their measurement. These measurements will focus on luminance maps and contrasts between pedestrians and background.

Keywords: Zebra crossing, Positive contrast, Negative contrast, Road lighting

1 Introduction

In the paper the listeners will be familiarized with the new criteria for resolving illumination of pedestrians on zebra crossings. In most cases zebra crossings are poorly illuminated. Attention is paid on illumination of the road – pedestrians see perfectly where they are stepping, but they are not seen by drivers. That is because it is neglected the crucial thing –vertical plane illumination of pedestrians.

There exist two ways to highlight a pedestrian on a zebra crossing, to ensure he will be visible:

- A negative contrast, when the pedestrian is seen like a dark figure on a light background.

© M. Krátký, J. Dvorský, P. Moravec (Eds.): WOFEX 2015, pp. 67–71.
VŠB – Technical University of Ostrava, FEECS, 2015, ISBN 978-80-248-3787-1.

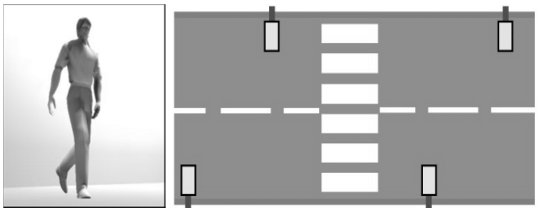

Fig. 1. A negative contrast and a way of reaching a negative contrast

- A positive contrast, when the pedestrian is seen as a light figure on a dark background.

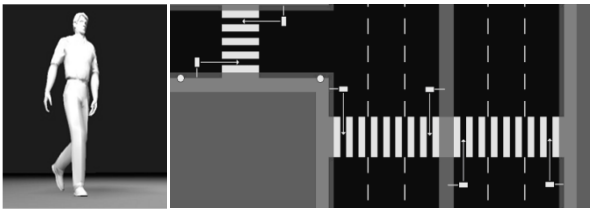

Fig. 2. A positive contrast and a way of reaching a positive contrast

2 Quantitative and qualitative requirements of iluminance of zebra crossing

A zebra crossing is divided into several sections. Each of these sections has different requirements for illumination. The basic part of a pedestrian crossing defines the space, which is located right at the crossed roads. The extended supplementary space is defined in the case of dividing each lane by central traffic island.

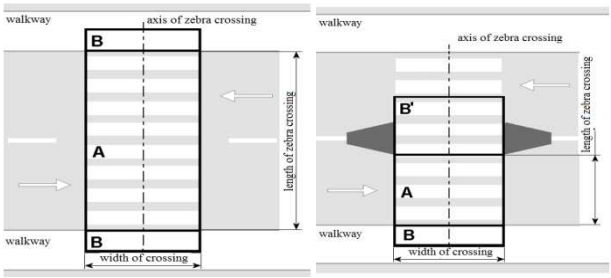

Fig. 3. Classical (to the left) and divided (to the right) zebra crossing

- A = the basic space
- B = the unextended supplementary space
- B‘ = the extended supplementary space

Table 1. Maintained average vertical illumination

Maintained value of		Average vertical iluminance (lx)		
Luminance of road (cd.m-2)	Horizontal iluminance of road (lx)	the lowest		the highest
		space		all space
		basic	supplementary	
$1.5 < \bar{L}$	$50 < \bar{E}$	Additional lighting is not required		
$1.0 < \bar{L} \leq 1.5$	$30 < \bar{E} \leq 50$	75	50	200
$0.75 < \bar{L} \leq 1.0$	$20 < \bar{E} \leq 30$	50	30	150
$0.5 < \bar{L} \leq 0.75$	$10 < \bar{E} \leq 20$	30	20	100
$\bar{L} \leq 0.5$	$\bar{E} \leq 10$	15	10	50

Table 1. shown a qualitative requirements of illuminance of zebra crossing. Maintained average vertical illuminance is prescribed for comparative vertical level at a height of 1 meter above the level of a zebra crossing. The selection is made according to the road luminance. When the luminance is unknown, the selection is based on the size of the maintained horizontal illuminance of the road.

The elongated supplementary space is quite important. It corresponds with that part of the crossing, which is located on the road itself, but it is already in the opposite direction from the point of view of a driver approaching the crossing. It is used in such case, when the pedestrian is somehow protected in the middle of the communication.

3 Situation at a zebra crossing

3.1 Good realized zebra crossing lighting systems (positive contrast)

If a pedestrian crosses the lighted zebra crossing – see Fig.4, his vertical surfaces are adequately lighted. Arriving driver can detect a pedestrian in a pedestrian crossing and also can adapt a ride to allow a pedestrian to cross the road safely. In this case the luminance of pedestrian is 2.39 cd/m2. In the comparison with the luminance of background which has the value less than 0.52 cd/m2, the luminance contrast is sufficient.

Fig. 4. Photo of zebra crossing and luminance analysis

Table 2. Evalution of good realized zebra crossing

		Luminance		
		L	Lmin	Lmax
		(cd/m2)	(cd/m2)	(cd/m2)
1	Pedestrian	2.39	0.39	10.87
2	Background	0.52	0.14	2.94
3	Crossing	2.11	0.42	4.09
Contrast (-)		3.60		

The contrast between pedestrian and background of zebra crossing is 3.60, which is a sufficient value.

3.2 Badly realized zebra crossing lighting systems (positive contrast)

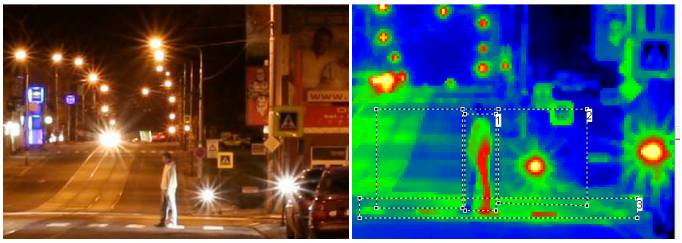

Fig. 5. Photo of zebra crossing and luminance analysis

Table 3. Evaluation of badly realized zebra crossing

		Luminance		
		L	L_{min}	L_{max}
		(cd/m^2)	(cd/m^2)	(cd/m^2)
1	Pedestrian	5.05	1.13	19.31
2	Background	3.03	0.62	139.3
3	Crossing	3.59	1.17	16.37
Contrast (-)		0.67		

The contrast between a pedestrian and a background of a zebra crossing is 0.67, which is too low value to recognize a pedestrian on a zebra crossing.

4 Conclusion

During the construction of pedestrian crossing and its lighting the issue is solved from the several points of views. We have to respect the legal requirements for the construction itself and also for the solution of lighting system.

It is necessary to combine public lighting with zebra crossing lighting together, because of good pedestrian's contrast (positive contrast is preferred) to the background. Public lighting has to prepare the appropriate value of luminance of background in front of and behind a zebra crossing. Ratio between pedestrian luminance and luminance of the background is good to be between borders 1-10.

5 References

1. EPE 2014. ISBN:978-147993806-3. Solution of lighting for pedestrian crossing to increase their visibility. Brno: EPE. Bláha Z., Novák T., Sokanský K.
2. Technické kvalitativní podmínky staveb pozemních komunikací, kapitola 15, Osvětlování pozemních komunikací, Dodatek č. 1 – Přisvětlování přechodů. Připravovaná revize TKP z roku 2006. Ministerstvo dopravy, odbor infrastruktury.
3. Bláha, Z.: Zkušenosti z návrhů osvětlení přechodů pro chodce pro ČEZ. In sborník Kurz osvětlovací techniky XXX, Ostrava, 2013, ISBN 978-80-248-3174-9
4. Lumen V4, 2014. Solution of lighting for pedestrian crossing to increase their visibility. Visegrád, Hungary: T. Maixner

Analysis of Data Measured on Co-generation Units in Biogas Station

Ladislav Novosád

Department of Electrical Power Engineering, FEECS,
VŠB – Technical University of Ostrava, 17. listopadu 15, 708 33 Ostrava – Poruba
ladislav.novosad.st@vsb.cz

Abstract. This paper deals with the measurement evaluation and power analysis of co-generation units in a particular biogas station. In the first part of the article, the measurement is described and the co-generation units which were used for measurement are stated there. Used measurement instruments are mentioned as well. In the second part of the article, the power analysis results of co-generation units in a biogas station are given.

Keywords: biogas station, power analysis, co-generation units, black out.

1 Introduction

Measurement took place in the Hraničář – Loděnice biogas station (BGS) near Opava. This BGS is equipped with four co-generation units (CGU) with a total installed electric power of 1,090kW and heat power of 1,080kW (1 x CGU: Agrogen BGA type 222–340kWe and 3 x CGU: Schnell ES 2507 type – 250kWe). Produced electric energy is then taken into a distribution board that is connected to a 0,4/22kV transformer station and using it, connected into a distribution grid of 22kV (DG).

Measurement period: 29/6/2013 (4:09am) to 5/8/2013 (8:31am) – total of 38 days
Place of measurement: RH1 BPS Loděnice distribution board

The measurement itself was conducted using an automatic digital measurement equipment MDS-U (Monitor of Distribution Grids). It is a device intended for a constant measurement of electric values (voltages, currents and power factors in low voltage/high voltage grids) and monitoring of HDO transmission. The measured values of effective phase voltages and currents were recorded in minute intervals. Counting the remaining quantities, i.e. active, reactive and apparent powers and also power factors was finished using this instrument. [2]

© M. Krátký, J. Dvorský, P. Moravec (Eds.): WOFEX 2015, pp. 72–77.
VŠB – Technical University of Ostrava, FEECS, 2015, ISBN 978-80-248-3787-1.

2 Measured Data Power Analysis

The following part shows the course of active and reactive power during the measured period. Graph no. 1 shows the course of total active power, supplied to the grid using all CGUs during the measurement period (38 days). The course of total active power P in the graph no. 1 is created by the sum of active powers in individual phases (P1 + P2 + P3).

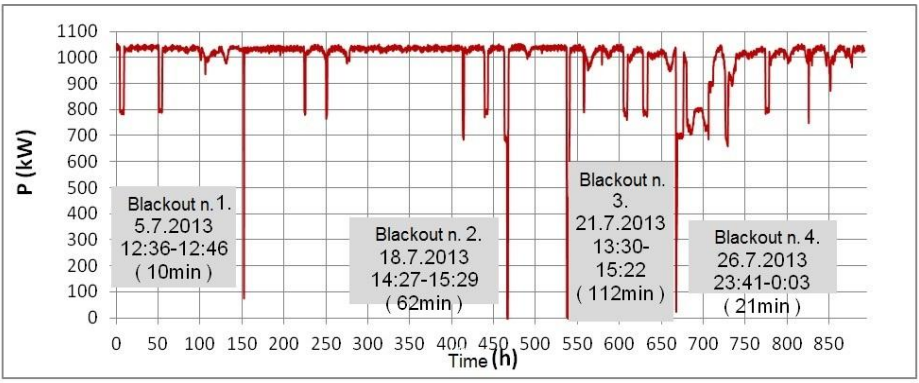

Fig. 1.: The course of the total active power of all CGUs supplied to the grid during the measurement period.

Referring to the above shown graph, it is obvious that a total of four complete black-outs occurred during the operation. The longest blackout came on 21/7/2013 at the time from 1:30pm to 3:22pm, with the power supply blackout taking 112 minutes. The total amount of time without the units not supplying any power to the grid is 207 minutes (i.e. 3 hours 27 minutes). This time takes approximately 0.387% of CGUs total operation time (892.383h). Furthermore, individual power decreases can be seen in the graph, too. This fluctuation was characterized by the active power decrease of ca. 250kW up to 300kW and by the time from the order of minutes up to several hours. The total time of these decreases was ca. 75.55 hours making it 8.466% of CGUs total operation time. In many cases, the power decrease was caused by switching one or more CGUs off. Most frequently, the switching off of one of the CGUs with the nominal electric power of 250kW occurred. The reason of blackouts or CGU switching off could not be closely clarified as the records of the BGS operation were not available. [1]

Graph no. 2 shows the histogram of total active power during the monitored period. Two smaller peaks (around the values of 721kW and 791kW) and one larger peak (ca. around the value 1,000kW) can be seen there. Therefore, it is possible to observe from the peak distribution in the histogram that the total active power supplied by all co-generation units to the grid during the measurement usually ranged around the value of ca. 1,000kW.

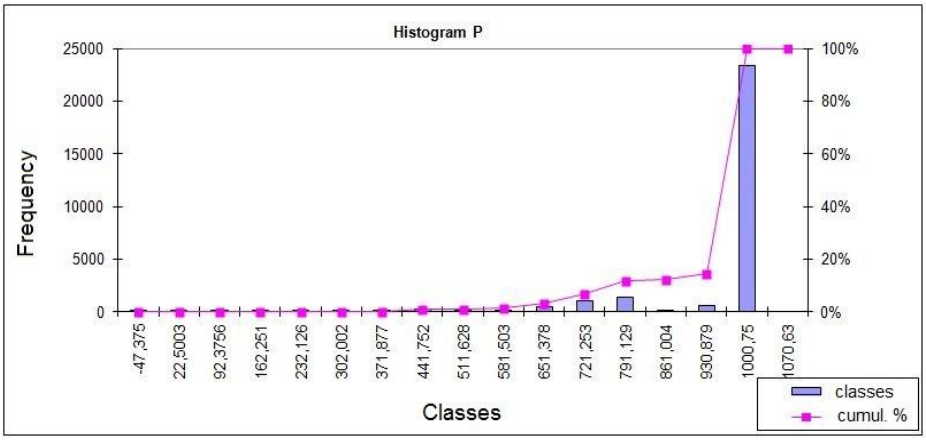

Fig. 2.: The histogram of total active power

The course of reactive power Q supply to the distribution grid is shown in Graph no. 3 and is created by the sum of reactive powers in individual phases (Q1 + Q2 + Q3), too. The reactive power was characterized by a considerably fluctuating course during the monitored period. The individual decreases of reactive power ranged approximately between 40 to 180kvar. [3]

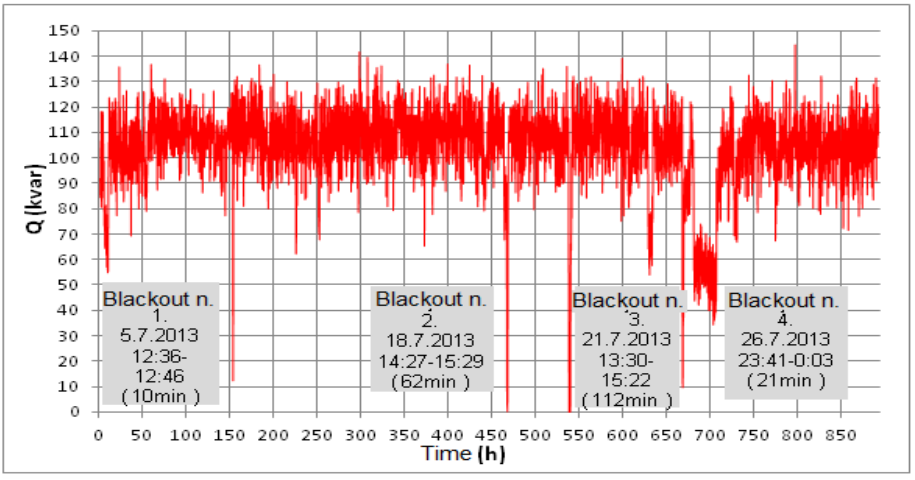

Fig. 3.: The course of the total reactive power of all CGUs supplied to the grid during the measurement period.

Regarding the fact that the value of active power in the individual phases was considerably different during the measurement, the histograms of reactive power in the individual phases are shown in the Graphs no. 4 to 6 for comparison.

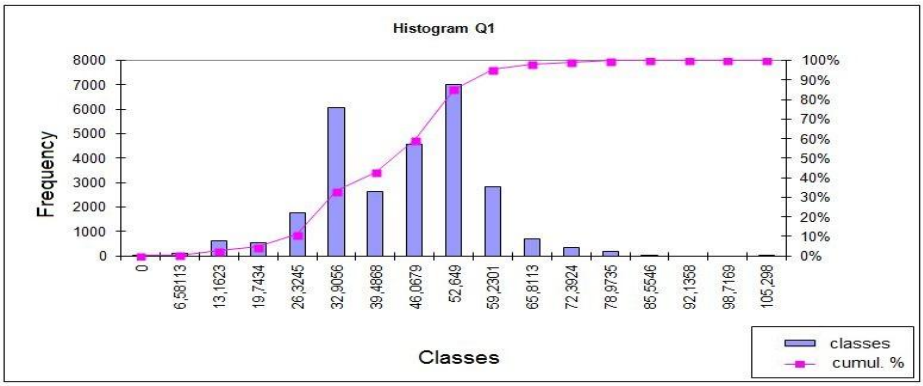

Fig. 4.: Histogram of reactive power in the 1st phase

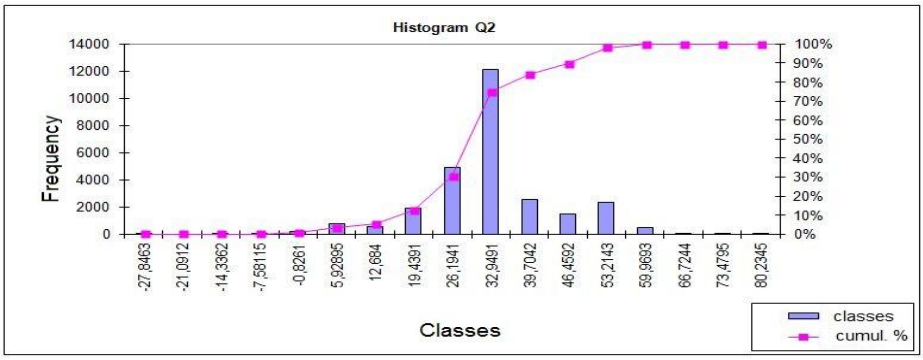

Fig. 5.: Histogram of reactive power in the 2nd phase

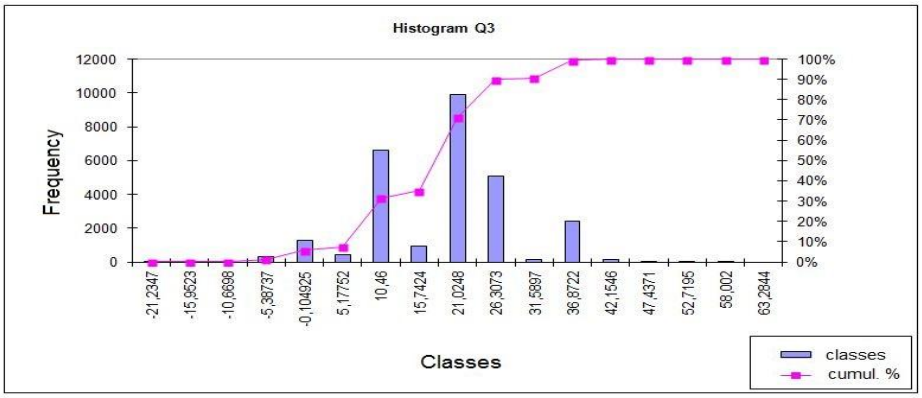

Fig. 6.: Histogram of reactive power in the 3rd phase

It can be seen from the histograms of the graphs no. 4 to 6 that the highest peaks in the 1st phase are between the values of 32kvar up to 52kvar of inductive character. In the 2nd phase, the reactive power values are concentrated mostly near the value of 32kvar of inductive character. In the 3rd phase, there are again two peaks lying ap-

proximately near the values of 11kvar and 21kvar of inductive character. Furthermore, there is one smaller peak near the value of -0.2kvar of capacity character in the 3rd phase. Different values between the individual phases can be caused by the BGS own technology or by unsuitable compensation setting.

3 Voltage Course Analysis

The following section shows the histograms of voltage in the individual phases. Regarding the supply voltage difference, any of the phases does not exceed the values stated in the relevant norm (±10%Un), corresponding to the values from the 207V–253V interval. In the graphs of all three phases, two distinct peaks appear while the second smaller of the peaks probably corresponds to the switching off of one of the CGUs and therefore, also to the decrease of supply power to the grid. Moreover, a small voltage asymmetry can be observed in the individual phases. This asymmetry manifests itself by increased voltage in the 1st phase approximately by 1–2V.

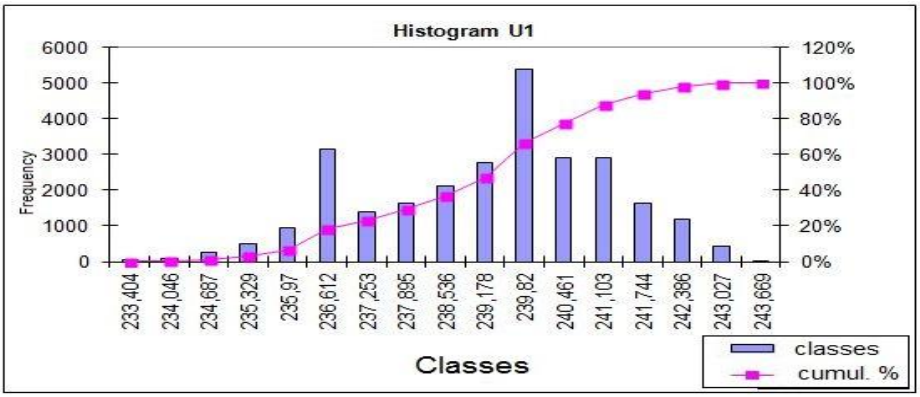

Fig. 7.: Histogram of voltage in the 1st phase

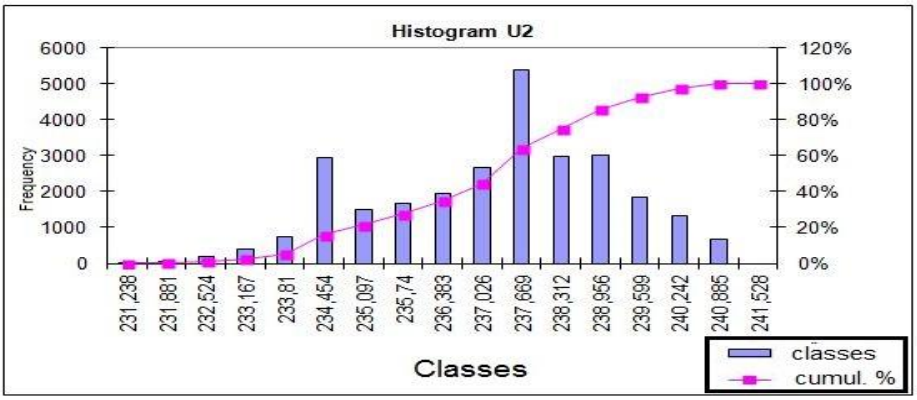

Fig. 8.: Histogram of voltage in the 2nd phase

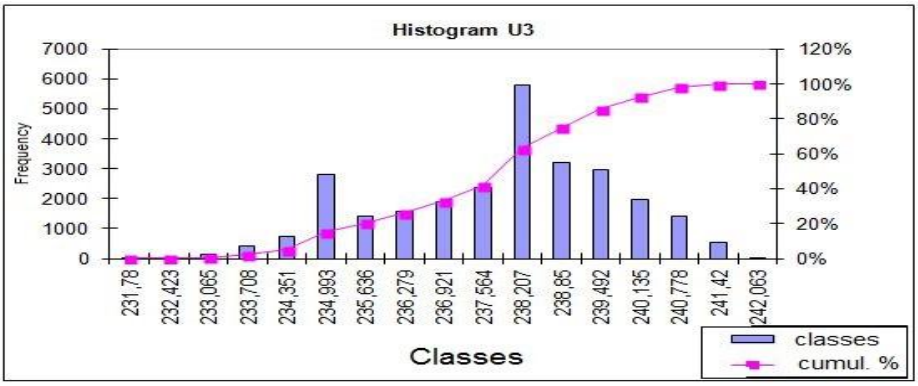

Fig. 9.: Histogram of voltage in the 3rd phase

4 Conclusion

This article is concerned chiefly with the analysis of power and voltage of the CGU in the Loděnice BGS. The main goal of the measured data analysis was to create a comprehensive notion about electric energy supply from BGS. Referring to the measured data or the created courses, it is possible to state that this biogas station is a stable and to a certain extent predictable electric energy source. From the operation and management point of view, the biogas station can be classified as a flexible and dynamic energy source. These sources should be able to accommodate to e.g. the stochastic courses of photovoltaic and wind power plants. Furthermore, this article serves as a source of information about the stability of powers from co-generation units for a possibility of further research. The research will deal with the cooperation of other renewable sources of electric energy and thus provide opportunities for 22kV grids supply stabilization.

References

1. L. Novosád, "Využití biomasy jako akumulační zdroj energie pro tepelné a elektrické sítě." 2014. Diplomová práce. Vysoká škola báňská - Technická univerzita Ostrava. Fakulta elektrotechniky a inf.. Vedoucí práce prof. Ing. Zdeněk Hradílek, DrSc.
2. J. Janša, Z. Hradílek, P. Moldřík, "Biogas station – operating measurement of electrical quantities", Proceedings of the 10th Workshop ELNET 2013, FEECS, VŠB - Technical University of Ostrava, 2013, ISBN 978-80-248-3254-8
3. L. Novosád, Z. Hradílek, "Power analysis of co-generation units at biogas station", Proceedings of the 16th International Scientific Conference on Electric Power Engineering (EPE) 2015 Dlouhé Stráně, 2015, ISBN 978-1-4673-6788-2

Evaluating Traction Currents at Electric Traction Stations

Jiří Plaček

Department of Electrical Engineering, FEECS,
VŠB – Technical University of Ostrava, 17. listopadu 15, 708 33 Ostrava – Poruba
jiri.placek@email.cz

Abstract. This paper describes the effects of currents caused by electrified railways. One of the main problems of DC railway electrification is electro-chemical corrosion. This paper sums up some theoretical knowledge about this problem. The author describes protective measures aimed to reduce the effects of stray currents. The most significant source of stray currents is the railway track, which is electrified by a DC system, where rails serve as overhead wires and part of the total reverse current flows through the ground. This is mainly due to the fact that the insulation of metal and reinforced concrete structures from the ground is not sufficient. For this reason, storage devices may lead current of a significant intensity, up to tens of amperes. Based on Faraday's Law, it may be deduced that in the course of one year, 1 A stray current will cause electro-chemical corrosion leading to the loss of 9.1 kg of iron at each current output. Stray currents are currents flowing through a conductive environment (e.g. soil, water or a storage device). Stray currents originate in electrical equipment that has not been sufficiently insulated from the environment, or when the ground is used as an overhead wire. Stray currents are divided into DC and AC.

Keywords: Stray current, electrochemical corrosion, storage devices, ground current fields; anti-corrosion protection

1 Introduction

Artificial ground current fields and their origin are closely linked to the origin of stray currents. Stray currents are currents which leak into the ground from a wire that is insufficiently insulated from the ground, or from a device which uses the ground as an overhead wire. These currents create ground current fields, which are the most dangerous because they lead to electro-chemical corrosion of storage devices. DC currents always flow along the path of least resistance. Depending on soil conductivity, they may spread within hundreds of metres or even kilometres from the line through which they were supposed to flow. The less conductive the soil, the farther they reach. On the other hand if the soil has a good conductivity, the reach is not so long.

Stationary current field distribution is characterised by the continuity equation. This equation states that the sum of currents flowing in and out through an enclosed

© M. Krátký, J. Dvorský, P. Moravec (Eds.): WOFEX 2015, pp. 78–83.
VŠB – Technical University of Ostrava, FEECS, 2015, ISBN 978-80-248-3787-1.

area around a certain object will appear as a time change of the charge contained in this volume.

Just like Maxwell's equations, this one is valid for all spatial points where J is a continuously differentiable function of the coordinates (1) and ρ is a continuously differentiable function of the coordinates and time (2).

$$\oiint_S \bar{J}\,\overline{\mathrm{d}S} = \frac{-\mathrm{d}Q}{\mathrm{d}t} \qquad (1)$$

$$\mathrm{div}J = -\frac{\partial \rho}{\partial t} \qquad (2)$$

$$\mathrm{div}J + \frac{\partial \rho}{\partial t} = 0 \qquad (3)$$

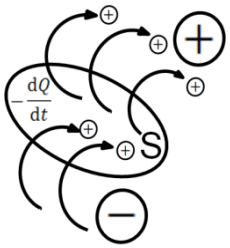

Fig. 1. Surface representation for [1] continuity equation

In a stationary current field, div J = 0, because at any given moment, charge flows in and out of every enclosed area.

$$\oiint_S \bar{J}\,\overline{\mathrm{d}S} = 0 \qquad (4)$$

In a stationary current field, continuity equation can be defined in the form of First Kirchhoff's Law.

$$\oiint_S J\,\mathrm{d}s = 0 = J_1S_1 + J_2S_2 + J_3S_3 + \ldots J_nS_n = I_1 + I_2 + I_3 + \ldots I_n = \sum I = 0 \qquad (5)$$

Equipotential Surface

An equipotential surface is characterised by a constant potential value. If charge moves along any given trajectory between two points of the same equipotential surface, no work needs to be performed by the electric field. This can be clearly seen in Relationship (6], which is going to be presented here for voltage.

$$U = \varphi_i - \varphi_f = -\frac{W}{Q} \qquad (6)$$

If $\varphi_i = \varphi_f$ then W=0.

It is obvious from the equation that no work needs to be performed by electrical forces to move a charged particle along an equipotential surface. This makes it possible to conclude that the E vector must be perpendicular at any point of the equipotential surface.

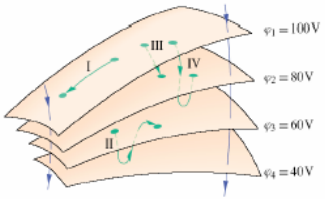

Fig. 2. Parts of four equipotential surfaces [1]

Fig. 2 shows several equipotential surfaces in an electrostatic field. When moving a charged particle from the starting point along Trajectories I or II, work performed by this field is equal to zero because, as it is shown in the picture, both trajectories begin and end on the same equipotential surface. This changes when charged particles are moved from starting point to final point along Trajectories III and IV, where work needed to move the charged particle is non-zero and besides identical in both cases. It is identical because potential values at the starting and final points of both trajectories are also identical.

2 Measurement on a Selected Segment of Traction Equipment

The segment which I have chosen for measurement belongs to Ostrava City tram tracks, which have a total length of 66.7 km. This segment is located on a single-rail track between the Zátiší and Vřesinská loops. This particular segment is 9.030 m long and the track is the only interurban tram track in the Ostrava region.

The tram track between the Poruba - Vřesinská and Zátiší loops is powered by two traction substations, in Vřesina and Dolní Lhota. The segment on which our measurement was performed is normally powered in a different way, but when we performed the measurement, it was switched to replacement power, preceded by short circuit tests, to ensure that the powered track segment was resistant to short circuits. During the measurement, the track segment was powered by the traction substation.

2.1 Selecting Measuring Location and Performing the Measurement

Based on measurement optimisation, suitable places were selected near the track, where it was possible to perform this measurement. There were six stations altogether.

Measurement on Location A.

Portable Cu/CuSO4 reference electrode was located near the rectifier substation to measure + polarity. A feedback bus leading from the rails back to the substation was used to measure – polarity.

Measurement on Locations B, C, D, E and F

The author performed a measurement at these measuring points to find out drop on both rails. For the actual measurement, measuring;g terminals were located within 4.8 m from each other. With the use of the measuring apparatus described above, the author measured voltage between rails and the potential of the ground against the rails.

The portable Cu/CuSO4 reference electrode was located within 40 m distance from the rails.

3 Evaluating the Obtained Data at Resistive Load

To evaluate this stray current related measurement, I used resistive load at the Zátiší loop, i.e. there was a constant current consumption for a certain period of time. In the course of this measurement, values were recorded on all five locations. The number of evaluated measurements at a constant current consumption was n = 942, from 13:14 to 13:22 p.m. Graph 1 shows waveforms measured at balanced resistive load, at the Zátiší loop.

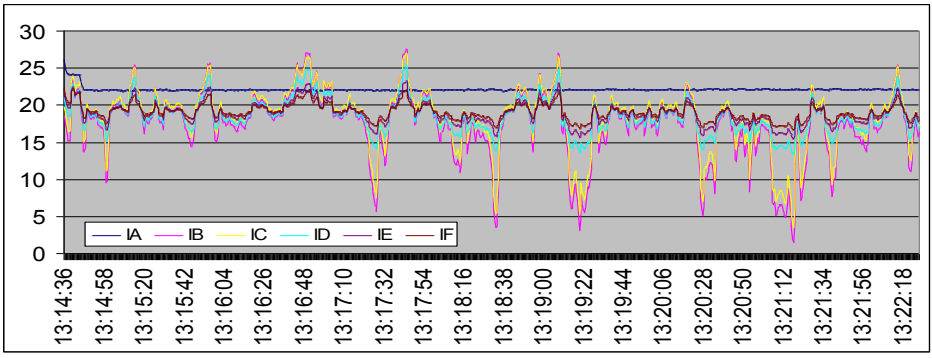

Graph 1. Current waveforms at resistive load, Zátiší loop

After that, the measurement was evaluated in Excel (see Table 1).

Table 1. Evaluation of the recorded data

	IA	*IB*	*IC*	*ID*	*IE*	*IF*
Stř. hodnota	22,10	17,46	18,34	18,50	18,89	19,07
Chyba stř. hodnoty	0,01	0,14	0,13	0,07	0,04	0,03
Medián	22,06	18,16	19,04	18,45	18,83	19,02
Směr. odchylka	0,32	4,52	4,04	2,28	1,49	1,05
Rozptyl výběru	**0,10**	**20,44**	**16,32**	**5,23**	**2,24**	**1,10**
Špičatost	57,22	1,09	1,34	0,09	0,03	0,17
Šikmost	7,14	-0,89	-1,03	0,33	0,33	0,39
Rozdíl max-min	4,26	26,09	23,45	12,07	7,78	5,66
Minimum	21,82	1,51	3,55	13,31	15,52	16,70
Maximum	26,08	27,60	27,00	25,38	23,31	22,36
Součet	20819	16449	17280	17435	17797	17965
Počet	942	942	942	942	942	942
Hladina spolehlivosti (95,0%)	0,02	0,28	0,25	0,14	0,09	0,06
	od	do				
942 měření	13:14:36	13:22:26				

By further analysis, it was found out that the obtained data showed variation even for the slightest currents. Even for the smallest consumption, there were differences between individual measured currents, e.g. the minimum is 1.5 A for Ib and 3.5 A for Ic. There were variations at the other locations as well, but it is obvious that the next highest average current after the substation is If, followed by Ie, Id, Ic and Ib, where it reached its lowest level.

Current values at different locations

I = (average value +- the absolute value of the variation

Ia = (22,101 +- 0,104) A; Ib = (17,462 +- 3,281) A; Ic = (18,344 +- 2,899) A;

Id = (18,509 +- 1,783) A; Ie = (18,893 +- 0,169) A; If = (19,072 +- 0,814) A

Ia current was measured at the substation with the use of a clamp ammeter, and for this reason its waveform is recorded differently than the other waveforms in the graph.

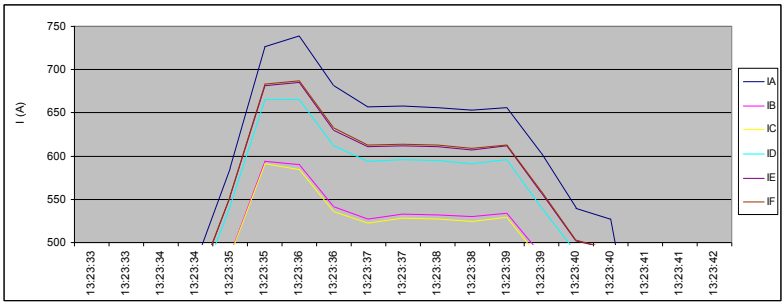

Graph 2. Evaluating current at the Zátiší loop; the highest current value was recorded for the substation (Ia), followed by If, Ie, Id, Ib and Ic.

The graph for 13:23:13 – 13:23:42 shows clearly that when traction vehicles are powered, current values are highest at the substation. Before the current reaches the end of the track, stray currents spread into the environment, as the value at the end of the measured segment is the second largest, right after the substation (Ia). Current value for Ic is slightly smaller than for the final point Ie. The least current flows through Ib and Ic, i.e. the points closest to the substation.

Current values from the highest to the lowest: Ia, If, Ie, Id, Ib, Ic.

4 Conclusion

This paper deals with current measurement at different locations of a traction equipment segment, demonstrating the influence of electrified vehicles on storage devices. It describes certain problems related to ground current fields as well as current measurement on traction equipment.

The measurement was performed, recording current as it flows from the substation through the individual locations. Current recordings for a certain time interval are presented in the form of graphs. Evaluation in graphs was performed within the same distance from the Vřesina substation.

The measured waveforms show a significant influence of stray currents. This unfavourable state is due to the fact that before the measurement was performed, the system by which the track was powered was changed. As a result, strong stray currents were found near the powered track segment, especially due to the great length of the segment without overhead cables. If this segment was supposed to be powered by the Vřesina substation very often, additional protective measures should be taken to avoid the risk of disturbing the reinforcement of reinforced concrete structures, cracks in concrete surfaces or even people getting hurt near traction devices.

The aim of this paper is to sum up and present the most important theoretical information related to this issue. This information may successfully be used in practice.

5 References

[1] FEYNMAN R. P., LEINGHTON R. B., SANDS M.: Feynmanovy přednášky z fyziky s řešenými příklady 2/3, 2001 Havlíčkův Brod: Nakladatelství Fragment, 806 s., ISBN 80-7200-420-4

[2] PALEČEK Josef: Napájení jednofázové vozby Českých drah z hlediska elektromagnetické kompatibility. Vyd. 1. Ostrava: VŠB - Technická univerzita Ostrava, 2000, 98 s. ISBN 80-707-8791-0

[3] V. KOLÁŘ, J. PALEČEK, T. MLČÁK, "Vliv provozu vodní elektrárny Lipno na kvalitu elektrické energie v souvislosti s trakčním odběrem," (The Influence of the Lipno Hydro Power Plant Operation on the Quality of Electric Energy in Connection with Traction Consumption) Electric Power Engineering 2012, Brno, 2012

[4] V. KOLÁŘ, R. HRBÁČ, Measurement of ground currents leaking from DC electric traction, 15th International Scientific Conference on Electric Power Engineering (EPE) 2014, p.p. 613-617, ISBN: 978-147993806-3, Brno, 2014

[5] ČSN EN 50122-2, Drážní zařízení - Pevná trakční zařízení: Část 2: Ochranná opatření proti účinkům bludných proudů, způsobených DC trakčními proudovými soustavami, Červenec 2001, Praha: Český normalizační institut, 2001.

[6] ČSN EN 50122-1 ed.2, Drážní zařízení-Pevná trakční zařízení-Elektrická bezpečnost, uzemňování a zpětný obvod: Část 1: Ochranná opatření proti úrazu elektrickým proudem, Listopad 2011, Praha: Úřad pro technickou normalizaci, 2011.

Measurement on the biogas plant Hodoňovice

Michal Špaček

Department of Electrical Power Engineering, FEECS,
VŠB – Technical University of Ostrava, 17. listopadu 15, 708 33 Ostrava – Poruba
michal.spacek.st2@vsb.cz

Abstract. This article deals with the evaluation of measured operating electrical quantities of biogas plants. The introduction describes the technology of biogas plants and involvement in the distribution network. The third part will evaluate the measured data with the application of mathematical and statistical methods in their final evaluation. The greatest emphasis is placed on evaluating the quality of supply. Another important process parameter is the total active power of everybody cogeneration units supplied into the grid of 22 kV. In conclusion, the evaluation of the quality of electricity supply according to DIN EN 50 160. Furthermore, it is evaluated from the perspectives of outages cogeneration unit.

Keywords: cogeneration unit, biogas plant, GE Jenbacher, BK ENA 330

1 Introduction

The biogas plant has a total installed electrical power of 1186 kW. All produced biogas is burned in cogeneration units with an internal combustion engine. All CHP units from one manufacturer GE Jenbacher. The production plant is made up of unit JGS 312 GS-B.LC 1x549 kW unit JGS 312 GS-B.LC 1x637 kW. The production plant is connected to the overhead line voltage 22 kV. Electrical power from cogeneration units with a voltage level of 400 V is transformed to 22 kV using a transformer with an output of 1,250 kVA, which is located in the kiosk. Connecting the transformer is DYN1. [1]

This research was partially supported by the SGS grant from VSB - Technical University of Ostrava (No. SP2015/192) and by the project LO1404: Sustainable development of ENET Centre.

© M. Krátký, J. Dvorský, P. Moravec (Eds.): WOFEX 2015, pp. 84–89.
VŠB – Technical University of Ostrava, FEECS, 2015, ISBN 978-80-248-3787-1.

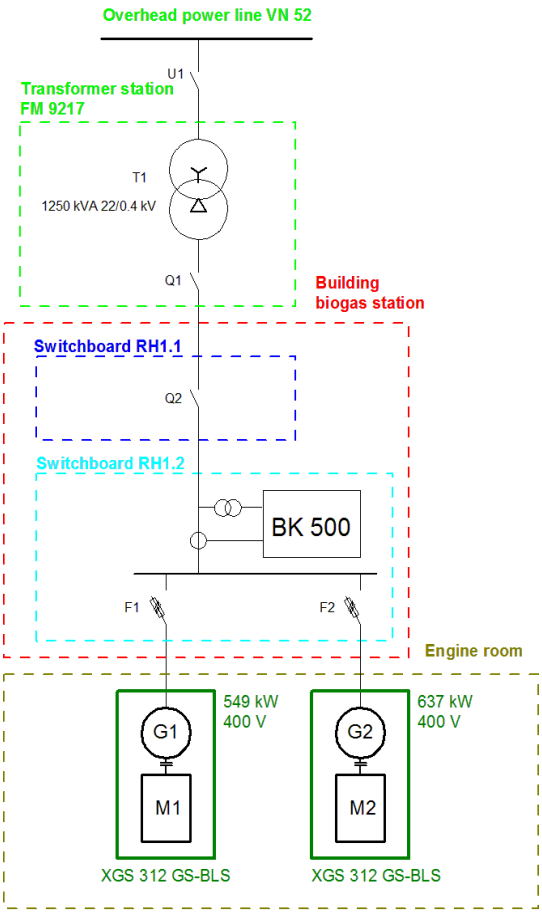

Fig. 1. Wiring diagram of cogeneration units to the grid

2 Measurement using BK ENA330 analysis

Measurements were made at the end of summer and the beginning of September in the summer of 2014, from August 20, 2014 to September 19, 2014, after a period of 31 days. Measurements were performed using the automatic operation of digital measurement equipment BK ENA 330 from manufacturer Elcom. ENA330 model is a compact power quality analyzer without display. The unit is equipped with four voltage and current inputs. ENA330 analyzer meets the requirements of standard EN 61000-4-30 for a class "A" voltage is measured directly on the bus in the switchboard and streams with flexible Rogowski coils - Ampflex. Measuring devices BK ENA 330 were connected in rozvači RH 1.2 BPS Hodoňovice (Figure 1). Interval recording (sampling frequency) was recorded after 1 minute. [2]

3 Evaluation of the measured data

During the measurement, the received a total of 44,640 lines corresponding to the recording sampling frequency of one minute after the time of 31 days. Measured data was assessed using the BK ELCOM 2.9 Report. Which meets all the requirements according to DIN EN 50160. When evaluating measured data were evaluated voltage drops in the network. Another evaluation parameter was the supply of electric power from cogeneration units. For this parameter will evaluate the progress of the power consumption and downtime for the measured period. Finally, the evaluation of quality power factor that corresponds to reactive power.

4 Electric output

The graph in Figure 2 presents the overall course of active power during operation of cogeneration units for the entire 31 days of measurements. Power (P) is the sum of the active power in each phase (P1 + P2 + P3). The graph (Figure 3) shows that for the duration of one measurement is a power failure and, on September 13, 2014 for a total duration of 13 minutes. Figure 3 shows a detailed view of the power failure of 13 September 2014 when the failure occurred during the 8:46 p.m. to 9:59 p.m.

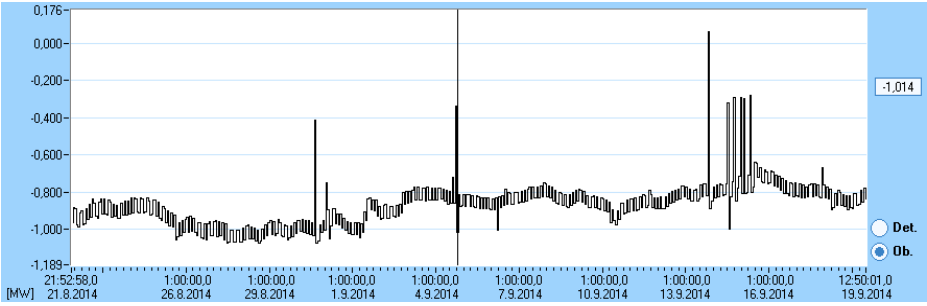

Fig. 2. The total active power supplied by all CHP (for the period from August 20, 2014 do 19 September 2014)

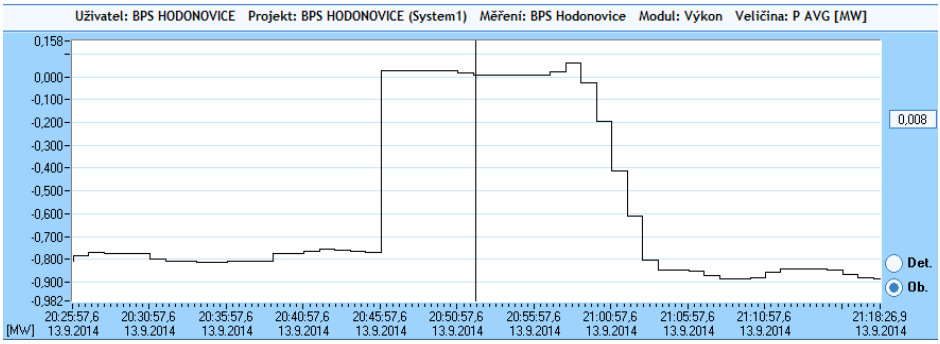

Fig. 3. Detail of failure of the active power supplied by all CHP September 13, 2014

5 Voltage measurement

If variations in the supply voltage (in all three phases) do not exceed the limits of ± 10% U_n corresponding to values in the range of 207-253 V satisfy the standard. Figure 4 shows the histogram of the voltage of each phase, Frequency dependence of the voltage in each class (value range).

Figure 4 shows histograms voltage for each phase. All phases are almost identical with the mean value with a margin of + 234,2V ±4,5V. Voltage waveform in phase L1 is displayed in red, phase L2 is blue and the L3 phase is green. Detailed voltage waveform is shown in Figure 6 on 4 September of 2014. Chosen was working day and 9:00 to 2:00 p.m. because of the observed voltage drops. The figure shows that about 11:00 to 12:30, there was an increase voltage. This was caused by reduced collection of electrical power which has strong links to the lunch break, when the firms are switched off major appliances. [3]

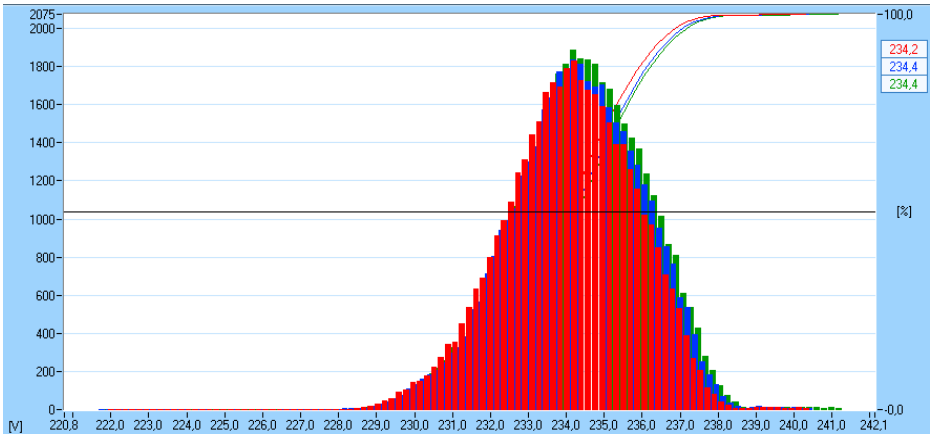

Fig. 4. Histogram of the total voltages measurement

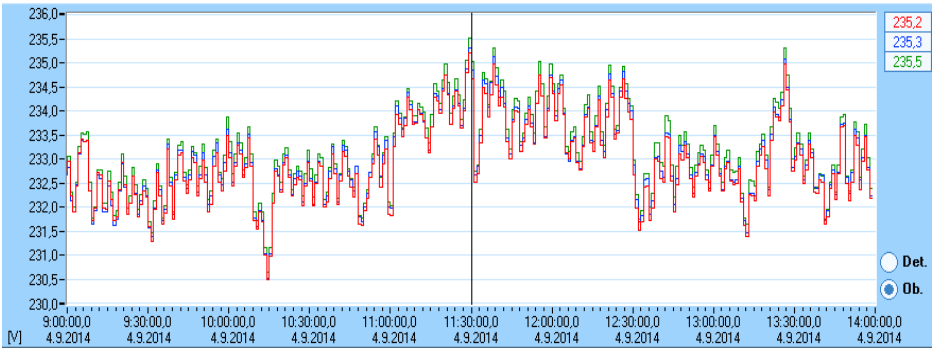

Fig. 5. Detailed voltage waveform of September 4, 2014 9:00 to 2:00 p.m.

6 Power factor measurement

The power factor is varied during measurement at all stages in the range from 0.989 to 1, and in more than 95% of cases. The exception was a power supply active power. Figure 6 shows a detail of the power factor of 4 September 2014. It was elected 9:00 to 2:00 p.m., and observing the performance changes. The biggest change over the power factor in phase L1 (drawn red line). The smallest are the stages of L2 and L3 (blue and green). During phase L3 (green line) is clearly visible that covers the course of phase L2 (blue curve). These curves are almost identical. [4]

Reactive power supplied for the overall measurements oscillated around the mean value of 25 kvar to 200 kvar deviation (range + 44 'inductive' to -18 kvar "capacity"). Figure 7 is shown in detail during the reactive power.

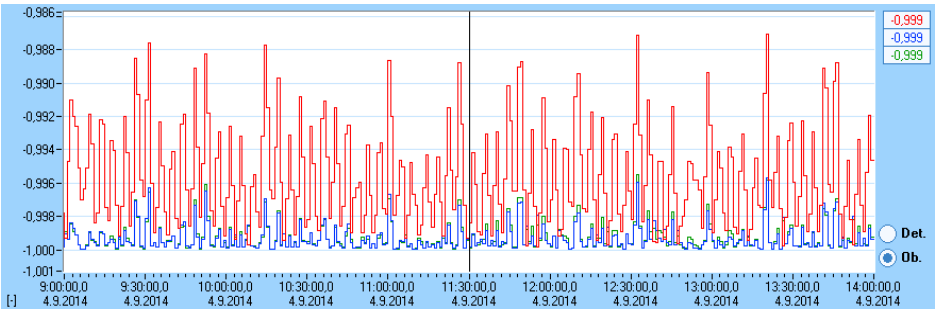

Fig. 6. Detail of the power factor in each phase of September 4, 2014 9:00 to 2:00 p.m.

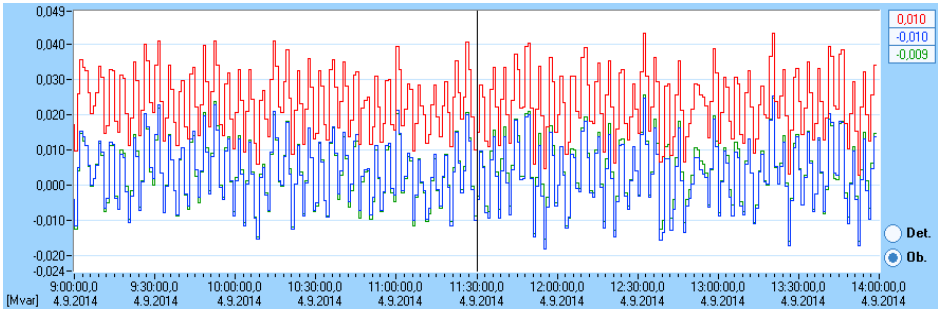

Fig. 7. Detail of reactive power in each phase of September 4, 2014 9:00 to 2:00 p.m.

7 Conclusion

In the context of this article were summarized interim results of research into the study of the impact on the quality of biogas voltage 22 kV distribution network. Over the entire period of measurement respond voltage range the indicated norm ČSN EN 50 160. From the measured data results high reliability of power to the grid (time outages is 0,029% of operating hours). The supply of electric output from biogas-fired cogeneration units can generally say that it is very stable. Most often affected by this power quality supplied biogas (methane percentage of CH_4 in biogas). Which has strong links to the quality of primary (organic) product.

References

[1] E. Dvorský, The combined production of electricity and thermal energy. 1. vyd. Praha: BEN technical literature, 2005, 286 s.

[2] J. Krbek, L. Ochrana, B. Polesný, Heating and cogeneration. 1. vyd. Brno: Academia, 1999, 141 s.

[3] Z. Hradílek, Elektroenergetika průmyslových a distribučních zařízení. 1. vyd. Ostrava: Academia, 2008, 315 s.

[4] Pravidla provozování distribučních soustav. [online]. 2015 [cit. 2015-08-09]. http://www.czrea.org/files/pdf/pravidla_ds.pdf

Simulation of Sliding Mode Observer in Speed Control Structure of Induction Motor Drive

Chau Si Thien Dong

Faculty of Electrical and Electronics Engineering, Ton Duc Thang University
Nguyen Huu Tho Street, Tan Phong Ward, District 7, Ho Chi Minh City, Vietnam
dongsithienchau@tdt.edu.vn

Abstract. The control of induction motor drives constitutes a vast subject, and the technology has further advanced in recent years. In control algorithms, continuous rotor position is mandatory. But the presence of encoder increases cost, reduces reliability. Therefore, elimination of this sensor is desirable. A sensorless of the vector controlled induction motor means the vector control without using any speed sensor. Speed is estimated using sophisticated techniques. Although the sensorless control is required in whole operation area of the induction motor drive, there are problems due to parameters variation, particularly near zero speed, which impose a challenge in the accuracy of the speed estimation. In the paper, there is a focus on basic theory of a sliding mode observer and its application in the sensorless control of the induction motor drive. The mathematical description and simulation results are presented in the paper.

Keywords: induction motor, vector control, speed control, sensorless control, sliding mode observer.

1 Introduction

Induction machines are used widely in practice. These machines are very economical, rugged and reliable. For the control of the induction motor, it is required rotor magnetic flux and rotor speed of the induction motor. The rotor magnetic flux and motor rotor speed can be provided by Hall sensors and encoder. Using these sensors implies more electronics, high cost, lower reliability, etc. The rotor speed and magnetic flux are estimated by using different types of observers such as MRAS observer, Kalman filter, Luenberger observer, and sliding mode observer (SMO).

However, the control and estimation of important quantities of AC drives with induction motors is difficult because of variable frequency of a supply stator phase voltages realized by frequency converters, complex dynamics of AC machines, machine parameters variations, and signal processing of feedback signals [1], [2].

In modern control techniques for induction motor (IM) with high dynamic requirements the speed transducer such as tachogenerator, resolver or mainly digital shaft position encoder are used to obtain speed information. These sensors are sources of trouble, mainly in hostile environments. The main reasons for the development of sensorless drives are: reduction of hardware complexity and cost, increased mechani-

© M. Krátký, J. Dvorský, P. Moravec (Eds.): WOFEX 2015, pp. 90–95.
VŠB – Technical University of Ostrava, FEECS, 2015, ISBN 978-80-248-3787-1.

cal robustness, higher reliability, working in hostile environments, lower maintenance requirements. Removing rotor position sensors or mechanical speed sensors from a control structure of electrical drive leads to so-called sensorless electrical drive, which naturally requires the sensors for the monitoring of stator currents and voltages.

The main objective of the sensorless control is to find an estimated position of the rotor and the mechanical angular velocity which is used for the vector rotation of the variables and for a speed feedback loop.

2 Mathematical model of the induction model

To analysis and control induction motor, the dynamic model of induction motor is defined. The dynamic of the induction motor is very complex because the three – phase rotor windings move with respect to the three – phase stator windings. The differential equations of an induction model are very complicated. However, it is much simpler by representing a three – phase machine by an equivalent two – phase machine. High performance control, such as vector control, is based on a dynamic model of the induction motor expressed in a rotating coordinate system which is oriented on the rotor magnetic flux vector.

State space equations which describe of the induction motor are written as follows:

$$\frac{d}{dt}\mathbf{x} = \mathbf{A}\cdot\mathbf{x} + \mathbf{B}\cdot\mathbf{v} \tag{1}$$

$$\mathbf{y} = \mathbf{C}\cdot\mathbf{x} \tag{2}$$

$$\mathbf{x} = \begin{bmatrix} i_{S\alpha} & i_{S\beta} & \psi_{R\alpha} & \psi_{R\beta} \end{bmatrix}^T \quad , \quad \mathbf{v} = \begin{bmatrix} v_{S\alpha} & v_{S\beta} \end{bmatrix}^T \tag{3}$$

$$\mathbf{A} = \begin{bmatrix} a_{11} & a_{12} & a_{13} & a_{14} \\ a_{21} & a_{22} & a_{23} & a_{24} \\ a_{31} & a_{32} & a_{33} & a_{34} \\ a_{41} & a_{42} & a_{43} & a_{44} \end{bmatrix} \quad , \quad \mathbf{B} = \frac{1}{\sigma L_S}\begin{bmatrix} 1 & 0 \\ 0 & 1 \\ 0 & 0 \\ 0 & 0 \end{bmatrix} \quad , \quad \mathbf{C} = \begin{bmatrix} 1 & 0 & 0 & 0 \\ 0 & 1 & 0 & 0 \end{bmatrix}. \tag{4}$$

$$a_{11} = -\frac{L_h^2 R_R + L_R^2 R_S}{\sigma L_S L_R^2} \ , \ a_{12} = 0 \ , \ a_{13} = \frac{L_h R_R}{\sigma L_S L_R^2} \ , \ a_{14} = \frac{L_h}{\sigma L_S L_R}\omega_r \tag{5}$$

$$a_{21} = 0 \ , \ a_{22} = -\frac{L_h^2 R_R + L_R^2 R_S}{\sigma L_S L_R^2} \ , \ a_{23} = -\frac{L_h}{\sigma L_S L_R}\omega_r \ , \ a_{24} = \frac{L_h R_R}{\sigma L_S L_R^2} \tag{6}$$

$$a_{31} = \frac{L_h R_R}{L_R} \ , \ a_{32} = 0 \ , \ a_{33} = -\frac{R_R}{L_R} \ , \ a_{34} = -\omega_r \tag{7}$$

$$a_{41}=0\ ,\ a_{42}=\frac{L_h R_R}{L_R}\ ,\ a_{43}=\omega_r\ ,\ a_{44}=-\frac{R_R}{L_R}\ ,\ \sigma=1-\frac{L_h^2}{L_S L_R}. \tag{8}$$

where $i_{S\alpha}$, $i_{S\beta}$ – stator current vector components in [α, β] stator coordinate system; $v_{S\alpha}$, $v_{S\beta}$ – stator voltage vector components in [α, β] stator coordinate system; $\Psi_{R\alpha}$, $\Psi_{R\beta}$ – rotor magnetic flux in [α, β] stator coordinate system; L_h – magnetizing inductance; L_R – rotor inductance; L_S – stator inductance; R_R – rotor phase resistance; R_S – stator phase resistance; σ – total leakage constant; ω_r – rotor angular speed.

3 Sliding mode observer

The sliding mode observer has some benefits in compared with above observers such as good estimation accuracy, robustness to parameter variations and its ability to handle nonlinear systems [3], [4].

$$\frac{d}{dt}\hat{\mathbf{x}}=\hat{\mathbf{A}}\cdot\hat{\mathbf{x}}+\mathbf{B}\cdot\mathbf{v}+\mathbf{G}\cdot\operatorname{sign}\left[\mathbf{y}-\hat{\mathbf{y}}\right] \tag{9}$$

$$\hat{\mathbf{y}}=\mathbf{C}\cdot\hat{\mathbf{x}} \tag{10}$$

$$\hat{\mathbf{A}}=\mathbf{A}_{(\omega_r=\hat{\omega}_r)} \tag{11}$$

Design of the sliding mode observer matrix **G** is based on the rule that the sliding mode observer must be stable and faster than observed system. In our case, it is the induction motor. The observer matrix **G** can be written as follows:

$$\mathbf{G}=\begin{bmatrix} g_1 & -g_2 \\ g_2 & g_1 \\ g_3 & -g_4 \\ g_4 & g_3 \end{bmatrix} \tag{12}$$

We can derive following equations for the calculation of **G** matrix elements [5]:

$$g_1=\lambda\left(k-1\right)\left(R_S L_R+R_R L_S\right)\quad,\quad g_2=-\left(k-1\right)\hat{\omega}_r \tag{13}$$

$$g_3=-\frac{\left(k-1\right)\left(R_R L_S-kR_S L_R\right)}{L_h}\ ,\ g_4=\frac{\left(k-1\right)}{\lambda L_h}\hat{\omega}_r\ ,\ \lambda=\frac{1}{L_R L_S-L_h^2}. \tag{14}$$

For the adaptation algorithm, there is possible to use a PI controller:

$$\hat{\omega}_r=K_P\cdot z+K_I\int z\cdot dt\quad,\quad z=\left(i_{S\alpha}-\hat{i}_{S\alpha}\right)\cdot\hat{\psi}_{R\beta}-\left(i_{S\beta}-\hat{i}_{S\beta}\right)\cdot\hat{\psi}_{R\alpha}. \tag{15}$$

where z is so-called correction member and K_P, K_I are controller constants.

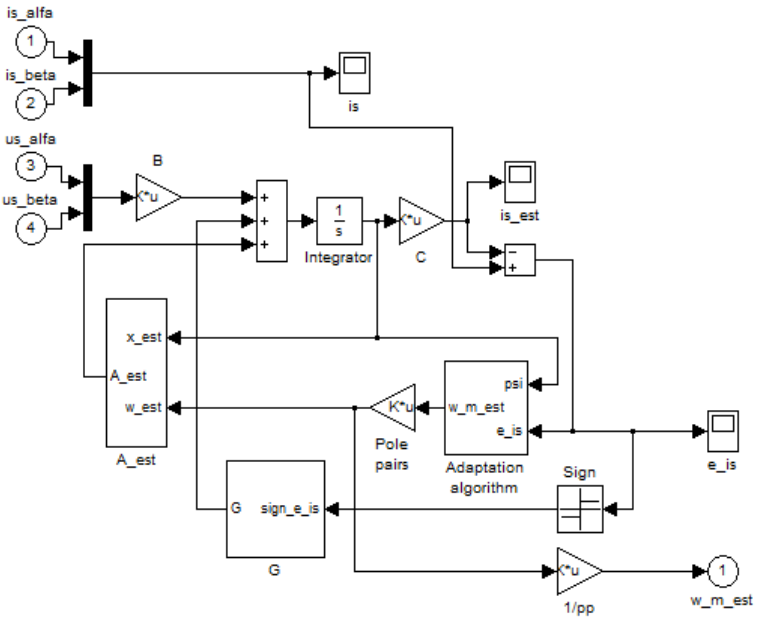

Fig. 1. Block diagram of the sliding mode observer in Matlab-Simulink

4 Simulation results

The described sliding mode observer was simulated by MATLAB-SIMULINK on a vector controlled AC drive with the induction motor (see Fig. 1). The controllers of quantities in control structure of AC drive with vector control were adjusted accordance with the following parameters of the induction motor (type P 112 M04):

- P_n = 2.7 kW, T_n = 19 Nm
- ω_{mn} = 1360 rpm, p_p = 2
- I_{Sn} = 7.51 A, I_{Rn} = 17 A
- I_{Sxn} = 6.8 A, I_{Syn} = 8.16 A
- U_{Sn} = 400/230 V, Ψ_{Sn} = 0.877 Wb
- R_S = 1.83 Ω, R_R = 2.19 Ω
- L_S = 0.137 H, L_R = 0.137 H
- L_m = 0.129H, T_R = 0.0546 s

To assess the control quality of simulated AC drive is important to assess the speed time course in different situations. The sliding mode observer was connected to a closed speed control loop. The estimated rotor angular speed, which was obtained on the output of the sliding mode observer, was used as feedback signal for the mentioned speed control loop.

The time courses of the actual rotor speed (see Fig. 2, estimated rotor speed (see Fig. 3) and speed difference (see Fig. 4) were obtained from the speed control structure at the jump of the load torque T_L = 5 Nm (see Fig 5).

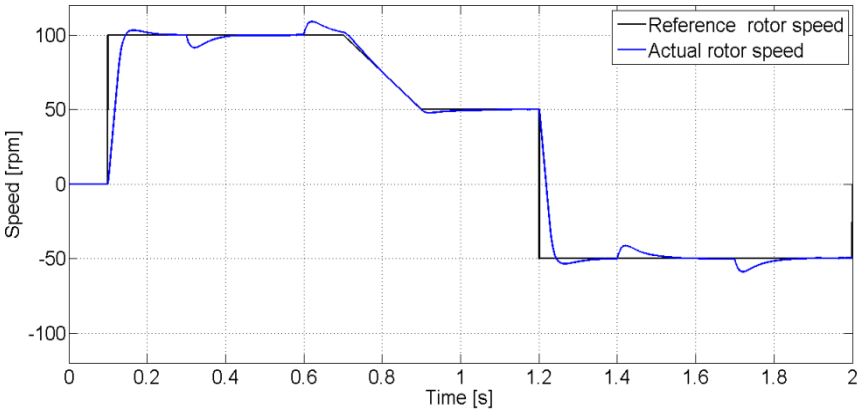

Fig. 2. Reference rotor speed (black) and actual rotor speed (blue) of the induction motor

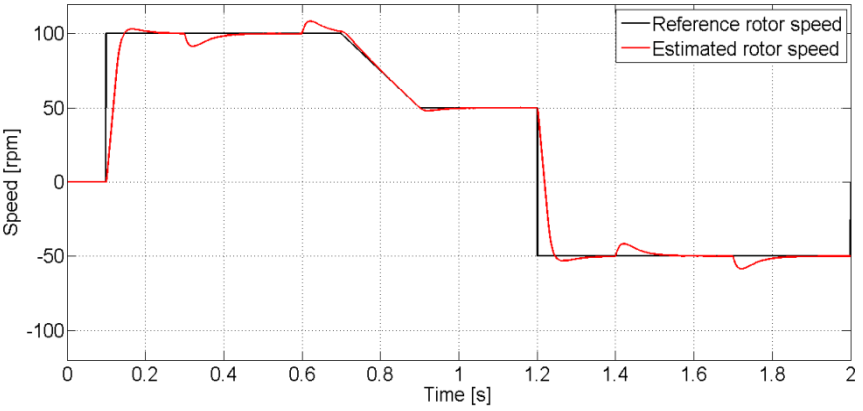

Fig. 3. Reference rotor speed (black) and estimated rotor speed (red) of the induction motor

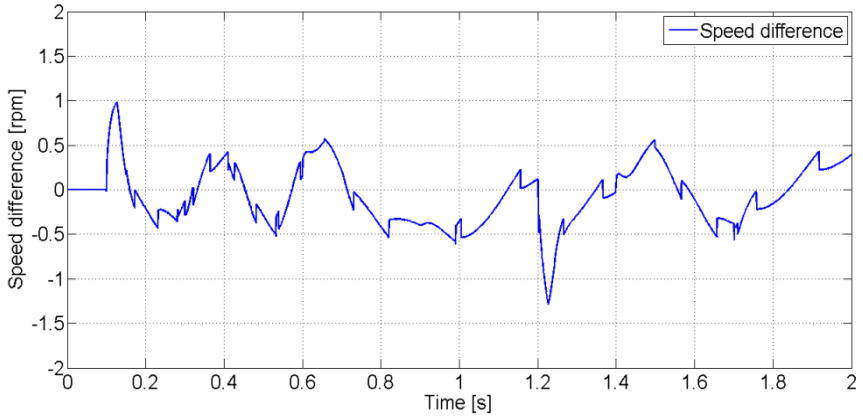

Fig. 4. Speed difference between actual and estimated rotor speed of the induction motor

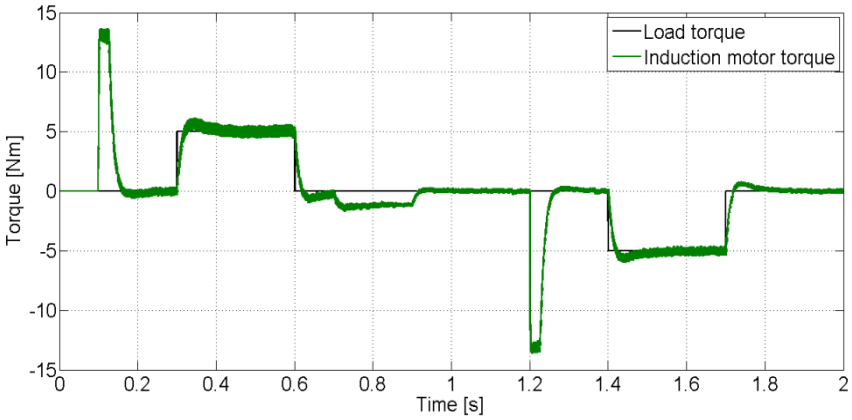

Fig. 5. Load torque (black) and induction motor torque (green)

5 Conclusion

The estimation technique for sensorless induction motor drive with vector control was presented in the paper. The speed estimator is based on application of the sliding mode observer. The induction motor drive with the presented speed estimator gives good dynamic responses and the estimation of the mechanical speed is good in steady state and also in transient state.

Acknowledgement

In the paper, there are the results of the project reg. no. SP2015/81 funded by the Student Grant Competition of VSB-Technical University of Ostrava. This research was supervised by Prof. Ing. Pavel Brandstetter, CSc.

References

1. K. B. Bose, Power Electronics and Modern Electric Drives. N. Jersey: Prentice Hall, 2002.
2. P. Brandstetter, AC Controlled Drives – Modern Control Methods. Ostrava, VSB-Technical University of Ostrava, 177 p., 1999.
3. D. G. Luenberger, An Introduction to Observers. Automatic Control, IEEE Transactions on Industrial Electronics, vol. 16, no. 6, pp. 596–602, 1971.
4. J. Gacho, M. Zalman, IM Based Speed Servodrive with Luenberger Observer, Journal of Electrical Engineering, Vol. 61, No. 3, 2010, pp. 149 – 156.
5. Y. Zhang et al., A Comparative Study of Luenberger Observer, Sliding Mode Observer and Extended Kalman Filter for Sensorless Vector Control of Induction Motor Drives. In Energy Conversion Congress and Exposition, San Jose, CA, pp. 2466 – 2473, 2009.

Controlled Systems with Electrical Drives Identification Using Genetic Algorithms

Jiri Hajovsky

Department of Electronics, FEECS,
VŠB – Technical University of Ostrava, 17. listopadu 15, 708 33 Ostrava – Poruba
jiri.hajovsky@vsb.cz

Abstract. The electrical controlled drives are described as controlled systems that contain one or two large time constants and several small time constants, whose influence is replaced by approximately sum time constant. The large time constants are then compensated by a serial correction using a controller, while the sum time constant remains uncompensated. The quality of the control is assessed according to the response of the control loop to step change of the input variable. In the paper, there is used a genetic algorithm to identify the unknown time constants of the controlled system with the electrical drive from the step response characteristic.

Keywords: Genetic algorithm, electrical controlled loop, time constants, control loop

1 Introduction

There are a lot of new approaches and principles which are based on a relatively new scientific discipline which is called soft computing. The main feature of soft computing is a departure from traditional modeling based on Boolean logic, analytical models, sharp classification and deterministic search. Among the main representative of soft computing we can include fuzzy logic, neural networks and genetic algorithms. Genetic algorithms solve optimization problems in different fields of the industry. In the field of electrical drives, the genetic algorithms can be used to identify the parameters of the controlled system, optimization of the controller parameters settings and optimization of the parameters adjustment of adaptive controllers.

2 Controlled systems with electrical drives

Different methods of analysis and synthesis are used to design of electric controlled drives which have to fulfill given static and dynamic requirements. The quality of the control is assessed according to the response of the control loop to step change of input variable (see Fig. 1). From a practical point of view, four factors are most im-

© M. Krátký, J. Dvorský, P. Moravec (Eds.): WOFEX 2015, pp. 96–101.
VŠB – Technical University of Ostrava, FEECS, 2015, ISBN 978-80-248-3787-1.

portant for the assessment of control quality: rise time t_r, settling time t_s, overshoot y_m and steady state error.

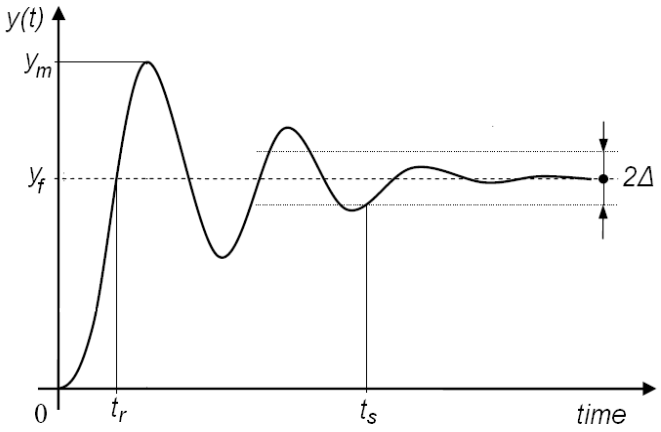

Fig. 1. Typical step response for an under damped second order system

The main requirements are a good dynamics of the control which is given by short rising time tr and small overshoot ym. These two parameters are contradictory and it is not possible to fulfill both of them at the same time. Appropriate settings of tr and ym determine the right curve shape of an open loop step response in time domain. In real control loop, there are some errors that it is not possible to compensate. These errors, for example voltage ripple, measurement errors and controller errors, determine the practical achievable static accuracy,

For the electrical controlled drives, a cascade structure is often used. The cascade control structure consists of several superior and subordinate control loops.

The serial correction method is mostly used to get right static and dynamic parameters of the control loop. For illustration, there will be considered the following transfer function of the controlled system in Laplace domain:

$$F_S(s) = \frac{K_S}{(1+sT_1)(1+sT_2).....(1+sT_n)} \tag{1}$$

The controlled systems with the electrical drives are described by the transfer function that contains one or two large time constants and several small time constants. The open control loop is described by transfer function:

$$F_{OL}(s) = F_C(s) \cdot F_S(s) = F_C(s) \cdot K_S \frac{1}{(1+sT_S)} \frac{1}{(1+sT_\Sigma)} \tag{2}$$

where $F_S(s)$ – transfer function of the controlled system; $F_C(s)$ – transfer function of the controller; K_S – gain of the controlled system; T_S – large time constant of the controlled system; T_Σ – uncompensated sum time constant.

For the control of the output quantity, it can be used the PI controller with the parameters K_{Ci} and T_{Ci}:

$$F_C(s) = K_{Ci} \frac{(1 + sT_{Ci})}{sT_{Ci}} \tag{3}$$

3 Simulation results

For the simulation, there was used the current loop of the vector controlled induction motor (IM) supplied by the frequency converter which consists of the input rectifier, DC voltage link and voltage source inverter (VSI). Basic parameters of the IM are: rated power 2.2 kW, rated speed 1420 rpm, rated voltage 230 V/400 V, rated current 8.4 A/4.7 A, rated torque 14.8 Nm, stator resistance 3.71 Ω, stator inductance 330 mH, leakage coefficient 0.0953, moment of inertia 0.005 kgm^2.

The resulting transfer function of the current loop that includes the voltage source inverter and its control part, current sensor and AD converter (ADC) is given:

$$\begin{aligned} F_{SI}(s) &= \frac{K_M K_I K_{AD}}{R_S} \frac{1}{(1 + sT_I)} \frac{1}{(1 + sT_\Sigma)} = K_{SI} \frac{1}{(1 + sT_I)} \frac{1}{(1 + sT_\Sigma)} = \\ &= 650.54 \frac{1}{(1 + s \cdot 0.00847)} \frac{1}{(1 + s \cdot 0.000125)} \end{aligned} \tag{4}$$

where K_{SI} – total gain of the current loop; K_M – voltage gain of the VSI, K_I – gain of the current sensor, K_{AD} – gain of the ADC, R_S – stator resistance, T_I – large time constant, T_{NKI} – small sum time constant.

The voltage gain of the VSI with the comparative PWM is defined as follows: $K_M = U_{DC\text{-}link} / U_{Cmax} = 650.54$, where $U_{DC\text{-}link}$ – DC-link voltage calculated for the rated stator voltage of the IM; U_{Cmax} – maximal control voltage with the value 1 which is given in the control software. The gain of the current sensor and ADC is defined in the control software: $K_I K_{AD} = 1$.

The large time constant T_I is calculated using IM parameters: $T_I = \sigma L_S / R_S = 0.0954 \cdot 0.33 / 3.71 = 8.47$ ms. Small sum time constant T_Σ is defined as follows: $T_\Sigma = 1.5 \cdot T_{SI} + T_{VSI} = 1.5 \cdot 50 \cdot 10\text{-}6 + 50 \cdot 10\text{-}6 = 0.125$ ms, where T_{SI} – sampling period of the current control loop; T_{VSI} – time delay of the VSI ($T_{VSI} = 1/2\ f_s$; switching frequency $f_s = 10$ kHz).

Step response in time domain (see Fig. 2) is described by the following equation:

$$y = K \left\{ 1 - \left[\left(\frac{T_1}{T_1 - T_2} \right) e^{-\frac{t}{T_1}} - \left(\frac{T_2}{T_1 - T_2} \right) e^{-\frac{t}{T_2}} \right] \right\} \tag{5}$$

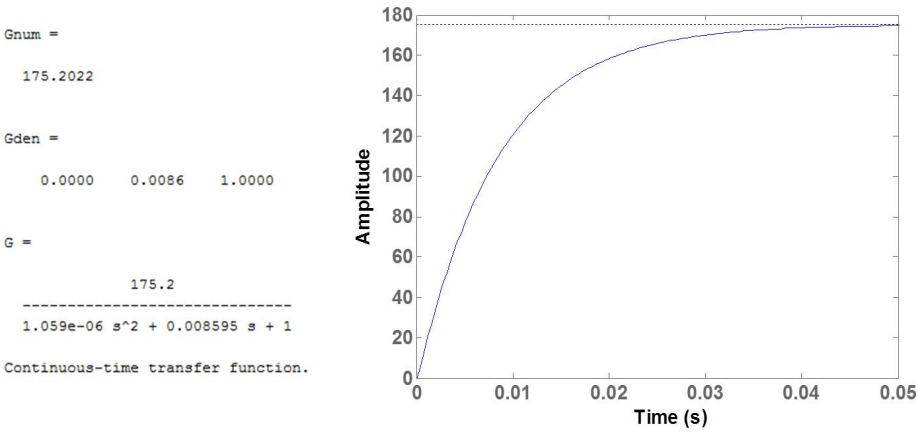

Fig. 2. Step response of the open current control loop

A few random points from step response were taken and applied into developed LabVIEW application based on the genetic algorithm. The equation of the step response in time domain is basically searched fitness function implemented into application. The genetic algorithm is used to find parameters $K = K_{SI}$, $T_1 = T_I$, and $T_2 = T_\Sigma$ of the step response in time domain. The population of 50 individuals and 60 generation were chosen.

Fig. 3 shows the improvement of the function graph with the best individual in each generation. In each generation the sum of the deviations is much smaller and the curve follows the given points. The obtained parameters of the controlled current loop using the described genetic algorithms are: $K = K_{SI} = 175.2035$, $T_1 = T_I = 0.00847085$ s, $T_2 = T_\Sigma = 0.00012495$ s.

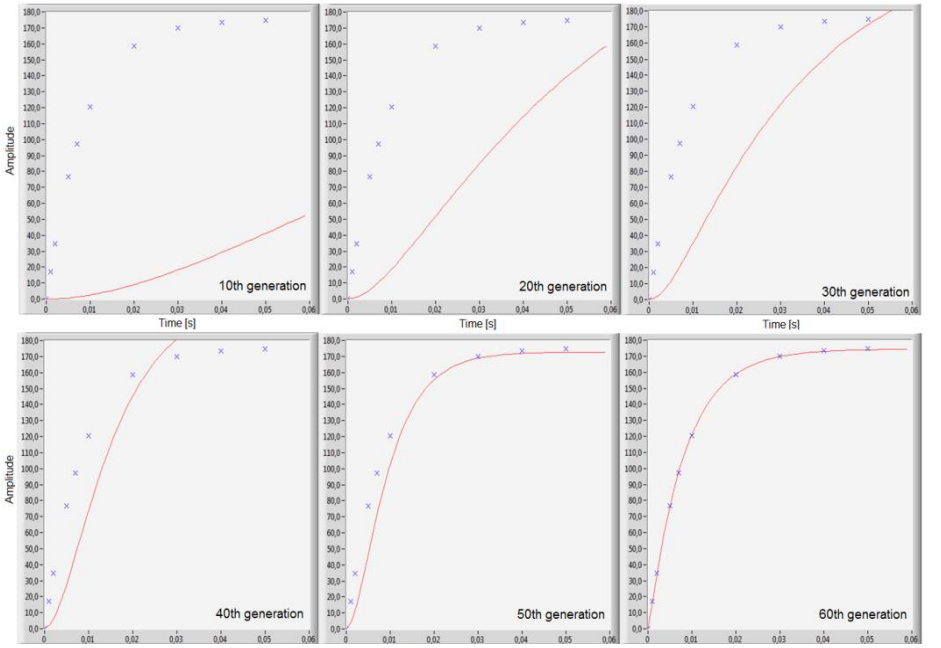

Fig. 3. Development of the fittest individuals in each generation

4 Conclusions

The designed GA application is able to find the important parameters of the controlled systems with the electrical drives. The achieved error is less than 0.1% in the sixtieth generation with the first population size of fifty individuals. This application can be used for almost every estimation tasks, if the controlled system is defined by the measured step response. The fitness function has to be chosen correctly.

5 Acknowledgement

In the paper, there are the results of the project reg. no. SP2015/81 funded by the Student Grant Competition of VSB-Technical University of Ostrava. This research was supervised by Prof. Ing. Pavel Brandstetter, CSc.

6 References

1. Ozturk, N.,"Speed control for dc motor drive based on fuzzy and genetic PI controller - A comparative study," *Elektronika Ir Elektrotechnika*, No. 7, 43-48, 2012.

2. Palacky, P., Hudecek, P. and A. Havel, "Real-Time Estimation of Induction Motor Parameters Based on the Genetic Algorithm," *Proceedings of the International Joint Conference CISIS'12-ICEUTE'12-SOCO'12 Special Sessions, Advances in Intelligent Systems and Computing*, Vol. 189, 401-409, 2013.
3. Fedor, P. and D. Perdukova, "Energy optimization of a dynamic system controller," *Proceedings of the International Joint Conference CISIS'12-ICEUTE'12-SOCO'12 Special Sessions, Book Series: Advances in Intelligent Systems and Computing*, Vol. 189, 361-369, 2013.
4. Rezazadeh, A., "Genetic algorithm based servo system parameter estimation during transients," *Advances in Electrical and Computer Engineering*, Vol. 10, No. 2, 77-81, 2010.
5. Finch, J. W. and D. Giaouris, "Controlled AC Electrical Drives," *IEEE Transactions on Industrial Electronics*, Vol. 55, No. 2, 481-491, 2008.
6. Kuzmanovic, D. and J. Lettl, "The Use of Prediction to Improve Direct Torque Control," *Proceedings of the Progress in Electromagnetics Research Symposium PIERS 2011*, Marrakesh, Morocco, 1411-1415, 2011.
7. Sladecek, V., Palacky, P., Slivka, D. and M. Sobek, "Influence of Power Semiconductor Converters Setup on the Quality of Electrical Energy from Renewable Sources," *Proc. of the 11th International Scientific Conference on Electric Power Engineering 2010*, Brno, Czech Republic, 527-531, 2010.
8. Chlebis, P., Vaculik, P., Moravcik, P. and Z. Pfof, "Direct Torque Control Methods for Three-level Voltage Inverter," *Proceedings of the 10th International Scientific Conference on Electric Power Engineering 2009*, Kouty nad Desnou, Czech Republic, 352-356, 2009.
9. Mitchell, M., An Introduction to Genetic Algorithms, A Bradford Book The MIT Press, Cambridge, Massachusetts; London, England, 1999.

Design and Simulation of Electric Traction Drive for 4WD Vehicles

Tomas Mrovec and Petr Chlebis

Department of Electronics, FEECS,
VŠB – Technical University of Ostrava, 17. listopadu 15, 708 33 Ostrava – Poruba
tomas.mrovec@vsb.cz

Abstract. In this paper, the basic simulation model of Individual-Wheel Drive (IWD) vehicle is demonstrated. The MATLAB/Simulink environment is used for simulation model of the real IWD vehicle called "Democar". The overall simulation model contains a few sub-models that represent the main structures of the vehicle. The mechanical parameters of the vehicle, ambient air, and terrain are aspects which affect the vehicle dynamics and are considered in sub-model. Each of the four wheels has its own electric driveline. For the torque management of individual drivelines and their coordination is designed control sub-system. Each of these main structures and their interlinkages are covered in the paper. A stable MATLAB/Simulink model was developed and validated, important results of simulation are presented. All results that are mentioned in the paper are made within the researcher activity in the branch of automotive electronics in the Department of Electronics, VSB-Technical University of Ostrava.

Keywords: IWD Drive; Vehicle Simulation Model; MATLAB/Simulink; PMSM; Democar; Torque Management;

1 Introduction

Today's vehicles are designed with one drive axle or 4x4, 4WD or AWD. Traditional four-wheel drive improves handling characteristics of the vehicle, but the vehicle has only one engine and torque is elaborated through gearboxes, clutches and axle to the driven wheels. In these conventional systems is very difficult to control the torque on each wheel individually, due to the mechanical linkages and a single source of torque moment. Individual wheel drive is used for electric vehicles. Each driven wheel has its own source of torque, usually the electric motor. The electrical drive unit is powered by batteries stored in the vehicle chassis. All power converters are connected to a control unit that ensures the distribution of torque to the wheels according to the current driving situation. The IWD system dramatically improves handling and vehicle stability. Vehicle dynamics can be tested experimentally on a testing track or using mathematical simulations. We are able to relatively credibly analyse behaviour of the vehicle under various conditions with modelling and simulation. The main advantages of the simulation also means that it is cheaper, because there is no destruction or stress tech-

© M. Krátký, J. Dvorský, P. Moravec (Eds.): WOFEX 2015, pp. 102–107.
VŠB – Technical University of Ostrava, FEECS, 2015, ISBN 978-80-248-3787-1.

niques. Today the development of every car starts with the use of modelling and simulation tools. The simulation is suitable for removing fundamental shortcomings and fatal errors before production of a prototype vehicle.

2 Conception of Demonstration IWD Vehicle

Chassis of the demonstration vehicle is taken from the quad Goes type 625i. Each wheel of the vehicle is equipped its own electric driveline. In the centre of chassis there is a battery box, which has a great effect on changing the weight distribution of the vehicle.

The vehicle is equipped with motors from Baumüller; type designation DSC100-S64U. It is a 10-pole, three-phase permanent magnets synchronous machines. Control is provided by the frequency converter from Baumüller labelled b Maxx 4400 type. On the vehicle used as an inverter only. The inverter consists of these basic blocks; voltage DC link with terminals and inverter. Voltage DC link of the converter has the terminals DC + and DC- that are used for its battery power.

The simulation model of the vehicle is made up of three subsystems which are connected into the overall model. The subsystems are structured systematically with respect to functional components of the electric drive. The vehicle model is therefore formed by the following subsystems: Central control unit for management of torque to each wheel; Drive unit with four independent electric machines; Mechanical part of the chassis realizing the driveability of the vehicle. Inputs into the model are torque request by an accelerator pedal and steering angle.

3 Simulation Sub-model of Vehicle Dynamics

The vehicle moves in space described axes *x*, *y* and *z*. This system is fixedly connected with the vehicle and its beginning is located in the centre of gravity of the vehicle. Consider the forces and dynamic quantities, as shown in the Fig. 1

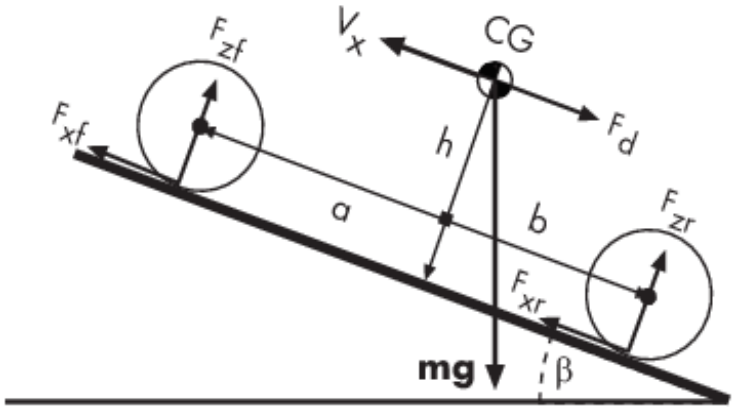

Fig. 1. Vehicle dynamics

The dynamic equation for the vehicle motion is

$$F_X = F_{RR} + F_{AD} + F_{HC} + F_{AC} \quad (1)$$

where F_X is total tractive force (forces are applied at the centre of gravity GC), F_{RR} is rolling resistance force, F_{AD} is aerodynamic drag force, F_{HC} is hill climbing force and F_{AC} is the force required to give linear acceleration and rotational acceleration.

The Tire block models a vehicle tire in contact with the road. The model provides the tire angular velocity ω_w and the longitudinal tractive force F_x on the vehicle as Simulink output signals. Front and rear longitudinal tractive forces F_{xf}, F_{xr} are applied at the front and rear wheel contact points, as well as the incline angle β.The block computes the vehicle velocity V_x and the front and rear vertical load forces F_{zf}, F_{zr} on the vehicle. Fig. 2 is shown the waveforms of vertical load forces. During acceleration is the load of a rear axle higher than a front axle. The simulation model includes only longitudinal motion and no camber, turning, or lateral motion.

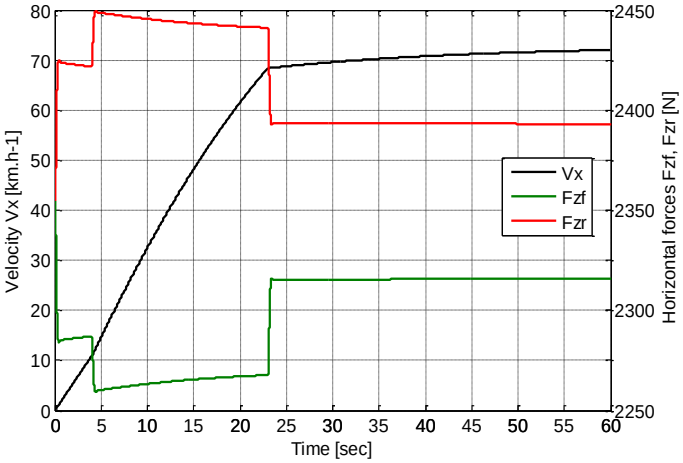

Fig. 2. Vertical load forces

4 Simulation Sub-model of Electric Drive

Many different architectures of an electric driveline exist as there are many possibilities. However, in this paper the architecture IWD is chosen. The traction power of the wheel is delivered by three-phase permanent magnets synchronous machines for each wheel. The torque and speed of the machines are controlled by the electric inverter which inverts DC voltage from battery pack. The model don't include the energy losses due to which aren't a part of the power chain, e.g. lighting system, steering, safety systems, etc.

4.1 Model of Battery Pack

The vehicle is equipped with a battery box, which consists of 200 pieces LiFePo4 cells. The LiFePo4 battery has many unique features s such as very high thermal runaway temperatures, very high discharge current capability, and high charge current. These special features make it more attractive in many applications, such as vehicle power train. Each cell has a nominal voltage of 3.3 V and is connected to it balancer.

4.2 Model of Three-phase Inverter

Here four the three-phase inverter are connected directly to the vehicle battery for each driveline. PMSM controller is contains a three-phase inverter, speed controller and VECT controller. Measuring block between the motor and the inverter provides current feedback.

This model uses the same firing pulses as for other power electronic devices and it correctly represents harmonics normally generated by the IGBT Bridge. The inverter is a voltage source inverter, controlled by PWM. The VECT controller block computes the three reference motor line currents corresponding to the flux and torque references and then generates a corresponding PWM using a three-phase current regulator. When the nominal flux is required, an optimal control is used in order to minimise the line current amplitude for the required torque.

4.3 Model of Electric Machine

Permanent magnet synchronous motors are increasing applied in several areas such as traction, automobiles, robotics and aerospace technology. The power density of permanent magnet synchronous motor is higher than one of induction motor with the same ratings due to the no stator power dedicated to the magnetic field production. Nowadays, permanent magnet synchronous motor is designed not only to be more powerful but also with lower mass and lower moment of inertia.

The permanent magnet synchronous machine is selected, due to its high power density and high efficiency. The electric machine is divided into an electric part and mechanic part. The electrical and mechanical parts of the machine are each represented by a second-order state-space model. Model of the electric part is modelled in the *dq*-dimension.

$$v_d = R_S.\, i_d + L_d.\frac{di_d}{dt} - \omega_e.\, L_q.\, i_q \tag{2}$$

$$v_q = R_S.\, i_q + L_q.\frac{di_q}{dt} - \omega_e.\, L_d.\, i_d + \omega_e.\, \lambda_{pm} \tag{3}$$

where R_s is stator phase resistance, ω_e is angular frequency of the stator and λ_{pm} is permanent magnet flux linkage. The Electromagnetic torque of machine is deduced from (4).

$$T_e = \frac{3}{2}.\frac{P}{2}(\lambda_{pm}.\, i_q + \left(L_d - L_q\right).\, i_q.\, i_q \tag{4}$$

where P is number of poles.

Results from simulation of electrical sub-model are presented in the Fig. 3. In this figure it can be the relationship between the electromagnetic torque of one electrical motor and vehicle speed. When the motor torque is increased, speed increases and the vehicle speed as well.

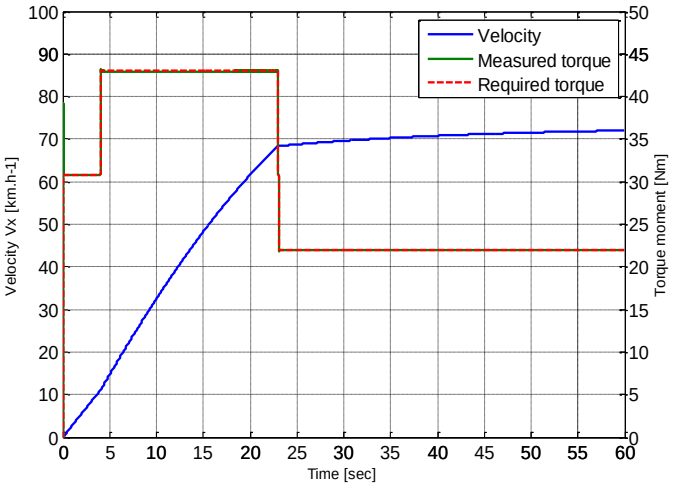

Fig. 3. Electromagnetic torque of one of all electrical machines

5 Simulation Submodel of Driveline Management

Torque management of the individual electrical driveline is provided by a central control unit CCU. The input values to the CCU are accelerator pedal position and the actual motor speed. Based on the torque demand and the actual engine speed is determined the required torque, which is sent to the speed controller for three-phase inverter. CCU acts as the electronic differential. Proper distribution of torque between the wheels is important for good vehicle driveability. Simulation diagram representing the calculation of the required torque for each driveline is shown in Fig. 4.

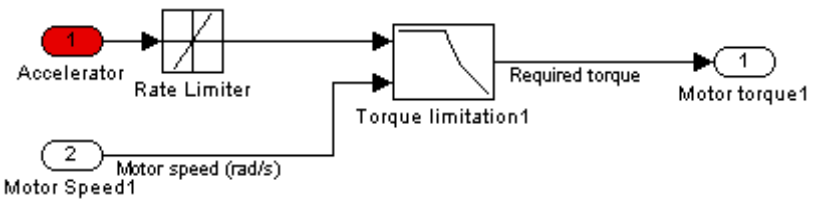

Fig. 4. Calculating of required torque

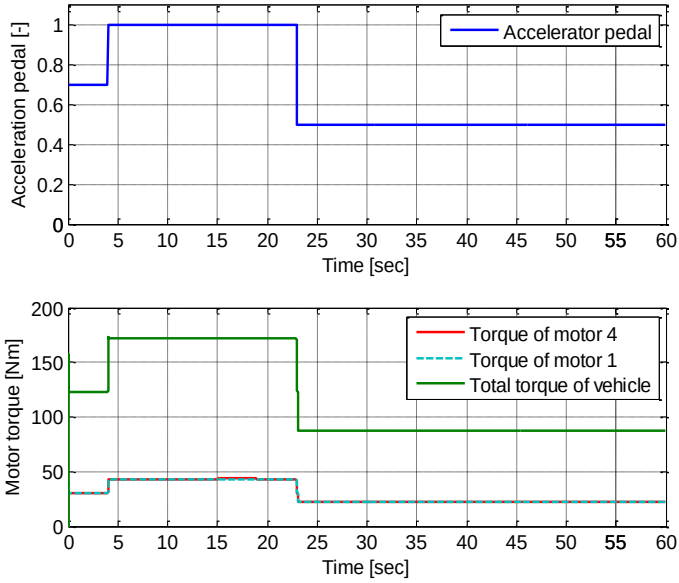

Fig. 5. Torque depending on the accelerator pedal

6 Conclusion

In this paper the electric driveline of the electric demonstration vehicle is modelled and simulated. At present is the results of simulation applied for design of control unit of the vehicle. The next stage of this simulation models will be also design new control algorithms of electric drive. Based on this model is also created another version of the simulation model including all wheel steering. All applications are realized within the research activity in the branch of automotive electronics in the Department of Electronics, VSB – Technical University of Ostrava.

7 Acknowledgment

Work is partially supported by Grant of SGS No. SP2014/119, VŠB - Technical University of Ostrava, Czech Republic, for which author express their sincere gratitude.

8 References

[1] I. Neborak, P. Simonik, and P. Odlevak, "Electric Vehicle Modelling and Simulation," In: 14th International Scientific Conference on Electric Power Engineering 2013, pp. 693-696, 2013.

[2] P. Chlebis, P. Moravcik, P. Simonik, "Method of Direct Torque Control for Three-level Voltage Inverter," EPE: 2009 13th European Conference on Power Electronics and Applications, vols 1-9, p. 4051-4056, September 2009.

The Enlarged Linear d-q Model of Induction Motor with the Iron Loss

Jan Otýpka

Department of Electrical Engineering, FEECS,
VŠB – Technical University of Ostrava, 17. listopadu 15, 708 33 Ostrava – Poruba
jan.otypka@vsb.cz

Abstract. The main aim of this article is presentation the linear model of induction motor with the iron loss and comparison with conventional model which neglected the iron loss. It is very important to note that the portion of iron loss is relatively small and it represents about 3 – 5% input power to the induction motor. Both models are simulated in the Matlab Simulink environment with the calculation of important variables and losses for dynamic analysis power in induction motor.

Keywords: Induction motor, d-q coordinate frame model, iron loss, saturation effect, magnetizing inductance, leakage inductance, T-form.

1 Introduction

The conventional model of induction motor is based on the classical T-form layout without the iron loss. This model is widely used for the operation of induction motor. The conventional model is presented many researchers [1]-[3]. In case of the operation of such motor with minimal losses or the power dynamic analysis of induction motors powered by the harmonic or nonharmonic source, the conventional model is not sufficient for the using. Hence, this model must be enlarged with the consideration of the iron loss.

This paper presents the enlarged model with the iron loss in d-q coordinate frame system. New model is compared with the conventional model for the starting of induction motor without a load. Each kind of loss is calculated by this model as the conventional model considers only the stator and rotor windings losses. On the other hand, the iron loss is not separated from the eddy-current loss and hysteresis loss, because the physical interpretation of both losses is relatively complicated. The possible solving of this problem is published in [4]. Therefore, the enlarged model operates only with one value of the resistance R_{Fe} represented the iron loss, which includes both losses.

© M. Krátký, J. Dvorský, P. Moravec (Eds.): WOFEX 2015, pp. 108–113.
VŠB – Technical University of Ostrava, FEECS, 2015, ISBN 978-80-248-3787-1.

2 The Model of induction motor with iron loss

The conventional model of induction motor is based on the classical equivalent circuit in T-form, from which derives the d-q coordinate frame model, presented in [1]-[3]. If this model is enlarged by the additional iron loss resistance R_{Fe}, the currents flowing in the transversal branch must be defined. The transversal branch is presented by the parallel combination of iron loss resistance R_{Fe} and magnetizing inductance L_m. The model of induction motor with the considering of iron loos is obtained, when the model derivation is based on the magnetizing current i_m, which flows through the magnetizing inductance L_m.

The derivation of the induction motor model is obtained from fig. 1, where the currents (the main current i_0, which flows through the transversal branch and the current in iron i_{Fe}) are defined by using the current divider. These currents are obtained as the function of the magnetizing current i_m. This approach for derivation of the induction motor model with iron loss is presented in [3], [4] and [5].

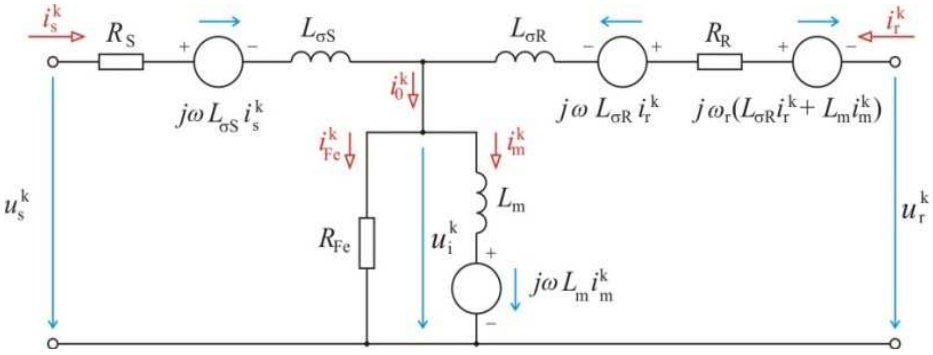

Fig.1. The equivalent circuit model of induction motor in T-form with the iron loss

The model of induction motor with the iron loss is given by these equations presented in [3], [4] and [5] for the general d-q coordinate frame system, which rotates with the general angle speed ω:

$$u_{ds}^k = R_S\, i_{ds}^k + L_{\sigma S}\frac{\mathrm{d}i_{ds}^k}{\mathrm{d}t} + L_m\frac{\mathrm{d}i_{dm}^k}{\mathrm{d}t} - \omega\left(L_{\sigma S}\, i_{qs}^k + L_m\, i_{qm}^k\right), \tag{1}$$

$$u_{qs}^k = R_S\, i_{qs}^k + L_{\sigma S}\frac{\mathrm{d}i_{qs}^k}{\mathrm{d}t} + L_m\frac{\mathrm{d}i_{qm}^k}{\mathrm{d}t} + \omega\left(L_{\sigma S}\, i_{ds}^k + L_m\, i_{dm}^k\right), \tag{2}$$

$$u_{dr}^k = R_R\, i_{dr}^k + L_{\sigma R}\frac{\mathrm{d}i_{dr}^k}{\mathrm{d}t} + L_m\frac{\mathrm{d}i_{dm}^k}{\mathrm{d}t} - (\omega-\omega_r)\left(L_{\sigma R}\, i_{qr}^k + L_m\, i_{qm}^k\right), \tag{3}$$

$$u_{qr}^k = R_R\, i_{qr}^k + L_{\sigma R}\frac{\mathrm{d}i_{qr}^k}{\mathrm{d}t} + L_m\frac{\mathrm{d}i_{qm}^k}{\mathrm{d}t} + (\omega-\omega_r)\left(L_{\sigma R}\, i_{dr}^k + L_m\, i_{dm}^k\right), \tag{4}$$

$$i_{\mathrm{d0}}^{\mathrm{k}} = i_{\mathrm{ds}}^{\mathrm{k}} + i_{\mathrm{dr}}^{\mathrm{k}}, \tag{5}$$

$$i_{\mathrm{q0}}^{\mathrm{k}} = i_{\mathrm{qs}}^{\mathrm{k}} + i_{\mathrm{qr}}^{\mathrm{k}}, \tag{6}$$

$$i_{\mathrm{d0}}^{\mathrm{k}} = i_{\mathrm{dFe}}^{\mathrm{k}} + i_{\mathrm{dm}}^{\mathrm{k}} = i_{\mathrm{dm}}^{\mathrm{k}} + \frac{L_{\mathrm{m}}}{R_{\mathrm{Fe}}}\left(\frac{\mathrm{d}i_{\mathrm{dm}}^{\mathrm{k}}}{\mathrm{d}t} - \omega i_{\mathrm{dm}}^{\mathrm{k}}\right), \tag{7}$$

$$i_{\mathrm{q0}}^{\mathrm{k}} = i_{\mathrm{qFe}}^{\mathrm{k}} + i_{\mathrm{qm}}^{\mathrm{k}} = i_{\mathrm{qm}}^{\mathrm{k}} + \frac{L_{\mathrm{m}}}{R_{\mathrm{Fe}}}\left(\frac{\mathrm{d}i_{\mathrm{qm}}^{\mathrm{k}}}{\mathrm{d}t} + \omega i_{\mathrm{qm}}^{\mathrm{k}}\right), \tag{8}$$

where ω_t is the electrical rotor angle frequency. The magnetic fluxes components are given by the equations in axis d and q:

$$\Psi_{\mathrm{ds}}^{\mathrm{k}} = L_{\sigma\mathrm{S}}\, i_{\mathrm{ds}}^{\mathrm{k}} + L_{\mathrm{m}}\, i_{\mathrm{dm}}^{\mathrm{k}}, \tag{9}$$

$$\Psi_{\mathrm{qs}}^{\mathrm{k}} = L_{\sigma\mathrm{S}}\, i_{\mathrm{qs}}^{\mathrm{k}} + L_{\mathrm{m}}\, i_{\mathrm{qm}}^{\mathrm{k}}, \tag{10}$$

$$\Psi_{\mathrm{dr}}^{\mathrm{k}} = L_{\sigma\mathrm{R}}\, i_{\mathrm{dr}}^{\mathrm{k}} + L_{\mathrm{m}}\, i_{\mathrm{dm}}^{\mathrm{k}}, \tag{11}$$

$$\Psi_{\mathrm{qr}}^{\mathrm{k}} = L_{\sigma\mathrm{R}}\, i_{\mathrm{qr}}^{\mathrm{k}} + L_{\mathrm{m}}\, i_{\mathrm{qm}}^{\mathrm{k}}. \tag{12}$$

The electromagnetic torque in general d-q coordinate frame is given by the interaction between rotor magnetic fluxes components and stator currents components:

$$T_{\mathrm{em}} = \frac{3}{2}\, p_{\mathrm{p}}\, \frac{L_{\mathrm{m}}}{L_{\sigma\mathrm{R}} + L_{\mathrm{m}}}\left[\Psi_{\mathrm{qr}}^{\mathrm{k}}\left(i_{\mathrm{ds}}^{\mathrm{k}} - i_{\mathrm{dFe}}^{\mathrm{k}}\right) - \Psi_{\mathrm{dr}}^{\mathrm{k}}\left(i_{\mathrm{qs}}^{\mathrm{k}} - i_{\mathrm{qFe}}^{\mathrm{k}}\right)\right], \tag{134}$$

The mechanical equation is given by:

$$J\,\frac{\mathrm{d}\Omega_{\mathrm{m}}}{\mathrm{d}t} = T_{\mathrm{em}} - T_{\mathrm{L}} - k_{\mathrm{F}}\,\Omega_{\mathrm{m}}, \tag{5}$$

where Ω_{m} is the mechanical angle speed, J is inertia, T_{L} is load torque and k_{F} is friction coefficient. The induction motor identified parameters are given in the following table. The parameters of longitudinal branch: rotor resistance R_{R}, leakage inductances $L_{\sigma\mathrm{S}}$ a $L_{\sigma\mathrm{R}}$ are obtained from the short circuit test. The parameters of transversal branch: magnetizing inductance L_{m} and the iron loss resistance R_{Fe} are obtained from the idle test. These parameters are considered to be constant in simulation.

Table 1. The table of identified parameters for specific type of induction motor

Parameter	*Sign*	*Value*
Nominal power	P_N	4 kW
Nominal voltage	U_N	400 V
Nominal current	I_N	8.1 A
Nominal frequency of mains	f_N	50 Hz
Nominal speed	n_n	1440 rpm
Effectivity clas		IE2
Stator resistance	R_S	1.1 Ω
Stator leakege induktance	$L_{\sigma S}$	9.5 mH
Rotor resistance	R_R	1.478 Ω
Rotor leakege induktance	$L_{\sigma R}$	14.8 mH
Magnetizing inductance	L_m	172.7 mH
Equivalent resistance for core loos	R_{Fe}	491 Ω
Inertia	J	0.02 Kg·m^2

The model of induction motor with the iron loss is created in the Matlab Simulink environment. The simulation is focused on the starting process without load, when the enlarged model of induction motor with the iron loss is compared with the conventional model. Both models are simulated in stationary d-q frame for angle speed $\omega = 0$ rad/s and supply voltage has amplitude 325V with frequency 50Hz. The simulation results are presented at following figures, where the electromagnetic torque T_{em}, the stator current of first phase i_{sa}, the magnetizing current i_m, the iron current i_{Fe} inducted voltage over magnetizing branch u_i are shown.

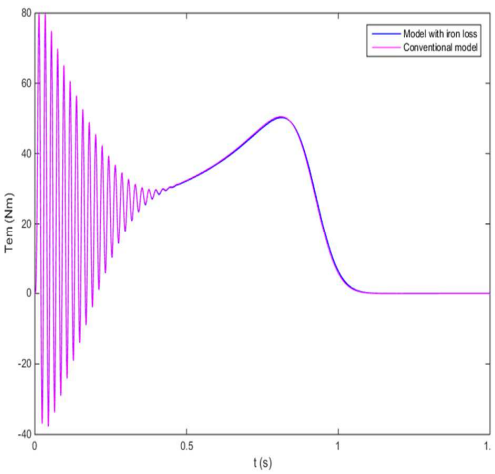

Fig. 2. The waveform of electromagnetic torque for both models.

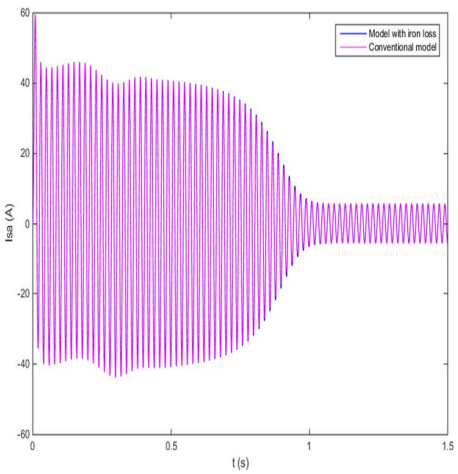

Fig. 3. The waveform of stator current in first phase for both models.

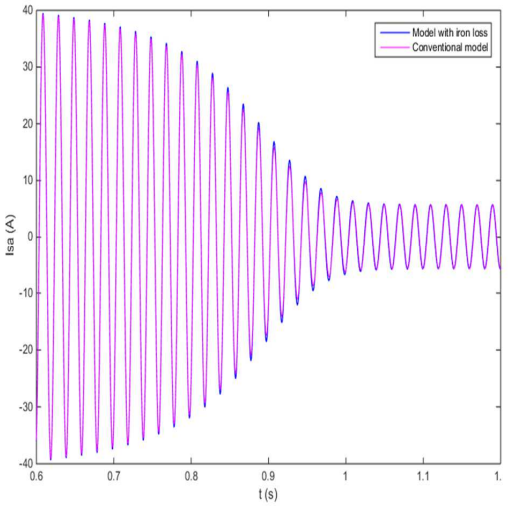

Fig. 4. The detail of stator current waveform for both models.

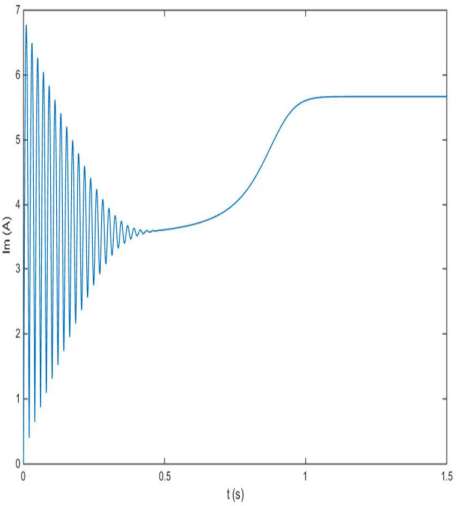

Fig. 5. The absolute value of magnetizing current i_m given by the vector sum of components in d and q axis for enlarged model of induction motor.

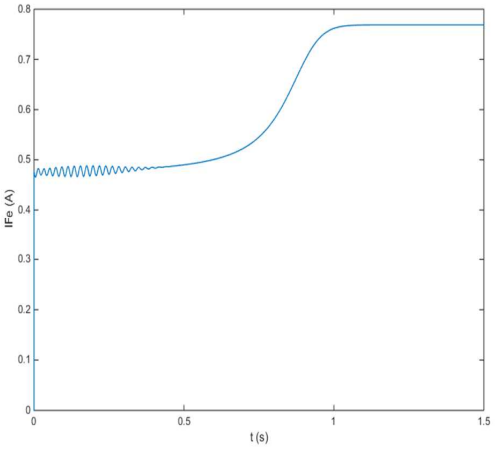

Fig. 6. The absolute value of iron current i_{Fe} given by the vector sum of components in d and q axis for enlarged model of induction motor.

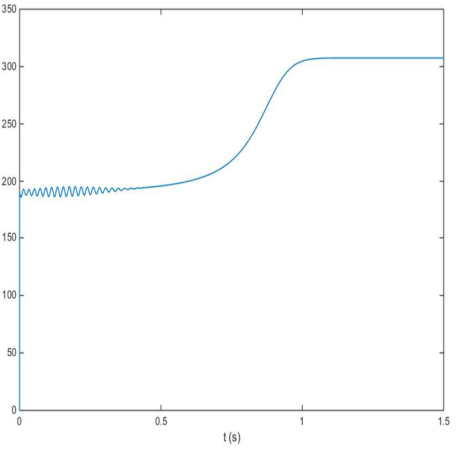

Fig. 7. The absolute value of inducted voltage over magnetizing branch u_i given by the vector sum of components in d and q axis for enlarged model of induction motor.

3 Conclusion

The simulations results show than the differences between the conventional model and the enlarged model with iron loss are negligible for normal operating conditions. The minor differences may appear in dynamic states. This fact is shown in fig. 2, 3 and 4, where the starting process of induction motor is shown. The correct solution of model with iron loss is confirmed, as the iron current is much smaller than magnetizing current ($i_{Fe} << i_m$). Therefore, the iron current does not considerably affect the stator current, as is shown in fig. 3 and 4. The simulated iron current caused the power dissipation 350 W in the steady state, confirms the values measured during the idle test.

Acknowledgment

The work is partially supported by Grant of SGS N°. SP2015/151, VŠB - Technical University of Ostrava, Czech Republic.

References

1. Krause, P. C., Wasynczuk, O., Sudhoff, S. D.: Analysis of Electric Machinery and Drive Systems, IEEE Press, NY: 2002.
2. Leedy, A. W.: Simulink / MATLAB Dynamic Induction Motor Model for use in Undergraduate Electric Machines and Power Electronics Courses, IEEE, NY: 2013.
3. Neborák, I.: Modelování a simulace elektrických regulovaných pohonů. Monografie, VŠB-TU Ostrava 2002, 172 stran, ISBN 80-248-0083-7.
4. Jung, J.: A Vector Control Scheme for EV Induction Motors with a Series Iron Loss Model, IEEE, Trans. Industry Electronics , 1998.
5. Lim, S., Nam, K.: Loss-minimising control scheme for induction motors, IEE Proc. – Electr. Power Appl., vol. 151, 2004.

Implementation of Luenberger Observer to Sensorless Vector Control Structure of Induction Motor Drive

Ondřej Petrtýl

Department of Electronics, FEECS,
VŠB – Technical University of Ostrava, 17. listopadu 15, 708 33 Ostrava – Poruba
ondrej.petrtyl@vsb.cz

Abstract. The aim of this paper is using of a sensorless vector control of a three-phase induction motor with the Luenberger observer. Theoretical assumptions for the mathematical model of the IM as well as for the vector control structure are given. Principles and settings for simulations in MATLAB Simulink, are presented. Results of simulations are presented.

Keywords: sensorless speed control, induction motor, luenberger observer, matlab simulink

1 Introduction

Sensorless drives are more and more popular, because of an absence of the speed or position sensor, it brings many advantages: lower maintenance requirements, a simpler construction and a higher reliability and mechanical robustness. A sensor brings more electronics, a higher cost and a lower reliability. Also a weight is increasing, the volume and the total moment of inertia of the drive are increasing as well. In sensorless drives the sensor of position or speed is replaced by using the machine model and an estimator as sensor. The sensorless control of induction motors (IM) is very popular nowadays. With decreasing prices and increasing performances of microprocessor control systems, they can provide a very good price-performance ratio. With a powerful processor all necessary variables of the complex control structure can be computed in real-time. [1] – [4]

Sensorless IM drives are used with intelligent and sophisticated control methods, such as the Vector Control (VC). The IM VC techniques use the information of the rotor speed coming from the speed sensor (positioning transducer) or the sensorless estimator. Speed estimators, operated on the motor model, can be divided into three groups: open-loop estimators, MRASs

© M. Krátký, J. Dvorský, P. Moravec (Eds.): WOFEX 2015, pp. 114–119.
VŠB – Technical University of Ostrava, FEECS, 2015, ISBN 978-80-248-3787-1.

and observers. The closed-loop (the observer-based) methods are more robust than the open-loop speed estimation techniques by introducing the error feedback of the current estimation. [1], [2], [5], [6]

2 Mathematical Model of Induction Motor

The mathematical model of the IM in the stator coordinate system is described by current-flux equations [13,17], which is shown by space equations (1), (2), where respective matrices are (3) – (5). [7], [8]

$$\dot{\boldsymbol{x}} = \boldsymbol{A}\boldsymbol{x} + \boldsymbol{B}\boldsymbol{u}, \tag{1}$$

$$\boldsymbol{y} = \boldsymbol{C}\boldsymbol{x}, \tag{2}$$

$$\boldsymbol{x} = [i_{s\alpha} \quad i_{s\beta} \quad \psi_{r\alpha} \quad \psi_{r\beta}]^T, \quad \boldsymbol{u} = [u_{s\alpha} \quad u_{s\beta}]^T, \tag{3}$$

$$\boldsymbol{A} = \begin{bmatrix} -\frac{{L_m}^2 R_r + {L_r}^2 R_s}{\sigma L_s {L_r}^2} & 0 & \frac{L_m R_r}{\sigma L_s {L_r}^2} & \frac{L_m}{\sigma L_s L_r}\omega_r \\ 0 & -\frac{{L_m}^2 R_r + {L_r}^2 R_s}{\sigma L_s {L_r}^2} & -\frac{L_m}{\sigma L_s L_r}\omega_r & \frac{L_m R_r}{\sigma L_s {L_r}^2} \\ \frac{L_m R_r}{L_r} & 0 & -\frac{R_r}{L_r} & -\omega_r \\ 0 & \frac{L_m R_r}{L_r} & \omega_r & -\frac{R_r}{L_r} \end{bmatrix}, \tag{4}$$

$$\boldsymbol{B} = \frac{1}{\sigma L_s}\begin{bmatrix} 1 & 0 \\ 0 & 1 \\ 0 & 0 \\ 0 & 0 \end{bmatrix}, \quad \boldsymbol{C} = \begin{bmatrix} 1 & 0 & 0 & 0 \\ 0 & 1 & 0 & 0 \end{bmatrix}, \tag{5}$$

$$\sigma = 1 - \frac{{L_m}^2}{L_s L_r}. \tag{6}$$

Where:

$\boldsymbol{i}_s^S$	Stator current space vector with components $i_{s\alpha}$, $i_{s\beta}$,
$\boldsymbol{u}_s^S$	Stator voltage space vector with components $u_{s\alpha}$, $u_{s\beta}$,
$\boldsymbol{\psi}_r^S$	Rotor magnetic flux space vector with components $\psi_{r\alpha}$, $\psi_{r\beta}$,
L_m	Magnetizing inductance,
L_s , L_r	Stator and rotor inductance,
R_s , R_r	Stator and rotor resistance,
ω_r	Electrical angular speed,
σ	Leakage factor.

3 Mathematical Model of Luenberger Observer

The Luenberg observer (LO) is a typical representative of the close loop estimators, so-called observers, namely of the deterministic observers. The expressions (7), (8) describe the basic Luenberger observer, which can be used for state estimation of a time invariant system. [7]

$$\dot{\hat{\boldsymbol{x}}} = \hat{\boldsymbol{A}}\hat{\boldsymbol{x}} + \boldsymbol{B}\boldsymbol{u} + \boldsymbol{G}\tilde{\boldsymbol{y}} = \hat{\boldsymbol{A}}\hat{\boldsymbol{x}} + \boldsymbol{B}\boldsymbol{u} + \boldsymbol{G}[\boldsymbol{y} - \hat{\boldsymbol{y}}], \tag{7}$$

$$\hat{\boldsymbol{y}} = \boldsymbol{C}\hat{\boldsymbol{x}}, \tag{8}$$

$$\hat{\boldsymbol{A}} = \boldsymbol{A}|_{\boldsymbol{\omega_r}=\hat{\boldsymbol{\omega}}_r}. \tag{9}$$

The observer state matrix $\hat{\boldsymbol{A}}$ is a transformed state matrix $\boldsymbol{A}$ by eqn (9). The input matrix $\boldsymbol{B}$ and output matrix $\boldsymbol{C}$ are same as in the IM description (6). The observer matrix $\boldsymbol{G}$ can be written as (10), and their components are described by (11) – (14). [9]

$$\boldsymbol{G} = \begin{bmatrix} g_1 & -g_2 \\ g_2 & g_1 \\ g_3 & -g_4 \\ g_4 & g_3 \end{bmatrix}. \tag{10}$$

Design of the observer matrix is based on the rule that the LO must be stable and faster than observed system, in our case the IM. [2]

$$g_1 = (k-1)(a_{11} + a_{33}), \tag{11}$$

$$g_2 = (k-1)\hat{\omega}_r, \tag{12}$$

$$g_3 = (k^2-1)(\mathrm{c}a_{11} + a_{33}) - \mathrm{c}(\mathrm{k}-1)(a_{11} + a_{33}), \tag{13}$$

$$g_4 = -\mathrm{c}(\mathrm{k}-1)\hat{\omega}_r, \tag{14}$$

$$c = -\frac{\sigma L_s L_r}{L_m}. \tag{15}$$

Where a_{11} , a_{31} , a_{33} are components of matrix $\boldsymbol{A}$ from (4). The estimated speed $\hat{\omega}_r$ is given by an adaptation algorithm, namely by integration with a proportional component (16). The correction term z is defined by (17). [2]

$$\hat{\omega}_r = K_P z + K_I \int z\, dz, \tag{16}$$

$$z = e_{is\alpha}\hat{\psi}_{r\beta} - e_{is\beta}\hat{\psi}_{r\alpha} = (i_{s\alpha} - \hat{\imath}_{s\alpha})\hat{\psi}_{r\beta} - (i_{s\beta} - \hat{\imath}_{s\beta})\hat{\psi}_{r\alpha}. \tag{17}$$

4 Simulation results

The simulation investigates the response for a multistep reference speed with reversing, shown by Fig. 1. The IM was tested under both motoring and generating modes and has been running at constant and at variable speed, too. The initial speed is 0 rpm. After half a second change to a constant value 100 rpm for one sec. Then the speed linearly decreases to 70 rpm during half a sec. Where it holds again for one sec. Then, the referenced speed reversed to -50 rpm for one sec. Finally at t = 4 s, the speed is set to 0 rpm again.

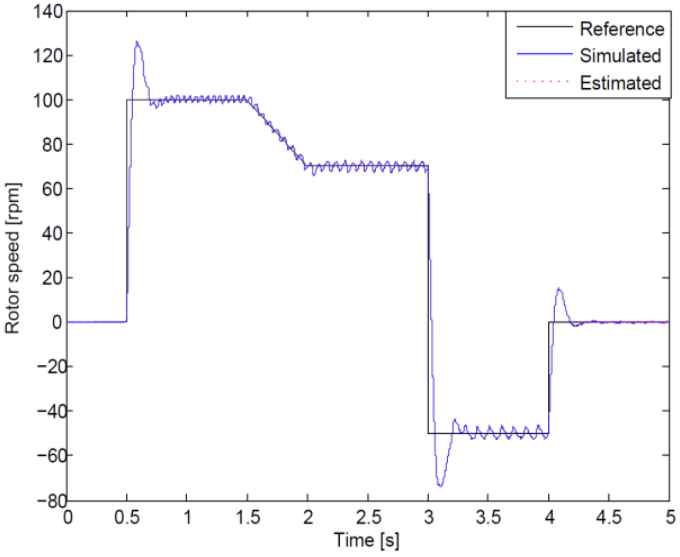

Fig. 1. Response for multistep reference speed with reversing.

According to the simulations, the difference between the simulated and the estimated speed quickly reduces down to zero after a change in the speed command, see the speed error shown in Fig. 2.

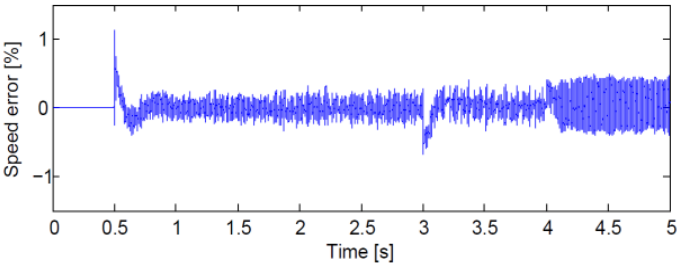

Fig. 2. Difference between simulated and estimated speed.

The simulated and the estimated currents (Fig. 3.), which are used as feedback in the observer, are also in good agreement, with a maximum error of 0.2 %, see Fig. 4. Note also the change in phases that can be seen at t = 3 s, where the speed is reversed.

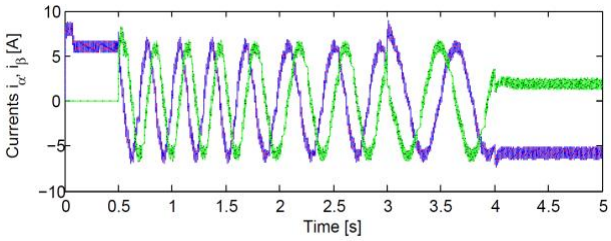

Fig. 3. Simulated (blue) and estimated (red) stator current i_α and simulated (green) and estimated (black) stator current i_β.

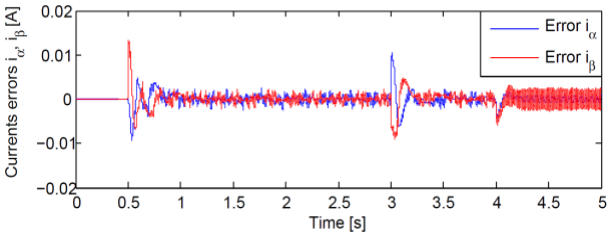

Fig. 4. Difference between simulated and estimated stator currents.

These simulation results substantiate the expected performance of the proposed algorithm based on the closed-loop estimation with the Luenberger Observer.

5 Conclusions

The aim of this paper is an implementation of the Luenberger Observer to the vector control scheme and verify a functionality. The simulations have been done and the simulation results have been evaluated and provided. Our implementation provides satisfactory results with a good level of an accuracy for a constant value of speed as well as for step or ramp changes and a reversing.

6 Acknowledgement

The paper was supported by the projects: Center for Intelligent Drives and Advanced Machine Control (CIDAM) project, reg. no. TE02000103 funded

by the Technology Agency of the Czech Republic and project reg.no. SP2015/81 funded by the Student Grant Competition of VSB-Technical University of Ostrava.

7 References

[1] Brandstetter, P. "AC Control Drives - Modern Control Methods," VSB - Technical University of Ostrava, 1999. ISBN: 80-7078-668.

[2] Brandstetter, P.; Friedrich, J. "Speed Estimation of Induction Motor Using Luenberger Observer," In Proc. of the Acta Tech. CSAV. vol. 57, pp. 113-126, 2012. ISSN: 0001-7043.

[3] Holtz, J. "Sensorless control of induction motor drives," Proceedings of the IEEE vol. 90, no. 8, pp. 1359-1394, 2002. DOI: 10.1109/JPROC.2002.800726, ISSN: 0018-9219.

[4] Demmelmayr, F.; Troyer, M.; Schroedl, M. "Advantages of PM-machines compared to induction machines in terms of efficiency and sensorless control in traction applications," IECON 2011 - 37th Annual Conference on IEEE Industrial Electronics Society, pp. 2762-2768, 2011. DOI: 10.1109/IECON.2011.6119749, ISBN: 978-1-61284-969-0.

[5] Stumper, J.-F.; Kennel, R. "Field-oriented control of a speed-sensorless induction motor for the complete speed range using a nonlinear observer," Sensorless Control for Electrical Drives (SLED), 2011 Symposium, pp. 107-113, 2011. DOI: 10.1109/SLED.2011.6051553, ISBN: 978-1-4577-1855-7.

[6] Zhang, Y.; Zhao, Z.; Lu, T.; Yuan, L.; Xu, W.; Zhu, J. "A comparative study of Luenberger observer, sliding mode observer and extended Kalman filter for sensorless vector control of induction motor drives," Energy Conversion Congress and Exposition, 2009. ECCE 2009. IEEE, pp. 2466-2473, 2009. DOI:10.1109/ECCE.2009.5316508, ISBN:978-1-4244-2893-9.

[7] Bose, B. K. "Modern power electronics and AC drives," Upper Saddle River, NJ : Prentice Hall PTR, 711 p., 2002, ISBN 0-13-016743-6.

[8] Neborak, I. "Modeling and Simulations of Electrical Controlled Drives," VSB-TU Ostrava, CZ, 172 p., 2002. ISBN: 80-248-0083-7.

[9] Kojabadi, H. M. - Chang, L. "Comparative Study of Pole Placement Methods in Adaptive Flux Observer," Control Engineering Practice 13, pp. 749-757, 2005. ISSN 0967-0661.

Optimization of the Rotor Part of a Interior Permanent Magnet Synchronous Generator

Ladislav Slíva

Department of Electrical Power Engineering, FEECS,
VŠB – Technical University of Ostrava, 17. listopadu 15, 708 33 Ostrava – Poruba
ladislav.sliva@vsb.cz

Abstract. The work is being focused on a rotor part of the interior permanent magnets synchronous machine (I-PMSM). The research had paid attention to the 5th and 7th harmonics. As it has been proven several times [1], [2], [3], [4], [5] a usage of multiple parallel magnets per a one pole instead of just one can affect specific operating properties. This study tries to find out how to divide a single magnet into more parallel ones and how to deploy them in appropriate way, with respect to a reduction amplitudes in selected harmonics. The issues has been solved using analytical calculations and also FEM analysis. The research was being made for a no-load state as well as for a rated load state. A prototype was produced at the end of this research, and likewise outputs of the model could be verified by measuring.

Keywords. synchronous machine, measurement, calculation, FEM, analysis, permanent, magnet, optimize, parameters, rotor.

1 Introduction

Nowadays, it's standard practice in designing and constructing of synchronous engines that magnets in one piece (i.e. single permanent magnet per pole – Fig. 1) could only be used when performance properties of the machine allows a manufacturing such engines. However this is not possible in case of high-power machines (and because of requirements of magnetic properties or of the high power), so it's necessary to split the single magnet into smaller ones and to place them next to each other (Fig. 2).

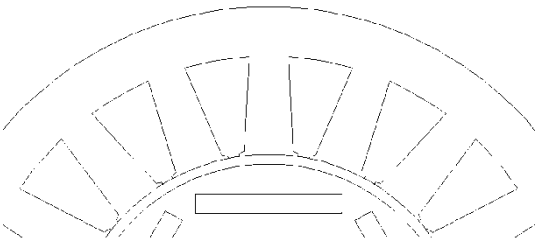

Figure. 1. Example – I-PMSM – one magnet per pole

© M. Krátký, J. Dvorský, P. Moravec (Eds.): WOFEX 2015, pp. 120–126.
VŠB – Technical University of Ostrava, FEECS, 2015, ISBN 978-80-248-3787-1.

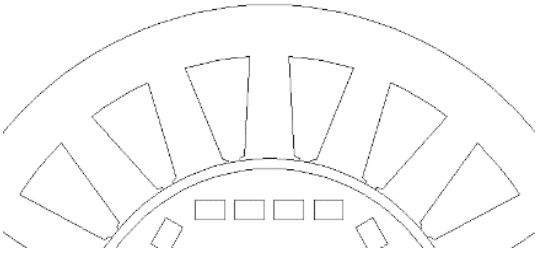

Figure. 2. Example – I-PMSM – more magnets per pole

A topology of parallel magnets per a pole hasn't required usage of this concept in low and middle power machines yet, well it has an influence on their specific operating properties anyway. We consider how an optimal splitting of magnets may improve the specific operating properties of the machine, especially how to reduce iron losses.

2 Analysed machine

The analysis of specific operating properties was done by measuring, calculating and using the FEM analysis. There is a prerequisite of conformity with measured, calculated and simulated waveform within a minimal variability, whether the correct procedure is followed. The parameters from the measuring, calculating and the FEM analysis will be applied in comparison with new topologies of the synchronous machine with permanent magnets. Rest of the parameters including machine geometry (Tab. I) we'd discovered during dismantling, these were not stated on the production plate.

Table 1. Parameters of analysed machine

P_n	2,2 kW	Rated power	2p	6	Number of poles
U_n	400 V	Rated voltage	N_s	420	Number of turns (one phase)
I_n	5,8 A	Rated current	l_i	0,08 m	Iron length
	Y	Stator winding	δ	0,8 mm	Air gap
f_n	50 Hz	Rated frequency	d	0,040 m	Outer rotor diameter
n_n	1000 min^{-1}	Rated speed	D	0,071 m	Outer stator diameter
Q	18	Stator slots	h_M	8,0 mm	Magnet height
q	0,5	Stator slots per pole and phase	w_M	25,0 mm	Magnet width
l_M	120 mm	Magnet length			

Before the FEM analysis itself it's needed to build a generator model. Main inputs for the FEM analysis cover basic diameters of the stator and the rotor (inside and outside diameter, length), layout of magnets on the rotor circumference and also material properties. Some values were evident, so it was possible to get them by a plain measuring and calculating, and properties of magnets and the magnetic circuit were taken from a design of the machine. Accuracy of FEM model had been still verified in se-

lected points of measured generator characteristic, so than we were able to approach the reality.

The Fig. 3 shows a magnetic induction layout of the original synchronous generator model in no-load state. The table II shows results from a harmonics analysis of the magnetic flux density progress in the middle of the air gap. This harmonics analysis was performed with use the FlexPro 9 application.

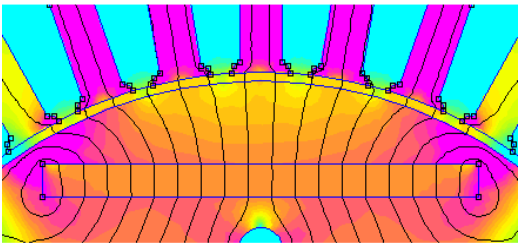

Figure. 3. Magnetic flux density (original model)

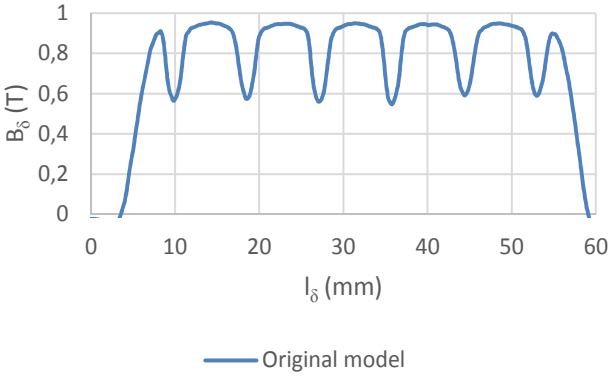

Figure. 4. Air gap magnetic flux density – original model

Table 2. Percentage content of harmonics and fundamental – original model (FlexPro 9)

Calculation type	Percentage content of harmonics and fundamental		
	1	5	7
Analytic	100	24,85	18,54
FEM	100	22,13	15,17

There on the Tab. II, you can see quite high amplitudes in the 5th and 7th harmonic order in terms of the fundamental harmonic. It is possible to reduce these 5th and 7th harmonic orders by dividing each single magnet per a pole into two parallel magnets in an appropriate way, this is solved and described by a mathematical model.

3 Mathematical Model

The mathematical model serves to determine a size of partial parallel magnets per a pole as accurate as possible, as well as to define a space (gap) between these partial magnets. The Fig. 5 shows a magnet of the analyzed machine. The width (longer side) of the magnet is expressed in degrees (deg.). The height of the magnet represents a maximum value of the magnetic flux density progress in the middle of the air gap inducted by this magnet.

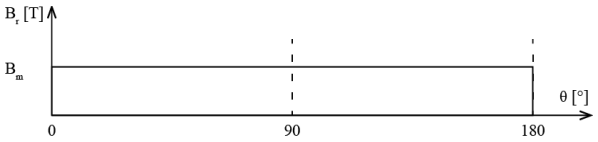

Figure. 5. Magnet of analysed machine

By arranging the sub-magnets properly, we can eliminate some terms of Fourier coefficients as many as the number of sub-magnets per pole (Fig. 5). In this article, we will eliminate two kinds of space harmonics (5th and 7th), and the air-gap flux harmonics are written as

$$b_h = \frac{2}{\pi}\int_0^{\pi} B_m(\theta)\sin(h\theta)\,d\theta \tag{1}$$

and with respect to Fig. 7 we can write

$$b_h = \frac{4}{\pi}\int_0^{\alpha_1} B_m(\theta)\sin(h\theta)\,d\theta + \frac{4}{\pi}\int_{\alpha_2}^{\pi} B_m(\theta)\sin(h\theta)\,d\theta \tag{2}$$

After the calculation we obtain

$$b_h = \frac{4B_m}{\pi h}[\cos(h\alpha_1) - \cos(h\alpha_2)] \tag{3}$$

Now we've got non-linear equation (3) as the base for a system of non-linear equations, where the number of unknowns (the number of angles from an appropriate magnet dividing) equals a number of non-linear equation in the system. In practise amplitude drops with the harmonic order and then it can be immeasurable, therefore we will by trying to focus on odd harmonics in 5th and 7th order. After the modification with regard to the (3) we obtain system of non-linear equations

$$\begin{aligned} \cos(5\alpha_1) - \cos(5\alpha_2) &= 0 \\ \cos(7\alpha_1) - \cos(7\alpha_2) &= 0 \end{aligned} \tag{4}$$

Because this kind of system of non-linear equations cannot be easily solved using methods of the linear algebra, we must usage of numerical methods - the Newton's method (also known as the Newton–Raphson method) is the most suitable in this case. The equations (4) can be solved when we substitute $b_n = 0$. In view of the fact that complexity and difficulty in solving of these kind of systems, it is recommended to use a computer.

4 Solving and evaluating mathematical and numerical model

The system of equations (4) was solved by using the MATLAB application and dividing angles of the magnet are $\alpha_1 = 15{,}42^o$ and $\alpha_2 = 87{,}42^o$. You may notice that 15% in total is removed from the original magnet (Fig. 8) and the Fig. 9 shows a part of optimized model of the machine.

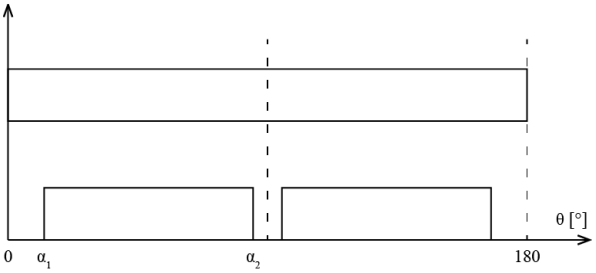

Figure. 6. Magnet of analysed and optimized machine

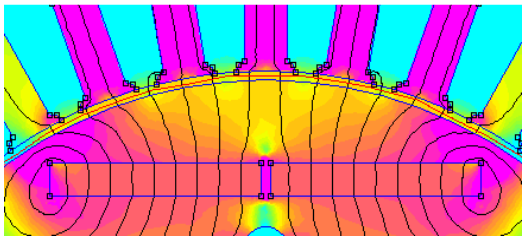

Figure. 7. Magnetic flux density (optimized model)

Also the Fig. 7 and Fig. 8 shows us that the magnetic flux density progress in the air gap dropped slightly from 0.892 T to 0.834 T, because have been removed magnet parts. Changing position of the magnet in the iron can help to eliminate this deficiency. Therefore let us apply Algorithms Artificial Intelligence.

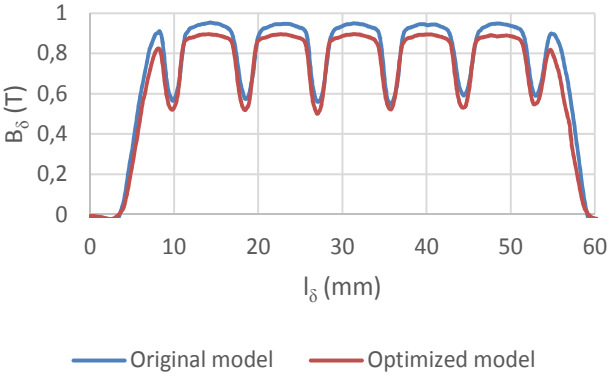

Figure. 8. Air gap magnetic flux density - comparison

Tab. 10 shows the results of harmonic analysis of optimized model. The amplitude the 5th and 7th harmonic order of magnetic flux density in the middle of the air gap dropped. Research results were being validated by analytical calculation too.

Table 3. Percentage content of harmonics and fundamental – optimized model (FlexPro 9)

Calculation type	Percentage content of harmonics and fundamental		
	1	5	7
Analytic	100	0	0
FEM	100	3,72	2,84

The Fig. 9 shows iron losses according to the change of no load speed. These losses are directly proportional to the magnetic flux density and the square wave of its frequency, also they are lower when using two parallel magnets per a pole instead of just one.

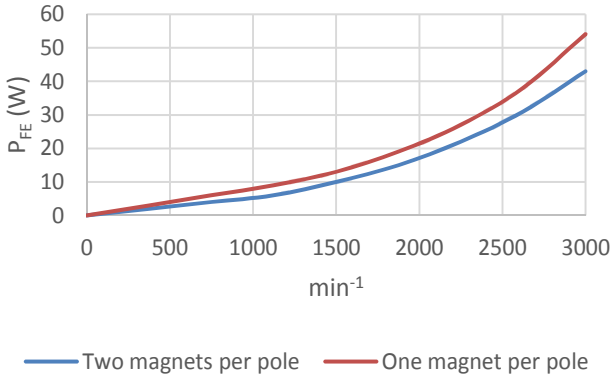

Figure. 9. Core loss

5 Concluson

A usage of two parallel magnets per a one pole instead of just one can reduce amplitudes of selected space harmonics on the base curve of the air gap magnetic flux density. This method can improve the selected operational characteristics of the synchronous machine with permanent magnets.

Based on results from comparison between the FEM analysis and analytical calculations, we can actually determine a validity of the technique and results. A prototype was designed for verification of results by measuring.

References

1. K. Yamazaki, Y. Fukushima.” Effect of Eddy-Current Loss Reduction by Magnet Segmentation in Synchronous Motors with Concentrated Windings”. IEEE Transactions on Industry Applications, vol. 47. pp. 779-788. 2011
2. J. Seo, S. Kwak, S. Jung, Y. Lee, CH. G. Chung, T. K. Jung. K. “A Research on Iron Loss of I – PMSM With a Fractional Number of Slot Per Pole”. Magnetics IEEE Transactions, 2009, str. 1824 – 1827, ISSN: 0018-9464
3. J. D. Ede, K. Atallah, G. W. Jewell, J. B. Wang, and D. Howe, "Effect of axial segmentation of permanent magnets on rotor loss in modular permanent-magnet brushless machines," IEEE Trans. on Ind. Appl., vol.43, no.5, pp. 1207-1213, 2007.
4. K. Yamazaki and A. Abe, "Loss investigation of interior permanent magnet motors considering carrier harmonics and magnet eddy currents," IEEE Trans. on Ind. Appl., vol.45, no.2, pp.659-665, 2009.
5. K. Yamazaki, M. Shina, M. Miwa and J. Hagiwara, "Effect of eddy current loss reduction by segmentation of magnets in synchronous motors: difference between interior and surface types", Intermag 2009, Sacrament, 2009.
6. A. Wang , H. Li , W. Lu and H. Zhao "Influence of skewed and segmented magnet rotor on IPM machine performance and ripple torque for electric traction", IEEE Int. Conf. Electric Machines and Drives (IEMDC\'09), pp.305 -310 2009
7. P. Reddy, R. Jahns, T.M. Lipo, T.A. Anbarasu, R. Sorensen, H.L. Osama, and M. Jensen,"Segmented permanent magnet synchronous machines for wind energy conversion system," Power Electronics and Machines for Wind and Water Applications (PEMWA), 2014 IEEE Symposium , vol., no., pp.1,8, 24-26 July 2014
8. S. Duan, L. Zhou and J. Wang, "Flux Weakening Mechanism of Interior Permanent Magnet Synchronous Machines With Segmented Permanent Magnets," Applied Superconductivity, IEEE Transactions on , vol.24, no.3, pp.1,5, June 2014
9. Z. Wu. and Z. Zhu. "Analysis of Air-Gap Field Modulation and Magnetic Gearing Effects in Switched Flux Permanent Magnet Machines," Magnetics, IEEE Transactions on , vol.PP, no.99, pp.1,1, January 2015

Control Methods of Induction Motor Drives

Thinh Cong Tran, Chau Si Thien Dong, Hau Huu Vo

Faculty of Electrical and Electronics Engineering, Ton Duc Thang University
Nguyen Huu Tho Street, Tan Phong Ward, District 7, Ho Chi Minh City, Vietnam
trancongthinh@tdt.edu.vn

Abstract. The paper deals with an overview of basic control methods which are used for induction motor drives. These methods include the scalar control, the vector control and the direct torque control. The paper contains basic description of the mentioned control methods. The simulation of the vector controlled induction motor drive with vector control was realized in Matlab-Simulink. The simulation results are presented in the paper.

Keywords: induction motor, speed control, scalar control, vector control, direct torque control.

1 Introduction

Induction motor drives with cage type machine have many applications in industry. For the control of induction motor drives, three main methods are used: Scalar Control (SC), Vector Control (VC) and Direct Torque and Flux Control (DTC). Thanks to VC or DTC it becomes possible to control, directly and separately, the torque and flux of the induction motors.

In scalar control, control variables are only varied in magnitude: voltage of an induction motor and frequency (or slip) can be controlled to control the flux and the torque respectively. The vector control technique demonstrates that an induction motor (IM) can be controlled like separately excited DC motor. The vector control and the corresponding feedback signal processing, particularly for modern sensorless vector control, are complex and the use of powerful DSP microcomputer control system is mandatory. The DTC has comparable performance with the vector control. In this control method, the torque and the stator flux are controlled directly by selecting voltage space vector of the voltage source inverter through a look up table [1]-[4].

2 Scalar control of induction motor drives

The scalar control is simple to implement, but the inherent the coupling effect (both torque and flux are functions of voltage or current and frequency) gives sluggish response and system can easily become unstable. These drives have been used commonly in industry [1]-[4].

© M. Krátký, J. Dvorský, P. Moravec (Eds.): WOFEX 2015, pp. 127–132.
VŠB – Technical University of Ostrava, FEECS, 2015, ISBN 978-80-248-3787-1.

2.1 Open loop voltage/frequency control

Normally, asynchronous machines have been used with open loop fixed-frequency power supplies for constant speed applications. For adjustable speed applications, frequency control is natural. However, voltage is required to be proportional to frequency so that the stator flux ($\Psi_S = V_S/\omega_e$) remains constant if the voltage drop on the stator resistance R_S is neglected. Fig. 1 shows block diagram of the voltage/frequency speed control.

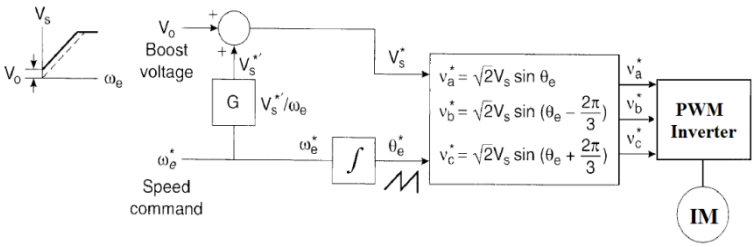

Fig. 1. Block scheme of the open loop voltage/frequency control

2.2 Speed control with slip regulation

This technique improves the performance of open loop voltage/frequency control (see Fig. 2). The speed error generates the slip command through PI controller. The addition of this signal and feedback signal is the frequency command. Since slip is proportional to the torque at constant flux, the scheme can be considered as an open loop torque control within a speed control loop. If the command speed is reduced by a step, the drive goes into regenerative or dynamic braking mode and decelerates with constant negative slip - ω_{sl}^*. If the load torque is increased, the speed will tend to drop. However, the speed control loop will increase the frequency until the original speed is restored.

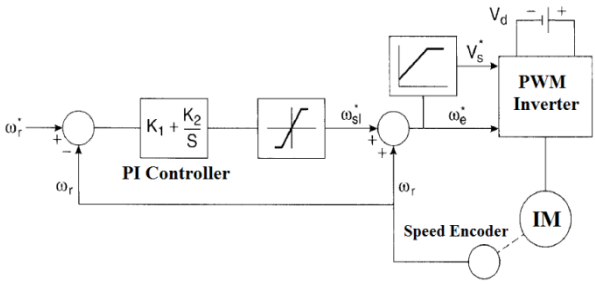

Fig. 2. Block scheme of the speed control with voltage/frequency control and slip regulation

2.3 Speed control with torque and flux control

The flux may drift in the voltage/frequency control technique, and as a result, the ratio between the torque and slip will vary. Fig. 3 shows a speed control system with close

loop flux and torque control. Many feedback signals make synthesis and system stabilization more complex. A torque loop within the speed loop improves the performance of the speed loop. The torque and flux estimation can be done with machine terminal voltages and currents. With constant rotor flux Ψ_r^* as the speed increase, the voltage increases proportionally until square-wave mode is reached and field-weakening mode starts.

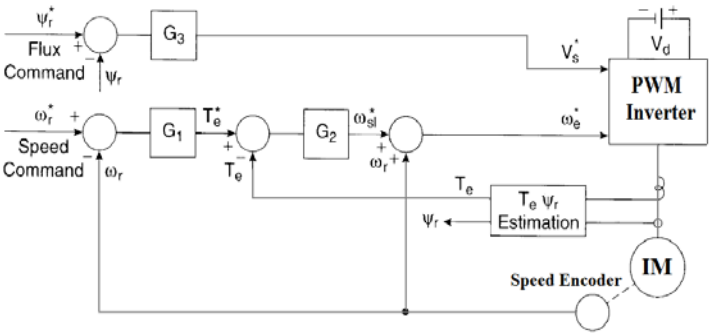

Fig. 3. Block scheme of the speed control with torque and flux control

3 Vector control of induction motor drives

The vector control is based on a dynamic model of the induction motor expressed in a rotating coordinate system *x*, *y* which is oriented on the rotor magnetic flux vector. Fig. 4 shows the basic block scheme of the vector control of the IM drive [5].

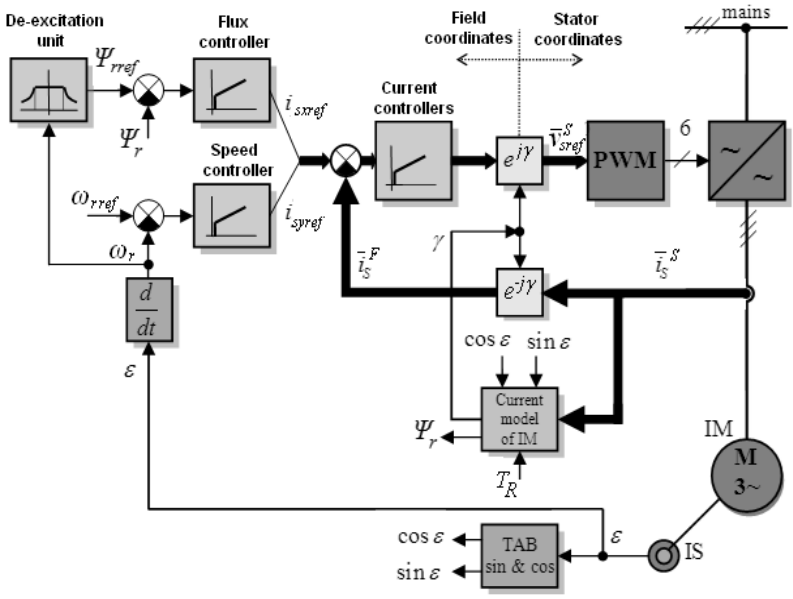

Fig. 4. Block scheme of the vector control

A flux control loop is used to control the rotor flux Ψ_r. A torque control is achieved through the torque current component i_{Sy} which is generated from the speed control loop. Two motor phase currents are measured by current sensors and are transformed by Clarke transformation module. The outputs of this projection are current components $i_{S\alpha}$ and $i_{S\beta}$. These two components enter into Park transformation that gives the current components i_{Sx}, i_{Sy} in the x, y rotating reference frame. These components are compared to the references i_{Sxref} and i_{Syref}. The outputs of the current controllers are v_{Sxref} and v_{Syref}; they are applied to the inverse Park transformation. The outputs of this projection are $v_{S\alpha ref}$, $v_{S\beta ref}$, which are the components of the stator vector voltage $\boldsymbol{v}_S^S$ in the α, β stator stationary reference frame. These components are the inputs of the vector PWM (Block of Pulse Width Modulation).

4 Direct torque and flux control of induction motor drives

The block diagram of the direct torque and stator flux control is shown in Fig. 5. Firstly, this technique compares the command torque and stator flux with estimated values. Then, the errors will be processed by hysteresis-band controllers [6].

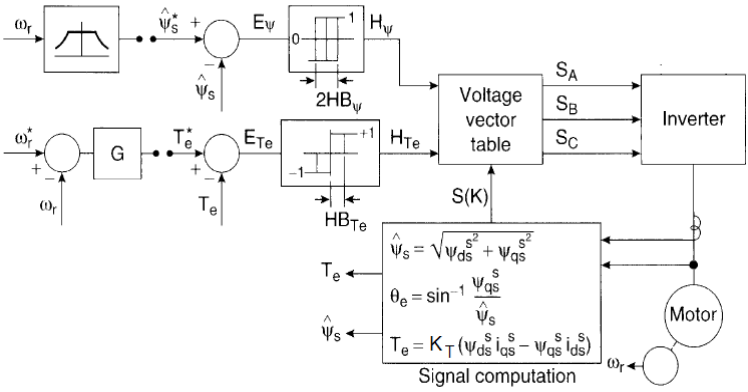

Fig. 5. Block scheme of the direct torque and stator flux control

The signal computation block (see Fig. 5) calculates signals from voltage model of the induction motor.

5 Simulation results

The described vector control of the IM drive was simulated using MATLAB-SIMULINK. The parameters of the induction motor (type P 112 M04) are: P_n = 2.7 kW, T_n = 19 Nm, ω_{mn} = 1360 rpm, p_p = 2, I_{Sn} = 7.51 A, I_{Rn} = 17 A, I_{Sxn} = 6.8 A, I_{Syn} = 8.16 A, U_{Sn} = 400/230 V, Ψ_{Sn} = 0.877 Wb.

The time courses of important quantities (see Fig. 6 - Fig. 9) were obtained from the speed control structure at the jump of the load torque TL = 5 Nm (see Fig 7).

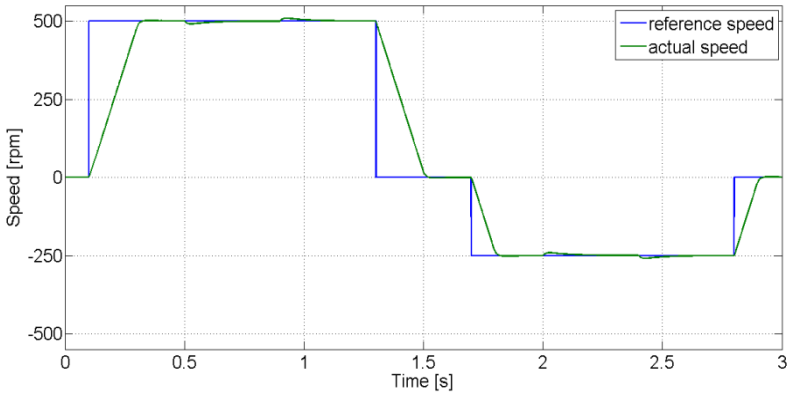

Fig. 6. Reference speed ω_{m_ref} and actual rotor speed of the induction motor ω_m

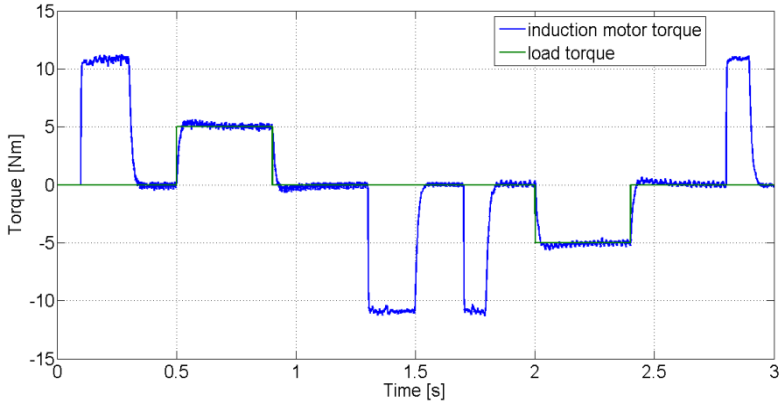

Fig. 7. Induction motor torque T_M and load torque T_L

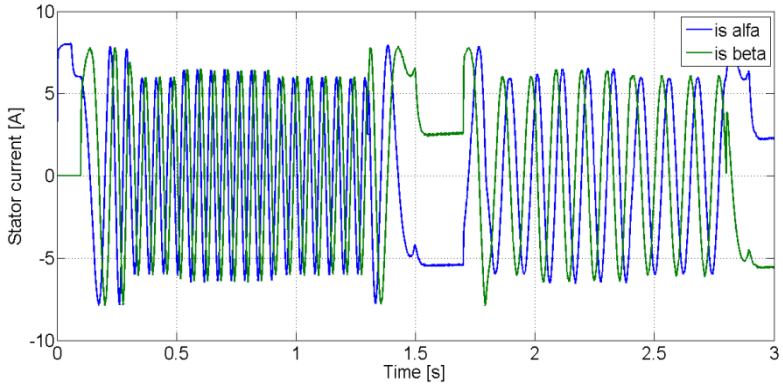

Fig. 8. Stator current vector components $i_{S\alpha}$, $i_{S\beta}$

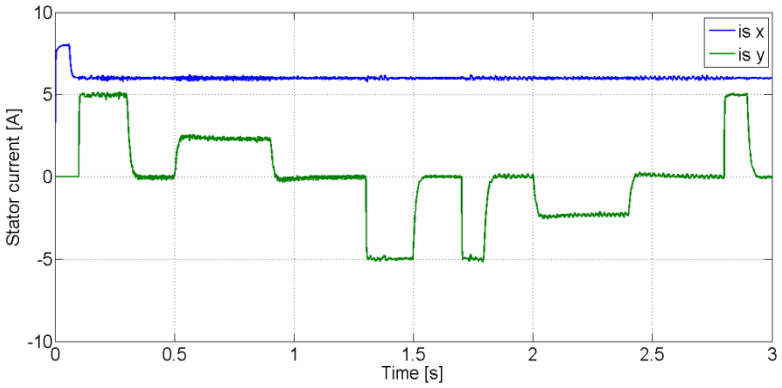

Fig. 9. Magnetizing current component i_{Sx} and torque current component i_{Sy}

6 Conclusion

The control methods for the induction motor drives were presented in the paper. The control structure of the induction motor drive with vector control was simulated using Matlab-Simulink. The induction motor drive gives good dynamic responses and the control of the mechanical speed is good in steady state and also in transient state.

Acknowledgement

In the paper, there are the results of the project reg. no. SP2015/81 funded by the Student Grant Competition of VSB-Technical University of Ostrava. This research was supervised by Prof. Ing. Pavel Brandstetter, CSc.

References

1. P. Vas, Sensorless Vector and Direct Torque Control, Oxford University Press, 1998.
2. J. Holtz, Sensorless Control of Induction Motor Drives, Proceedings of the IEEE, vol. 90, n. 8, pp. 1359-1394, 2002.
3. K. B. Bose, Power Electronics and Modern Electric Drives. N. Jersey: Prentice Hall, 2002.
4. A. Bellini, S. Bifaretti, Sensitivity to Parameters' Variations in Sensorless Induction Motor Drives Using a Reduced Order MRAS Observer, International Review of Electrical Engineering - IREE, vol. 2, n. 2, pp. 242-249, 2007.
5. P. Brandstetter, AC Controlled Drives – Modern Control Methods. Ostrava, VSB-Technical University of Ostrava, 177 p., 1999.
6. P. Brandstetter, P. Chlebis, P. Palacky, Direct Torque Control of Induction Motor with Direct Calculation of Voltage Vector. Advances in Electrical and Computer Engineering, vol. 10, no. 4, pp. 17-22, 2010.

MRAS Techniques for Sensorless Control of Induction Motor With Using Artificial Neural Network

Tomáš Verner

Department of Electronics, FEECS,
VŠB – Technical University of Ostrava, 17. listopadu 15, 708 33 Ostrava – Poruba
tomas.verner1@vsb.cz

Abstract. The paper describes the Model Reference Adaptive System (MRAS) observers techniques as the modern way for the control of an induction motor (IM). The induction motor drive is a dynamic nonlinear system with uncertainty in the machine parameters. The main aim is to improve tracking performance of the induction motor drive etc. A method for controlling induction motor drive and speed estimation with MRAS and (based) Artificial Neural Networks (ANN). One of the important reason for controlled induction motor drives without mechanical speed sensors at the motor shaft are that have the attractions of low cost and high reliability. The artificial neural network, MRAS-based speed estimation is used. The error between the reference model and the neural network based adaptive model is used to adjust the weights by on-line Back propagation training algorithm. Artificial Neural Networks (ANN) is successfully used in many areas such as fault detection, control and signal processing in our daily technology. Matlab-Simulink is software which used to develop a three phase induction motor model and we can use to the creation of simulation models for the sensorless control and another methods for motor drives.

1 Introduction

By using modern resources used in the regulation of AC drives can be considerable savings and improvements in the control of the drives. Currently, high attention is paid to a sensorless control of the AC machines whose basic advantages such as a reduction of hardware complexity and cost, increasing mechanical robustness, higher reliability, lower maintenance demands and cost, working in hostile environments, etc., led to the development of different sensorless methods for rotor position and mechanical speed estimation of electrical drives with the induction motors [4], [5]. Several speed estimators for sensorless vector control of induction motor have been proposed. They can be divided into two groups, the model-based estimators and signal injection-based estimators. Among the first group the MRAS, the adaptive Luenberger observers and the extended Kalman-filter. These methods perform well at low and zero speed regions, they suffers from, computational complexity, the need of external hardware for signal injection and the adverse effect of injecting signal on the machine performance. Therefore, due to their simplicity, model-based methods and especially MRAS-based methods are, until now, the most widely used [6], [7].

© M. Krátký, J. Dvorský, P. Moravec (Eds.): WOFEX 2015, pp. 133–138.
VŠB – Technical University of Ostrava, FEECS, 2015, ISBN 978-80-248-3787-1.

2 Model Reference Adaptive System (MRAS) Observer

Mr.Tamai has proposed one speed estimation technique based on the Model Reference Adaptive System (MRAS) in 1987. Two years later, Mr.Schauder presented an alternative MRAS scheme which is less complex and more effective. The MRAS approach uses two models. The model that does not involve the quantity to be estimated (the rotor speed, ω_r) is considered as the reference model. The model that has the quantity to be estimated involved is considered as the adaptive model (or adjustable model). The output of the adaptive model is compared with that of the reference model, and the difference is used to drive a suitable adaptive mechanism whose output is the quantity to be estimated (the rotor speed). The adaptive mechanism should be designed to assure the stability of the control system. A successful MRAS design can yield the desired values with less computational error (especially the rotor flux based MRAS) than an open loop calculation and often simpler to implement [8]. The adaptation mechanism has two parts: evaluation of the adaptation signal Φ(e) and it´s following minimalization using classical PI-controller which produces the estimated value of the rotor speed for the adaptive model. The block of structure of the MRAS is shown in the figure 1 [2].

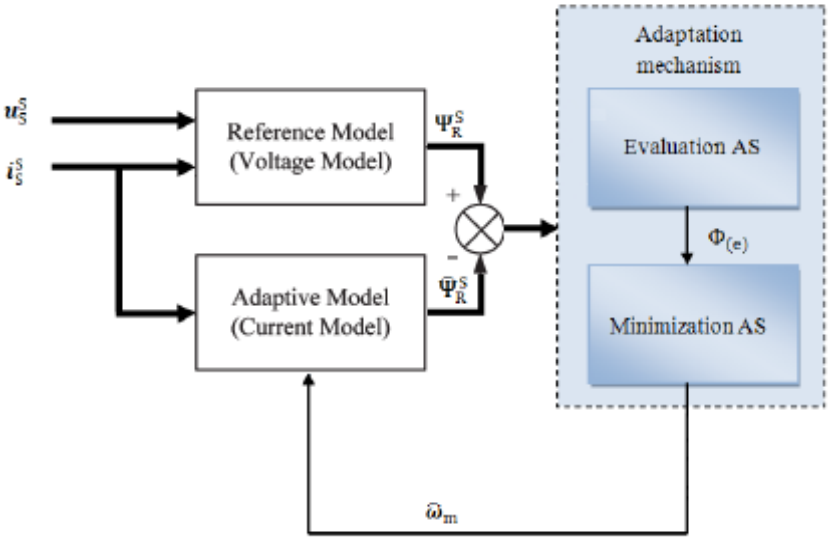

Fig.1. Structure of the model reference adaptive system (MRAS) for estimation [2].

The model reference adaptive system (MRAS) is one of the major approaches for adaptive control. The model reference adaptive system (MRAS) is one of many promising techniques employed in adaptive control. Among various types of adaptive system configuration, MRAS is important since it leads to relatively easy-to-implement systems with high speed of adaptation for a wide range of applications [8].

2.1 Simulation block of MRAS-ANN in MATLAB-SIMULINK

Figure 2 shows the simulink block diagram Model Referencing Adaptive System with artificial neural networks (MRAS-ANN). Which is consists Two blocks one is called Reference Model with ANN and other is Adaptive Model. The voltage model's stator-side equations are defined as a Reference Model and the simulink block diagram of Reference Model. The Adaptive Model receives the machine stator voltage and current signals and calculates the rotor flux vector signals, as indicated by equations. By using suitable adaptive mechanism the speed ω_r, can be estimated and taken as feedback [8].

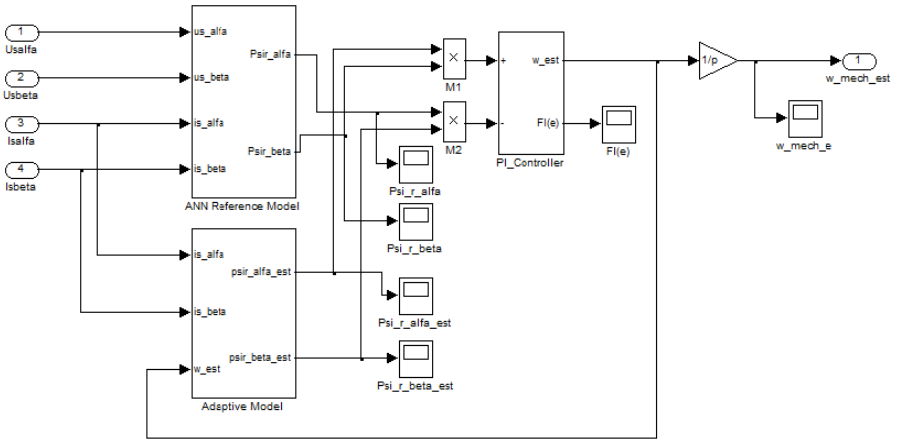

Fig.2. Simulation model of ANN-MRAS for model referencing adaptive system.

In the system of MRAS performs the function reference model, artificial neural network, which is trained off-line using the models obtained from the current model of induction machine, which uses vector control with the sensors. The current model then performs the function of the adaptive system MRAS model.

The adaptive model is described by equations [2]:

$$\hat{\bar{\Psi}}^{S}_{R(AM)} = \int \left[\left(j\hat{\omega}_R - \frac{1}{T_R} \right) \cdot \hat{\bar{\Psi}}^{S}_{R} + \frac{1}{T_R} \cdot L_m \bar{i}^{S}_{S} \right] dt \qquad (1)$$

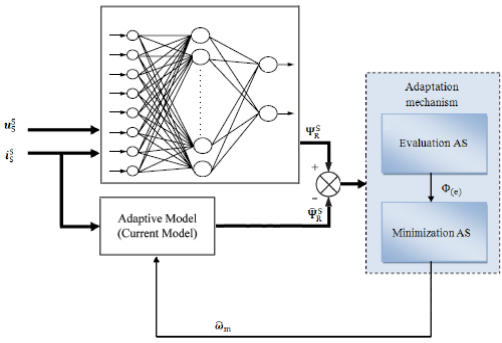

Fig.3. Block diagram of the ANN-MRAS speed observer.

3 Reference Frame Model Reference Adaptive System (RF-MRAS)

In general, we can decompose the determination of the neural network parameters into two phases. At first, the default values of all attributes are determined. In the second phase, these values are adapted by the appropriate algorithm.

The adaptive model of the reference frame MRAS (RF-MRAS) is described with the following equation no.1 (on page 3), which contains the rotor angular speed as changing parameter.

The reference model is described with the following equation:

$$\overline{\Psi}^{S}_{R(RM)} = \frac{L_R}{L_m}\left[\int\left(\bar{u}^{S}_{S} - R_S\bar{i}^{S}_{S}\right)dt - \frac{L_S L_R - L_m^2}{L_R}\cdot\bar{i}^{S}_{S}\right] \qquad (2)$$

The integration, however, would be subject to long term drift in practice and special measures should be taken to correct this drift. There was used I controller with the limitation. By help of the limitation war removed the influence of the offset on the calculation of the rotor flux in the reference model. The adaptation algorithm is described with the next equations [2]:

$$\Phi(e) = \hat{\overline{\Psi}}^{S}_{R(AM)} x \overline{\Psi}^{S}_{R(RM)} = \hat{\Psi}_{R\alpha(AM)}\Psi_{R\beta(RM)} - \hat{\Psi}_{R\beta(AM)}\Psi_{R\alpha(RM)} \qquad (3)$$

$$\hat{\omega}_R = K_1\Phi(e) + K_2\int_0^t \Phi(e)dt \qquad (4)$$

Where K1 > 0, K2 > 0.

If we look carefully to RF-MRAS structure, we can see, that for rotor flux flows directly from the reference model. This means that RF-MRAS works as open-loop estimator of rotor flux. And as it was written before, open-loop estimators have so many disadvantages, that they are unusable for traction drive purposes. Where upon we can claim that RF-MRAS is not a perspective solution. Purpose it is not necessary to implement any feedback, because the most important quantity for vector control.

4 Simulation Results

The simulations of sensorless vector control of induction motor have been carried out using MATLAB/Simulink platform and the estimators were implemented in the structure of vector control.

Next figure shows the speed response of the MRAS speed estimator when the induction motor is operated at different reference speeds. It shows that the estimated speed tracks the actual speed reasonably well at high speed and even at low speed. But, as the speed decreased, the steady state values of the estimated speed tend to deviate from actual speed. The performance of the estimators has been studied in terms of its ability to converge to the actual speed and the response of the estimators towards parameters changes. Thus, to fit that purpose, the values of parameter in the induction motor are kept unchanged while the values of the estimators are varied from its rated value [9].

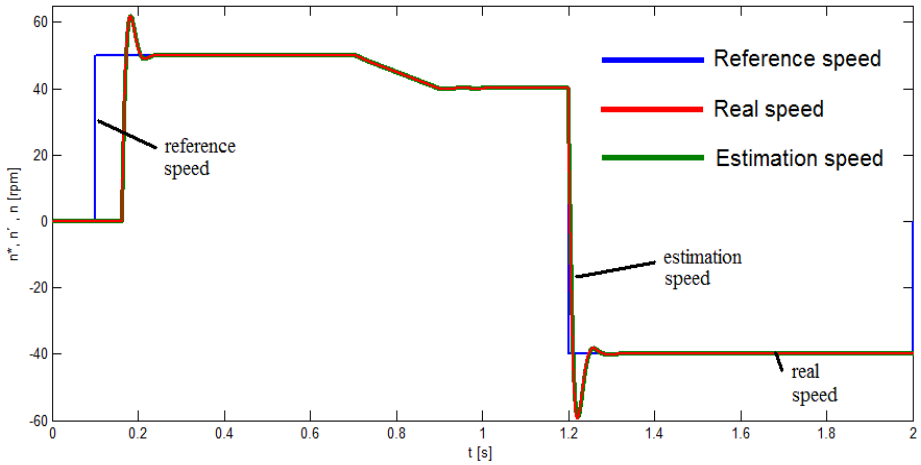

Fig.4. Compared reference, real and estimation speed during simulation of MRAS sensorless control

Figure 4 shows the MRAS performance for step changes in speed rererence. The MRAS responds well to these changes in speed reference as can be seen from the plot, but the network have a small problem with the change during step change. But even with these small problems, the application of model reference adaptive system have good properties.

5 Conclusion

This paper has described the use of Model Reference Adaptive System (MRAS) to identify and control the induction machine in the basic application. Article shows a possible application of MRAS and ANN-MRAS techniques in the control of induction motor A.C. drives. A multilayer feedforward ANN estimates the rotor flux components from present and past samples of reference stator voltages and measured currents. The scheme makes use of the offline-trained ANN observer as a reference model in MRAS scheme. MRAS rotor speed observer was proposed to improve the performance of sensorless vector controller of induction machine. The control robustness is achieved by a new approach by controller. In this approach is the robustness of the proposed observer regarding load torque and stator resistance variations, especially at low and zero speed, is much better than the classical observer. The MRAS technique is used for simultaneous estimation based on measured terminal voltages and currents. The validity of the proposed Sensorless Speed Control with MRAS for Induction Motor Drive was also proven by simulation and the results confirm the effectiveness and the good dynamic performances of the proposed method.

Acknowledgement

In the paper, the results of the project SP2015/81, which was supported by Student Grant Competition of VSB - Technical University of Ostrava. This research was supervised by Prof. Ing. Pavel Brandštetter, CSc.

References

[1] BRANDŠTETTER, Pavel. *AC controlled drivers – modern control methods*. Ostrava, VŠB-TU Ostrava, 177p, 1999, ISBN 80-7078-668-X. (in Czech language)

[2] BRANDŠTETTER, Pavel. *Sensorless Control Of Induction Motor Using Modified MRAS.* International Review of Electrical Engineering (I.R.E.E), Vol.7, N.3, 4404-4411, ISNN 1827 – 6660.

[3] VERNER, Tomáš. *Control of Induction Motor Using Artificial Neural Networks.* WOFEX 2014, pp.132–137. Ostrava, VŠB – TU Ostrava, FEECS, 2014. ISBN 978-80-248-3458-0.

[4] BRANDŠTETTER, P., DOBROVSKÝ, M. *Speed Estimation of Induction Motor Using Model Reference Adaptive System with Kalman Filter.* Theoretical and applied electrical engineering, Vol.12, N.1, March 2013.

[5] HOLTZ, J. *Sensorless Control of Induction Motor Drives*. Proceedings of the EEE. 2002, vol. 90, ISSN 0018-9219. DOI: 10.1109/JPROC.2002.800726.

[6] BENLALOUI, I., DRID, S. and coll.: *Implementation of a New MRAS Speed Sensorless Vector Control of Induction Machine.* IEEE 2014,Transaction on energy conversion.

[7] HA, J-I., SUL, L-K. *Sensorless field-orientation control of an induction machine by high-frequency signal injection. IEEE Trans. Ind. Appl.*, vol. 35, no. 1, pp. 45–51, Jan./Feb. 1999.

[8] KUMAR, K.K., SASIKANTH, S., DINESH, L.: *Simulation Of Sensorless Induction Motor Based On Model Reference Adaptive System (MRAS)*. International Journal of Engineering Research and Applications (IJERA), Vol. 2, Issue 6, November- December 2012, pp.255-260, ISSN: 2248-9622.

[9] HARON, A.R., IDRIS, N.R.: *Simulation of MRAS-based Speed Sensorless Estimation of Induction Motor Drives using MATLAB/SIMULINK*. First International Power and Energy Conference (PECon), November 2006, Malaysia.

Simulation of MRAS Observer in Direct Torque Control Structure of Induction Motor Drive

Hau Huu Vo

Faculty of Electrical and Electronics Engineering, Ton Duc Thang University
Nguyen Huu Tho Street, Tan Phong Ward, District 7, Ho Chi Minh City, Vietnam
vohuuhau@tdt.edu.vn

Abstract. The paper deals with a rotor speed estimation for an induction motor. The Model Reference Adaptive System method (MRAS) is chosen for its good tracking capability and moderate demands on the DSP unit. The paper contains basic mathematical description of the direct torque control of the induction motor and MRAS observer. In the paper, there is a focus on basic theory of the MRAS observer and its application in the sensorless control of the induction motor drive with the direct torque control. The simulation results are presented in the paper.

Keywords: induction motor, direct torque control, speed control, sensorless control, MRAS observer.

1 Introduction

The control and estimation of induction motor drives is almost unbounded subject, and the technology has been developing very strong in last few decades. The induction motor drive with cage type machine have many applications in industry such as pumps and fans, paper and textile mills, subway and locomotive propulsions, electric and hybrid vehicles, machine tools and robotics, home appliances, heat pumps and air conditioners, rolling mills, wind generation systems. These applications often require adjustable speed and wide power range from several hundreds to multi-megawatts. Besides that, the energy-saving capability of variable frequency drive is getting a lot of attention nowadays.

The control and estimation of AC drives in general are more complex than those of DC drives, and this complexity increases substantially if high performance are demanded. The main reason of this complexity is need of variable frequency, harmonically optimum converter power suppliers, the complex dynamics of AC machines, machines parameter variations, and difficulties of processing feedback signals in the presence of harmonics [1], [2].

The selection of the drive for the induction motor control is based on considering several questions such as:

- One-, two- or four-quadrant drive?

© M. Krátký, J. Dvorský, P. Moravec (Eds.): WOFEX 2015, pp. 139–144.
VŠB – Technical University of Ostrava, FEECS, 2015, ISBN 978-80-248-3787-1.

- Torque, speed, or position control in the primary or outer loop?
- Single- or multi- motor drive?
- Range of speed control? Does it include zero speed and field-weakening regions?
- Accuracy and response time?
- Robustness with load torque and parameter variations?
- Control with speed sensor or sensorless control?
- Type of front-end converter?
- Efficiency, cost, reliability, and maintainability?
- Line power supply, harmonics, and power factor?

2 Direct torque control of the induction motor

The direct torque control (DTC) has comparable performance with the vector control. In this scheme, the torque and the stator flux are controlled directly by selecting voltage space vector of the inverter through a look up table. The block diagram of DTC is shown in Fig. 1. Firstly, this techniques compare the command torque and stator flux with estimated values. Then, the errors will be processed by hysteresis-band controllers [3].

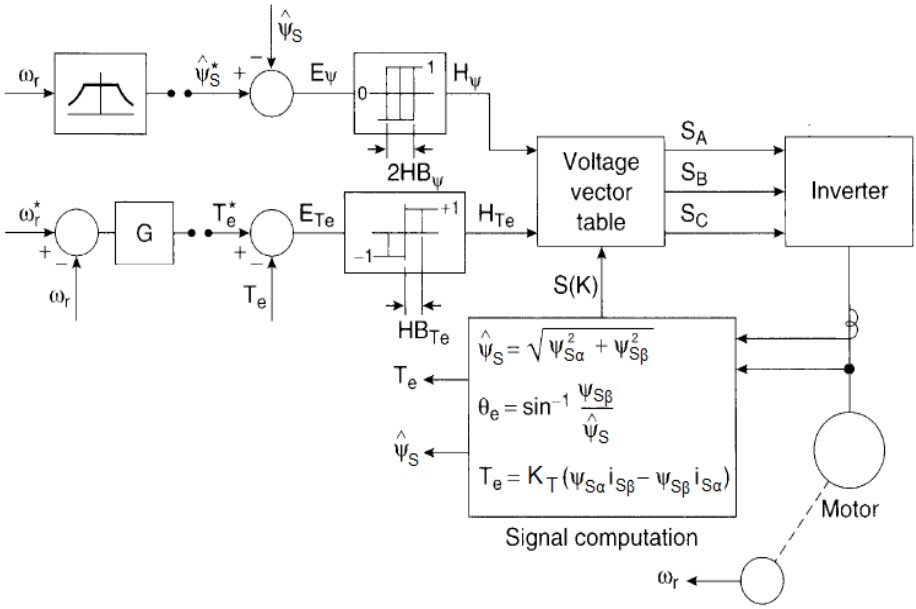

Fig. 1. Block scheme of the direct torque control

High performance control, such as vector control, is based on a dynamic model of the induction motor expressed in a rotating coordinate system which is oriented on the rotor magnetic flux vector.

The flux controller has two levels:

$$H_{\psi} = 1 \quad \text{for} \quad E_{\psi} > +HB_{\psi}$$
$$H_{\psi} = -1 \quad \text{for} \quad E_{\psi} < -HB_{\psi} \tag{1}$$

The torque controller has three levels:

$$H_{Te} = 1 \quad \text{for} \quad E_{Te} > +HB_{Te}$$
$$H_{Te} = -1 \quad \text{for} \quad E_{Te} < -HB_{Te} \tag{2}$$
$$H_{Te} = 0 \quad \text{for} \quad -HB_{Te} < E_{Te} < +HB_{Te}$$

The signal computation block (see Fig. 1) calculates signals from voltage model of the induction motor. This block also seeks where stator flux vector lies (see Fig. 2).

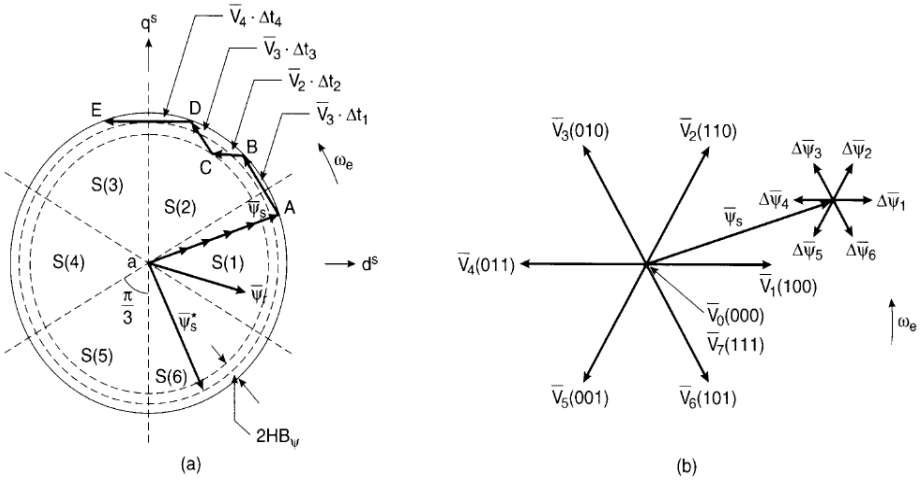

Fig. 2. Trajectory of the stator flux vector in DTC Control, (b) Inverter voltage vectors and corresponding flux variation in time Δt

DTC technique has some special features:

- no feedback current control,
- no traditional PWM algorithm,
- no vector transformation,
- feedback signal processing is similar to stator flux-oriented vector control,
- hysteresis-band controller generates flux and torque ripple and switching frequency is not fixed (like hysteresis-band current control).

3 MRAS observer

The rotor speed can be estimated by the Model Reference Adaptive System (MRAS) observer [4], [5]. The output of the MRAS observer is compared with the output of an adaptive or adjustable model until the errors between the two models is equal to zero.

The speed estimation diagram is shown in Fig. 3. The stator voltage and current signals are measured and used for calculating the rotor flux vector in this figure.

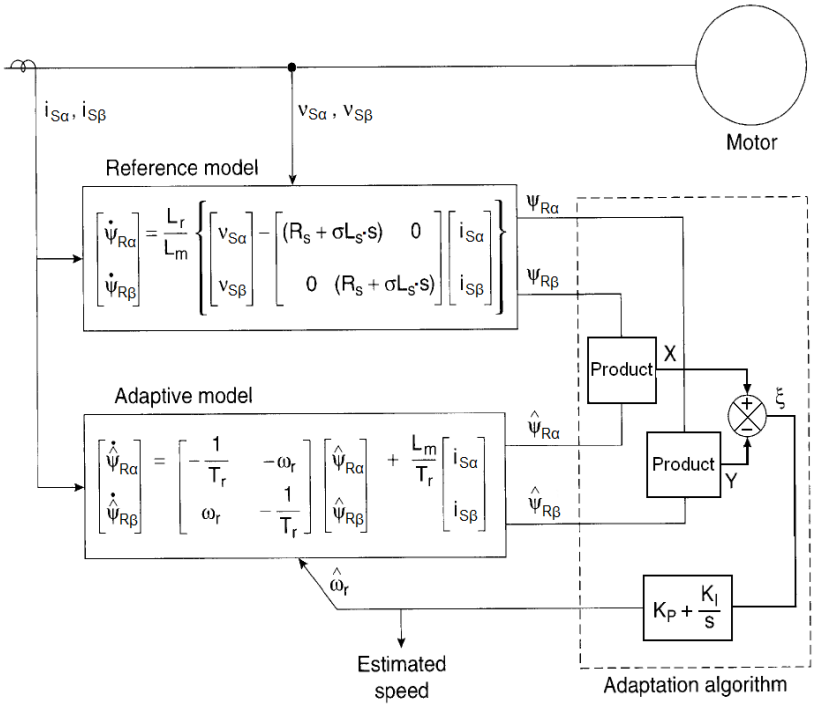

Fig. 3. Block scheme of the speed estimation using MRAS

In this model, we can get rotor flux vector components from the inputs (stator voltages and stator currents) only if we know the rotor speed ω_r exactly. Ideally, the rotor flux vector components from two models (reference and adaptive) will match. An adaptation algorithm with PI control can be used to tune the speed so that an adaptation signal ξ reach to zero.

The adaptation algorithm is described with the following equations:

$$\xi = \hat{\psi}_{R\alpha}\psi_{R\beta} - \psi_{R\alpha}\hat{\psi}_{R\beta} \tag{3}$$

$$\hat{\omega}_r = K_1\xi + K_2\int_0^t \xi dt \tag{4}$$

where $K_1 > 0$, $K_2 > 0$.

In practice, this method is difficult to implement, particularly at low speeds because of the pure integration of the voltage signals. The integration, however, would be subject to long-term drift in practice and special techniques should be taken to correct this drift. For example, the I-controller with the limitation can be used. Besides that, the estimation accuracy can be good if parameters of motor are constants. However, accuracy is decreased due to parameter variation.

4 Simulation results

The described induction motor drive with the DTC was simulated using MATLAB-SIMULINK. The basic parameters of the induction motor (type P 112 M04) are: P_n = 2.7 kW, T_n = 19 Nm, ω_{mn} = 1360 rpm, p_p = 2, I_{Sn} = 7.51 A, I_{Rn} = 17 A, U_{Sn} = 400/230 V, Ψ_{Sn} = 0.877 Wb.

The time courses of important quantities (see Fig. 6 - Fig. 9) were obtained from the speed control structure at the jump of the load torque TL = 2 Nm (see Fig. 7).

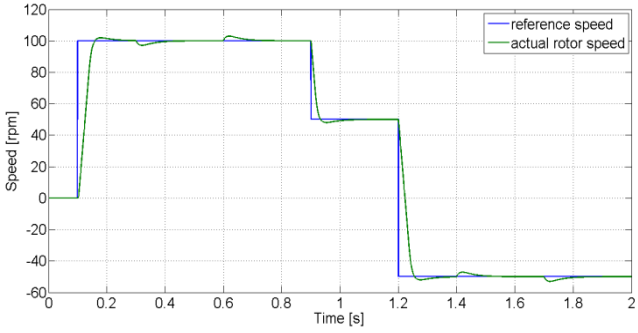

Fig. 4. Reference speed ω_{m_ref} (blue) and actual rotor speed of the induction motor ω_m (green)

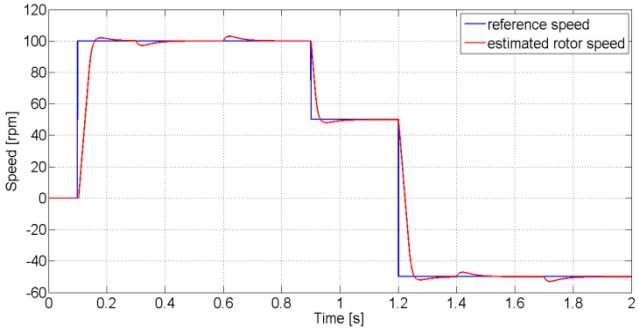

Fig. 5. Reference speed ω_{m_ref} (blue) and estimated rotor speed of the induction motor ω_m (red)

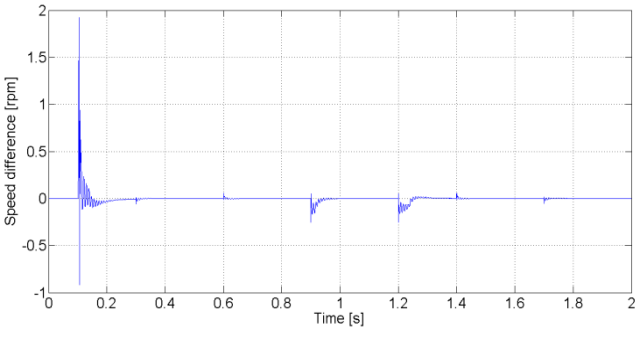

Fig. 6. Speed difference between actual and estimated rotor speed of the induction motor

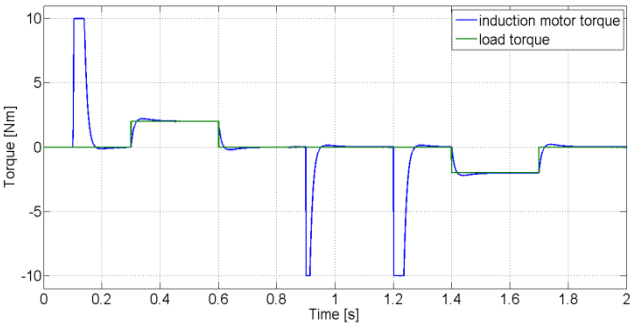

Fig. 7. Load torque (green) and induction motor torque (blue)

5 Conclusion

The estimation technique for sensorless induction motor drive with the direct torque control was presented in the paper. The speed estimator is based on application of the MRAS observer. The induction motor drive with the presented speed estimator gives good dynamic responses and the estimation of the mechanical speed is good in steady state and also in transient state.

Acknowledgement

In the paper, there are the results of the project reg. no. SP2015/81 funded by the Student Grant Competition of VSB-Technical University of Ostrava. This research was supervised by Prof. Ing. Pavel Brandstetter, CSc.

References

1. P. Vas, Sensorless Vector and Direct Torque Control, Oxford University Press, 1998.
2. J. Holtz, Sensorless Control of Induction Motor Drives, Proceedings of the IEEE, vol. 90, n. 8, pp. 1359-1394, 2002.
3. P. Brandstetter, P. Chlebis, P. Palacky, Direct Torque Control of Induction Motor with Direct Calculation of Voltage Vector. Advances in Electrical and Computer Engineering, vol. 10, no. 4, pp. 17-22, 2010.
4. T. Orlowska-Kowalska, M. Dybkowski, Stator-Current-Based MRAS Estimator for a Wide Range Speed-Sensorless Induction-Motor Drive, IEEE Transactions on Industrial Electronics, vol. 57, n. 4, pp. 1296-1308, 2010.
5. P. Brandstetter, Sensorless Control of Induction Motor Using Modified MRAS. International Review of Electrical Engineering - IREE, Vol. 7, N. 3, pp. 4404-4411, 2012.

Coupling of DC sources

Katerina Baresova

Department of Electronics, FEECS,
VŠB – Technical University of Ostrava, 17. listopadu 15, 708 33 Ostrava – Poruba
katerina.baresova@vsb.cz

Abstract. In recent years there is a growing interest in the development of new types of electric networks, which contain elements of accumulation of electrical energy in electrochemical sources. Accumulation units may cover the peak of electric power consumption, voltage stabilization, or improvements of power quality in distribution networks. To achieve the highest capacity of the accumulation unit, it is necessary to couple different types of accumulation technologies into serial-parallel connected units. This paper deals with ways of coupling these accumulation units to obtain larger amount of stored energy and obtaining greater loadability of accumulation systems. This paper describes options of solutions suitable for coupling elements accumulation DC sources and focuses on the use of the principle of resonance in this application.

Keywords: DC source, coupling, energy.

1 Theory of coupling sources

In simple terms we divide electrical sources to voltage sources and current sources, according to whether the source holds at the load a constant voltage at current variable both in terms of its polarity, or circuit load "pushes" a constant current regardless of the voltage polarity that its terminals create. A typical representative of the voltage source is ideal charged capacitor with infinite capacity. In this paper we will not deal with current source type. For solving electrical circuits we consider the voltage source for solving electrical circuits either as ideal or as real.
Real voltage source usually consists of an ideal voltage source with a serial resistor, which represents the internal resistance of the voltage source. The principle shows that with different parameters voltage and partially with internal resistance a parallel connection of voltage sources is very difficult or even impossible. Even when the voltage of sources is the same, it depends on the size of the internal resistance, because these resistances determine the embranchment of current at individual sources. The condition of identical voltage is difficult to realize in practice. Failing this condition means the creation of equalization currents at voltage sources, and equalization voltage at current sources. Their size depends on different parameters of coupled sources. The situation is illustrated in Fig. 1.

© M. Krátký, J. Dvorský, P. Moravec (Eds.): WOFEX 2015, pp. 145–150.
VŠB – Technical University of Ostrava, FEECS, 2015, ISBN 978-80-248-3787-1.

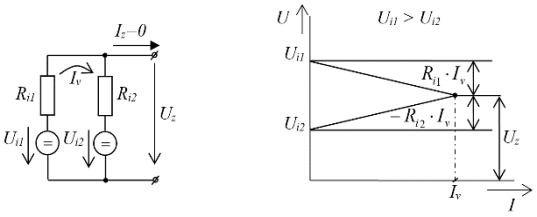

Fig. 1. Parallel connection of two voltage sources without load

In a parallel connection of two or more sources without load creates equalizing current I_v between sources, which corresponds to the difference between the open circuit voltage of each sources and the size of their internal resistance. These internal resistors create a voltage divider, which determines the value of output open circuit voltage U_z for the entire system of sources. [1, 7, 8]

2 Use of resonance for energy transmission

This designed conception allows transferring equalizing energy between DC sources in pulses, which are used in energy transfer at resonance. This principle is often used in intermediate circuits of indirect frequency converters with the so-called resonance DC link. To illustrate this principle, first we must analyze the activities of the resonant circuit to the mathematical description of resonant transfer energy unit.
The simplest second-order circuit is the uncontrolled circuit having one capacitor and one inductor, shown in Figure 2. It is lossless because it contains no elements that dissipate energy. That is, it contains no resistors. It is uncontrolled because it contains no independent sources to provide external stimuli. Therefore, it offers us the opportunity to focus on the internal, or homogeneous, behavior of the circuit itself. More about this analysis is in literature [2].

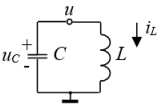

Fig. 2. A simple second-order circuit.

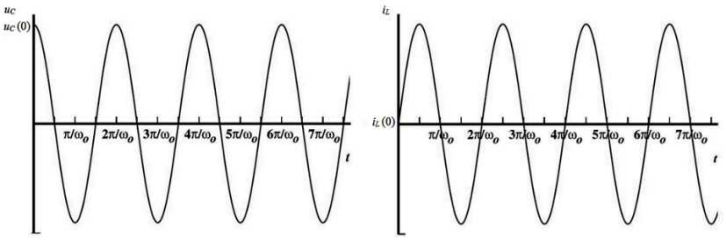

Fig. 3. Waveforms of i_L and u_C for the undriven LC circuit for the special case of $i_L(0) \equiv 0$

A close look at Figure 3 shows that, for all choices of initial condition, i_L and u_C are sinusoidal functions that are a quarter cycle out of phase with each other. The initial conditions affect only their amplitudes and their common absolute phase. Therefore, we can illustrate the behavior of the circuit without loss of understanding by considering the special case of

$$i_L(0) \equiv 0$$

The resulting expressions for i_L and u_C for $i_L(0) \equiv 0$ are given as follows, and Figure 3 shows the corresponding evolution of both i_L and u_C:

$$u_C(t) = u_C(0)\cos(\omega_0 t) \tag{1}$$

$$i_L(t) = \sqrt{\frac{C}{L}}u_C(0)\sin(\omega_0 t) \tag{2}$$

Figure 3 illustrates several important points. As mentioned earlier, both branch variable states are sinusoidal in time. Because of this, the peaks of one state occur at the zeros of the other. Given the definitions of positive i_L and u_C in Figure 4, u_C leads i_L by a quarter cycle. Thus, the greatest positive slope in i_L occurs at the positive peaks of u_C, and the greatest negative slope in i_L occurs at the negative peaks of u_C, in accordance with the constitutive law for the inductor. Similarly, the greatest positive slope in u_C occurs at the negative peaks of i_L, and the greatest negative slope in u_C occurs at the positive peaks of u_C, in accordance with the constitutive law for the capacitor. So, each state drives the growth of the other.

There is also an important energy interpretation to Figure 3. It is that the oscillations in i_L and u_C carry out a repetitive exchange of energy between the inductor and the capacitor. Indeed, the state of each element drives the growth of the other at the expense of the energy it stores. To see this, consider the energy w_E stored in the capacitor, the energy w_M stored in the inductor, and the total energy w_T stored between them. [2]

The total energy in the circuit w_T is is given by:

$$w_T = w_E + w_M = \frac{1}{2}Cu_C^{\,2}(0) + \frac{1}{2}Li_L^{\,2}(0) \tag{3}$$

Thus, the total energy w_T is constant in time. This is the case because there are no resistors in the circuit that could dissipate the energy. Note too that the energy completely exchanges between the two elements since both w_E and w_M periodically go to zero. This behavior is also identical to that of many other lossless second-order mechanical oscillators in which kinetic and potential energies are repetitively exchanged. To illustrate this, Figure 4 shows the w_E, w_M, and w_T for the special case of $i_L(0) \equiv 0$. Note that the energies exchange at the frequency $2\omega_0$ because both i_L and u_C go to zero twice during the period $2\pi/\omega_0$.

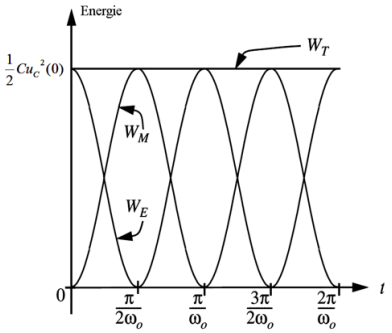

Fig. 4. Energy w_E, w_M, and w_T for the circuit for the special case of $i_L(0) \equiv 0$

Function of resonant circuit makes it possible to transfer energy between sources by converting the form of electrical and magnetic energy. [1, 5, 6]

3 The results of numerical model

The figure below shows the results of simulation of the resonant circuit coupling the two voltage sources. Waveform in middle shows the voltage on the capacitor, which represents the energy w_E, the waveform below shows the current of inductance coupling of individual sources, thus the energy w_M of these coupling coils. This principle has also been verified by simulations for block arrangement, when the resonant currents were divided into coupling coils of multiple sources. [3, 4]

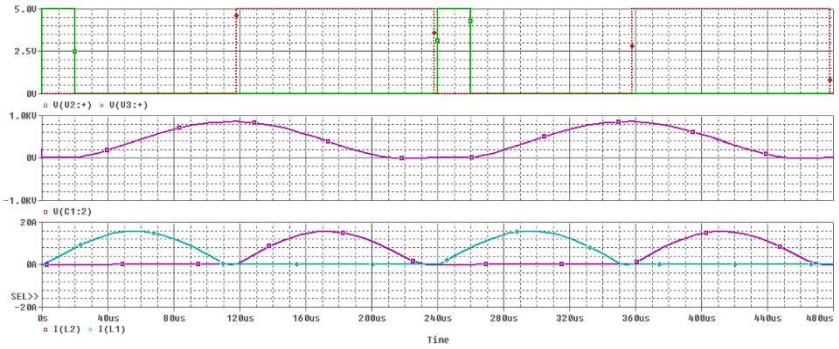

Fig. 5. Waveforms: controlling impulses (top), the voltage on the capacitor (center), current resonance coils (bottom)

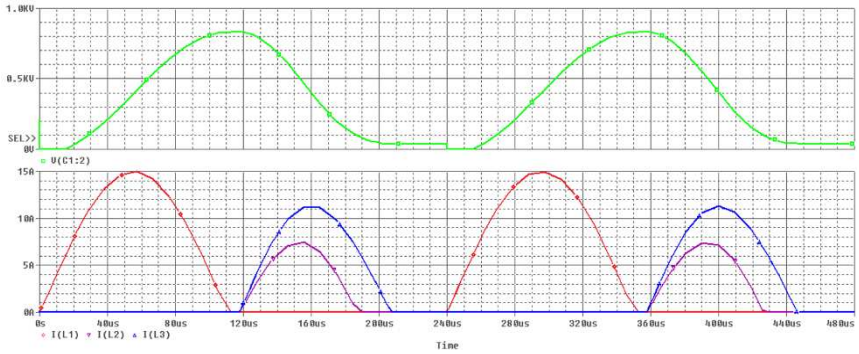

Fig. 6. Waveforms: capacitor voltage (top), current resonance coils (bottom)

4 Conclusion

The paper deals with a very actual issue of coupling DC sources with different parameters. This topic is especially interesting in connection with the implementation of distributed storage systems. In the paper is conducted a basic analysis of the theoretical assumptions of coupling sources, the basic description of the function of the oscillating LC second-order circuit, which became the basis for a new concept and further verification of that principle by using numerical simulations. The advantage of designed solution is that the switching of devices occurs at zero current or voltage. Therefore it is called soft switching of semiconductor devices. The advantage of designed solution is that it enables without any problems equalization of voltage in multiple sources simultaneously. This mentioned solution is currently the subject of a patent application.

Acknowledgment

The presented research was supervised by prof. Ing. Petr Chlebis, CSc. from Department of Electronics, VSB - TU Ostrava, Czech republic. This paper was funded by a grant of SGS (No. SP2015/174) from the VSB - Technical University of Ostrava, Czech Republic.

References

1. Kijonka, J. a kolektiv: Teorie obvodů I, Ostrava 2007, ISBN 978-80-248-1488-9.
2. Anant Agarwal, Jeffrey H. Lang: Foundations of Analog and Digital Electronic Circuits, San Francisco 2005, ISBN 1-55860-735-8.
3. Chlebiš, P.: Polovodičové měniče s měkkým spínáním, Ostrava 2004, ISBN 80-248-0643-6.
4. Baresova, K.: Teze disertační práce, Rezonanční vazební měnič pro systémy akumulace elektrické energie, Ostrava 2015.

5. Thomas C. Greening, William C. Athas, P. Jeffrey Ungar: Parallel battery architecture with shared bidirectional converter, IPC: H01M2/26, H01M4/82, H02J7/00, Cupertino California, Patentový spis, US2009325056 (A1), 31.12.2009.
6. Kolektiv řešitelů pod vedením prof. Ing. Petra Chlebiše, CSc.: Akumulace energie, základní koncepce návrhu projektu akumulace, interní materiály v Projektu ENET cz.1.05/2.1.00/03.0069.
7. Chlebis, P., Tvrdon, M., Baresova K., Havel, A.: The System of Fast Charging Station for Electric Vehicles with Minimal Impact on the Electrical Grid, Advances in Electrical and Electronic Engineering Journal – AEEE 2015, ISSN 1336-1376, ISSN 1804-3119.
8. Chlebis, P., Havel, A., Sobek, M., Baresova, K.: ZCS Concept of Single-Phase Traction Supply Converters, 16th Electric Power Engineering – EPE 2015, May 20 – 22, Kouty nad Desnou, Czech Republic.

The Properties of Bidirectional Coupling Converter with Galvanic Insulation

Martin Borski

Department of Electronics, FEECS,
VŠB – Technical University of Ostrava, 17. listopadu 15, 708 33 Ostrava – Poruba
martin.borski@vsb.cz

Abstract. This paper describes the properties of bidirectional coupling converter with galvanic insulation. At the beginning of this article is shown the connection and description the bidirectional coupling converter. The base of this converter is H-bridge, high frequency transformer and matrix converter. Together it creates topology of the semi-matrix dual active bridge (SM-DAB). The parts used in connection are design on the basis of silicon-carbide (SiC), which enables to converter operates on the high switching frequencies. The functions are verified by a several simulations.

Keywords: bidirectional coupling converter, high frequency transformer, matrix converter, silicon-carbide.

1 Introduction

One of the current characteristics of power engineering is an effort to maximize the use of renewable sources of energy. This effort is not give a range of existing supply mains, but also efforts to improve the environment and limiting conventional fuel sources. Although these renewable sources currently account for only a small part of the production of electric energy, their importance continues to grow. The disadvantage of renewable sources is their variability, which enforces the use of new technologies for stabilizing power supply in networks and brings new requirements for the accumulation systems production. These accumulation systems must contain converters for bidirectional flow, whether in the excess energy produced or a lack of energy in the electric network. Accumulation systems to equalize the balance of production and consumption of electrical energy, such as photovoltaic or wind power plants.

The basic requirement for converters that will work with renewable sources and accumulation systems is a two-way, it means the ability to transfer energy from input to output and back. This condition is easily met with converters that are galvanic connected with both systems. Relatively difficult is achievable with converter or systems that require galvanic insulation. In this case, it is necessary to make solutions of new technologies and topologies of converter so that we could transfer the energy at the highest possible frequency and thereby achieve optimization both in terms of size and

© M. Krátký, J. Dvorský, P. Moravec (Eds.): WOFEX 2015, pp. 151–156.
VŠB – Technical University of Ostrava, FEECS, 2015, ISBN 978-80-248-3787-1.

in terms of efficiency of power transmission. The possibility of performance enhancement is also conditional on the development of new components that will increase the switching frequency of the converters and thus their efficiency.

2 Design and Describe of Bidirectional Coupling Converter with Galvanic Insulation

The circuit diagram of reversible converter is in the figure 1. There is connected single-phase voltage inverter in H-bridge on the primary side. High frequency pulse transformer with ratio 1:1 provides galvanic insulation. On the secondary side there is matrix converter of the current character. The switches in matrix converter are connected to the bidirectional nonconductive off. This can be achieved transistors and diodes in anti-series configuration. The diodes prevent current flow in the opposite direction. If, the transistor Q8 is switched on, current flows in this transistor and diode D7. Unless the switching transistor Q7, diode D7 protects current flow in the opposite direction.

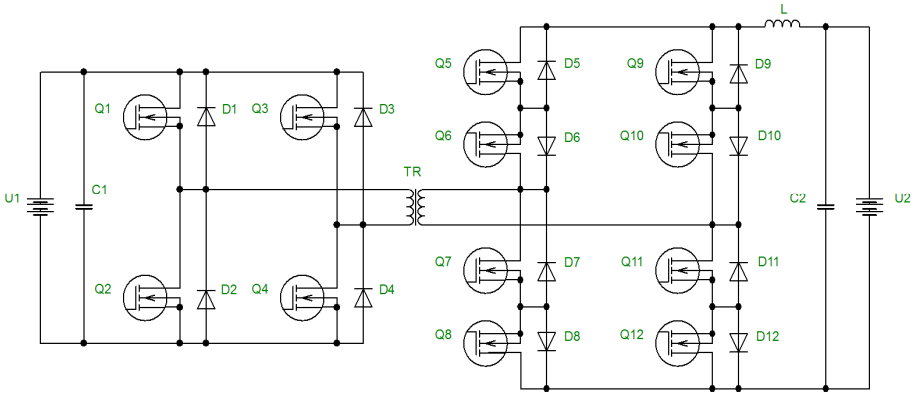

Fig. 1. Connection diagram of the bidirectional coupling DC/DC converter

Function this converter was above mentioned. We distinguish two modes. Energy is transferred in the direction from source U1 to U2 or in the opposite direction. Every time is activated only one of the converters. The second converter is used for rectification of energy, which is flowed via pulse transformer. Width of the pulse controls quantity of transmitted energy. This pulse is brought to transformer from a primary side. When we ignore short dead time, the maximum width of pulse is half of the switching period. It is T/2 and the ultimate energy is transmitted. [1], [2], [3], [4].

2.1 Design of High Frequency Pulse Transformer

Pulse transformer is used for transmission commonly orthogonal pulse. This pulse has one or two polarity. Requirement for the transmission of the undistorted pulses

influences the choices of the magnetic materials, core shape of the pulse transformers and layout of the winding. Voltage and current part of converter are bridges therefore there are rectangular pulse on the winding of transformer, which have a positive and negative polarity. The producer informs about magnetic induction B_{SAT} in datasheet. This value is significant from the point of view operation of converter. In view of the fact that saturation of the magnetic core is undesirable we determine maximum value of magnetic induction B_{MAX}, is the following formula. [5]

$$|B_{MAX}| < |B_{SAT}|\ [T;T] \tag{1}$$

Magnetic induction stroke ΔB is determined by the following formula.

$$\Delta B = 2 \cdot |B_{MAX}|\ [T;T] \tag{2}$$

The proposal is based on the known relationship and transformer must be able to operate at high frequencies. There is a connection between magnetic induction with frequency and losses in magnetic core. The Number of the windings of transformer is related to width of the transmitted voltage rectangular pulse. The Number of windings on the primary and secondary windings is identical because a turn ration is 1:1. Core size is depended on transmitted power and determines from the root mean square of the core section and winding area.

3 Simulation of Bidirectional Coupling DC/DC Converter and Analyze of the Results

The connection of the reversible DC/DC converter was made in simulation program OrCAD PSpice to verify theoretical supposition. It is possible to use some simplified supposition.

3.1 Simulation in the Process of Transfer of the Energy from Source U1 to U2

The matrix converter has function as push–pull bridge rectifier when the energy flows from source U1 to source U2. That we have voltage inverter in the input and we connect rectifier in the output. The connection scheme is in the figure 2.

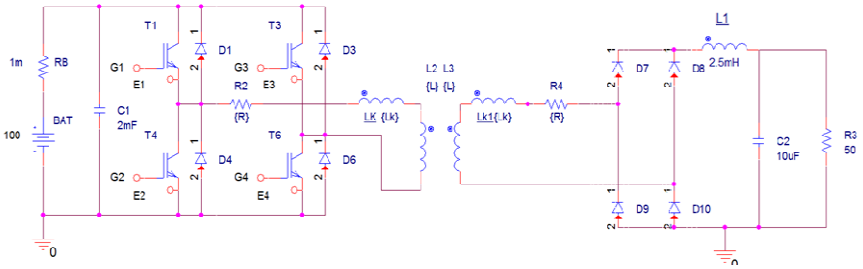

Fig. 2. OrCAD PSpice simulation diagram of bidirectional coupling converter in the process of transfer of the energy from sources U1 to sources U2

In the figure 3 there are drawn waveforms of voltage and current in the primary and secondary transformer winding. These waveforms were taken in the process of energy transmission from the source U1 to source U2. Voltage delay in the secondary winding is result of effect dispersion inductance L_k It is a cause of unfaithful energy transmission by transformer. A part of this energy flows back to the source as reactive component. This process arises in time when current commutates over reverse diode. This description is important due to control of matrix converter. Matrix converter has to be controlled with delay similar to delay of voltage on secondary winding.

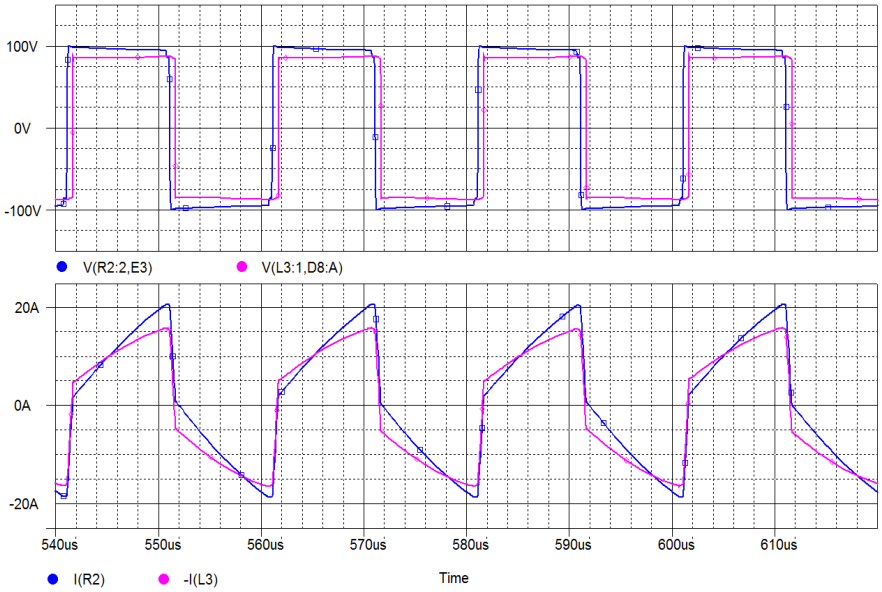

Fig. 3. The waveform of the voltage and current in the primary a secondary winding

3.2 Simulation in the Process of Transfer of the Energy from Source U2 to U1

There is a possibility to use the simplified supposition again. Single-phase inverter is replaced by two-pulse bridge rectifier according to figure 4. Transformer consists of inductance L2 and L3 which have common coupling. When this value is set on number 1, it is ideal transformer, which doesn´t show leakage inductance and the other parasitic properties.

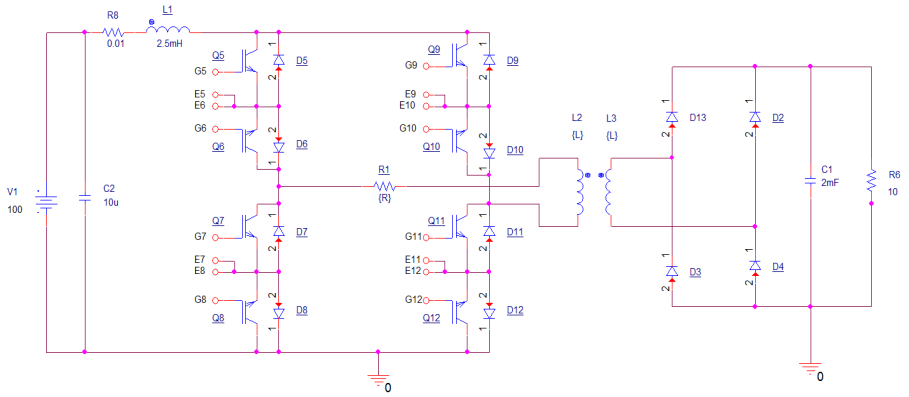

Fig. 4. OrCAD PSpice simulation diagram of bidirectional coupling converter in the process of transfer of the energy from sources U2 to sources U1

Using simulation profile are pictured important waveform of current and voltage on the coil L1 and on the inductances L2 and L3 which is creating the transformer. On the picture 5, there are waveforms of the current and voltage of primary and secondary winding. Thanks to the fact that the ideal transformer is set, the waveforms of current and voltage on the primary and secondary winding are the same. Waveform of current is inverted due to clear arrangement. The load affects current of primary winding.

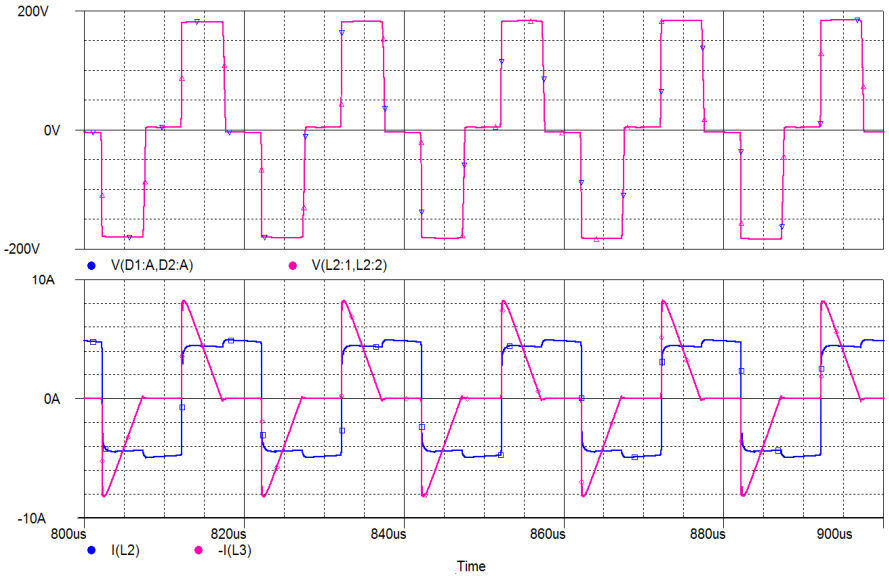

Fig. 5. Waveform of the voltage and current to primary a secondary winding

4 Conclusion

The main object of this paper was analysis the properties of bidirectional coupling converter with galvanic insulation and design high-frequency pulse transformer. This converter operates in the high switching frequency. In this paper we verify armchair knowledge by simulation. This created simulation will be used for the next research.

5 Acknowledgment

This paper was funded by a grant of SGS No. SP2015/174 from the VSB - Technical University of Ostrava, Czech Republic. This research was supervised by prof. Ing. Petr Chlebiš, CSc. from Department of Electronics, VSB - TU Ostrava

6 References

1. Palacky P., Hudecek P., Havel A.: Real-time Estimation of Induction Motor Parameters Based on the Genetic Algorithm. 7th International Conference on Soft Computing Models in Industrial and Environmental Applications, SOCO 2012, September 5-7, Ostrava, Czech Republic, Vol. 189, p. 401-409, 2013, ISBN 978-3-642-33017-9, ISSN 2194-5357, DOI: 10.1007/978-3-642-33018-6_41.
2. Havel A., Chlebis P., Simonik P., Hromjak M.: Active Charging Stations for Electric Vehicles Charging. Progress in Electromagnetics Research Symposium, 31th PIERS 2012, March 27-30, Kuala Lumpur, Malaysia, PIERS Proceedings p. 995 – 998, ISBN 978-1-934142-20-2, ISSN 1559-9450.
3. Palacky P., Slivka D., Havel A., Vaculik P.: Electric Vehicle Control Units Communication. Advances in Electrical and Electronic Engineering Journal - AEEE 2012, March, Vol. 10, Is. 1, p. 17-21, 2012, ISSN 1336-1376, DOI: 10.15598/aeee.v10i1.557.
4. Vondrášek, F., Výkonová elektronika, svazek 3, Měniče s vlastní komutací a bez komutace. *Plzeň: Západočeská univerzita*, 2003, 267s. ISBN 80-7082-980-X
5. Faktor, Z.: Transformátory a tlumivky pro spínané napájecí zdroje, Vyd. 1., BEN – technická literatura, Praha, 2002, 248s, ISBN 80-86056-91-0

The investigation of reverse impacts of a six pulse controlled rectifier to a power supply

Jiří Špička

Department of Electronics, FEECS,
VŠB – Technical University of Ostrava, 17. listopadu 15, 708 33 Ostrava – Poruba
jiri.spicka@vsb.cz

Abstract. The harmonic analysis of an input current of a six pulse uncontrolled rectifier is widely known. However, little has been known about harmonic of the input current of three phase controlled rectifier. This article describes the measured results of the six pulse controlled rectifier and influences of harmonic distortion of phase current are investigated. The changes of induction load and the effects of power supply reactance, which are represented by a commutation inductors, are parameters for measurement.

Keywords: controlled rectifier, reverse impacts, harmonics, ripple current, commutation, total harmonic distortion (THD)

1 Introduction

Semiconductor converters generate interference radiated to its area. This interference can be divided into a low-frequency and a high-frequency interference. The low-frequency interference results from consumption of the non-sinusoidal shape of current from the supply source which is the typical for rectifier. The next various influences affecting this current are described below. [1]

Measurement was taken on the six-pulse control rectifier for analyze of the influence to a harmonic spectrum of phase current. It is researched influence of an internal reactance of source to the harmonic distortion of the size of single harmonic wave. The influence of the ripple of output current to the harmonic distortion has been part of the research as well. Dependence of the harmonic distortion of phase current to the delay angle of the rectifier has been verified.

The adverse effects of the harmonic distortion in the input current come in many forms. One detrimental effect is that input current harmonic distortion can lead to voltage distortion further up the line due to the line impedance. This harmonics may reach the distribution transformers which are not rated to handle large amounts of harmonics. [2][3][4][5][6]

© M. Krátký, J. Dvorský, P. Moravec (Eds.): WOFEX 2015, pp. 157–162.
VŠB – Technical University of Ostrava, FEECS, 2015, ISBN 978-80-248-3787-1.

2 Description of power circuit with the rectifier

Figure 1 shows a power schematic of the six pulse controlled rectifier circuit. The rectifier is connected via a commutation inductors to AC input and a resistive-inductive load output. Commutation inductors Lk represent the influence of internal reactance of the power supply. The input variables are measured by harmonic analyzer Fluke Norma 4000.

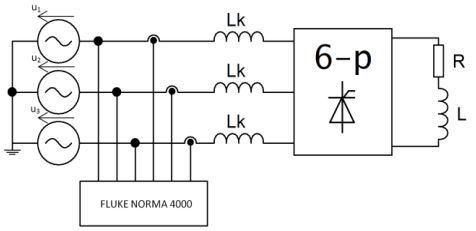

Fig. 1. Power circuit with the rectifier.

3 Effect of ripple current of the load to THD

The value of inductive load causes ripple current of the load. The resistive-inductive load has constant resistance 450Ω. Differential current ripple factor is calculated as:

$$\sigma_I = \frac{i_{d\max} - i_{d\min}}{i_{d\max} + i_{d\min}} \tag{1}$$

where σ_I stands for ripple current, $i_{d\,max}$ represents the maximum value of load current and $i_{d\,min}$ represents the minimum value of load current. Next figure show example of load current with values of ripple current.

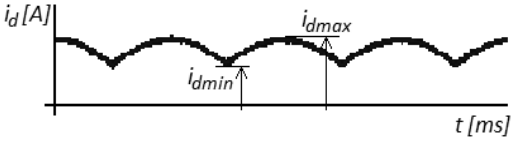

Fig. 2. Example of ripple current of the load.

The total harmonic distortion (THD) determines the amount of content of harmonics in the signal. Analyzer Fluke calculates THD by the following formula:

$$THD_I = \frac{\sqrt{I_{RMS}^2 - I_1^2}}{I_1} \tag{2}$$

where I_{RMS} is rms of current and I_1 is rms of first harmonic.

Table 1. Dependence of σ and THD on load inductor.

L [mH]	0	200	480	660	830
σ [-]	0,092	0,059	0,042	0,035	0,032
THD [%]	31,517	31,709	31,961	31,99	32,149

The measured values of ripple current and the calculated values of THD are shown in table 1. Parameter of measurement is the load inductor.

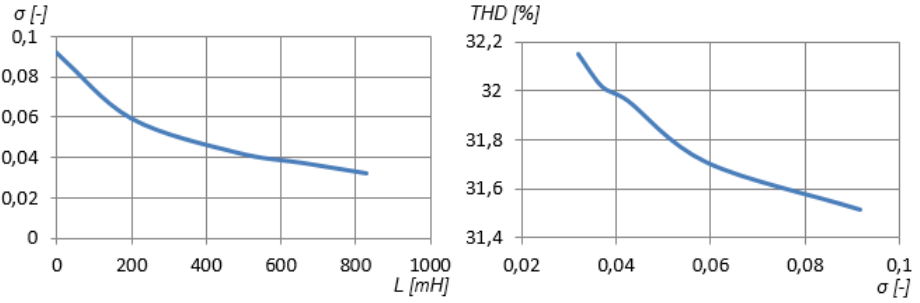

Fig. 3. Dependence of σ on L and dependence of THD on σ.

The measured dependences are shown in the figure 3. It has been shown that the higher the value of inductance in the load, the smoother is the load current. Also the ripple current is lower. The lower ripple leads to a rise in adverse harmonics of phase current. Larger inductance of the load means greater THD of phase current.

The measured values of output voltage and values of phase currents expressing different ripple current created by different inductive load are shown in the following figure:

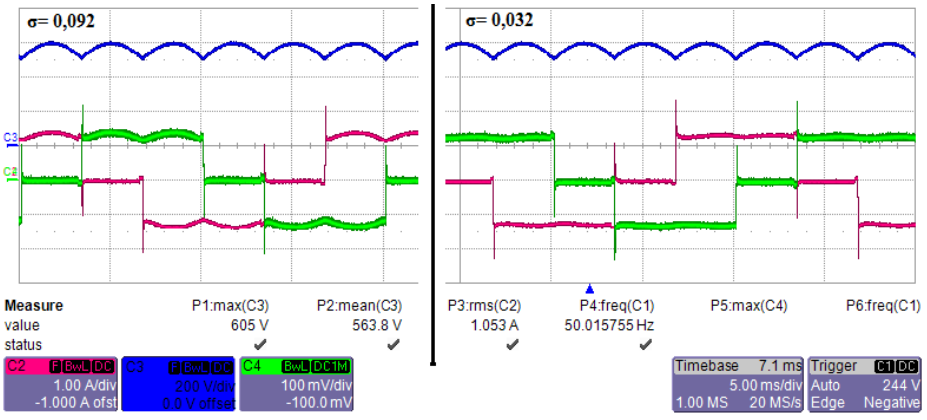

Fig. 4. Output voltage (blue) and phase currents (red, green).

4 Effect of internal reactance of the power supply

The commutation of current between a pair of SCRs in the rectifier bridge takes time, which is primarily determined by the reactance of the power supply. The reactance of power source is represented by commutation chokes Lk. Higher value of Lk causes slower commutation time μ.

In the next table are measurement values, based on the change of commutation chokes. The measurement was performed at zero firing angle and resistive-inductive load with R = 450Ω, L = 830mH.

Table 2. Dependence of μ and THD on commutation chokes.

Lk [mH]	0,0	0,5	1,0	1,5	2,0	2,5	3,0
THD [%]	32,059	31,062	30,678	30,379	30,192	30,023	29,901
μ [μs]	38	130	165	200	230	260	280

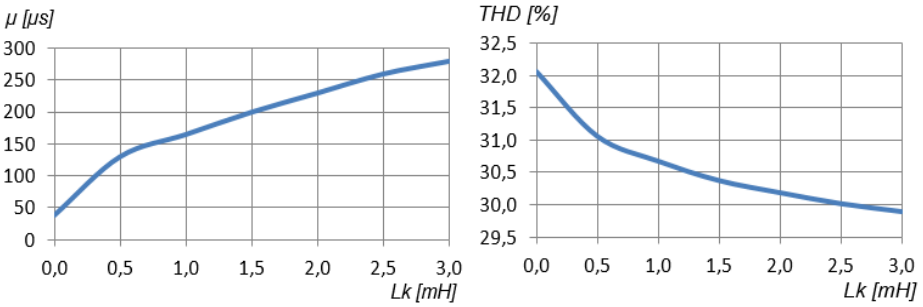

Fig. 5. Dependence of μ on Lk and dependence THD on Lk.

The measured dependence of commutation time on value of commutation choke is almost linear. The measurement leads to the conclusion: the reactance of the power source reduces the THD, but increases commutation time and commutation drops of output voltage.

The Figure 6. shows measured harmonics of phase current up to the 40th order. The most important are the characteristic harmonics based on the Formula 3. The individual harmonic of phase current should be lower when Lk = 2,5 mH than the relevant harmonic of phase current when Lk = 0 mH. The slight variations can be caused by unstable voltage value of the three-phase AC power supply.

$$n = k \cdot p \pm 1 \quad k \in N^{+} \tag{3}$$

where p represents the number of pulses.

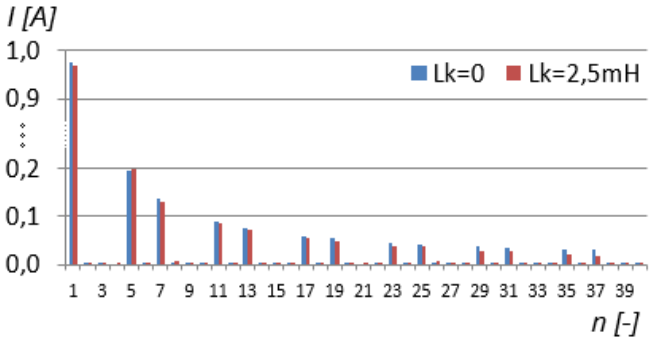

Fig. 6. Harmonic spectrum of phase current with different commutation chokes.

5 Effect of firing angle on harmonic distortion of phase current

The firing angle α has an effect on harmonic distortion of phase current. Figure 7. shows dependence of THD on the firing angle. The value of commutation choke is a parameter of measurement. The commutation angle μ decreases depending upon increasing firing angle α and THD is increasing.

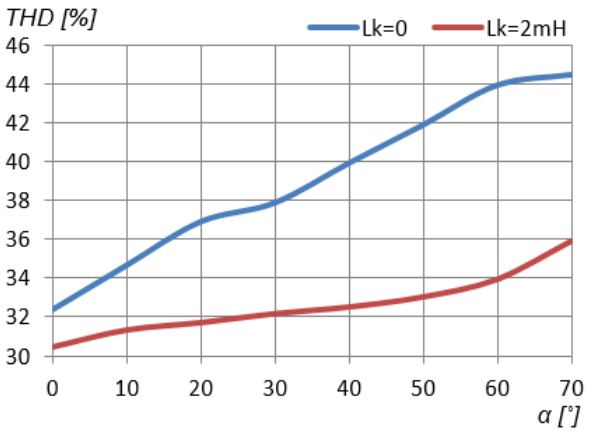

Fig. 7. Dependence of THD on firing angle.

6 Conclusion

In this article the total harmonic distortion (THD) of a six-pulse controlled rectifier was investigated. The measurement was taken on the six-pulse controlled rectifier to analyze the influence of the harmonic spectrum of phase current.

The effect of internal reactance of power supply to THD of the size of single harmonic wave and the effect of output current ripple to the harmonic distortion was researched. Dependence of the harmonic distortion of phase current to delay angle of

the rectifier was verified. This article demonstrates the impact of the harmonic distortion at the input of devices, and provides the required theoretical formulas for predicting the THD of input current of a six pulse controlled rectifier.

THD was assessed by measurement. THD testifies to content of higher harmonics of phase current. The value of THD was measured on various parameters of the power circuit.

This was followed by another measurement: the change of the ripple current in the load referred to the inverse proportion between ripple current and THD. This particular measurement showed an inverse proportion: the larger the value of load inductance, the higher harmonic distortion.

The effect of reactance of the power supply to the harmonic distortion was measured as well. Reactance of the power supply is represented by commutation chokes in input of the controlled rectifier. The greater the commutation chokes, the longer the commutation times of phase current. This inverse proportion affects harmonic distortion as well. Between commutation time and THD of phase current is also inverse proportion: the higher reactance of the power supply, the lower THD. But the higher reactance of the power supply, the slower commutation times.

The effect of the firing angle was measured up to 70° angle. The values of THD considerably increase by increasing firing angle. The commutation time is shorter when the firing angle is increased. The difference between the zero commutation chokes and THD is approximately 12% in the control range from 0 to 70˚.

7 Acknowledgment

This paper was funded by a grant of SGS No. SP2015/174 from the VSB - Technical University of Ostrava, Czech Republic.
This research was supervised by prof. Ing. Petr Chlebiš, CSc. from Department of Electronics, VSB - TU Ostrava.

8 References

1. Kůs, V.: *Vliv polovodičových měničů na napájecí soustavu*. 1. vyd. Praha: BEN - technická literatura, 2002, 183 s. ISBN 80-7300-062-8.
2. Kennedy, B. W.: *Energy Efficient Transformers*, McGraw-Hill Professional, 1997.
3. Barnes, R.: *Harmonics in power systems*, Power Engineering Journal, Volume 3, Issue 1, pp 11 – 15, January 1989.
4. Maslowski, W. A.: *Harmonics in power systems*, Proc. IEEE 1992 Annual Textile, Fiber and Film Industry Technical Conference, pp. 11/1 – 1110, 1993.
5. Stratford, P. R.: *Rectifier harmonics in power systems*, IEEE Trans. On Industry Applications, Volume IA-16, Issue 2, pp. 271 – 276, March 1980.
6. McCarty, M., Taufik, T., Pratama, A., Anwari, M.: *Harmonic Analysis of Input Current of Single Phase Controlled Bridge Rectifier,* IEEE ISIEA 2009, pp. 520 -524, October 4-6, 2009

Application of Modern Active Structures in Signal Generators

Radek Šulák

Department of Electronics, FEECS,
VŠB – Technical University of Ostrava, 17. listopadu 15, 708 33 Ostrava – Poruba
radek.sulak@vsb.cz

Abstract. The main aim of this paper is simulation RC sine generator and function generator with constant frequency, in which new active structure (CFA) is used. This article introduces generator with sine waveform and function generator with only commercially available current conveyor, which is the non – invert positive current II. generation conveyor (CCII+) and active structure - , a voltage source controlled by current is created. A circuit provides generating of signals for frequencies up to 100kHz with small waveform distortion is presented. This new functional structure is consequently demonstrated in electronic circuit mentioned above.

Keywords. current conveyor, RC sine generator, functional generator, voltage source controlled by current, CFA

1 Introduction

In 1966, the concept of an active element was introduced, which surpassed the characteristics of operational amplifiers. Three generation of current conveyors exists.. In these days, current conveyor is found as part of another complex structure. These elements are now used in electronic circuits with many advantages, such as: it extends frequency range of processed signals, it increases frequency, at which circuit can operate (up to several hundred MHz), it extends frequency range of processed signals, it significantly improves dynamics of the circuit (increases slew rate), it improves circuit's noise immunity at low supply voltage, and most importantly, it can operate at very low supply voltage.

Electrical signal generators are devices generated time-varying electrical signals without external excitation. According to the shape of electrical signal waveform, generators are divided into harmonics generators (oscillators), and function generators generate triangular, rectangular, ramp signals or pulses. Furthermore, generators are categorized according to the following criteria [5,6]:

- repetition rate f and a period time T
- stability (stability frequency generated voltage)
- tunable (frequency variation)
- constant frequency generators

© M. Krátký, J. Dvorský, P. Moravec (Eds.): WOFEX 2015, pp. 163–168.
VŠB – Technical University of Ostrava, FEECS, 2015, ISBN 978-80-248-3787-1.

- a variable frequency generators

If generator have oscillate, the circuit must contain one or more storage elements that are used to collect energy. This energy is supplied to the circuit in certain clock and a certain amount so that generated oscillations kept on a constant value. Therefore, the circuit include the element which automatically controls at what time will be energy bring to the oscillating circuit. This element is classified among source of electricity and circuits with storage elements [5].

Schematic symbol of the current conveyor is shown in Fig.1. Most commonly, the conveyors have only three terminals. These terminals differentiate from each other by function and properties [1]. The current I_x is independent value which it is always conveyed from terminal X (current input) to the terminal Z by the current follower. The terminal Z is current output terminal of current conveyor [2]. We choose the voltage system (U_x, U_y, U_z) on the individual gates and we orient this voltage system to common node. The voltage *Uy* is transfer from gate Y (high – impedance non-inverting voltage input) to the gate X by voltage follower and this gate can also be considered as the voltage output gate.

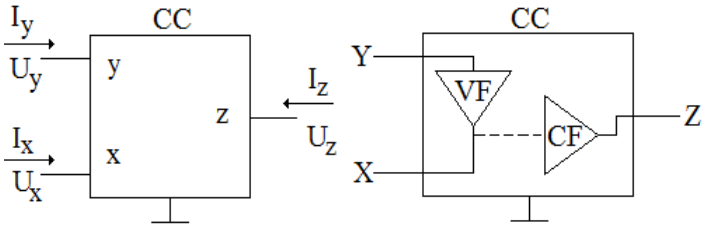

Fig. 1 Schematic symbol and block scheme of current conveyor

The behavior between input and output terminals of current conveyor [1]:

$$u_X = u_Y, i_Y = i_X, i_Z = i_X \tag{1}$$

Another important element is the universal current conveyor (UCC) which it can represent every mention current conveyor any generation.

3 Basic structure with current conveyors (CFA)

The best description every active element is by a set of controlled sources, which can describe all the structures [3]. These are: a voltage source controlled by voltage, a current source controlled by voltage, a voltage source controlled by current, a current source controlled by current.

The structure that is used in the article is the structure (CFA) [3] which replaces the operational amplifier. The structure consist of current conveyor and voltage follower. Gate Y is represented by the non-inverting input and the gate X is invert input. Gate Z is the output of the element and it is coupled to the voltage follower. An impedance Z have important role in this structure. It is the input resistance of the voltage follower,

which leads to the actual voltage gain of this structure. It is required that the impedance Z as big as possible, ideally infinite, because setting the value of the impedance significantly affects the course of the characteristics of the circuit.

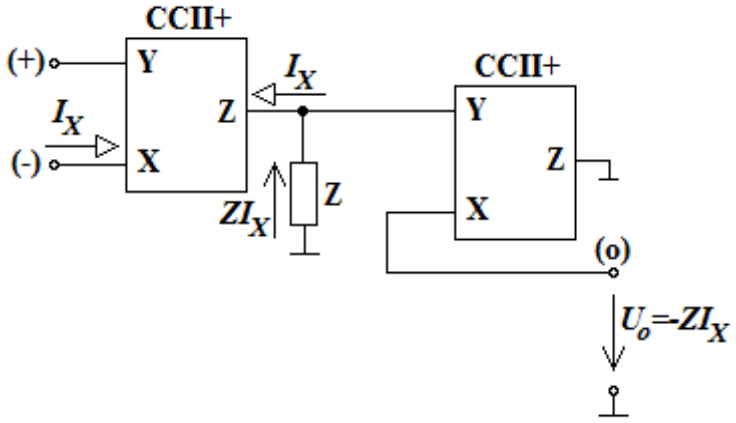

Fig. 2 Function block structure with current conveyors (CFA) [3]

4 Generators with structure based on current conveyors

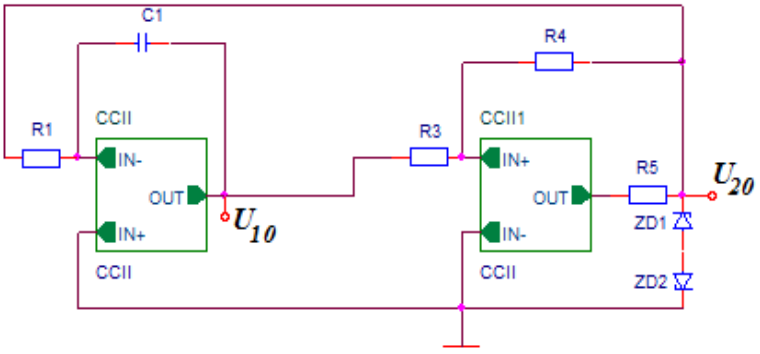

Fig. 3 Function generator with constant frequency

The equal for period and frequency of output voltages:

$$T = 4 \cdot R_1 \cdot C \cdot \left(\frac{R}{R_4} \right) \tag{2}$$

$$f_G = \frac{1}{T} = \frac{1}{4R_1C} \frac{R_4}{R_3} \tag{3}$$

Frequency fg = 1MHz is set by integrator which generates a periodic triangular and rectangular signal. The selection of Zener diodes is very important because it must complies a condition $\pm U_{20} = \pm (U_Z + U_{FZ})$ and they limit output voltage of comparator.

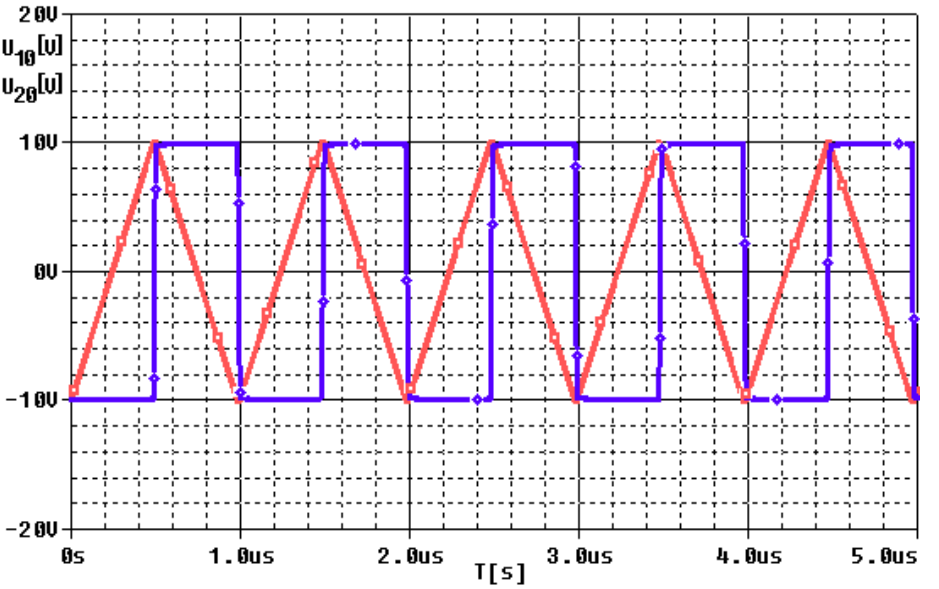

Fig. 4 The waveform of functional generator (*f* = 1MHz)

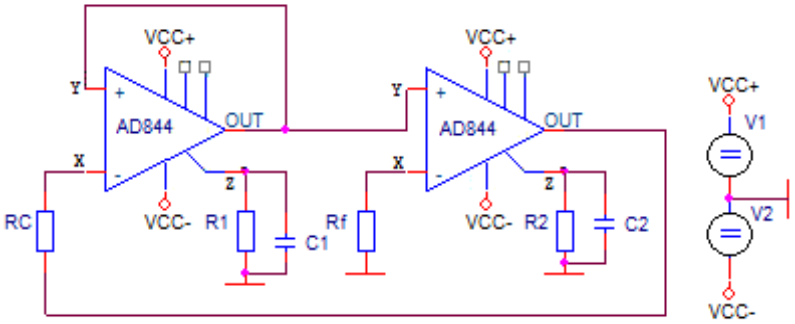

Fig. 5 RC generator [4]

RC sine wave generator use a second-generation current conveyors. It is shown in Figure 5. It uses circuits AD844. They have implemented just mentioned second-generation current conveyors. For reasons of simplicity, the circuit elements are selected R1 = R2 = R and C1 = C2 = C [4].

The oscillator oscillated constantly and must be satisfied:

$$R_C = \frac{R}{2} \tag{4}$$

The angular frequency is defined as

$$\omega = \frac{1}{R \cdot C} \tag{5}$$

Oscillations, on the other hand, can disappear if $R_C \rangle \frac{R}{2}$. Oscillation can be controlled using the resistor Rf without any effect on oscillation waveform. The value of the resistor Rf should be less or equal to R. [4]

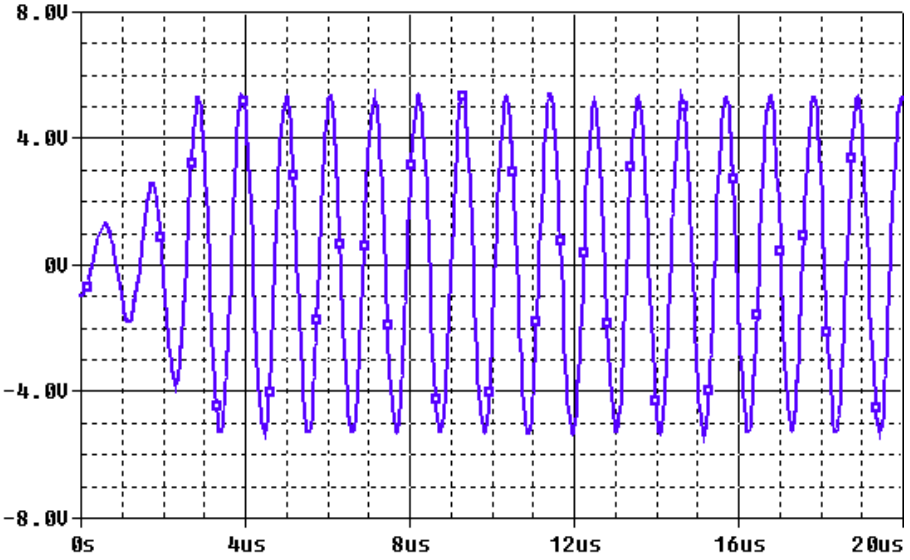

Fig. 5 The waveform of RC generator (f = 1MHz)

5 Conclusion

The paper describes basic structure CFA based on current conveyors and its using in RC generator and functional generator. From graph, we can see that waveform is in very good condition. We can speculate that on higher frequencies frequencies that waveforms could have deformation because any element isn't ideal. But is is con-

firmed that the current conveyor of II. generation can operate on very high frequencies. This can be also seen in the provided waveform graph. Especially in case of frequency dependent circuits.

Acknowledgement

In the paper there are the results of the project SP2015/81 which was supported by Student Grant Competition of VSB - Technical University of Ostrava. This research was supervised by Prof. Ing Pavel Brandstetter, CSc..

References

[1] ČAJKA, Josef, Tomáš DOSTÁL a Kamil VRBA. *New terminology and unifying view of the current conveyors* [online] (in Czech language). 2001[cit. 2012-04-30]. Available from: http://www.elektrorevue.cz/clanky/01024/index.html

[2]. KLEIN, Lukáš. *The current and voltage conveyors*. Additional instructional text,(in Czech language) Ostrava: Vysoká škola báňská – Technická univerzita, 2011.

[3] PUNČOCHÁŘ, Josef. *History and present of operational amplifiers*. BEN. Praha, 2002. ISBN 80-7300-047-4.

[4] A. A. Khan, S. Bimal, K. K. Dey and S. S. Roy, *Novel RC sinusoidal oscillator using sekond generation current conveyor"* IEEE Transactions on instrumentaion and measurement, Vol.54, No.6, 2005.

[5] VRBA K., LATTENBERG I., MATĚJÍČEK L., *Analogová technika*, Study text, FEKT VUT, Brno, 2004.

[6] BRANDŠTETTER, Pavel. *Elektronika*. Ostrava : Vysoká škola báňská - Technická univerzita, 2005.

Automotive Communication Buses and Their Analysis

Jiří Takáč

Department of Electronics, FEECS,
VŠB – Technical University of Ostrava, 17. listopadu 15, 708 33 Ostrava – Poruba
jiri.takac@vsb.cz

Abstract. The paper provides review of based theory of analysis vehicle communication data buses. The techniques and principles for understanding the structure of communication particular data bus used in automotive. Understanding the principles of particular data bus is important for their diagnosis and faults diagnosis of the vehicle. Data structure of particular buses is shown primarily in the paper. All results that are mentioned in the paper are made within the researcher activity and diploma theses in the branch of automotive electronics in the Department of Electronics, VSB-TU Ostrava.

Keywords: CAN-Bus; communication; identifier; K-line; synchronization; baud rate; vehicle bus

1 Introduction

Implementation of electronic systems into the construction of modern vehicle is based on the many different requirements for increased efficiency, safety and comfort. Modern electronic systems provide control of particular vehicle systems and driver can concentrate to traffic situation. Electronic systems ensure process control of individual actuators and process signals from sensors and switches based on the program stored in the memory. Control of the electronic system is implemented by Electronic Control Unit (ECU) connected to other components via wiring. ECU can be connected to each other via communication wiring.

With the development of electronic system increases their complexity. Increasing number of electrical components in the vehicle means a huge number of electric cables and heavier vehicles. Therefore are advanced vehicle systems connected by communication buses, that allow sharing of particular components, e.g.: wheel speed sensor for ABS is also used for speedometer in instrument cluster etc. With the development of electronics in automotive are generated greater demands on communication between particular systems. Communication must be reliable, fast enough and enable error detection. Based on these requirements were developed several communication lines and buses.

© M. Krátký, J. Dvorský, P. Moravec (Eds.): WOFEX 2015, pp. 169–174.
VŠB – Technical University of Ostrava, FEECS, 2015, ISBN 978-80-248-3787-1.

2 Types of communication lines and buses

2.1 CAN-Bus

CAN-Bus is designed specifically for automotive applications. It is multi-master serial bus implemented by two twisted wires. Principle of communications:

- *Peer to peer* – one system nodes are equal.
- *Frame* – communication is based on frame format massages. There are four types of frames: Data frame, Remote frame, Error frame, Overload frame.
- *Frame ID* – nodes aren't addressed, but massage has unique identifier *Error detection* - if any fault is detected communicating node is sent an error frame, and a faulty massage is sending again.
- *Multi*-master - each node is able to send and receive messages.

Physical layer specifies the form of communication due to the electrical properties. There are defines two logic level bit - Dominant (active state) and Recessive (passive state). Dominant state corresponds to a logical "0" and Recessive to a logical "1". CAN bus is designed in order to implement function of logical AND. Logical values aren't strictly determined by the voltage level depending on the ISO standard. Table 1 provides an overview of the most commonly used ISO standards. The ECU, which is connected to bus, must have a CAN-Bus unit, whose block diagram is shown in Figure 1.

Table 1. Iso standard of Can-bus

Standards	Physical layer properties		
	Baud rate	Min. voltage	Max. voltage
ISO 11898 – 2	up to 1 Mb/s	1.5 V	3.5 V
ISO 11898 – 3	up to 125 kbit/s	0 V	5 V
ISO 11519	up to 125 kbit/s	1 V	4 V
SAE J2411	33.3 kbit/s	0 V	4,1 V

Fig. 1. Block diagram of CAN-Bus unit in ECU

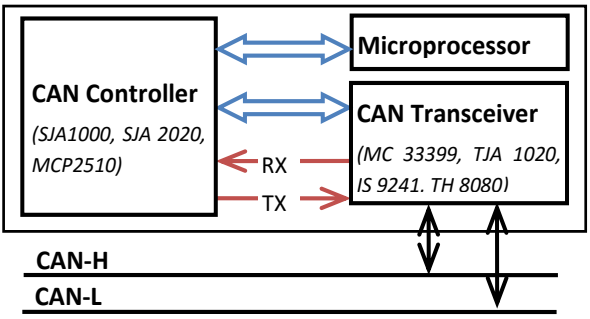

2.2 LIN-Bus

LIN-Bus is based on master-slave serial communication and realized on one wire. It was developed as substitute CAN-Bus, because implementation of CAN-Bus is more expensive and more difficult for simple applications. Range of baud rate for this bus is 2400 – 19200 b/s. To bus can be connected one master unit and up to sixteen slave units. Physical layer is derived from ISO 9141 diagnostic standard (see K-Line) and there are defined two states – *Dominant* (logical "0") and *Recessive* (logical "1"). LIN-Bus is designed in order to implement function of logical AND. Voltage level on wiring is derived from voltage of the vehicle battery. Dominant state corresponds to a battery voltage lower than 40 % and recessive state corresponds to a battery voltage higher than 60 %.

Fig. 2. Block diagram of LIN-Bus hardware implementation

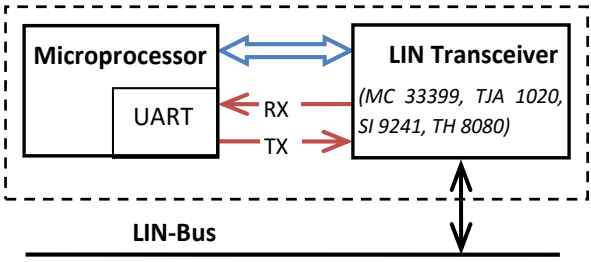

2.3 K-Line

K-Line is developed for diagnostic data transfer on standard ISO 9141-2. The Line is used for on board diagnostics (OBD) – transfer between diagnostic tester and ECU. It's a single wire serial communication. Physical layer is similar to that LIN-Bus and there are defined two states – *Dominant* (logical "0") and *Recessive* (logical "1"). There is difference from LIN-Bus in voltage level of logical state. For dominant state is a voltage lower than 30 % of battery voltage level and for recessive state a voltage higher than 70 % of battery voltage level.

Fig. 3. Block diagram of K-Line hardware implementtion

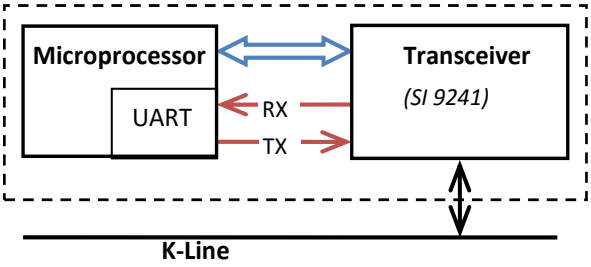

3 Techniques for analysis

This paper deals with the analysis of the most frequently used buses and lines in modern vehicles. Few diagnostic tools were used to understand the principles of bus and data transmission protocol. For analysis CAN-Bus was applied these tools:

3.1 USB to CAN Converter

This tool is designed for analysis, received and sends data, and simulation of CAN-Bus. The device realizes transfer between USB port of computer and bus. Communication on the bus is displayed using the software on computer, and user can use plugins to work with the data, and send their own data on the bus. The device includes a circuit SJA1000 as CAN BUS controller, PIC microcontroller for transfer CAN communication and for USB communication (FTDI). Screen of the application software – PP2CAN is shown on the Fig. 4.

Fig. 4. Screen of application SW for USB to CAN converter

3.2 LeCroy VBA 64Xi

This device is professional analysis oscilloscope for data buses of vehicle. Primarily used for physical layer diagnosis, and enables measurement of up to four buses at a time. By displaying signal waveform of the buses it is possible to diagnose faults and interference on wiring of the buses. The main features are: the bus load measurement, decodes CAN serial data into text directly on the oscilloscope display, uploading custom DBC database file.

4 Analysis of CAN-Bus communication

CAN bus protocol used in the automotive industry is mainly governed by the norm ISO 11898-2 for “High-speed”, and norm ISO 11519-2 for “Low-speed” communica-

tion. In this paper is described analysis of ISO 11898-2 for CAN-motor in Volkswagen Group vehicles.

Fig. 5. Structure of Data frame CAN-Bus 2.0A

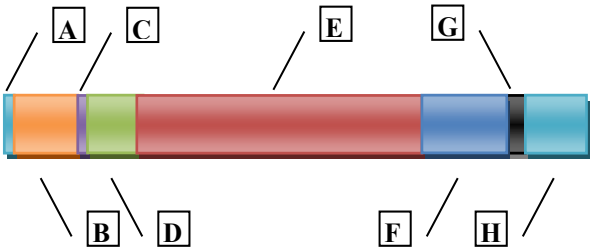

A – Start bit (1 bit), B – Identifier (11 bits), C – Remote transmission request bit RTR (1 bit), D – Control field (6 bits), E – Data field (0 – 64 bits), F – CRC field (16 bits), G – Ack field (2 bits), H – End of frame (7 bits)

The each frame has a unique identifier (ID) specifying information about data is contains. The each devices interconnected to bus, must has a DBC database. This database is described contents of the data in frame from ID. For the analysis of CAN-Bus communication was used USB to CAN analyzer. USB to CAN device is connected to the vehicle CAN-Bus, and with the application software is displayed the communication. In order to understand the structure of communication must be the assignment of ID and the associated ECU. It is possible to recording a communication with complete ECUs. After, each ECU is disconnected from the CAN-Bus and recording a communication again. This procedure can be analyzed most of the ID. Another step is the analysis of the data in these frames. Length of the data field can be from 0 to 64 bits, respectively from 0 to 8 bytes, and each bit can represent state value of some element (state of switch) or each byte can represent physical value (value of the engine speed). Analysis of particular data is possible to monitoring the values of the bits in each frame [1]. Monitoring is done in the response to changes in the value of search. Example to identify the location data of engine speed is monitored the changes in the values of bits in the frame, which transmits the engine ECU.

Fig. 6. Tool for analysis of bit value in data field

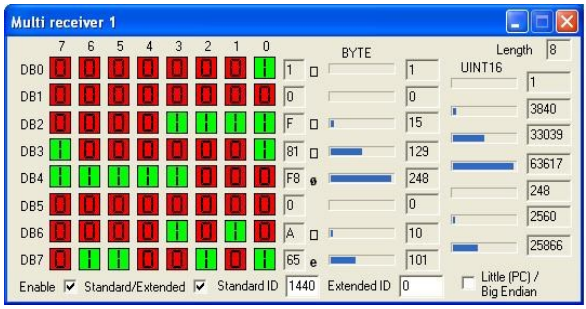

Fig. 7. Laboratory model of power steering

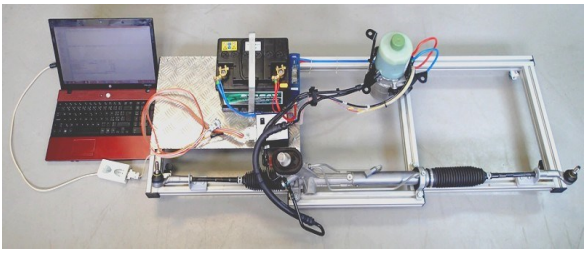

The results of CAN-bus analysis was used for laboratory model of power steering. This type of power steering needs to know information about vehicle speed or engine speed, etc. This information is sent to the ECU of power steering via CAN-Bus and received information about the state of power steering. Principle of estimation was verified as in [2].

In order to protect of intellectual ownership aren't purposefully presented the exact results of analysis. The results can be partly discussed at the conference.

5 Acknowledgment

Work is partially supported by Grant of SGS No. SP2014/119, VŠB - Technical University of Ostrava, Czech Republic, for which author express their sincere gratitude.

6 References

1. Brandstetter P., Chlebis P., Palacky P., Skuta O.: Application of RBF Network in Rotor Time Constant Adaptation. Elektronika Ir Elektrotechnika, Issue 7, pp. 21-26, 2011, ISSN 1392-1215.
2. KASCAK, S., DOBRUCKY, B., PRAZENICA, M.: A New Approach for Estimation of Speed/Position of Two-Phase Induction Machine Using Virtual High Frequency Injection Method, In: International Review of Electrical Engineering -IREE, Vol. 8, No.4, 2013, pp. 1156-1161, ISSN 1827-6660, simulations, In: Electrical Engineering - ArchivfürElektrotechnik, 2013, 5/95, ISSN 0948-7921, ElectrEng DOI 10.1007/s00202-013-0284-8, ADC, CC.

Accumulation system of electric vehicle

Kristýna Friedrischková, David Vala, and Bohumil Horák

Department of Cybernetics and Biomedical Engineering, FEECS,
VŠB – Technical University of Ostrava, 17. listopadu 15, 708 33 Ostrava – Poruba
kristyna.friedrischkova@vsb.cz

Abstract. Electric cars are becoming a serious competition for the common artificial fuel driven cars in small city agglomerates and short distances. With the new developments on the field of state-of-art accumulators, electric cars are becoming much more that just a single use items, but can serve a number of roles. One of them is possibility to use excessive energy stored in the batteries and its rerouting from the car to other systems (such as offices, family houses, lighting etc.). This brief article is making a suggestion on usage and lifecycle of traction batteries, interconnection of the house and its electric car. Additionally, logic and control of such a transfer processes is put to the test for conclusion, that the electric car can be used as both the mean of transportation as well as energy source while in the meantime its primary function is not dampened at all.

Keywords: battery, electric vehicle, smart grid, smart discharging, transfer energy

1 Introduction

Due to increasing number of cases where local energy sources are disrupted by climatic changes or by due to human interventions, there is ever increasing need for independent energy and heat sources. Also related to those, there is a high demand for "clean energy sources" and small energy producing units that are capable of sustaining local establishments, such as family houses etc. Hand in hand with these demands, there is also a pressing need to properly store unused energy for later usage by the residents or users.

1.1 Energy consumption of family houses

Energy consumption of family house is dependent on many different home appliances, but due to better access to state of the art products, consumption can be better distributed and lowered (side demand management).

Days when most consumption was created by heating and water management are over, almost 50% of the current consumption is created by home appliances that are becoming more and more common in most homes. Some of them, like a fridge, needs to be turned on and connected 24/7, others can be connected when needed (oven, microwave and others).

© M. Krátký, J. Dvorský, P. Moravec (Eds.): WOFEX 2015, pp. 175–180.
VŠB – Technical University of Ostrava, FEECS, 2015, ISBN 978-80-248-3787-1.

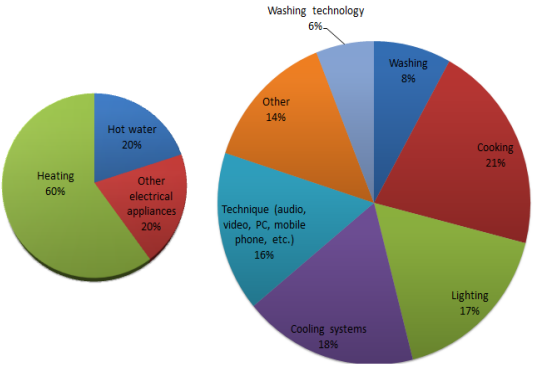

Fig. 1. Graphical balance of the consumption

It appears from the measurements that the customs and behavior of the members of particular household differs during work-days (most consumption happens during 2 PM to 8PM) and weekends (most con-sumption happens during 7 AM to 12 AM).

The weekly consumption in house with 4 family members is average 25kWh.

1.2 Traction battery

In connection with this main idea, research and development was conducted during the period of 2009 - 2012, involving commercial co-investigators, on electric drive unit. This project included four prototypes of vehicles (K0-electric vehicle for suburban traffic, K1- electric vehicle for long range, K2 - electric vehicle with Range Extender to extend the range, K3 - hybrid vehicle, into which it is possible to build in various types of sources (batteries, range extender for LPG, CNG, petrol, diesel or hydrogen)).

Fig. 2. A prototype electric vehicle K0

The implemented experiments then demonstrated that vehicles consume an average of 10kWh/100km.

The drive is designed for suburban traffic and maximum speed is 65 km/h. Set of 100 LiFePO4 batteries with a voltage of 320 V and 40 Ah capacity is giving the vehicle „Action range“ of 300 000 km. The system is built for charging at 400V/32A and full charge is achieved under 2 hours (you can also charge at up to 120A).

Elaborated study on transport services in Ostrava showed that the average vehicles daily driving distance is up to 50km. The remaining energy (14kWh) in a vehicle can be used for other purposes.

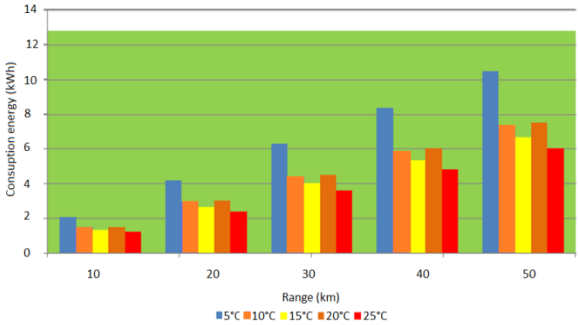

Fig. 3. Consumption of electricity electric vehicle depending on the distance and temperature

2 Experiments

2.1 Charging and discharging battery cells

Testing of the battery is performed during cyclic charging and discharging while balancing the system. Use it to determine the number of cycles the batteries hold until they have the appropriate characteristics.

The testing device serves as charging and discharging power through electronic decade. One of the charging sources has to charge using the large current and a second small current. Charging a small current is used for charging multiple batteries and is only used to recharge the batteries when charging and battery balancer has limits. Discharge electronic decade can be firmly set on the discharge current or adjusted continuously according to the required parameters during the discharge.

The process control computer is used to program measuring card in LabVIEW. Measuring card controls the measuring device and the relay to switch between charging and discharging of the battery.

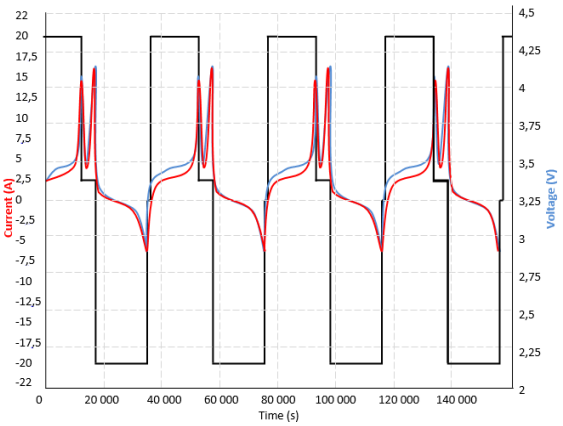

Fig. 4. Lifetime battery cells

On the figure 8 is showing that charging has two parts - charging of battery and balancing of battery. For charging 9 Amps were used from mains (i.e 2 kW - limited by local power net). After the first, cell of traction battery charged to charging voltage (in this case 3.8V) the charger was switched by balancing subsystem to balancing mode (i.e less than 2.5A) next it is possible to observe cyclical interruption of balancing current. This is caused by necessity of heat transfer from balancing module to the cooling medium (air) and also give a time to chemistry of battery to better absorption of energy (pulse charging).

Furthermore, long-term tests of the battery cells were performed in order to verify of capacity decrease by 10% after 3000 cycles which was declared by manufacturer.

One of the main things extending the life time of the battery is a battery management system.

2.2 Charging traction battery from household electric grid

Traction batteries in the electric vehicle are equipped by integrated charger and balancing subsystem to be able to store electric energy.

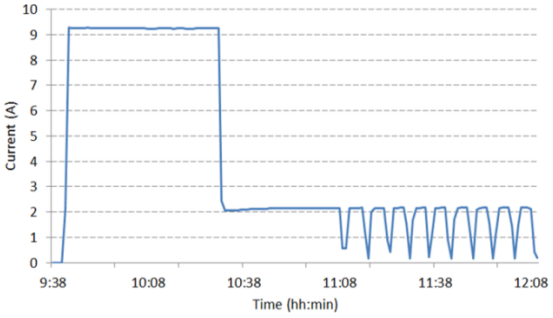

Fig. 5. Charging electric vehicle

There is graph of input power of traction battery charging from home mains for our experi-mental electric vehicle. As is evident from the graph, the current for charge was 9A.

2.3 Discharging traction battery into the household grid

The experimentally was verified by the connection of electric vehicle to the infra-structure of family house. Measurement was aimed to different setting of discharging circuit and mainly on several limitations of discharging of traction battery of electric vehicle. For the testing the minimum voltage has been setup for the traction battery to the 319 V and maximum power to the mains to the 2 kW.

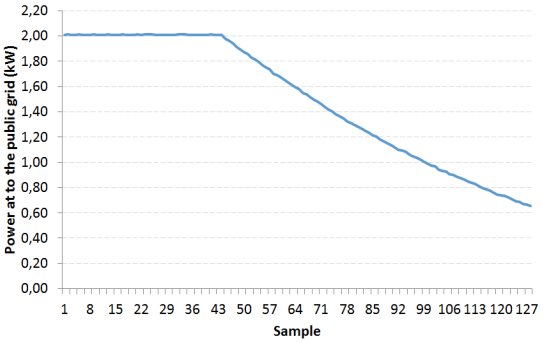

Fig. 6. Discharging electric car to the home grid

3 Conclusion

Usage of the new technologies and energy sources are a viable way for the people to get rid of the dependency on international companies and state regulatory charges.

The implementation of a house that is electrically and thermally independent is do-able, if we take into consideration proper measurements and adjustments that are needed to establish precise environ-mental concept of the house.

We need to take into account appliances and behavioral statistics of the occupants it is much easier to create a proper list of energy sources and their optimal implemen-tation.

Thanks to the boom of automotive industry, we could say, that most advanced and also easily accessible are electrochemical accumulators that in state of the art can go through up to 8 000 cycles with 20% capacity drop and without memory effect.

This allows used electric cars as a supplemental accumulation unit for the family house that, in case of the implementation of the sophisticated control system, will then operate both as consumer and supplier of the energy into the family house grid and can compensate for energy generation inconsistencies.

Some experts do claim that this way of storing energy into mobile solutions is con-tra productive, because of the fact, that in most times that there is an energy produc-

tion peak, the electric car is usually away from the house. In this case we need to take into consideration fact, that both car and houses energy center can be in constant communication via remote access. Only necessity in this case is the connection of the car into public grid, which then may be used as a "transfer medium".

4 Acknowledgements

This project was supported by European sources within the project Pre-seed activities VSB-TUO II - Energy, CZ.1.05/3.1.00/13.0317. And the work was partially supported by Grant of SGS No. SP2015/42, VSB - Technical University of Ostrava, Czech Republic.

5 References

1. Horak, B., Minarik, D., Friedrischkova, K., Vala, D., Kazarik, J.: The development of drive units for electric cars KaipanVoltAge. Proceedings of the 14th International Scientific Conference Electric Power Engineering 2013. VŠB – TU Ostrava 2013. 978-80-248-2988-3
2. Haluza, M., Macháček, J.: Spotřeba elektrické energie domácností, predikce a potenciální úsporypomocí BACS. TZB info: Technická zařízení budov [online]. 7.5.2012, [cit. 2014-07-15]. Available from: http://elektro.tzb-info.cz/8570-spotreba-elektricke-energie-domacnosti-predikce-a-potencialni-uspory-pomoci-bacs
3. WOODBANK COMMUNICATIONS LTD,.The electropaedia [online]. 2005. vyd. South Crescent Road, Chester, CH4 7AU, (United Kingdom), 2005 [cit. 2015-01-31]. Available from: http://www.mpoweruk.com/index.htm
4. M. Swierczynski, D. Stroe, and et al., “Field tests experience from 1.6MW/400kWh Li-ion battery energy storage system providing primary frequency regulation service,” IEEE 4th European Innovative Smart Grid technologies, in press, 2013.
5. B. Dunn, H. Kamath, and et al., “Electrical energy storage for the grid:a battery of choices,” Science, pp. 928–35, 2011.
6. SWIERCZYNSKI, Maciej, Ana-Irina STAN a Remus TEODORESCU. 2013. (6825 - 6830): 6. Available from: http://ieeexplore.ieee.org/xpl/login.jsp?tp=&arnumber=6700262&url=http%3A%2F%2Fieeexplore.ieee.org%2Fiel7%2F6683943%2F6699103%2F06700262.pdf%3Farnumber%3D6700262
7. CONDUCTED BY GROUP WPS4 - 1050. 2011. ACCELERATED LIFE TESTING AND LIFE PREDICTION OF LITHIU ION BATTERIES CONNECTED TO WIND TURBINE: Accelerated life testing and life-time prediction of Lithium Ion batteries connected to Wind Turbine [online]. Aalborg University [cit. 2015-05-12]. Dostupné z: http://projekter.aau.dk/projekter/files/52684684/Report_WPS4_1050.pdf. STUDENT REPORT. AALBORG University.
8. KAZARIK, J., SLANINA, Z., VALA, D., Long - Time Battery Testing. VSB – TU Ostrava, Faculty of Electrical Engineering and Computer Science, Department of Cybernetics and Biomedical Engineering, 17. Listopadu 15, Ostrava - Poruba, Czech republic, 2010

Fuzzy Clusterization of Obese Patients

Jakub Hlavica, Michal Prauzek, and Marketa Michalikova

Department of Cybernetics and Biomedical Engineering, FEECS,
VŠB – Technical University of Ostrava, 17. listopadu 15, 708 33 Ostrava – Poruba
jakub.hlavica@vsb.cz

Abstract. Patients suffering from obesity have different demands for medical treatment regarding the causes of their metabolic disorders. To propose new medical solutions to weight reduction, it is desirable to group patients exhibiting similar characteristics. This contribution describes an automatic fuzzy classification system capable of dividing obese patients into groups of diverse metabolic types. Metabolic data were acquired through energometry tests and bioimpedance measurements. Methods considered in this paper are particularly Principal Component Analysis used for data set's reduction and fuzzy clustering method dividing patients into groups called clusters. The results are subsequently tested and medically evaluated and possible research methods are eventually described in conclusions.

Keywords: Fuzzy cluster analysis, PCA, Metabolic data, Obesity

1 Introduction

Obesity is a typical representative of disorders affecting particularly people in developed countries. However, it is not necessarily a consequence of an unhealthy lifestyle. Patients having complex metabolic disorders or serious diseases may suffer from obesity as well. It is important to detect whether the cause is an excessive income of food associated with a limited physical activity or an effect of metabolic problems, such as low fat-burning rate or an increased level of insulin in the blood.

Therefore, it is convenient to group patients suffering from obesity and then, on the basis of medical examinations, describe a typology of people depending on the type of metabolism [2], [7], eventually recommending an individual treatment [6]. Such examinations could be based on metabolic energometry tests, bioimpedance measurements [5], blood analyzes, and other methods that are assessed subjectively without standardization [9].

As it is noted in abstract, the methods applied in this paper are Principal component analysis and fuzzy clustering method. Other methods possible to use are Adaptive neuro fuzzy inference system [8] or fuzzy genetic algorithms [3].

2 Metabolic data acquisition

Metabolic data were obtained in collaboration with patients suffering from obesity. Almost 4000 persons underwent a series of energometry tests during eight

© M. Krátký, J. Dvorský, P. Moravec (Eds.): WOFEX 2015, pp. 181–186.
VŠB – Technical University of Ostrava, FEECS, 2015, ISBN 978-80-248-3787-1.

years of this research in Hradec Kralove hospital, Czech Republic. Eventually, 254 patients with a complete diagnosis in the year 2008 were chosen for this study. Energometry tests were based on measurements of body composition and reaction to food utilization. Additional metabolic data were obtained by bioimpedance measurements of a human body and biochemical blood samples analyses.

3 Data normalization

Data normalization is necessary to balance the ratio of data with different statistical properties. It ensures that each dimension of multidimensional data will be treated equally in classification space, with the same weight. There are two basic algorithms for data normalization applied in this paper: normalization in the range (also called Feature scaling) and normalization in the statistical variance (also known as Standard score).

4 PCA analysis

Principal Component Analysis (PCA) is a data decorrelation method. Applying PCA, the original data set's quantity of parameters is reduced whereas an excessive information loss is prevented. The new reduced data set is composed of vectors, so-called principal components, and is obtained using a linear transformation based on variance characteristics of the original data set.

PCA was performed on the data set, thus creating new variables that represent an information entropy of the original data set.

As it is a linear method, the transformation was executed using a linear transformation matrix, described by formula 1, which is composed of PCA coefficients. Therefore, columns represent one principal component.

$$\mathbf{COEFF} = \begin{pmatrix} k_{11} & k_{12} & \dots & k_{1n} \\ k_{21} & k_{22} & \dots & k_{2n} \\ \vdots & \vdots & \ddots & \vdots \\ k_{m1} & k_{m2} & \dots & k_{mn} \end{pmatrix} \tag{1}$$

5 Reduction of data set

The reduction of data set needs to be done at first. Insignificant measurement parameters have to be eliminated because the reduced set produces better estimation in classification space. There are several ways to reduce data set.

Information criteria are reduced according to the sum of the information from first two principal components. This is an objective criterion. The first two principal were selected in order to create two dimensional classification space. The coefficient 0.8, which represents 80 % of the new values in the first two components, is used to determine the information criteria. This rule is described

in formula 2. This condition guarantees adequate representation in the clustering analysis. It is also possible to reduce data set by other methods. The other two reduction criteria are rather subjective. The parameters are deleted according to difficulties in economic or technical process of the measured parameter. Also, a physical redundancy can be applied by a medical doctor.

$$0.8 < I_1 + I_2 \tag{2}$$

After the reduction, the data set is ready for clustering. If it is necessary to increase information criteria for more principal components, then the reduction coefficient has to be altered. However, it is no longer possible to display the clustered data in two dimensional space.

6 Clusters estimation and clusterization

Fuzzy clustering analysis contains membership degree of each data [1]. This analysis was chosen specifically for this application due to the mentioned degree of belonging to individual clusters. Thus, it is possible to distinguish the types of patients belonging to particular clusters with the same characteristics and also determine the degree of membership of individual patients.

Selection of the number of clusters is crucial for the clustering algorithm. It is simpler to determine the number of clusters of a data set in applications where it is clear what types of data are input and what are the main categories. In multiparametric analysis however, it is not that obvious and there must be used a lot of criteria which predict the suitability of the cluster number. Two criteria are used in this research.

$$PC(c) = \frac{1}{N} \sum_{i=1}^{c} \sum_{j=1}^{N} (\mu_{ij})^2 \tag{3}$$

The first criterion denoted Partition Coefficient (PC) is calculated by using formula 3. The parameter μ_{ij} defines the membership of data with index j to cluster i. If the coefficient PC is increased, then the cluster approximation is more accurate.

$$CE(c) = -\frac{1}{N} \sum_{i=1}^{c} \sum_{j=1}^{N} \mu_{ij}.log(\mu_{ij}) \tag{4}$$

Another factor describing cluster appropriate approximation is Classification Entropy (CE) calculated by formula 4. This coefficient is very similar to PC parameter, but the optimal number of clusters reaches a minimum of the function.

Results of the test are displayed in Figure 1. Graphs represent functions of number of clusters. Indicator PC reaches a local minimum in value 3 and the global minimum is value 6. Coefficient CE indicates optimum in values of 3 and 6, as the function reaches its local maximums in these values. Division into 3 clusters was chosen according to these calculations because the aim was to find the best approximation with low number of clusters.

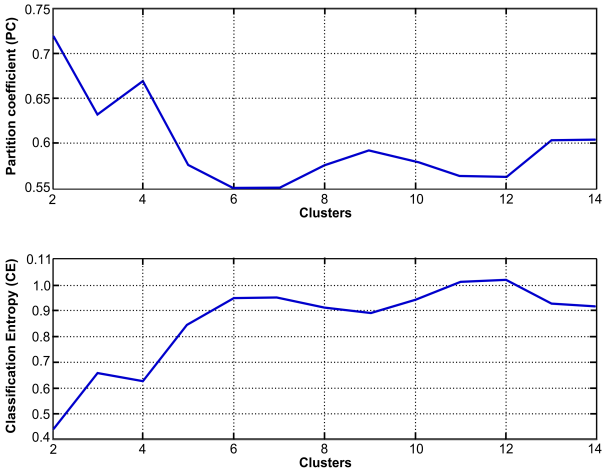

Fig. 1. Partition coefficient and Classification Entropy function

Fuzzy c-means method is used in this research as it allows to separate patients into several clusters. The algorithm can calculate degree of belonging to these clusters and get the individual parameters [4].

Figure 2 shows clustering test estimated by two main components. In each cluster, a centroid (in form of a red circle) is located. These centroids represent the geometric centers of the clusters. The data are normalized before the test by the range algorithm in order to normalize data within the range of 0 and 1 [1].

7 Testing and evaluation of the results

Results interpretation of clusterization is the most important part. Patients were divided into 3 the clusters. It is necessary to evaluate the critical degree of fuzzy membership. Experimental procedure for membership degree estimation is shown in the formula 5. Coefficient n represents the number of clusters in the clusterization and φ represents final degree of fuzzy membership. Minimal membership degree for 3 clusters is set to 50 %. Therefore, a patient with a degree over 50 % is considered to be a typical representative of the cluster. As the number of clusters increases, the degree of membership lowers.

$$\varphi = \frac{200}{n+1} \tag{5}$$

Representatives of individual clusters were selected according to the membership degree. Various statistical parameters were calculated for representatives. Results of medical evaluation are shown in table 1. This evaluation is based on medical diagnosis of patients' groups and assessed by standard range levels of metabolic indicators.

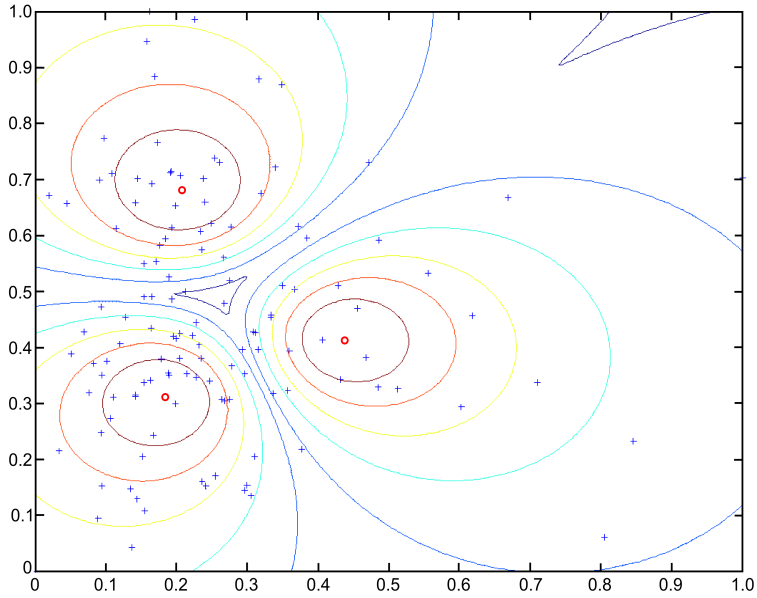

Fig. 2. Clustering test in two dimension

Table 1. Results of medical evaluation

Clusters	Obesity	Glucose processing	Average fat	Cholesterol
Cluster I.	Class II	Very limited	45,22 %	Elevated
Cluster II.	Class II	Limited	32,65 %	Normal
Cluster III.	Overweight	Very limited	34,59 %	Elevated

The average patient in the first cluster has class II obesity, and after eating glucose the ability to burn fat is very limited. Average values of insulin also reach very high level after eating glucose. Cholesterol levels are increased.

The average patient in the second cluster also suffers from obesity class II, as well as patients in first cluster. However, this patient has better fat-burning ability. Patient has also increased parameters of insulin, but he reduces insulin and C-peptid more rapidly. Cholesterol level is within the normal range.

The average patient in third cluster is only overweight, but his fat-burning ability is at the same level as the patient in the first cluster. Insulin is at lower levels than those in two previous clusters. Body composition is similar to the patient in the second cluster. Cholesterol level is increased here.

8 Conclusion

This paper applies Principal component analysis and fuzzy clustering to determine the metabolic types. Data are firstly normalized and then transformed us-

ing Principal component analysis. Clustering method implements fuzzy c-means algorithm.

It was found that patients with metabolic diseases can be divided into three basic groups. The first group consists of obese patients who have a failure of fat-burning ability and obesity is caused by the excesses of fat tissue. The second group are patients who have fat burning within the standard range, but their overweight is caused by the accumulation of active body mass and body water. The last group of patients is characterized by worsened fat-burning ability, but fat tissue excess is not produced. However, their health is also at risk.

This clustering can lead to improved diagnostic procedures and can change obesity treatment. If standardized procedure for the obesity treatment was found, it would be possible to ensure greater efficiency of medical procedures. Other differences in individual groups and more structured treatment can be obtained by similar mathematical methods.

As for the future work, a classification of patients for application purposes is to be performed in order to develop an effective medication methods.

Publication. This work was presented and published at 7th Cairo International Biomedical Engineering Conference (CIBEC), 11th-13th December 2014, Giza, Egypt.

References

1. Abonyi, J., Feil, B.: Cluster analysis for data mining and system identification. Birkhauser Basel (2007)
2. Deng, J., Hu, J., Chi, H., Wu, J.: An improved fuzzy clustering method for text mining. In: NSWCTC 2010 - The 2nd International Conference on Networks Security, Wireless Communications and Trusted Computing. vol. 1, pp. 65–69 (2010)
3. Hong, T.P.: On genetic-fuzzy data mining techniques. In: Granular Computing, 2007. GRC 2007. IEEE International Conference on. pp. 3–3 (Nov 2007)
4. Jing, H.: Application of fuzzy data mining algorithm in performance evaluation of human resource. In: IFCSTA 2009 Proceedings - 2009 International Forum on Computer Science-Technology and Applications. vol. 1, pp. 343–346 (2009)
5. Michalikova, M., Prauzek, M.: A hybrid device for electrical impedance tomography and bioelectrical impedance spectroscopy measurement. Canadian Conference on Electrical and Computer Engineering (2014)
6. Paul, R., Hoque, A.: Clustering medical data to predict the likelihood of diseases. In: 2010 5th International Conference on Digital Information Management, ICDIM 2010. pp. 44–49 (2010)
7. Saha, I., Maulik, U., Nilanjan: Differential fuzzy clustering for categorical data. In: Proceedings of International Conference on Methods and Models in Computer Science, ICM2CS09 (2009)
8. Tafti, A., Sadati, N.: Fuzzy clustering means data association algorithm using an adaptive neuro-fuzzy network. In: Aerospace conference, 2009 IEEE. pp. 1–5 (March 2009)
9. Vanisri, D., Loganathan, C.: Fuzzy pattern cluster scheme for breast cancer datasets. In: Proceedings of 2010 International Conference on Communication and Computational Intelligence, INCOCCI-2010. pp. 410–414 (2010)

Corpus callosum tilt estimation algorithm for imaging systems

Radek Hrabuška[1] and Niranjana Sampathila[2]

[1]Department of Cybernetics and Biomedical Engineering, FEECS,
VŠB – Technical University of Ostrava, 17. listopadu 15, 708 33 Ostrava – Poruba
radek.hrabuska@vsb.cz
[2]Dept. of Biomedical Engineering, Manipal Institute of Technology, Manipal
University, Manipal- 576 104, Karnataka, India
niranjana.s@manipal.edu

Abstract. Corpus callosum is proved to be effective marker of brain related diseases. Clinical research requires autonomous methods for estimation of corpus callosal properties. Proposed simple algorithm looks for described points in corpus callosum contour. Algorithm is able to estimate tilt in usual range of -30 to 30 degrees in mid sagittal plane. All images have been preprocess and segmented by watershed segmentation algorithm. Tilt is successfully estimated in 82% of normal cases and 57% of abnormal cases.

Keywords: MRI, CT, corpus callosum, brain tilt

1 Introduction

Tilt estimation is challenging issue for the machine recognition of brain structures. Correct value of tilt is required for further processing and evaluation of morphological structures. Due to high discomfort during a MRI and CT sessions it is highly recommended for a patient to take at least partially relaxed position, especially when it comes to children and elderly patients, resulting in a head slightly tilted in various directions. Minor tilt might come from improper application of fixing aids, but the main problem to be addressed is varying physiological location within skull. This requires manual processing of the images. This algorithm focuses on tilt estimation in a mid-sagittal plane. For example the tilt estimation might contribute to correct classification of various corpus callosum (CC) abnormalities occurring with diseases such as Parkinson's disease [1], Autism [2], Multiple Sclerosis [3], Hydrocephalus [4] and Alzheimer's disease [5]. Some methods of the CC classification use witelson's protocol [6] to estimate morphological features.

Main purpose of the algorithm is to estimate CC tilt for proper classification of diseases. Proposed method finds point described in witelson's protocol [6] and adds its counterpart (G2) to calculate angle of the line connecting them. This angle is considered

© M. Krátký, J. Dvorský, P. Moravec (Eds.): WOFEX 2015, pp. 187–192.
VŠB – Technical University of Ostrava, FEECS, 2015, ISBN 978-80-248-3787-1.

to be estimated CC tilt. Points are found by sliding over the contour until the point meeting criteria is found.

2 Dataset specification

Data used for processing are originally in courtesy of longitudinal OASIS database [7], they are free to use with agreed terms. Data from longitudinal database consists of 103 patients divided into two groups (Demented, Non-demented). In addition some of the patients had more than two MRI sessions. In figure 1 there are shown the original data acquired by MRI of 4 patient. Dataset was chosen to represent even abnormal population to test robustness of the algorithm.

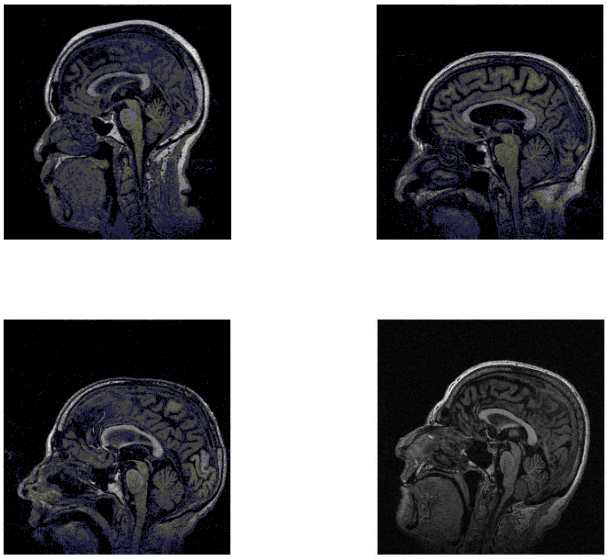

Fig. 1. MRI original data

3 Image pre-processing and segmentation

Preprocessing is done by thresholding by Otsu's method [8] and multilevel thresholding of areas with higher brightness than threshold by Otsu's method [9]. Next stage segments the image by watershed image segmentation [10] and indexes objects in the picture. Indices include information about position, dimensions, brightness and placement. Database was checked for images not respecting the same orientation (nasion on the left, inion on the right), and unfitting images were mirrored.

Objects with rating better than threshold are compared with template [11], which is obtained as sum of normal CC's segmented by hand and tilt corrected. Best match is considered to be CC.

4 Corpus callosum tilt estimation

Some of methods of the CC classification use witelson's protocol [6] to estimate morphological features. Witelson's protocol require to divide into upper and lower segment for which it is needed to estimate its tilt. For this application was into the witelson's protocol added the G2 point as in figure 2.

Fig. 2. The sub-regions of normal CC by Witelson with highlighted G and G2 point

It is needed to choose starting point to find G and G2 points in the image. In this case starting point in the half-way of the objects centroid and inner curvature. Indices of centroid are calculated as mean of each pixels X and Y coordinates.

In each iteration current pixel's neighborhood properties are evaluated and when the conditions are not met algorithm moves towards Y = 0 column around the contour. Algorithm is also described in figure 3.

In the same way G2 point location is estimated on mirrored image. Finally the line equation (1) parameters (2, 3) and tilt angle α (4) of G-G2 line segment are calculated.

$$y = kx + q \quad (1)$$

$$q = \frac{Y_G}{X_G} \quad (2)$$

$$k = \frac{(Y_{G2} - Y_G) - q}{(X_{G2} - X_G)} \quad (3)$$

$$\alpha = \tan\left(\frac{Y_{G2} - Y_G}{X_{G2} - X_G}\right) \quad (4)$$

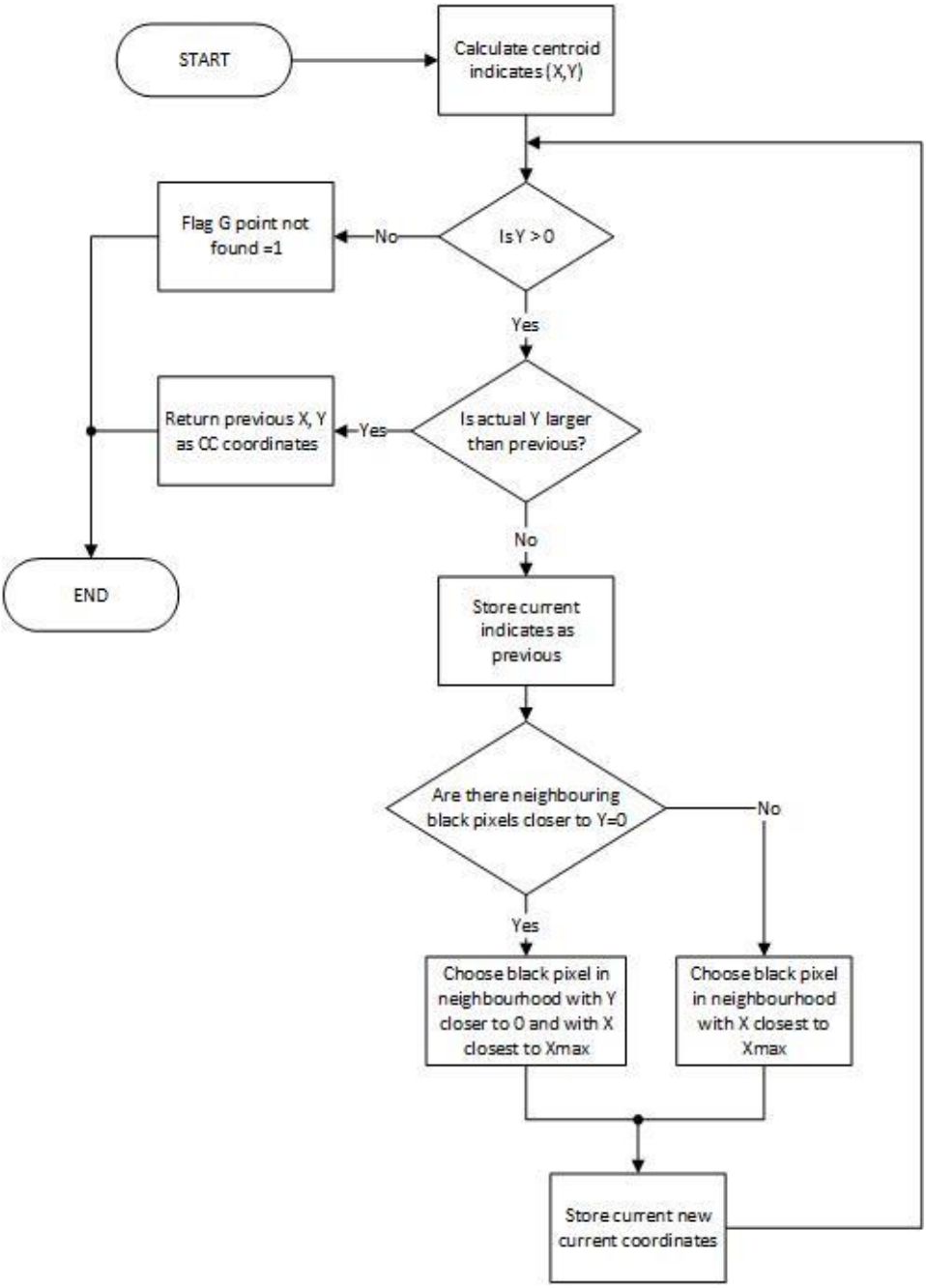

Fig. 3. Flow chart of the G point estimating algorithm

5 Conclusion

From total number of 171 tested pictures were properly segmented 129. G or G2 points were not properly found in 13 from 73 of normal cases (82%) and in 24 from 56 (57%) cases with dementia. In figure 4 there are shown 4 CCs with highlighted G and G2 points.

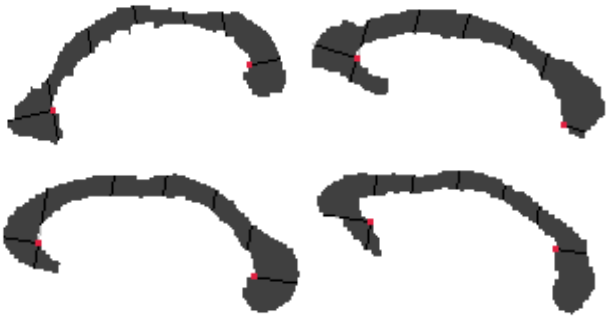

Fig. 4. CCs with properly found G and G2 point (left column) and CCs with improperly found G and G2 point (right column) with witelson's division

Proposed algorithm works well as a part of larger project which investigates corpus callosal morphological properties and their use in brain disease diagnosis. Accuracy shows that tested approach is promising for future use. Better accuracy might be achieved through better segmentation and point definition.

Following work can be focused on correction of head tilt based on CC tilt and pitfall prevention.

Acknowledgement

Author is thankful to Dept. of Biomedical Engineering, Manipal for providing the best possible amenities to carry out research work to and is also thankful IAESTE organization which provided opportunity of internship at Manipal Institute of technology, Manipal University.

References

1. C. Salvatore, A. Cerasa, I. Castiglioni, F., Gallivanone, A. Augimeri, and M. Lopez, et al., "Machine learning on brain MRI data for differential diagnosis of Parkinson's disease and progressive supranuclear palsy," Journal of neuroscience methods, vol.13, pp.230-237, Jan.2013.

2. A.C.C. Modeling, “Abnormalities in MRI traits of corpus callosum in autism subtypes,” in International conf. Engineering in Medicine and Biology Society, Canada, 2008, pp. 3900-3903.
3. R. Bakshi, A.J. Thomson, M.A. Rocca, D. Pelletier, V. Dousset, and F. Barkhof, et al., “MRI in multiple sclerosis: current status and future prospects,” Lancet Neurology, vol.7, pp.615-625, Jul.2008.
4. R. Hurley, W.G. Bradley, H.T. Latifi, and K.H. Taber, “Normal pressure hydrocephalus: Significance of MRI in potentially treatable dementia,” The Journal of Neuropsychiatry and Clinical Neurosciences, vol.11, no.3, pp.297-300, 1999.
5. M.S. de Oliveira, M.L.F. Balthazar, A.D’ Abreu, C.L. Yasida, B.P. Damasceno, and F. Cendes, et.al., “MR Imaging Texture Analysis of Corpus Callosum & Thalamus in Amnestic Mild Cognitive Impairment & Mild Alzheimer Disease,” American Journal of Neuroradiology, vol. 32, pp.60-66, Jan.2011.
6. S.F. Witelson, “Hand and sex differences in the isthmus and genu of the human corpus callosum: a post-mortem morphological study,” Brain: A Journal of Neurology, vol.112, pp. 799-835, Jun.1989.
7. OASIS brain MRI database, available on: http://www.oasis-brains.org/
8. N. Otsu.” A Threshold Selection Method from Grey-Level Histograms”. IEEE Transactions on Systems, Man, and Cybernetics, Vol. 9, No. 1, pp. 62-66, 1979.
9. Ping-Sung Liao, Tse-Sheng Chen, Pau-Choo Chung“, A Fast Algorithm for Multilevel Thresholding”. Journal of Information Science and Engineering, vol. 17 (5), pp. 713–727, 2001.
10. F. Meyer, “Topographic distance and watershed lines”, Signal Processing, July 1994, vol. 38, pp. 113-125.
11. M. Muja,D.G. Lowe.” Fast Matching of Binary Features”. Conference on Computer and Robot Vision, CRV 2012.

Implementation and Comparison of Algorithms for Discreet Fourier Transform

Michal Kelnar

Department of Cybernetics and Biomedical Engineering, FEECS,
VŠB – Technical University of Ostrava, 17. listopadu 15, 708 33 Ostrava – Poruba
michal.kelnar@vsb.cz

Abstrakt Signal processing in the frequency domain is currently one of an essential means of machine cognition of the surrounding world. Fourier transform (FT) plays the important role of these means. This article discusses the implementation of algorithms for calculating the discrete Fourier transform (DFT) on embedded devices with 8-bit micro-controller (MCU). Algorithms were implemented in C language environment Atmel Studio.

Keywords: Fourier transform, decimation in time, decimation in frequency, decomposition

1 Introduction

The Fourier transform plays a very important role in the analysis of continuous signals. Discrete version of the Fourier transform (DFT) is in the discrete-time signals. [8,4].

This article aims to the implementation and comparison of three algorithms to calculate the DFT. In principle, the individual DFT algorithms differs in processing speed of the transformation, which is associated with the number of mathematical operations (sums and multiplications). DFT algorithms for the N elements that achieve higher processing speeds, are known as fast Fourier transform (FFT) algorithms.

In some cases, where only a few values of DFT are required, algorithms like Goertzel or chrip transform (mostly based on direct DFT) are more efficient and flexible than FFT algorithms, see [3].

However, this article is aimed directly to a group of FFT algorithms. This group of algorithms uses three basic principles that each FFT algorithms combine, see [10]. The first is decomposition of calculating a DFT of N elements to calculate several DFTs of less number of elements. The second principle uses symmetry or periodicity of $e^{\left(\frac{-2\pi}{N}nk\right)}$ series; which is always known before calculating the DFT and its size depends on the number of elements N. And the last principle is to reduce the number of multiplications at an increase of number of sum operations.

The group of FFT algorithms contains basis algorithms as decimation-in-time (DIT) and decimation-in-frequency (DIF), which divides DFT computation for

© M. Krátký, J. Dvorský, P. Moravec (Eds.): WOFEX 2015, pp. 193–198.
VŠB – Technical University of Ostrava, FEECS, 2015, ISBN 978-80-248-3787-1.

N elements involved in the calculation of DFT for a smaller number of elements in a series in time or frequency domain, see [9,8]. Wherein the class of DIT and DIF algorithms require the number of series elements equal to the square of 2. Further FFT algorithms use a convolution as basis for calculation the DFT, such as Winograd's, Rader's, Bluestein's algorithms, see [2]. These classes of algorithms can process FFT for series with variable or other specific number of elements.

The aim of this work is the design, implementation, and comparison of selected FFT algorithms for embedded device with MCU (for systems like [6,5]). The selected algorithms are DIT for the number of elements corresponding to 2 square base (DIT radix-2), DIT for the number of elements corresponding to 4 square base (DIT radix-4), and Bluestein's algorithm. These algorithms were implemented for an 8-bit MCU ATXmega192D3 (see [1]) in C language in development environment – Atmel Studio.

2 Algorithms for FFT

The FFT algorithms are based on the direct DFT for finite number of elements, see definition at Eq. (1).

$$F_n = \frac{1}{\sqrt{N}} \sum_{k=0}^{N-1} f_k \cdot e^{-\frac{2\pi i}{N} nk}, \qquad n = 0 \dots N-1. \tag{1}$$

Whereas, substitution can be introduced

$$\omega_N = e^{-\frac{2\pi i}{N}}, \omega_N^{nk} = e^{-\frac{2\pi i}{N} nk}, \tag{2}$$

thus the simplified equation is defined Eq. (3).

$$F_n = \frac{1}{\sqrt{N}} \sum_{k=0}^{N-1} f_k \cdot \omega_N^{nk}, \qquad n = 0 \dots N-1. \tag{3}$$

2.1 FFT DIT Radix-2

The DIT FFT algorithm for finite number of elements in integral powers of a base 2 (known as radix-2) uses decomposition of DFT into multiple smaller DFTs and also uses symmetry and periodicity of the complex series $e^{-\frac{2\pi i}{N} nk}$, see [7].

Decomposition it the time domain is performed for the odd and even indexes of input series of the total number of elements N, whereby the couple of DFT for $N/2$ elements (odd and even) arises. The idea of that algorithm is entered in base DFT relation Eq. (1) and transformed into a relation Eq. (4) while introducing substitution according to Eq. (2). From this relationship is evident

decomposition of DFT at even elements E_n and odd elements O_n.

$$F_n = \underbrace{\frac{1}{\sqrt{N}} \sum_{k=0}^{\frac{N}{2}-1} f_{2k} \cdot \omega_{\frac{N}{2}}^{nk}}_{E_n} + \omega_N^n \cdot \underbrace{\frac{1}{\sqrt{N}} \cdot \sum_{k=0}^{\frac{N}{2}-1} f_{2k+1} \cdot \omega_{\frac{N}{2}}^{nk}}_{O_n}, \qquad n = 0 \dots N-1 \quad (4)$$

The introduction of the above mentioned adjustments of resulting relationship gets algorithm for DIT radix-2 given by relations Eq. (5) and Eq. (6).

$$F_n = E_n + \omega_N^n \cdot O_n, \qquad n = 0 \dots \frac{N}{2} - 1 \quad (5)$$

$$F_{n+\frac{N}{2}} = E_n - \omega_N^n \cdot O_n, \qquad n = 0 \dots \frac{N}{2} - 1 \quad (6)$$

Implementation of FFT DIT radix-2 algorithm uses principle of Splitting method, which was published by authors J. W. Cooley a J. W. Tukey.

The last step is the distribution Eq. (6) to the real and imaginary components via Euler relationship. The importance of mentioned distribution of computation to real and imaginary part is unavailability of native support for complex data type, as well as the importance of prepared tables for trigonometric constants.

3 FFT DIT Radix-4

The FFT DIT algorithm for finite number of elements in integer powers of a base 4 (known as radix-4) uses decomposition of DFT into multiple smaller DFTs and also uses symmetry and periodicity of the complex series $e^{-\frac{2\pi i}{N} nk}$, see [7].

Decomposition in the time domain is performed for indexes $4k + i$, where $i = \{0, 1, 2, 3\}$. Using this considerations into relation Eq. (3); the following equation Eq. (7) is obtained with simultaneous expression of individual subtransforms A_n, B_n, C_n, D_n.

$$\begin{aligned} F_n = & \underbrace{\frac{1}{\sqrt{N}} \sum_{k=0}^{\frac{N}{4}-1} f_{4k} \cdot \omega_{\frac{N}{4}}^{nk}}_{A_n} + \omega_N^n \underbrace{\frac{1}{\sqrt{N}} \sum_{k=0}^{\frac{N}{4}-1} f_{4k+1} \cdot \omega_{\frac{N}{4}}^{nk}}_{B_n} + \\ & + \omega_N^{2n} \underbrace{\frac{1}{\sqrt{N}} \sum_{k=0}^{\frac{N}{4}-1} f_{4k+2} \cdot \omega_{\frac{N}{4}}^{nk}}_{C_n} + \omega_N^{3n} \underbrace{\frac{1}{\sqrt{N}} \sum_{k=0}^{\frac{N}{4}-1} f_{4k+3} \cdot \omega_{\frac{N}{4}}^{nk}}_{D_n}, \end{aligned} \quad (7)$$

pro $n = 0 \dots N-1$.

By splitting exponential series to portions of Eq. (7) a constants for individual quarters can be quantified:

$$\begin{aligned} \omega_N^{\frac{N}{4}} &= -i, & \omega_N^N &= 1, \\ \omega_N^{\frac{N}{2}} &= -1, & \omega_N^{\frac{3N}{2}} &= -1, \\ \omega_N^{\frac{3N}{4}} &= i, & \omega_N^{\frac{9N}{4}} &= -i. \end{aligned} \quad (8)$$

Quantified constants are written in modified relation Eq. (7) ant the result is a prescription Eq. (9) for DIT FFT radix - 4 algorithm for $n = 0 \dots \frac{N}{4} - 1$.

$$\begin{aligned} F_n &= A_n + \omega_N^n B_n + \omega_N^{2n} C_n + \omega_N^{3n} D_n \\ F_{n+\frac{N}{4}} &= A_n - i\omega_N^n B_n - \omega_N^{2n} C_n + i\omega_N^{3n} D_n \\ F_{n+\frac{2N}{4}} &= A_n - \omega_N^n B_n + \omega_N^{2n} C_n - \omega_N^{3n} D_n \\ F_{n+\frac{3N}{4}} &= A_n + i\omega_N^n B_n - \omega_N^{2n} C_n - i\omega_N^{3n} D_n \end{aligned} \tag{9}$$

Like implementation of the FFT DIT radix-2 algorithm, the Splitting method is also used to implement this algorithm. Also, the relationship Eq. (9) had to be distributed to the separate calculation of real and imaginary components, which is analogous to the described radix-2 algorithm.

3.1 Bluestein's algorithm

Bluestein's algorithm (sometimes known as „chirp z-transform algorithm“) is based on the expression of DFT as a convolution. The main advantage of this algorithm is its ability to work with different numbers of elements of input series, including the prime-factor numbers, see [7].

Product nk deriving from the exponential relationship original sequence Eq. (1) for DFT computation is replaced by identity

$$nk = -\frac{(n-k)^2}{2} + \frac{n^2}{2} + \frac{k^2}{2}. \tag{10}$$

After substitution to an original relation the algorithm relationship is achieved, see Eq. (11).

$$F_n = \frac{1}{\sqrt{N}} e^{-\frac{\pi i}{N} n^2} \cdot \sum_{k=0}^{N-1} \left(f_k \cdot e^{-\frac{\pi i}{N} k^2} \right) \cdot e^{\frac{\pi i}{N} (n-k)^2}, \qquad n = 0 \dots N-1. \tag{11}$$

Subsequently for this relation the convolution kernel b_{n-k} is defined and also input series a_n is defined.

$$\begin{aligned} a_k &= f_k \cdot e^{-\frac{\pi i}{N} k^2}, && n = 0 \dots N-1 \\ b_k &= e^{\frac{\pi i}{N} k^2}, && n = -N+1 \dots N-1 \end{aligned} \tag{12}$$

The Bluestein's algorithm equation is obtained by substitution b_{n-k} and a_n back to Eq. (11).

$$F_n = \frac{1}{\sqrt{N}} b_n^{-1} \sum_{k=0}^{N-1} a_k \cdot b_{n-k}, \qquad n = 0 \dots N-1. \tag{13}$$

The last step, similary in cases of previous algorithms, the algorithm calculation is separated into real and imaginary parts (see Eq. (14)).

$$\begin{aligned}
\mathbf{Re}(a_k) &= f_k \cdot \cos\left(\frac{\pi}{N}k^2\right), \\
\mathbf{Im}(a_k) &= -\, f_k \cdot \sin\left(\frac{\pi}{N}k^2\right), \\
\mathbf{Re}(b_k) &= \cos\left(\frac{\pi}{N}k^2\right), \\
\mathbf{Im}(b_k) &= \sin\left(\frac{\pi}{N}k^2\right).
\end{aligned} \tag{14}$$

4 Results

Computation performance comparison of mentioned FFT algorithms implemented in C for 8-bit MCU are showen in the Table 1. Processing time is measured using an oscilloscope for short periods (up to units of seconds) and a stopwatch for timer periods exceeding approximately 10 s. Processing speed of FFT algorithms are always measured for the actual computing core, it means that preparation of tables of constants are not included in this measuring. The results are available for different number of elements in series N for each mentioned FFT algorithms.

Tabulka 1. Comparison of the time-consuming processing of FFT algorithms implemented in C for MCU ATxmega192D3

N	DFT	Bluestain	Radix2	Radix4
[-]	[s]	[s]	[s]	[s]
4	0.00324	0.00237	0.000265	0.000257
8	0.01348	0.00816	0.000718	—
16	0.0542	0.0291	0.001828	0.00188
32	0.217	0.111	0.00442	—
64	0.868	0.429	0.01042	0.01094
128	3.46	1.962	0.02392	—
256	10.6	6.8	0.0479	0.0582
512	56.5	26.2	0.121	—
1024	—	—	0.267	0.288

4.1 Conclusion

According to the results of comparison of the algorithms for calculating the FFT on the 8-bit MCU is concluded that DIT radix-2 is the most effective for a number of samples of the input signal 8 and higher. Algorithm implementation DIT radix-4, when analyzing the processing speed of the algorithm in a given range

of input signal samples, showed about the same time as processing DIT radix-2. This may be due to the relatively high overhead mathematical operations for indexing the data structures in this implementation.

Acknowledgments

This work is partially supported by the Science and Research Fund 2014 of the Moravia-Silesian Region, Czech Republic and project SP2015/181 of Student Grant System, VŠB – Technical University of Ostrava.

Reference

1. Atmel Corporation: ATxmega192D3 – Technical Data Sheet (2014), http://www.atmel.com/products/microcontrollers/avr/AVR_XMEGA.aspx
2. Beaudoin, N., Beauchemin, S.: An accurate discrete fourier transform for image processing. In: Pattern Recognition, 2002. Proceedings. 16th International Conference on. vol. 3, pp. 935–939 vol.3 (2002)
3. Davis, J., Gravagne, I., Marks, R.: Time scale discrete fourier transforms. In: System Theory (SSST), 2010 42nd Southeastern Symposium on. pp. 102–110 (March 2010)
4. Hsue, W.L., Chang, W.C.: Multiple-parameter real discrete fractional fourier and hartley transforms. In: Digital Signal Processing (DSP), 2014 19th International Conference on. pp. 694–698 (Aug 2014)
5. Konecny, J., Kelnar, M., Prauzek, M.: Advanced waste rock exploring by mobile robot. Applied Mechanics and Materials, vol. 313-314, pp. 913–917 (2013), www.scopus.com
6. Krejcar, O., Janckulik, D., Kelnar, M.: Visualization of Measured Data for Wireless Devices BluesenseAD. In: 5th Kuala Lumpur International Conference on Biomedical Engineering 2011 (BIOMED 2011). IFMBE Proceedings, vol. 35, pp. 363–366. Springer, 233 Spring Street, New York, NY 10013, United States (2011)
7. Qadeer, S., Khan, M., Sattar, S., Ahmed: A radix-2 dit fft with reduced arithmetic complexity. In: Advances in Computing, Communications and Informatics (ICACCI, 2014 International Conference on. pp. 1892–1896 (Sept 2014)
8. Voronenko, Y., Puschel, M.: Algebraic derivation of general radix cooley-tukey algorithms for the real discrete fourier transform. In: Acoustics, Speech and Signal Processing, 2006. ICASSP 2006 Proceedings. 2006 IEEE International Conference on. vol. 3, pp. III–III (May 2006)
9. Xie, G., chun Li, Y.: Parallel computing for the radix-2 fast fourier transform. In: Distributed Computing and Applications to Business, Engineering and Science (DCABES), 2014 13th International Symposium on. pp. 133–137 (Nov 2014)
10. Zhao, L., Gao, S., Hao, Y.: Improved fast fourier transform processing on fast acquisition algorithms for gps signals. In: Electronic Measurement Instruments, 2009. ICEMI '09. 9th International Conference on. pp. 4–221–4–224 (Aug 2009)

Exergaming Rehabilitation System for 3D Motion Analysis of Wobble Board

Jana Krohova and Maros Smondrk

Department of Cybernetics and Biomedical Engineering, FEECS,
VŠB – Technical University of Ostrava, 17. listopadu 15, 708 33 Ostrava – Poruba
jana.krohova@vsb.cz

Abstract. This paper describes the design and implementation of telemetric rehabilitation system for motion analysis of the wobble board. Balance exercises on the wobble board are used for rehabilitation of different diagnosis (e.g. poor posture, different types of fractures and postsurgical states of lower extremity, and etc.). The rehabilitation system compromises wobble board which measuring part consists of an inertial measurement unit. The inertial measurement unit measures orientation of the wobble board (pitch, roll and yaw). The motion analysis of the wobble board provides important information about the quality of undertaken exercise.

Keywords: rehabilitation; bluetooth 4.0; wobble board; orientation; rotation

1 Introduction

The lack of movement usually leads to uneven loading of musculoskeletal system, decreasing of the exteroceptive and proprioceptive excitation resulting in decreased stimulation of the central nervous system. The result is the development of various muscle imbalances, incorrect posture, incorrect movement patterns, increased risk of accident conditions (ankle sprain, knee injury), and risk of falls in elderly people. [1]

In many rehabilitation centres balance exercise is used for aforementioned problems. Balance exercise is particularly indicated for the diagnosis such as lower limbs fractures, instability of the knee joint, plastic of the knee joints, etc. A musculoskeletal lower leg injury such as an ankle sprain has affected balance capabilities [2]. Balance exercise is part of physical therapy which actively relaxes, stretches, stabilizes and strengthens the deep muscles of legs and back. The main principle of balance exercises is to balance on the rehabilitation tool. The most commonly used balance tool is wobble board. Its symmetrical shape allows a patient to move in the range from 0 to 30 degrees.

The quality of the rehabilitation and progress of the patient is usually evaluated only subjectively and depends on theoretical and practical knowledge of the physiotherapist. Various studies have shown improvements of postural control, ankle sprain prevention, etc. through the balance training programs [3], [4].

© M. Krátký, J. Dvorský, P. Moravec (Eds.): WOFEX 2015, pp. 199–203.
VŠB – Technical University of Ostrava, FEECS, 2015, ISBN 978-80-248-3787-1.

It follows from the foregoing that the need for an objective assessment of the balance rehabilitation process and progress of the patient has reasonable importance and great benefit to physiotherapist and patient.

2 Problem Definition

The system for interactive rehabilitation balance exercises on the wobble board has been designed and tested. The main aim of this work was to design and implement a rehabilitation tool which will be able to evaluate objectively the progress of rehabilitation and display both qualitative and quantitative information about the performed exercise.

3 System Description

Proposed device consists of an inertial measurement unit and a module platform OLP425.The OLP425 is the Bluetooth Low Energy (BLE) platform module which integrate two specific features: low energy consumption due to wireless communication technology Bluetooth 4.0 and small physical dimensions. The small physical dimensions allow it to use in plenty of applications where limitation of dimensions are crucial. The communication between the CC2540 and the IMU is implemented using I^2C bus. [5], [6]

As IMU we have used a commercial available 9-axis motion tracking device MPU-9150 from InvenSense. It comprises a 3-axis accelerometer, a 3-axis gyroscope, and a 3-axis magnetometer which are integrated in one package. [7]

The orientation of the proposed system is estimated using the 3D raw data provided by the accelerometer and magnetometer. The gyroscope was not used due to its considerable power consumption. The presented work aims to perform an orientation estimation algorithm on the PC in order to ensure low power consumption. Proposed device is embedded into a rehabilitation wobble board whose shape allows the patient to move in limited ranges. This movement is reduced to a rotation around 3 axes without a translational motion. In other words we assume that the wobble board is not affected by linear acceleration during rehabilitation, it is affected only by rotation around one fixed point. Consequence of this simple assumption results in errors in orientation estimation during undergoing linear acceleration of the wobble board. The rotation of the wobble board is in the range of ±30°in x, y axis and full 360° in z axis.

The orientation of rehabilitation wobble board is represented by Euler angles: roll, pitch and yaw. Roll is defined as the angle between the y axis and the horizontal plane, pitch as the angle between the x axis and the horizontal plane, and yaw as the angle between the x axis and the magnetic north on the horizontal plane. [8]

The accelerometer output is used for roll and pitch estimation as follows, [9]:

$$roll = tan^{-1}(A_Y/A_Z) \tag{1}$$

$$pitch = tan^{-1}\left(-A_X/\sqrt{A_Y^2 + A_Z^2}\right), \tag{2}$$

where A_X is the normalized accelerometer reading in *x*-axis, A_Y is the normalized accelerometer reading in *y*-axis and A_Z is the normalized accelerometer reading in *z*-axis.

The accelerometer readings have to be preprocessed before applying formula (roll and pitch) in order to calibrate its outputs. This task includes determination of the accelerometer offset, the scale factor and the misalignment matrix between the accelerometer sensing axes and the device body axes. The objective of the accelerometer calibration is determining these parameters in order to get normalized accelerometers values from raw accelerometer measurements. [9]

In order to estimate yaw, on the magnetometer outputs are applied following formula, [8]:

$$yaw = \arctan\left(\frac{yaw_Y}{yaw_X}\right), \tag{3}$$

where yaw_X is the horizontal component of local earth magnetic field H in axis X and yaw_Y is the horizontal component of local earth magnetic field H in axis Y.

Aforementioned horizontal components are defined as follows [8]:

$$yaw_X = M_X.\cos(pitch) + M_Z.\sin(pitch)\,, \tag{4}$$

$$yaw_Y = M_X.sin(roll).sin(pitch) +$$

$$+M_Y.cos(roll) - M_Z.sin(roll).cos(pitch)\,, \tag{5}$$

where M_X is the normalized magnetometer reading in *x*-axis, M_Y is the normalized magnetometer reading in *y*-axis and M_Z is the normalized magnetometer reading in *z*-axis. As in the case of the accelerometer, the magnetometer raw readings have to be calibrated in order to get normalized values of earth's magnetic field strength. In determination of the magnetometer offset, the scale factor and misalignment matrix with respect to the device body, the geographical position of the device has to be taken into account. [8], [10] - [12]

3.1 Software

The proposed software consists not only of rehabilitation software it is also comprised of the firmware of the measuring part (OLP425 and MPU-9150) which ensures the acquisition of measured data from the sensors and data transmission to the PC. The therapeutic software was developed in the MATLAB R2011a environment. It provides real-time graphical representation of the patient (wobble board) motion during the rehabilitation exercises.

The rehabilitation programs were designed with cooperation with physiotherapists of the Therapeutic Rehabilitation Clinic of the University Hospital of Ostrava. The therapeutic software is designed for patients with the poor posture, the flat foot, the hip arthritis, the attention deficit hyperactivity disorder, with different types of fractures. More information about the rehabilitation software can be found in [13].

3.2 Testing

Until these days, more than thirty patients at the age of 12 to 30 participated in testing of proposed system. The preliminary results indicate higher motivation of the patients. Their exercises were simply evaluated by score as the ratio between the number of samples which were in the tolerance area and the number of samples which were outside. In the next step the measured data will be processed and classified in order to estimate the function state of the patient's locomotive system.

4 Discussion

The proposed system is based on the combination of the accelerometer and the magnetometer as the sensor part. The proposed rehabilitation programs designed with cooperation with physiotherapist provides more specific exercise tasks depending patient's diagnosis and mobility. In each rehabilitation program is implemented a virtual line which patient has to track. The space for movement is limited by different types of tolerance area. The maximal wobble board tilt of deflection is a user selectable. These types of rehabilitation tasks could provide a variety of parameters for example maximal and minimal deflection, required time to finish rehabilitation task, deflection from virtual line, jerkiness or movement sharpness, etc. These parameters could be used for complex evaluation of patient progress during rehabilitation process.

5 Conclusion

Many various studies have shown improvements of postural control, fall prevention, function of the lower extremity after previous injury or disease through the balance training on the wobble board. In this paper the design and implementation of the interactive low energy balance rehabilitation system has been presented. The main advantages and disadvantages of the related available solutions were also pointed and the optional parameters from motion analysis of the wobble board were discussed.
We would like to focus on the feature extraction from the measured data in order to estimate and evaluate the patient's progress in our future work.

6 References

1. R. Dvorak, "Fundamentals of kinesiotherapy," 3th ed. Olomouc: Palacky University in Olomouc, 2007.
2. A. Mitchell, R. Dyson, T. Hale, and C. Abraham, "Biomechanics of Ankle Instability. Part 2," Medicine & Science in Sport & Exercise, vol. 40, issue 8, pp. 1522-1528, 2008. doi: 10.1249/MSS.0b013e31817356d6.
3. V. M. Clark, A. M. Burden, "A 4-week wobble board exercise programme improved muscle onset latency and perceived stability in individuals with a functionally unstable ankle," Physical Therapy in Sport, Volume 6, Issue 4, pp. 181-187, November 2005, ISSN 1466-853X, doi: 10.1016/j.ptsp.2005.08.003.

4. T. A. McGuine, J.S. Keene, “The Effect of a Balance Training Program on the Risk of Ankle Sprains in High School Athletes, ” American Journal of Sports Medicine, vol. 34, issue 7, pp. 1103-1111, February 2006. doi: 10.1177/0363546505284191.
5. Connectblue, 2014. cB-OLP425 cB-OLS425 cB-OLS426 Electrical Mechanical Data Sheet. 31 January 2014, [Online]. Available: http://support.connectblue.com/display/PRODBTSPA/cB-OLP425+cB-OLS425+cB-OLS426+Electrical+Mechanical+Data+Sheet.
6. Texas Instruments, 2013. 2.4-GHz Bluetooth® low energy System-on-Chip (Rev. F). June 2013, [Online]. Available: http://www.ti.com.cn/cn/lit/ds/symlink/cc2540.pdf.
7. InvenSense, 2013. MPU-9150 Product Specification Revision 4.3. 8 September 2013, [Online]. Available: http://support.connectblue.com/display/PRODBTSPA/cB-OLP425+cB-OLS425+cB-OLS426+Electrical+Mechanical+Data+Sheet.
8. STMicroelectronics, 2010. Using LSM303DLH for a tilt compensated electronic compass. August 2010, [Online]. Available: http://www.pololu.com/file/download/LSM303DLH-compass-app-note.pdf?file_id=0J434.
9. Freescale Semiconductor, 2013. Tilt Sensing Using a Three-Axis Accelerometer. March 2013, [Online]. Available: http://www.freescale.com/files/sensors/doc/app_note/AN3461.pdf.
10. Freescale Semiconductor, 2012. Implementing a Tilt-Compensated eCompass using Accelerometer and Magnetometer Sensors. January 2012, [Online]. Available: http://freescale.com.hk/files/sensors/doc/app_note/AN4248.pdf.
11. Freescale Semiconductor, 2013. Calibrating an eCompass in the Presence of Hard and Soft-Iron Interference. April 2013, [Online]. Available: http://www.freescale.com/files/sensors/doc/app_note/AN4246.pdf.
12. M. Penhaker, M. Stankus, M. Prauzek, O. Adamec, T. Peterek, M. Cerny, and V. Kasik, “Advanced Experimental Medical Diagnostic System Design and Realization,” Electronics and Electrical Engineering, vol. 117, issue 1, pp. 89-94, January 2012. doi: 10.5755/j01.eee.117.1.1060.
13. J. Krohova, M. Smondrk, M. Cerny, I. Chwalkova, M. Zadrapova, “Interactive rehabilitation system for balance exercises on the spherical cap,” In Proc. 18th International Conference on Applied Electronics 2013, pp. 145-148, September 2013.

Articular Cartilage Chondromalacia Detection Based on Soft Thresholding Segmentation Approach

Jan Kubicek

Department of Cybernetics and Biomedical Engineering, FEECS,
VŠB – Technical University of Ostrava, 17. listopadu 15, 708 33 Ostrava – Poruba
jan.kubicek@vsb.cz

Abstract. Article deals with design of complex method for image segmentation of articular cartilage. This work is mainly focused on detection of early stage pathological changes. These pathological lesions are classified into for stages. Individual stages reflect level of cartilage´s damage and consequent treatment. The presence of chondromalacia is detected on the base of examination by Magnetic resonance (MRI). In terms of image processing, first stage of chondromalacia is the most interesting. In this particular case pathological lesions are badly recognizable. The Goal of proposed solution is design of complex software algorithm which approximates cartilage area to contrast color map. On the base this procedure individual tissue's structures are precisely differentiated. The main benefit of proposed algorithm is precise localization of physiological cartilage and adjacent pathological lesions.

Keywords: Image segmentation, Soft thresholding, Membership function, MRI, MATLAB, Articular cartilage

1 Introduction

Cartilage is a specialized type of fibrous tissue. It is composed of different substances, each of them responsible for its overall integrity, deformability, hardness and the ability to repair itself. Cartilage is created from mesenchymal cells at the ends of the epiphyses of bones during embryonic development in human foetuses.

Histologically, it is classified into three basic types: elastic, fibrous and hyaline. The contact surfaces of joints are covered with hyaline cartilage. Cartilage is organized into a layered structure, which is functionally and structurally divided into four layers. The surface layer is responsible for its smoothness and is resistant to friction. It makes up about 10-20% of the total depth of the cartilage. It can compress about 25 times more than the middle layer.

Adult cartilage is composed of 75% water and 25% solid compounds. The metabolism of cartilage is mainly anaerobic. Due to cartilage's shortage of its own vascular supply and nerve fibres, it has a very low ability to repair itself or remove metabolites. Despite its low metabolic turnover, the replacement and the continuous exchange of cells occurs in cartilage. [1, 2, 3, 4]

© M. Krátký, J. Dvorský, P. Moravec (Eds.): WOFEX 2015, pp. 204–209.
VŠB – Technical University of Ostrava, FEECS, 2015, ISBN 978-80-248-3787-1.

2 Chondromalacia

Chondromalacia or chondropathy is a pathological condition in which there is softening of the cartilage and damage to the lattice, often with its erosion and fissuration caused by damage to adjacent bone. Chondrocytes have only limited ability to self-repair. When there is a defect, they do not travel into the affected site and are able to only synthesize new cartilage in their immediate vicinity.

According to the extent of macroscopic disability, the degrees of disability of chondromalacia are most often judged according to the Outerbridge classification:

- Degree 0 – physiological cartilage;
- Degree I – cartilage with swelling and softening;
- Degree II – partial rupture with a crack on the surface that does not interfere with the subchondral bone;
- Degree III – a crack extending to the subchondral bone with a diameter of up to 1.5 cm;
- Degree IV - exposed subchondral bone. [5, 6]

3 A Fast Thresholding Algorithm

The proposed fast thresholding algorithm can be used, in particular, for segmentation of tissues that contain rather different structures. The core of this approach is to determine a suitable membership function for each pixel in the input image and then match pixels with the same properties into output classification classes. This approach represents the main difference from standard hard thresholding methods where the input decision-making criterion is a fixed thresholding value.

The algorithm can be divided into two main parts:

pre-processing of the input image data

outputting for creating color mapping of tissue structures.

It is assumed that the image signal, whitch is defined by function f(x,y) that is represented by the histogram H(i) is the input for the algorithm,

where:

i is the image intensity,

x, y - coordinates of individual pixels

The first step in segmentation is dividing the input image into N corresponding different regions.

The second step in segmentation is defining partial membership functions, typically for the n^{th} output region:

$$n = 1, 2, ...N \tag{1}$$

The next step is normalising the input image's histogram. The approach is practically identical to all other thresholding methods because the histogram is the basis for identifying the minimum and maximum values for the decisive threshold. Sometimes, problems can appear in the separation of tissues in medical images because individual levels of tissue structures are quite often not known, this being, for instance, the case with articular cartilage mapping. In that case, it is recommended to unify the input image as much as possible – of course, all remote values should be, ideally, removed. Thus, it is possible to restrict the interval in a closed interval [0,1].

An important segment of the algorithm is the detection and analysis of maximum values. The basic assumption for this step is that the number of histogram peaks corresponds to the number of output classes. When mapping complex tissue structures, it frequently occurs that the tissue being mapped is comprised of many different intensities that should be distinguished reliably and efficiently. This is a big advantage of the proposed solution. The number of histogram peaks can be determined as follows:

$$N = NUM_{MAX} \tag{2}$$

Where:

NUM_{MAX} is number of histogram's peak.

The final part in detecting the maximum values is filtration of the output image. A low-pass filter was used for filtering. The output histogram downstream from the filter can be described as follows:

$$H_{LP}(i) = H(i) * K \tag{3}$$

After the maximum values are detected, it is necessary to adjust N known distributions of image intensities. This adjustment is made using the formula that is made up of contributions from all partial probability distributions:

$$H_{LP}(i) \approx \sum_{n=1}^{N} \Omega_n p_n(x) \tag{4}$$

Where:

Ω_n is a specific weight function

$p_n(x)$ is the distribution probability

An optimising procedure should be performed to adjust each image intensity. In order to minimise errors in image intensity, a gradual iteration algorithm has been used. The optimising issue can be described as follows:

$$\min_{l \in N} | H_{LP}(I) - \sum_{n=1}^{N} \Omega_n p_n(x) |^2 \tag{5}$$

The next step derives the membership function for each output region. This key phase is divided into several parts. First, it is necessary to estimate the probability that the x pixel in the input image is a part of the REG_n region. Using the standard definition of probability, the estimate can be formulated as follows:

$$p(REG_n) = \frac{p(x \mid REG_n)p(REG_n)}{\sum_{n=1}^{N} p(x \mid REG_n)p(REG_n)} \tag{6}$$

The key objective is to use the membership function. For this, regularities of the histogram are used to model the resulting Fuzzy sets. The sets provide us information about the membership. The standard Gaussian function of relevance appears to be a very efficient approach.

Now it is necessary to define and assign the membership function for the respective region. The membership function of the input image f(x) in the respective output REG_n region can be defined as $\mu_n(f(x))$. Let us assume that the following restrictions apply with respect to that function:

$$\sum_{n=1}^{N} \mu_n(f(x)) = 1 \tag{7}$$

If the input image is segmented in iteration steps, the first iteration step will be:

$$TI(y) = \max_n \mu_n(f(x)) \tag{8}$$

TI(y) is the output image with thresholding. Of course, this is the example with the simplest thresholding. More detailed segmentation needs the neighbouring membership values, so it is advisable to carry out another step in the process.

A common issue that should be kept in mind is the maximum possible noise invariance. Color mapping close to object edges where the intensity of pixels changes rather dramatically appears which, of course, impairs the segmentation results. For this reason, it is recommended to optimise the process in order to achieve greater noise resistance, especially close to the object edges. These artefacts appear typically in bone - muscle tissue borders. This approach is linear. For a non-linear process, a median can be used for each channel. The final mathematical model is:

$$\mu_n(f(x)) = med_n(\mu_n(f(x))) \tag{9}$$

A median is normally used as a robust indicator of position which is robust against remote observations. The median is calculated for the environment of each pixel. In some cases, a rather good solution has been to replace the median with another averaged operation. But here, only the medial with the best noise resistance is used. Using the non-linear approach, the final thresholding image can be formulated using the formula below:

$$TI(y) = \max_n(med_n(\mu_n(f(x)))) \tag{10}$$

[1, 2]

4 Algorithm Testing

The following output shows the using of the proposed algorithm for real patient data. A very important aspect for physicians is the identifying regions of interest (RoI) of the analyzed image of the suspected pathology. Consequently, it is necessary to interpolate the selected area in order to improve the quality of the analyzed record. It is important to note that the quality of the input image largely affects the quality of segmentation and hence the relevance of the results obtained.

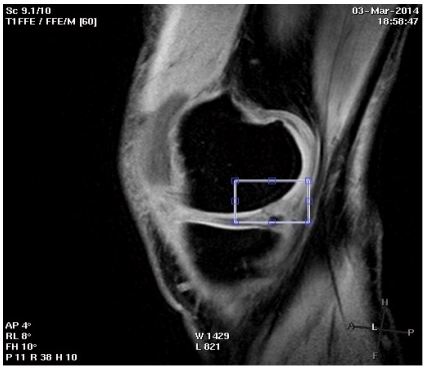

Fig. 1 A Sagittal T1 WATS-c sequence selectively displaying articular cartilage with the maximum suppression of signals of the surrounding tissues

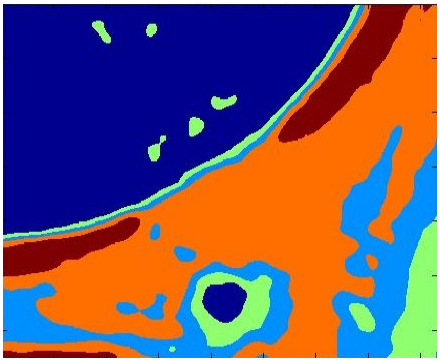

Fig. 2 A Sagittal T1 WATS-c sequence selectively displaying articular cartilage with the maximum suppression of signals of the surrounding tissues - colour mapping with interpolation

5 Conclusion

Image segmentation has a very wide application for medical image analysis. Images from magnetic resonance form the core basis for the analysis and detection of pathological changes in knee cartilage. The main disadvantage is that the pathologies of cartilage are often poorly identifiable. It is often a pressing issue for the physician to detect locations subject to pathological changes as those locations are typically presented by a minor change in the brightness scale which is almost impossible to recognise for a human eye. The only chance to improve visibility of pathological changes is supply of a contrast substance which, however, loads a human organism with a radiation dose and effects of such examination are not too satisfactory. The proposed segmentation method can efficiently separate each tissue structure and identify locations subject to pathological changes. This is of a major benefit for the physicians who may perform a better diagnosis even with pathological changes being in an early stage.

6 Publications

1. Kubicek, J., Penhaker, M., Fuzzy algorithm for segmentation of images in extraction of objects from MRI (2014), Proceedings of the 2014 International Conference on Advances in Computing, Communications and Informatics, ICACCI 2014, art. no. 6968264, pp. 1422-1427.
2. Kubicek, J., Penhaker, M., Bryjova, I., Kodaj, M., Articular cartilage defect detection based on image segmentation with colour mapping (2014), Lecture Notes in Computer Science (including subseries Lecture Notes in Artificial Intelligence and Lecture Notes in Bioinformatics), 8733, pp. 214-222.
3. Kubicek, J., Penhaker, M., Pavelova, K., Selamat, A., Majernik, J., Hudak, R., Segmentation of MRI Data to Extract The Blood Vessels Based on Fuzzy Thresholding In 7th Asian Conference on Inteligent Information and Database Systems ACIIDS 2015. 23th - 25th March, 2015 Bali, Indonesia
4. Kubicek, J., Valosek, J., Selamat, A., Penhaker, M., Bryjova, I., Grepl, J. Extraction of Blood Vessels Using Multilevel Thresholding with Color Coding In the 2nd International Conference on Communication and Computer Engineering, 9th - 11th June, 2015 Phuket, Thailand
5. Kubicek, J., Bryjova, I., Penhaker, M., Javurkova, J., Kolarcik, L. Segmentation of Macular Lesions Using Active Shape Contour Method In the 1th European-Middle Asian Conference on Computer Modelling, 25th - 27th August, 2015 Issyk Kul, Kyrgyzstan
6. Bryjova, I., Kubicek, J., Dembowski, M., Kodaj, M., Penhaker, M. Reconstruction of 4D CTA Brain Perfusion Images Using Transformation Methods In the 1th European-Middle Asian Conference on Computer Modelling, 25th - 27th August, 2015 Issyk Kul, Kyrgyzstan
7. Kubicek, J., Timkovic, J., Augustynek, M., Penhaker, M., Pokryvkova, M. Optical Nerve Disc Segmentation Using Circual Integro Differencial Operator In the 2nd International Conference on Communication and Computer Engineering, 9th - 11th June, 2015 Phuket, Thailand

Simulation of technological process using .NET for control system design

Martin Mikolajek

Department of Cybernetics and Biomedical Engineering, FEECS,
VŠB – Technical University of Ostrava, 17. listopadu 15, 708 33 Ostrava – Poruba
martin.mikolajek@vsb.cz

Abstract. This article contains the methods of communication in industrial automation area. The article is about the data exchange between the PLC systems and PC. The data exchange between PC and PLC system is usually used for control and display process values. However a PC with appropriate software may allow simulation of technology for design and debug PLC programs. The main part of this paper contains simulation of industrial technology via the PC by .NET use.

Keywords: Simulation, .NET, PC, PLC, Ethernet, C#

1 Introduction

This article is about on data transmission in industrial automation. Selecting the type of communication usually depends on the features of the devices used for communication. Each of the communication devices is limited to certain hardware and software parameters. Communicating devices are limited ways of using physical communication interface or physical communication layer. Selected devices can use, for example, communication via Ethernet, Profibus, RS485 and so on. Communication methods generally affect the chances of transmission. It is mainly due to the sampling rate or the amount of transmitted information. In the topic of this paper is used only type by Ethernet connection. Other types of communications not contained in this article. Next problem is choice the desired communications protocols and means for transmitting data. Then it is possible to provide and represent data in the HMI system, or in the trend viewer. Description of the optimal method of transferring data between devices is graphically described through standardization ISO / OSI model. Software means for providing connection with industrial automation can then be divided into several parts, and according to the requirements of their use.

The first area includes the area HMI systems in which the emphasis is usually on the versatility and ease of connection, there is usually not important critical system response in milliseconds. For this application the most commonly used means of communication based on OPC server – client architecture. Namely for this application, we can choose, for example, Siemens S7 PLC connection using the OPC Server for Siemens PLCs, Siemens SIMATIC TI505 OPC Server, KepServer etc. [1]

© M. Krátký, J. Dvorský, P. Moravec (Eds.): WOFEX 2015, pp. 210–215.
VŠB – Technical University of Ostrava, FEECS, 2015, ISBN 978-80-248-3787-1.

Next areas include the disclosure of data for the trend viewer. For such cases usually just we need time deterministic data. Methods require specific communication approaches, which usually must be selected according to exactly the selected PLC. [1] [2] This may be a type of communication through the use of Ethernet TCP / IP etc. This type of connection use special communication trend visualization means such as: PLC-ANALYZER pro 5, AutoSPy etc.

The last area of use of communication methods in automation is focused on solutions for the realization of simulation the technological processes. For these applications are usually used the criteria such as a high refresh sample rate and universal connection. The simulations of technologies are used for the design and testing of software for PLC devices. Simulation test mode contains input and output signals from input/output PLC circuits. Simulation software control inputs and outputs values like running in real technology.

Can be used at last some of the available software means like e.g. WinMod. These software tools are usually highly efficient, but the price of licenses is usually high. Payments for these systems are cost-effective only for create big comprehensive simulation technology. [3]

For school teaching laboratory supplies PLC was needed to model a simulated technology. Task can be easily destroyed if prepared program will be incorrect. In simulated technology students will not damage the real model technology. Simulation model represent a model of the elevator. Simulation of elevator used freeware library of Snap7 and programming language C#. [3]

2 WinMOD

WinMOD software is a tool for Virtual Commissioning of machines and plants. It allows simulating machine behavior from real technology. WinMOD supports the quality

management with continuous software tests according to actual the development status. Through the combination of WinMOD with the automation system can be created the virtualized machines. This allows training of operating personnel before the commissioning of the real machine. Data exchange between PLCs and PLC can be used by communication possibilities of Ethernet, Profibus etc. Specific devices can be simulated by an implementer GSD files to simulation software. These files contain the communications configuration. [3]

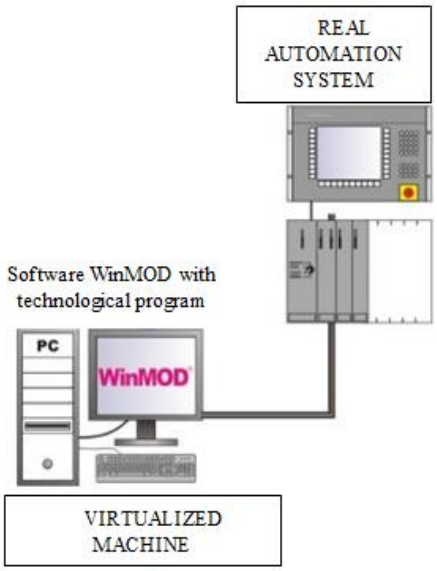

Fig. 1. Topology of WinMOD network [4]

3 Programing elevator simulation model

Simulation of the elevator is created by using .NET. in form of implementing a WF (Windows Forms) application, an using a Snap7 communication library. The Snap7 technology is an open source including a 32/64-bit, multi-platform Ethernet communication suite for communication with Siemens S7 PLCs. The purpose of the Snap7 is to fully integrate a PC station into a PLC network, namely without any significant difference. This library also contains three objects, i. e. the Client, the Server, and the Partner. Program can communicate with PLC by using the memory area. Software contains information about the dedicated memory for communication in Help section. [5]

Simulation software needs information about selected speed from 0 to 5 for moving the elevator, and binary information to output (e.g. a command to run an engine). This software uses several windows. The first main window contains parts for control and visualization of the elevator. The next windows are “Console”, and “Help” to inform about a memory allocation of the PLC. The last window is centered on setting-up the parameters for S7 PLC communication. Data communication is distributed from Siemens PLC to PC thru Ethernet. Communications library Snap7 in application need information about position of plc processor in rack and rack number. Application is ready for simulation after successful connect to PLC.

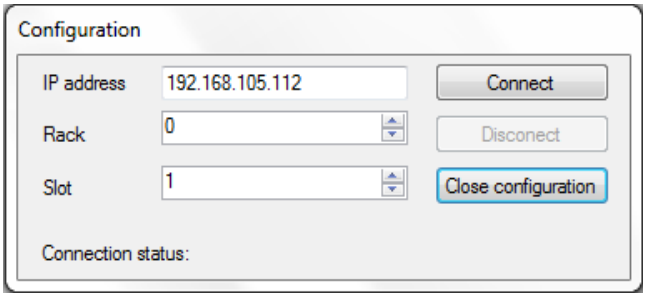

Fig. 2. Windows form with connection parameters.

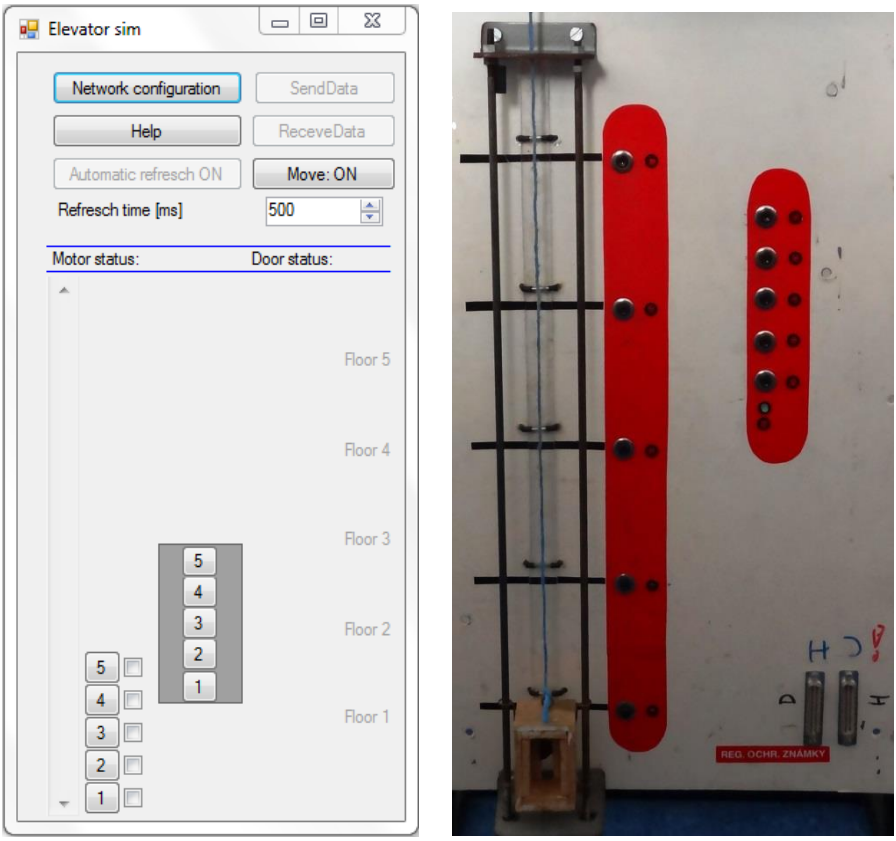

Fig. 3. The simulated model (left) and the real laboratory model (right).

A button “Automation refresh ON” is activated after the connection to PLC. The simulation software writes data to the PLC memory area. Position of the elevator is controlled automatically by simulation or manually. Mode of moving can be choice by a button “Man. Move ON or OFF”.

	Name	Data type	Address
1	IN_CabButton1	Bool	%M200.0
2	IN_CabButton2	Bool	%M200.1
3	IN_CabButton3	Bool	%M200.2
4	IN_CabButton4	Bool	%M200.3
5	IN_CabButton5	Bool	%M200.4
6	IN_Button1	Bool	%M201.0
7	IN_Button2	Bool	%M201.1
8	IN_Button3	Bool	%M201.2
9	IN_Button4	Bool	%M201.3
10	IN_Button5	Bool	%M201.4
11	IN_ActualElevatorPoz1	Bool	%M202.0
12	IN_ActualElevatorPoz2	Bool	%M202.1
13	IN_ActualElevatorPoz3	Bool	%M202.2
14	IN_ActualElevatorPoz4	Bool	%M202.3
15	IN_ActualElevatorPoz5	Bool	%M202.4
16	OUT_ActualFloorLed1	Bool	%M300.0
17	OUT_ActualFloorLed2	Bool	%M300.1
18	OUT_ActualFloorLed3	Bool	%M300.2
19	OUT_ActualFloorLed4	Bool	%M300.3
20	OUT_ActualFloorLed5	Bool	%M300.4
21	OUT_MotorON	Bool	%M302.0
22	OUT_MotorDown	Bool	%M302.1
23	OUT_MotorUp	Bool	%M302.2
24	OUT_DoorOpen	Bool	%M302.3
25	OUT_DoorClose	Bool	%M302.4
26	OUT_Speed_value_0-5	Int	%MW303
27	OUT_ActualFloorButtLed1	Bool	%M301.0
28	OUT_ActualFloorButtLed2	Bool	%M301.1
29	OUT_ActualFloorButtLed3	Bool	%M301.2
30	OUT_ActualFloorButtLed4	Bool	%M301.3
31	OUT_ActualFloorButtLed5	Bool	%M301.4

Fig. 4. This image shows memory area in simulated model elevator

4 Conclusion

At the beginning of this paper is written on the basic issues of communication possibilities and methods in industrial automation. This topic did not bring revolutionary new technology in industrial automation communication. The topic idea was about use affordable communication technology for improving teaching in laboratories PLC lessons Solution simulation model using .Net gives several benefits. Because the

application is developed using .Net technology, simulation can be running on each PC. Therefore, each student can work on a given task in laboratories separately and is not limited by the number of real available laboratory devices. The program is divided into a communication and simulation parts and it can therefore be easily modified to another simulation technology tasks. It should be noted that in this modification of the simulation is not as easy as in commercially available products for technological simulation (like WinMOD), but a simulation of small learning tasks using the library Snap7 and custom applications in C# is easy to create.

References

1. Mikolajek, M. Design and Implementation of Universal Data Interface for Actual and Historical Trending in .NET, Master thesis, VSB (2013).
2. Otevrel, V. Design and Implementation of real and Historical Trend Viewer in .NET Environment for Industrial Automation Area, Master thesis, VSB (2012).
3. http://winmod.de/en/index.php?page=ziele
4. http://winmod.de/en/uploads/WinMOD_for_Manufacturing%20Technology_en.pdf [download 9.8.2015].
5. http://snap7.sourceforge.net/ [download 9.8.2015].

Electrical Impedance Tomography Image reconstruction with RBF Neural Network

Marketa Michalikova

Department of Cybernetics and Biomedical Engineering, FEECS,
VŠB – Technical University of Ostrava, 17. listopadu 15, 708 33 Ostrava – Poruba
marketa.michalikova@vsb.cz

Abstract. Electrical impedance tomography (EIT) is a non–invasive imaging method, where the inner distribution of resistivity corresponding to different resistivity properties of different tissues, is estimated from voltage potentials measured on the boundary of inspected object. The major problem of EIT is how to reconstruct the image of inner resistivity. In this article we adopted the use of Radial Basis Function (RBF) neural network for image reconstruction and compared it to reconstructed images obtained using EIDORS software.

Keywords: Electrical impedance tomography, Image reconstruction, RBF neural network

1 Introduction

EIT problematics comprises solution of forward and inverse problem. The forward problem in EIT is how to get the voltage on the boundary of object corresponding to its inner distribution of resistivity. The inverse problem solves how to estimate the inner resistivity distribution from voltages gained on the boundary of examined object - in fact this stands for image reconstruction. The relationship between inner resistivity distribution and boundary voltages is determined by the Laplace equation and boundary conditions [1].

There are several methods to solve the inverse problem, as described in [2]. Another approach to solve this non–linear problem is to use Neural Network for image reconstruction. Neural network is a powerful instrument which is now being used in different branches of biomedical engineering for example as described in [3] and it has also been used in image reconstruction in Electrical capacitance tomography [4] and in EIT [5], [6], [7]. The objective of this work is to demonstrate that the usage of neural networks for the image reconstruction in EIT is feasible.

2 Electrical Impedance Tomography

The goal of EIT is to map the inner impedance distribution ρ of an object Ω (which is considered as a volume conductor). As stated in introduction this

© M. Krátký, J. Dvorský, P. Moravec (Eds.): WOFEX 2015, pp. 216–221.
VŠB – Technical University of Ostrava, FEECS, 2015, ISBN 978-80-248-3787-1.

requires the solution of forward and inverse problem. Mathematical model of EIT is described with generalized Laplace equation(equation 1) and boundary conditions (equation 2, 3)([2]):

$$\nabla \cdot \left(\rho(x,y)^{-1} \nabla \Phi \right) = 0, (x,y) \in \Omega \tag{1}$$

$$\Phi(x,y) = \Psi, (x,y) = \partial\Omega \tag{2}$$

$$\rho^{-1} \frac{\partial \Phi}{\partial n} = J_n, (x,y) = \partial\Omega \tag{3}$$

whereas $\Phi(x,y)$ is electrical potential inside the Ω, $\rho(x,y) > 0$ is resistivity distribution inside the Ω object, n stands for outer unit normal vector to $\partial\Omega$, J_n is the electrical current density on the boundary and Ψ is potential on the boundary.

Forward problem solution comprises calculation of voltage that can be measured with electrodes on the surface for particular impedance distribution, whereas both the impedance distribution of given object and applied current value are known. The most common method to obtain numerical solution of EIT forward problem is Finite Element Method (FEM). The forward problem is modeled with Laplace equation and boundary conditions, as stated above. Using the FEM method, the region Ω is partitioned into a two-dimensional model of elements, which have a node in their each corner. There is an assumption that each of elements has its uniform resistivity ([8]),

The a priori knowledge of the resistivity distribution and appropriate voltage on the boundary (meaning the numerical solution of forward problem) is essential for image reconstruction - the inverse problem. It was proved that the complete knowledge of the relationship between voltage and current at the boundary determines the inner resistivity uniquely ([9]).

To compute the resistivity distribution inverse problem solution uses the knowledge of current patterns and voltages measured on the boundary ([7]).

In solution of inverse problem the applied current value and the voltage on the boundary, measured with electrodes are used to evaluate the estimated inner distribution of resistivity([10], [6]).

3 Image reconstruction using RBF NN

Radial basis function (RBF) neural network is frequently exploited type of NN [5],[6]. Compared to other feedforward neural networks, RBF networks have better approximation ability, classification ability and the learning of network is faster as was pointed out in [4].
A typical radial basis function network has three layers: (1) an input layer, (2) one hidden layer and (3) one output layer, see Fig. 1.

The hidden layer contains a variable number of neurons N, whereas the optimal number of neurons is determined by the training process. Any of neurons

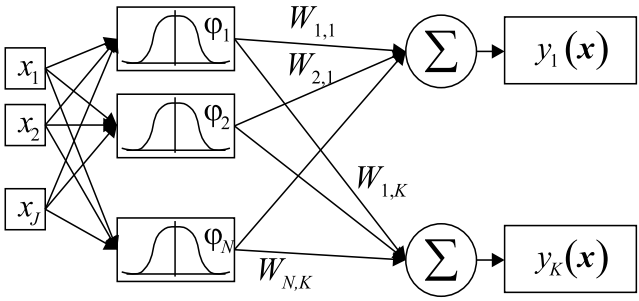

Fig. 1. Radial Basis Function network schematic

in hidden layer comprises a nonlinear Radial Basis function as the neuron activation. Such a radial basis function, particularly the Gaussian function denotes equation 4 [11].

$$\varphi_n(x) = e^{-\beta \|x-\mu_n\|^2} \tag{4}$$

The RBF neural network was created and trained using Neural Network Toolbox in MATLAB. As network training data, we used EIDORS software [12] to solve the EIT forward problem - in other words we used EIDORS to create a set of Finite Element Method (FEM) based models of different resistivity distribution and to obtain boundary voltages. Every generated FEM model has 3214 triangular elements and 1714 nodes. In this work we considered simulation of measurement with 32 electrodes, so we gained 928 boundary voltage measurements per each model as a result of measurement simulation. This implies the properties of the RBF network: it has 928 inputs (input layer) and 3214 outputs (output layer), corresponding to number of elements in FEM model. We also performed the reconstruction of image in EIDORS, particularly the difference reconstruction for every generated model in order to have output training vector and to have a comparison to neural network reconstructed images.

4 Results

At first we performed the training of the network in MATLAB nntool using 100 pairs of input and corresponding output patterns. One input stands for one set of 928 simulated measured voltages for one model and corresponding output is a set of 3214 element data values computed with EIDORS software. We generated another set of 100 models with EIDORS software for testing. We also used the simulation of measurement on those models to get boundary voltages. Such obtained data we used as inputs to RBF network and performed the image reconstruction. Several RBF NN reconstructed images compared to EIDORS reconstructed images can be seen on figure 2. To have a comparison of reconstructions we calculated the Mean Squared Error (MSE) of each reconstructed picture related to the original model as stated in equation 6:

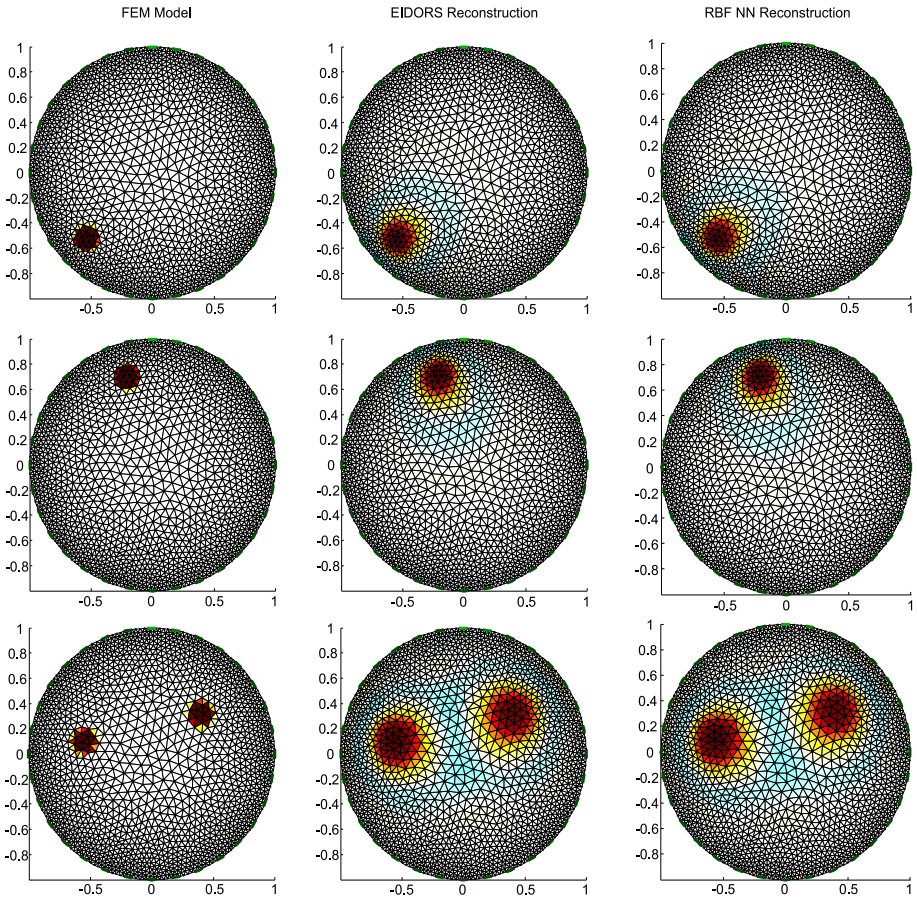

Fig. 2. Comparison of results

$$MSE = \frac{1}{n}\sum_{i=1}^{n}\left(\hat{Y}_i - Y_i\right)^2 \tag{5}$$

The boxplot of MSE is depicted on figure 3. The numerical expression is in table 1.

5 Conclusion and future work

The aim of this work was to validate the approach of usage the Radial Basis Function neural network for image reconstruction in Electrical Impedance Tomography. As a reference solution we used already existing software EIDORS intended for model generating, simulations of measurement, various image reconstructions and other related problems. As it can be seen from results depicted

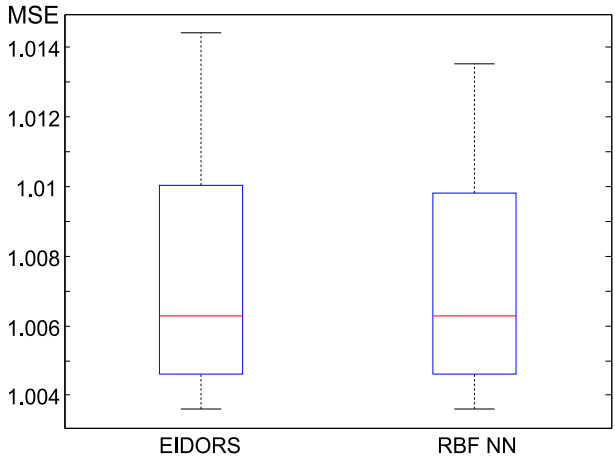

Fig. 3. Boxplot of MSE

Table 1. Mean squared error summary

MSE	EIDORS	RBF NN
median	1.0063	1.0063
std. deviation	0.000179	0.000191
maximum	1.0144	1.0135
minimum	1.0036	1.0036
n. of outliers	0	0
n. of images	100	100

on figure from the statistical point of view there are no significant differences between images reconstructed with the neural network and images reconstructed using EIDORS. It is obvious also from the computed Mean squared error, that the network is trained to produce almost equal results as the EIDORS. It means, that the difference reconstruction algorithm, which EIDORS uses can be replaced by neural network solution. The goal of this work was to prove this fact and to create the basis for the ongoing research. In the future work we will focus on improvement of neural network implementation to get better results than can be obtained using EIDORS difference reconstruction. Certainly, it requires to train the network on the values of the original model, not to the reconstructed image, as it was done in this work. As the neural network is being trained on the simulated data, we assume, that such trained network will be able to compute corresponding image of inner resistivity distribution with real measured input data. The measurement on phantom is the objective of the future study.

References

1. H.-C. Kim, K. Kim, J. Park, and H. Lee, "Electrical impedance tomography reconstruction algorithm using extended kalman filter," *IEEE International Symposium on Industrial Electronics*, vol. 3, pp. 1677–1681, 2001.
2. K. Wu, J. Yang, X. Dong, F. Fu, F. Tao, and S. Liu, "Comparative study of reconstruction algorithms for electrical impedance tomography," *IFMBE Proceedings*, vol. 39 IFMBE, pp. 2296–2299, 2013.
3. M. Prauzek, T. Peterek, and S. Conforto, "Reconstruction of ecg precordial leads by pca and neural networks," *IFMBE Proceedings*, vol. 39 IFMBE, pp. 414–417, 2013.
4. X. Chen, H. Hu, J. Zhang, and Q. Zhou, "An ect system based on improved rbf network and adaptive wavelet image enhancement for solid/gas two-phase flow," *Chinese Journal of Chemical Engineering*, vol. 20, no. 2, pp. 359–367, 2012.
5. C. Wang, J. Lang, and H.-X. Wang, "Rbf neural network image reconstruction for electrical impedance tomography," *Proceedings of 2004 International Conference on Machine Learning and Cybernetics*, vol. 4, pp. 2549–2552, 2004.
6. P. Wang, H.-L. Li, L.-L. Xie, and Y.-C. Sun, "The implementation of fem and rbf neural network in eit," *ICINIS 2009 - Proceedings of the 2nd International Conference on Intelligent Networks and Intelligent Systems*, pp. 66–69, 2009.
7. P. Wang, L. Xie, and Y. Sun, "Application of pso algorithm and rbf neural network in electrical impedance tomography," *ICEMI 2009 - Proceedings of 9th International Conference on Electronic Measurement and Instruments*, pp. 2517–2521, 2009.
8. G. Xu, Q. Wu, Q. Yang, Y. Li, and W. Yan, "A reconstruction algorithm based on wavelet network in electrical impedance tomography," *Annual International Conference of the IEEE Engineering in Medicine and Biology - Proceedings*, vol. 26 II, pp. 1435–1438, 2004.
9. D. S. Holder, *Electrical Impedance Tomography: Methods, History and Applications (Series in Medical Physics and Biomedical Engineering)*. IOP Publishing Ltd., 2005.
10. X. Zhang, G. Xu, S. Zhang, Y. Li, Y. Guo, Y. Li, Y. Wang, and W. Yan, "A numerical computation forward problem model of electrical impedance tomography based on generalized finite element method," *IEEE Transactions on Magnetics*, vol. 50, no. 2, 2014.
11. C. M. Bishop, *Neural Networks for pattern recognition*. Oxford University Press, 1995.
12. A. Adler and W. Lionheart, "Uses and abuses of eidors: An extensible software base for eit," *Physiological Measurement*, vol. 27, no. 5, pp. S25–S42, 2006.

Application for Evaluation of Biological Signals

Agáta Mročková, Martin Pieš, and Miroslav Pokorný

Department of Cybernetics and Biomedical Engineering, FEECS,
VŠB – Technical University of Ostrava, 17. listopadu 15, 708 33 Ostrava – Poruba
agata.vaverkova.st@vsb.cz

Abstract. This thesis deals with the creation of the user interface for processing and evaluation of biological signals. Biological signal is a special type of signal that is caused by the existence of a living organism or organism is scanned. The aim was to create a user environment for processing actigraphy records of lower limbs, in order to determine the pathophysiology of sleep. It was evaluated as to whether it is advantageous to use a scan from the lower leg instead of a typical diagnostics methods for certain sleep disorders. Actigraphy recorded from the lower limbs can also be used to demonstrate the efficacy of treatment medicine for diseases characterized with tremors and cramps (muscle cramps) in the legs. The potential for more accurate and detailed actigraphy lower extremity we can see at screening patients who showed a suspected sleep disorder and for children for whom the routine examination by polysomnography is frustrating. To propose a computer aided decision making evaluation system an expert fuzzy-logic base system will be used.

Keywords: Actigraphy, pathophysiology of sleep, diagnostic methods, sleep, expert system, fuzzy logic

1 Introduction

This research was base of the idea, if it possible to use several sensors to detect motion in a 3D view, and whether this will show due the appropriate software, can be used in medical practice to detect sleep disorders. The result is unique software, which is able to provide view of the patient's quality of sleep at home and for his pleasant environment to which they are accustomed. During the data collection has an examinee fix the measuring unit on leg. This unit records data that are evaluated by a doctor. To propose a computer aided decision making record evaluation system an expert fuzzy-logic base system will be used.

© M. Krátký, J. Dvorský, P. Moravec (Eds.): WOFEX 2015, pp. 222–227.
VŠB – Technical University of Ostrava, FEECS, 2015, ISBN 978-80-248-3787-1.

2 Sleep physiology

Sleep is characterized by:

- Stereotypical position of body.
- Minimal movement.
- Decreased reactivity to external stimulus
- Reduced body temperature.
- Relatively easy reversibility (possibility of awakening-unlike coma or hibernate).

Sleep has several stages, the most important being called REM phase, which occurs under closed eyelids for fast moving eyeballs. This phase is characterized by the presence of dreams. The REM sleep inducing part of the hindbrain – bridge of Varol.

The second major phase is non-REM sleep, which is further divided into four stages according to the depth of sleep. REM is primarily used for mental relaxation, NREM stage rather to relax the muscles.

During sleep [1], the REM and NREM cycled. Sleep of adult human usually begins with gradual by changing NREM stages 1 to 4. This procedure is sometimes interrupted body movements and partial awakening. After about 70-80 minutes, typically dormant briefly back to the third or the second stage and follows the first REM phase, which lasts about 5-10 minutes. The length of the cycle from the beginning of the first stages of NREM after completion of the first REM is about 90 to 110 minutes. In typical cases, this cycle is repeated four to six times per day and in each cycle, the third and fourth stage NREM became shorter, while increasing the length of REM. The exact course of the sleep cycle is different for each individual and varies with age.

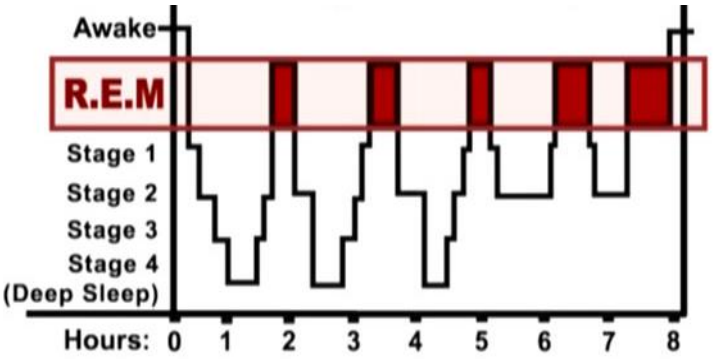

Fig. 1. Sleep cycle [1]

In each of these stages of sleep can occur something not physiological. These sleep disorders are nowadays a large amount and sometimes is not possible to confirm their

presence and define the correct diagnosis. General term for disorders relating to quantity, quality, or timing of sleep is called a dyssomnia.

Dyssomnias can accompany severe neurological diseases and mental disorders. These symptoms can be divided into three groups:

- Disorders manifested by sleep duration.
- Disorders manifested by parasomnias.
- Disorders manifested by limb movements in sleep.

3 Diagnostic methods

For diagnostics of sleep disorders are most commonly used polysomnografics record. Polysomnography is the examination for evaluation of sleep throughout the night. The patient is monitored for extended time periods. Should be recorded electroencephalography, electrooculography and electromyography. By measuring and recording these variables, can be distinguish different stages of sleep and wakefulness.

Fig. 2. Polysomnografics record

Besides these records, can still scan electrocardiography, monitored breath and breathing movements, heart rate, oxygen saturation, and blood pressure.

Polysomnography examination should take place in a well soundproofed, dark room. Most of the rooms for polysomnogarfické examination is equipped with a camera recording. The patient bad is scanned by infrared light. During the examination, the examinee has secured the appropriate sensors and electrodes, whose records are displayed worker in the next room. The resulting notation is referred to as a polysomnogram, or recording physiological parameters during sleep.

4 System of monitoring at home

Even if the patient is examined more than two days, the sleep disorder may not occur due to stress from a foreign environment and abnormal mental disposition.

In this case we can use a device for monitoring at home. This device is x-IMU.The x-IMU was designed to be the most versatile Inertial Measurement Unit (IMU) and Attitude Heading Reference System (AHRS) product available. Its host of on-board sensors, algorithms and congurable 8-channel auxiliary port make the x-IMU both a powerful sensor and controller. Communication is enabled via USB or Bluetooth for wireless applications. The on-board SD card, battery charger (via USB), real-time clock/calendar and motion trigger wake up also make the x-IMU an ideal stand-alone data logger.

The open source x-IMU GUI allow users congure all internal x-IMU settings, view sensor data in real-time and export data to software such as MATLAB and Microsoft Excel.

Device is attached before sleep on limb. SD record is activated by movement in any direction. When handing over equipment to the doctor, the data are loaded into a computer, where they are analyzed by software Leg's Actigraphy.

We get information about the quality of sleep. We are interested in duration of sleep, activity of the limbs in various stages of sleep. Character of motions - movement speed, direction and duration. Some diseases are characterized by a set of movements, increasing the number of movements, tremor, excavations of the limbs, but also walking during sleep, or a tendency to cringe limb to the body.

5 GUI

Was used Matlab and GUI. In computing, a graphical user interface or GUI, is a type of interface that allows users to interact with electronic devices through graphical icons and visual indicators such as secondary notation, as opposed to text-based interfaces, typed command labels or text navigation.

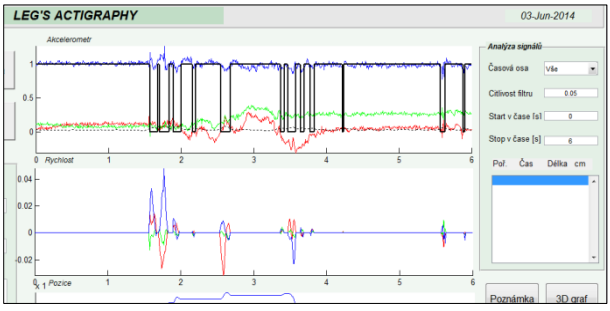

Fig. 3. User interface

6. Computer Aided Record Evaluation

Standard records evaluation thru a doctor – neurologist is done. Machine formalization of decision making role assumed a utilization of special programme system which decides on the basis of knowledge of a doctor-expert. Such system is included in tools of artificial intelligence discipline and expert system is known. The participial scheme of diagnostic expert systems - see [4].

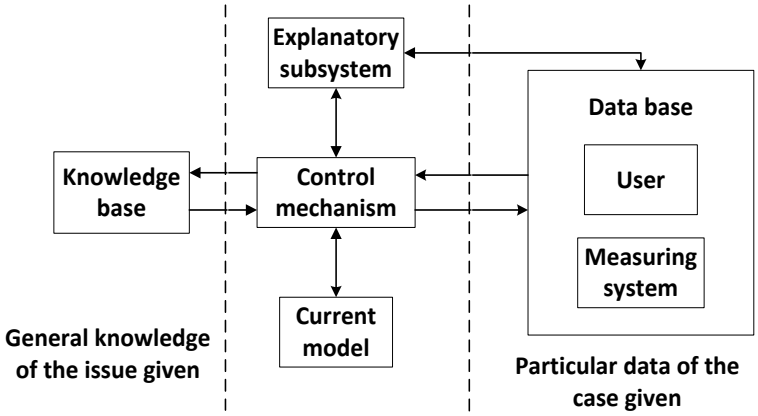

Fig. 4. Expert system scheme

To create the expert system the expert´s knowledge computer representation is necessary to create. To knowledge representation the fuzzy rule based model and fuzzy-logic based algorithms will be used to expert decision-making procedure formalization.

7 Conclusion

The software is able to display all measured data. It provides the option timelines, several filters, provide basic information about the characteristics of the measured data. The user can analyze the signal, allowing the focus directly on selected portions of selected important recording without lengthy passing through the records. Spite of all features of the software, the main data analysis makes the physician on the basis of their knowledge and visual assessment. For better and faster data handling software will be expanded and will use fuzzy logic. Each step leading to faster data analysis will be beneficial for physicians. It will be appreciated that the data can be collected several weeks. To propose a computer aided decision making record evaluation system an expert fuzzy-logic base system will be used.

References

1. X-IMU-User-Manual.pdf, x-io Technologies, 2013.
2. NEVŠÍMALOVÁ, Soňa a Karel ŠONKA. *Poruchy spánku a bdění*. 2., dopl. a přepr. vyd. Praha: Galén, 2007. 345 s. ISBN 978-80-7262-500-0.
3. BORZOVÁ, Claudia. *Nespavost a jiné poruchy spánku*. 1. vyd. Praha: Grada, 2009. 141 s. ISBN 978-80-247-2978-7.
4. ZAPLATÍLEK, Karel a Bohuslav DOŇAR. MATLAB, *tvorba uživatelských aplikací*. 1. vyd. Praha: BEN - technická literatura, 2004. 215 s. ISBN 80-7300-133-0.
5. POKORNÝ, Miroslav Umělá inteligence v modelování a řízení, BEN – technická literatura Praha, 1996, 189 str., ISBN 80-901984-4-9.
6. POKORNÝ, Miroslav Expertní systémy, OSU Ostrava (2012)

Controlling of Non-Stationary Systems Based on Fuzzy-Logic Approaches

Jana Nowaková and Miroslav Pokorný

Department of Cybernetics and Biomedical Engineering, FEECS,
VŠB – Technical University of Ostrava, 17. listopadu 15, 708 33 Ostrava – Poruba
{jana.nowakova,miroslav.pokorny}@vsb.cz

Abstract. In the article I try to introduce the final state of the solution of the Ph.D. thesis. In the Ph.D. thesis some improvements are planned, but it does not change the sense of the work. The idea is to design intelligent controller, where for the main tasks non-conventional methods are used. The main problem of controlling of systems is to achieve required quality of the control process in time for often non-stationary systems. As the main parts of such intelligent controller system identification, quality assessment and controller parameters design are considered and are described in the article.

Key words: Fuzzy application, controlling, soft-computing, quality assessment, identification, system, genetic algorithms, optimization.

1 Introduction

Many of real technological controlled systems have the property of non-stationary typically time-variant parameters [1]. To permanently achieve the desired quality of control of such systems it is necessary to follow the actual characteristics of the system continuously and if it is necessary - to re-adapt the actual parameters of its controllers.

All the above mentioned tasks are design in non-conventional way, using fuzzy expert systems and genetic algorithms. The fuzzy rule based systems introduced in this paper are determined to improve the quality of a classical PID controller, which is considered in negative closed feedback loop. The aim of the presented paper is to describe non-conventional re-adaptation system of PID controller, which is called intelligent controller (Figure 1).

To realize these tasks the special cybernetic and informatics procedures is necessary to design. The first expert system (ES1) for monitoring of control process quality is of Mamdani type. Its rule base is created within two input linguistic variables - namely the relative settling time and relative overshoot are mentioned. Output of this expert system is decision if the PID controllers parameters should be changed.

© M. Krátký, J. Dvorský, P. Moravec (Eds.): WOFEX 2015, pp. 228–233.
VŠB – Technical University of Ostrava, FEECS, 2015, ISBN 978-80-248-3787-1.

For the identification (IS) of the controlled system, it is used optimization of the parameters of its difference equation by the genetic algorithms.

The second expert system (ES2) for determination of parameters of PID controller is of Takagi-Sugeno type. Its knowledge base is built on know-how obtained from the combination of the frequency response method and the step response Ziegler-Nichols design method.

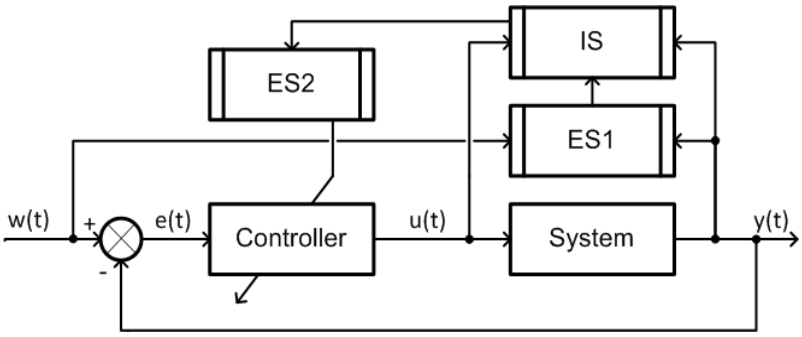

Fig. 1. The schema of the concept of intelligent controller

All the applied systems are open and it is possible to add any other aspect to their structures. The designed processes could be done in real time. The proof of efficiency of the proposed method and a numerical experiment was presented by the simulation in the software environment Fuzzy Toolbox and Matlab-Simulink. It is shown that presented monitoring system with following design of PID controller is useful for family of second order controlled systems.

2 Monitoring System - ES1

The monitoring system is fuzzy expert system [2] of Mamdani type with two inputs, knowledge base with linguistic rules and one output, which indicates if it is necessary to re-adapt the PID controller or not.

2.1 Inputs - Relative Overshoot and Relative Settling Time

For understanding, it is necessary to describe, firstly, input called as relative overshoot (RO) - the difference between the controlled value (CV) and the required value (RV) is rated relatively to the required value (1).

$$RO = \frac{|CV - RV|}{RV} \tag{1}$$

The maximal overshoot of the time response of the system is detected after the fast step change of timing, the fast step changes in timing could be caused by

the e.g. change of the controlled system or change of the required value.. The value of the overshoot is stored in the memory and then used with the settling time for determining the score.

And also the second input - settling time (RST), as the name says, it is not the classic settling time (ST_k), it is defined as the part or multiple of previous settling time ($ST_k - 1$)(2). So as the overshoot, the classic settling time from previous step is also stored in the memory. The linguistic variable relative settling time is defined as the ratio of current settling time and previous settling time.

$$RST_k = \frac{ST_k}{ST_{k-1}} \tag{2}$$

For evaluation of the settling time the 3 % standard deviation from steady-state value [2]. The linguistic values of both linguistic variables are expressed by fuzzy sets, for each linguistic variable by three linguistic values [3].

2.2 Output - Score

The output of the monitoring fuzzy expert system is the score, which is also the linguistic variable and its linguistic values are expressed by fuzzy sets. As the fuzzy expert system of Mamdani type is used [2], the linguistic variable score must be defuzzificated. For defuzzification it is used the COA method (Center of Area). The score more than 2 means that the time response with the current controller can be considered as appropriate. The score less than 2 is considered as not satisfactory and the controller has to be re-adapted [3].

$$Score \quad \left\{ \begin{matrix} \geq 2 & \text{do not re-adapt} \\ < 2 & \text{re-adapt} \end{matrix} \right\}. \tag{3}$$

The knowledge base is formed by nine linguistic IF-THEN rules of the Mamdani type [2], the example of the rules:

$$\text{If } (RO \text{ is } High) \ \& \ (RST \text{ is } Same) \text{ then } (Score \text{ is } Small)$$

3 Identification System - IS

The new added part is the identification system. The proposed method, which is described further can be also used for any system of any order and with any shape of the transfer function. The only necessary thing is to be able to define the difference equation of the identified system. Described method can be used both for continuous and discrete system [4], [5]. The identification of the parameters of difference equation is done using genetic algorithms (GA).

3.1 Discretization of Continuous Transfer Function of the Defined System

As it was mentioned proposed method can be used both for continuous and discrete systems, but for the continuous systems it is needed to discretize chosen system. The discretization is done using $\mathcal{Z}$-transform considering zero-order hold [5] with T as an optional sampling period.

Using $\mathcal{Z}$-transform and after substitution for bigger clarity the system can be described using difference equation which can be written as a simple regression function

$$\begin{aligned} a_k y(k) + a_{k-1} y(k-1) + a_{k-2} y(k-2) = \\ = b_{k-1} u(k-1) + b_{k-2} u(k-2), \end{aligned} \tag{4}$$

where the parameters a_{k-1}, a_{k-2}, b_{k-1} and b_{k-2} are parameters of the difference equation to be identified using GA. The equation (4) can be also written in the shape

$$\begin{aligned} y(k) = \frac{-a_{k-1}}{a_k} y(k-1) - \frac{a_{k-2}}{a_k} y(k-2) + \\ + \frac{b_{k-1}}{a_k} u(k-1) + \frac{b_{k-2}}{a_k} u(k-2), \end{aligned} \tag{5}$$

3.2 Genetic Algorithm Synthesis

For the identification of the coefficients of difference equation of the re-identified system the minimization of fitness function [6] can be expressed in the form of

$$J = \frac{1}{N} \sum_{j=1}^{N} \left[y^0(x_j) - y^*(x_j) \right]^2 \to 0, \tag{6}$$

where N is size of the set of input-output, y^0 is measured value and y^* value identified by GA [7]. The fitness function was set according the equation 6 with the computation of the y^* according to the (5). The minimization of fitness function J (6) by embedded function of genetic algorithm in Optimtool in Matlab environment is used and it is also programmed in C++ for proofing.

4 PID Parameter Design System - ES2

As it was mentioned also for design parameters of conventional PID controller fuzzy expert system (ES2) is used [1], [8]. It uses know-how obtained from the combination of the frequency response method and the step response Ziegler-Nichols design method [9].

Expert design system is model of Takagi-Sugeno type [10] so it does not require defuzzification. The knowledge base of the ES2 is consisted of 27 linguistic rules. For detailed information see [8], the example of one linguistic rule:

$$\text{If}(a_2 \text{ is } S)\&(a_1 \text{ is } L)\&(a_0 \text{ is } L)\text{then}(KKNOW_r = K_9)\&(TIKNOW_r = T_{i_9})\&(TDKNOW_r = T_{d_9})$$

5 The Description of Implemented Algorithm

The process of re-adaptation of PID controller is based on tasks (Figure 2), which are chronologically defined as

- continuous storage of required and controlled values with forgetting (values of previous cycle can be forgotten)
- detection of every change of required or controlled value (without change of required value)
- detection of relative overshoot and settling time and storage into the memory
- obtaining of the score using ES1
- if the value of the score is less than 2, the identification procedure of the system using IS is started
- according to the identified values of the parameters of the system, the parameters of the PID controller using ES2 are changed (only after change of required or controlled values)

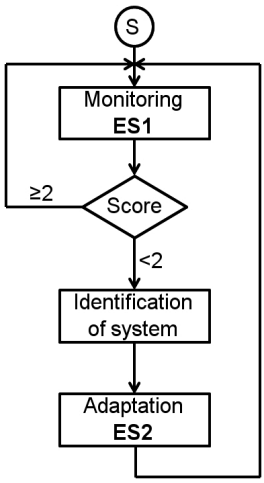

Fig. 2. The flowchart of monitoring and readaptation procedure

6 Verification of Created System

As all the parts ES1, IS and ES2 were verified (using in Matlab-Simulink) in [10], [8], [3], [4] and [5], the proof of efficiency was done, the verification is not shown because the limited space of the paper.

7 Conclusion

Subscribed solution is used for continuous adaptation of controller using soft-computing approach. The design of intelligent controller is going to be widen for bigger family of controlled systems, the idea is to proof the method for PID

controller parameters design for systems with other order and the identification procedure is going to be parallelized.

The results of my work is published in thirteen papers, where four of them are published in journals with impact factor and one of them in Q2 category. For the last year work I received the support of Science and Research Fund 2014 of the Moravia-Silesian Region, Czech Republic and IRP project.

Acknowledgements This work has been partially supported by Grant SP2015/84, VB - Technical University of Ostrava, Czech Republic supported by Project SP2015/84, of the Student Grant System, VŠB - Technical University of Ostrava and Science and Research Fund 2014 of the Moravia-Silesian Region, Czech Republic.

References

1. Nowaková, J. - Pokorný, M. (2012), *On PID Controller Design Using Knowledge Based Fuzzy System.*, Advances in Electrical and Electronic Engineering, **10(1)**, 18-27.
2. Nowaková, J. - Pokorný, M. (2013) *Double Expert System for Monitoring and Re-adaptation of PID.* In Advances in Intelligent Systems and Computing, Volume 237, 2014, pp 85-93. DOI 10.1007978-3-319-01781-5_8. Print ISBN 978-3-319-01780-8. Online ISBN 978-3-319-01781-5, Springer Berlin Heidelberg.
3. Nowaková, J. - Pokorný, M. (2013), *Rule Based Systems for Monitoring and Controller Re-adaptation.*, 16th Czech-Japan Seminar on Data Analysis and Decision Making under Uncertainty Marinsk lzn, September 2013.
4. Nowaková, J. - Pokorný, M. (2014), *System Identification Using Genetics Algorithm.*, 5th International Conference on Innovations in Bio-Inspired Computing and Applications, June 2014.
5. Nowaková, J. - Platoš, Jan - Snášsel, V. (2014) *Automatic power system identification using genetic algorithms.* In 6-th International Conference on Intelligent Networking and Collaborative Systems INCoS-2014, 2014. Salermo, Italy.
6. Nowaková, J. - Pokorný, M. (2013) *Fuzzy linear regression analysis.* In IFAC Proceedings Volumes (IFAC-PapersOnline).12th IFAC Conference on Programmable Devices and Embedded Systems, PDeS 2013. Volume 12, Issue PART 1, 2013, Pages 245-249.
7. Nowaková, J. - Pokorný, M. (2014) *On multidimensional linear modelling including real uncertainty.* Advances in Electrical and Electronic Engineering, **12(5)**, 511–517.
8. Nowaková, J. - Pokorný, M. (2012), *Fuzzy rule based optimization of systems control.*, 15th Czech-Japan Seminar on Data Analysis and Decision Making under Uncertainty Osaka, September 2012.
9. Nowaková, J. - Pokorný, M. - Pieš, M. (2013) *Takagi-Sugeno Fuzzy Model in Task of Controllers Design.* In Advances in Intelligent Systems and Computing, Volume 189 AISC, 2013, pp 391-400. DOI: 10.1007978-3-642-33018-6_4. ISSN: 21945357, ISBN: 978-364233017-9, Springer Berlin Heidelberg.
10. Nowaková, J. - Pokorný, M. - Pieš, M. (2015) *Conventional Controller Design Based on Takagi-Sugeno Fuzzy Model.* Journal of Applied Logic.

Multi-source energy unit for family house

Vít Otevřel, Zdeněk Slanina, and Bohumil Horák

Department of Cybernetics and Biomedical Engineering, FEECS,
VŠB – Technical University of Ostrava, 17. listopadu 15, 708 33 Ostrava – Poruba
{vit.otevrel, zdenek.slanina, bohumil.horak}@vsb.cz

Abstract. This paper is focused on multi-source energy unit for family house. The device is consisted from some technologies and these technologies is needed control and visualize. The paper is focused for communication possibilities of these technologies and their connection and visualization.

Keywords: Multi-source energy unit, solar collector, photovoltaic panel, battery, balancing system, battery management system, heat pump, co-generation unit, server, communication converter, Ethernet, IP[1], TCP[2], UDP[3].

1 Introduction

Nowadays is mentioned still more and more ecology, usage of renewable sources or energy self-sufficiency of objects, buildings or family houses. Multi-source energy unit is intended for smaller objects or family houses. The device is installed as prototype in object of civic association Trianon in Český Těšín. The unit is consisted from some technologies:

- Production and accumulation electric energy - photovoltaic panels with inverter (charger or regulator), LiFePO4 batteries and balancing or battery management system (BMS[4]).
- Production and accumulation thermal energy - solar collectors with regulator and accumulation boiler for PWH[5].
- System for changing thermal energy - water-air heat pump.
- System for production thermal and electric energy from natural gas - hybrid co-generation unit with power about 7 kW (thermal) and 3 kW (electrical) energy.
- Technology for system control and visualization - computer (server).

[1] Internet Protocol.
[2] Transmission Control Protocol.
[3] User Datagram Protocol.
[4] Battery Management System.
[5] Portable Water Hot.

© M. Krátký, J. Dvorský, P. Moravec (Eds.): WOFEX 2015, pp. 234–239.
VŠB – Technical University of Ostrava, FEECS, 2015, ISBN 978-80-248-3787-1.

Individual parts are from various brands therefore in the system is used some communication interfaces and protocols. All important data are transferred to server and all communication was converted to Ethernet. It is allowed to install easier cabling in the object with technology installation.

2 Technology scheme

On Fig. 1 is shown connection scheme of multi-source energy unit.

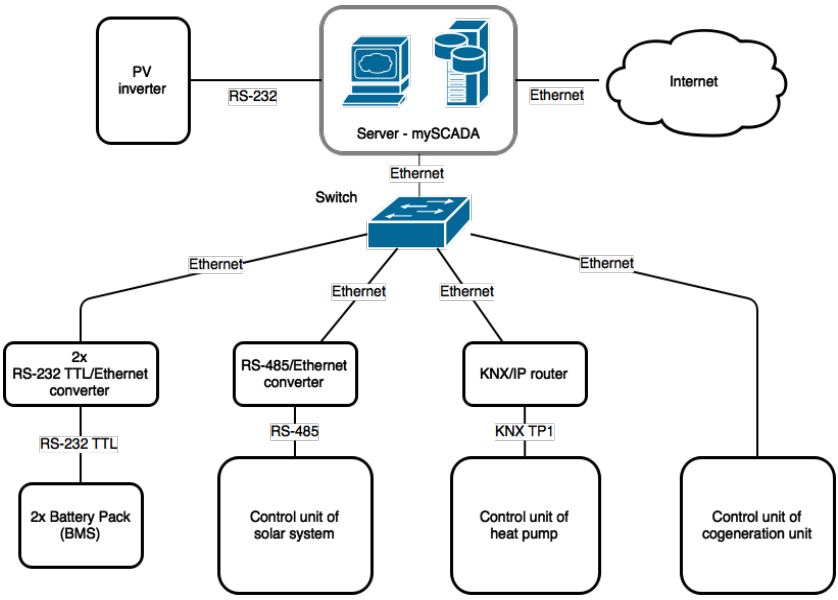

Fig. 1. Connection scheme of multi-source energy unit.

In the server were installed two network cards. By this step was separated communication (communication between server and other devices in technology) from Internet traffic. Currently, the photovoltaic charger is not connected to server via Ethernet. The charger is connected to server via RS-232 interface because the device is location in same room as server.

3 Communication possibilities

3.1 mySCADA Pro 6

Server is computer with installed operation system Linux (Xubuntu 14.04 LTS[6]). For visualization was used visualization software mySCADA Pro 6. It is product

[6] Long Term Support.

from Czech company mySCADA Technologies. It is standard HMI[7]/SCADA[8] software with support the three most widely used operation systems: Linux, Mac OS and Windows. This is modern and web oriented visualization based on technologies as HTML5[9], JavaScript and SVG[10]. The software is very user friendly for end user. For watching the visualization is needed to install only a modern web browser on your computer. mySCADA contains standard visualization parts as trends, data logging, alarms or reports generating. The software also included some drivers for communication with PLC[11] via the most widely used interfaces or protocols (EtherNet/IP, Siemens S7, Modbus, Melsec, Toyopuc, OPC UA). User have choice to make own scripts in JavaScript language and Node.js API[12] (Node.js API is part of runtime interface Node.js).

3.2 Photovoltaic system

Main part of photovoltaic system is charger (inverter). The charger controlling flow electric energy (PV panels, distribution network, battery charging, etc.).

Table 1. Communication interfaces - photovoltaic system.

Count	Type	Interface	Note
1	Axpert Inverter 5KVA-48-PAR-A	RS-232	PV charger
2	Active balancig system UTP 16x7.5 A	RS-232 TTL	BMS for LiFePO4 batteries
2	WIZnet WIZ107SR	RS-232 TTL/Ethernet	RS-232 TTL/Ethernet converter

The Voltronic Power company created own communication protocol called "Axpert KS RS232 communication protocol" for communication with inverter. The protocol contains nine commands for reading actual measurement values and nine commands for setting the inverter. The script was created in visualization and it is launched periodically and read the actual values from the inverter.

BMS control unit is based on universal board Arduino Mega. Communication interface is RS-232 with TTL levels (UART[13]). Communication with BMS was converted to Ethernet via WIZnet WIZ107SR converters. The control unit sending data via serial line every five seconds. Ethernet converter is configured for sending frames as UDP packets from BMS to visualization.

[7] Human Machine Interface.
[8] Supervisory Control And Data Acquisition.
[9] HyperText Markup Language.
[10] Scalable Vector Graphics.
[11] Programmable Logic Controller.
[12] Application Programming Interface.
[13] Universal Asynchronous Receiver/Transmitter.

3.3 Solar system

Main part of solar system is pump control unit ZPS 18e-01 from Hewalex brand. It contains pump, control unit and sensors. The control unit is called Geco G-422-P07 and it using RS485 interface for communication. Temperatures in solar circuits, pump and pump flow-meter are connected to pump control unit.

Table 2. Communication interfaces - solar system.

Count	Type	Interface	Note
1	Hewalex ZPS 18e-01 pump control unit	RS-485	Pump with control unit Geco G-422-P07
1	EKO-LAN module	RS-485/Ethernet	RS-485/Ethernet converter
1	WIZnet WIZ108SR	RS-485/Ethernet	RS-485/Ethernet converter

3.4 Heat pump

In the system was used water-air heat pump and it is controlled by Siemens Synco controller. The unit using KNX[14] interface with physical layer KNX TP1. KNX/IP router was used for conversion KNX TP1 on Ethernet. All sensors are connected to control unit Siemens Synco RMH760B or their extension module RMZ787. The KNX/IP router converting data from KNX TP1 to Ethernet and UDP protocol. All UDP packets are sent as UDP multicast packets.

Table 3. Communication interfaces - heat pump.

Count	Type	Interface	Note
1	Siemens Synco RMH760B	KNX (TP1)	Heating control unit
1	KNX/IP router	KNX/Ethernet	KNX TP1/Ethernet converter

3.5 Hybrid co-generation unit

In the co-generagion unit is used motor for natural gas. The unit produce about 7 kW (thermal) and 3 kW (electrical) energy. PLC Siemens Simatic S7-1200 is used as control unit.

[14] World standard for home and building control.

Fig. 2. The electronics of heat pump.

Table 4. Communication interfaces - co-generation unit.

Count	Type	Interface	Note
1	Siemens Simatic S7-1200	Ethernet/Profinet	PLC, CPU 1212 DC/DC/DC (6ES7212-1AE40-0XB0)

4 Visualization

The most communications were converted to Ethernet and UDP protocol. In the visualization was created scripts with UDP servers. The servers are launched on background and received data from devices. In the next step, the data are parsed and visualized. Communication with co-generation unit is easier because mySCADA contains driver for PLC Siemens Simatic S7-1200 connection.

5 Acknowledgement

This work was supported by projects CZ.1.05/3.1.00/14.0317 ”Pre-seed activities Technical University of Ostrava - Energetics” and SP2015/184, ”Control of power systems with renewable and alternative energy sources.” of Student Grant System, VSB-TU Ostrava.

6 Conclusion

All communications were united via converters to one communication medium - Ethernet. The communication was tested with some configuration with TCP and

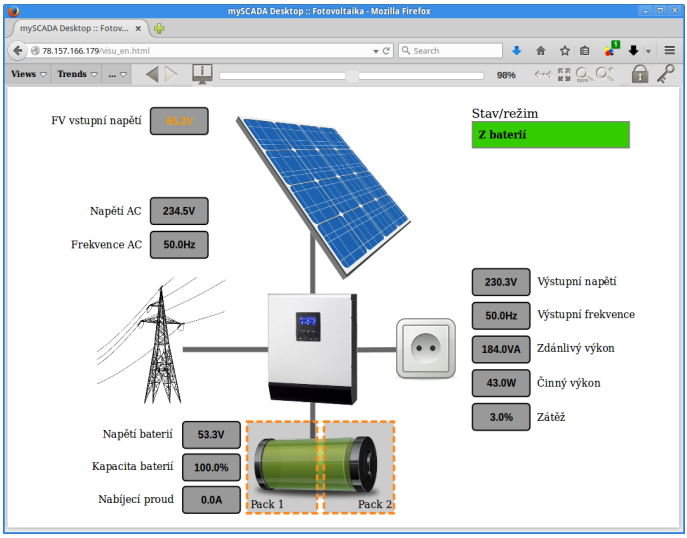

Fig. 3. Example of visualization - photovoltaic system.

UDP protocols. UDP protocol was used for less overhead and because it do not use confirmation packets. The converters to Ethernet between some interfaces (RS232, RS485) was installed. Next step was create visualization of technology. The installed system is prototype and it is used for cover consumption of electric energy in SVMC object and for production and accumulation PWH for the object.

References

1. HORÁK, B. *Vícezdrojová energetická jednotka rodinného domu.* Published in NZEE 2015.
2. FRIEDRISCHKOVA, K. *Metodika řízení energetických soustav rodinného domu, elektromobilu a fotovoltaické elektrárny.* Published in NZEE 2015.
3. IEEE Standard for Ethernet. In: IEEE Std 802.3-2012 [online]. 2012 [cit. 2015-07-28]. Available from: http://standards.ieee.org/getieee802/download/802.3-2012_section1.pdf
4. mySCADA professional HMI/SCADA Solution. [online]. [cit. 2015-07-28]. Available from: http://www.myscadatechnologies.com/
5. *Solar and heat pump systems for houses.* S.l.: Ernst & Sohn, 2014. ISBN 3433030405.
6. LANGLEY, Billy C. *Heat pump technology.* 3rd ed. Upper Saddle River, N.J.: Prentice Hall, c2002, viii, 536 p. ISBN 0130339652.
7. KOLANOWSKI, by Bernard F. *Small-scale cogeneration handbook.* 4th ed. Lilburn, Ga: Fairmont, 2011. ISBN 143987624x.
8. DUNLOP, James P. *Photovoltaic systems.* 3rd ed. Orland Park, IL: American Technical Publishers, Inc, 2010. ISBN 1935941054.

Multichannel Photoplethysmography; Possibility How to Noninvasively Determine State of Cardiovascular System

Lukas Peter

Department of Cybernetics and Biomedical Engineering, FEECS,
VŠB – Technical University of Ostrava, 17. listopadu 15, 708 33 Ostrava – Poruba
lukas.peter@vsb.cz

Abstract. Cardiovascular system is one of the most important system in human body and it is necessary to oversee its right function. For medical doctor it would be interesting to have possibility how to evaluate state of cardiovascular system without using invasive entrance and to have information about state of all main parts of cardiovascular system. Measurement of pulse wave could be one of the possibility how to noninvasively evaluated state of cardiovascular system and its individual parts. The paper introduces methodology of measurement pulse waves from several places of human body and ECG signal simultaneously. There is also describe its hardware and software solution and it shows some preliminary results.

Keywords: ECG, Multichannel photoplethysmography, State of cardiovascular system, PWV, LabView

1 Introduction

In the World are cardiovascular diseases the most frequent causes of death. This is very known and discussed problem, and yet many people underestimate risks connected with formation of these diseases. Medical doctor together with engineers try to find some reliable and noninvasive method which helps evaluated rate of cardiovascular problems. As one of possible method could be pulse wave measurement.

Parameters of pulse wave give good information about heart rate, right work of heart because of information about start and end of systole and, what is very important, it gives information about pulse wave velocity. Pulse wave velocity could be used for evaluation stiffness of blood vessel or for evaluation of blood pressure which is complex indicator about state of cardiovascular system [1], [2].

Pulse wave is most of time measured from periphery as fingertip or from places where is good blood perfusion as ear lobe, nose or forehead. Measuring is noninvasive and relative comfortable for patient. It is reason why diagnostic methods based on processing of pulse wave could have a big potential for prevention of cardiovascular failure.

© M. Krátký, J. Dvorský, P. Moravec (Eds.): WOFEX 2015, pp. 240–245.
VŠB – Technical University of Ostrava, FEECS, 2015, ISBN 978-80-248-3787-1.

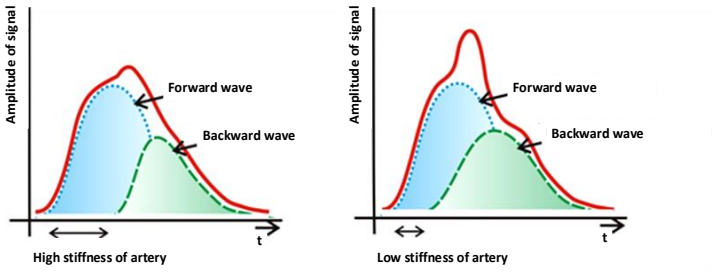

Fig. 1. Comparison of shape of pulse wave based on stiffness of artery. If is stiffness high waves are faster and backward wave makes blood pressure higher. If is stiffness low backward wave is slower and it positively affects blood flow.

2 Problem definition

Thanks to the shape and properties of pulse wave; as pulse wave velocity or pulse transmit time which are dependent on properties of blood vessel and work of the heart; is possible to noninvasively evaluate state of cardiovascular system. From pulse wave is also possible to evaluate right work of heart because of its anacrotic and catacrotic part. Anacrotic part is increasing part of pulse wave which is produced by systole and catacrotic part is slowly decreasing part which captures moving of artery wall during diastole.

Pulse waves which are measured on different places of human body has different properties. It can be recognized differences of state of cardiovascular segments.

3 Implementation of new solution

Our main objective was to develop measuring circuit which will be able to noninvasively measure pulse wave from several parts of human body simultaneously. Our solution consists from two parts; hardware part for analogue preprocessing of measured signal and for AD conversion and software part as graphical user interface for display of measured signal and digital signal processing.

Developed hardware includes 6 channels for PPG measurement, one channel for ECG measurement and AD convertor. Software part includes digital filtering of measured signals and signal processing which is needed for evaluation of state of cardiovascular system.

3.1 Measuring hardware

Whole measuring hardware was developed as independent device for measurement of biological signals. For our purpose was important to measure all of signals very precisely with higher sampling rate than is usual and to assure simultaneously measurement all of signals without time delay between analog channels.

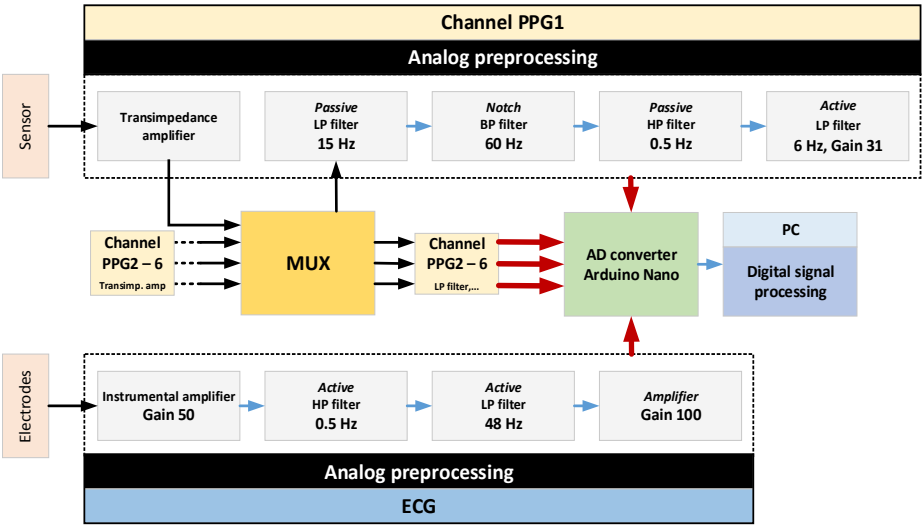

Fig. 2. Block scheme of developed hardware part. Device includes six PPG channels and one ECG channel. Signal from each channel was processed by analogue for better digital conversion. Signal from PPG channels are bring to multiplexor because of biological calibration of each channel.

PPG and ECG signals were preprocessed by analog part for better conversion to digital form.

We used standard reflexive and transmission PPG sensors. All of these sensors were photoplethysmography sensors so they included one IR LED as transmitter and one photodiode as receiver. It is measured small value of current from photodiode. For digital conversion of signal was better to measure value of voltage so it was needed to current to voltage. Each PPG channel included transimpedance amplifier as adjustment of signal from PPG sensor. Directly after this amplifier are signals bring to multiplexor. This multiplexor is control by developed software and it is there add because of biological calibration of all of channels. When calibration is active signal from one channel is send into all of channels for analogue preprocessing of PPG. Thanks it, it is possible to discovered small time differences between channels and make compensation.

For analogue preprocessing of measured signal from PPG sensor there were put series of filters for removing of undesirable components of signal. PPG signals were filtered by active and passive. Frequency spectrum which was useful for our measurement was choose 0.5 Hz – 6 Hz.

For digital conversion of signal was used Arduino Nano. This module includes 10 bits eight channel microcontroller. This microcontroller is also used for control of multiplexors thanks to PWM.

Device was connected by USB connector to computer which was also used as power supply.

Fig. 3. Multichannel photoplethysmography device with three connectors for ECG electrodes. ECG is in this device use as time synchronization of all of pulse wave during one cardiac cycle.

3.2 Developed software

Developed software consists from two parts. Acquiring and visualization of measured signals was made by LabView software as real time measurement. Digital signal processing of signals was made by Matlab software as online processing.

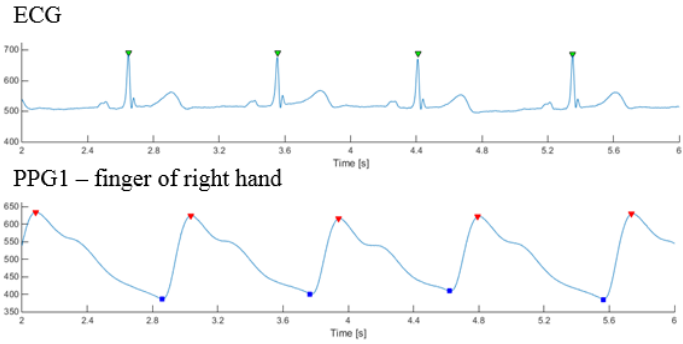

Fig. 5. Detection of significant points on measured signals. It was detected each R wave as point of heart's systole and peak and valley of each pulse wave. All of these point were used for statistical analysis and evaluation of relationship between parameters of pulse wave and state of cardiovascular system.

4 Analysis of signals

It was measured group of six people. It was choose three categories of age and in each categories man and woman. The youngest category were two healthy sportsmen without any chronic disease. Second category were man and woman middle age with adequate body. Woman treats hypertension for long time. During testing measurement hypertension was also found in man. The oldest category of patients were two people with cardiac problems. Man had few time heart attack. He has two times bypass. Woman had also heart attack and she has stent in coronary venous.

All of patients were measured during a rest. Each patient was sitting on a chair and except pulse waves and ECG was also measured noninvasively blood pressure by standard automatic tonometer.

Pulse waves were measured from index finger of right hand (PPG1); index finger of left hand (PPG2); second finger of right foot (PPG3); second finger of left foot (PPG4); right temporal bone (PPG5); left temporal bone (PPG6).

It was determined length of anacrotic part of pulse wave as time delay between valley and peak of pulse wave; length of catacrotic part as time delay between peak of one wave and valley from next wave; time of whole pulse wave; time delay (PTT) between pulse wave and R wave from ECG and pulse wave velocity thanks to equation [6]:

$$PWV = \frac{D}{PTT} \tag{1}$$

Where D is distance between heart and place where pulse wave was measured. This distance was measured by tape.

It was also evaluated expandability of blood vessels thanks to equation [6]:

$$Expandability = \left(\frac{3.57}{PWV}\right)^2 \tag{2}$$

After finding and evaluation all of parameters it was made statistical analysis based on linear regression. It was made analysis of relationship between expandability of blood vessel and age of patient.

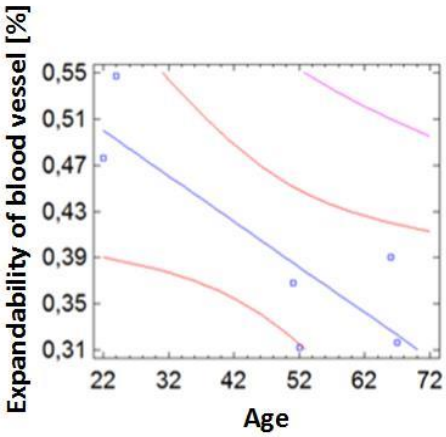

Fig. 6. Relationship between expandability of blood vessel and age of patient. With increasing of age; expandability of blood vessel decreases. Picture shows analysis which was made on signal from PPG1 (index finger of right hand).

It can be seen that with increasing of age of patient expandability of blood vessel decreases.

Expandability of blood vessel and time of anacrotic part of pulse wave can be good indicator of state of cardiovascular system. These parameters are parameters which affects blood pressure and heart's work. It can be seen in Table 2 where is comparison between all of these parameters all of patients.

5 Conclusion and summary

It is very important to monitor state of cardiovascular system. There are many parameters which can bring significant information about its condition. Good indicator is value of blood pressure. This value gives global information about state of cardiovascular system but many times it is more useful to know information about each part of cardiovascular system. Possibility how to evaluated parameters of each parts is to measure pulse wave which gives information about state of blood vessel which reflects state of cardiovascular system.

Our main objective was to developed system which could be used for evaluation of each part of cardiovascular system and gives complex information about state of cardiovascular system. This system should be accurate and comfortable for patient because of possibility of continuous long time monitoring.

Out measurement was based on developed multichannel photoplethysmograph which was tested on group of six people. It was measured six photoplethysmography signals from different places on human body and made analysis of these signals.

Out device and methodology bring us promising results. It was tested in laboratory conditions and now it is ready to use it during clinical test. For validation of this method it is necessary to measure bigger group of patients and results from this measurement to compare with standard method for evaluation stiffness of blood vessels or blood pressure.

Multichannel photoplethysmography is promising method for long time monitoring of state of cardiovascular system which will bring better information about treatment of this system and it could prevent heart failure or; in the worst case, premature death.

6 Publications

1. Peter, Lukas, and Martin Cerny. "Pulse Transmit Time Laboratory Measurement Solution." *Programmable Devices and Embedded Systems*. Vol. 12. No. 1. 2013.
2. Peter, Lukas, and Martin Cerny. "Hardware for precise in vivo pulse transmit time CNIBP tests." *Applied Electronics (AE), 2013 International Conference on*. IEEE, 2013.
3. Peter, Lukas, Noury, Norbert, and Cerny Martin. "A Review of methods for non-invasive and continuous blood pressure monitoring: Pulse Transit Time method is promising?" (in proceeding IRBM)
4. Peter, Lukas; Foltyn, Jan; Cerny, Martin. Pulse wave velocity measurement; developing process of new measuring device. *In: Applied Machine Intelligence and Informatics (SAMI)*, 2015 IEEE 13th International Symposium on. IEEE, 2015.
5. Peter, Lukas; Neprasova, Iveta; Cerny, Martin, Make life easier based on detection of eyes movements; laboratory measurement, PDeS2015
6. Peter, Lukas; Neprasova, Iveta; Cerny, Martin, Detection of eyes movement; possibility how to control world, IUPESM2015

Classification of Actual Fetal State Determination using Random Forests

Tomas Peterek, Maros Smondrk and Jana Krohova

Department of Cybernetics and Biomedical Engineering, FEECS,
VŠB – Technical University of Ostrava, 17. listopadu 15, 708 33 Ostrava – Poruba
maros.smondrk@vsb.cz

Abstract. The proposed paper deals with an algorithm for the automatic recognition of ten basic fetal states. These states are obtained from the cardiotocography record. This diagnostic method measures heart activity, uterine contraction, and movement of a fetus. The Random Forests algorithm was used as a classification method.

Keywords: Cardiotocography; actual fetal state; Random Forests

1 Introduction

Cardiotocography (CTG) is a widely used technique for assessing a fetal state (fetal surveillance) in prenatal care. It records heart rate variability, uterine contractions, and fetal movements simultaneously. It is provided by an obstetrician with information about the cardiovascular system of the fetus and the fetus movements in order to prevent adverse fetal outcomes.

There are four basic parameters, which can be extracted from the CTG records: heart rate and its variability, decelerations, and accelerations. According to the analysis of these parameters doctor may classify a fetus into three basic groups: physiological, suspicious, and pathological group.

The physiological group can be split into five classification subgroups (A, B, C, D, and DC). The first physiological classification subgroup is a peaceful sleep (A – subgroup). This state is characterized by low baseline variability which is around 5 beats per minute (bpm) even less and no heart acceleration of the fetus. The second subgroup is REM sleep (B – subgroup) comparable to neonatal REM sleep. The CTG in this phase shows normal baseline variability but rare fetal movement. The third subgroup is a quiet awake state (C – subgroup). In this the CTG would show normal baseline variability and at least two movement accelerations of the fetus in twenty minutes. The next subgroup is an active awake state (D – subgroup) characterized by a lot of fetal movements and a high baseline variability. The last physiological classification subgroup is baseline accelerations or decelerations patterns (AD – subgroup) caused by stress.

The suspicious group consists of the three classification subgroups (SH, DE, and S). The first suspicious classification subgroup is a so-called shift pattern (SH – sub-

© M. Krátký, J. Dvorský, P. Moravec (Eds.): WOFEX 2015, pp. 246–249.
VŠB – Technical University of Ostrava, FEECS, 2015, ISBN 978-80-248-3787-1.

group), which is a similar to a peaceful sleep pattern but with small differences. The next subgroup is so-called decelerations patterns (DE – subgroup) as the result of Vagus nerve stimulation. All remaining suspicious states are in the last suspicious classification subgroup (S – subgroup).

The pathological group includes two classification subgroups (LD and FS). The so-called large decelerative pattern (LD – subgroup) and the flat sinusoidal pattern (FS – subgroup) defined by periodical oscillations of baseline variability in range of 5 to 10 bpm. It is typically reflective of severe anaemia. [1]

2 Dataset

A database contains 2,126 CTG records. These records have been independently annotated by three obstetricians. Each record contains information about its morphological pattern (physiological, suspicious, and pathological). There are 1,655 normal records, 295 of them are suspicious and 176 are labelled as pathological. Twenty-one statistical features were extracted using the software SiSPorto 2.0. Their description and definition are presented in Table 1. The dataset was downloaded from the UCI machine repository. [2]

Table 1. Features description and explanation.

Feature	Explanation
Uterine contraction	
UC	Number of uterine contractions per second (frequency)
Baseline fetal heart rate (FHR)	
LB	Fetal Heart rate baseline (beats per minute)
FM	Number of fetal movements per second
Baseline FHR variability	
ASTV	Percentage of time with abnormal short term variability
MSTV	Mean value of Short term variability
ALTV	Percentage of time with abnormal long term variability
MLTV	Mean value of long term variability
Presence of accelerations	
AC	Number of accelerations per second (frequency)
Presence of deceleration	
DL	Number of light decelerations per second (frequency)
DS	Number of severe decelerations per second (frequency)
DP	Number of prolonged decelerations per second (frequency)
Characteristics of histogram	
WIDTH	Width of fHRV histogram
MIN	Minimum of fHRV histogram
MAX	Maximum of fHRV histogram
NMAX	Number of histogram peaks
NZEROS	Number of histogram zeros
MODE	Histogram mode
MEAN	Histogram mean
MEDIAN	Histogram median
VARIANCE	Histogram variance
TENDENCY	Histogram tendency

3 Random Forests

The choice of a classifier is a very complex task and it mainly depends on experience and on many other factors, e.g. some algorithms can be sensitive to presence of outliers, noise, and data balance. In general, there is no universal algorithm for correct classification of general data.

Random Forests algorithm is one of the most successful data classification methods. It was designed by Leo Breiman and can be used for classification or regression. This method uses a group of classification trees and classifies samples into classes. Advantages of this method are: the possibilities for explanation and visualization of its output, does not overfit, the fast classification, the noise robustness, etc. Using this method we can simply describe the importance of the individual variables, as well as detect outliers. The overall error should be minimized by optimization of two important parameters of the Random Forests: the number of trees and the number of predictive variables used to split the nodes. [3-4]

4 Results

The dataset was randomly divided in ratio 1:1 into training and testing set. The outliers were preserved, because they could bring beneficial information about pathological states. Different number of trees in the forest (10, 50, 100, 500, and 1,000) and different number of features in each tree (5, 10, 15, and 20) were tested. Precision, sensitivity and specificity values of each state were observed. The confusion matrix for the Random Forests classifier is shown in the Table 2.

Table 2. The confusion matrix of the Random Forests classifier.

	A	**B**	**C**	**D**	**SH**	**AD**	**DE**	**LD**	**FS**	**S**
A	172	12	6	0	6	2	4	0	2	11
B	11	270	2	9	5	12	0	0	0	2
C	0	0	17	0	0	0	0	0	0	0
D	0	2	0	29	0	0	0	0	0	0
SH	3	0	0	1	18	0	0	0	0	1
AD	0	4	0	2	1	147	5	0	0	0
DE	2	1	1	0	0	5	115	5	0	0
LD	0	0	0	0	0	0	1	48	0	0
FS	0	0	0	0	0	0	0	0	23	2
S	4	1	0	0	6	0	1	0	10	82
Precision [%]	80.00	86.82	100.00	93.55	78.26	92.45	89.15	97.96	92.00	78.55
Sensitivity [%]	89.58	93.10	65.38	70.73	50.00	88.55	91.27	90.57	65.71	83.67
Specificity [%]	95.06	94.70	100.00	99.80	99.51	98.66	98.51	99.90	99.81	97.72

The best classification performance was achieved by the Random Forests algorithm, which consists of 500 trees and each tree contains 15 variables.

5 Conclusion

In this work, the classification of the actual fetus states using Random Forests algorithm was performed. The main aim was to recognize ten basic fetal states: peaceful sleep, REM sleep, quiet awake state, active awake state, accelerations or decelerations patterns, shift pattern, decelerations patterns, suspicious states, large decelerative pattern, and flat sinusoidal pattern. Different parameters of Random Forest algorithm were tested. The best results achieved by the Random Forests algorithm was with overall accuracy of 87.6 %. The obtained results could be very useful as a decision support for obstetrician's clinical practice.

6 References

1. Debdas, AK: Practical Cardiotocography, (2005), Jaypee
2. Ayres de Campos et al. (2000) SisPorto 2.0 A Program for Automated Analysis of Cardiotocograms. J Matern Fetal Med 5:311-318
3. Breiman, Leo (2001). "Random Forests". Machine Learning 45 (1): 5–32. doi:10.1023/A:1010933404324
4. Kulkarni, V.Y.; Sinha, P.K., "Pruning of Random Forest classifiers: A survey and future directions," Data Science & Engineering (ICDSE), 2012 International Conference on , vol., no., pp.64,68, 18-20 July 2012 doi: 10.1109/ICDSE.2012.6282329

Magnetometer with protection against detection by electronic countermeasure

David Vala

Department of Cybernetics and Biomedical Engineering, FEECS,
VŠB – Technical University of Ostrava, 17. listopadu 15, 708 33 Ostrava – Poruba
david.vala@vsb.cz

Abstract. This contribution describe invention of Magnetometer with protection against detection by electronic countermeasure (ECM) registered by Czech patent office as patent no. 305322. Magnetic sensors are often part of dual use or security instruments and equipment. For this purpose is very interesting to build sensor with is hidden against electronic countermeasure. In this case is very important level and behavior of electromagnetic noise produced by sensor. And also electromagnetic compatibility of electronic devices is the area which significance grows nowadays too. As the consequence of this growth there is a continuous process of making more strict standards focused on electromagnetic radiation of electronic devices. Sensors technology begins to be a part of these issues due sensors bandwidth increasing and approaching to frequency of radio communication band. Nowadays microcontrollers and similar digital circuits are integrated into sensors devices and it brings new sources of electromagnetic radiation in modern smart sensors

Keywords: Anisotropic magnetoresistors, AMR, magnetic sensor, EMC, weak magnetic field, electronic countermeasure, ECM

1 Introduction

Anisotropic Magneto-Resistive (AMR) sensors are fabricated with permalloy (NiFe) thin films that create changes in resistivity with respect to external magnetic fields. More information you can find in [1], [2], [3], [4] or [5]. These film materials are similar to magnetic recording tapes in that strong magnetic fields can disrupt the magnetic domains of the film particles from a smooth factory orientation to arbitrary directions. Accuracy and resolution of these sensors will suffer until the film magnetic domains are "reset" to recreate a uniform direction. In application notes [6] [7 or [8] is detailed description of the set and reset functions for AMR sensors including the reasons to perform this function, characteristics of set/reset components, and example circuits showing the present state of the art in set/reset pulse generation.

© M. Krátký, J. Dvorský, P. Moravec (Eds.): WOFEX 2015, pp. 250–255.
VŠB – Technical University of Ostrava, FEECS, 2015, ISBN 978-80-248-3787-1.

AMR sensors are designed in Wheatstone bridge configurations, with four magneto-resistive elements that remain identical electrically when no external magnetic fields are applied. With linear-mode AMR sensors, the externally applied magnetic fields are to be limited in strength so as to not disrupt the factory set magnetic domains of the permalloy thin-film elements. Figure 1 shows three examples of magnetic orientation of the film domain structure.

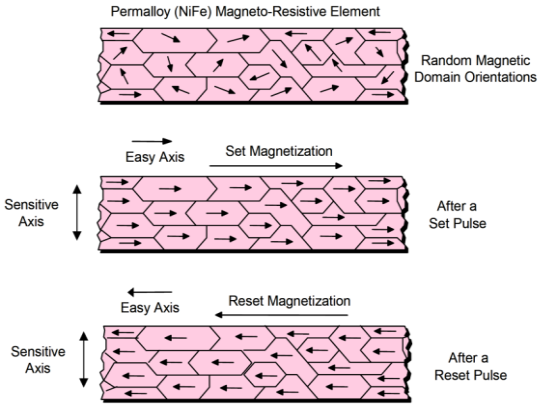

Fig. 1. Domain orientation in permalloy magneto-resistive elemnt [8]

The alignment of the magnetic domains is up along the "easy" axis of the material. The "sensitive" axis is perpendicular to the easy axis direction and serves as the driving function of the magneto-resistive characteristic curve shown in [7]. When an external magnetic field has a vector component in the sensitive axis, the field rotates the magnetic moment creating a change in resistance. If the external magnetic fields are in the operational field range, the magnetic moments will return to their set or reset orientations after the field is removed. To put some numbers on the magnetic fields involved, typically a "set" or "reset" field requires about 4 mT or more to be applied to completely orient the magnetic domains.

2 Why bi-directional magnetization

The reasons to perform a set or reset on an AMR sensor are:

1. to recover from a strong external magnetic field that likely has re-magnetized the sensor,
2. to optimize the magnetic domains for most sensitive performance, and
3. to flip the domains for extraction of bridge offset under changing temperature conditions.

Strong external magnetic fields that exceed a 1 to 2 mT "disturbing field" limit, can come from a variety of sources. The most common types of strong field sources come from permanent magnets such as speaker magnets, nearby high-current conductors such

as welding cables and power feeder cables, and by magnetic coils in electronic equipment such as CRT monitors and power transformers. Magnets exhibit pole face strengths up to unit of Tesla. These high intensity magnetic field sources do not permanently damage the sensor elements, but the magnetic domains will be realigned to the exposed fields rather than the required easy axis directions. AMR sensors are also ferromagnetic devices with a crystalline structure. This same thin film structure that makes the sensor sensitive to external magnetic fields also has the downside that changing magnetic field directions and thermal energy over time will increase the self-noise of the sensor elements. This noise, while very small, does impair the accurate measurement of sub-micro Tesla field strengths or changes in field strength in nano Tesla increments. By employing frequent set and reset fields on the sensor, the alignment of the magnetic domains in each permalloy element drops the self-noise to its lowest possible level. More information you can find in [6], [7], [12].

The above description explained that providing pulses of electrical current creates the needed magnetic fields to realign the magnetic domains of the sensor resistive elements. Also the rationale for performing these set and reset pulses has been justified. The following paragraphs shall show when and how to apply these pulsed currents, and circuits to implement them. The tempco math shows the importance of choosing appropriate strap voltages to create the correct strap currents and that both resistances and currents are variables to be dealt with. The direction of the strap currents also determines what is considered a “set” or a “reset” pulse. Set pulses are defined as pulsed currents that enter the positive pin of the set/reset strap. For more information look for example [8],[11],[15]

3 Electronic countermeasure

An electronic countermeasure (ECM) is an electrical or electronic device designed to trick or deceive radar, sonar or other detection systems, like infrared (IR) or lasers. It may be used both offensively and defensively to deny targeting information to an enemy. The system may make many separate targets appear to the enemy, or make the real target appear to disappear or move about randomly. It is used effectively to protect aircraft from guided missiles. Most air forces use ECM to protect their aircraft from attack. It has also been deployed by military ships and recently on some advanced tanks to fool laser/IR guided missiles. It is frequently coupled with stealth advances so that the ECM systems have an easier job. Offensive ECM often takes the form of jamming. Defensive ECM includes using blip enhancement and jamming of missile terminal homers. For more information look for example [23] or [24].

4 Measurement and reduction of set reset pulse radiation

Each current pulse can product wide spectrum of electromagnetic radiation. This radiation can disturb another devices or measurement itself especially in multisensory application. For this reason I’m aimed to reduce this source of radiation because shielding of sensor is in direct conflict with function of the sensor.

Fig. 2. Measurement equipment and workplace for measurement of electromagnetic radiation

As is shown on figure 2 is by the fusion of techniques from telecommunication technologies whit sensor techniques reduced the radiation of AMR magnetic sensor at least of 3 dB in worst case but generally is the radiation reduction significantly higher. For more information about spread spectrum techniques you can look for example here [16],[17],[18],[19].

Fig. 3. Measurement of spectrum of magnetization circuit without and with reduction techniques.

5 Intellectual property

Results of this invention was reworked to patent registration. The schematic block diagram of invention is on figure 4 or in [22]. Specific involvement magnetometer using magnetic feedback is shown. In addition to the magnetometer contains 2.0 AMR sensor, comprising bridged arranged given anisotropic magnetoresistor 1.0., other circuits for the function of the magnetometer. Measuring bridge AMR sensor sensing elements formed 2.0 is supplied with direct current from a current source 2.1 signal of the AMR sensor 2.0 is amplified in the amplifier 2.4 and subsequently fed to the synchronous detector 2.5, which compensates the direction of magnetization of the sensor 2.0. Subsequently, the output signal from synchronous detector 2.5 is fed to the controller feedback 6.2 here, the excitation current for generating the compensation coil of the sensor 2.0 and reads information on the size of the compensating coil current 1.3 to 2.7 the

output block, because a compensation magnetic field is directly proportional to the current compensation coil 03. To ensure repeated magnetization is placed in a magnetometer clock circuit generates 2.3 bar to control the magnetization of the sensing element 1.1, which is carried by a magnetic field that is created by the magnetizing coils 1.4 For this purpose, the output of the switching circuit 2.3 is fed to the exciter magnetizing 2.2 Furthermore, the output of the switching circuit block 2.3 is fed to synchronous detector 2.5 is based on the polarity of the clock pulse sets the correct polarity of the measured output signal from the synchronous detector 2.5 Block clock circuit generates the clock signal 2.3 just such a way that its spectrum is spread over a wider frequency area. Thus it is achieved that the spectrum of the excitation signal from the exciter magnetizing block 2.2 is spread in the same manner. Since the output signal of the AMR sensor 2.0 is dependent on the magnetization direction of the sensing element 1.1 (part of the magnetoresistor 1.0), and this signal is spread into a wider frequency area in case that the output of the AMR sensor 2.0 will be nonzero.

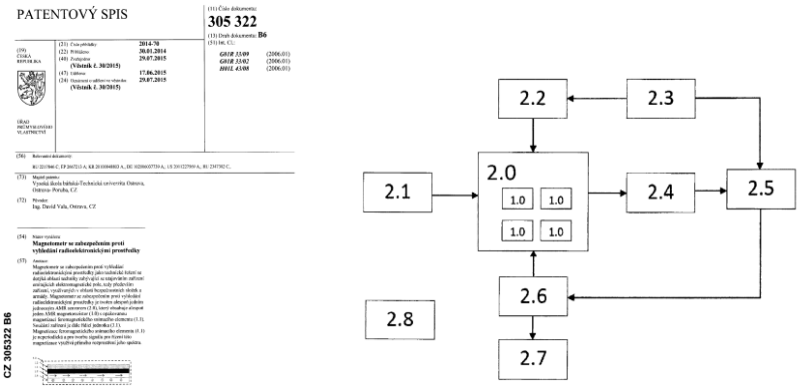

Fig. 4. Copy of patent registration and basic schematic of invention [22]

6 Conclusion

Detailed description of techniques for reducing of electromagnetic radiation of AMR magnetoresistive sensor is possible to find in internal documents [20] and [21]. This technique is also detailed described in application of the invention on Czech Industrial property office under number E193142 from 30 of January 2014 which is now public as Czech patent [22]. Upper described invention can reduce electromagnetic noise of AMR based magnetometer and help to make sensor invisible for electronic countermeasure devices.

Acknowledgement

This work was supported by the project SP2014/188 "*Řízení technologických soustav s OAZ pro komplexní energetické systémy 2015*" within the student's grant compeition

(VŠB-TU Ostrava) and This work is supported by project SP2013/135, named "Control of technological systems with OAZE providing an independent sustainable development of complex systems" of Student Grant Agency (VSB - Technical University of Ostrava)

Reference

1. Ripka, P., Magnetic sensor and magnetometers, Artech House, Norwood, MA, USA,2001 ISBN 1-58053-057-5
2. Fuka, J., Havelka, B.: Elektřina a magnetismus, vydání 3, SPN, Praha, 1979
3. Stork, T.: Electronic Compass Design using KMZ51 and KMZ52, Philips Semiconductors Systems Laboratory Hamburg, Germany, 2000
4. Data sheet: KMZ52 Magnetic Field Sensor, Philips Semiconductors
5. Hauser, H., Stangl, G., Fallmann, W., Chabicovsky, R., Riedling, K.: Magnetoresistive Sensors, Preparations, Properties and Applications of Thin Ferromagnetics Films, June 2000, Vienna, Austria
6. Handling Sensor Bridge Offset AN212, Honeywell, 2002
7. Set/Reset Pulse Circuits for Magnetic Sensors AN-201, Honeywell
8. Reference Design: Low Cost Compass AN214, Honeywell, 2002
9. Caruso, M., J.: Applications of Magnetoresistive Sensors in Navigation Systems, Honeywell Inc., 1998
10. Caruso, M., J.: Applications of Magnetic Sensors for Low Cost Compass Systems, Honeywell
11. Horák, B., Vala, D.: Smart Digital Magnetometer Application in Navigation Subsystem of Mobile Robot, VŠB – TU Ostrava
12. Vala, D.: Mini Flux-gate Sensor, INPF-LMN/LEG Grenoble, 2002
13. Caruso, M., J.: Applications of Magnetic Sensors for Low Cost Compass Systems, Sensors and Actuators 1997, SAE SP-1220, February 1997, 15-21
14. Caruso, M., J., Bratland, T., Smith, C., H., Schneider, R.: A New Perspective on Magnetic Field Sensing, Honeywell, SSEC Nonvolatile Electronics Inc.
15. Vala, D., Návrh a realizace systému autonomního měření polohy bezpilotního letového prostředku Kavka, Diplomová práce, kat.455, VŠB-TU Ostrava, 2003
16. Nevřiva, P., Analýza signálů a soustav, BEN, Praha 2000, ISBN 80-7300-004-0
17. Boashash, B., Time Frequency Signal Analysis and Processing, Elsevier,Oxford, 2003 ISBN 0-08-044335-4
18. Markey,H.,K.Antheil,G. Secret communication system, US Pat. 2,292,387
19. Meel,J., Spread Spectrum, Sirius Communication, Rotsellar, Belgie 1999
20. Vala,D. Způsob zvýšení utajení zařízení pro měření změny slabých magnetických polí před vyhledávaním radioelektronickými prostředky. Interní dokument VŠB-TU Ostrava, ev. č .040/02-09-2011, Ostrava, 2011
21. Vala, D., Buzení demagnetizace AMR magnetorezistoru rozprostřeným spektrem, Interní dokument VŠB-TU Ostrava, ev. č. 039/02-09-2011, Ostrava, 2011
22. Vala, D.: Magnetometr se zabezpečením proti vyhledání radioelektronickými prostředky, http://spisy.upv.cz/Patents/FullDocuments/305/305322.pdf.
23. Electronic countermeasure, https://en.wikipedia.org/wiki/Electronic_countermeasure.
24. Electronic counter-countermeasure, https://en.wikipedia.org/wiki/Electronic_counter-countermeasure.

Microsoft Azure Machine Learning and market prediction, performance

Marian Bielik

Department of Computer Science, FEECS,
VŠB – Technical University of Ostrava, 17. listopadu 15, 708 33 Ostrava – Poruba
marian.bielik.st@vsb.cz

Abstract. Microsoft Azure Machine Learning (ML) is a service that can be used to build predictive analytics models. In this case stock markets data are used. Neural network regression and linear regression are used for prediction of markets close prices. The key factor is a performance of cloud based machine learning platform.

Keywords: Microsoft Azure, machine learning, neural network regression, deep learning, linear regression, market prediction, performance, Azure Machine Learning Studio

1 Introduction

Azure Machine Learning (ML) is a cloud based machine learning platform. This service runs in Microsoft Azure [1] and was released on February, 2015. Predictive analytics is the underlying technology behind Azure Machine Learning. ML supports different categories of machine learning algorithms like classification algorithms, regression algorithms and clustering algorithms, described in [2].

In this paper are used Azure build in linear regression and neural network regression. Both are used to predict market data close prices.

Key point of this analysis is performance of training prediction models in cloud based Azure ML service.

2 Experiment Design

Azure ML has already implemented set of algorithms for prediction. Azure also provides set of various data with hundreds of rows. This paper uses IBM minute data from January 1998. Data file has about 2 million rows and has about 100 MB size and is used as impute for prediction algorithms and performance testing. Market data are described by date time, open, high, low, close prices and volume columns.

Using Descriptive Statistics module are data inspected for missing values. Missing data could be removed or replaced with mean, median using module Missing Values Scrubber.

© M. Krátký, J. Dvorský, P. Moravec (Eds.): WOFEX 2015, pp. 256–260.
VŠB – Technical University of Ostrava, FEECS, 2015, ISBN 978-80-248-3787-1.

In this paper is used close price as a prediction value. Filter Based Feature Selection module is used to determine the features of the dataset that are most relevant for the prediction. In this case, it is date time, open, high, low and close from previous tick. Algorithms that are available in Filter Based Feature Selection are Pearson Correlation, Mutual Information, Kendall Correlation, Spearman Correlation, Chi Squared, Fisher Score and Count Based.

Whole dataset is split using Split module. The first part of the data, that is 75%, are used to train the model and the rest is used to score the trained model.

Modules that are used for prediction are Linear Regression and Neural Network Regression. Linear regression is using Ordinary Least Squares. Neural network [3] settings are set to use 500 hidden nodes (Fully-connected case), learning rate is 0.005, number of learning iterations are 500, the initial learning weights diameter is 0.1, momentum is 0 and the type of normalizer is Min-Max normalizer. Neural Network Regression algorithms are widely known for use in deep learning. Whole design is shown in Figure 1.

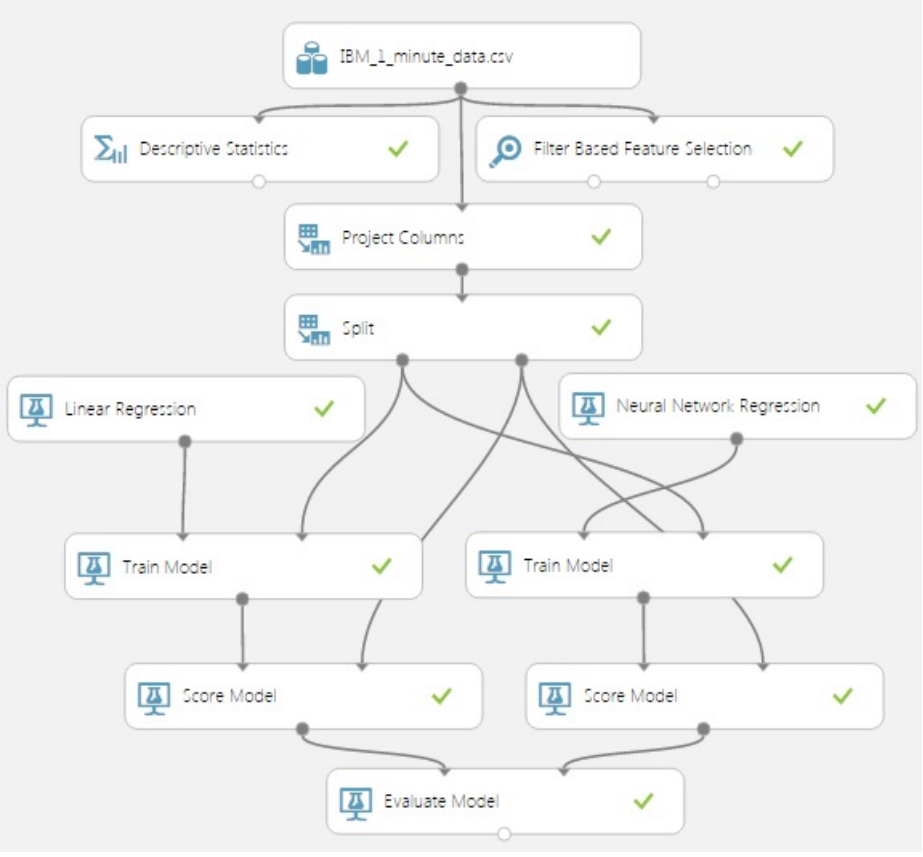

Fig. 1. Algorithm design

3 Results

Linear regression results are shown on figure 2. Predicted close price is almost same as original real closed price. But algorithm just follows trend.

More realistic results are shown on table 1. There can be seen, that predicted winning trends are 189903, but predicted loosing trends are 238197. As a result, linear regression can predict trends with 44.36% success.

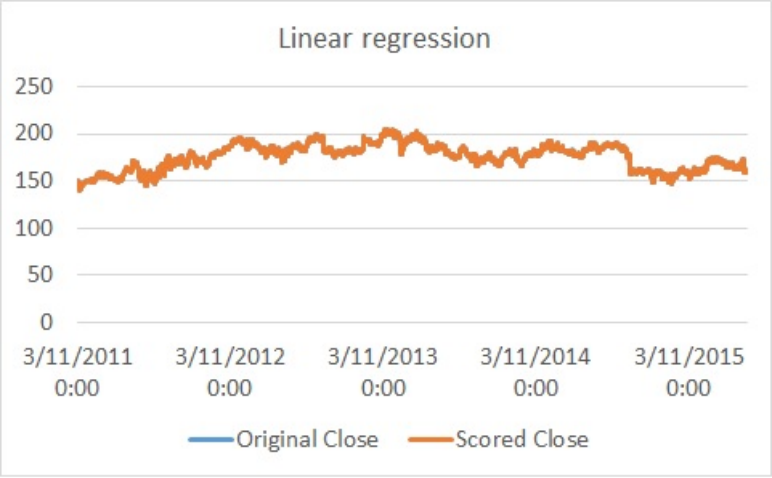

Fig. 2. Linear regression prediction

Trend prediction	Linear regression
Successful increasing	95660
Successful decreasing	94243
Winning total	189903
Losing total	238197
Percentual	44.36%

Table 1. Linear regression results

Neural network regression results are shown on figure 3. Predicted close price is a little different, than original close price. But more important are results shown in table 2. There is shown, that predicted winning trends are 189622 and predicted loosing trends are 238478, which means, that neural network regression can predict trend with 44.29% success.

Table 3 shows another key point of this paper and it is performance. Linear regression takes only 5 seconds for training and neural network regression takes

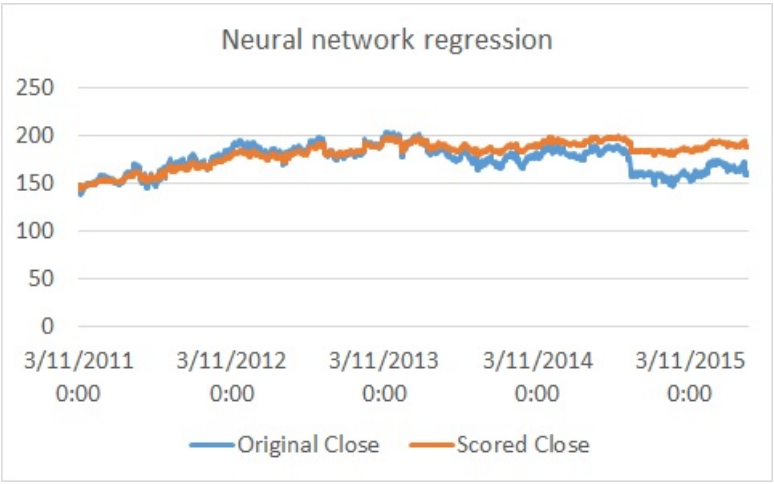

Fig. 3. Neural network regression prediction

Trend prediction	Neural network regression
Successful increasing	94050
Successful decreasing	95572
Winning total	189622
Losing total	238478
Percentual	44.29%

Table 2. Neural network regression results

50 minutes and 41 seconds. Learning process is quite fast, comparing to personal computers, but not so fast, as can be expecting from data center. Important is the fact, that training process is running simultaneously, which means, that multiple models can be trained during same time. For example, multiple neural networks can run with different initial setting, or different input/output values. Microsoft says, that you can utilize hundreds of thousands of CPU cores to solve your most difficult computational problems.

	Linear regression	Neural network regression
Training time duration [hh:mm:ss]	00:00:05	00:50:41

Table 3. Performance

4 Conclusions

Both strategies linear regression and neural network regression are losing. Azure build in predictive algorithms maybe can be used as a part of bigger algorithm.

Azure ML supports R code and Python, algorithm can use own code, that will be executed directly in Windows Azure.

Another possibility how to use Azure ML, is to use it for time-consuming operations that can be divided in smaller subtasks. These tasks can run simultaneously and use benefits of cloud based service running in big datacenters.

Trained models can be easyly (just one click) used as a service, that can using inputs, calculate and predict outputs. This functionality can be used as a part of bigger algorithm.

ACKNOWLEDGMENT

The following grants are acknowledged for the financial support provided for this research: Grant Agency of the Czech Republic - GACR P103/13/08195S, is partially supported by Grant of SGS No. SP2014/159, VB - Technical University of Ostrava, Czech Republic, by the Development of human resources in research and development of latest soft computing methods and their application in practice project, reg. no. CZ.1.07/2.3.00/20.0072 funded by Operational Programme Education for Competitiveness.

References

1. Michael Collier, Robin Shahan, 2015, Fundamentals of Azure: Microsoft Azure Essentials
2. Jeff Barnes, 2015, Azure Machine Learning: Microsoft Azure Essentials
3. Ivo Vondrk, 2009, Neural Networks

Data Classiffication using Evolutionary Algorithms

Petr Buček

Department of Computer Science, FEECS,
VŠB – Technical University of Ostrava, 17. listopadu 15, 708 33 Ostrava – Poruba
petr.bucek.2@vsb.cz

Abstract. The classification is one of frequently used method in data processing. Input of the classification algorithm is collection of uncategorized objects, while on output, each object must be assigned to appropriate category, which is chosen based on previous data processing. There are a lot of algorithms, which can be used for, such as statistical methods or Support Vector Machines. Evolutionary algorithms can be also used for classification, as described in this paper.

Keywords: classification, evolutionary algorithms

1 Introduction

Classification is method able to predict category of previously uncategorized object. It is used in a lot of science disciplines, such as image processing, text processing, filtering or machine vision [1][3][7].

In this paper, evolutionary algorithms are used to solve classification problem. This idea was first introduced in [9] (with algorithm Particle Swarm Optimization).

For predict category of previously uncategorized object is used classifier. Classifiers can predict category by model, based on categorized objects of training set. There are a lot of methods, how to calculate classifier, but the biggest issue is the increasing learning time which depends on the amount of the input data. This is the reason for using evolutionary based algorithms for classification problem.

Next important thing is how to measure similarity between objects. There are a lot of methods, but in this case, cosine similarity is used. Each object is represented as vector. For determining similarity of vectors u and v is cosine similarity defined as [9]:

$$sim(u, v) = \frac{u \cdot v}{\|u\| \, \|v\|}$$

For our purposes, we are testing classification with few other evolutionary based algorithms and compare its quality. Implemented and tested algorithms are:

© M. Krátký, J. Dvorský, P. Moravec (Eds.): WOFEX 2015, pp. 261–265.
VŠB – Technical University of Ostrava, FEECS, 2015, ISBN 978-80-248-3787-1.

- Bat Algorithm (BA) [11]
- Cuckoo Search Algorithm (CSA) [14]
- Firefly Algorithm (FA) [10]
- Flower Pollination Algorithm (FPA) [12]
- Particle Swarm Optimization (PSO) [4]

2 Classification with Evolutionary Based Algorithms

As stated in introduction, cosine similarity is used for comparing two objects. In evolutionary based algorithms, each object represents one particle. Cost function used in all evolutionary based algorithms is computed as the similarity between particles.

Because we are using text document datasets (one document is an object), document is assigned to the category if its similarity is smaller than predefined treshold.

In this section is explained general description of each used algorithm and calculation method.

2.1 Bat Algorithm

Bat Algorithm is meta-heuristic algorithm developed by Xin-She Yang (2010). Similar to PSO algorithm, each object is represented as particle (bat) with own set of properties. Behavior of swarm is inspired by bat echolocation.

Each particle has following properties: Position (x_i), frequency (f) and velocity (v_i). Movement is done by rules:

$$f_i = f_{min} + (f_{max} - f_{min})\beta$$
$$v_i^t = v_i^{t-1} + (x_i^t - gBest)f_i$$
$$x_i^t = x_i^{t-1} + v_i^t$$

where $\beta \in [0, 1]$ is a random vector (uniform distribution). Variables f_{max} and f_{min} are parameters of the algorithm and depends on the requirements of the task. There is also used $gBest$ global best solution, found by all bats [11].

2.2 Cuckoo Search

Cuckoo Search was developed by Xin-She Yang and Suash Deb (2009) [14]. Particles in this algorithm has behavior inherited from cuckoo species and its brood parasitism. This behaviour is simulated with Lévy flights. New solution is represented by the following equation:

$$x_i^{t+1} = x_i^t + \alpha \oplus Levy(\lambda)$$

where $\alpha > 0$ represents maximum size of move. Operator $\oplus$ is entry-wise multiplication with Lévy flight vector.

Update phase of CS algorithm is consist of these steps:

- Each cuckoo lays only one egg to random nest.
- Only eggs with high quality of solutions are passed to the next update phase.
- There is probability $p_a \in [0, 1]$ to discover cuckoo egg by host bird. In this case, there are three variants:
  - Host bird can build a new nest.
  - Host bird can abandon its nest.
  - Host bird can remove cuckoo egg [5].

These steps are repeated until the optimal solution is found.

2.3 Firefly Algorithm

Firefly Algorithm was published by Xin-She Yang (2008) in [10]. Particles in this algorithm has properties derivated from fireflies. Their flashing characteristics represents their attractiveness to other fireflies. Intensity of their light is also affected by the distance [13]. There are several variants of FA, but basically, update phase has following rules [8]:

- Each firefly is attracted to each others.
- Movement direction of firefly is to a brighter one or random, if there is no one brighter.
- Brightness of firefly depends on solution of the cost function.

The simple form of the light intensity $I(r)$ is:

$$I(r) = \frac{I_s}{r^2}$$

where I_s is the light intensity at the source and r is the distance. This is a simplified equation ignoring the factor of absorption λ. The movement of a firefly i is specified as:

$$x_i = x_i + \beta_0 e^{-\gamma r_{ij}^2}(x_j - x_i) + \alpha\epsilon_i$$

where second term represents attraction and last term is randomisation (with parameter $\alpha \in [0, 1]$). Parameter γ is a light absorption coefficient [10].

2.4 Flower Pollination Algorithm

FPA was developed in 2012 and it is based on idea of pollen transport between flowers. Each particle represents one flower and update phase has following rules:

- Biotic and cross-pollination has a global approach and it is provided by Lévy flights.
- Abiotic and self-pollination has a local approach.
- Reproduction has same probability as value of similarity of the flowers.
- Local and global pollination have probability $p \in [0, 1]$.

Flowers are evaluated by:

$$x_i^{t+1} = x_i^t + Levy(x_i^t - gBest)$$

where $gBest$ is the best known flower [12].

2.5 Particle Swarm Optimization

Particle Swarm Optimization was first time announced in [2, 4]. PSO algorithm represent each object as particle which movement is derivated from the behavior of the bird swarm. Particles are moved to find optimal (minimum or maximum) value of cost function. Vector value of each particle represents its position. Except the position, each particle has its own velocity vector. Current particle velocity and the position of the best particle is used for movement in update phase of algorithm. The velocity v_i^{t+1} of i-th particle in iteration $t+1$ is defined as follows:

$$v_i^{t+1} = wv_i^t + c_1 r_1 \times lBest - x_i^t + c_2 r_2 \times gBest - x_i^t$$

where r_1, r_2 are randomly generated numbers in the interval $\langle 0, 1)$, c_1, c_2 are parameters of the algorithm called learning factors, x_i^t is the position of the i-th particle in iteration t and w is a inertia factor of the algorithm. $lBest$ and $gBest$ are local and global best found solution.

3 Experiments and Conclusion

Classification with evolutionary based algorithms was applied to document datasets, described in table 1. Computation was paralelized on GPU, with following optimizations:

- Similarity was calculated on normalized vectors.
- Calculation was separated to two parts, preparation and particle movement.
- The cost function was calculated in same time for each particles.
- For paralelization was used MPI and CUDA combination.
- Matrix multiplication was realized with cuBlas CUDA library.

Dataset	Full size	Training set	Test set	Attributes
Higgs	11.000.000	10.500.000	500.000	28
Sussy	5.000.000	4.500.000	500.000	18

Table 1. Datasets

Computed F-score of all used algorithms was between 0.66–0.71 for first dataset and between 0.71–0.82 for second dataset. Only PSO and FA algorithms has F-score better ~ 0.0189 (first dataset) and ~ 0.0872 (second dataset) than others. Aquired results achieved by all used algorithms are very good [6][9].

References

1. I. Androutsopoulos, J. Koutsias, K. V. Chandrinos, G. Paliouras, and C. D. Spyropoulos. An evaluation of naive bayesian anti-spam filtering. *arXiv preprint cs/0006013*, 2000.
2. R. Eberhart and J. Kennedy. A new optimizer using particle swarm theory. In *Micro Machine and Human Science, 1995. MHS '95., Proceedings of the Sixth International Symposium on*, pages 39 –43, oct 1995.
3. R. Jain, R. Kasturi, and B. G. Schunck. *Machine vision*, volume 5. McGraw-Hill New York, 1995.
4. J. Kennedy and R. Eberhart. Particle swarm optimization. In *Neural Networks, 1995. Proceedings., IEEE International Conference on*, volume 4, pages 1942 –1948 vol.4, nov/dec 1995.
5. P. Manikandan and S. Selvarajan. *Data Clustering Using Cuckoo Search Algorithm (CSA)*, pages 1275–1283. 2012.
6. J. Platos, V. Snasel, T. Jezowicz, P. Kromer, and A. Abraham. A pso-based document classification algorithm accelerated by the cuda platform. In *Systems, Man, and Cybernetics (SMC), 2012 IEEE International Conference on*, pages 1936–1941. IEEE, 2012.
7. F. Sebastiani. Machine learning in automated text categorization. *ACM Comput. Surv.*, 34(1):1–47, Mar. 2002.
8. P. R. Srivatsava, B. Mallikarjun, and X.-S. Yang. Optimal test sequence generation using firefly algorithm. *Swarm and Evolutionary Computation 8 (2013) 4453*, 2012.
9. Z. Wang, Q. Zhang, and D. Zhang. A pso-based web document classification algorithm. In *Proceedings of the Eighth ACIS International Conference on Software Engineering, Artificial Intelligence, Networking, and Parallel/Distributed Computing - Volume 03*, SNPD '07, pages 659–664, Washington, DC, USA, 2007. IEEE Computer Society.
10. X.-S. Yang. *Nature-Inspired Metaheuristic Algorithms Second Edition*, pages 81–89. Luniver Press, 2010.
11. X.-S. Yang. A new metaheuristic bat-inspired algorithm. *Nature Inspired Cooperative Strategies for Optimization*, 2010.
12. X.-S. Yang. Flower pollination algorithm for global optimization. *Unconventional Computation and Natural Computation 2012*, 2012.
13. X.-S. Yang. *Nature-Inspired Optimization Algorithms*. School of Science and Technology Middlesex University London, London AMSTERDAM, 2014.
14. X.-S. Yang and S. Deb. Cuckoo search via lvy flights. *Proc. of World Congress on Nature & Biologically Inspired Computing*, 2009.

Analysis and Implementation of the Active Demand Side Management in the Off-grid System

Tomas Burianek

Department of Computer Science, FEECS,
VŠB – Technical University of Ostrava, 17. listopadu 15, 708 33 Ostrava – Poruba
tomas.burianek.st1@vsb.cz

Abstract. The Off-Grid systems are energetic objects independent of an external power supply. It uses primarily renewable sources. For safe running of the system the Active Demand Side Management must be implemented. The Active Demand Side Management controls switching of appliances based on given plan that must be optimized by information obtained from forecasting of production of energy from photovoltaic power plant and also power quality. This paper introduces analysis of a parameters in the Off-Grid system and subsequent forecasting of production and power quality based on statistical and bio-inspired machine learning algorithms.

Keywords: Active Demand Side, Off-grid system, Time-series forecasting, Neural Networks

1 Introduction

The Off-Grid system is an energy unit that is independent of an external energy power source. It uses mainly renewable sources (RES) namely photo-voltaic power plan and wind turbine. The Off-Grid system can be divided to two basic parts. Basic block scheme of the Off-Grid system is shown in Figure 1. First one is a hardware part (power sources, part of electrical consumption, parts of energy transfer and energy conversion). Second one is a software part called the Active Demand Side (ADSM) that includes inputs such as weather forecast, energy production forecast, consumption plan(forecast), load configuration, power quality parameters(PQP) forecast and implementation of a new protection scheme. The ADSM is a computing core that optimizes plan of appliances based on consumption profile of each appliance and available production of energy from RES to meet the basic requirements of house inhabitants. Also this plan optimization must count with forecasting of PQP for safe working of appliances. For PQP and production forecasting is important to understand relations between those PQ parameters, other electrical parameters and meteorological conditions that affect running of the whole system.

© M. Krátký, J. Dvorský, P. Moravec (Eds.): WOFEX 2015, pp. 266–271.
VŠB – Technical University of Ostrava, FEECS, 2015, ISBN 978-80-248-3787-1.

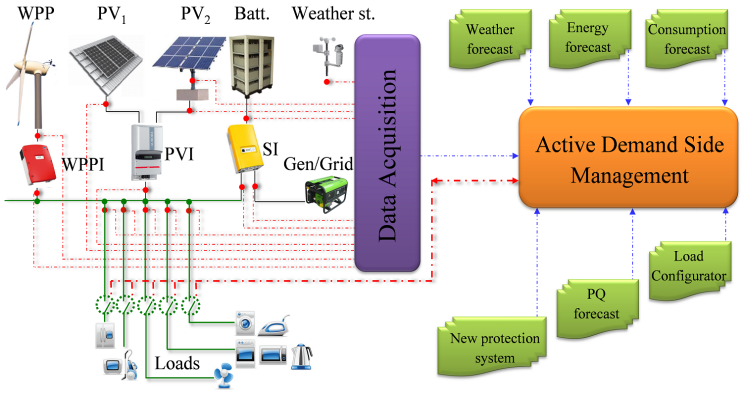

Fig. 1. Active energy unit

In this paper, the statistical and bio-inspired methods are employed such as Feed-Forward Multilayer Neural Network and Recurrent Neural Network in problem of forecasting and Self-organizing Map, Dimensionality Reduction and Clustering methods in analysis of parameter time-series.

This paper is organized as follows: Section 2 describes proposed method for the Off-grid parameters analysis, Section 3 presents Power Quality forecasting approach, in Section 4 the Photovoltaic Power Plan Production Forecasting is presented and in Section 5 conclusions and future work are given.

2 Off-Grid Parameters Analysis

In the Off-Grid system it is important to understand dependency and relations between measured parameters for further forecasting. Parameters are divided to three groups. First group of parameters are PQ parameters namely THDu, THDi, Plt, Pst and frequency. Second group are electrical power parameters such as voltages, currents, performances and other parameters measured on specific parts of the Off-Grid system. Last group consists of meteorological parameters for instance global solar irradiation, atmospheric pressure, temperatures, wind direction and so on.

The proposed method for parameters analysis consists of four main steps. In the first step a data set is constructed from all parameters, where each row is a time-series of each parameter. Further normalization an pre-processing is performed. The second step consist of dimensionality reduction [2] of the data set to a specific dimension where only important features extracted from the original high-dimensional data and speeds up the following step. Principal Component Analysis [3] is used for this task. In the next step the reduced data set is processed by the Self-organizing Map [4], where map prototype nodes are labeled by parameters names. The assumption is that related and dependent parameters

are close on this two-dimensional map. In the last step the k-means clustering algorithm [5] is used for identification of parameters groups.

Experiments were performed on 117 Off-Grid parameters where each parameter time-series consists of 14400 one-minute ticks. Th resulted Self-organizing Map labeled by names of all parameters are shown in Figure 2. Different clusters computed by k-means algorithm are highlighted by distinct colors of cells. This

Fig. 2. Labeled Self-Organizing Map with highlighted clusters

analysis shows obvious relations between similar parameters but also revealed unknown relations. Example of this is association of voltage on each part of Photovoltaic power lant (PV) string U_{FVE_1} and U_{FVE_2} which are in relation with frequency $freq$ in the Off-Grid System that subsequently affect PF_{SI} - a power factor of Off-Grid inverter. Other power quality parameters such as THDu and THDi are grouped in cluster with consumption in the system P_{1avg} and also with global irradiation that can be assumed as an energy production from a PV. Also other weather parameters such as atmospheric pressure are in relation with parameters of PV.

More details of this proposed method and its results are described in [1].

3 Power Quality Parameters Forecasting

Power Quality parameters include Total harmonic distortion of voltage - THDu (%), Total harmonic distortion of current - THDi (%), Long-Time Flicker severity - Plt (-) and Power Frequency - f (Hz). It is needful to keep PQ parameters in

defined limits for a restraint of a reliable and safe running all of the appliances in the system. PQP out of desired limits may cause reduction of a service life of the appliances and in the worst case may cause damage. Then it is important to forecast development of these parameters in time to prevent its behavior out of limits. For the task of forecasting the Feed-Forward Multilayer Neural Network [7] was employed.

Experiments were performed on the dataset constructed from Off-Grid parameters. Data were 15 minutes median ticks. Based on results in Section 2 the global solar irradiation, actual consumption in the system ($P_1 avg$) and also predicted PQ parameter itself were selected for forecasting of each PQ parameter with 10 ticks of these parameters in the past. Forecasting was done for 1st, 2nd, 3rd and 4th tick to the future for each PQ parameter. Example of the result is presented in Figure 3 for THDi forecasting 1st tick to the future. More details

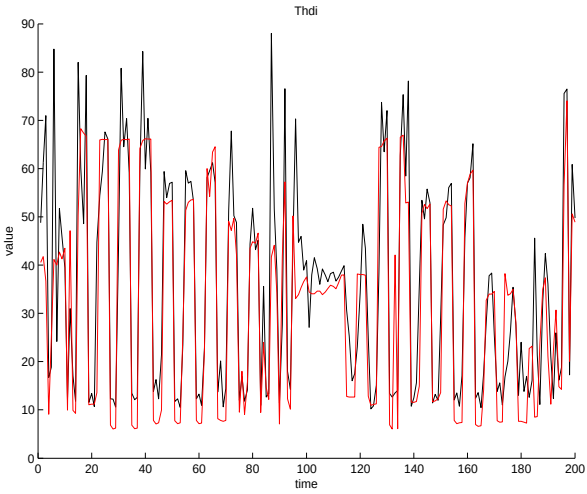

Fig. 3. THD_i result for $1st$ data sample prediction (black) compared to target output (red) on data for time periods 0 to 200.

about presented PQP forecasting approach and obtained results are described in [8].

4 Photovoltaic Power Plan Production Forecasting

The photovoltaic power plant production forecasting is mainly dependent on solar irradiance that is influenced by actual weather conditions. Proposed forecasting model is based on a meteorological forecasting data. These data along

with a real historical production from the reference solar power plant form time-series data. For time-series forecasting the Recurrent Neural Networks are suitable for this kind of task because it can capture sequence data relations in time in contrast to Feed-Forward Neural Network.

Forecasting data are obtained four times a day with six hour gap and each forecasting contains 55 hours of predicted data ahead and it is comprised of many attributes namely *humidity*, *temperature*, *windspeed*, *atmosphericpressure* and *cloudiness*. The main effect on a solar irradiation has the *cloudiness* data. These data contains four classes of cloudiness: *low*, *medium*, *high*, *total*. For a real production from a photovoltaic power plant affected by clouds is crucial to know unaffected clear production for every day of the year. The approximate clear production is possible to construct from a collected historical data of the reference solar power plant by picking only sunny days and approximating its curve through the whole year. It is important to know times of sunrises and sunsets of all days in the year for correct formatting of power curves. The approximate clear production data and the cloudiness data are then used to construct dataset applied in supervised learning. The input part of the dataset contains one column of approximate clear production and four columns of cloudiness classes composed of forecasting data. The output part is then one column of the real production from the photovoltaic power plant that is affected by presented inputs of cloudiness and the clear production at the same hour. Proposed model for solar power production forecasting uses Recurrent Neural Network as a supervised learning technique [6] with Backpropagation Through Time learning algorithm [9].

Experiments were performed on constructed dataset with 2970 data rows as hours representing 124 days of the data. Error during training and testing was measured by Mean Square Error (MSE). Final MSE for training was $9.956e-3$ and for testing $15.329e-3$. Results are presented for picked cloudy day and sunny day in Figure 4. It is obvious that precision of the model is mainly affected

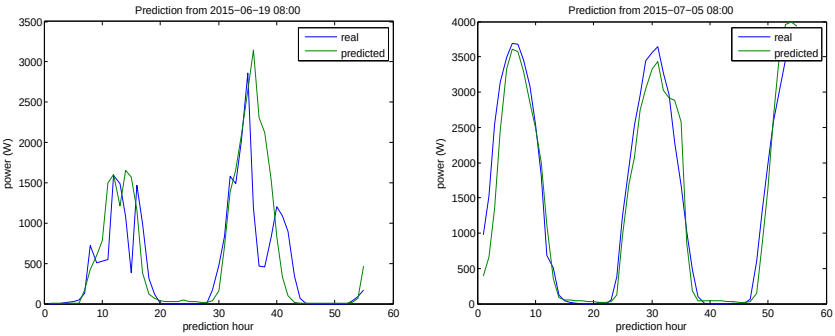

Fig. 4. Prediction for cloudy days in left and sunny days in right

by obtained meteorological forecasting data. Even though obtained results are very close to the real output production and the presented model is suitable for approximate solar power production forecasting. More details about proposed method and its results will be presented in forthcoming conference paper.

5 Conclusion and Future work

Proposed methods for analysis, forecasting of PQ parameters and production from photovoltaic power plant were applied with good experimental results. The forecasting methods are important inputs for optimization of appliance plan for safely running of appliances and sufficient supply of energy for complete independence from external power source. These methods are implemented as separated online web services that together serve as important parts of the ADSM. In the future work these methods must be thoroughly tested for real traffic of appliances in the Off-Grid system.

References

1. Burianek, T., Vantuch, T., Stuchly, J., Misak, S.: Off-grid parameters analysis method based on dimensionality reduction andself-organizing map. In: Matouek, R. (ed.) Mendel 2015, Advances in Intelligent Systems and Computing, vol. 378, pp. 235–244. Springer International Publishing (2015)
2. Cunningham, P.: Dimension reduction. In: Machine Learning Techniques for Multimedia, pp. 91–112. Springer (2008)
3. Jolliffe, I.: Principal Component Analysis. Springer Series in Statistics, Springer (2002)
4. Kohonen, T.: Self-organized formation of topologically correct feature maps. Biological Cybernetics 43(1), 59–69 (1982)
5. MacQueen, J.B.: Some methods for classification and analysis of multivariate observations. In: Cam, L.M.L., Neyman, J. (eds.) Proc. of the fifth Berkeley Symposium on Mathematical Statistics and Probability. vol. 1, pp. 281–297. University of California Press (1967)
6. Pearlmutter, B.A.: Dynamic recurrent neural networks. Tech. rep., Carnegie Mellon University (1990)
7. Rosenblatt, F.: Principles of neurodynamics; perceptrons and the theory of brain mechanisms. Spartan Books Washington (1962)
8. Stuchly, J., Misak, S., Vantuch, T., Burianek, T.: A power quality forecasting model as an integrate part of active demand side management using artificial intelligence technique - multilayer neural network with backpropagation learning algorithm. In: Environment and Electrical Engineering (EEEIC), 2015 IEEE 15th International Conference on. pp. 611–616 (June 2015)
9. Werbos, P.: Backpropagation through time: what it does and how to do it. Proceedings of the IEEE 78(10), 1550–1560 (Oct 1990)

Moodle logs analysing web application

Michal Čerbák

Department of Computer Science, FEECS,
VŠB – Technical University of Ostrava, 17. listopadu 15, 708 33 Ostrava – Poruba
michal.cerbak.st@vsb.cz

Abstract. This paper deals with created system for LMS Moodle log analysis. This system is composed from three key parts including: Moodle plugins whose provide extracting user acitivity log files from Moodle appication; web service for log data processing and finaly web application with interactive user interface for downloading logs, managing and visualization of processed logs. The whole app will provide an interactive way for finding differences between students.

Keywords: LMS Moodle, log processing, user acitivy analysis

1 Architecture

Web application architecture is developed to decrease load on web server hosting LMS Moodle. It is reason for using independent server for graph analysis web application, and also for log data processing web service. Architecture can be divided into three logical parts: LMS Moodle, Moodle graph analysis web application, log data processing web service.

Moodle graph analysis web application can be considered as core part. This web app mediates autentization and communication with LMS Moodle, allows calling Moodle functions to view and download Moodle logs and finaly creates interface for processing and visualising these logs. And it is possible within one web app.

2 Communication with LMS Moodle

Communication with the system uses Moodle Web Services (External services). These services allow external applications to call functions of Moodle API that provides a set of built-in features or functionalities available through the installed plugins. To allow user calling remote functions, Moodle must have enabled Web services with assigned privileges for this user.

© M. Krátký, J. Dvorský, P. Moravec (Eds.): WOFEX 2015, pp. 272–276.
VŠB – Technical University of Ostrava, FEECS, 2015, ISBN 978-80-248-3787-1.

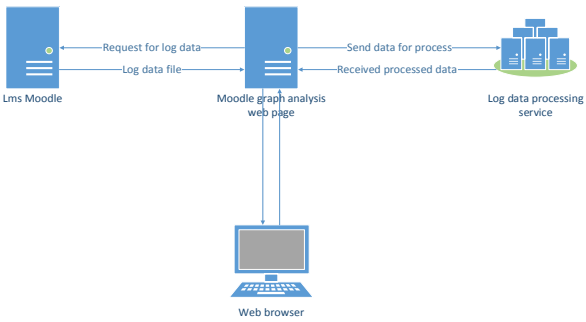

Fig. 1. Architecture overview

2.1 Web services

There are two Web services created and activated within Moodle. Web services can be accessed only by authorized users whose need to be assigned by a particular Moodle system administrator. Communication uses two-step verification, Moodle user name and password, and communication token, what brings even more security and disallow anautorized access to web services.

Web service dp application Only one user representing the external application is assigned to this web service. This user also have to be assigned to the communication token, which is manually generated. This token will not expire and remains the same for all time. The Web service exposes function required to authenticate the user to the system via an external Moodle application and verification of whether the user has assigned the required system role (Webservice User).

Web service dp user Web Service has assigned users who will be able to generate and retrieve log files. These users are not manually assigned to a communication tokens. Token generation is proceeded by sending a secure HTTPS request. Based on the transmitted data system authenticates the user. In case of successful authentication sends back the generated token. The Web service exposes the functions needed to generate a tree of categories and relevant courses, as well as a function for obtaining information about the course, based on an identifier of the course itself and obtaining the relevant course log entries.

3 Communication with log processing web service

Communication is based on sending HTTP requests, which are processed by web service and through HTTP response sended back to web application.

3.1 Log data processing and analyzing

The basis of processing and analyzing of resulting log file is communication between ASP.NET application and application containing WCF service. This WCF application is running on a Windows server and provides several methods for processing transmitted log file.

ASP.NET web application can store multiple requests for the analysis of log files in the database. Each request has the attribute State which indicates the current status of log file analysis. Attribute Token is used in communication with WCF services. Token is used for identification of current partial subtasks state within processing of the log file. New analysis request is created only after successful acquisition and downloading of non-empty log file. After this web app generates file name composed of the user identifier and date time of log downloading. Then request is queued for processing.

Particular requests for log processing are stored in a queue. Whole operation runs asynchronously because of time-consuming processing of the log file. User only starts request processing, all further steps are performed automatically. On succesfull end of processing is user informed abbout sucessfull processing by web app which moves log to processed logs.

The processing operation is asynchronous. This allows easier processing within web service and also this queue approach runs all processing subtasks sequentialy. It avoids problems with concurent access to the same file. Web application doesnt need remote scheduler or web service for queue processing. I developed mechanism which can wake up page at constant intervals, due to registering cache entries with expiration time as a interval. When cache expires, server executes a registered callback. This starts processing of queue and if it finds any pending analysis, continues or starts the process. Atfer porcessing web register another cache entry.

The whole process is divided into the tasks. This allows a reasonable response to possible errors in processing, such as web services shutdown, unavailability of internet connection and so on. In this case, the web application attempts to repeat the current task. If the error persists, analysis stays in the current task and another analysis run its own current task. If the task will execute without error, web application processing moves to the next task. This approach has the additional advantages: processing in nature is executing a collection of tasks. If additional functionality is needed then it only requires a new task added to collection, or if some operation is needed to be disabled then it only requires to remove task from the collection.

Anonymize task In order to maximize Moodle users anonymity is first task anonymizing users. Parser goes through the entire log file and finds the username. It is stored in a database and all its occurances in the log file are replaced with anonymous form $StudentXX$, where XX is a number allowing deanonymization. This ensures that the Web service does not handle real names.

Upload task The log file is uploaded to the Web services server. All the processing on the Web service is also divided to tasks because this processing can also cause

an error. This approach can determine which part of the processing has been completed correctly and which must be done again.

Preprocess after load task Log file preprocessing request is sent to the web service.

Get base profile task Web app tries to get processed basic user profiles from web service.

Prepare user graph task Graph data processing request is sent to the Web service.

Get users graph task Web app gets processed graph data.

Parse to JSON task On the side of the web application are precessed data converted to JSON, in order to be easily used in the visualization.

Delete processed task Processed files are deleted from the Web server. This is happening mainly because of safety. On server remain only two files stored in JSON format, whose contain only anonymous data. This approach is even economic to disk space, because only necessary files for visualization remains on disk.

Set complete task It is the last task that moves analysis into processed analyzes allowing the resulting visualization.

4 Final visualization

The most important part of the whole application is an interactive visualization of the results. Visualization is based on javascript libraries D3.js. This library offers multiple graph layouts. One of many possible layouts is Force Layout, which is also used by the application to render the resulting graph. This layout allows setting specific properties: friction, charge, gravity, etc, whose can affect the behavior of the entire visualization.

There are several tasks wose need to be done before generating and displaying the graph, such as setting some important variables, retrieve JSON file containing nodes and edges of the graph, verifying the existence of respective nodes to all edges in the graph, initial creation of networks, calculation of the nodes (nodes degree) of all nodes in the graph, initialization of interactive elements, etc.

If a user with insufficient permissions that are assigned on the basis of the LMS Moodle login tries to access visualization, JSON file stays anonymised and displays anonymized visualization. Otherwise, using a login with sufficient privileges, system automaticaly preforms deanonimization and renders visualization of real Moodle users.

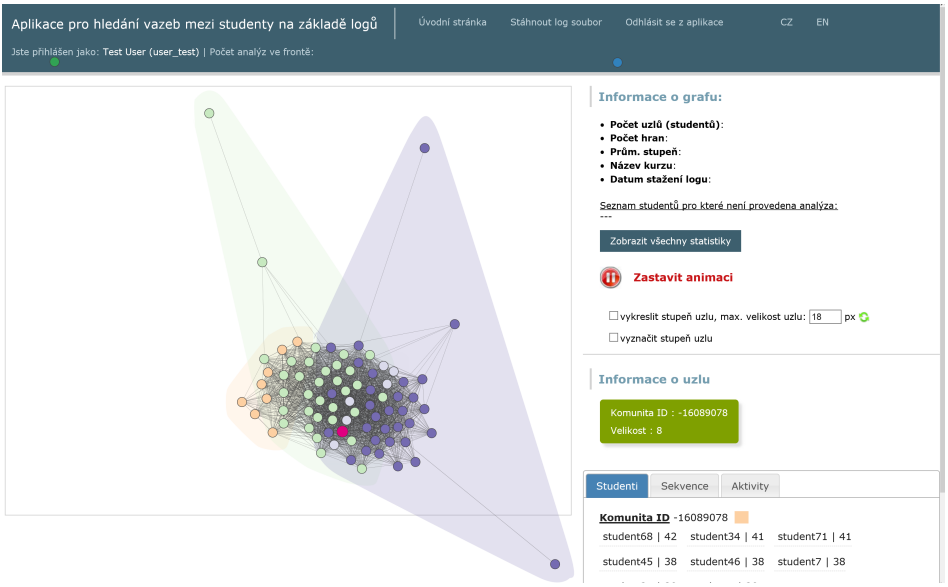

Fig. 2. User interface

5 Conclusion

This paper discribed developed system for log files analysis. The result is a web application for LMS Moodle users - teachers. They can easily see the most frequent activities for chosen course. They can see who did the excercise, who read the given text etc. Students are divided into groups based on their activities. Teachers can easily separate and identify students whose are different from the mass and help them or focus on them in order to achieve better results.

References

1. BUŠTÍKOVÁ, Lenka. Analýza sociálních sítí. Sociologický časopis [online]. 1999, Vol. 35 (No. 2: 193-206) [cit. 2015-07-25]. Dostupné z: http://sreview.soc.cas.cz/uploads/42a6c78198cacdc20c3a2da286e0c226ef935606_210_193BUSTI.pdf
2. BOSTOCK M., OGIEVETSKY V., and HEER J. D3: Data-Driven Documents [online]. 2011 [cit. 2015-08-02]. Dostupné z: http://d3js.org/
3. CAMPUS SOURCE. CampusSource Software Moodle [online]. 2014 [cit. 2015-08-02]. Dostupné z http://www.campussource.de/org/software/moodle/.
4. Core APIs - MoodleDocs [online]. 2014 [cit. 2015-07-22]. Dostupné z http://docs.moodle.org/dev/Core_APIs.
5. MARTINOVIČ J., DRÁŽDILOVÁ P., SLANINOVÁ K., KOCYAN T., and SNÁŠEL V. Left-Right Oscillate Algorithm for Community Detection Used in E-learning System. In ComputerInformationSystemsandIndustrialManagement,volume7564ofLecture Notes in Computer Science, pages 278–289. Springer Berlin Heidelberg, 2012.

Software Process Resource Modeling based on UPMM

Jan Czopik, Jakub Stolfa, Svatopluk Stolfa, and Ivo Vondrák

Department of Computer Science, FEECS,
VŠB – Technical University of Ostrava, 17. listopadu 15, 708 33 Ostrava – Poruba
{jan.czopik, jakub.stolfa, svatopluk.stolfa, michal.kosinar, ivo.vondrak}@vsb.cz

Abstract. In software process engineering, the ability to simulate software process before it is deployed to some kind of workflow system for automated execution allows us to simulate and tune the process to maximum efficiency, stripping it off any defects it might have along the way. Our simulation of software process (the dynamic part) is extended by static aspects (mainly resources) and thus we could obtain even more accurate data on how software process behaves under scenarios possible only by adding resources into the equation. And of course, use those results to analyze, verify and improve the process itself. All of this using standard UML and CPN, based on our Unified Process Meta-model.

Keywords: Software process, UML, CPN, OWL, Resource utilization, Unified Process Meta-model

1 Introduction

Business process modeling basically means to capture the structural, behavioral and functional aspects of the modeled company. The need to have a stable reusable models that can be easily used for simulation has raised [1, 5, 8]. Many research groups have been investigating various methodologies, adaptive process techniques, etc. [7, 12]. Other solutions involve utilization of formal systems, knowledge bases and mathematical models (e.g., Discrete-Event Simulation, System Dynamics, etc.). By the implementation of formal rules and facts, the process model and its execution may be more adaptive to an unexpected situation and events.

This paper proposes a combined solution of UML's ease of use and understandability and CPN's strong semantics and verification, validation and simulation possibilities to allow process specialists to incorporate static aspects (mainly resources) to their models and thus enhance the simulation and analytical capabilities. Our approach is based on Unified Process Meta-model introduced in [9] and it is an outcome (and refinement) of our previous work presented in [3, 2].

© M. Krátký, J. Dvorský, P. Moravec (Eds.): WOFEX 2015, pp. 277–282.
VŠB – Technical University of Ostrava, FEECS, 2015, ISBN 978-80-248-3787-1.

2 State of the Art

These days process modeling presents many modeling techniques as is mentioned in Vergidis's paper [16]. However according to paper [4] software process has been characterized as "the most complex endeavor humankind has ever attempted". It is caused by that the software process is quite specific [3].

In this paper we are focused on the converting software process models modeled in UML2 Activity diagrams to their Colored Petri Nets (CPN) counterparts to get advantages of well-formed formal language. Some of the researchers [14, 13, 11, 4] are focusing on using Petri nets for resource utilization modeling and simulation. They are mainly using colorless Petri nets meaning the expressivity of their models is limited and some of them are trying to overcome it by supplying the net with additional external software components which are not native to Petri nets [11] and therefore all the aspects of the Petri net itself are not present in the structure of the net and therefore the verification and analysis can't be sound. Our solution is based solely on CPN and their core features so everything is built-in to the structure of the net and inscriptions providing sound analysis and verification. Others [14, 4] deal only with rules specification but there is no proper connection to an executable model.

The strongpoint of our approach is its simplicity with maintaining completeness and simple extensibility.

3 Our Approach and UPMM Metamodel

We have introduced the basics of our approach in previous papers [3, 2]. Now, we are focusing on definition of transformation rules mainly concerning resources. The whole approach is based on and benefits from our unified Process Meta-model (UMPMM) based on formal OWL language. There are many process meta-models each focused on slightly different process aspects. Our UPMM is combining all the metamodels and adds some other aspects to form a complex generally usable metamodel and is a basement for all necessary models in our methodology for modeling [10].

Our UML to CPN transformation approach is based on a small part of the UPMM shown in Fig. 1. It shows the relationship between Process step (whether it is an Event, a Task or a sub Process) and some Role in which some Resource (Inanimate or Human) is then executing the Process step. It also shows a relationship between Resource and Role through Competence.

As in real world, resources (whether inanimate or human) can appear under roles. Roles are important from constraint and security point of view. But using role based model is not enough. We need to refine the role by adding competence as well as skill level. Hence the resource is not defined just by its role, but also by its competence. The relation is depicted in Fig 1.

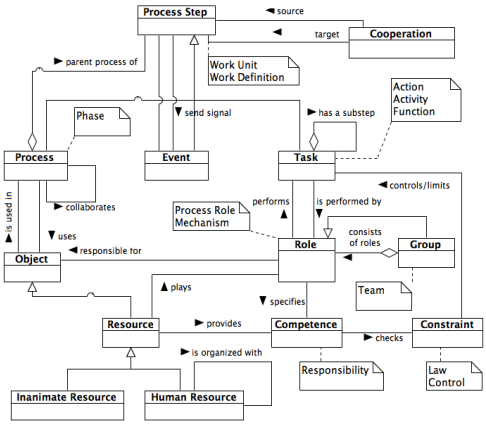

Fig. 1. Part of UPMM regarding resources and competences

4 Resource Modeling And Transformation

Main element of every Activity diagram is an activity (activities), it represents a task (or tasks in case when activity has actions), piece of work to be done. Activity is performed by a resource (preferably in a role) with certain competences. Activity can also consume (or utilize) passive resource (which is not performing the activity itself) and produce an artifact.

A part of UML model in Fig. 2 shows an activity which is performed by a resource (represented by role) with some competence (on some level), consumes a passive resource and produces an artifact. Please notice that UPMM uses one more element between a Competence and Task called Constraint. In example on Fig. 2 we are using an anonymous Constraint (not exactly specified) represented by object flow with a guard. The guard restricts level of the competence and it reflects the data property Skill level in UPMM. It means that activity *Code integration into source control* can be performed only by a *Developer* with competence *Source control* on level greater than 70.

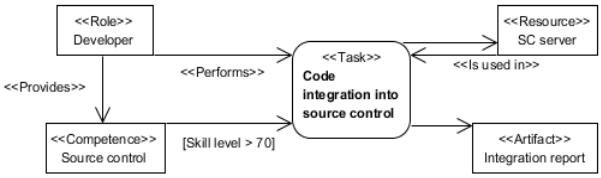

Fig. 2. UML resource modeling complaint to UPMM

4.1 CPN Insciptions

Based on newly added information from the UPMM we have extended [2] the generated colorsets definitions of two new colorsets, SkillLevel, Competences and Constraints.

All colorsets (except SkillLevel colorset, which is independent) are generated based on a concrete model (or set of models). Example of the colorsets regarding Fig. 2 would be generated like (example is written in CPN ML language and provided without core colorsets described in our previous paper [3]):

```
colset Resources = with SCServer;
colset Artifacts = with IntegrationReport;
colset Workers = with Developer;
colset SkillLevel = int with 0..100;
colset Competences = with SourceControl;
colset Constraints = product Competences * SkillLevel;
var sl : SkillLevel;
```

4.2 CPN transformation rule

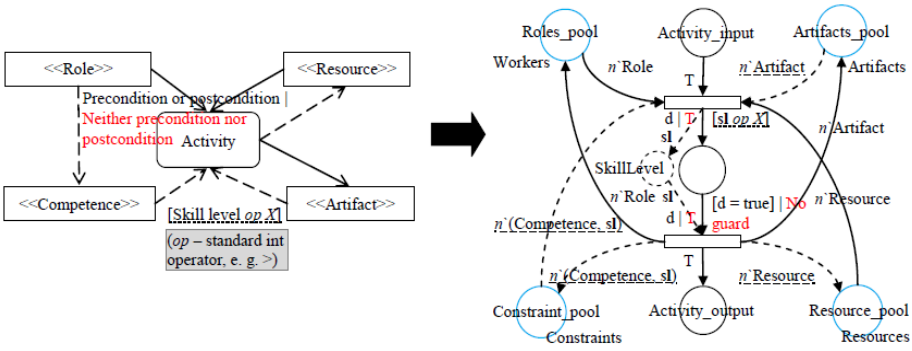

Fig. 3. Transformation rule

As you can see on Fig. 3 we have added two new places, the Constraint_pool with tokens of type Constraints and an anonymous place with tokens of SkillLevel. The Constraint_pool represents the same idea as other pools, acting as a reservoir of competences (with different skill level) which resources might have. If an activity needs resource (in a role) with certain competence (possibly with certain skill level), the competence needs to be available in the pool, otherwise the activity has wait for its execution. Constraint_pool place is connected with outgoing arc with first internal transition of the activity and a n`(Competence, sl) is used as an arc expression. This expression evaluates to multiset tuple, where the tuple is of product colorset, in this case the Constraints colorset. The first part of the expression (in brackets) tells us that we require a specific Competence, the second is a variable which will be (if possible) bound to certain value (from multiset of the place), more in [6]. The variable represents concrete Skill level value of a Competence which might be required by the activity. We use variable for two reasons. The first is, the Skill level was not specified (so we can use any matching Competence without paying attention to concrete level value). The second is, we can use sign operators (like greater than, lesser than etc.) to constrain the level, not only equals or not equals operator. Speaking of constraining the level value, the transformation rule contains a guard expression [sl op X], on the

first internal transition of the activity, which mirrors the guard in UML (of course the operator op is transformed from UML to CPN script language accordingly). As next, the anonymous place of type SkillLevel is then used for passing through the already binded sl variable so the incoming arc back to Constraint_pool place from second internal transition returns the same multiset of Constraints it took from Constraint_pool place when executing the first internal transition. Hence the same arc expression for the second arc between Constraint_pool place and an internal transition of the activity.

Object flows are drawn in dashed line as well as certain matching arcs (and arc expression underlined with that very same dashed line) and the skill level guard is underlined in dotted underline. It is because we are trying to point out that the competence mechanism is optional (hence the dashed lines and underlines) and specifying the skill level is even more optional. If execution of an activity is not restrained by competence mechanism, the arcs from Constraint_pool to internal transitions are not generated as well as the anonymous place used for passing the sl variable. Nevertheless, the Constraint_pool is always generated, it just not connected in case were competences are not needed. If an activity requires a resource with some competence but it doesn't require specific skill level, the skill level guard is not generated into CPN structure.

We have also decided to refactor artifact related arcs. We are not using the arc with n`ArtifactAsResource expression anymore to model situation where an artifact can be later used as resource. Instead we have replaced it with input arc to first internal transition from Artifact_pool which allows us to use artifacts also as resources. As with the dashed line in competence case, the dashed arc between first internal transition and Artifact_pool place suggest the arc is generated optionally based on whether any artifact is used as resource.

You can also notice the arc between Resource_pool and second internal transition is drawn as dashed. It means it is optional. The arc will be generated when specific resource is utilized. The arc won't be generated when resource is consumed, it means the concrete resource token won't return to Resource_pool place and therefore is lost.

5 Conclusion and Future Work

In this paper we have presented a refinement of our current research in terms of core modeling principles and the most important, the transformation rules. We have based our approach on our meta-model called Unified Process Meta-Model because we see great potential in this particular meta-model. The approach was enhanced by adding competences and few important changes were made mainly regarding modeling roles and artifacts. We have mentioned the ways you can analyze the CPN models and interpret data gained from simulation.

In the future, we would like to focus on enhancing the models even more with timed CPN which would allow us to incorporate duration information and make simulation and therefore simulation report (log) data more precise which would result in deeper process analysis and more precise error correction.

References

1. Aalst, W.M.P. van der, Hee, K.M., van, Houben, G.J. (1994). Modeling Workflow Management Systems with High-Level Petri-Nets, In G. De Michelis, C. Ellis, and G. Memmi, editors, Proceedings of the second Workshop on Computer-Supported Cooperative Work, Petri nets and related formalisms, pages 31-50, 1994.
2. Czopik J, Kosinar A. M., Stolfa J, Stolfa S. (2014). Addition of Static Aspects to the Intuitive Mapping of UML Activity Diagram to CPN. Paper presented at the Proceedings of the 1st international conference on Afro-European Conference for Industrial Advancement, Addis Ababa, 2014.
3. Czopik J, Kosinar A. M., Stolfa J, Stolfa S. (2014). Formalization of Software Process Using Intuitive Mapping of UML Activity Diagram to CPN. Paper presented at the Proceedings of the 5th international conference on Innovations in Bio-Inspired Computing and Applications, Ostrava, 2014.
4. Gomez-Perez A, Ramirez J, Villazon-Terrazas B. (2007). An ontology for modelling human resources management based on standards. Presented on 11th International Conference on Knowledge-Based Intelligent Informational and Engineering Systems.
5. Jennings, N.R., Faratin, P., Norman, T.J., O'Brien, P., Odgers, B. (2000). Autonomous agents for business process management, International Journal of Applied Artificial Intelligence 14(2), pp. 145–189.
6. Jensen, K., Kristensen, L.M. (2009). Coloured Petri Nets: modelling and validation of concurrent systems. Dordrecht: Springer. ISBN 978-3-642-00283-0.
7. Kammer, P.J., Bolcer, G.A., Taylor, R.N., Hitomi, A.S., Bergman, M. (2000). Techniques for supporting dynamic and adaptive workflow, Computer Supported Cooperative Work 9(3–4), pp. 269–292.
8. Klein, M., Dellarocas, C., (2000). A knowledge-based approach to handling exceptions in workflow systems, Computer Sup- ported Cooperative Work 9(3–4), pp. 399–412.
9. Kosinar A. M., Czopik J., Stolfa J., Penhaker M. (2015). Knowledge Framework for Clinical Processes Architecture and Analysis. Paper presented at the Proceedings of the 13th international Symposium on Applied Machine Intelligence and Informatics , Herlany, 2015.
10. Košinár, M., Štolfa, J., Štolfa, S. Knowledge Support for Software Processes (revisited). Paper presented at the 24th European-Japanese Conference on Information Modeling and Knowledge Bases, Kiel, Germany, 2014
11. Kuchar S, Martinovic J. (2013). Human Resource Allocation in Process Simulations Based on Competency Vectors. Presented on 7th conference on Soft Computing Models In Industrial And Enviromental Applications.
12. Narendra, N.C. Flexible support and management of adaptive workflow processes, Information Systems Frontiers 6(3), pp. 247–262, 2004.
13. Pesic M., van der Aalst W.M.P. (2007). Modelling work distribution mechanisms using colored Petri nets.
14. Radevski V, Trichet F. (2006). Ontology-based systems dedicated to human resources management: An application in e-recruitment. France.
15. Raffo, D.M. (1996). Modeling software processes quantitatively and assessing the impact of potential process changes on process performance, Carnegie Mellon University.
16. Vergidis K., Tiwari A., Majeed B., Business Process Analysis and Optimization: Beyond Reengineering. Systems, Man, and Cybernetics, Part C: Applications and Reviews, IEEE Transactions on 38 (1): 69-82, 2008.

A New Photogrammetric Tool for the Automatic Detection and Segmentation of Circular Objects in Low-quality Images

Karolína Feberová

Department of Computer Science, FEECS,
VŠB – Technical University of Ostrava, 17. listopadu 15, 708 33 Ostrava – Poruba
karolina.feberova@vsb.cz

ABSTRACT. The proposed paper describes an enhanced method for the automatic image object detection and segmentation. The presented method was added as a fully functional module into the new version of our photogrammetric software for the advanced image processing and analysis FOTOM^{NG}. The method has specialized in localization and processing of circular object despite its eventual inconsistency. Hough transformation was used for the circle detection. Consequently, the obtained information was used in the following segmentation using the active contour driven by the local Gaussian distribution fitting energy. Additionally, the segmentation and further processing of several objects simultaneously has been allowed from now.

Keywords: object detection, image segmentation, Hough circle transform, active contour model, level set method, ultrasound image

1 INTRODUCTION

The number of applications dealing with information hidden in images rises. This eventuates in strong demand for the computerization in the image processing. The new method for the detection and segmentation of mainly circular objects was developed for extending the existing photogrammetric software FOTOM^{NG}. The tool is capable of finding and signing the circle even in the low-quality, noisy or intensity inhomogeneous image. Moreover, the circular border of the object can be disrupted due to the high occurrence of artefacts within the certain images. And thus the following segmentation of that object would be imprecise. There is a need for the method efficient at recognition of small nuances in shape of particular object while respecting its circular basis.

The medical ultrasonic images of the carotid artery were chosen as a set of images apt for demonstrating the use of the newly developed tool. The assumption of pure circular lumen of artery was insufficient. In many cases, there was an atherosclerotic plaque fasten on the interior surface of artery and from the diagnostic's point of view, it was necessary to segment this plaque off.

© M. Krátký, J. Dvorský, P. Moravec (Eds.): WOFEX 2015, pp. 283–288.
VŠB – Technical University of Ostrava, FEECS, 2015, ISBN 978-80-248-3787-1.

2 MATERIALS AND METHODS

2.1 Image analysis and carotid artery detection

There are two main necessary pre-processing steps – contrast adjustment and image filtering. The contrast and the brightness in the ultrasound images are generally low. The CLAHE (Contrast Limited Adaptive Histogram Enhancing)[1] method was used as a first step of pre-processing process which leads to significantly better results in the subsequent artery detection.
The next pre-processing step is the speckle noise filtering, [2, 3]. During testing, it was experimentally determined that for subsequent edge detection and Hough transform, the conventional median filter seems to get the best results.
Edge detection is realized by a classical Sobel filter, followed by an iterative adaptive thresholding method.
The Hough transform (HT) has been used for artery detection in the edge image, especially HT for circle detection. Although the artery does not always have a circular shape, results obtained by artery detection with HT for circle detection were much better in comparison with the generalized HT detection and also with less computational complexity.

2.2 Artery reconstruction

An acoustic shadow artefact appeared in most of the analysed carotid artery ultrasonic images, especially when calcified plaque is present at the upper part of the artery. In this case, information about a large part of the artery wall is missing, which results in an unwanted contour development outside the area of interest. The solving algorithms for these phenomena are presented in [4].

2.3 New method for artery segmentation

In this section we introduce a method for segmentation based on a geometric active contour, especially contour minimizing Gaussian fitting energy [5] which we have modified in manner that acoustic shadow impact is being eliminated.
One of the most important geometric active contours based on level set methods is Chan and Vese contour [6]. Disadvantages of this contour reveal themselves during the segmentation of the image with brightness inhomogeneities like in the case of ultrasound images. This issue is solved by contours with local binary fitting energy [7]. This contour computes average values f_1 and f_2 in near area of each pixel only:

$$\begin{aligned} E^{LBF}(\phi, f_1, f_2) = {} & \lambda_1 \int \left[\int K_\sigma(x-y)|I(y) - f_1(x)|^2 H(\phi(y))dy \right] dx \\ & + \lambda_2 \int \left[\int K_\sigma(x-y)|I(y) - f_2(x)|^2 \left(1 - H(\phi(y))\right) dy \right] dx \\ & + \upsilon \int |\nabla H(\phi(x))|dx + \mu \int \frac{1}{2}(|\nabla\phi(x)| - 1)^2 dx \quad (1) \end{aligned}$$

λ_1a λ_2 are coefficients of data terms, υ is coefficient of smoothness, μ is a coefficient of regularization term minimizing distance of Level set space from a unit function and K_σ is a Gaussian distance function.
Gaussian fitness energy works locally, too. Data terms are based on probability model, such as

$$E_x^{LGDF} = \sum_{i=1}^{2} \int_{\Omega_i \cap O_x} -\omega(x-y) \log p_{i,x}(I(y)) dy \quad (2)$$

where

$$p_{i,x}(I(y)) = \frac{1}{\sqrt{2\pi}\sigma_i(x)} e^{\left(-\frac{(u_i(x)-I(y))^2}{2\sigma_i(x)^2}\right)} \quad (3)$$

Contour is trying to minimize probability that each pixel y with brightness value I(y) lies in a neighbourhood of pixel x belonging to the inner and outer area of contour, respectively. The level set is being deformed by minimization of following functional

$$E(\phi, u_1, u_2, \sigma_1^2, \sigma_2^2) = E^{LGDF}(\phi, u_1, u_2, \sigma_1^2, \sigma_2^2) + \upsilon L(\phi) + \mu P(\phi) \quad (4)$$

where

$$P(\phi) = \int \frac{1}{2} (|\nabla\phi(x)| - 1)^2 dx \quad (5)$$

is regularization term again and

$$L(\phi) = \int |\nabla H(\phi(x))| dx \quad (6)$$

is length term.
As mentioned before, ultrasound images of carotid artery contain acoustic noise artifact, especially when calcified atherosclerotic plaque is present. Since we know the position of artery center x_s in the image and its radius r_t from the previous step we can use this information in energy functional of contour as follows:

$$E_x^{LGDF} = \sum_{i=1}^{2} \int_{\Omega_i \cap O_x} -\varpi(x_s - y)\omega(y-x) \log p_{i,x}(I(y)) dy \quad (7)$$

where ϖ is new distance function given by

$$\begin{cases} \varpi(x_s - y) = 1; (x_s - y) \le r_t \\ \varpi(x_s - y) = 0; (x_s - y) > r_t \end{cases} \quad (8)$$

By Euler Lagrange minimization and gradient descent numeric solution we get

$$\frac{\partial\phi}{\partial t} = -\delta_\varepsilon(\phi)(e_1 - e_2) + \upsilon\delta_\varepsilon(\phi) \operatorname{div}\left(\frac{\nabla\phi}{|\nabla\phi|}\right) + \mu\left(\Delta\phi - \operatorname{div}\left(\frac{\nabla\phi}{|\nabla\phi|}\right)\right) \quad (9)$$

where

$$e_1(x) = \int_\Omega \varpi(x_s - y)\omega(y-x)\left[\log(\sigma_1(y)) + \frac{(u_1(x) - I(y))^2}{2\sigma_1(x)^2}\right] dy \quad (10)$$

and

$$e_2(x) = \int_{\Omega} \varpi(x_s - y)\omega(y - x)\left[\log(\sigma_2(y)) + \frac{(u_2(x) - I(y))^2}{2\sigma_2(x)^2}\right] dy \quad (11)$$

The advantage of this method is that the contour worked with original image without need of pre-processing operations. Difference between classical Gaussian fitting energy contour result and our modified contour result is shown in Figure 1.

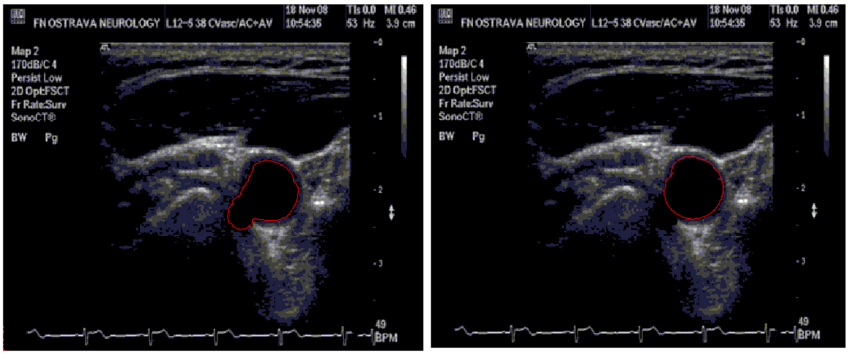

a b

Fig. 1. a) segmentation with classic Gaussian fitting energy contour, b) segmentation with modified Gaussian fitting energy contour

3 IMPLEMENTATION

The developed method was implemented into the photogrammetric software FOTOM[NG] [8] based on NetBeans platform. The various post-processing methods can be performed on the selected grey scale image. It is possible to simplify the continuous curve into the points of the polygon as shown in Figure 2. This formation could be forwarded to another module for further processing, e.g. the 3D modeling, or the measurement technics. The selection of fitting points enables computations in real metrics.

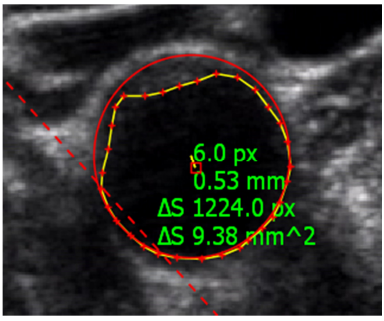

Fig. 2. Detected and segmented artery in FOTOM[NG]

4 RESULTS AND DISCUSSION

4.1 Artery detection results

For the artery detection algorithm testing, 1100 ultrasound images with transversal scan of carotid artery were taken. The artery was correctly found in 870 images. Tested data is available on our website [9].

4.2 Artery segmentation results

Results of artery segmentation algorithm were compared with manually obtained contours. All the tested results were obtained with following parameters of contour: Sigma of the Gaussian distance function was 5, λ_1 and λ_2 were 1, data term α was 20 and the length term μ was 65.025. The initial circle contour is placed into the found HT center and its radius was 25 pixels.
Static ultrasound picture evaluation is very subjective in many cases. It is often impossible to differentiate between the plaque and the noise, the obtained result rather depends on physician's experience. Despite these facts, the manually obtained contour was considered as a correct (reference) measurement. The area signed by the described automatic artery segmentation algorithm that does not overlap the reference regions, was taken as an error measured in mm2. The segmentation was tested on 60 images. Results are shown in Figure 3.

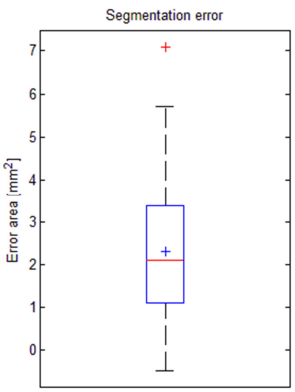

Fig. 3. Segmentation error boxplot

5 CONCLUSION

This paper presented the new method for automatic detection and segmentation of circular objects in low-quality images. The detection was performed using the

Hough transform, the segmentation stemmed from active contour driven by local Gaussian distribution fitting energy, but was modified with respect to circular character of the object. The research showed that the reliability of the proposed method is 79.1% in detection. Average segmented error area is 2.311mm2. The method was implemented into the modular photogrammetric software FOTOM^{NG}.

ACKNOWLEDGEMENTS.

The following grant is acknowledged for the financial support provided for this research: partially supported by Grant of SGS No. SP2015/142.

REFERENCES.

[1] Pizer S.M., Amburn E.P. A Austin, J.D., Adaptive Histogram Equalization and Its Variations. Computer Vision, Graphics, and Image Processing, vol. 39, pp 355-368, 1987.

[2] Szabo T. L., Diagnostic ultrasound imaging: inside out. 1st ed., Boston: Elsevier Academic Press, 2004, ISBN 01-268-0145-2.

[3] Loizou C., Ultrasound image analysis of the carotid artery. Disertation. Kingston university, School of Computing and Information Systems, London, 2005. Retrieved from http://www.medinfo.cs.ucy.ac.cy/doc/Publications/PhD/CLoizou/PhD_CLoizou.pdf.

[4] Ličev L., Tomeček J., a Farana R., Adjusting the input ultrasound image data and the atherosclerotic plaque detection in the carotid artery by the Fotom^{NG} system, Biotechnology & Biotechnological equipment, pp 567-575, 2013. ISSN 1310-2818

[5] Wang L., He L., Mishra A., Li C., Active contours driven by local Gaussian distribution fitting energy, Signal Processing [online], vol. 89(12), pp 2435-2447, 2009. [cit. 2015-01-31].

[6] Chan T.F., Vese L.A., Active Contours Without Edges. IEEE Trans. on Image Proces., vol 10, pp 266-277, 2001.

[7] Li C., Kao C.-Y., Gore J.C., Ding Z., Minimization of Region-Scalable Fitting Energy for Image Segmentation, IEEE Transactions on Image Processing [online], vol. 17(10), pp 1940-1949, 2008. [cit. 2015-01-31].

[8] FOTOM^{NG} available from http://www.cs.vsb.cz/licev/

[9] Ultrasound test images retrieved from www.cs.vsb.cz/licev/experiments/test4.zip

PUBLICATIONS PRESENTING AND ACHIEVEMENTS

Lichev, L., Feberová, K., Tomeček, J. a Hendrych, J.: A NEW PHOTOGRAMMETRIC TOOL FOR THE AUTOMATIC DETECTION AND SEGMENTATION OF CIRCULAR OBJECTS IN LOW-QUALITY IMAGES, Albena, Bulgaria: 15th International Multidisciplinary Scientific GeoConference SGEM 2015, 8 p., p. 003-010, ISSN 1314-2704, 17-25. June. 2015.

High Performance Computing Framework for Uncertainty Modelling in a Flood Monitoring System

Martin Golasowski

Department of Computer Science, FEECS,
VŠB – Technical University of Ostrava, 17. listopadu 15, 708 33 Ostrava – Poruba
martin.golasowski@vsb.cz

Abstract. Uncertainty modelling is a vital part of flood monitoring and prediction process. Rainfall-Runoff simulations enhanced by uncertainty modelling have better informational value for the end-user and can siginificantly improve disaster management process in case of an ongoing emergency. This paper describes high performance uncertainty modelling framework which was developed as a part of the Floreon$^+$ disaster management system.

Keywords: rainfall-runoff, flood, uncertainty modelling, high performance computing, framework

1 Introduction

Main purpose of an automatic online flood monitoring and prediction system is to provide accurate and actual insight to current development of hydrologic situation on a river and to provide an early warning in case of ongoing flood situation. The system gathers current meteorological data from various sources and periodically runs hydrologic models. Results of the simulations are visualised in a web-based interactive map application. The application is used by local authorities in the event of an extreme weather as an additional source of current information in the disaster management process. Architecture and operation of such system is described in Section 2.

Our primary goal is to assure best possible accuracy of the simulations which can be negatively affected by several factors. These factors include inaccuracy of the modelling methods and inaccuracy of the input data. Influence of the first factor can be lowered by using several different types of models in single simulation and by interpreting the results together. The second factor can be lowered by running uncertainty simulation of selected input parameters (e.g. forecasted rainfall). Results of the uncertainty simulation combined with output of a regular simulation provide additional information to the end-user and enables a probabilistic view on a possible scenarios that can occur in the near future.

Running an uncertainty simulation usually involves running a large number of independent simulations which can be a lengthy task using conventional computers. Beside computational complexity, time constraint is another very important

© M. Krátký, J. Dvorský, P. Moravec (Eds.): WOFEX 2015, pp. 289–294.
VŠB – Technical University of Ostrava, FEECS, 2015, ISBN 978-80-248-3787-1.

factor in a flood monitoring system since we have to deliver the most actual results as soon as possible with the best accuracy. Hence, usage of highly scalable algorithms developed and executed on high performance computing (HPC) infrastructure is very convenient. Our proposal for uncertainty modelling method based on the well known Monte Carlo approach [5, 7] is described in Section 3

However, a several problems appeared when we attempted to apply our uncertainty modelling method on several different hydrologic models which are primarily unsuitable to run in the HPC environment. Each model uses different formatting of input and output data and is executed differently. We had to create a software framework which provides a common interface for input and output data and for execution of multiple model simulations in parallel. Detailed description of the framework as well implementation of the uncertainty modelling method is described in Section 4. The created framework have been integrated and extensively tested with hydrologic models which are part of the Floreon$^+$ system [2]. Results of scalability experiments based on real-world data are presented in Section 5.

2 Flood monitoring and prediction process

This section describes flood monitoring a prediction process implemented in the Floreon$^+$ disaster management system. Two main types of input data are retrieved at the beginning of the process. Measured data are provided by the Odra catchment management office from their network of hydrologic gauges every 10 minutes. The data set contains current observed water levels, discharge values, precipitation rates and temperatures. Meteorological forecast is the second type of the input data and is provided by Academy of Sciences of the Czech Republic from their MEDARD regional model approximately every 6 hours. These forecasts contain precipitation rates, temperatures, wind velocities and wind directions and are issued for the next 72 hours.

2.1 Rainfall-runoff simulations

Rainfall-runoff (RR) model is a dynamic mathematic model that transforms rainfall to water discharge levels by modelling individual parts of the RR process [1]. Two models used in the Floreon$^+$ system are HEC–HMS model which is developed by US Army corps of engineers and Math1D model which is developed internally. Both models are semi–distributed event RR models. Standard RR simulation consists of 5-day long period of measured precipitation, 2-day long period of forecast precipitation, each set having a time step of one hour.

3 Uncertainty modelling of input parameters

Our uncertainty modelling approach is an implementation of the well known Monte Carlo method. Large number of input data sets are sampled from the RR

model input space represented by a probability distributions corresponding to each modelled parameter. RR simulation is executed for each of the generated input data sets. By picking selected p-percentiles from all results of the performed RR simulatons, confidence intervals of the simulated water discharge are formed. Each interval represents boundaries in which values of a model output can occur with a certain probability. The intervals are combined with output of a given standard RR simulation to provide additional information about precision of the simulation output.

Input space of the RR model can be roughly divided in two parts. First part is the parameterization of modelled catchment area represented by various fitted parameters such as Manning's roughness coefficient or CN curve number (SCS-CN method) [1]. It is difficult to obtain correct probability distributions for these parameters as their values are usually obtained as a result of calibration or are determined by a domain expert, hence our method allows to use only known probability distributions such as the Gaussian or uniform [5, 7].

Second part of the input space is the precipitation which can be either measured or forecast. This part of the input space has much larger influence on the output of the model and its precision can significantly affect precision of the RR simulation result. Common sources of precipitation forecast are global or regional numerical models (such as ALADIN or MEDARD). Using statistical analysis of historic forecast and measured precipitation data probability distribution of the forecast error can be determined. Probability distribution of the forecast error is inferred using a non-parametric kernel density method. Precipitation forecast data sets for the individual Monte Carlo runs are generated using the obtained probability distribution [5, 7].

4 Modelling framework

Uncertainty modelling has a positive impact on precision of RR simulations. However, problems arise when attempting to implement uncertainty modelling method for different RR models. Altough the modelling method is universal in the RR modelling domain, each model used in the Floreon$^+$ system has a different interface for communication.

At the same time, execution of the models has to be as fast as possible which is only achievable by concurrent execution of the simulations on the HPC infrastructure. This lead us to idea to create an application framework that would allow us to generalize paramerization, execution and gathering of results of all supported models. Various methods including calibration and uncertainty modelling can be built on top of the framework sharing the same interface for communication with models. Execution of the model itself can be parallelised independently on the method and vice versa. Deployment of the framework to the HPC infrastructure assures short execution times which is very convenient for its application in the Floreon$^+$ system.

Structure of the framework is shown in Figure 1. The topmost layer of the framework is represented by abstract class *ModelAdapter* which contains a con-

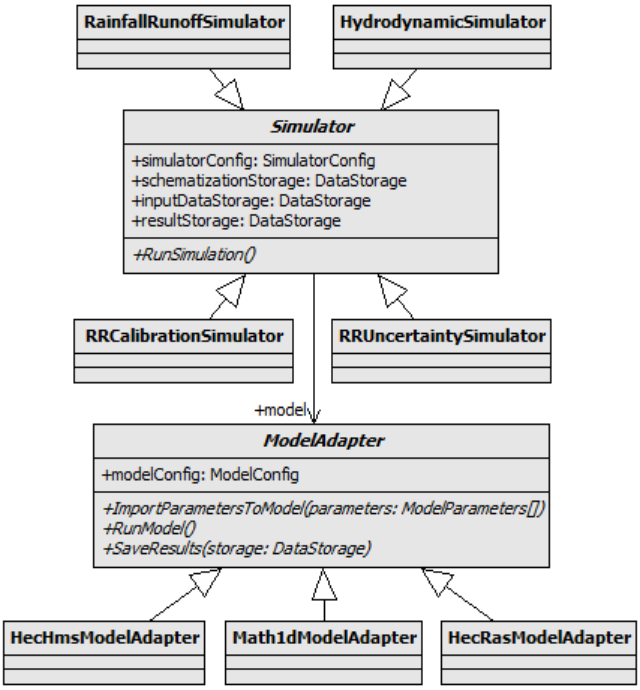

Fig. 1: Class structure of the simulator framework

figuration for the currently used model (e.g. information about the model executable, specific internal parameters, log files, etc.) and three main abstract methods *ImportParametersToModel()*, *RunModel()* and *SaveResults()*. Concrete subclass of this abstract class provides implementation of these methods for specific model, e.g. HEC-HMS.

Second layer of the framework is the *Simulator* abstract class and its subclasses. This layer contains implementation and high-level parallelization of modelling and simulation methods used in the Floreon$^+$ system and use the model abstraction layer for their execution.

5 Experiments

Experiments presented in this section were performed for heavy rainfall situation which occured between 12–15 May 2010 at catchment area of the Ostravice river. The river is located in Moravian–Silesian region of the Czech Republic. Measured rainfall data were used for the first 5–day period of the simulation, forecast data were used for the last 2 days. Both types of data have frequency of 1 hour. All experiments were performed on the Anselm supercomputer which is operated

by the IT4Innovations Czech supercomputing center. Results of the scalability experiments are presented in Table 1.

Table 1: Run times [s] of uncertainty simulations for given model

(a) Math1D

MPI Ranks	Samples			
	1,000	10,000	50,000	100,000
1	30	296	1,391	2,774
2	48	143	719	1,431
4	43	76	381	741
8	46	62	226	431
16	78	99	189	297
32	165	175	240	298

(b) Math1D HEC-HMS

MPI Ranks	Samples	
	1,000	10,000
1	2,964	–
2	1,139	–
4	541	–
8	318	6,077
16	274	3,107
32	247	2,311

The Math1D model simulations scale successfully for up to 16 MPI processes for 100 000 samples. The HEC-HMS simulations stop scaling around 16 MPI processes for 1000 samples and around 32 MPI processes for 10 000 samples.

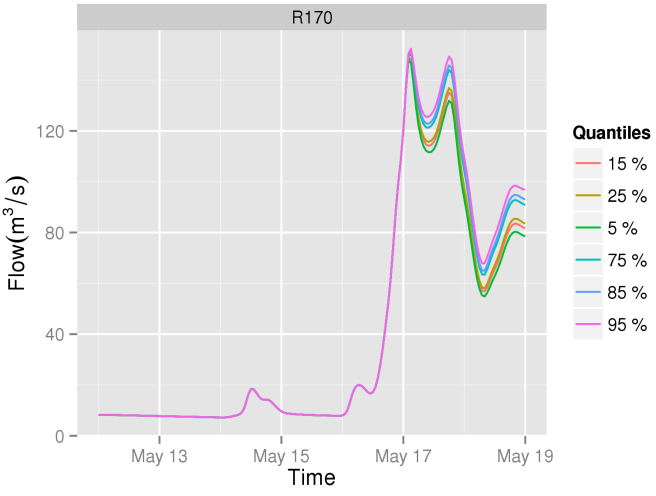

Fig. 2: Uncertainty simulation for 10 000 samples for station Sviadnov

The Math1D simulations are executed on 16 threads per MPI process simultaneously and have smaller memory footprint that HEC-HMS simulations. This

allows us to effectively run simulations up to 100 000 samples. In the case of the HEC-HMS model the model itself runs in 16 Java threads, therefore it is not viable to run more than one instance of the model per MPI rank. Example of hydrograph with confidence intervals formed by uncertainty simulation is in Figure 2.

6 Conclusion and future work

Thanks to the created framework we have been able to implement the uncertainty modelling method universally for the Math1D and HEC-HMS RR models. The framework further enables us to implement various uncertainty and calibration methods only once and apply them to any supported model.

The total duration of simulations for all catchments in the Moravian-Silesian region would take several hours to complete when ordinary personal computers are used. Thanks to the framework and its deployment to a HPC cluster we are able to deliver results from uncertainty simulations to end-users much faster in a matter of minutes. More results of work based on this research has been published in [3–7].

References

1. Beven K. Rainfall-Runoff Modelling – The Primer, Wiley-Blackwell, Second edition, 2012.
2. Martinovic J., Kuchar S., Vondrak I., Vondrak V., Sir B., Unucka J. Multiple Scenarios Computing In The Flood Prediction System FLOREON, in Proceedings of the 24th European Conference on Modelling and Simulation, Simulation Meets Global Challenges (ECMS 2010), Kuala Lumpur. ECMS, 2010, pp. 182–188.
3. Portero A., Kuchar S., Vavrik R., Golasowski M., Vondrak V. System and Application Scenarios for Disaster Management Processes, the Rainfall-Runoff Model Case Study, 13th International Conference on Computer Information Systems and Industrial Management Applications, CISIM'2014. November 2014, Ho Chi Minh City, Vietnam.
4. Kuchar. S., Golasowski. M., Vavrik. R., Podhoranyi, M., Sir B., Martinovic, J. Using High Performance Computing for Online Flood Monitoring and Prediction World Academy of Science, Engineering and Technology, International Science Index 101, International Journal of Environmental, Ecological, Geological and Geophysical Engineering ,2015, 9(5), pp. 267–272.
5. Golasowski M., Kuchar S., Podhornyi M., Vojtek D., Uncertainty Modelling in Hydrodynamic Simulations using the Parallel Monte Carlo Method, in Proceedings of the Fourth International Conference on Parallel, Distributed, Grid and Cloud Computing for Engineering , Civil-Comp Press, Stirlingshire, UK, Paper 10, 2015.
6. Vondrak V., Kuchar S., Golasowski M., Vavrik V. and Martinovic J. Scalable Algorithms for Inverse and Uncertainty Modelling in Hydrology The Fifteenth International Conference on Civil, Structural and Environmental Engineering Computing (CC2015) Prague, Czech Republic (accepted and revised)
7. Golasowski, M., Litschmannova M., Kuchar S., Podhoranyi M., Martinovic J. Uncertainty Modelling In Rainfall-Runoff Simulations Based On Parallel Monte Carlo Method Neural Network World (accepted and revised)

Analysis of Medical Images, Using Active Contours Optimized by Self-Organizing Migration Algorithm

Jakub Hendrych and Radim Kunčický

Department of Computer Science, FEECS,
VŠB – Technical University of Ostrava, 17. listopadu 15, 708 33 Ostrava – Poruba
{jakub.hendrych, radim.kuncicky}@vsb.cz

Abstract. In this paper, we deal with the image segmentation performed by active contours and optimized by evolution algorithm. The purpose of this algorithm is to find best possible parameters of the active contour for the segmentation of objects of interest in ultrasonic images. The segmentation of these objects is highly significant from a medical perspective, considering for example atherosclerostic plaque in carotid arteries. Here, we describe procedures employing a combination of common methods and evolutionary algorithms, namely the self-organizing migrating algorithm (SOMA). We use SOMA to optimize the energy function of deformable models used to approximate the locations and shapes of object boundaries in images. We suppose that SOMA can be used to find the desired global solution. Evolutionary algorithms are based on evolution principles found in nature and respect Darwin's theory of natural selection according to the defined cost function and gene recombination and mutation.

***Keywords*:** medical, imaging, artery, segmentation, contour, snake, SOMA, evolutionary algorithms

1 Introduction

This article describes the process of segmentation based on active contour model optimized by evolution algorithm. With the help of this algorithm we are looking for ideal parameters to optimize the energy of active contours used in segmentation of objects within the medical. From a medical point of view, it is important to be able to segment objects such as atherosclerotic plaque in carotid arteries [1] or the intima-media thickness in the distal part of the common carotid artery.

Evolutionary algorithms are search methods that can be used for solving optimization problems. They mimic working principles from natural evolution by employing a population–based approach, labeling each individual of the population with fitness and including elements of random, albeit the random is directed through a selection process. In this paper, we review the basic principles of selected evolutionary algorithm and discuss its use in com-

© M. Krátký, J. Dvorský, P. Moravec (Eds.): WOFEX 2015, pp. 295–300.
VŠB – Technical University of Ostrava, FEECS, 2015, ISBN 978-80-248-3787-1.

puter graphics. In doing so, it is particularly shown how the fundamental understanding of natural evolution processes has cleared the ground for the origin of evolutionary algorithms. The self-organizing migrating algorithm (SOMA) [2] belongs to the family of evolutionary algorithms. This algorithm works with a population of individuals that migrate in the space of possible solutions.

In addition, this article describes procedures that employ common principles and methods for recognizing regions of interest in images that may serve in finding and determining the coordinates, shape properties and other valuable parameters of the analyzed objects. There is an entire class of algorithms and methods for extracting segments with certain parameters from rather specific classes of medical images. The rest of the paper briefly describes individual medical examinations, addresses some common tools for image segmentation, focuses on active contours and describes the optimization of active contour parameters by SOMA.

2 Materials and Methods

2.1 Segmentation, active contours and objects of interest recognition

With technological development of tools the subsequent images are getting more efficient. But even so, we need to distinguish every single object of interest, which will be further processed. One technique of digital image processing is segmentation, which provides methods for dividing an image into different regions with common characteristics.

Example of such method is active contour (snakes). Unlike thresholding, this method is preferred for multimodal images containing noise. The input of this method is initializing of a contour (curve), which surrounds a segment containing the object of interest. The output is an exact contour of the object. The principle is therefore based on the edge detection of the object in an image. Successive shaping of contour is controlled by two forces. The first one, internal force, is control bending, stretching curve and forming the contour towards to the edge of the object of interest. The second one, external force, usually represents the initial location of contour in the analyzed image. In recent years the trend is to use the above mentioned method of segmentation to identify objects of interest. Yet the most common problems, for example with using active contours, is forming boundary concavities at the edges or placing initialization curve, which should be as close to the edge of the object of interest, otherwise the algorithm may lead to an incorrect result. In [3], authors deal with these problems of active contours. They describe a new class of external forces, called Gradient Vector Field (GVF). We adopt this approach in our attempt to obtain the contour of the object of our interest in a medical image.

The active contour (snake) is represented as a curve $\boldsymbol{x}(s) = [x(s), y(s)]$, $s \in [0, 1]$, that moves through the spatial domain of an image I to minimize the energy functional:

$$\boldsymbol{E} = \int_0^1 \frac{1}{2}(\boldsymbol{\alpha}|\boldsymbol{x}'(\boldsymbol{s})|^2 + \boldsymbol{\beta}|\boldsymbol{x}''(\boldsymbol{s})|^2) + \boldsymbol{E_{ext}}(\boldsymbol{x}(\boldsymbol{s}))\boldsymbol{ds} \qquad (1)$$

Where α and β represent the weighting parameters that control the tension and rigidity of the curve, $x'(s)$ and $x''(s)$ denote the first and second derivatives of $x(s)$ with respect to s. External energy is represented by the function denoted E_{ext} and can be computed as:

$$\boldsymbol{E_{ext}}(\boldsymbol{x}, \boldsymbol{y}) = -|\boldsymbol{\nabla}[\boldsymbol{G_\delta}(\boldsymbol{x}, \boldsymbol{y}) * \boldsymbol{I}(\boldsymbol{x}, \boldsymbol{y})]|^2 \qquad (2)$$

Where G_δ denotes a two-dimensional Gaussian function with standard deviation δ and ∇ denotes the gradient operator. A contour that minimizes energy E must satisfy the Euler equation, which can be viewed as a force balance equation:

$$\boldsymbol{F_{int} + F_{ext} = 0} \quad (3)$$

Where $F_{int} = \alpha \boldsymbol{x}''(s) - \beta \boldsymbol{x}''''(s)$ and prevents the curve from excessive stretching and bending. The $F_{ext} = -\nabla E_{ext}$ pulls snake towards the desired image contour. To find a solution to equation (3) we need to make it dynamic in time t until it stabilize. Then we still need to define external force F_{ext}. In [3] F_{ext} is defined as $\boldsymbol{v}(x, y)$, where $\boldsymbol{v}$ represents the Gradient Vector Field (GVF). After substituting the term $-\nabla E_{ext}$ we get:

$$\boldsymbol{x_t(s,t) = \alpha x''(s,t) - \beta x''''(s,t) + v} \quad (4)$$

Where $\boldsymbol{v}$ is evaluated as $\boldsymbol{v}(x, y) = [u(x, y), v(x, y)]$, that minimizes the energy functional:

$$\boldsymbol{\varepsilon = \iint \gamma\left(u_x^2 + u_y^2 + v_x^2 + v_y^2\right) + |\nabla f|^2 |v - \nabla f|^2 dx\, dy} \quad (5)$$

Where f denotes the edge map [3]. The parameter γ is a regularization parameter governing the tradeoff between the first term and the second term. This parameter should be set according to the amount of noise present in the image (more noise, increase γ).

In (5) we see that, when ∇f is zero, the energy is dominated by partial derivatives of the vector field. But if ∇f has large value, the second term dominates the integrand, and is minimized by setting $\boldsymbol{v} = \nabla f$.

2.2 Selected parameters

To obtain the desired contour, we should investigate every possible combination of selected GVF field and contour evolution parameters. We selected 4 distinct parameters. Values of these parameters represent innovative implementation in the medical image processing field. Namely α, β, γ and Gaussian kernel width. Those parameters are forming 4-dimensional parameter space. Evolutionary algorithm (EA) is expected to find the optimal parameters in terms of better convergence of the contour energy function (i.e. obtaining the solution in significantly lesser number of steps in comparison to the naive approach when the user is responsible for setting the right parameters for every processed image).

2.3 Used evolution algorithm

To find the optimal values of selected parameters for active contour algorithm, we have used Self-Organizing Migration Algorithm (SOMA) [3, 4]. It is a member of the evolutionary algorithm class because of similar results obtained with EA that are equivalent to the results from one generation derived by the classic EA except the fact that there are no new individuals – offspring. It also behaves similarly like Genetic Algorithms (GA) [5, 6] and Differential Evolution (DE) [7, 8].

The principles of SOMA can be described as follows. Each specimen is fully described by vector of parameters. Each parameter is of certain type (e.g. real or integer) with some predefined upper and lower borders representing the valid range of values. The population consists of many individuals and can be represented as an M × N matrix, where M stand for number of parameters and N represents number of individuals. Each individual represents an estimate trying to minimize (or maximize) the cost function. In the ideal state when we get exactly the desired solution, value of the cost function will be maximal. It is clear that such a function is multimodal and it is difficult to find its global minimum. The cost function is described in detail in the next chapter. At the beginning of the evolutionary process we randomly initialize each specimen of the population.

This algorithm works on the following principle: In the first population, the SOMA parameters are set randomly according to their low and high bounds. The fitness function is computed on the basis of active contours result. Then the algorithm continues like standard AllToOne SOMA algorithm. If the fitness computation is necessary, algorithm for active contours is used and parameters from the individual are used as parameters of the algorithm for active contours computation. Intrinsic parameters of SOMA algorithm were set according the guidance of [2, 4].

The main strategy has been briefly outlined above. Now the algorithm SOMA – AllToOne will be described in detail. The algorithm works with population of individuals, which migrates, to the best individual, we call it Leader. Leader has the best fitness value (the smallest or the greatest value) in the actual migration loop. During each migration cycle new Leader is chosen. Each individual moves to the Leader in steps (the parameter is marked as Step) as long as the Step value does not overshot the value of the parameter PathLength. The individual can move to the Leader in many directions. Parameter PRT means perturbation and it determines in which direction the individual will move. The PRT vector prevents the individual from movement in a given dimension in scanned space.

The precise equation of the individual motion to the Leader is described in Eq. (3):

$$\boldsymbol{x}_{i,j}^{ML+1} = \boldsymbol{x}_{i,j,start}^{ML} + \left(\boldsymbol{x}_{L,j}^{ML} - \boldsymbol{x}_{i,j,start}^{ML}\right) * \boldsymbol{t} * \boldsymbol{PRTVector}_j \qquad (3)$$

Where $\boldsymbol{x}_{i,j}^{ML+1}$ is the value of j-th parameter of the i-th individual in the next migration loop $ML+1$, $\boldsymbol{x}_{i,j,start}^{ML}$ is the value of the i-th individual with parameter j in the actual migration loop ML, $\boldsymbol{x}_{L,j}^{ML}$ is the value of the j-th parameter of the Leader in current migration loop. Parameter t denotes value of Step and $PRTVector_j$ is the j-th parameter of $PRTVector$ [9].

2.4 Fitness Function

The linkage between the SOMA algorithm and the active contour model is the cost (fitness) function. The function has to be designed in manner that it describes the quality of the resulting contour. During the research, we experimented with number of different types of functions. The function overlap ratio turned out to be the most appropriate for our purposes. It described the coverage of desired element very well, it was sensitive for inaccurate segmentation and it correctly penalized even small imprecisions. Overlap ratio is defined as:

$$\boldsymbol{Overlap\ ratio} = \frac{\boldsymbol{TP}}{\boldsymbol{FN+TP+FP}} \qquad (4)$$

Where TP are correctly indicated points, FN are false positive and TN are true negative. The function reaches its global maximum in 1 and that comports with the moment when the contour generated by computer corresponds to the reference image.

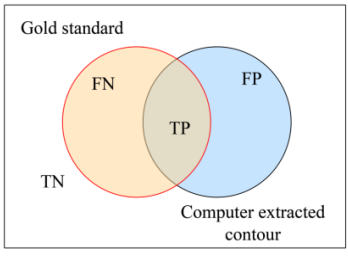

Fig. 1. Overlap areas

Table 1. Used SOMA parameters

PathLength	3
Step	0.11
PRT	0.15
PopSize	60
Migrations	30
MinDiv	0.005

3 Results and Discussion

In this research paper one of modern evolutionary algorithms, class of memetic / swarm intelligence algorithms called SOMA has been used for segmentation methods. Parameters of the algorithm used during the experiment are listed in the table 1. It is obvious that the algorithm was set for the possibly most sensitive searching in space.

In the figure 2, there are the leaders of population during the algorithm process. The figure shows the very low quality of the population in the beginning. However, during the next few migrations, it improved rapidly. The consequent migrations brought only the partial improvement. Parameters of population before and after the optimization are taken down in the table 2. The low variance of the generated population is caused by the very high occurrence of individuals with low or even zero value of the cost function.

Table 2. Results of algorithm

Before:	Leader:	0,3048	Running time:	1 372 min
	Mean of population	0,0236	Number of evaluated contours:	50 971
	Variance of population	0,0034	Processing speed:	37 / min
After:	Leader:	0,9871		
	Mean of population	0,8629		
	Variance of population	0,0848		
Testing system: AMD Phenom II X6 1055T, 4GB RAM, Parallelized				

There is a disadvantage - computation of the gradient vector field and the development of active contours are computationally very demanding and therefore it is necessary to use powerful computers. Using these tools were identified objects of interest, in the image, calculated its position and figure orientation. All this improvements led to the better object's parameter identification. The use of evolutionary algorithms was achieved repeatable measurement accuracy excluding the impact of the human factor, producing uncertainty, with guaranteed sufficient quality evaluation area of all objects, with subsequent use of FOTOM^{NG} in clinical practice.

It should be mentioned that during testing the ultrasound images that were previously handled by the system FOTOM^{NG} were used. The processing included binary thresholding and repair of artery borders. These tools are the first step of preprocessing and makes the whole process easier for the user.

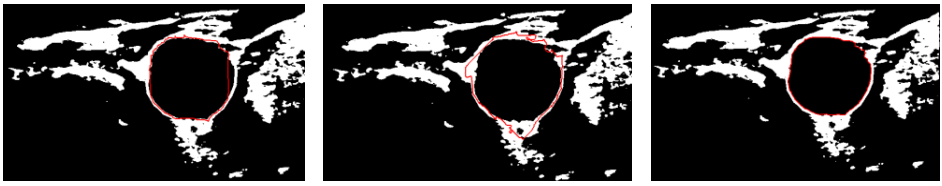

a) 3 - 0.84 **b**) 4 - 0.92 **c**) 20 - 0.98

Fig. 2. a - c Leader progress during migrations. Migration – fitness.

4 Conclusion

In this paper we have described our experience with medical image segmentation. We focused on active contour algorithm based on GVF field for segmenting challenging images of carotid artery.

To accommodate the algorithm to medical practitioners we use the SOMA algorithm to automatically refine the parameters of GVF computation and active contour evolution part. In the further development we would like to extend the number of those parameters (e.g. parameters of initial curve) to handle wider range of images. The devised approach is repeatedly applicable on various medical images depicting objects of our interest.

Used SOMA algorithm was set according to the best knowledge [2] and obtained results was sufficient. For the future research we plan to use more modern evolutionary algorithms in order to get richer set of mutually comparable results. All the processing algorithms were implemented into the photogrammetric software FOTOM^{NG}.

Acknowledgements

The following grant is acknowledged for the financial support provided for this research: partially supported by Grant of SGS No. SP2015/142.

References

1. Bar, M., Roubec, M., Farana, R., Ličev, L., a Školoudík, D. Interrater Agreement in Carotid Atherosclerotic Plaque Quantification by 3D Ultrasound. Journal Cerebrovascular Diseases, 2013, 35:390-390.
2. Zelinka, I.: SOMA - Self Organizing Migrating Algorithm. In: Onwubolu, Babu, B. (eds.) New Optimization Techniques in Engineering. Springer, New York (2004).
3. Xu Ch., Prince J. L. Snakes, Shapes, and Gradient Vector Flow, IEEE Transactions on Image Processing, 1998, 7:359-369.
4. Onwubolu, G. C. Babu, B. V. New Optimization Techniques in Engineering, Springer, 2004.
5. Back, T., Fogel, B., Michalewicz, Z.: Handbook of Evolutionary Computation, Institute of Physics, London (1997)
6. Holland, J.: Genetic Algorithms. Sci. Am., 44–50 (1992)
7. Feoktistov, V.: Differential Evolution - In Search of Solutions. Springer, Heidelberg (2006)
8. Price K., Storn R., et al.: Differential Evolution – A Practical Approachto Global Optimization. Springer, Heidelberg (2005)
9. Coelho, L. S.: Self-organizing migration algorithm applied to machining allocation of clutch assembly, Mathematics and Computers in Simulation. 2009; 80:427-435.

Geodesic Distance and k-max Geodesic Distance in Image Segmentation

Michael Holuša

Department of Computer Science, FEECS,
VŠB – Technical University of Ostrava, 17. listopadu 15, 708 33 Ostrava – Poruba
michael.holusa@vsb.cz

Abstract. The geodesic distance is commonly used when solving image processing problems. In noisy images, unfortunately, it often gives unsatisfactory results. This fact was a motivation to find a new distance that performs better. Therefore, we proposed a k-max geodesic distance whose length of path is defined as the sum of the k maximum edge weights along the path. The distance is defined as the length of the path that is the shortest one in this sense. With an appropriate choice of the value of k, the influence of noise can be reduced substantially. The properties of this distance are demonstrated on the image segmentation and the results are compared with the results of geodesic distance.

1 Introduction

Finding the distance between points is an important task in computer science with many applications in data clustering or image processing [2, 4]. The geodesic distance [7] is a commonly used distance measure in many tasks of image processing, especially in the image segmentation [3, 1, 6, 8]. This distance is defined as the shortest path in the weighted graph that corresponds to the image (the weights reflect the brightness differences between the endpoints of edges).

Although this distance is frequently used, it is also known that it is sensitive to noise in image, which negatively influences the results. This was a motivation to find a distance that ignores the noise if possible and takes into account only the important brightness changes, such as edges. If we assume that the noise is reflected by the low-weighted edges, while the relevant image information is in the edges with higher weights, the sensitivity to noise may decrease by considering only few edges on each path with the highest weights.

Therefore, we proposed the k-max geodesic distance, where the length of path is defined as the sum of the k maximum edge weights along the path. For illustrating the properties of the k-max geodesic distance and for its comparison with the geodesic distance, the image segmentation is used.

The paper is organized as follows. The problems of geodesic distance are presented in Section 2. Section 3 describes the k-max geodesic distance. The results and comparisons of both distances are presented in Section 4. Section 5 is a conclusion. We note that in the rest of the paper, we will simply say k-max distance instead of the long name k-max geodesic distance.

© M. Krátký, J. Dvorský, P. Moravec (Eds.): WOFEX 2015, pp. 301–306.
VŠB – Technical University of Ostrava, FEECS, 2015, ISBN 978-80-248-3787-1.

2 Geodesic Distance

In this section, we focus on the geodesic distance and its behavior in images. Consider a graph with two nodes, denoted by A and B, respectively. Let P be a path connecting A and B; $P = (v_{p_1}, v_{p_2}, v_{p_3}, \ldots, v_{p_n})$, where v_{p_i} are the nodes through which the path is running; $v_{p_1} \equiv A$, $v_{p_n} \equiv B$. The geodesic length of path is the sum of the weights of all its edges, i.e., $l_{\mathrm{g}}(P) = \sum_{i=1}^{n-1} w_{(p_i,p_{i+1})}$. Let $\mathcal{P}_{AB}$ be the set of all existing paths between A and B in the graph. The geodesic distance between A and B is then defined as $d_{\mathrm{g}}(A, B) = \min_{P \in \mathcal{P}_{AB}} l_{\mathrm{g}}(P)$.

In image processing, the weight of edge is often determined by the equation

$$w_{i,j} = 1.0 - e^{-\frac{(b_i - b_j)^2}{2\sigma_w}} + \beta\,, \tag{1}$$

where b_i, b_j are the values of brightness at the v_i and v_j node, respectively; σ_w is a constant. The value of β determines the price for using the edge regardless how big the brightness difference between its endpoints is. It can also be $\beta = 0$, which reflects the fact that the pixels with the same brightness are regarded as close to each other; the points may be geometrically distant in the xy plane but they should create one segment. In the rest of the paper, we consider $\beta = 0$.

Fig. 1. An example of image with two segments. The segments are labeled by the seed points (black and white point).

Let us now show the behavior of geodesic distance in the image segmentation. Consider an image with two segments: the object and the background (see Fig. 1). Let O and B denote the object (black dot) and the background (white dot) seed, respectively. Let x measure the coordinates of points along the shortest path between O and B; $I(x)$ stands for brightness at x; $d_{\mathrm{g}}(O, x)$ is the distance between the object seed and the point whose coordinate is x. Similarly, $d_{\mathrm{g}}(B, x)$ is the distance from the background seed. The big change of $I(x)$ is the place where the edge separates the object and the background, which is also the place where the diagrams of the functions $d_{\mathrm{g}}(O, x)$ and $d_{\mathrm{g}}(B, x)$ should intersect if segmentation is done on the basis of distance. Fig. 2(a) shows how the situation may turn out in the noisy images. The equality of distances may occur at other place than the edge, which leads to incorrect segmentation. This problem is caused by summing many small and unimportant values, which may overshadow the values that are important.

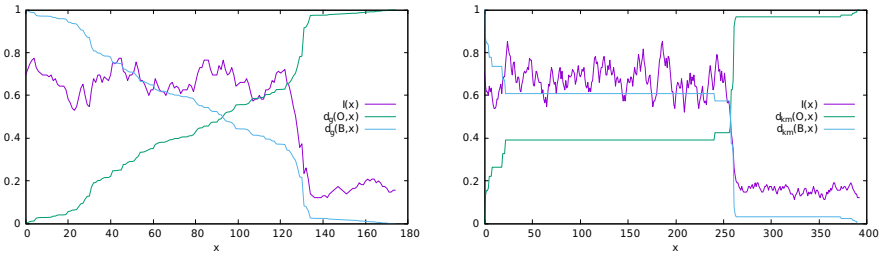

(a) (b)

Fig. 2. The diagram of the geodesic distance (a) and the k-max distance (b) along a path between the object seed and the background seed; x measures the coordinate along the path (for the object seed, we have $x = 0$); $d_\cdot(O, x)$ stands for the distance between the object seed and the point whose coordinate along the path is x. Similarly, $d_\cdot(B, x)$ is the distance from the background seed. $I(x)$ stands for the brightness at x.

3 *k*-max Geodesic Distance

In this section, we introduce the k-max distance. Let $\sum_{\text{top}_k}(.)$ stand for the sum of the k highest values in a collection of nonnegative real numbers (the edge weights in our case). We define the length of path as a sum of the k highest weights on it, i.e., $l_{k\text{m}}(P) = \sum_{\text{top}_k}(w_{(p_1,p_2)}, w_{(p_2,p_3)}, \ldots, w_{(p_{n-1},p_n)})$, where P is a path. Let $\mathcal{P}_{AB}$ be the set of all paths between A and B. The k-max distance between A and B is then defined as $d_{k\text{m}}(A, B) = \min_{P \in \mathcal{P}_{AB}}\{l_{k\text{m}}(P)\}$. For high values of k, the k-max distance is approximating the geodesic distance, for $k = \infty$, $d_{\text{g}}(A, B) \equiv d_{k\text{m}}(A, B)$.

We tested how the k-max distance behaves along the shortest path between the object and background seed, similarly as we did for the geodesic distance. The result is shown in Fig. 2(b). It can be seen that the k-max distance is much less sensitive to noise and the edge position is detected correctly. (The range on the x axis is bigger than in the case of geodesic distance since the shortest k-max path is longer in the xy plane than it was for the geodesic distance in Fig. 2(a). This conforms with the expectation since we have $\beta = 0$ in Eq. (1)).

The description of algorithm that computes the k-max geodesic distance can be found in our paper (see Author's publication). We only note here that the algorithm is based on the well-known Dijkstra algorithm, but, comparing to the geodesic distance where only one value is stored in each node, a list of vectors containing k maximum weights has to be associated with each node when computing the k-max distance.

4 Experiments

In this section, we evaluate the distance-based methods on the image segmentation. Firstly, we show the properties on the segmentation of synthetic images with two segments. With such images, it is easy to measure the error rate of

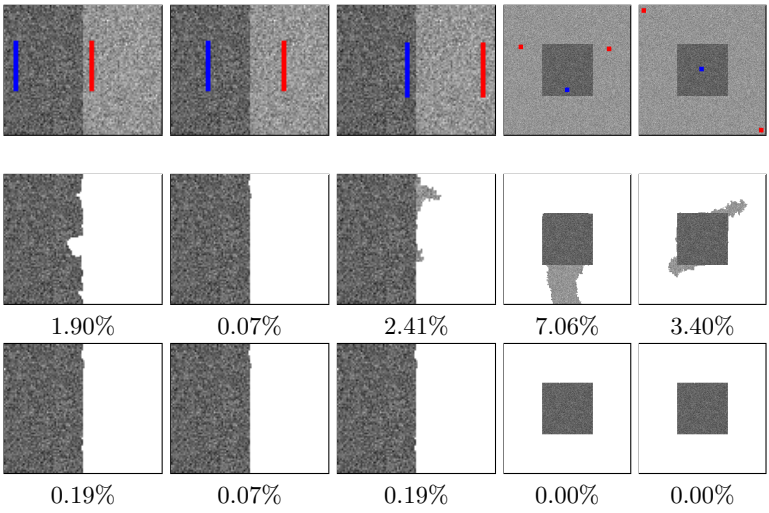

Fig. 3. The sensitivity to the seed positions. The input images with the seeds (first row), the results of segmentation using the geodesic distance (second row), the results of segmentation using the k-max distance, $k = 2$ (third row). The segmentation error rates are below each image.

segmentation since the ground truth images are unambiguous (the error rates are below each segmented image in Fig. 3 and Fig. 4). Then, we show how the choice of k influences the quality of segmentation. This is shown on selected real-life images obtained from the Berkeley segmentation dataset [5]. In all the experiments, we set the parameters from Eq. (1) to $\sigma = \frac{1}{3}$ and $\beta = 0$.

In the first experiment, we focus on the relationship between the segmentation results and the position of seeds, i.e. how the position of seeds influences the segmentation. The results are shown in Fig. 3. It can be seen that the results of geodesic distance (row 2) are dependent on the seed positions, which is undesirable. The reason of such behavior was explained in the previous chapters and corresponds to the diagram in Fig. 2(a). The k-max distance provides much better results (row 3), which is mainly due to the fact that it does not sum the noise values that are unimportant.

In the second test, we focus on how the amount of noise influences the segmentation. We prepared several images affected by Gaussian noise with various standard deviations σ_b in the background area and a constant σ_f in the foreground area. The seeds stay fixed for all the images. The results are shown in Fig. 4. It is seen that the amount of noise influences the results of geodesic distance (row 2). The distance from the seed raises faster in the areas with higher noise, which causes incorrectly detected edge inside this area. Since the k-max distance takes into account only the highest values, it is less sensitive to the noise amount and the images are segmented with a lower error rate (row 3).

In the last experiment, we show that the value of k affects the result of segmentation. In Fig. 5, the results of segmentation are presented for the geodesic

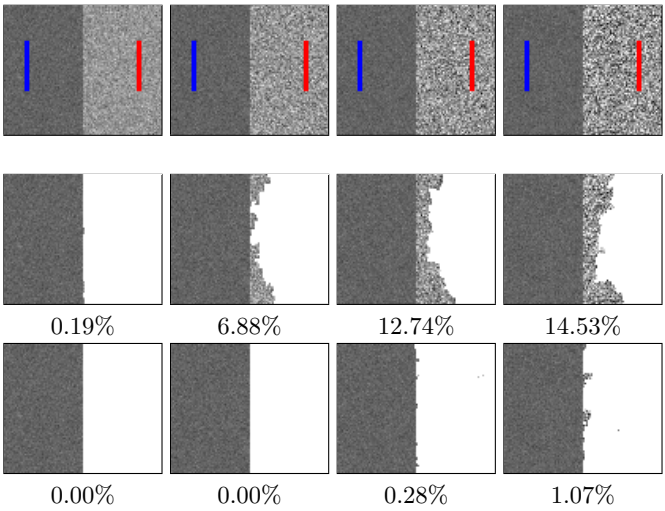

Fig. 4. The sensitivity to the noise amount. The input images with the seeds (first row), the results of segmentation using the geodesic distance (second row), and using the k-max distance with $k = 2$ (third row). The noise in the background area σ_b is set as $2\sigma_f$ (col 1), $3\sigma_f$ (col 2), $4\sigma_f$ (col 3) and $5\sigma_f$ (col 4), where σ_f is the noise amount in the foreground area. The segmentation error rates are below each image.

distance (column 2) and for the k-max distance for several k values ($k = 1$, $k = 6$, and $k = 20$; column 3-5). In the first image (row 1), the goal is to segment only the yellow umbrella into which the object seed is scribbled. The segmentation based on the geodesic distance is apparently bad. In the case of the k-max distance, the segmentation is close to the desired result if low values of k (even $k = 1$) are used. For $k = 20$, the detected object segment "overflows" from the true object, and the result becomes similar to the result of the geodesic distance (as was mentioned in Section 3, this behavior is expected). On the other hand, a good segmentation of the gravestone in the second image (row 2) is achieved with a relatively high value of k ($k = 20$); lower values of k lead to an incomplete object. We can conclude that the choice of the k value is not universal, but it depends on image properties.

5 Conclusion

In this paper, we described the geodesic distance and the k-max geodesic distance. We demonstrated the problems of geodesic distance and we showed that the k-max distance has a chance to overcome them. The properties of both distances were illustrated on the image segmentation problem. According to the results, the k-max distance achieves better results than the geodesic distance. On the other hand, its computation requires more time and memory than the computation of the geodesic distance. The universal choice of k for different images is another open issue.

Fig. 5. On the influence of the k value on the segmentation result. The input images with the seeds (the first column), the results of segmentation based on the geodesic distance (the second column), and the results of segmentation based on the k-max distance for various values of k (the columns 3-5).

Author's publication

Holusa M. and Sojka E.: A k-max Geodesic Distance and its Application in Image Segmentation. In Computer Analysis of Images and Patterns - 16th International Conference, CAIP 2015, Valletta, Malta, September 2-4, 2015 (to appear).

References

1. Bai, X., Sapiro, G.: Geodesic matting: A framework for fast interactive image and video segmentation and matting. Int. J. Comput. Vision 82(2), 113–132 (2009)
2. Borgefors, G.: Distance transformations in arbitrary dimensions. Computer Vision, Graphics, and Image Processing 27(3), 321 – 345 (1984)
3. Criminisi, A., Sharp, T., Blake, A.: Geos: Geodesic image segmentation. In: Proceedings of the 10th European Conference on Computer Vision: Part I. pp. 99–112. ECCV '08, Springer-Verlag, Berlin, Heidelberg (2008)
4. Hajdu, A., Kormos, J., Nagy, B., Zrg, Z.: Choosing appropriate distance measurement in digital image segmentation. Annales Univ. Sci. Budapest. Sect. Comp 24, 193–208 (2004)
5. Martin, D., Fowlkes, C., Tal, D., Malik, J.: A database of human segmented natural images and its application to evaluating segmentation algorithms and measuring ecological statistics. In: Proc. 8th Int'l Conf. Computer Vision. vol. 2, pp. 416–423 (2001)
6. Price, B.L., Morse, B.S., Cohen, S.: Geodesic graph cut for interactive image segmentation. In: CVPR. pp. 3161–3168. IEEE (2010)
7. Toivanen, P.J.: New geodesic distance transforms for gray-scale images. Pattern Recogn. Lett. 17(5), 437–450 (1996)
8. Wang, J., Yagi, Y.: Shape priors extraction and application for geodesic distance transforms in images and videos. Pattern Recogn. Lett. 34(12), 1386–1393 (2013)

Detection of Corners in LIDAR Data via Neural Network

Branislav Holý

Department of Computer Science, FEECS,
VŠB – Technical University of Ostrava, 17. listopadu 15, 708 33 Ostrava – Poruba
branislav.holy@vsb.cz

Abstract. Detection of corners is an important task in many computer science fields. In computer vision, it is mostly used to find landmarks for motion detection, image registration, or video tracking. It is similar in robotics, where the robot is often equipped with a laser scanner. In this field, the corners may be used for localization of the robot, registration of LIDAR data, or the SLAM algorithms. This paper presents a new algorithm for corner detection based on a multilayer neural network. The novelty of the proposed method is the feature vector that is used to describe the surrounding of the corner in appropriate distance from the corner along the edge. The algorithm has been tested in a simulated environment and is able to detect corners with high accuracy.

Keywords: corner detection, neural network, LIDAR

1 Introduction

Many algorithms in robotics need reliable landmarks that can be found in input LIDAR data. The landmarks are used for example in navigation, localization, or in many simultaneous localization and mapping algorithms. The corners as landmarks are ideal for indoor environments. They can be relatively easily described by their surrounding which makes the corner detection fast and reliable.

Since the robot scans LIDAR data from different angles, the description of surrounding has to be invariant to rotation. For this reason, the presented method uses the feature vector with angles between edges around the corner in certain distances.

This paper is organized as follows. Brief descriptions of previous methods are contained in the next section. Section 3 describes the new algorithm and especially the feature vector more deeply. Section 4 shows the results of experiments. The conclusion is presented in the final section.

2 Previous Work

Many computer vision algorithms for corner detection have been used with LIDAR data as well. Rasterization of 2D LIDAR data and range images of 3D

© M. Krátký, J. Dvorský, P. Moravec (Eds.): WOFEX 2015, pp. 307–312.
VŠB – Technical University of Ostrava, FEECS, 2015, ISBN 978-80-248-3787-1.

data provide the input images for algorithms like Harris corner detector [4], faster SUSAN [8] that exploits normals directly, SIFT detector [7], and BRISK: Binary robust invariant scalable keypoints [5]. Different approaches with neural networks have been also used with focus on image data [2, 1].

Extraction of features from LIDAR data is studied in [6]. It also needs rasterized LIDAR data and detects corners by the adapted Kanade-Tomasi corner detector [10]. Some methods use Freeman chain code [3] to detect corners in LIDAR data. The Freeman chain code consists of eight values that represent the directions of neighbouring points. One of them [9] uses Freeman chain code and a neural network for classification.

3 New Algorithm

The presented method works directly with LIDAR data (concretely with points created from LIDAR data) and no rasterization is needed. The method checks every input point and its neighbourhood to decide if the examined point is a corner or not. Since the LIDAR data are ordered in the same order as they were obtained from the scanner, it is fast to find neighbouring points. The method investigates the neighbourhood by the feature vector of angles between edges around the examined point. The feature vector is used as an input vector of a neural network.

3.1 Feature Vector

As mentioned above, the feature vector describes the surrounding of examined point via angles. Our method uses a vector of eight values $f = [\alpha_1, \alpha_2, ..., \alpha_8]$ where α_i is the normalized angle ($\alpha_i \in \langle 0; 1 \rangle$) between vectors a_i and b_i (see Fig. 1). The first endpoint of the vectors a_i and b_i is the examined point p and the second endpoint is the point lying on the edge at the distance i.

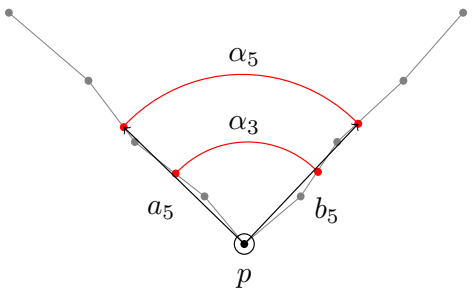

Fig. 1. The example of feature vector. The image shows two values of the feature vector (α_3 and α_5). The value α_5 is computed as the angle between vectors a_5 and b_5. The angle α_3 would be computed similarly.

Since LIDAR data are noisy, the values for small i are not reliable. For this reason, the presented method uses the feature vector consisted from values $f = [\alpha_3, \alpha_4, ..., \alpha_{10}]$.

3.2 Neural Network

The proposed method uses a neural network with a single hidden layer to classify a point as a corner or a point at edge. The input vector has dimension 8 and the output vector has dimension 2. The parametrized backpropagation method has been used for the learning.

3.3 Learning

A simulated environment was used to learn the network. Every corner in the map (see Fig. 2) has red colour and the path of robot is coloured blue. Scans from 10 random poses were used for the learning.

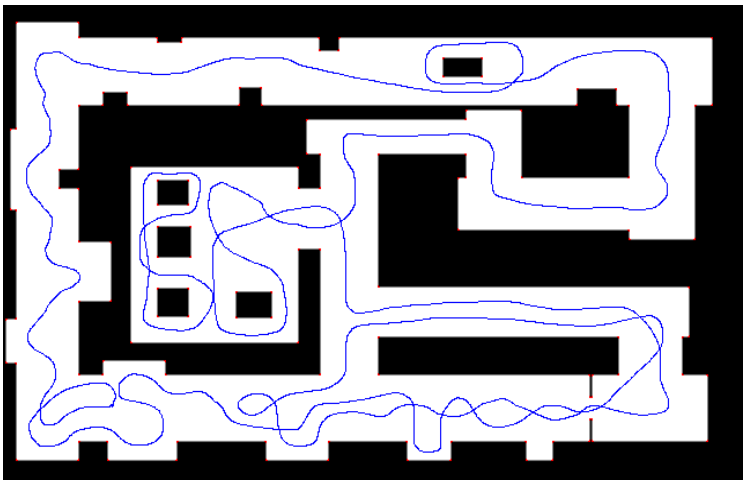

Fig. 2. The map used for the learning. The corners are coloured red and the path of robot has blue colour.

Since the robot can scan a corner without enough information about its surrounding (see Fig. 3), it is necessary to distinguish these corners (the green ones in Fig. 3) from the ones with the information (the red ones in Fig. 3). The corner is marked red, if the distances between consecutive points are below a threshold. We check all points that are looped through until the second endpoint of the vector is found. The green corners are not used only with this scan but they can be used in different scans if they meet the condition.

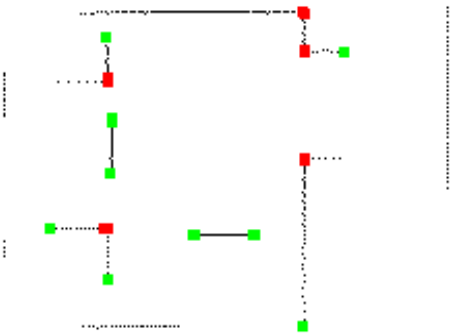

Fig. 3. An example of scan. Green corners do not have enough information about their surrounding so they are not used for the learning. Only the red ones are used with this scan.

4 Results

The algorithm has been tested with three different maps overall with 12,631 scans and 3,078,526 tested points. The first map was the same as the map used for the learning (Fig. 2) but this time, we used all 5,392 scans. This map contains 124 corners and all of them were successfully detected (Fig. 4). However, some corners were marked as "not a corner" (green colour in Fig. 4) but only from certain positions, different positions marked those corners successfully. It increases false positive detection as is shown in Table 1.

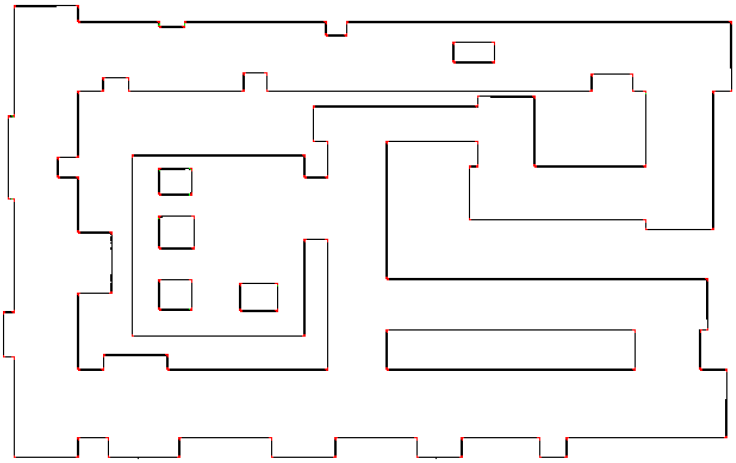

Fig. 4. The result of corner detection of the first map. Black colour represents all scanned points, the detected corners have red colour and false positive detections have green colour.

Similar results were obtained with the second and third testing map. The second map was scanned from 668 different positions and contains 18 corners (Fig. 5a). The third map was scanned from 6,571 poses and has 160 corners (Fig. 5b). All of them were detected with few false positive detections.

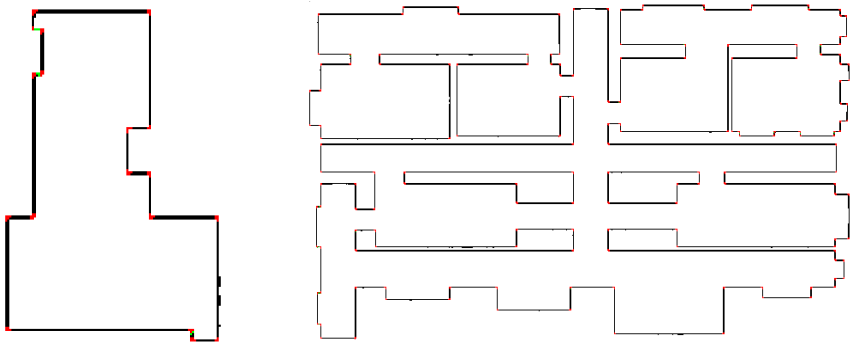

(a) (b)

Fig. 5. The result of corner detection of the second (a) and third (b) map. Black colour represents all scanned points, the detected corners have red colour and false positive detections have green colour.

The results of experiments are shown in Table 1. The true positive (TP) shows how many times the corners were successfully detected. The false negative (FN) displays the unsuccessful detections. The true negative (TN) represents the correct edge detections and the false positive (FP) the incorrect ones. The true positive rate (TPR) was computed as $TPR = TP/(TP+FN)$ and the true negative rate (TNR) as $TNR = TN/(TN + FP)$.

Table 1. The results of the presented algorithm.

	Map 1	Map 2	Map 3	Total
Corners	124	18	160	302
Scans	5,392	668	6,571	12,631
Tests	1,275,714	183,167	1,619,645	3,078,526
True positive	39,144	7,547	50,269	96,960
False negative	3,591	1,169	5,923	10,683
True negative	1,232,435	174,318	1,562,681	2,969,434
False positive	544	133	772	1,449
True positive rate	91.60%	86.59%	89.46%	90.08%
True negative rate	99.96%	99.92%	99.95%	99.95%

5 Conclusion and Future Work

This paper presents a new algorithm for detection of corners in 2D LIDAR data. The detection is based on a multilayer neural network where the input feature vector represents the surrounding of examined point. This new representation is invariant to rotation which is necessary due to various angles from which the corner can be scanned. The algorithm has been tested with three different maps and the results proved the successfulness of the presented method. The future work will be focused on a 3D variant of the method for a wider use.

References

1. Chen, W.C., Rockett, P.: Bayesian labelling of corners using a grey-level corner image model. In: Image Processing, 1997. Proceedings., International Conference on. vol. 1, pp. 687–690. IEEE (1997)
2. Dias, P., Kassim, A., Srinivasan, V.: A neural network based corner detection method. In: Neural Networks, 1995. Proceedings., IEEE International Conference on. vol. 4, pp. 2116–2120. IEEE (1995)
3. Freeman, H., Davis, L.S.: A corner-finding algorithm for chain-coded curves. IEEE Transactions on Computers (3), 297–303 (1977)
4. Harris, C., Stephens, M.: A combined corner and edge detector. In: Alvey vision conference. vol. 15, p. 50. Citeseer (1988)
5. Leutenegger, S., Chli, M., Siegwart, R.Y.: Brisk: Binary robust invariant scalable keypoints. In: Computer Vision (ICCV), 2011 IEEE International Conference on. pp. 2548–2555. IEEE (2011)
6. Li, Y., Olson, E.B.: Extracting general-purpose features from lidar data. In: Robotics and Automation (ICRA), 2010 IEEE International Conference on. pp. 1388–1393. IEEE (2010)
7. Lowe, D.G.: Distinctive image features from scale-invariant keypoints. International journal of computer vision 60(2), 91–110 (2004)
8. Smith, S.M., Brady, J.M.: Susana new approach to low level image processing. International journal of computer vision 23(1), 45–78 (1997)
9. Subri, S.H., Haron, H., Sallehuddin, R.: Neural network corner detection of vertex chain code (2006)
10. Tomasi, C., Kanade, T.: Detection and tracking of point features. School of Computer Science, Carnegie Mellon Univ. Pittsburgh (1991)

The Radio Direction Finding with Advantage of the Software Defined Radio

Josef Hrabal

Department of Computer Science, FEECS,
VŠB – Technical University of Ostrava, 17. listopadu 15, 708 33 Ostrava – Poruba
josef.hrabal@vsb.cz

Abstract. The software defined radio has gained a lot of popularity in the last years and its applications can be found in many sectors. The software defined radio platform enables a rapid development of almost any radio system. In this paper we present a realization of the Pseudo-Doppler radio direction finding system. We have constructed a Pseudo-Doppler antenna array and implemented signal processing using tools available in the GNU Radio package.

Keywords: radio direction finding, RDF, software defined radio, SDR, Pseudo-Doppler

1 Introduction

Radio direction finding (RDF) is the measurement of the direction from which a received signal was transmitted. This has many applications in different sectors. The RDF is used for example in the navigation of ships and aircrafts, for tracking wildlife, and to locate not only emergency transmitters but also illegal or interfering ones.

Nowadays, most of the radio frequency bands are occupied. Fast classification and location of the source of an illegal or interfering transmitters could be very helpful, especially when transmitters or networks are being built and maintained. The classification and locating can be simplified thanks to *software defined radio* (SDR).

2 Radio Direction Finding

The RDF is nearly as old as radio itself. Earliest experiments in the radio direction finding were carried out by Heinrich Hertz in 1888. Since then many types of radio direction finding techniques were discovered. The mostly used ones are the Watson-Watt and the Doppler technique.

2.1 Watson-Watt radio direction finding system

The first one from the mentioned techniques is older and was introduced by Robert Watson-Watt before the World War II. It utilises an antenna array consisting of four equidistant vertical elements (known as Adcock antenna [8]) and

© M. Krátký, J. Dvorský, P. Moravec (Eds.): WOFEX 2015, pp. 313–318.
VŠB – Technical University of Ostrava, FEECS, 2015, ISBN 978-80-248-3787-1.

two separated precisely calibrated receivers. The *angle of arrival* (AOA) is then determined from the signals level difference. Presence of the two receivers is the main disadvantage of this technique [1].

2.2 Doppler radio direction finding system

The second technique uses the Doppler effect. This effect was described by Austrian physicist Christian Doppler in 1842 in Prague. Most people associate the Doppler effect with acoustic waves, but the theory is also applicable to radio waves as well. This well known effect describes a difference between the observed and emitted frequency of a wave for an observer which is moving relative to the source of the waves.

The earliest Doppler direction finding systems used a single antenna placed on a fast rotating turntable. As the receiving antenna approaches the transmitter, the frequency increases and as the antenna recedes from the transmitter, the frequency decreases. The receiver then observes a frequency modulated signal at a rate equal to the frequency of the rotation (rotation tone). The received signal is then de-modulated by FM receiver, which then produces the demodulated rotation tone. The angle of arrival is then determined from phase offset between the original and the demodulated rotation tone [2].

Spinning the turntable fast enough to produce high frequency signal efficiently is very difficult. Because of this, the physically rotated antenna could be replaced by an antenna array. This array can consist of three or more separate omnidirectional antennas placed evenly along the perimeter of a circle. Each one of the antennas is switched successively to make an illusion of the physical rotation. This modified system is known as the Pseudo-Doppler direction finding system and is a result of combination of the Earp and Godfrey system [3] and the Whale system [2].

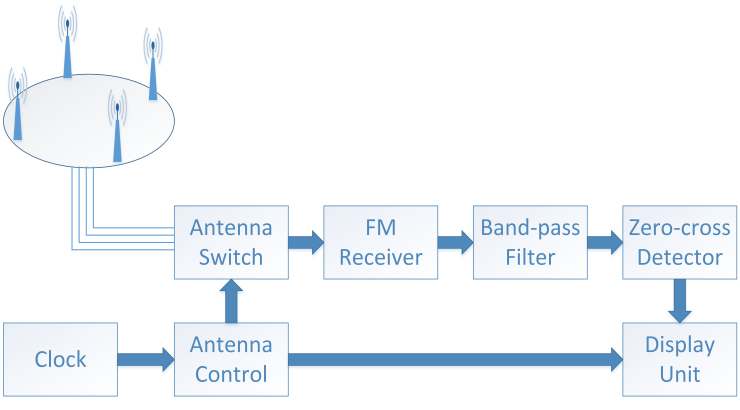

Fig. 1. Pseudo-Doppler block diagram

Block diagram of a simple Pseudo-Doppler direction finding system is shown in the Figure 1. The Pseudo-Doppler antenna array is located in the top left corner of the image. In this case the array is assembled from four omnidirectional antennas. The antenna array is then connected to the antenna switch. This switch is driven by the antenna control unit and its purpose is to handle sequential switching of the antennas in the array. The radio signal then runs to a FM receiver, where is demodulated. In the next step the audio output of the receiver is fed into a band-pass audio filter which passes frequencies within a range of rotation tone and rejects frequencies outside that range. To determine the angle of arrival, phase offset of this filtered audio signal is needed. This is carried out by the Zero-cross detector block. In the last step, phase offset of the signal is compared with the rotation tone and the angle of arrival is obtained.

2.3 Software Defined Radio

SDR is a radio communication system where components (such as demodulators, filters, amplifiers, etc.) that have been typically implemented in hardware are instead implemented as a software on a personal computer. The concept of SDR is not new, its origins can be tracked back to 1970's. For a long time computers were too slow to accomplish this task. As price of SDR hardware decreased in last years, SDR has gained a lot of popularity and its applications can be found in many sectors.

Main purpose of a SDR receiver is to transform desired frequency to an intermediate frequency and then to convert it to digital data by a high speed A/D converter. Result of this process is a stream of digital information which represents the original radio signal by values of its sine and cosine component.

3 Doppler antenna array design and construction

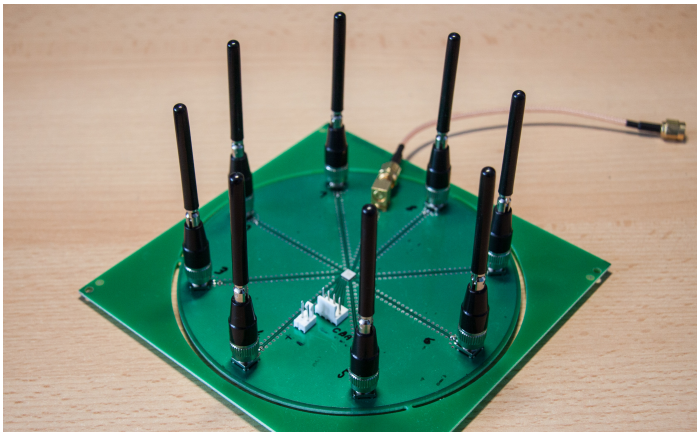

Fig. 2. Pseudo-Doppler antenna array

For testing purposes, we decided to use the 860 MHz band which is regulated by general authorization VO-R/10/05.2014-3 and does not require a licence to use it. Band 860 MHz contains ultra short waves ($\lambda \sim 35$ cm) which allows us to combine antenna switch and antenna array base together easily. Maximum spacing between each separate antenna of the array is limited to less than $\frac{\lambda}{2}$ [4]. Too small spacing increases mutual coupling between antennas, which in turn increases amplitude directivity of the antennas and reduces the Doppler tone strength in the receiver.

Because we wanted to include more usage scenarios in one design, we decided to make the antenna array as universal as possible. Pseudo-Doppler antenna array with eight omnidirectional antennas mounted is depicted in the Figure 2. Each antenna is connected through a SMA connector. This solution allows to mount any number of antennas or use this array only as antenna switch.

High frequency electronic antenna switch implemented as integrated circuit HMC253LC4 is placed in the center of the antenna array. The circuit is able to process radio signal up to 3.5 GHz with maximum switching speed of 10 MHz. Insertion loss is less than 1.7 dB in the entire bandwidth. Communication is done by a simple parallel interface consisting of three binary input pins. Each binary combination connects one of the eight inputs to the output [5].

4 Signal processing using GNU radio

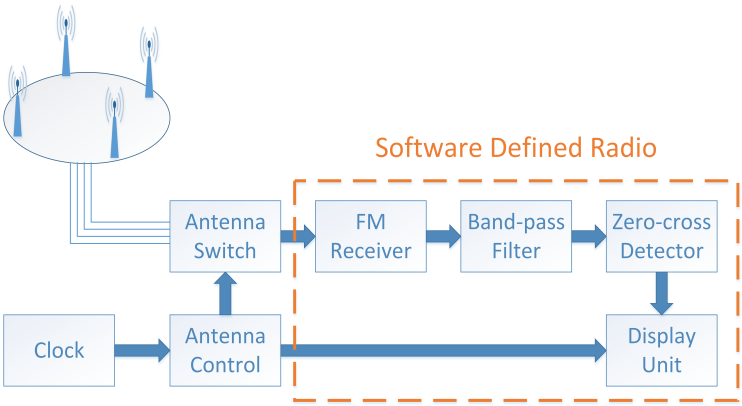

Fig. 3. Pseudo-Doppler block diagram with SDR

Signal processing is based on the well known open source project GNU Radio [7]. This software development toolkit provides a signal processing runtime and processing modules with convenient tools for creating software radio implementations. As a software defined radio receiver we used the HackRF One from

Great Scott Gadgets company [6] which is a very powerful and affordable open source hardware platform.

Part of the Pseudo-Doppler direction finding system which is implemented in software is enclosed by an orange box in Figure 3. To achieve a good synchronization between the data stream and the antenna rotation, the internal clock of the HackRF One is used. Other tasks like tuner settings, FM demodulation or band-pass filtering are implemented in a very simple way with the help of the GNU Radio modules. On the other hand, comparison of a phase offset is a much harder task.

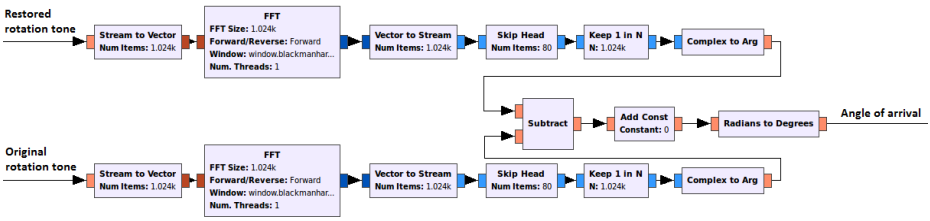

Fig. 4. GNU Radio flow diagram

The filtered signal cannot be compared directly because of the different power levels, interferences etc. The Figure 4 depicts processing of both rotation tones and angle of arrival calculation. The output data stream must be converted from the time domain to the frequency domain. This is done by Fast Fourier Transformation (FFT). Part of the data, whose size is equal to the size of the FFT window, is captured by the *Stream to Vector* module and processed by the *FFT* module and converted back to a data stream by the *Vector to Stream* module. The data are in the frequency domain now and the data relevant to the rotation tone can be now separated. This is done by the *Skip Head* and *Keep 1 in N* modules. The Eq. (1) is used to determine the number of the data samples to be skipped.

$$N = \frac{f_s f_r}{N_{FFT}}, \tag{1}$$

where:

N	Number of elements to skip
f_s	Sample rate
f_r	Rotation tone frequency
N_{FFT}	Size of FFT

Since all digital samples of the signal are represented as complex numbers, the phase of the rotation tone is determined by their argument. The argument is

obtained by the *Complex to Arg* module for each of the rotation tones. The phase offset, which is equal to the angle of arrival, is obtained after subtracting tones from each other.

Purpose of the *Add const* module is to calibrate angle of arrival with respect to the north. This calibration is needed after each start of the system. Automatic calibration with usage of the HackRF One is a subject of a future work.

5 Conclusion

The software defined radio brings a new possibilities to a many sectors and implementation of the radio direction finding system is not an exception. Prototype of the Pseudo-Doppler direction finding system based on the software defined radio is presented in the article. The antenna array was designed, constructed and tested. The hardware implementation of the system was transferred to software and difficult parts of the specific implementation was presented.

Main advantage of the designed system is a possibility to analyse the entire bandwidth which the software defined radio can provide at once. Number of the parallel analysed signals is limited only by performance of the used computer. This is an enormous improvement against the hardware implementation, where a separate receiver is needed for each signal.

References

1. RDF Products. "Basics of the Watson-Watt Radio Direction Finding Technique" White Paper WN-004, Rev. B-01, 2007
2. H.A. Whale. "A Rotating Interferometer for the Measurement of the Directions of Arrival of Short Radio Waves" Proc. Phys. Soc. B 67 553, 1954
3. C.W. Earp and R.M. Godfrey. "Radio direction-finding by the cyclical differential measurement of phase" Journal of the Institution of Electrical Engineers - Part IIIA: Radiocommunication, Volume 94, Issue 15, 1947, p. 705 - 721
4. Peavey, David, and T. Ogumfunmi. "The single channel interferometer using a pseudo-doppler direction finding system." Acoustics, Speech, and Signal Processing, 1997. ICASSP-97., 1997 IEEE International Conference on. Vol. 5. IEEE, 1997.
5. Analog Devices, Inc. "GaAs MMIC SP8T Non-reflective switch, DC - 3.5 GHz" HMC253LC4 Datasheet v02.0414
6. Great Scott Gadgets, "HackRF One" 2015. [Online]. Available: http://greatscottgadgets.com/hackrf/ [Accessed Aug. 3, 2015].
7. GNU Radio, "The Free and Open Software Radio Ecosystem" 2015. [Online]. Available: http://gnuradio.org/redmine/ [Accessed Aug. 3, 2015].
8. Adcock, Frank. "Improvement in means for determining the direction of a distant source of electromagnetic radiation." British patent 130490, 1919.

Differential Evolution based Cluster Forest Algorithm

Jan Janoušek

Department of Computer Science, FEECS,
VŠB – Technical University of Ostrava, 17. listopadu 15, 708 33 Ostrava – Poruba
jan.janousek@vsb.cz

Abstract. Cluster Forest (CF) is relatively new ensemble clustering method inspired by Random Forest algorithm. The main idea behind of the existing algorithm consists in a construction of a larger number of partial clusterings for feature subsets using K-means algorithm. At the end, these clusterings are aggregated using a method of spectral clustering. This article describes a new application of Differential Evolution that replaces the K-means algorithm in the computation pipeline.

Keywords: Cluster Forest, clustering, ensemble clustering, optimization, Differential Evolution, soft computing

1 Introduction

Clustering represents one of the main machine learning research area. It aims to partitioning data points into groups based on their similarity. Points in the same group should be as similar as possible in comparison to the points in another group. Concrete number of clusters is mostly unknown. Clustering is often called unsupervised learning, because there are no information on classes. A large number of clustering algorithms has been developed in past decades. One of the best known clustering algorithms is k-means [1]. This method assign each point into the cluster with the nearest mean. k-means is very popular method because it is fast and provide relatively good results. Other examples of well known clustering algorithms are hierarchical clustering [2], DBSCAN [3], OPTICS [4], Fuzzy c-means [5], and many others [6] [7].

The ensemble methods became popular in the past years. One of the best known ensemble method is Random Forests (RF) [8], that is commonly used for classification and regression. The same idea, that is behind Random Forests, was introduced as "Cluster Forests" [9] that proposed a new clustering method. Authors made the comparison of CF with other ensemble methods like Bagged clustering, Evidence accumulation, and Random Projection as well. Finally, they shown that CF can outperform these algorithms.

A new modification of CF is introduces in this article. It utilizes Differential Evolution [10], that replaces k-means clustering algorithm within CF.

© M. Krátký, J. Dvorský, P. Moravec (Eds.): WOFEX 2015, pp. 319–325.
VŠB – Technical University of Ostrava, FEECS, 2015, ISBN 978-80-248-3787-1.

2 Cluster Forest algorithm

As is was already mentioned, Cluster Forest was inspired by Random Forests algorithm. Both algorithms can be divided into two main phases. The first phase covers an application of multiple weak learners (base clustering/classification algorithms). Particular application results in assignment of input points to clusters. Then, all the assignments are aggregated in the second phase of algorithm. The original CF uses k-means in the second phase. There exists a hidden constrain that weak learners must not produce the same assignments. Otherwise, the aggregation does not bring any additional information. This is the main disadvantage of k-means algorithm whose frequent application produces almost the same results. In RF, the mentioned problem is solved using bagging and random selection of features. CF solves this problem using the *clustering vector growing method* (CVG) shown in Algorithm 1. Here, the Cluster vector is a subset of features used for clustering, hence it will be called the feature vector. In the first step of CVG, the feature vector is initialized with n randomly selected features. Then, k-means algorithm is applied and quality of obtained clustering is evaluated using Formula 1, where c is the clustering, SS_w is the within cluster sum [11] of squares and SS_b is the between cluster sum of squares [11].

$$\rho(c) = \frac{SS_w(c)}{SS_b(c)} \tag{1}$$

After this, other n features are selected randomly and merged with the previous feature vector. k-means algorithm is applied to this temporary created vector and if the quality of obtained clustering is higher, then the previous feature vector is replaced by the new one.

All features are selected randomly in each step. This can lead to poor selection if the data contains only small number of significant features. To solve this problem, feature competition is used for feature vector initialization. In this procedure, base clustering algorithm is applied to multiple randomly selected feature subsets. And subset with the highest quality is selected as initial vector.

The output of the CVG described above is represented by the final feature vector and related clustering. This clustering is equivalent to a single tree in the RF algorithm. The algorithm must be executed multiple times to build the set of clusterings.

In the second phase, all results of the weak learners are aggregated. Spectral clustering [12] was selected as an optimal aggregation method, that is based on the spectral graph theory. The spectral clustering is applied on the matrix M whose elements a_{ij} are give by Formula 2. Matrix M is regularized using thresholding, when element a_{ij} is set to zero, if it is less then configuration parameter β with value in interval $(0, 1]$. After this, all elements of matrix D are scaled using $a_{ij} = exp(\gamma a_{ij})$, where γ is a configuration parameter with the value in interval $[0, 1]$.

$$a_{ij} = exp\left(\frac{1}{T}\sum_{t=1}^{T}\begin{Bmatrix}1\ if\ c_t(i) = c_t(j)\\ 0 \quad otherwise\end{Bmatrix}\right) \tag{2}$$

Algorithm 1 Cluster vector growing method

Require:
f: list of all features
$sampleFeatures$: randomly sample n features
$KMeans$: k-means clustering

1: $iter = 0 v$ = featureCompetition(f)
2: $clustering_{old}$=KMeans(v)
3: **while** $iter < iter_{max}$ **do**
4: $iter = iter + 1$
5: v_{tmp} = sampleFeatures(f)
6: $clustering_{new}$ = KMeans(v_{tmp})
7: **if** $\rho(clustering_{old}) > \rho(clustering_{new})$) **then**
8: $v = v_{tmp}$
9: $clustering_{old} = clustering_{new}$
10: $iter = 0$
11: **end if**
12: **end while**

where $i, j \in \{1, \ldots, n\}$, and T is the total number of iterations, and c_t returns a cluster index to which a point j was assigned to in the iteration t.

3 Differential Evolution (ED)

Bio-inspired methods make a subset of algorithms that are inspired from nature. A large proportion of these methods is represented by optimization algorithms and can be applied to wide range of machine learning methods focused on finding global optima, solutions of real problems. In our case, selected Differential Evolution was implemented within the clustering algorithm. Its implementation leads to function minimization problem where the clustering error is computed as an output of fitness function, e.g. *within-cluster sum of squares* [11], *Davies-Bouldin index* [11], or *Dunn index* [11]. Davies-Bouldin index was used in our experiments that is described by Formula 3.

$$fit = \frac{1}{K} \sum_{i=1}^{K} \max_{j \in K, j \neq i} \left(\frac{\frac{1}{N_i} \sum_{\vec{x} \in C_i} d(\vec{x}, c_i) + \frac{1}{N_j} \sum_{\vec{x} \in C_j} d(\vec{x}, \vec{c}_j)}{d(\vec{c}_i, \vec{c}_j)} \right) \tag{3}$$

where K is the number of clusters, N_i is the number of points in cluster C_i for $i \in \{1, \ldots, K\}$, N_j is the number of points in cluster C_j for $j \in \{1, \ldots, K\}$, c_i is the center of cluster i, and d is the distance function.

All clusters have to be represented as single vector

$$v = (c_{1,1}, \ldots, c_{1,n}, \ldots, c_{K,1} \ldots, c_{K,n})$$

to be able to apply DE, where K is number of clusters as n is the number of features.

DE [10] is a representative of evolutionary algorithms. In this method, candidate solutions are called "agents". These agents are initialized randomly. In each step of the algorithm, every agent picks N (N is set to three by default) different agents, e.g. "a", "b" and "c", and generates random number R between 0 and F, which is the number of features of the agent. After this, a new agent is created using Formula 4, that is applied to each feature independently, if $rand(0,1) < CR$. If $rand(0,1) >= CR$ then $x_i^{new} = x_i$. Variables CR and W are configuration parameters called "crossover probability" with value in interval $[0,1]$ and "differential weight" with value in interval $[0,2]$. If the new created agent is better then the original one, then the original agent is replaced.

$$x_i^{new} = a_i + W \times (b_i - c_i) \tag{4}$$

4 Data collections

For our experiments we used 8 freely available dataset from UC Irvine Machine Learning Repository [13].

Table 1. Data collections

Dataset	Instances	Features	Classes
Statlog (Heart)	270	13	2
Image Segmentation	2100	19	7
Madelon	2000	500	2
Robot Execution Failures	164	90	5
Soybean	47	35	4
SPECT Heart	267	22	2
Wine	178	13	3
Breast Cancer Wisconsin (Diagnostic)	569	30	2

These collections were chosen for purposes of comparison with the original version algorithm, published in the paper [9].

5 Experiments

Two main experiments was performed. The quality of clustering was compared using already described bio-inspired methods in the first experiment. In the second experiment, results achieved by the best bio-inspired methods were compared with the results made by the original CF and others clustering methods.

There exists a lot of metrics that can be used for clustering quality comparison. Two metrics based on classification performance were used. The first metric is ρ_r:

$$\rho_r = \frac{\sum_{i=1}^{N}\sum_{j=1}^{N}\sigma(O_i,O_j)\sigma(A_i,A_j)}{N(N-1)} \quad i \neq j \tag{5}$$

where σ is the function that returns 1 if the values of both attributes are the same, 0 otherwise. O is the vector of original (expected) classes and A is the vector of assigned classes. N is the number of classified vectors. This metric is based on an assumption that all possible pairs of vectors that have the same class in the original class vector, should have the same class in the assigned class vector.

The second metric is ρ_c:

$$\rho_c = \underset{\tau \subset T}{max} \left\{ \frac{1}{N} \sum_{i=0}^{N} \sigma(\tau(O_i), A_i) \right\} \tag{6}$$

where T is the set of all class permutations. σ, O_i and A_i have the same meaning like in Formula 5. This metric is equivalent to the standard classification accuracy. For both metrics, the higher value the better result.

All published results in both experiments are means of 20 subsequent executions of the algorithms. The maximum threshold of the fitness function was set to 300. This number was chosen empirically.

There are results of comparisons between cluster forest based on DE (CF-DE) with the original cluster forest and standard clustering methods like k-means and three others ensemble methods called "bagged clustering" (bC2) [14], "evidence accumulation" (EA) [15] and "random projection" (RP) [16] in Tables 2 and 3. All results for bC2, EA and RP are taken from the paper [9].

From Table 2 can be seen that CF-DE outperforms the other clustering methods including original version of CF in all but one cases for metric ρ_r. In Table 3, there are results for metric ρ_c, where CF-DE outperforms other algorithms in 7 of 8 cases.

Table 2. Comparison of results for metric ρ_r

Dataset	Custer Forest Variants					
	CF-DE	CF	k-means	bC2	EA	RP
Statlog (Heart)	**62.39**	56.8	47.3	51.50	53.20	52.41
Image Segmentation	80.25	79.71	23.61	82.19	85.75	**85.88**
Madelon	**51.21**	50.76	49.98	49.98	49.98	50.82
Robot Execution Failures	**68.53**	63.42	53.26	39.76	58.31	41.52
Soybean	**95.46**	92.36	85.14	83.16	86.48	87.04
SPECT Heart	**59.28**	56.78	49.22	50.61	51.04	49.89
Wine	**91.26**	79.7	32.05	71.97	71.86	71.94
Breast Cancer Wisconsin	**83.26**	79.66	82.14	74.87	75.04	74.89

6 Conclusion

In this article, application of DE to original Cluster Forest (CF) algorithm was presented. The main goal was the substitute the standard clustering method,

Table 3. Comparison of results for metric ρ_c

Dataset	Custer Forest Variants					
	CF-DE	CF	k-means	bC2	EA	RP
Statlog (Heart)	**71.94**	68.26	57.3	59.10	59.26	60.54
Image Segmentation	47.82	48.24	43.42	49.91	**51.30**	47.71
Madelon	**55.78**	55.12	51.73	50.20	50.30	55.19
Robot Execution Failures	**46.58**	41.2	42.05	35.37	37.19	35.50
Soybean	**91.7**	84.43	82.142	72.34	76.59	71.83
SPECT Heart	**71.59**	68.02	55.9	56.28	56.55	61.11
Wine	**93.11**	79.19	46.53	70.22	70.22	70.79
Breast Cancer Wisconsin	**91.18**	88.7	82.142	85.38	85.41	70.79

that was used within CF, by selected bio-inspired method. Eight datasets that differ in the number of instances, features and classes were used in performed experiments. As it can be seen in the result tables, the Cluster-Forest algorithm with Differential Evolution (CF-DE) does not bring the better result just in one case that will be the subject of further research and observations.

References

1. J. A. Hartigan, M. A. Wong, Algorithm AS 136: A k-means clustering algorithm, Applied Statistics 28 (1) (1979) 100–108. doi:10.2307/2346830.
2. T. Hastie, R. Tibshirani, J. Friedman, The Elements of Statistical Learning: Data Mining, Inference, and Prediction, Second Edition (Springer Series in Statistics), Springer, 2009.
3. M. Ester, H. peter Kriegel, J. S, X. Xu, A density-based algorithm for discovering clusters in large spatial databases with noise, AAAI Press, 1996, pp. 226–231.
4. M. Ankerst, M. M. Breunig, H. peter Kriegel, J. Sander, Optics: Ordering points to identify the clustering structure, ACM Press, 1999, pp. 49–60.
5. J. C. Bezdek, Pattern Recognition with Fuzzy Objective Function Algorithms, Kluwer Academic Publishers, Norwell, MA, USA, 1981.
6. P. Yang, B. Huang, A spectral clustering algorithm based on normalized cuts, in: Computer Science and Software Engineering, 2008 International Conference on, Vol. 4, 2008, pp. 329–331. doi:10.1109/CSSE.2008.910.
7. T. S. Madhulatha, An overview on clustering methods, CoRR abs/1205.1117.
8. L. Breiman, Random forests, Machine Learning 45 (1) (2001) 5–32.
9. D. Yan, A. Chen, M. I. Jordan, Cluster Forests, ArXiv e-printsarXiv:1104.2930.
10. R. Storn, K. Price, Differential evolution a simple and efficient heuristic for global optimization over continuous spaces, Journal of Global Optimization 11 (4) (1997) 341–359. doi:10.1023/A:1008202821328.
11. M. Halkidi, Y. Batistakis, M. Vazirgiannis, Clustering validity checking methods: part ii, ACM Sigmod Record 31 (3) (2002) 19–27.
12. J. Shi, J. Malik, Normalized cuts and image segmentation, in: Computer Vision and Pattern Recognition, 1997. Proceedings., 1997 IEEE Computer Society Conference on, 1997, pp. 731–737. doi:10.1109/CVPR.1997.609407.
13. M. Lichman, UCI machine learning repository (2015).
URL `http://archive.ics.uci.edu/ml`

14. S. Dudoit, J. Fridlyand, Bagging to improve the accuracy of a clustering procedure, Bioinformatics 19 (9) (2003) 1090–1099. doi:10.1093/bioinformatics/btg038.
15. A. L. Fred, A. K. Jain, Data clustering using evidence accumulation, in: Pattern Recognition, 2002. Proceedings. 16th International Conference on, Vol. 4, IEEE, 2002, pp. 276–280.
16. X. Z. Fern, C. E. Brodley, Random projection for high dimensional data clustering: A cluster ensemble approach, in: ICML, Vol. 3, 2003, pp. 186–193.

Replacing Pseudo-inverse in the Extreme Learning Machine Algorithm to Improve Algorithm Speed on GPU

Tomáš Ježowicz

Department of Computer Science, FEECS,
VŠB – Technical University of Ostrava, 17. listopadu 15, 708 33 Ostrava – Poruba
tomas.jezowicz@vsb.cz

Abstract. Extreme learning machine (ELM) is a novel learning algorithm that is fully comparable to other well known learning algorithms like SVM, neural networks, etc. ELM is widely used in recent years due to fast learning speed and good performance that in many cases outperforms other approaches. The algorithm may be further improved as described in this article. A three approaches was proposed to improve speed of the ELM algorithm. Experiments have shown that proposed approaches are faster while performance of the algorithm is the same as the original.

Keywords: Extreme Learning Machine, speedup, ELM, GPU, speedup, pseudo-inverse

1 Introduction

The ELM is special case of a single-hidden-layer feed-forward neural network. The advantage of the ELM is that the weights of this network can be computed analytically without expensive back propagation. The ELM is able to fit training dataset with zero error when the number of hidden neurons in the network is equal to number of vectors in training set [6]. Notice that the number of hidden neurons is much smaller in practice. ELM is able to provide a good generalization performance which means that it performs well on an unknown data.

This paper proposes a three approaches that speed up ELM algorithm with usage of parallel architecture CUDA. General Purpose GPU (GPGPU) utilize graphics processing units (GPUs) to perform computations that are usually handled by a common CPU. A parallel nature of graphic chips provides advantages for specific applications that may outperform current multi-core CPUs. One of the GPGPU framework is NVIDIA CUDA which was launched in 2006. CUDA is comprehensive development environment for C and C++ developers. It allows a heterogeneous programming model where part of a code is processed by CPU and another part on GPU.

© M. Krátký, J. Dvorský, P. Moravec (Eds.): WOFEX 2015, pp. 326–331.
VŠB – Technical University of Ostrava, FEECS, 2015, ISBN 978-80-248-3787-1.

2 Related work

Huang introduced the ELM algorithm in 2004 in the paper [6] where the ELM was compared to other learning algorithms. Also other comparison of ELM with many standard classification algorithms have been made in recent years. For example a comparison with SVM was studied in [5] where the ELM achieved similar or better results and much faster learning speed. In 2014 the paper [4] showed that ELM outperforms deep auto-encoder on embedding and clustering tasks. The ELM was also used in many areas like biomedical and medical applications [10], image processing [8] or computer vision [1][2]

In recent years there were proposed several methods that speedup the ELM algorithm using a parallel approach. The ELM algorithm that solves a large-scale regression was proposed in the paper [9]. Next, a map reduce framework was designed and implemented in paper [3].

3 Extreme Learning Machine

Algorithm 1 ELM classification algorithm

Require: D input data (training dataset)
Require: T target output for classification
1. $W = rand()$ // Random input weights
2. $B = rand()$ // Random bias; same for every neuron
3. $H = DW$ // Multiply data with input weights
4. $H = H + B$ // Add biases
5. $H = 1./(1 + e^{-H})$ // Calculate hidden neurons
6. $\beta = H^{+}T$ // Pseudo-inverse

The training phase of the ELM classification algorithm is described in the Algorithm 1. The inputs of this algorithm are dataset D (matrix in row-major format) and column vector T that represents a required (target) output. The input weights W and biases B of the hidden neurons are randomly set. The number of hidden neurons L is a user parameter. The resulting matrix H is basically a non-linear transformation of the input data D. Final step consist of computing a pseudo-inverse of the matrix H. The result of this algorithm are output weights β. Also, the input weights W and biases B must be stored to perform a testing phase.

4 Proposed Approaches

The whole ELM algorithm was implemented on GPU. The last step of the ELM algorithm was implemented in three variants.

The following libraries were used in all experiments:

- CULA[1] math library for GPU (dense version).
- cuBLAS[2] for matrix-matrix multiplications on GPU.
- cuRAND[3] for random number generator on GPU.

4.1 GPU full QR decomposition (GPU_F)

The least-squares problem is solved by computing full QR decomposition of the matrix H on GPU. This variant requires more than twice of the size of the matrix H memory space. Also, the CULA library buffers needs to be released in case of the large matrix H. The advantage of this variant is that it does not require additional data manipulation.

4.2 GPU + pseudo-inverse on CPU (GPU_I)

Second variant proposed to reduce a GPU memory limitations by computing pseudo-inverse on CPU. In this case the matrix H and target T is copied back to the CPU memory space. This variant is advantageous when the dataset and the matrix H are large or the GPU memory is limited for some reasons. The disadvantage is slower speed.

4.3 GPU + reduced pseudo-inverse (GPU_M)

The last proposed variant is the fastest one in most of the cases. It runs completely on GPU and solves least-squares problem in the following way:

$$(H^T H)^{-1} Hx = P_i^{-1} Hx = T$$

Notice that the additional memory allocations are required:

$$Mem(H_{help}) = H_{row} * H_{col}$$
$$Mem(P_i) = min(H_{row}, H_{col})^2$$
$$Mem_{total} = Mem(H_{help}) + Mem(P_i)$$

where Mem is a function that returns required memory, H_{help} is an auxiliary variable of size $H_{row} \times H_{col}$ (same size as matrix H). The matrix P_i is used to store results from $H^T H$ which means that its size is $min(H_{row}, H_{col})^2$. $P_i = H^T H$ and $P_i^{-1} = (H^T H)^{-1}$.

This variant computes the inverse of the reduced matrix P_i by calling culaDeviceSgetrf and culaDeviceSgetri CULA functions. In many datasets the number of vectors in the dataset is much larger than number of hidden neurons ($L << N$) and the matrix P_i is relatively small.

[1] `http://www.culatools.com`
[2] `https://developer.nvidia.com/cuBLAS`
[3] `https://developer.nvidia.com/cuRAND`

5 Performance and Quality Experiments

For all experiments a server with AMD FX-8150 Eight-Core processors 3.61GHz, 32GB RAM, Windows 8.1 OS, GeForce GTX 970 with 4GB RAM was used.

The first experiment measured a computation time with different settings of hidden neurons L. The matrix multiplication is done on GPU without data transfers and thus the GPU_M is not affected by L. Even if the matrix H is small ($L = 500$) the GPU processed computations in very short time. The final speedup is in the Table 1.

The second experiment measured the influence of the number of vectors N in the dataset. The table 2 shows the achieved speedup for different N. The QR decomposition (in GPU_F) is very sensitive to N but not so much to L. The speedup was about 92× for large data.

Table 3 shows the influence of the number of attributes M in the dataset to the computational times. The number of attributes is very important as shown in the Table 3. It is caused by $H = DW$ matrix multiplication, because the D is of size $N \times M$. The final speedup is showed in the last column of the table.

The last experiment tried to compare the original ELM to the proposed solutions. The approaches were tested on four datasets (Ionosphere[4], Sonar[5], Heart[6] and Diabetes[7]). A standard 10-fold cross-validation approach was used in all experiments. Table 4 shows an accuracy for each dataset. It is clear that all proposed approaches does not have an influence to the accuracy.

	CPU	GPU_F	GPU_I	GPU_M	Speedup
50	21.7812	7.5938	14.4218	0.1251	174.1382
100	46.2657	18.2344	31.6720	0.3752	123.3236
150	74.0001	23.4531	53.2188	0.5157	143.4814
200	104.1410	31.9531	77.4846	0.7655	136.0483
250	138.1090	38.9688	105.6410	1.0781	128.1029
300	173.1250	45.6875	134.3910	2.0781	83.3085
350	212.8280	51.4062	170.9840	2.8750	74.0274
400	254.6570	61.0312	206.7190	2.6562	95.8712
450	300.1100	66.7343	248.6570	3.5780	83.8758
500	347.0780	74.6250	292.6720	5.1406	67.5168

Table 1. Computation times with different numbers of hidden neurons (L) for every implemented approach.

[4] https://archive.ics.uci.edu/ml/machine-learning-databases/ionosphere/

[5] https://archive.ics.uci.edu/ml/machine-learning-databases/undocumented/connectionist-bench/sonar/

[6] https://archive.ics.uci.edu/ml/datasets/Statlog+%28Heart%29

[7] https://archive.ics.uci.edu/ml/machine-learning-databases/pima-indians-diabetes/

	CPU	GPU_F	GPU_I	GPU_M	Speedup
100 000	31.4796	7.0983	24.4443	0.5110	61.6013
200 000	66.4026	16.2059	50.6739	0.7820	84.9098
300 000	100.6510	25.1843	79.8904	1.0890	92.4286
400 000	136.6470	33.0817	105.5150	1.4864	91.9327
500 000	171.5780	44.6104	133.1660	1.8671	91.8955

Table 2. Computation times with different numbers of input vectors (N) for every implemented approach.

	CPU	GPU_F	GPU_I	GPU_M	Speedup
10	28.4427	7.1264	24.4673	0.5060	56.2082
20	31.4915	7.0013	24.8495	0.5150	61.1459
40	47.3815	8.2495	24.7176	0.4290	110.4400
80	90.8629	7.8224	25.2374	0.4412	205.9585
160	144.2400	7.4523	24.8906	0.4650	310.1762
320	264.0990	7.7694	25.0805	0.5060	521.9111
640	496.8640	7.8964	24.5113	0.6381	778.6678

Table 3. Computation times with different dimensions of input vectors (M).

	Ionosphere	Sonar	Heart	Diabetes
L	72	79	16	9
CPU	88.49±1.27	76.81±2.13	83.39±0.64	76.54±0.54
GPU_F	88.30±1.36	76.88±2.14	83.35±0.61	76.55±0.48
GPU_I	88.42±1.15	77.24±2.17	83.56±0.64	76.60±0.49
GPU_M	88.12±1.14	77.41±2.38	83.42±0.70	76.43±0.66

Table 4. Accuracy comparison (4 datasets, 4 approaches). L is a number of hidden neurons.

6 Conclusion and Future Work

This paper proposed a three different approaches that implements ELM classification algorithm on GPU. All three approaches were faster and reached the same accuracy as C++ version.

The proposed method GPU_M is able to achieve speedup more than 700x compared to the CPU approach. The method runs completely on GPU and uses reduced pseudo-inverse for solving leas-squares problem. Second proposed approach GPU_I is suitable in situations when GPU has not enough memory.

Approaches GPU_F and GPU_M run on GPU completely and thus they may be integrated within other GPU algorithms or applications effectively.

Projects and Publications

The extended version of this paper is to be published [7]. This work was supported by the IT4Innovations Centre of Excellence project (CZ.1.05/1.1.00/02.0070), funded by the European Regional Development Fund and the national budget of the Czech Republic via the Research and Development for Innovations Operational Programme and by Project SP2015/105 "DPDM - Database of Performance and Dependability Models" of the Student Grand System, VÅăB âĂŞ Technical University of Ostrava and and by Project SP2015/146 "Parallel processing of Big data 2" of the Student Grand System, VŠB âĂŞ Technical University of Ostrava, and it was also supported by Czech Science Foundation (GACR), grant No. P103/13/08195S.

References

1. Aryaz Baradarani, QM Jonathan Wu, and Majid Ahmadi. An efficient illumination invariant face recognition framework via illumination enhancement and dd-dtcwt filtering. *Pattern Recognition*, 46(1):57–72, 2013.
2. Bo He, Dongxun Xu, Rui Nian, Mark van Heeswijk, Qi Yu, Yoan Miche, and Amaury Lendasse. Fast face recognition via sparse coding and extreme learning machine. *Cognitive Computation*, 6(2):264–277, 2014.
3. Qing He, Tianfeng Shang, Fuzhen Zhuang, and Zhongzhi Shi. Parallel extreme learning machine for regression based on mapreduce. *Neurocomputing*, 102:52–58, 2013.
4. Gao Huang, Shiji Song, Jatinder ND Gupta, and Cheng Wu. Semi-supervised and unsupervised extreme learning machines. 2014.
5. Guang-Bin Huang, Hongming Zhou, Xiaojian Ding, and Rui Zhang. Extreme learning machine for regression and multiclass classification. *Systems, Man, and Cybernetics, Part B: Cybernetics, IEEE Transactions on*, 42(2):513–529, 2012.
6. Guang-Bin Huang, Qin-Yu Zhu, and Chee-Kheong Siew. Extreme learning machine: theory and applications. *Neurocomputing*, 70(1):489–501, 2006.
7. Tomas Jezowicz, Petr Gajdos, Vojtech Uher, and Vaclav Snasel. Classification with extreme learning machine on gpu. In *7-th International Conference on Intelligent Networking and Collaborative Systems INCoS-2015*. IEEE, 2015.
8. Weitao Li, Dianhui Wang, and Tianyou Chai. Burning state recognition of rotary kiln using elms with heterogeneous features. *Neurocomputing*, 102:144–153, 2013.
9. Mark van Heeswijk, Yoan Miche, Erkki Oja, and Amaury Lendasse. Gpu-accelerated and parallelized elm ensembles for large-scale regression. *Neurocomputing*, 74(16):2430–2437, 2011.
10. Zhu-Hong You, Ying-Ke Lei, Lin Zhu, Junfeng Xia, and Bing Wang. Prediction of protein-protein interactions from amino acid sequences with ensemble extreme learning machines and principal component analysis. *BMC bioinformatics*, 14(Suppl 8):S10, 2013.

Comparison of variable neighborhood search algorithm and particle swarm algorithm using travelling salesman problem optimization task

Adam Kašpar

Department of Computer Science, FEECS,
VŠB – Technical University of Ostrava, 17. listopadu 15, 708 33 Ostrava – Poruba
adam.kaspar@vsb.cz

Abstract. This paper discusses about comparison of Variable Neighborhood Search (VNS) and Particle Swarm Algorithm (PSO). The work is focused mainly on performance analysis of these two metaheuristic optimization methods, using TSP (Travelling Salesman Problem) optimization task. Beginning of this thesis will discuss about basic description of VNS and PSO algorithms. Next chapter will discuss about measured results. Conclusion will discuss about the future work.

Keywords: metaheuristic, optimization, PSO, TSP, VNS

1 Introduction

Travelling Salesman Problem is a well-known optimization problem. Main idea is based on finding of shortest cost of path between all cities. Basic solution is to go through all possible paths between cities. We should be able to find best possible cost of path, after all paths was passed.

The problem arises with growing number of cities, when computing time becomes intolerable. Possible solution is using one of metaheuristic, optimization algorithms, in our case VNS and PSO. Results of both algorithms, solving TSP problem are included in the last chapter of this thesis.

2 Computational methods

As computational method for TSP were picked VNS a PSO algorithms. We were mainly interested in different performance results between these metaheuristic methods.

2.1 Variable Neighborhood Search

This metaheuristic method was proposed by Hansen Mladenović in 1997. Method is useful for solving of global optimization problems. Basic process consists of few steps.

© M. Krátký, J. Dvorský, P. Moravec (Eds.): WOFEX 2015, pp. 332–336.
VŠB – Technical University of Ostrava, FEECS, 2015, ISBN 978-80-248-3787-1.

Local search. Local search. This computational methods is one part of VNS. At the beginning of all, initial solution x is established. Next, algorithm searches descent from x within neighborhood location of this x, let´s name it as $N(x)$ and moves to the minimum of $f(x)$ within $N(x)$ along that direction. Heuristic search is stopped, if no direction of descend is found. If descent is found, than neighborhood is iterated. At the end, the best direction (local minimum) is used [1].

Let's demonstrate this process with following algorithm.

```
Function BestImprovement(x)
    repeat
        x' ← x;
        x ← f(min(y ∈ N(x)));
    until (f(x) ≥f(x'));
return x;
```

(Example of BestImprovement method from Hansen, P., Mladenović., N.: Variable Neighborhood Search Methods. Les Cahiers du GERAD, Montreál/Uxbridge (2007))

As we can see entire neighborhood of x is searched. This approach is very timeconsuming, better approach is to use first descent heuristic method, in example is called as FirstImprovement function [2].

```
Function FirstImprovement(x)
    repeat
        x' ← x; i ← 0;
        repeat
            i ← i + 1;
            x ← min(f(x), f(xi), xi ∈N(x)
        until(f(x) < f(xi) or i = |N(x)|)
    until (f(x) ≥f(x'))
return x;
```

(Example of FirstImprovement method from Hansen, P., Mladenović., N.: Variable Neighborhood Search Methods. Les Cahiers du GERAD, Montreál/Uxbridge (2007))

In the case of FirstImprovement function is obvious, that inner and outer loop is terminated, if first improvement in neighborhood x is found.

Basic schemes. Basic schemes. Let´s have set of pre-selected neighborhoods N_k, where value of k is from 1 to k_{max} and set of solutions $N_k(x)$ in the kth neighborhood of x. If minimum (optimal solution or global minimum) in one of neighborhood is found, then is marked as x_{opt}. We can call $x' \in X$ of particular neighborhood N_k as local minimum, if there´s no exists any other solution $x \in Nk(x') \subseteq X$ such that $f(x) < f(x')$.

In basic variable neighborhood change algorithm (BVNS) is need to change neighborhood area in case of, that no improvement is done, see the following function [1].

```
Function NeighborhoodChange(x)
if f(x') < f(x) then
    x ← x'; k ← 1 /*Make a move*/;
else
    k ← k + 1 /*Next neighborhood*/;
```

(Example of NeighborhoodChange method from Hansen, P., Mladenović., N.: Variable Neighborhood Search Methods. Les Cahiers du GERAD, Montreál/Uxbridge (2007))

Basic VNS. Basic variable neighborhood search algorithm is combination of determin-istic and stochastic changes of neighborhood. Variable x is shook in the Shake function. This step is necessary to avoid cycling. Next, FirstImprovement method was used. Obtained variable x'' is then compared with neighborhood change method. If value of function $f(x'')$ is better than value of $f(x)$, then original variable x is replaced with x'' and neighborhood k is set to initial value 1. This case is called as "move" to new vector x. On the other hand, if there is no improvement in comparison between x and x', then neighborhood k is replaced with $k + 1$ value. This case means, that algorithm was switched to another neighborhood.

At the end of each loop, k value is checked. If k equals to k_{max}, then loop is terminated (maximal count of searched neighborhoods without any improvement has been reached). CpuTime is also checked, if measured time is smaller, then t_{max} value, then algorithm continues with next iteration, otherwise VNS execution is terminated [3].

For demonstration purposes, see pseudo-VNS function in VNS algorithm.

```
Function VNS(x, kmax, tmax)
repeat
    k ← 1;
    repeat
        x' ← Shake(x, k) /*Shaking*/
        x'' ← FirstImprovement(x') /*Local search*/
        NeighborhoodChange(x, x'', k) /*Change neighborhood*/
    until k = kmax
    t ← CpuTime()
until t > tmax
```

(Example of VNS method from Hansen, P., Mladenović., N.: Variable Neighborhood Search Methods. Les Cahiers du GERAD, Montreál/Uxbridge (2007))

2.2 Particle Swarm Optimization

Particle swarm optimization (PSO) is a population based stochastic optimization technique. It was first introduced by J.Kennedy and R.Eberhart [4] in 1995. More

specifically, PSO is method, designed to optimize concrete problem by iterative way [5].

Description. Description. Basic version of PSO works with population (swarm) of candidate solutions (particles). Algorithm moves with these candidate solutions through searchspace. Base for these moves are is particle´s and swarm´s best known positions in the searchspace.

If better positions for swarm are found, then these positions replaces old swarm positions. This process is repeated as long as optimal solution is found. On the other side, metaheuristics such as PSO do not guarantee an optimal solution is ever found [6].

3 Results

Both described algorithms were subjected to performance measurement. As base optimization problem was determined Travelling Salesman Problem [7].

It was performed about 5 measurements with different number of cities for each of both algorithms. For PSO, maximal number of epochs was chosen as 10000. For VNS, maximal number of iterations without improvement was chosen as 100. All tests ran in Java environment. Table 1 shows measured results.

Table 1. Results of comparison between PSO and VNS using TSP.

Alg. name	Num. of cities	Min. cost	Total time [s]
PSO	50	2349	26
	100	3532	54
	200	4666	112
	250	5540.8	147
	280	5815.7	216
VNS	50	644	1
	100	1126	4
	200	2200	25
	250	2774	33
	280	2853	66

As we can see, VNS was efficient in all performed measurements. Average performance for VNS was mostly more than 2 times better than PSO.

4 Conclusion and future work

My intent is to use both described algorithms in my future work. My work is focused on research of swarm intelligence. Future research will be also focused on another optimization algorithms and methods with aim to upgrade them, if it will be possible.

References

1. Hansen, P., Mladenović., N.: Variable Neighborhood Search Methods. Les Cahiers du GERAD, Montreál/Uxbridge (2007)
2. Hansen, P., Moreno Peréz, J.A., Mladenović, N.: Variable neighbourhood search: methods and applications. Springer-Verlag, Montreál/Uxbridge/La Laguna (2008)
3. Hansen, P., Mladenović, N.: Variable neighborhood search: Principles and applications. Gerad, Montreál (1999)
4. Kennedy, J., Eberhart, R.: Neural Networks. IEEE, Perth (1995)
5. Kaur, A., Kaur, M.: A Review of Parameters for Improving the Performance of Particle Swarm Optimization. Guru Nanak Dev University, Jalandhar (2015)
6. Zhenhua, L.: Computational Intelligence and Intelligent Systems. Springer-Verlag, Wuhan (2012)
7. Gutin, G., Punnen, A.P.: The Traveling Salesman Problem and Its Variations (Combinatorial Optimization). Kluwer Academic Publishers, AH Dordrecht (2002)

Analytic programming on CPU and GPU

Lumír Kojecký

Department of Computer Science, FEECS,
VŠB – Technical University of Ostrava, 17. listopadu 15, 708 33 Ostrava – Poruba
lumir.kojecky@vsb.cz

Abstract. Analytic programming is one of methods of symbolic regression that is composing simple elements into more complex units. This process can be used e.g. for approximation of measured data with suitable mathematical formula. To find the most suitable mathematical formula it is necessary to use an evolutionary algorithm. Since the process of estimation is too slow, the algorithm was also implemented in one of the most widespread programming architecture NVIDIA CUDA and the results in terms of execution time are compared.

Keywords: Analytic programmming, SOMA, parallelization, CUDA

1 Introduction

Symbolic regression [3] is a process in which are composed simple elements into more complex units – programs. This process can be used for logic circuit synthesis, neural network synthesis or approximation of measured data with most suitable mathematical formula. There are several approaches to symbolic regression, for example Genetic programming [5], Grammatical evolution [9], or Analytic programming (AP) [11], [12].

In Analytic programming, that is used for approximation of measured data with most suitable mathematical formula, programs can consist of mathematical operators, functions, variables or constants. These elements are placed in General Functional Set (GFS). As an input, AP takes a set of numbers that are pointers to the GFS. From these elements then AP composes an output expression. Process of the expression composing is visualized in Fig. 1.

To find the most suitable mathematical formula it is necessary to use an evolutionary algorithm that will provide the input sets of numbers to convert. For AP purposes can be used an arbitrary evolutionary algorithm like Particle Swarm Optimization [4], Differential Evolution [10], or Self Organizing Migrating Algorithm (SOMA) [7], [2]. For the output mathematical formula is then calculated difference (area) between the formula and measured data, that is used as fitness for a particular individual. As a representative evolutionary algorithm was chosen SOMA algorithm.

SOMA is a stochastic optimization algorithm imitating the social behavior of cooperating individuals. At the beginning, the population is randomly initialized and evaluated. Then is chosen an individual with the highest fitness –

© M. Krátký, J. Dvorský, P. Moravec (Eds.): WOFEX 2015, pp. 337–342.
VŠB – Technical University of Ostrava, FEECS, 2015, ISBN 978-80-248-3787-1.

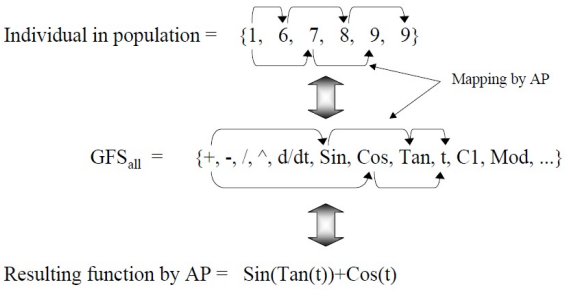

Fig. 1. Main principle of AP [12]

the leader. In each migration loop, all other individuals are moving through the space towards the leader and seeking their best position with the highest fitness. Movement in allowed dimensions is controlled before each individual's step by creation of binary perturbation vector.

In AP there are several options how to handle constants. One of the methods is to place many randomly generated constant values to GFS [5] – in this case, number of possible generated formulas rapidly increases. In this paper we use a method that adds only one general indexed constant K (1) to GFS. Values of all indexed constants are estimated using a second evolutionary algorithm. Unfortunately, due to this estimation, the whole process becomes too slow. This algorithm was therefore implemented in one of the most widespread programming architecture NVIDIA CUDA which allows us to reduce the computational time.

$$K_1 \cdot (x + K_2) \tag{1}$$

2 Code Design on the GPU

2.1 NVIDIA CUDA

The Compute Unified Device Architecture (CUDA) [6] is one of the most widespread parallel programming architecture invented by NVIDIA. It provides us a platform for accessing the NVIDIA GPU for processing in essence by extensions to standard programming languages like C/C++.

In CUDA language, functions that are launched from CPU are named kernels. Each kernel consists of blocks that are executed independently from each other on multiple Streaming Multiprocessors. Each block is divided into threads. These threads have access to the registers and shared memory in a block they belong to. Kernels can be executed on any combination of blocks and threads – this depends only on the application requirements.

In Table 1 there are summarized several types of GPU memories, having each its capabilities and purpose, differing in access latency, size, address space, scope, lifetime and whether it is cached or writable.

Table 1. Summary of the scope and lifetime of CUDA memories

Memory	Scope EA	Lifetime
Global	Grid	Application
Constant	Grid	Application
Shared	Block	Kernel
Register	Thread	Kernel
Local	Thread	Kernel

2.2 Implementation Details

When designing the code on the GPU [1], [8], it is highly desirable to write bigger kernels with more functionality instead of many small kernels. Not only fitness function evaluation [1], but all computation tasks are also moved from CPU to GPU. It is also desirable to avoid many memory transfers between CPU to GPU. In this application, all memory transfers are reduced to only 3 cases:

1. Transferring the GFS and the measured data to GPU from application configuration file.
2. Transferring number of constants in an expression from GPU to CPU to decide whether to run the inner evolution to estimate the constants or not.
3. Transferring the final expression from GPU to CPU.

One of the most crucial steps is using shared memory as much as possible due to very high access latency of global memory. In this program, shared memory is widely used – each individual or expression is processed in one block so this is an ideal candidate for using shared memory:

- Mathematical fitness function evaluation – all values are loaded into shared memory at once (by multiple threads) and sequentially processed within this fast memory.
- Composing expressions – GFS, as well as appropriate indexed expressions, is loaded into shared memory at once and one by one processed within this fast memory. This includes pairing expressions with other ones and checking whether the final expression is pathological or not.
- Expression evaluation – each expression is concurrently evaluated in 50 measured points that are loaded into shared memory as well as the evaluated expression.

It is also necessary to appropriately design the grid to efficient use of GPU resources – one individual, as well as one expression, is here processed by one block of threads. The grid consists of $PopSize$ blocks and each block consists of Dim threads. This grid layout (illustrated in Fig. 2) allows us to efficiently utilize shared memory.

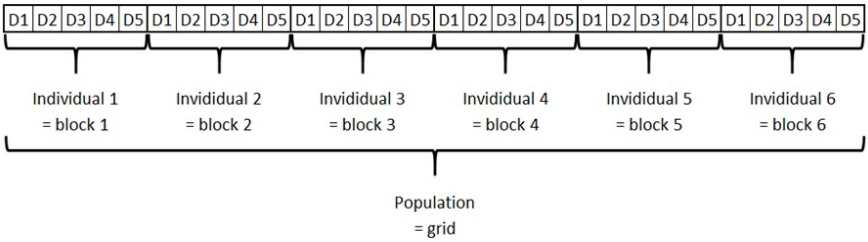

Fig. 2. CUDA Grid layout design

3 Simulations and Results

Experiments done in this paper were focused on performance measurement of the new GPU application and its comparison with current single-thread C# application. All simulations were done on a desktop PC with Intel Core i7 at 3.4 GHz and NVIDIA GeForce 750 Ti that operates on 1,020 MHz core clock speed and compute capability version 5.0.

At first was measured performance of standalone SOMA (version AllToOne), optimizing Schwefel's function (2). Then was measured performance of basic AP (without estimation of constants) and also AP algorithm with estimation of constant values by means of secondary evolutionary algorithm, approximating 50 points of Quintic equation (3) in interval $[-1, 1]$.

$$\sum_{i=1}^{n} -x_i \sin(\sqrt{|x_i|}) \tag{2}$$

$$x^5 - 2x^3 + x \tag{3}$$

Each experiment was repeated 50 times. Operating parameters for all use cases of SOMA are given in the Table 2.

Table 2. Algorithm settings for SOMA. The dimension of the inner EA equals to the number of estimated constants.

Parameter	Outer EA	Inner EA	Basic AP	SOMA only
Dimensions	50	-	$[20, 30, 50]$	$[20, 30, 50]$
PopSize	100	50	100	100
Migrations	12	11	100	200
PRT	0.1	0.1	0.1	0.1
PathLength	3	2	3	3
Step	0.11	0.21	0.11	0.11

The results from all simulations are summarized in Tables 3-5. In each Table there is recorded the maximal, median, average and the minimal execution time of all 50 simulations for both C# and CUDA implementations.

Table 3. SOMA Algorithm runtime [s]

	Dimension 20				Dimension 30				Dimension 50			
Language	Max	Med	Avg	Min	Max	Med	Avg	Min	Max	Med	Avg	Min
C#	3.07	2.88	2.90	2.85	4.24	4.20	4.20	4.17	7.56	7.20	7.22	7.14
CUDA	0.16	0.06	0.06	0.05	0.20	0.06	0.07	0.06	0.21	0.11	0.11	0.10
Speedup	19.19	48.00	48.33	57.00	21.20	70.00	60.00	69.50	36.00	65.45	65.64	71.40

Table 4. Basic AP version runtime [s]

	Dimension 20				Dimension 30				Dimension 50			
Language	Max	Med	Avg	Min	Max	Med	Avg	Min	Max	Med	Avg	Min
C#	6.32	6.19	6.18	6.02	9.96	9.70	9.68	9.33	18.23	17.70	17.67	16.99
CUDA	0.30	0.11	0.12	0.11	0.26	0.15	0.15	0.15	0.41	0.29	0.30	0.29
Speedup	21.07	56.27	51.50	54.73	38.31	64.67	64.53	62.20	44.96	61.03	58.90	58.59

Table 5. AP-meta version runtime [s]

	Dimension 50			
Lang.	Max	Med	Avg	Min
C#	2210.68	1735.53	1726.06	1262.56
CUDA	116.60	111.63	111.68	106.94
Speedup	18.96	15.55	15.46	11.81

4 Conclusion

In this paper was implemented CUDA-based Analytic programming by means of SOMA algorithm in three versions: standalone SOMA, basic AP without estimation of constants and AP with estimation of constants.

Simulations showed us that average speedup of CUDA implementation of standalone SOMA and basic AP was from 48× to 65× and speedup of full version of AP was 15×. This speedup was achieved especially by proper use of shared memory and minimizing memory transfers between the CPU and GPU.

However, the smaller speedup of full AP was caused by too big problem size. One graphic card cannot process all data in one big transaction – the transaction has to be divided into more smaller transactions.

In the future research of the algorithm parallelization field, we want to utilize more than one CUDA GPU or to utilize the other parallel platforms to achieve even better results. Currently, we are preparing similar simulations under Open MPI architecture that can run on Anselm, x86-64 Intel based supercomputer hosted at VSB-Technical University of Ostrava.

The extended version of this paper was published in the conference Mendel 2015.

Acknowledgment

The following grants are acknowledged for the financial support provided for this research: Grant Agency of the Czech Republic – GACR P103/15/06700S and partially supported by Grant of SGS No. SP2015/142, VSB-Technical University of Ostrava.

References

1. Davendra, D., Gaura, J., Bialic-Davendra, M., Senkerik, R.: Cuda based enhanced differential evolution: A computational analysis. In: ECMS. pp. 399–404 (2012)
2. Davendra, D., Zelinka, I.: Flow shop scheduling using self organizing migration algorithm. In: Modelling and Simulation.[Proceedings of the European Conference.] Nicosia: European Council of Modelling and Simulation. pp. 195–200 (2008)
3. Davidson, J., Savic, D.A., Walters, G.A.: Symbolic and numerical regression: Experiments and applications. Information Sciences 150(1), 95–117 (2003)
4. Kennedy, J., Kennedy, J.F., Eberhart, R.C.: Swarm intelligence. Morgan Kaufmann (2001)
5. Koza, J.R.: Genetic programming III: Darwinian invention and problem solving, vol. 3. Morgan Kaufmann (1999)
6. Nvidia, C.: Nvidia cuda c programming guide. NVIDIA Corporation 120 (2011)
7. Onwubolu, G.C., Babu, B.: New optimization techniques in engineering, vol. 141. Springer Science & Business Media (2004)
8. Pospichal, P., Jaros, J., Schwarz, J.: Parallel genetic algorithm on the cuda architecture. In: Applications of Evolutionary Computation, pp. 442–451. Springer (2010)
9. Ryan, C., Collins, J., Neill, M.O.: Grammatical evolution: Evolving programs for an arbitrary language. In: Genetic Programming, pp. 83–96. Springer (1998)
10. Storn, R., Price, K.: Differential evolution–a simple and efficient heuristic for global optimization over continuous spaces. Journal of global optimization 11(4), 341–359 (1997)
11. Zelinka, I.: Analytic programming by means of soma algorithm. In: Proceedings of the 8th International Conference on Soft Computing, Mendel. vol. 2, pp. 93–101 (2002)
12. Zelinka, I., Oplatkova, Z., Nolle, L.: Analytic programming–symbolic regression by means of arbitrary evolutionary algorithms. Int. J. of Simulation, Systems, Science and Technology 6(9), 44–56 (2005)

Parallelization of Cellular Automaton using Kaira

Lukáš Kroczek

Department of Computer Science, FEECS,
VŠB – Technical University of Ostrava, 17. listopadu 15, 708 33 Ostrava – Poruba
lukas.kroczek@vsb.cz

Abstract. This paper focuses on a cellular automaton and describes how the performance of cellular automaton can be improved by using parallel computation techniques called Kaira. The paper describes how a code can be created in Kaira without knowledge of MPI. Auto-generated code will use MPI.

Keywords: cellular automaton, parallelization, Kaira, MPI

1 Introduction

Parallel computing gives us possibility to decrease computational time or runs applications that are too large for a single machine. These benefits are connected with more complex development of the applications using parallel computing. Since programming and debugging of the parallel applications can be too hard for some developers, Kaira was developed.

Kaira allows to create a visual model of communication and parallelism of a program and the developer can insert his own sequential code written in C++ into this model. The visual models in Kaira are based on variant of Colored Petri nets (CPN) [4].In the result, Kaira generates parallel backend-threads or Message Passing Interface (MPI) [5].

2 Experiment Design

2.1 Cellular Automaton

A cellular automaton is a model of a world with very simple physics. Cellular means that the space is divided into discrete chunks, called cells. An automaton is a machine that performs computationsit could be a real machine, but more often the machine is a mathematical abstraction or a computer simulation.

Automata are governed by rules that determine how the system evolves in time. Time is divided into discrete steps, and the rules specify how to compute the state of the world during the next time step based on the current state. [3]

A self-reproduction automaton was first presented by Von Neumann. He considers such a model, and incorporated a cellular model into his "universal

© M. Krátký, J. Dvorský, P. Moravec (Eds.): WOFEX 2015, pp. 343–347.
VŠB – Technical University of Ostrava, FEECS, 2015, ISBN 978-80-248-3787-1.

constructor". A CA consists of regular square cells with discrete variables. The actual value of each cell is updated simultaneously based on the value of current and neighbors cells at the preceding step and according to a definite set of a local rules. Since the local rule is defined so as to govern only local relationships among the neighbors cells, the governing equation for the whole domain is not necessary.

More information about cellular automaton you can find in [8].

2.2 About Kaira

This section shortly describes Kaira basics. More details about Kaira can be found in papers [6] (where was Kaira introduced) and [7].

Kaira [1] is as an open-source development environment for MPI (Message Passing Interface) applications. Kaira tries to provide an unified environment for activities for development: prototyping, programming, testing, debugging, profiling, performance prediction, and verification.

The main idea is to use visual models (inspired by Colored Petri Nets). This model is designed to catch parallel aspects and communication inside of the developed application. Kaira does not want to program applications completely in a visual way, so our models can be enriched by any sequential C++ code. With such model, a user can generate MPI applications, run simulations, or start a state-space analysis.

A program in Kaira consists of a visual program (net), sequential codes embedded into the net and global configurations. This text starts with the most important part, the visual language for describing nets. The goal of the visual language is to describe data-flows and communication in the developed program. It consists of four main elements: Places, Transitions, Arcs, and Init areas.[2]

Everything that can be done with Kaira can be also achieved by the direct use of C++ and MPI. The opposite direction does not hold. The current version of Kaira does not use collective communication i.e. all communication are realized through point-to-point sends.[2]

Some attributes of an element contain C++ expressions. Each expression should not have any side effect and a returned value should depend only on the values of its free variables. The user cannot make any assumption about when and how many times any one of the expressions is evaluated. [2]

2.3 Cellular Automaton in Kaira

Design of parallel processed cellular automaton consist of 4 main steps that are running in loop:

1. Split
2. Distribute
3. Compute
4. Merge

Except these 4 steps, the program includes an initialization logic (a logic before the first step) and a logic for keeping all results.

Split In the split step we provide splitting 1 big array into P smaller arrays where P means number of running processes. Each small array will consist his part of array and neighbor cell on each side except the first and the last array which will consist of array and neigbour cell only on the side where it is ending (for the first array) or starting (for the last array).

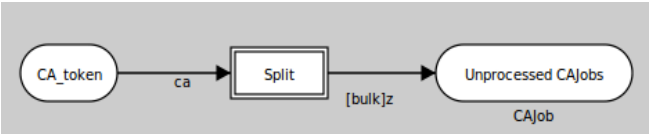

Fig. 1. Process of splitting

Distribute This part of the process provides distributing of array parts into available processes. The current implementation includes a load balancer (a balancer is for the case when we will split an array into bigger number of small arrays than is the number of processes).

Compute Here is the main computing logic. When the computing is finished, the process that provides computation is put on the list of free processes (for the correct working of the load balancer).

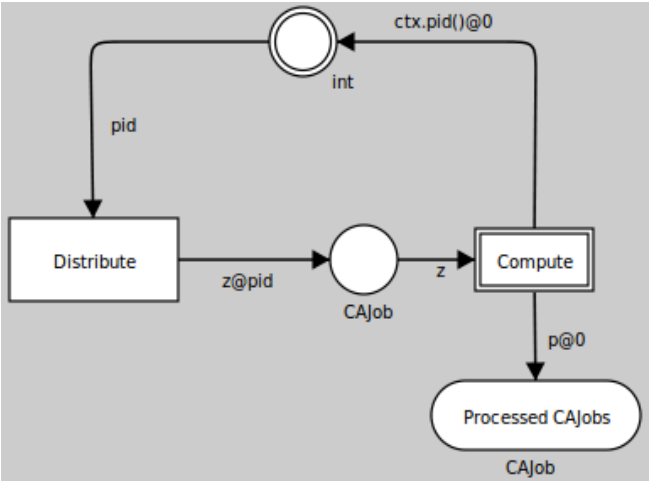

Fig. 2. Process of distributing and computing with used load balancer

Merge When all small arrays are counted, then merging of all small array to one big array is provided. Important is merging arrays in the correct order.

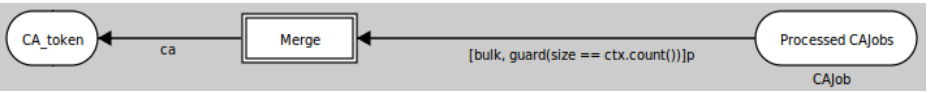

Fig. 3. Process of merging

Init step Init step defines the starting point of the application and specifies the starting array. The program provides checking of input parameters here.

Saving result This part saves the result of each step and stops the program when we compute selected number of iterations.

When we merge all these steps we will receive process shown in Fig. 4. The steps can contain C++ logic inside the transitions (for more details see [2]).

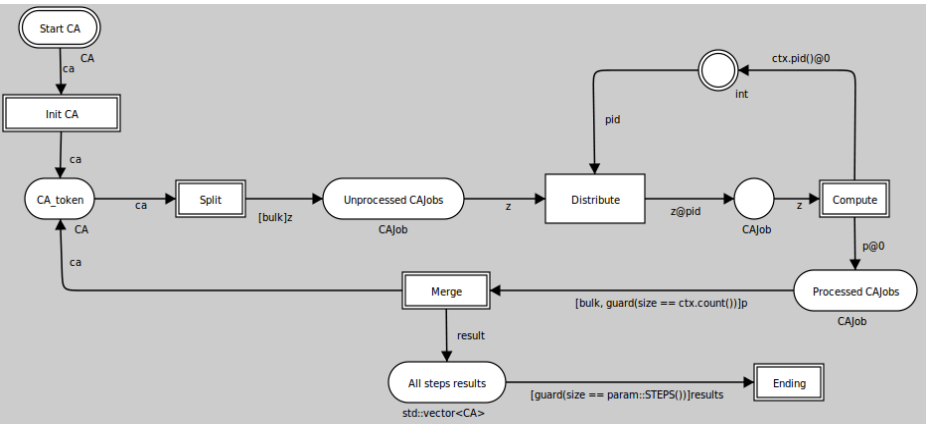

Fig. 4. Complete process schema in Kaira

3 Results

The experiments done in this paper were focused on validation and performance measurement and comparison with multi-thread C# application.

The experiment was repeated for 100 times, results are summarized in Table 1. In table are showed maximum, minimum and average execution time counted for 100 executions for C# multi-thread application, for Kaira back-end code using threads and Kaira back-end code using MPI. Both Kaira back-end codes are auto-generated from the identical visual model. Cellular automaton setting were set k=2 and r=1, size of array to 100 cells. One execution provides 10000 iterations (steps) of cellular automaton.

Table 1. This table shows performance results

Implementation	Min [s]	Max [s]	Average [s]
C# multithreads	0.35	0.511	0.419
Kaira Threads	0.184	0.452	0.302
Kaira MPI	0.148	0.384	0.223

All results were measured on the same machine. Programs generated by Kaira were running in a virtual machine, so the performance was degraded.

4 Conclusion and Future Work

Implementation of Cellular Automaton is presented. Future work will focus on implementation of Cellular automaton in another parallel technologies, e.g. CUDA, MPI and similar. Then I will compare these parallel technologies and choose the best technology based on time.

References

1. Kaira: About, http://verif.cs.vsb.cz/kaira/
2. Bohm, S.: Unifying framework for development of message-passing applications (2013), http://verif.cs.vsb.cz/sb/thesis.pdf
3. Downey, A.B.: Think complexity: Complexity science and computational modeling (2012)
4. Jensen, K., Kristensen, L.M.: Coloured petri nets - modelling and validation of concurrent systems. Berlin/Heidelberg: Springer, 2009 (2009)
5. M. Snir, S.O., et al.: Mpi-the complete reference, volume 1: The mpi core. 2nd (revised). Cambridge: MIT Press (1998)
6. S. Bohm, S.B.: Kaira: Modelling and generation tool based on petri nets for parallel applications. 13th International Conference on Computer Modelling and Simulation (UKSim 2011) (2011)
7. S. Bohm, S.B., Garnczarz, O.: Developing parallel applications using kaira
8. Wolfram, S.: A new kind of science. Wolfram Media, Champaign, Ill. (2001)

Cost Estimations in XML Queries

Petr Lukáš

Department of Computer Science, FEECS,
VŠB – Technical University of Ostrava, 17. listopadu 15, 708 33 Ostrava – Poruba
petr.lukas@vsb.cz

Abstract. Storing and querying data in a form of relations is not always the best choice. There are alternatives like an XML data model that are more suitable in certain situations. The main advantage of the XML data model is a dynamic schema. There are many approaches dealing with the problem of storing and querying such a model. However, there are still opportunities to improve effectiveness of XML query evaluation. In this paper we show how to estimate a cost of an XML query with respect to persistent data structures of a native XML database.

Keywords: XQuery, XML, query processing, TPQ, cost-based optimizations

1 Introduction

In [7], we proposed a novel cost-based optimization method of holistic twig join algorithms. These algorithms evaluate *twig pattern queries*[1] (TPQ) representing a simplified model of XML queries used by many approaches [3, 2, 7, 1]. Namely, we proposed Cost-Twig Join (CTJ) algorithm [1] that is capable of using two index data structures (see Section 2). This algorithm is implemented in our prototype of a native XML database management system (DBMS) called RadegastXDB (originally QuickXDB) [8].

Any cost-based optimization method is based on a cost formula that evaluates a cost of a query plan (see Section 2.1). A cost formula often consists of variables that are estimated using several statistics of persistent data structures. In this paper, we show what statistics do we need and how the estimations should be done in order to use the proposed CTJ algorithm.

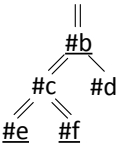

Fig. 1. TPQ Example

2 Cost-Twig Join

The CTJ algorithm is based on two persistent data structures. We call them *document index* and *partition index*. Similar structures can be found in any native XML DBMS.

[1] TPQ is a labeled rooted tree, where the nodes represent tag predicates and the edges represent required relationships. An example of a TPQ can be found in Figure 1.

© M. Krátký, J. Dvorský, P. Moravec (Eds.): WOFEX 2015, pp. 348–353.
VŠB – Technical University of Ostrava, FEECS, 2015, ISBN 978-80-248-3787-1.

The document index is a primary storage (i.e. all other indices can be build from this structure). It is a B^+-tree where a *node label* servers as a key. A node label is a unique identifier of each XML data node and knowing two node labels, we can immediately resolve their structural relationship.

The partition index is also a B^+-tree, but with a node tag as a key. The leaf entries of the B^+-tree point to paged arrays of node labels that correspond to data nodes of a given tag. The node labels in the arrays are sorted according to the document order.

The key idea of the CTJ algorithm is that some of query nodes are evaluated using the partition index (we call the nodes *partition query nodes*), while the rest of the query nodes is evaluated using the document index (we call them *document query nodes*). This is in contrast with traditional holistic joins, that use only the partition index (or a similar structure).

2.1 Cost Analysis

Before a TPQ can be evaluated using the CTJ algorithm, a *query plan* has to be known. A query plan divides query nodes onto partition and document query nodes. An example of a plan is also given in Figure 1 – partition query nodes ($\#b$, $\#e$ and $\#f$) are underlined.

$$Cost = \frac{reads}{size_s} + \beta * seeks * height + \alpha * \frac{moves}{size_t} \quad (1)$$

Different query plans have different costs. The cost can be computed using Equation 1. The formula is explained in [7] in a more detail. In this paper, we are interested in variables that are computed using statistics of the persistent data structures. Those variables are: *reads*, *seeks* and *moves*.

3 Statistics and Estimation

We can never compute the *reads*, *seeks* and *moves* variables precisely, since they depend on a particular TPQ and data. Instead, they have to be estimated.

3.1 Partition Index

The partition index is used to evaluate a part of a TPQ that consists only of partition query nodes. We call such a part a *core subquery*. A core subquery of the TPQ in Figure 1 is depicted in Figure 2.

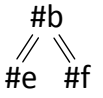

Fig. 2. Core subquery

The evaluation of the core subquery is performed such that arrays of node labels matching to the partition query nodes are merged together. The variable *reads* reflects a number of node labels retrieved from the partition index. Since we need to read the whole arrays, the value of *reads* is computed by summing

sizes of the arrays. The only statistic we need is a size of array for each node tag.

However, the situation becomes more complicated in practice if we consider the *early termination property* of holistic twig joins (see [1]). Breafly, it is not always necessary to read the whole arrays. When performing the merge, when we reach end of any array, the rest of the other arrays can be skipped. To solve this problem, we use 1-dimensional histograms [6] reflecting a distribution of XML nodes of a given tag among an XML document.

3.2 Document Index

The variables *seeks* and *moves* are related to the document index. The value of *seeks* represents a result size of the core subquery and this is exactly the number of range queries that have to be performed in the document index to resolve the rest of the relationships of the original TPQ. The value of *moves* is the total number of leaf entries read from the B^+-tree of the document index during the range queries. Since each range query searches for descendants of an XML node, the value of *moves* also reflects the number of descendants of XML nodes retrieved by the core subquery.

Note, that a result of a TPQ depends on *output query nodes*. In the case of the core subquery, an output query node is each partition query node having a document query node as a child in the original TPQ and not having another output query node as a parent. In our example (see Figure 1 and Figure 2), it is the query node $\#b$.

Usually, there is exactly one output query node in the core subquery and we will consider only this variant from this point. However, generally, there may be situations, when there are more output nodes, and those are discussed in [1].

Each TPQ with a single output node can be written as an XPath expression. The *seeks* and *moves* values are computed using two *auxiliary* XPath queries that are both constructed from the core subquery. We are only interested in their result sizes, we do not need the complete result.

The auxiliary query computing *seeks* is constructed directly from the core subquery. The auxiliary query computing *moves* is constructed so that we add a wildcard query node (i.e. `//*`) at the end of the *seeks* auxiliary query.

In the case of the core subquery in Figure 2, the auxiliary queries are:
seeks = `count(//b[.//e and .//f])`,
moves = `count(//b[.//e and .//f]//*)`.

Clearly, the estimation of the *seeks* and *moves* values is transformed to the estimation of an XPath query result size. There are many approaches dealing with this problem [12, 11, 5, 9]. We use two of them in this paper: (1) *XSketch synopsis* [11], which is considered one of the state-of-the-art selectivity estimation techniques, and (2) the *sampling* based estimation [9]. In the following paragraphs, we briefly describe both methods.

XSketch synopsis is an oriented labeled graph, where nodes correspond to disjoint sets of XML nodes [11]; these sets are called *extents*. The graph is fully

loaded into the main memory to provide a low response time. The estimation is then based on forward and backward stabilities between the extents [10]. More precisely, we use the f-XSketch variant [4], where fractional stabilities are utilized instead of binary value stabilities. This simple improvement provides a more accurate estimation of the query result size.

Sampling is a simple estimation method [9]. A query is processed on a small sample XML document constructed from the original XML document. The result size is then multiplied by a fraction N_{out}/n_{out}, where N_{out} and n_{out} are the numbers of nodes with the tag *out* in the sample and the original XML document, respectively (the tag *out* is a tag searched by the output query node).

4 Experimental Results

In this section we show the advantage of CTJ over a traditional holistic join algorithm with respect to a statistic that is used to estimate values of *reads*, *seeks* and *moves* variables which in turn yield a cost of a query. For the partition index, the 1-dimensional histograms are always used. For the document index, we have two statistic available – XSketch synopsis and a sample. Moreover, we can use various sampling ratios that produce samples of different sizes. Concretely, we use two samples – one of 100 kB size and one of 1 MB size.

We tested four XML data collections: XMark[2] (1.11 GB), SwissProt (109 MB), DBLP (127 MB) and TreeBank (82 MB).[3] We generated 250 testing XPath queries with varying selectivity for each data collection.

Summarized results are shown in Figure 3. The values represent a relative speed-up of CTJ over a traditional holistic twig join. Horizontal axes mean selectivity of a group of queries. Circles represent the best possible speed-up of the CTJ algorithm, i.e. we know the best possible plan in advance. Crosses represent a speed-up, when the plan is selected using a particular statistic – 100 kb sample, 1 MB sample or XSketch. An optimization overhead is taken into account.

We can see that usually the statistics choose the best or almost the best query plans for all the collections except TreeBank. TreeBank is the smallest collection, but it contains a lot of recursive elements that make result size estimations complicated and non-accurate. For the f-XSketch statistic, there are no results for this collection, since it was not possible to build the synopsis.

There are no major differences between the 100 kB sample, 1 MB sample and the XSketch. However, there were group of queries (see XMark collection and queries with selectivity up to 0.05) where the XSketch synopsis choose worse plans than the samples. There is also a significant practical advantage of sampling-based estimations over the XSketch synopsis. Building of a sample can be done almost immediately as an XML document is being indexed. On the other hand, building of an accurate XSketch takes much more time (several hours on a common PC).

[2] `www.xml-benchmark.org/generator.html`

[3] All collections except XMark:
`cs.washington.edu/research/xmldatasets/www/repository.html`

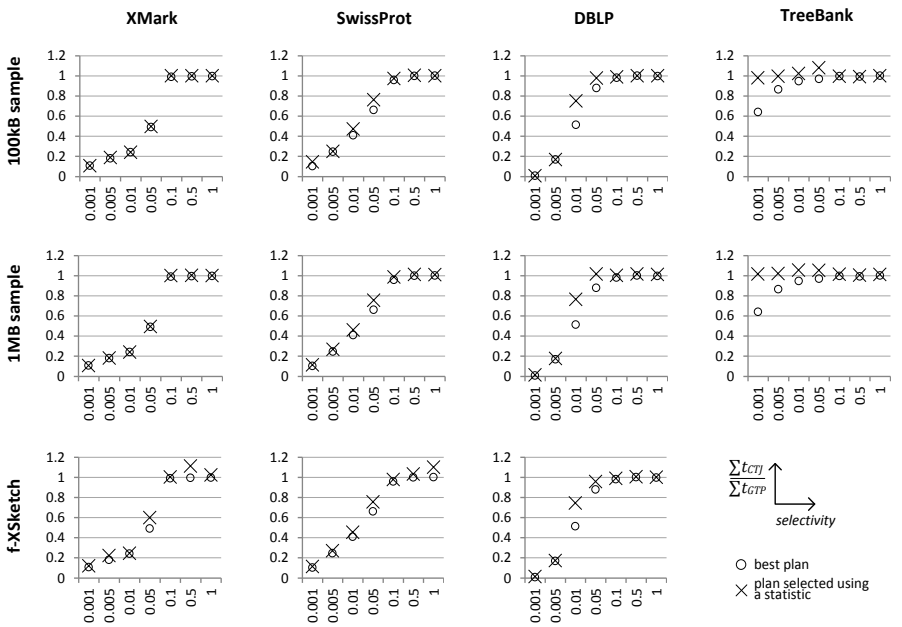

Fig. 3. Experimental results

5 Conclusions and Future Work

In this paper, we have shown what statistics and estimation techniques are needed to make a novel CTJ algorithm working effectively. Especially, for highly selective queries, the CTJ algorithm is 10 – 100 times faster and this is achieved by a selection of an appropriate query plan.

Holistic twig joins are not the only algorithms that can evaluate TPQs. There is also another family of algorithms called binary structural joins that evaluate TPQs successively by query edges. These algorithms ale often criticized because of large intermediate results they produce. However, there is a large class of XML queries that can be evaluated using pipelined binary joins, where there is no need of any intermediate result. Our initial experiments show that these pipelined binary joins can outperform the holistic twig joins. Our future work will be focused on integrating such joins into our XML database prototype and comparing the two families – holistic twig joins and binary structural joins.

Author Publications

1. R. Bača, P. Lukáš, and M. Krátký. Cost-based holistic twig joins. *Information Systems*, 52:21–33, 2015.

2. R. Bača, P. Chovanec, M. Krátký, and P. Lukáš. QuickDB – Yet Another Database Management System?. *Dateso 2014*. Pages 91–99. Písek, April 2014. ISBN 978-80-01-05482-6.
3. P. Lukáš, R. Bača, and M. Krátký. QuickXDB: A Prototype of a Native XML DBMS. *Dateso 2013*. Pages 36–47. Písek, April 2013. ISBN 978-80-248-2968-5.

Author Projects

– SP2015/170 – doc. Ing. Stanislav Mišák, PH.D. Vývoj detektoru poruch izolačních systémů s podporou databázových systémů

References

1. R. Bača, P. Lukáš, and M. Krátký. Cost-based holistic twig joins. *Information Systems*, 52:21–33, 2015.
2. R. Bača, M. Krátký, T. Ling, and J. Lu. Optimal and efficient generalized twig pattern processing: a combination of preorder and postorder filterings. *The VLDB Journal*, 22(3):369–393, 2013.
3. N. Bruno, D. Srivastava, and N. Koudas. Holistic Twig Joins: Optimal XML Pattern Matching. In *Proceedings of ACM SIGMOD 2002*, pages 310–321. ACM Press, 2002.
4. N. Drukh, N. Polyzotis, M. Garofalakis, and Y. Matias. Fractional xsketch synopses for xml databases. In *Database and XML Technologies*, pages 189–203. Springer, 2004.
5. D. K. Fisher and S. Maneth. Structural selectivity estimation for xml documents. In *Data Engineering, 2007. ICDE 2007. IEEE 23rd International Conference on*, pages 626–635. IEEE, 2007.
6. Y. Ioannidis. The history of histograms (abridged). In *Proceedings of the 29th international conference on Very large data bases-Volume 29*, pages 19–30. VLDB Endowment, 2003.
7. P. Lukáš. Cost-based optimizations of xml queries. *Ph.D. Workshop of Faculty of Electrical Engineering and Computer Science*, pages 383–389, 2014.
8. P. Lukáš, R. Bača, and M. Krátký. QuickXDB: A Prototype of a Native XML DBMS. In *Proceedings of the Dateso 2013 Annual International Workshop*, pages 36–47. FEE CS, 2013.
9. C. Luo, Z. Jiang, W.-C. Hou, F. Yu, and Q. Zhu. A sampling approach for xml query selectivity estimation. In *Proceedings of the 12th International Conference on Extending Database Technology: Advances in Database Technology*, pages 335–344. ACM, 2009.
10. R. Paige and R. E. Tarjan. Three partition refinement algorithms. *SIAM Journal on Computing*, 16(6):973–989, 1987.
11. N. Polyzotis and M. Garofalakis. XSKETCH Synopses for XML Data Graphs. *ACM Trans. Database Syst.*, 31(3):1014–1063, 2006.
12. Y. Wu, J. M. Patel, and H. Jagadish. Using histograms to estimate answer sizes for xml queries. *Information Systems*, 28(1):33–59, 2003.

Improvements of Formal Veriffication in Kaira

Ondřej Meca

Department of Computer Science, FEECS,
VŠB – Technical University of Ostrava, 17. listopadu 15, 708 33 Ostrava – Poruba
ondrej.meca@vsb.cz

Abstract. The research of a group which the author is a member is focused on simplifying the process of developing parallel programs with distributed memory. We are developing a tool named Kaira. It is a high-level visual prototyping tool that combines an abstract computational model (that captures parallel behavior and communication) with sequential C++ codes to automatically produce MPI applications. Kaira provides several supportive activities that help a user to develop their programs. Nowadays, the most developed activity is the formal verification. In Kaira, verification is based on a state-space analysis of an application with a particular input and a given number of processes. However, the number of reachable states can be huge even for small examples, hence, some reduction has to be used. The reduction in Kaira exploit the abstract computational model. It allows us to efficiently implement a particular reduction method and significantly reduce the state space and improves the verification performance. Achieved results are compared on a few examples with patterns that commonly occurs in the distributed programming.

Keywords: verification, distributed memory systems, MPI, high-level model, Petri Nets

1 Introduction

In recent years, parallel computers have become more and more common. Besides standard personal computers with several cores, there are many new supercomputers with thousands of computational nodes which can be utilized for various data or time demanding tasks like weather forecasting, simulation of flows or chemical reactions. The majority of supercomputers operate with a distributed memory where each process has its own memory space isolated from the others and the computation is controlled by passing messages among them.

The de-facto standard of an interface for this communication is *Message Passing Interface* (MPI)[1]. However, it represents quite a low-level interface. Users usually have to use other tools for activities connected with the parallel programming like debugging or performance analyses. Since MPI is commonly used, there exist many tools for this purpose. However, tools from different areas usually do

[1] http://www.mpi-forum.org/

© M. Krátký, J. Dvorský, P. Moravec (Eds.): WOFEX 2015, pp. 354–359.
VŠB – Technical University of Ostrava, FEECS, 2015, ISBN 978-80-248-3787-1.

not cooperate with each other and even an experienced programmer of sequential applications can spend a lot of time by learning a new set of complex tools. Therefore, for many non-experts in the area of the parallel computing, it can be difficult to create, debug, and analyse their distributed applications. Besides specialized tools, we develop unifying tool Kaira[2] [2]. Kaira is a development environment for MPI applications aimed at easy prototyping and unifying common activities that occur during development.

Nowadays, the most developed activity is the formal verification. While by the common testing a user checks only few runs, verification systematically explores all possible runs. It reveals all errors connected with a non-determinism introduced by the MPI. In Kaira, verification is based on a state-space analysis of an application with a particular input and a given number of processes. The current version provides the detection of a deadlock, finding cycles in a computation, and checking some uniqueness properties of computations.

To make verification more practical, it is important to be able to verify real-world examples, it means to handle as big instances as possible. The overall strategy how to achieve this is to reduce the state space itself and reduce its memory usage. One of the known techniques how to reduce the state space is usage of general principles of a *partial order reduction*(POR) [4]. POR exploits the fact that many actions in parallel applications are independent, i.e. the order of these actions does not have an impact on the application's global state and actions can be executed in arbitrary orders. Besides recognition of actions' independence, a correct reduction needs to find out a set of actions that can be executed in the future. It is a complicated task in general, hence, an over-approximation has to be used. In Kaira, an over-approximation utilizes information from its abstract computational model. The implemented reduction algorithm together with several memory optimizations result in a significant speed up and a reduction of memory used in Kaira's verification engine.

This paper reports on a work in progress, after a completion it is planned to be submitted to a relevant peer-reviewed conference. The paper has the following structure. Section 2 briefly describes tool Kaira and basic principles of the partial order reduction. Section 3 shows improvements achieved by the implementation of the reduction algorithm on a few examples that represent standard patterns in the parallel programming.

2 Kaira

In this section, Kaira [1, 2] is briefly introduced to give the reader a flavour of the tool. The design goal is to provide an environment where users can implement and experiment with their ideas in a short time, create a real running program, and verify its performance, scalability, and correctness. An important aspect is a unification of development activities such as debugging, performance analysis, and verification. As a unifying element, an abstract computational model is used.

[2] `http://verif.cs.vsb.cz/kaira/`

The model is based on *Coloured Petri Nets* (CPNs) [5]. They naturally describe a distributed computation and they have a natural visualization. Because of the specific needs of Kaira, we have modified and extended CPNs to be more suitable for the parallel programming with MPI. The most distinctive element is the usage of queues to store tokens instead of multisets. In addition, for simpler control of a created application, we add priorities to transitions.

Programs in Kaira are written in a *visual programming language* that describes parallel aspects and communication. Sequential parts are written in C++. In such an environment, it is easier to capture a distributed state of a computation because it is defined only by the visual part.

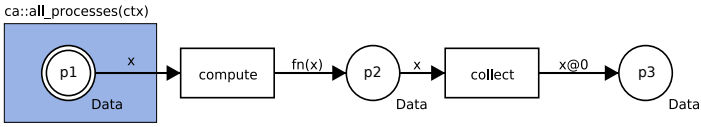

Fig. 1: A simple program in Kaira

A simple example of a program in Kaira is shown in Figure 1. Similarly as in CPNs, places (circles) contain values that represent data and transitions (squares) represent operations with data. Input arcs (arcs from places to transitions) specify what values a transition needs to be *enabled*. An enabled transition can be executed. If a transition is executed, it consumes values according to input arcs and produces values according to output arcs (arcs from transitions to places). An element with a double border contains sequential codes inside. Places execute inside codes at the beginning of the computation, transitions execute inside codes at all transitions' executions. By blue areas a user can specify processes where Kaira creates data at the beginning of the computation. For an interprocess communication, arcs inscriptions can contain symbol '@'. An expression after that symbol determines a target process where a transition sends produced data. In addition, all arcs have *settings*. In the default settings an input arc consumes the first value from an input place. The settings can be changed by an expression in square brackets. For example, an arc can consume all values from an input place by using expression "bulk" in square brackets.

Even though the example on picture 1 is very simple, the computation can have several different runs. Transition *compute* has to precede transition *collect*, but only in the same process. Transitions *compute* in different processes can be executed in arbitrary orders. For catching all possible behaviour of the application with the fixed input we can compute the state space, i.e. a graph of all possible runs where nodes are states of an application and arcs represent actions. Because the state space catches all possible runs of an application, it is possible to check properties of the application by checking properties of the state space.

The state space of the example in Figure 1 is shown in Figure 2a. Names of arcs are composed from a name of a transition and a process where it was

executed. There are also arcs for receiving data from another process. Receive actions are not a part of the Kaira's abstract model, but is automatically generated by Kaira from arcs sending data to other processes. As Figure 2a shows, there are many different paths in the state-space graph. However, many of them end at the same state, no matter how actions are ordered. In this situation not all paths have to be included to the state space to keep all its studied properties. For example the state space from Figure 2a can be reduced to the state space on Figure 2b. This situation is common in parallel applications and utilization of this fact can lead to saving resources and make manageable a verification of much bigger examples. It was implemented in Kaira, the results summarize the next section.

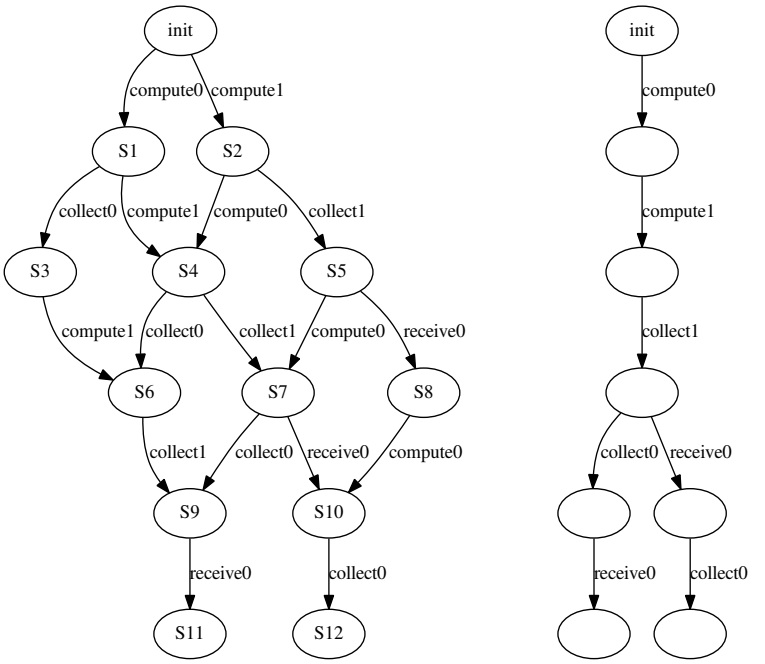

(a) A full graph (b) A reduced graph

Fig. 2: State spaces of the example in Figure 1.

3 Benchmarks

In this section, the performance of POR in Kaira is measured on five MPI programs with patterns that commonly occur in the distributed programming. The deadlock detection was performed in all cases. All experiments were performed on Intel i5-3570 3.40GHz with 8GB RAM. The time limit for all experiments was

Table 1: Execution times of verification

Program	MPI procs.	with POR		without POR	
		ver. time	number of states	ver. time	number of states
W(50 intervals)	3	0.190s	20872	0.306s	39696
W(500 intervals)	3	12.4s	1.9M	28.6s	3.9M
W(10 intervals)	5	0.9s	100k	6.4s	411k
W(20 intervals)	5	61s	5.7M	438s	23M
W(10 intervals)	10	213s	12.2M	>1h	>50M
HF	4	0.175s	1206	94s	256k
HF	16	0.724s	4818	>1h	>2M
HF	64	9.745s	19266	>1h	>2M
MM	4	0.004s	32	0.152s	1863
MM	16	0.022s	212	>1h	>6M
MM	64	0.655s	1604	>1h	>6M
SE	4	1.8s	60k	319s	3.9M
SE	6	687s	12M	>1h	>15M
JS(2 jobs)	3	0.338s	12945	0.417s	23256
JS(4 jobs)	3	10.125s	321k	16.96s	779k

one hour. Execution times are summarized in Table 1. The following programs are used in the experiment:

- Program *Workers* (W) represents a standard centralized parallelization with the manager-workers pattern. The manager process distributes work to other processes. In our case workers compute prime numbers in a given interval. The interval was set to 10 numbers.
- Program *Heatflow* (HF) computes spreading of a heat on a cylinder by an iterative process. The cylinder is discretized by a grid and a new temperature of a cell is derived from a temperature of neighbor cells. The grid is divided among processes. Each process exchanges border parts of the computed area with two neighbor processes. The program was verified with the grid size 64x64 and 100 iterations.
- Program *Matrix multiplication* (MM) implements the well-known Cannon's algorithm for a distributed matrix multiplication using systolic arrays [3, Chapter 4.6.3]. Verification was performed with rectangular input matrices and the both were divided to sub-matrices with sizes 3x3.
- Program *Sieve of Eratosthenes* (SE) implements the algorithm of the same name. In our case, the sieved interval is divided among computing nodes. At the beginning, the first process starts to generate primes and sends them to other processes. Multiples of received primes are marked as composed numbers. When a process sieves all its numbers, it informs the next process and primes are generated on the next process. It is repeated until all primes are found. The verified program sieves the interval of 1000 numbers in all cases.
- Program *Job stealing* (JS) represents a decentralized load-balancing algorithm. All processes are computing assigned jobs. When a process finishes

its jobs, it asks its neighbors for a new work. When a process receives such request, it sends some of its incomplete jobs to the requesting process. All computed results are sent to the first process. When all results are collected, the first process stops the computation. The number of assigned jobs to each process is in Table 1.

For understanding the results we shortly describe the programs behavior. HF and MM represent programs that are internally deterministic. It can be proven, that their structure of communication allows exploring just a single representative execution to exclude all deadlocks. The reduction algorithm recognize this and verification is very fast. W, SE, and JS are more complicated. These examples inherently include non-deterministic behavior. The speed of each process has an impact not only on an order of actions but also on programs' behavior. Hence, the number of states grows fast even with reduction. When the system has not enough memory to save the whole state space to RAM, verification is rapidly slower. Even the POR does not prune the state space in these examples to only one run, it helps to save a significant amount of memory to make verification faster.

4 Conclusion

The paper contains the improvements of the verification engine achieved by the implementation of the partial order reduction in Kaira. The results show that our algorithm successfully recognizes situations when an arbitrary order of actions leads to the same state. Besides the speed up of verification it also reduces the amount of a used memory and make possible to verify bigger instances.

Acknowledgment The work was supported by the student project SP2015/123.

References

1. S. Böhm. *Unifying Framework For Development of Message-Passing Applications.* PhD thesis, FEI VŠB-TUO Ostrava, 17. listopadu 15, Ostrava, 11 2013. `http://verif.cs.vsb.cz/sb/thesis.pdf`.
2. S. Böhm, M. Běhálek, O. Meca, and M. Šurkovský. Kaira: Development environment for MPI applications. In G. Ciardo and E. Kindler, editors, *Application and Theory of Petri Nets and Concurrency*, volume 8489 of *Lecture Notes in Computer Science*, pages 385–394. Springer International Publishing, 2014.
3. I. Foster. *Designing and Building Parallel Programs: Concepts and Tools for Parallel Software Engineering.* Addison-Wesley Longman Publishing Co., Inc., Boston, MA, USA, 1995.
4. P. Godefroid. Partial-order methods for the verification of concurrent systems - an approach to the state-explosion problem, 1995.
5. K. Jensen, L. Kristensen, and L. Wells. Coloured Petri Nets and CPN Tools for modelling and validation of concurrent systems. *International Journal on Software Tools for Technology Transfer*, 9:213–254, 2007.

A survey of semantic database benchmarking

Roman Meca

Department of Computer Science, FEECS,
VŠB – Technical University of Ostrava, 17. listopadu 15, 708 33 Ostrava – Poruba
roman.meca@vsb.cz

Abstract. Because the field of semantic databases is undergoing rapid development, the comparison and evaluation of the performance of semantic database systems is necessary. This survey describes some selected problems of benchmarking. The survey also compares well-known semantic database benchmarks and their abilities. Finally, we discuss some issues related to the OWL specification.

1 Introduction

Benchmarking databases is a very specific field, because there is a large number of variables. For example the measured values will change not only when we modify a software, but also if we make some changes to hardware, network, data or queries.

An ideal benchmark has to be scalable, to implement the newest specifications and the result has to be unambiguous. Of course, this requirements also cause problems with older implementations of semantic databases, which do not implement newer specifications.

One of the main problems are differences in hardware. This problem can be solved by testing other well-known semantic database system under the same conditions as we test a new database system. This practise also eliminates differences of network connections.

The metric of benchmarks is also very important. The first which comes to mind is the query processing time, but we also use logical and physical accesses to pages of data structures. These two values well characterized a performance of query processing algorithms.

In this short article, some important specifications for semantic databases are presented. Next, the comparison of commonly known benchmarks for testing semantic databases are described. Moreover, two techniques enabling to run newer benchmarks on older semantic databases are discussed. Finally, we evaluate the benchmarks.

2 Most Important Specifications

In semantic databases there are several crucial specifications. All of them are managed by W3C. The first and the most important is RDF or Resource Description Framework [6] which describes the basic data format. This specification also defines the RDF triple, which presents an atomic unit of data.

© M. Krátký, J. Dvorský, P. Moravec (Eds.): WOFEX 2015, pp. 360–364.
VŠB – Technical University of Ostrava, FEECS, 2015, ISBN 978-80-248-3787-1.

The next important specification is SPARQL 1.1 [5] describing a query language over RDF data. This language contains all features which we expect of a modern query language and in many ways it is similar to the well-known SQL. A SPARQL query always describe searched sub-graph in semantic data some of query shapes are presented in figure 1.

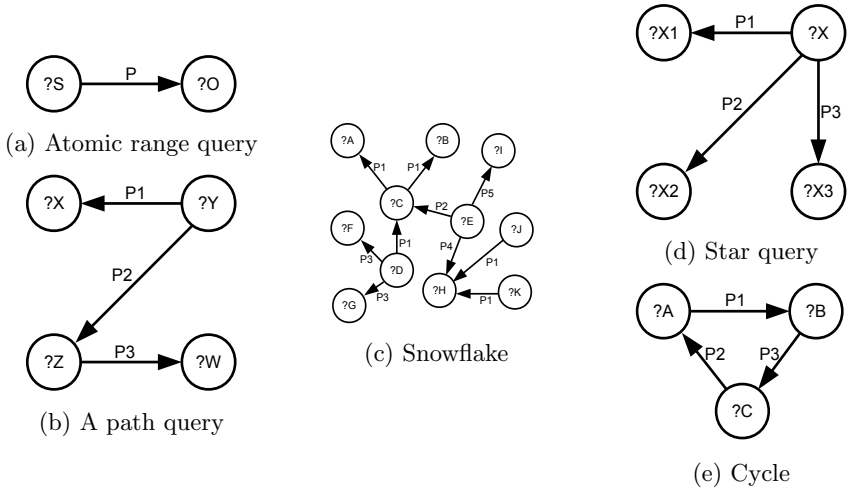

(a) Atomic range query

(b) A path query

(c) Snowflake

(d) Star query

(e) Cycle

Fig. 1: Common SPARQL query graph shapes

The last important specification is OWL [7] which can extract new facts from a vocabulary.

3 Semantic Benchmarks

Each semantic benchmark needs data or a data generator, a query test collection is also needed. Ideally, test queries have to represent all possible query types. In some cases, a support of the OWL specification is also necessary. On the other hand, for testing older or experimental databases not supporting OWL, OWL parts of the benchmarks have to be disabled. A good benchmark should also include a test client supporting a standardized way of communication with a semantic database, for example SPARQL end point.

The first and probably the most known and used benchmark is Lehigh University Benchmark (LUBM). LUBM is well defined and also very simple. We need the JAVA virtual machine to run the data generator and test client. Queries are sent directly to the SDBMS or via the simple test client. The LUBM benchmark also support OWL.

[1] `http://www.ldbcouncil.org/`

[2] `https://github.com/facebook/linkbench`

[3] `http://lodqa.wbsg.de/`

Name	Data	Client	Query	Source	OWL
LUBM [4]	Generator	Yes	Select	Yes	Yes
SP^{2}Bench [8]	Generator	No	Select	Yes	No
BSBM [2]	Generator	Yes	Select, Update	Yes	Yes
WatDiv [1]	Generator	Yes	Select, Update	Yes	Yes
LDBC [1]	Generator	Yes	Select, Update	Yes	Yes
LinkBench[2]	Generator	Yes	Select	Yes	Yes
LODQA [3]	Static	Yes	No	No	No
LODIB [3]	Static , Generated	Yes	No	Yes	No

Table 1: Table of semantic database benchmarks

Another benchmark is SP^{2}Bench. The queries of this benchmark are more complex compared to LUBM. But unlike LUBM, this benchmark does not support any test client. As result, queries must be directly sent to the SDBMS or we have to implement own test client.

The next well-known benchmark is Berlin SPARQL Benchmark (BSBM), which is practically the successor of LUBM. This benchmark, unlike LUBM, defines not only Select, but also Update queries. The implementation of the client is much more sophisticated and queries are parametrized.

Even more complex benchmark is WatDiv. This benchmark can generate sets of test queries, his scalability is higher compared to BSBM.

The most complex benchmarks are Semantic Publishing Benchmark (SPB) and Social Network Benchmark (SNB) from Linked Data Benchmark Council (LDBC). These benchmarks are suitable for testing enterprise solutions. The most important feature of these benchmarks is the ability to simulate complex interactive workload. The benchmarks have a special place in our survey. The main goal of LDBC is to play the role of TPC [4] benchmarks proposed for relational DBMS in the field of semantic databases.

Sophisticated benchmarks also usually propose additional evaluation metrics than the query processing time. For example benchmarks from LDBC use a number of operations per second, some other benchmarks like for example BSBM also include a count of clients.

Another interesting benchmark which was developed to evaluate specific test case is LinkBench [5]. LinkBench was developed by Facebook. So this benchmark is focused to the field of social networks and their specific problems.

In addition, there is some highly specialized benchmarks like Linked Open Data Quality Assessment LODQA. This benchmark is designed to test data loading and data error recovery. Or Linked Open Data Integration Benchmark (LODIB), which is focused on notation polymorphism of RDF data.

[4] `http://www.tpc.org/`
[5] `https://github.com/facebook/linkbench`

Unfortunately, sophisticated benchmarks are not so easy to set-up. They usually run on clusters like Hadoop [6], LinkBench even uses relational database to help generate data and workload.

In the end of the benchmark survey we have to mention real world data like Uniprot [7] or DBpedia data set [8]. These data can be used for benchmarking too, but they are published without a test queries or test clients and they are not scalable. For these reasons benchmarking with these data is not appropriate.

4 Workaround methods

The main problem of a older or experimental semantic databases is that they do not implement OWL standard. There is one widely used workaround technique how to enable OWL knowledge base to SDBMS which do not implement OWL specification. We also present alternative to this method.

The First and most simple and used method is to generate owl invented triples and add them to basic data set so that database would not have to do OWL processing.

This method is not ideal because it can discriminate newer semantic database which implement OWL standard in phase of query solving. To solve this issue we have to disable OWL standard in each tested database system and load extended data so that the benchmark conditions were the same. Another problem of this approach is the obvious growing of data size so the loading time will be significantly longer.

The other approach does not modify the data to enable solving of OWL base query, but it modifies the query itself. This approach does not affect data loading, but to achieve the same query results as in first case, much more complicated logic is necessary.

In each case we have to use well-known tools to derive facts from the given OWL. Here we can mention JENA [9] or SEZAME[10] frameworks. Other possibility is to implement a similar tool of our own.

5 Conclusion

As a conclusion we can state that each benchmark is appropriate for different conditions. Also there are many benchmarks which are outdated and in case of real world data not standardized.

The LUBM benchmark is the most simple and it implements all important technologies, so we would recommend it as a first choice, mainly because this benchmark is used in many articles and also because it is the most suitable for

[6] `https://hadoop.apache.org/`
[7] `http://www.uniprot.org/`
[8] `http://wiki.dbpedia.org/`
[9] `https://jena.apache.org/`
[10] `http://rdf4j.org/`

experimental databases when we use one from workaround technique mentioned earlier in this article.

From other benchmarks we can recommend BSBM as the more complex successor of LUBM. This benchmark has the ability to simulate more real workload than LUBM so it is suitable for testing fully functional semantic databases.

The most complex and best described are the benchmarks from LDBC. These benchmarks are suitable for testing enterprise solutions and they are comparable to TCP benchmarks.

There are also highly specialized benchmarks like LODQA, LODIB or LinkBench, but these benchmarks are not widely used.

Autor Publications

- Roman Meca, Michal Krátký, Peter Chovanec, Filip Krizka: "Data Structures for Indexing Triple Table". DATESO 2015: 13-27

Autor Projects

- Inovace výuky databázových předmětů (FRVS2015/90), Ing. Pavel Bednář
- Vývoj detektoru poruch izolačních systémů s podporou databázových systémů, (SP2015/170), doc. Ing. Stanislav Mišák, Ph.D.

References

[1] Güneş Aluç et al. "Diversified stress testing of RDF data management systems". In: *The Semantic Web–ISWC 2014*. ISBN: 978-3-319-11964-9.

[2] Ch. Bizer and A. Schultz. *The berlin sparql benchmark*. 2009. URL: `http://www.researchgate.net/publication/220123872_The_Berlin_SPARQL_benchmark`.

[3] Schultz A. Carlos R. R. Ruiz D. Bizer Ch. "Benchmarking the performance of linked data translation systems". In: *Proceedings of Linked Data On the Web (LDOW)*. 2012.

[4] Y. Guo, Z. Pan, and J. Heflin. "LUBM: A benchmark for OWL knowledge base systems". In: *Web Semantics: Science, Services and Agents on the World Wide Web* 3.2 (2005), pp. 158–182.

[5] S. Harris and A. Seaborne. "SPARQL 1.1 query language". In: *W3C Recommendation* (2013). URL: `http://www.w3.org/TR/sparql11-query/`.

[6] F. Manola, E. Miller, B. McBride, et al. "RDF primer". In: *W3C recommendation* 10 (2004). URL: `http://www.w3.org/TR/rdf-primer/`.

[7] D. L McGuinness, F. Van Harmelen, et al. "OWL web ontology language overview". In: *W3C recommendation* 10 (2004).

[8] M. Schmidt et al. "SP^{2}Bench: a SPARQL performance benchmark". In: *Proceedings of International Conference on Data Engineering, ICDE'09*. IEEE. 2009.

Identity of users publishing on the Internet and their research area

Adam Ondrejka

Department of Computer Science, FEECS,
VŠB – Technical University of Ostrava, 17. listopadu 15, 708 33 Ostrava – Poruba
adam.ondrejka.st@vsb.cz

Abstract. We created our own method for identifying users of various Internet services. We summarize our original approach to finding unique identity of Internet users. Mainly, we are estimating the authors' areas of research by an analysis of publications and publicly available metadata of digital libraries and the information about authors published on social networks.

Keywords: user identity, digital library, social network, data mining

1 Introduction

The boom and making the Internet accessible for the public in recent years has enabled people all over the world to publish information about their personal info. Unfortunately, there are many places where a person may publish and present themselves and the situation is not simplified by the fact that a lot of people could have the same names. Some situations are then very complicated, one example might be a case conferences. The conference organizer needs to select appropriate reviewers for each registered paper. This task is not difficult in the case of smaller conferences, the chairman knows the other members and the number of submitted papers is not great. However, the situation is considerably more difficult for larger conferences when it is no longer possible to keep knowledge about the area of research of the individual reviewers.

The main goal of this work was to create an algorithm that finds the authors of the papers on the social networks and estimates their area of research by publicly available information. It would then be easier to facilitate the assessment of the organizers. The main idea is shown in Figure 1.

2 State of the Art

This work builds and partially summarize information described in our publications [4, 5].

Elie Raad in [3] uses similar principles in a vector space. For each keyword adds weight and also compares the entire sentence on user profiles. The result, if users are the same or not is ultimately determined by the score of similarity between the profiles and by the manually set value. Mutschke and Haase Ain in

© M. Krátký, J. Dvorský, P. Moravec (Eds.): WOFEX 2015, pp. 365–369.
VŠB – Technical University of Ostrava, FEECS, 2015, ISBN 978-80-248-3787-1.

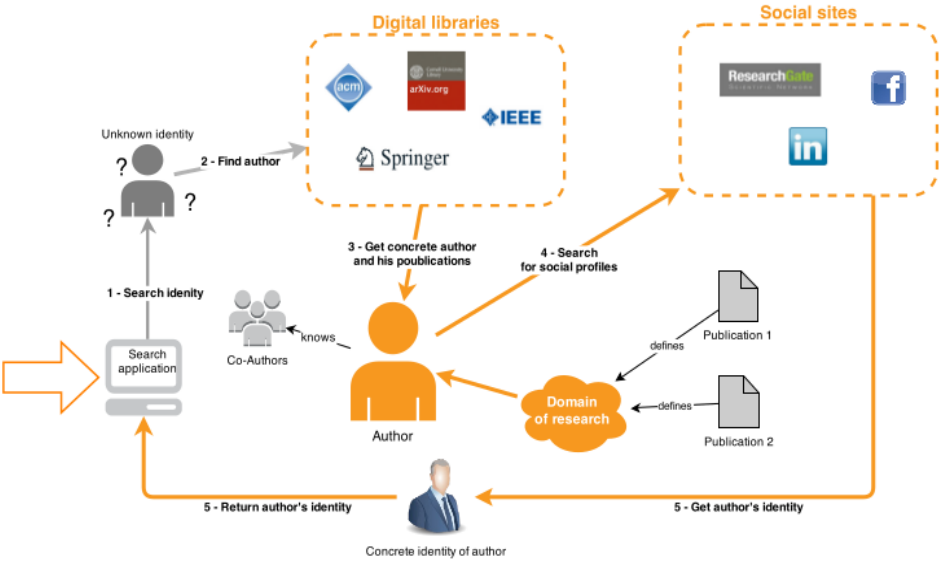

Fig. 1. Finding user identity

[2] made network analysis of users based on bibliographic records containing keywords publication and subsequent application of the analysis of socio-cognitive networks.

In the field of digital libraries Martin published in the article [1] techniques to find similar scientific articles by using the language models. The principle is based on an estimate of whether a text can generate words from the text of another one. The estimate is based on a previous analysis of abstracts, keywords and by subsequent machine learning and may be an alternative or possible supplement to comparing publications in a vector space.

3 Finding user's identity

The main idea of the search for the author's identity on social networks and digital libraries are built on the types of information that users publish about themselves and which describe him. These two types are named as *general* and *unique*. Into *general* attributes can be included, for example. *sex*, *residence*, or *name* and *surname*. In terms of characteristics that confirm and identify users, but cannot definitely decide whether one is a really wanted person. On the other hand, *unique* attributes concretize user's profile. *Email* or *telephone number* should be used really only by one person, of course, we assume a scenario where the user fills truthful information. Any further general attribute may be just the

profile pictures showing *users* face. By finding a sufficient number of common attributes and at least one unique, we can relatively accurately determine a user's identity across different networks. Above is Equation 1 used in algorithm (based on emthod described in [4]).

$$sim_{u,p} = \begin{cases} \sum_{i=0}^{n} w_i \cdot sim(a_{i,u}, a_{i,p}) & \text{if } sim(a_{name}) > th_{name} \\ 0 & \text{else} \end{cases} \quad (1)$$

where $sim(a_{name})$ is a similarity between the names;th_{name} is the threshold for determining whether the names match; n is the number of compared attributes; w_i is weight compared attributes; a_p is a set of attributes in user profile; a_u is the set of attributes of searched user in a database; $sim(a_{i,u}, a_{i,p})$ is a similarity between the profile and attributes of the selected user

When comparing attributes can not rely on simple string comparison. One identical entity can be expressed slightly differently on different networks, e.g. phone numbers can be separated by spaces on one website and not separated on the other. The address in digital libraries is also very often written differently, example is the expression *VSB - Technical University of Ostrava* and *VSB Tech. Univ.* of Ostrava. To determine compliance text strings we used partial matching algorithm, namely *Levensthein distance*. A more detailed description of the algorithm is described in the publication [4].

3.1 Digital libraries

In the case of digital libraries we analysed the public metadata of publications authors. As crucial were shown attributes that define the social network of the author, which greatly reflects its connection with other users on other social networks. It is mainly about the *co-authors* and *institutions*.

3.2 Social networks

Unlike digital libraries, social networks are different and specific, users choose information to publish on the network. In most cases, *general* attributes can be checked, such as the address or the gender.

4 Experiment

In the experiment, we examined whether algorithm will correctly find identities of the 180 randomly selected writers of different nationalities or not. For digital libraries were selected ACM Digital Library[1] , IEEEXplore[2] and SpringerLink[3] and from social networks LinkedIn[4] and ResearchGate[5].

[1] http://dl.acm.org/
[2] http://ieeexplore.ieee.org/Xplore/home.jsp
[3] http: //link.springer.com/
[4] https://www.linkedin.com/
[5] http://www.researchgate.net/

In the first step, we tested the identity searching using only the co-author and institutions attributes in digital libraries, the results are in Table 1. Out of the 180 authors were found correctly 118 authors (column "C"), 3 different authors were incorrectly merged under one identity (column "MI") and 59 authors were incorrectly identified as more authors (column "MA"). The accuracy of the algorithm in this case was 65.5 %, the error rate of about 34.5 %.

Table 1. Experiment of finding identities

	C	MI	MA
Co-authors	118	3	59
Co-authors + Social networks	132	3	45
Co-authors + Social networks + Keywords	166	14	0

In the second step we have added a comparison of data from social networks. Correctly found 132 authors, 3 authors still remained improperly merged, and 45 of them remained incorrectly created multiple identities. The correctness of the algorithm rose to 73.3 % and the error rate has dropped to 26.7 %.

In the final, third step of the experiment, we have added to social networks comparing keywords of publications and other attributes of social networks, such as interests, experience, etc. There were 166 authors correctly found, unfortunately the number of authors merged under one identity was 14. Conversely, multiple identities were not created for any authors. Correctness in the final stage was 92.2 %, error rate fell to 7.8 %. However it should be noted that increased worse scenario where one author is assigned sections and publications of other people, which can significantly distort the further work with the data obtained.

5 Conclusion

We created an algorithm to find the user's identity in digital libraries and social networks. The results of our experiment showed that the user identification was correct for 92 % of the total of 180 authors.

This work was the first step in research seeking a unique identity of the user on the Internet regardless of the type of website and research recommending accordance unique identity and stereotypes user behaviour. The next step in the research will incorporate verification into existing face recognition algorithms identify users on the Internet. The main contribution of this work is to connect two different types of web services, the digital libraries and the social networks, to find the user's identity.

References

1. G. Hurtado Martín, S. Schockaert, Ch. Cornelis, and H. Naessens. Finding similar research papers using language models. In *2nd workshop on semantic personalized information management : retrieval and recommendation, Proceedings*, pages 106–113. University College Ghent, 2011.
2. P. Mutschke and A. Haase. Collaboration and cognitive structures in social science research fields. towards socio-cognitive analysis in information systems. *Scientometrics*, 52(3):487–502, 2001.
3. E. Raad, R. Chbeir, and A. Dipanda. User profile matching in social networks. In *Network-Based Information Systems (NBiS), 2010 13th International Conference on*, pages 297–304, Sept 2010.
4. Petr Saloun, Adam Ondrejka, and Ivan Zelinka. Estimating users' areas of research by publications and profiles on social networks. In *Hypertext 2014 Extended Proceedings: Late-breaking Results, Doctoral Consortium and Workshop Proceedings of the 25th ACM Hypertext and Social Media Conference (Hypertext 2014), Santiago, Chile, September 1-4, 2014.*, 2014.
5. Petr Saloun, Jakub Stonawski, and Ivan Zelinka. Recommending new links in social networks using face recognition. In *8th International Workshop on Semantic and Social Media Adaptation and Personalization, SMAP 2013, Bayonne, France, December 12-13, 2013*, pages 89–94, 2013.

Universal B-tree

Jakub Ondruš

Department of Computer Science, FEECS,
VŠB – Technical University of Ostrava, 17. listopadu 15, 708 33 Ostrava – Poruba
jakub.ondrus.st@vsb.cz

Abstract. There are a lot of applications of multidimensional data structures. One of them, the Universal B-tree (UB-tree), provides some important properties, for example their sibling regions are not intersected. The paper describes this data structure.

Keywords: Multi-dimensional indexing; UB-tree; Z-region; Z-address

1 UB-tree

The UB-tree is multidimensional access method developed by Rudolf Bayer. This method uses a combination of the B-tree and a space-filling curve.

1.1 Z-curve

In our project we decide to use one of a space-filling curves, called Z-curve, because it has a simple implementation and high rate of transformation. The Z-curve is a partitioning technique that transforms multidimensional data tuple to coordinates (Z-address). Spatial proximity enables clustering of these points allowing better data storage to disk pages, similar data are store close to each other.

© M. Krátký, J. Dvorský, P. Moravec (Eds.): WOFEX 2015, pp. 370–375.
VŠB – Technical University of Ostrava, FEECS, 2015, ISBN 978-80-248-3787-1.

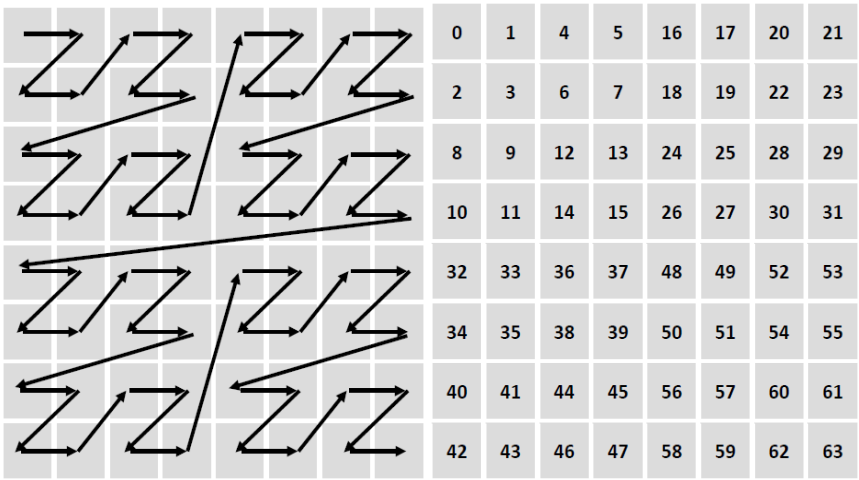

Fig. 1. Z-curve on 8 x 8 space

1.2 Z-address

The Z-address is unique for each point in space (on a Z-curve) and calculating Z-address is easy if use binary representation of each coordinates. For calculation is use a bit-interleaving algorithm. This algorithm in every step of the cycle “cut” one bit of all coordinates (in binary representation) and then “glue” it together. In the end of this transformation we have one bit-string, which we call the Z-address. An example for bit-interleaving is in Figure 2.

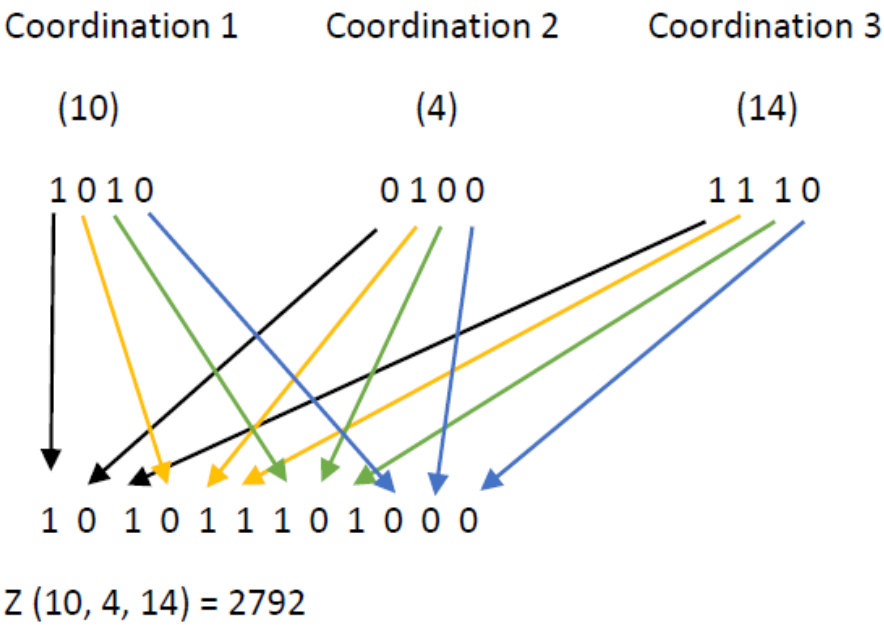

Fig. 2. Transformation of coordination to Z-address

1.3 Z-region

In the UB-tree we also meet with the Z-region, which is in node and indicates interval on Z-curve. Entire universe is divide by Z-regions to subsections. Each Z-region contain upper and lower border for leafs in this node. One Z-region has determined the maximum tuple and each Z-region is stored in one page on disk. Inserting into UB-tree and necessary adjustments of the UB-tree contain the Z-Region will be explained in chapter Insert. The Z-region also introduce super Z-region notion. The super Z-region consists from nodes that do not point to tuples but on the other Z-regions (Figure 3).

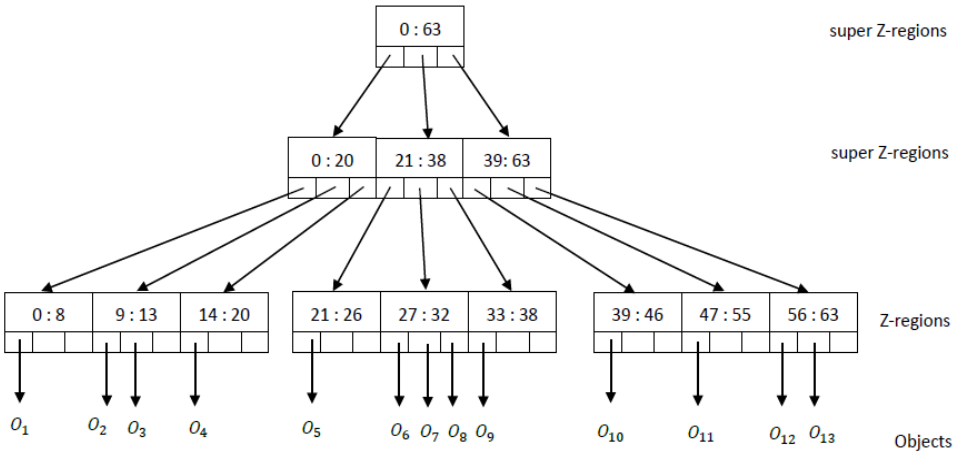

Fig. 3. UB-tree

2 Inserting into UB-tree

For the inserting is important capacity of the region (capacity of disc page). Because the algorithm before insert checks if region capacity is exceeded. If so, then the Z-region has to be split into two regions. The objects will be redistributed to the two regions. Below a few examples:
The maximum page capacity is three points and we are inserting first points.

1) Inserting of first three points. All three points are stored in one region (one leaf) that means entire universe is in this region.

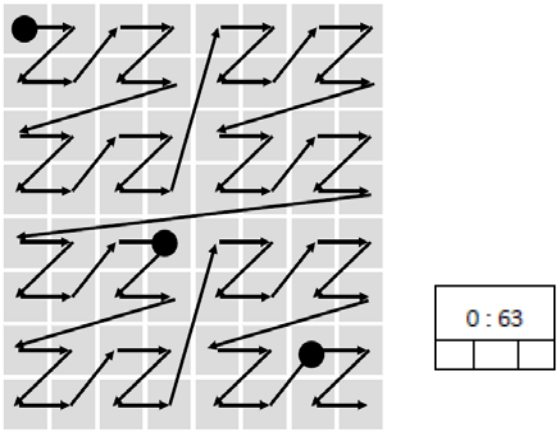

Fig. 4. UB-tree insert 1

2) We insert new point, which is white, because capacity is exceeded, we need to split region into two regions. Data are distributed into these regions.

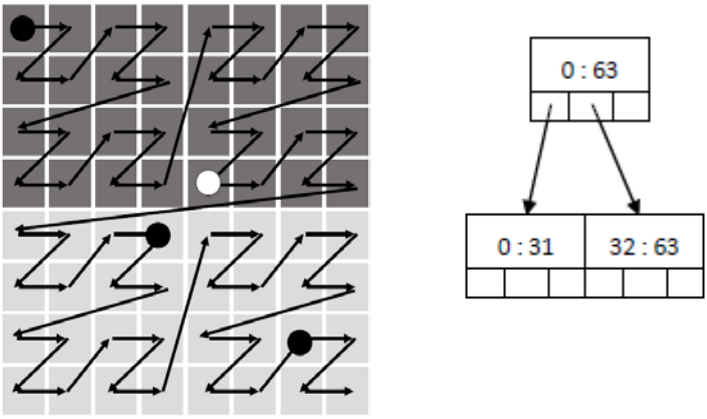

Fig. 5. UB-tree insert 2

3) We insert two more points (white points), because capacity is exceeded, we need to split upper region into two regions.

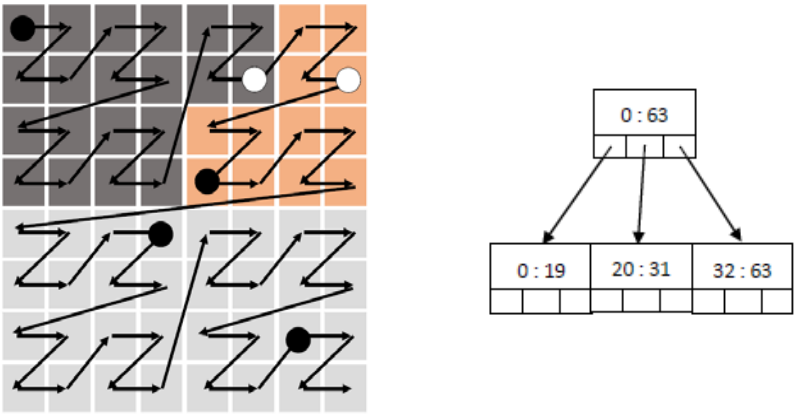

Fig. 6. UB-tree insert 3

In case we need to insert more data and we already exceeded capacity of regions, we have to split super Z-region into two regions.

3 Searching algorithm

In case of point query, coordinates are transformed into Z-address and with this address the tree is searched and output is the Z-region that contains this coordinates. This region is loaded from disc and the Z-address is in this disc page.

If we have the range query, we need to load into memory every region, which are included in range of the query. In these pages we are searching for results of the query.

4 What is done

In our project we try to add this UB-tree implementation into bigger framework. The Z-address calculation is done and now we implements insert into UB-tree, which contain dividing universe into the Z-regions and the super Z-regions and inserting data into leaf. For now I do not have any results that could be present.

5 References

1. SKOPAL, Tomáš, Michal KRÁTKÝ, Jaroslav POKORNÝ a Václav SNÁŠEL. A new range query algorithm for Universal B-trees. *Information Systems* [online]. 2006, **31**(6): 489-511 [ref. 2015-08-08]. DOI: 10.1016/j.is.2004.12.001. ISSN 03064379. Available from: http://linkinghub.elsevier.com/retrieve/pii/S0306437905000116
2. BAYER, Rudolf. *The universal B-tree for multidimensional indexing: General concepts* [online]. In: Proceedings of the International Conference on Worldwide Computing and Its Applications: Springer, 1997, p. 198 [ref. 2015-08-08]. DOI: 10.1007/3-540-63343-X_48. Available from: http://link.springer.com/10.1007/3-540-63343-X_48
3. RAMSAK, FRANK, VOLKER MARKL, ROBERT FENK, MARTIN ZIRKEL, KLAUS ELHARDT a RUDOLF BAYER. *Integrating the UB-Tree into a Database System Kernel* [online]. In: Procs. of the 26th Int. Conf. on Very Large Databases, 2000, 263-272 [ref. 2015-08-08]. Available from: http://www.vldb.org/conf/2000/P263.pdf
4. GHANJAOUI, Yacine. Indexing *Indexing Techniques in Data Warehousing Environment The UB-Tree Algorithm* [online]. 2003 [ref. 2015-08-08]. Available from: http://www.aui.ma/personal/~H.Haddouti/UB_Tree_paper.pdf

Efficient data routing system ForceB – Webinar

Martin Prokeš

Department of Computer Science, FEECS,
VŠB – Technical University of Ostrava, 17. listopadu 15, 708 33 Ostrava – Poruba
martin.prokes@vsb.cz

Abstract. This paper deals with the system for organizing the webinars called ForceB - Webinar. The article will focus on the technological background of this system, especially the efficient distribution of data over the Internet between all participants in real time. To ensure the communication among particular servers and clients, there was designed an algorithm and a communication protocol called ForceB (further only the FBP) which provides a transfer of data. In this article, we will describe given protocol and presents the issues of data transmission in the environment of Internet.

Keywords: Webinar, ForceB, Fbp, Tree topology, Routing data

1 ForceB - Webinar

ForceB is the system designed for organizing the web seminars in environments of the Internet and university network. It allows organization of the seminars theoretically for hundreds of participants thanks to its own communication protocol ForceB. The objective was to design and implement a tool for remote tuition. The endeavour was to select a new technologies based solution that will be further extensible in easy way for support of new features in the form of plug-in modules. Courses are easily accessible without the need to install additional software or special hardware. It is a SaaS solution in another words the software as a service. The key features of the ForceB system are:

- Videoconference towards the audience.
- Teleconference between all participants.
- Chat.
- Electronic boards.
- Sharing entire desktop of the screen.
- Sharing window of the specific application.

2 Data transmission on internet

The use of webinars is associated with the demanding conditions imposed on the communication network. Data must be transmitted in real time. For this

© M. Krátký, J. Dvorský, P. Moravec (Eds.): WOFEX 2015, pp. 376–381.
VŠB – Technical University of Ostrava, FEECS, 2015, ISBN 978-80-248-3787-1.

reason not only the bandwidth, plays a major role but the delay and QOS as well. Whether the seminar runs on university network or on the Internet, it is necessary to have sufficiently large network throughput. The biggest problem is not data transfer from the presenter to the server but it is transfer of these data from server to the remaining clients.

2.1 Methods of sending the IP datagrams

Multicast There are technologies that solve the sending of data from one source to the group of more end-stations such as the multicast [2]. Instead of posting individual packets to each destination, just a single packet is sent.

The problem of multicast technology is the need to ensure proper configuration for this type of transfer on all elements within the network (routers, switches, etc.). This can be achieved in the corporate or local networks but not on the Internet where there are countless of these elements owned by different providers. For our purposes of organizing the web seminars we need to ensure the availability of ForceB system from the Internet and for that reasons the multicast type of data transmission is not suitable.

Unicast Unicast is the type of transfer where the data are transmitted only to a single destination. That destination may be the node or the end-station. It is the most commonly used method of data transfer in the Internet. Unicast use the protocols such as http, ftp, pop3, smtp, etc. At these protocols always only two stations communicate with each other. And just this type of data transfer was selected for the ForceB application.

2.2 The network topology

Star topology A star topology, see Figure 1, is often selected for communication among more clients. The presenter sends the data to one central element in this case the server and this distributes it to all logged clients.

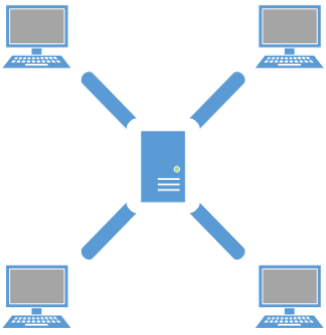

Fig. 1. Architecture overview

This method of data transfer has one significant disadvantage. If we want to send the same data to more target stations then, in the case of the Unicast transfer, each packet must be sent to each station separately. For that reason the server is very limited by its maximum bandwidth and can handle only a limited number of connected clients.

The tree topology The tree topology, meaning a tree-shaped, is best suited for the dynamic load distribution. It originates from a star topology incurred by connection of individual servers that are in the centres of particular stars. This topology can be divided into three parts. First part is the central server which forms the root of the tree (root). This server manages the communication itself. The nodes of tree, further the nodes only, are another important part. They are connected to a central server or linked to each other. Exactly those serve to forward the communication among clients. Each client is connected not to a central server but to one of the nodes, see Figure 2.

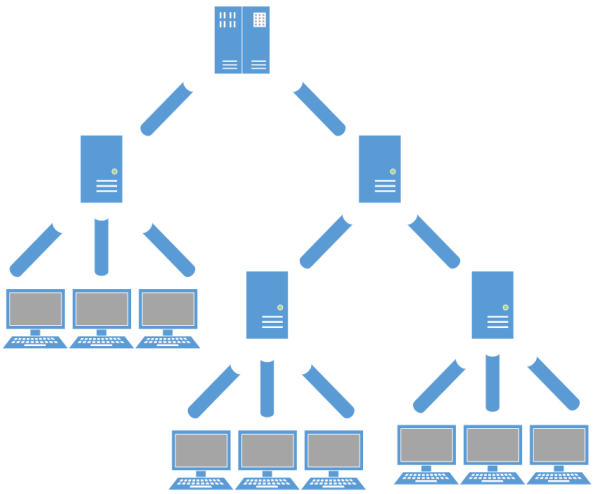

Fig. 2. Architecture overview

In a such way designed network, there must be carried out the routing based on which we can transfer data from any client in the network to another. Own protocol performs this routing the within ForceB network. Thanks to this topology we can increase the maximum capacity to a size which we would never achieve with a single server. If the capacity of one node runs out then every other client is connected to another node which still has the free capacity. On the basis of routing that is carried out in the network, we are able to transfer the data to all participants even if they are not connected to one node.

3 ForceB protocol – FBP

If two endpoints want to communicate together, there must the convention exist under which bases an electronic communication and data transfer are carried out. These conventions or also standard are called the protocol. The system ForceB communicates on the basis of its own application protocol FBP (ForceB protocol). This defines the rules that are used in transmission and receiving of data. It further defines the control syntax, semantics, and synchronization of mutual communication. The protocol generally specifies many characteristics among which for example belong:

- Negotiation of various connection parameters.
- How to start and end the message.
- How to format messages.
- How to end the session or connection.
- What to do with damaged or incorrectly formatted data.
- How to detect unexpected loss of connection or what to perform as the further action.

3.1 Architecture FBP

Data transfer is in the FBP divided into two parts. The first part consists of the overhead data. Here are the data related to individual participants. These are for example routing data, the data about transmitted streams and statistical data. These data are called FBP Control Data. The second part of the transmitted data is already form by the actual content. This can be further subdivided into audio data, video data, text data, and many others.

Own connection exists for all transmitted data. A unique identifier is assigned to this. Every sent datagram is then identified on the basis of this identifier. We can imagine this connection as a stream of data. This may include for example an image from the specific webcam or a specific sound from sound card. Thanks to identifier in the header of each sent datagram, it is possible to distinguish clearly the individual streams of data. The participant can select only that stream of data he is having interest about. In case of insufficient connection to the Internet he can select in a videoconference, for example, to receive only the audio track.

4 Routing the FBP

The added value of the ForceB protocol is its ability to route data. This helps to determine the paths of datagrams in the ForceB network environment. All elements in the network deal with routing. Not only nodes and server ensure it but the end-stations as well. Its task is to ensure the delivery of datagrams to the addressee.

Routing in the ForceB network is similar to routing in computer networks. However here, the routing of data is carried out among the individual elements

at application layer of the ISO/OSI model. The bitrate is thus controlled among individual elements that are involved in the communication using the FBP protocol. Packet transmission among the individual elements in a computer network is controlled by lower layers of the ISO/OSI model.

Similarly as in computer networks, the network infrastructure of the ForceB network between the sender and the addressee of datagram may be very complex. Therefore the routing generally does not deal with full path of datagram but it always solves only one step, i.e. whom to pass the datagram as the next. Each element in the network has a set of rules that say where to forward datagrams towards the designated targets. These rules are contained in so called routing table. On its basis the data are transferred to one of the neighbouring elements and there the decision-making process repeats according to local rules.

4.1 Routing table

The routing table contains information which is necessary during deciding making about next routing of the packet. Each of the elements in ForceB network (server, node, and client) creates its own routing table. Changes in this table that are associated with ambient elements are further distributed. So not all information is sent but only those records what make sense for the target element.

Records in the routing table are divided into rows while each contains the one routing information. Each entry refers to one participant and includes information on his transmitted data stream. Such a record contains, among other things, the unique identifier of the participant identifier of data stream, the type of transmitted data, the list of target addressees and more.

4.2 Formation of the routing table

The routing table of recipient arises on the basis of the transmitted data streams of each sender. The necessary routing information is generated with each newly created stream of data. These are sent to its recipient in periodic intervals. On its bases he updates his routing table. To every recipient is thus sent only the information that is useful to him.

4.3 Routing according to the routing table

Thanks to this method of routing the every superior element knows all participants who are in its subnets. The root of the tree subsequently knows about each connected element in ForceB network. However it does not know exact location of connected element but only the following node, so called next hop. On the bases of this information it is always possible to send the content to the target addressee without this participant would be directly connected to the server or specific node. Demonstration of routing in the network is shown in Figure 3.

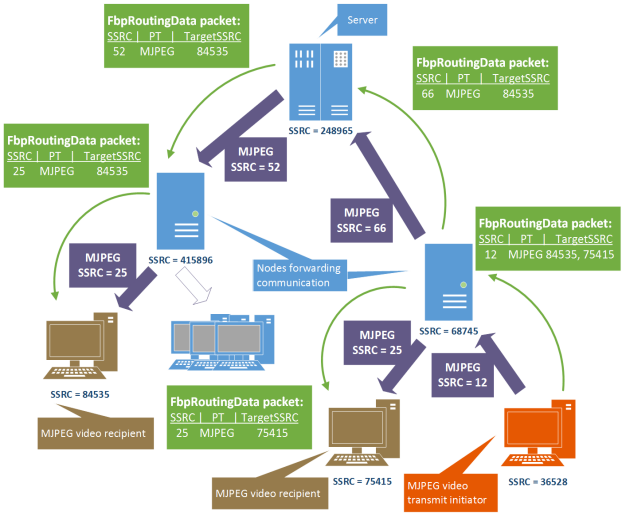

Fig. 3. Architecture overview

5 Conclusion

The article describes the ForceB system as a system for organizing web seminars and its principles of data transmission. It deals with the main aspects related to the issue of holding such seminars in the Internet environment. Emphasis is put primarily on the data transmission and associated development of own communication protocol FBP. The article describes basic principles and architecture of this protocol.

Our goal is to design and implement a system for organizing seminars which would enable to hold the courses for up to hundreds of participants. Solution is built on new technologies.

6 References

1. PROKES, Martin a Radoslav FASUGA. Tool for desktop sharing and remote teaching - ForceB. In: 2012 IEEE 10th International Conference on Emerging eLearning Technologies and Applications (ICETA) [online]. 2012 [cit. 2015-08-06]. DOI: 10.1109/iceta.2012.6418615.
2. KIM, Ki-Il, Jeoung-Lak HA, Eun-Hee HYUN a Sang-Ha KIM. Internet multicast provisioning issues for hierarchical architecture. In: Proceedings. Ninth IEEE International Conference on Networks, ICON 2001 [online]. 2001 [cit. 2015-08-06]. DOI: 10.1109/icon.2001.962375.
3. TRAN, D.A., K.A. HUA a T. DO. ZIGZAG: an efficient peer-to-peer scheme for media streaming. In: IEEE INFOCOM 2003. Twenty-second Annual Joint Conference of the IEEE Computer and Communications Societies (IEEE Cat. No.03CH37428) [online]. 2003 [cit. 2015-08-06]. DOI: 10.1109/infcom.2003.1208964.

Differential Evolution Dynamics Analysis by Complex Networks

Lenka Skanderova and Tomas Fabian

Department of Computer Science, FEECS,
VŠB – Technical University of Ostrava, 17. listopadu 15, 708 33 Ostrava – Poruba
{lenka.skanderova, tomas.fabian}@vsb.cz

Abstract. In this paper, the complex networks are used to visualize the differential evolution dynamics. Individuals are modeled by the nodes and the relationships between them by the edges of the graph. For each node representing the individual the weighted clustering coefficient is computed and incorporated as the property into the individual. In the process of parent selection in the mutation step, the individuals are selected on the basis of their weighted clustering coefficient. Our enhancement has been incorporated in the differential evolution with composite trial vector generation strategies and control parameters (CODE). Finally, a set of well-known benchmark functions (including 21 functions) has been used to test and evaluate the performance of the proposed enhancement of the differential evolution.

Keywords: Differential evolution dynamics, complex network, weighted clustering coefficient, hybrid mutation operator, self-adapting parameter

1 Differential Evolution Dynamics Modeled by Complex Networks

Despite the fact that we test our approach in three different variants of DE, the principle of the CN creation is the same for all of them. The main goal of this work is not to develop a new algorithm that would be better than the others but to find out the appropriate way how to select parents in the mutation step to improve the convergence speed of the original variants. Our research is based on the idea that the best individual from the population can be selected not only on the base of its fitness value. CN help us to visualize the relationship between individuals in the population and provide us a new view to the problem. In the following rows, we would like to familiarize the reader with the principle of the CN creation and interpretation of its properties.

The CN can be described as the graph with non-trivial topological features, i.e. features that do not occur in the simple networks but occur in the real networks [2]. CN can be represented by the directed or undirected graph $G = (V, E)$ where $V = \{v_1, \ldots, v_N\}$ denotes the set of vertices (nodes) and $E = \{e_1, \ldots, e_K\}$ is the set of the edges where the edge $e_{i,j}$ connects vertices v_i and v_j [1].

© M. Krátký, J. Dvorský, P. Moravec (Eds.): WOFEX 2015, pp. 382–387.
VŠB – Technical University of Ostrava, FEECS, 2015, ISBN 978-80-248-3787-1.

1.1 Graph Creation on the Basis of DE Dynamics

We will build one graph for each generation of the DE algorithm. Thanks to this mechanism we will be able to track the development of the relationships between individuals. One node of the graph represents one individual in the population. The edge between two nodes models the relationship between two individuals (actual individual is always connected with its parents). We have mentioned that in the mutation step of DE/rand/1/bin three mutually different random parents are selected. Let $\boldsymbol{x}_i^G$ be the actual individual and $\boldsymbol{x}_{r_1}^G$, $\boldsymbol{x}_{r_2}^G$, and $\boldsymbol{x}_{r_3}^G$ the randomly selected parents. The noise vector $\boldsymbol{v}_i^{G+1}$ and the trial vector $\boldsymbol{u}_i^{G+1}$ are created as common. If $f(\boldsymbol{u}_i^{G+1}) < f(\boldsymbol{x}_i^G)$, the edges between the node representing the original individual and each node representing the parent will be created such that each edge will lead from the parent node to the node representing the original individual. Otherwise no edge will be created. In the other words we record just the individuals which contributed to the improvement of the population. At the end of the generation the adjacency matrix A_G is created on the basis of the recorded relationships between the nodes (individuals). The adjacency matrix consists of the weights of the edges between the individuals. In the next generation, the adjacency matrix A_G is upgraded to A_{G+1}, i.e. the weights of the edges between the individuals are recomputed, etc.

1.2 Incorporation of the Weighted Clustering Coefficient to the Parent Selection

The main goal of this work is to find out the way how to select the parents in the mutation step to improve DE convergence rate. In the variant DE/best/1/bin, the best individual is the individual with the smallest (in minimizing problems) or greatest (in maximizing problems) fitness value. As it was described in [3], DE/best/1/bin does not reach the best results in the non-separable and multimodal functions. This fact led us to search for another criterion of the best individual selection. From the rules that we have presented above, we know that the edges between nodes representing the individuals are created only if the individuals represented by these nodes contributed to the population improvement. The nodes representing the individuals becoming the parents more often will have the greater out-degree (the number of out-going edges will be greater) and the weights of the edges leading from these nodes will be higher. Such parents have the genomes of the high quality and in our opinion it is important to spread these genomes. The weighted clustering coefficient is one of the most appropriate candidate to be chosen as the criterion of parents selection in the mutation step from two reasons:

1. It enables to capture spreading of the genomes from the node to another node.
2. Unlike the local clustering coefficient the weights of the edges are took into account.

When the adjacency matrix A^G for the generation G is created, the weighted clustering coefficient of each node is computed according to the following equation [7]:

$$\widetilde{C}_{i,Z} = \frac{\sum_{j,k} \hat{w}_{i,j}\hat{w}_{i,k}\hat{w}_{j,k}}{\left(\sum_k \hat{w}_{i,k}\right)^2 - \sum_k \left(\hat{w}_{ik}\right)^2}, \tag{1}$$

where the weights of the edges are normalized by the maximal weight such that $\hat{w}_{i,j} = \frac{w_{i,j}}{max(w)}$. Weighted clustering coefficient according to B. Zhang $\widetilde{C}_{i,Z}$ has been selected because it is purely weighted based and it is not sensitive to additive noise [4].

When each individual has its own weighted clustering coefficient, the probability of selection is computed for each of them according to the following equation:

$$p_i = \frac{\widetilde{C}_{i,Z}}{\sum_{j=1}^{NP} \widetilde{C}_{j,Z}}, \tag{2}$$

where p_i denotes the probability of the i-th individual selection and $\widetilde{C}_{i,Z}$ is the weighted clustering coefficient of the node representing the i-th individual. Individual represented by the node with the higher weighted clustering coefficient has the higher probability to be selected as the parent in the mutation step.

2 Experimental results

In the full version of the paper called "Differential Evolution Dynamics Analysis by Complex Networks", we have selected three variants of DE to be enhanced by our approach of the parents selection in the mutation step – classical DE, jDE, and CODE. These algorithms are implemented in C#, .NET Framework 4.5.1 and run on a computer with CPU Intel(R) Xeon(R) 2.83 GHz. To evaluate the performance of the presented algorithms, 21 benchmark functions from [6] have been used. In this short version, we will present just results of CODE because it is relatively new version of DE, moreover the enhanced CODE reached surprisingly good results from the view of the convergence rate.

The population size has been set to $NP = 100$. The maximum number of generations for all benchmark functions are mentioned in Table 1. These values have been selected according to [8] except function f_8 where we have selected maximum number of generations to be just 2000. The algorithm CODE has been enhanced by our approach of the parents selection in the mutation step. No other step of the algorithm has been modified. The initial population is generated randomly with the uniform distribution. The results are the minima and standard deviations that have been reached during 50 independent runs. To make a fair comparison, the Wilcoxon signed-rank test at the $\alpha = 0.05$ level has been conducted between the original CODE and its enhanced variant. If both comparing algorithms reach the global minimum and the standard deviation equals to 0, the mean number of the cost function evaluation will be mentioned. We consider

the algorithm is better if the number of the cost function evaluations is lower by at least 5%. In Table 2 "+","=" and "–" indicate that the enhanced CODE reached better, similar or worse results than the compared original version.

Table 1. Maximum generation number of benchmark functions.

Maximum number of generations	Benchmark functions
1500	f_1, f_6, f_{10}, f_{12}, f_{13}
2000	f_2, f_8, f_{11}
3000	f_7
5000	f_3, f_4, f_5, f_9
100	f_{14}, f_{15}, f_{16}, f_{17}, f_{18}, f_{19}, f_{20}, f_{21}

2.1 Comparison of CODE and Enhanced CODE

CODE algorithm uses the pool of DE strategies, namely DE/rand/1/bin, DE/rand/2/bin and DE/current-to-rand/1/bin. For these strategies, the different values of the control parameters are set. In our experiments, for the variant DE/rand/1/bin $F = 1.0$ and $CR = 0.1$, for DE/rand/2/bin $F = 1.0$, and $CR = 0.9$, and for DE/current-to-rand/1/bin $F = 0.8$, and $CR = 0.2$ as suggested in [5]. The population size has been set as well as in the previous cases to $NP = 100$ and the maximal numbers of generations are mentioned in Table 1. The results of the experiment can be seen in Table 2.

For the first function f_1 the results are comparable. In the rest of the unimodal functions f_2–f_5, Step function f_6, Noisy quartic function f_7, multimodal functions f_8–f_{13} and low-dimensional functions f_{16} and f_{18}–f_{20}, the enhanced algorithm of CODE reached better results than the original version. In the case of the low-dimensional functions f_{14} the enhanced CODE reached the worse results. For the rest of the testing problems the results are comparable.

3 Conclusion

In this paper, we have proposed the enhanced algorithm based on the analysis of the DE dynamics by the complex networks where the individuals are modeled by the nodes and the relationships by the edges of the graph representing evolution of population. In the enhanced algorithm (CODE), the key modification we have proposed is that the parents are selected with the probability based on their weighted clustering coefficients in the mutation step, see Eq. 2. This modification stems from the assumption that the individuals with the high weighted clustering coefficient have the genomes of the high quality and from this reason they should be used more frequently in the process of mutation. To prove the validity of our strategy, the performance of the enhanced CODE algorithm is evaluated on the

well known Yao's benchmark functions [6]. The enhanced CODE is compared with its original version in term of the convergence rate. Another contribution is that our approach offers a new perspective to the DE dynamics analysis. The main disadvantage of our approach is that the complex network creation is time-consuming and it works well just for the greater populations ($NP \geq 70$). The elimination of these lacks is one of the goal of the future research as well as to apply the next properties of the complex networks to the DE. The full version of this paper has been submitted to the journal Soft Computing, IF = 1.271.

4 Acknowledgement

The following grant are acknowledged for the financial support provided for this research: Grant Agency of the Czech Republic - GACR P103/15/06700S, partially supported by Grant of SGS No. SP2015/142, VSB - Technical University of Ostrava.

References

1. Boccaletti, S., Latorab, V., Morenod, Y., Chavezf, M., Hwanga, D.U.: Complex networks: Structure and dynamics. Physics Reports **424**, 175–308 (2006)
2. Kim, J., Wilhelm, T.: What is a complex graph? Physica A: Statistical Mechanics and its Applications **387**, 2637–2652 (2008)
3. Mezura-Montes, E., Velasquez-Rezes, J.: A comparative study of differential evolution variants for global optimization. In: Proceedings of the 8th annual conference on Genetic and evolutionarz computation, pp. 485–492. ACM (2006)
4. Saramaki, J., Kivela, M., Onnela, J.P., Kaski, K., Kertes, J.: Generalizations of the clustering coefficient to weighted complex networks. Physical review E **75** (2007). DOI 10.1103/PhysRevE.75.027105
5. Wang, Y., Cai, Z., Zhang, Q.: Differential evolution with composite trial vector generation strategies and control parameters. Evolutionary Computation **15**, 55–66 (2011)
6. Yao, X., Liu, Y., Lin, G.: Evolutionary programming made faster. IEEE Transactions on Evolutionary Computation **3**, 82–102 (1999)
7. Zhang, B., Horvath, S.: A general framework for weighted gene co-expression network analysis. Product Information Statistical Applications in Genetics and Molecular Biology **4** (2005). DOI 10.2202/1544-6115.1128
8. Zhou, Y., Li, X., Gao, L.: A differential evolution algorithm with intersect mutation operator. Applied Soft Computing **13**, 390–401 (2013)

Table 2. Experimental results for CODE and enhanced CODE. To make a fair comparison, the Wilcoxon signed-rank test at the $\alpha = 0.05$ level has been conducted. The results are mentioned in the format: *the minimum value (standard deviation)*. In the cases denoted by † both algorithms reached the global minimum and the standard deviation equals to 0. From this reason we mention the average number of the cost function evaluation.

Function	CODE		Enhanced CODE
f_1	5.8E-11 (3.35E-11)	=	1.03E-12 (1.70E-12)
$f_2^\dagger$	**476038**	+	**428260**
$f_3^\dagger$	**476164**	+	**427060**
f_4	**1.87E-03 (2.90E-04)**	+	**3.68E-05 (1.91E-05)**
f_5	**0.17E+00 (0.37E+00)**	+	**6.38E-03 (0.07E+00)**
$f_6^\dagger$	**112942**	+	**103780**
f_7	**8.84E-03 (2.83E-03)**	+	**6.14E-03 (2.58E-03)**
$f_8^\dagger$	**497422**	+	**438238**
$f_9^\dagger$	**638638**	+	**555160**
f_{10}	**1.85E-06 (4.31E-07)**	+	**2.36E-07 (9.89E-08)**
f_{11}	**8.11E-15 (2.43E-14)**	+	**0.00E+00 (0.00E+00)**
f_{12}	**8.99E-12 (4.89E-12)**	+	**6.62E-14 (2.47E-13)**
f_{13}	**4.20E-11 (1.76E-11)**	+	**2.92E-13 (8.81E-13)**
f_{14}	0.9980038 (3.37E-16)	–	0.9980038 (5.61E-16)
f_{15}	1.91E-05 (3.77E-06)	=	3.30E-05 (2.17E-06)
f_{16}	**-1.0316285 (4.00E-15)**	+	**-1.0316285 (1.42E-15)**
f_{17}	24838	=	24712
f_{18}	**3.000 (4.49E-16)**	+	$3.000(0.00E+00)$
f_{19}	**-10.1532 (1.56E-06)**	+	**-10.1532 (6.83E-07)**
f_{20}	**-10.4029 (4.53E-07)**	+	**-10.4029 (2.01E-07)**
f_{21}	-10.5364 (6.95E-07)	=	-10.5364 (6.92E-07)
+	16		
=	4		
–	1		

Techniques of Czech Language Lossless Text Compression

Jiri Sevcik

Department of Computer Science, FEECS,
VŠB – Technical University of Ostrava, 17. listopadu 15, 708 33 Ostrava – Poruba
jiri.sevcik.st5@vsb.cz

Abstract. For lossless data compression of the texts of natural language and for achieving better compression ratio we can use linguistic and grammatical properties extracted from the text analysis. This work deals with usage of word order, word categories and grammatical rules in sentences and sentence units in Czech language. Special grammatical properties of this language which are different from for example English language are used here. Further, there is an algorithm designed for searching similarities in analyzed sentence structures and its next processing to final compressed file. For analysis of the sentence units a special tool is used which allows parsing on more levels.

Keywords: lossless data compression, czech language, linguistic, morphology, graphs

1 Introduction

Within the compression we can encounter several data types. These types can be graphic data, sound data or a text in natural language. All these types have different statistic properties and dependences following from them. In case of the text compression we can point out that the character of given language has an influence on the compression itself. From this finding we can deduce that knowledge of the language structures and rules can influence the final compression ratio if we use it properly. Our work focuses on these properties. It is not a general system which processes any kind of language, but Czech language.

2 Language Categories

Czech belongs to Slavic languages. This category is interesting from morphological point of view, because on this level there is a possibility of dividing languages into other categories. The most important category for this work is an inflected language category, which is characterized by using inflection for expression of the grammatical functions. The inflection adjusts grammatical categories grammatical case, number, gender etc. The words are divided into inflectional and non-inflectional, it depends on the fact if we can use the inflection or not. In case

© M. Krátký, J. Dvorský, P. Moravec (Eds.): WOFEX 2015, pp. 388–393.
VŠB – Technical University of Ostrava, FEECS, 2015, ISBN 978-80-248-3787-1.

of inflexible words we can distinguish type of inflection: declension and conjugation. Flexible words have its basic which is called lemma. Another category is analytic languages category where we can put English language.

The number of language properties which are different for described categories is higher, but it is sufficient for basic understanding. Thanks to this understanding we can point out the fact that in case of inflected languages is the word arrangement looser than in the analytic languages. The word order is mainly influenced by semantic point of view of the whole sentence or by its grammatical arrangement. Knowledge of this property is one of the crucial features of our work and the whole principle of the data preprocessing for compression is built on this property.

3 Previous Work

We can find a large number of researches or works that deal with the compression which specializes on a particular language. The largest amount of them deals with English text or with Indo-European languages[1][2]. We can find also special compressing methods for different language categories such as Arabic[3] or Chinese[5] language

In a number of these works we can encounter also preprocessing. It divides the compression into two sequential parts preprocessing algorithm and compression algorithm. First algorithm transforms the input data for the compression based on its own compression scheme and these modified data he will deliver to the second algorithm which will, based on some standard or special methods, compress it. Decompression works just the opposite way. In the case of preprocessing algorithm we can encounter various general methods. The closest one to the topic of this work is the one on the level of words[4], symbols or sentential units. Another interesting method is the compression based on syllables[6].

4 Linguistics

The problem of compressing a natural language is therefore large and we can approach it with different perspectives. The aim of this work is to use some of these specific attributes and characteristics of Czech language and with the use of that attain a better compression ratio. Therefore we have to use possibilities of a science related to the language linguistics. We can divide it into general linguistics, applied linguistics or language linguistics. Further we can divide it based on its aims in our case we will specialize in descriptive linguistics and theoretical linguistics. On theoretical level we can divide these subsystems into three categories: phonetics, grammar and syntax. Related to the aim of this work we will specialize on the second category which is divided into morphology and syntax. Morphology we can describe as a discipline which deals with the study of the creation of words their declension and deriving of new words. Further we analyze the structure of particular words or whole word form. For the analysis of words we use morphematics. Basic morphological unit is an component which

has a particular meaning morpheme. If standing alone it may not be even a word. In the basic division morpheme may be lexical (word base) root of the word which represents action or characteristic or morpheme gramattical (*afix*) which defines grammatical categories (*sematics*)[8].

The opposite procedure of analysis is the morphological synthesis. Here, in order to acquire a particular word we need to know its basic lemma form and morphological tag. There are various morphological taggers for the Czech language and each processes the text in a different way. Among the most well-known belong Free morphology tagger of Jan Haji[11] and Ajka system[12]. Another category is the syntactic discipline.

In European linguistics the dependency description is used to describe the structure of the sentence. Here, the verb is considered to be the central part of the clause or the sentence. The whole structure of the sentence is described in the form of tree where each node represents an individual constituent. The borders between the nodes represent dependency relations and each node has only a single superordinate parent node. Here the verb is the root node. The nodes in the tree are arranged structurally according to their dependency relations and also linearly according to their sequence in the sentential word order.

5 Computer Linguistics

The described linguistic disciplines are difficult and complex field and a "handmade" analysis of the grammatical constituents or units is very demanding not only with the respect to time. Here the use of computers comes in the picture. Such processing is called Natural language processing.

The corpus is the important term here. It is a structured set of texts/literature or even transcriptions of a spoken language. This set includes other information about the linguistic informations of the given text. Such information is crucial for us because they are syntactic and morphological. For our task the Prague Dependency Treebank[9] is the most interesting. This corpus, besides other functions, includes two aforementioned levels, that is the *morphological layer* (m-level) and *analytical/syntactic layer* (a-level). A *tectogrammatical layer* is also included, however it is not crucial for our task. The actual data is stored in the structured format *PML* (Prague Markup language) which is based on the well-known marking XML and thus the computer data processing is made easier.

The resulting dependency tree includes the description of dependencies in the line descendant parent between the individual constituents of the sentential whole. Such analytical tag is called afun and there are twenty-eight types of them. The second most important information included is the morphological part which records the lemma form to each grammatical constituent and a complete morphological tag. The last presented tool is *Treex*[10] which is capable of processing the text, creating its morphological and syntactic analysis and generate the resulting *PML* set.

6 Our Work

6.1 Processing of the text

Treex analyser is to be used for the analysis of the compressed text. The program can be used in a graphic mode via web program as well as a console application. After morphological and syntactic analysis is done, the output is transferred to the next part of the algorithm.

6.2 Similarities in tree structures

For our case, the searching for similarities in graphs is the most important. The search is to be done in two, mutually collaborating levels. The algorithm works in several phases:

1. **The initial phase** takes place during the actual processing of the input text in *Treex* analyser. Here we observe whether the afun *Coord* appears in the morphological analyses because here it serves as the coordinate function for grammatical constituents; Namely the symbols "*,*" and "*a*". In such case the whole tree is divisible into grammatical constituents. After the conclusion of this initializing phase the trees are divided in two sets (hereinafter referred to as A and B).
2. **The first similarity phase**: Here, and also in the following phase, the work is done by the general algorithm for similarity search in the graph. The manner and evaluation of similarities is to be discussed later. The algorithm first processes the set tagged as divisible i.e. A. In case there are more trees with necessary similarity, they are moved into resultant set C.
3. **The phase of division** A division into sentential units is to be done for all the remaining trees from the set A. The division is made on the spot of the occurrence of the *Coord* afun. Thus two subtrees are created, to which we assign the information about the linking coordinating function and which tree is their parent. The division into subtrees is done recursively because of the possibility of several *Coords* appearing in the single tree. After all subtrees are determined for the individual tree, they are moved into set B where all trees gained from the first phase can be found.
4. **The second similarity phase**. The same procedure as in the set A is used for the set B with the exception that all trees are to be moved into the resultant set.

As another possibility we have synthesis and modification of these phases in two which shall look as follows:

1. **The first phase** after processing the text in *Treex*, the sentences where *Coord* afun occurs, will be divided into subtrees that will be saved into set together with all other trees that could not be divided.
2. **The second phase** The similarity algorithm is applied on the whole set.

In the current phase of this work we cannot decidedly tell which procedure shall bear better results. It can be assumed that the processing of divided sentential units[7] will enhance the overall compression ratio but considering the small modification of preprocessing algorithm both alternatives shall be tested.

6.3 Comparing the similarity in graphs

The issue of comparing and defining the similarity of graphs is not unusual and there are many theoretical and practical works that deal with the topic. Thus there is plenty of research material and completed theoretical solutions. We are especially interested in the research group created under Czech Technical University in Prague. This group which consists of the members of well-known The Prague Stringology Club created a research group Arbology in 2008 [13].
Structural similarity A clause or a grammatical constituent can be regarded as a tree without further research of its attributes and dependency functions between the individual nodes.
Word-order similarity This similarity has already been mentioned there are certain similarities to be found even in the free word-order.
Morphological similarity The most frequent similarity can be found in the same grammatical case of the words.

It can be seen that the similarity of the grammatical constituents can be found on several levels. Our goal is to create such an algorithm that will be capable of processing all input trees and create the smallest possible output set of trees for them on all similarity levels. The algorithm will be capable to determine whether it is suitable for particular clause to create a new tree if there is a similarity with the already existing output tree. Or whether an existing should be used considering that the original tree is modified and the modification is saved as the additional information. The modification will be most commonly used in addition or removal of the node in the tree or change of some morphological tags.

Another no less important part of our way of compression is the processing of individual words. Because the structure of the clause and its morphological elements will be already saved in trees we can then just use a lemma basis of each word. This option is very economical because the set of all words will be drastically smaller. For compression of these words various algorithms from the category LZ[14] can be used.

There is a greater number of available options for improvement of compression but in the initial phase of our research we take into account only the conversion of numerals from the textual form into number and their subsequent compression according to the already existing algorithm suitable for this type of data. The resulting compressed file will have a following structure:

- a set of morphological tags corresponding to some of these trees
- a list of words
- a set of structures representing the original text.

6.4 Decompression

From our method we expect that the decompression will be quick mainly due to a fact that the complex process of obtaining sentential structure will not be necessary. The lemma basis should be sufficient for acquiring the original word and its corresponding form should be acquired from its morphological tag with help of morphological synthesis in Treex. The original words should be then compiled into corresponding trees. Thanks to our way of compression of the individual clauses, with no regard to other clauses, the decompression can be sped up with applying of parallel processing.

6.5 Future works

Our further work should go towards the greatest possible use of the Czech grammar while searching for similarities. In this most important phase it will be possible to use successive testing of the individual types of texts such as texts in standard language or transcription of the spoken word where we can expect a better compression ratio due to usage of the lesser number of words and especially the lesser number of similar sentential structures.

References

1. Yuret D.: *Discovery of Linguistic Relations using Lexical Attraction*, PhD Thesis, Massachusetts Institute of Technology, 1998
2. Bach J., Witten H.: *Lexical Attraction for Text Compression*, Proceedings of Data Compression Conference, pp. 516-516, 1999.
3. Awajan A.: *Multilayer model for Arabic text compression*, Int. Arab J. Inf. Technol., vol. 8, no. 2, pp. 188196, 2011.
4. Moffat A.: *Word-Based Text Compression*, Software, Practice and Experience, pp. 185-198, 1989
5. Chang K. Y., Yang G. T.: *A Data Compression System for Chinese Fonts and Binary Images Using Classification Techniques*, Pr. Exp., vol. 22, no. 12, , 1992.
6. Lansk J., Zemlicka M.: *Compression of Small Text Files Using Syllables*, Technical Report of Department of Software Engineering No. 2006- 1, 2006
7. Kazik O.: *Lingvistick komprese textu*, Diploma Thesis, Charles University in Prague, 2009
8. Hajicova E., Panevova J, Sgall P.: *vod do teoretick a potaov lingvistiky, I. svazek - Teoretick lingvistika*, Nakladatelstv Karolinum, Praha, 2002.
9. Honetschlger V. a kol.: *The Prague Dependency Treebank 3.0*, https://ufal.mff.cuni.cz/pdt3.0
10. *Treex Highly Modular NLP Framework*, http://ufal.mff.cuni.cz/treex
11. Haji, J.: *Disambiguation of Rich Inflection (Computational Morphology of Czech)*, Karolinum, Praha, 2004
12. Sedlacek R.: *Morfologicky analyzator cestiny*, Diploma thesis, Masaryk university Brno, 1999
13. Melichar B., Janousek J., Flouri T.: *Introduction to Arbology*, Czech Technical University in Prague, 2008
14. Ziv J., Lempel A. *A universal algorithm for sequential data compression*, IEEE Transactions on Information Theory 23 (1977), 337 343

Introduction to Integration of the Process Mining to the Knowledge Framework for Software Processes

Jakub Stolfa

Department of Computer Science, FEECS,
VŠB – Technical University of Ostrava, 17. listopadu 15, 708 33 Ostrava – Poruba
jakub.stolfa@vsb.cz

Abstract. Systems started to be more process oriented during last decades. The shift to process oriented systems was motivated by the idea of supporting systems for the daily businesses. The knowledge has moved from humans to systems and systems has more and more knowledge about the process. This paper presents an approach to the integration of the process mining, process modeling and process standards supported by the formal layer.

Keywords: process mining, process modeling, formal approach, OWL

1 Introduction

Process is ordered set of the steps that leads to some goal. In the reality there is a process that is executed by persons, machines, etc. Process that is followed in the information system is called workflow. In last decades, systems started to be more and more process oriented. The shift to process oriented systems was motivated by the idea of supporting systems to the daily business, to shift the knowledge about operations that could be described as processes from humans to systems. Process oriented systems started to be worshiped as the only way to control the processes and activities that has to be enacted. The knowledge about the processes and their enactment was transferred to the systems by defining the workflow. The shift from the data oriented systems to the process oriented systems brought possibilities for further analysis of controlling and checking the enactment of the processes and resources that are involved.

Execution of the process in the information system generates data that is called event data and it can be examined by the process mining [8, 9]. Process mining is an approach that is used for the analysis of real enactment of the processes. Process mining uses logs of real process enactments to analyze the process itself. Process mining could discover the process model that is really followed in the reality. In other words it could create the process model from the "bottom".

On the other hand stands the Business process modeling [1]. Business process modeling is the activity of creating a process model that should be followed then. The aim of the business process modeling is to capture reality and create the process model

© M. Krátký, J. Dvorský, P. Moravec (Eds.): WOFEX 2015, pp. 394–399.
VŠB – Technical University of Ostrava, FEECS, 2015, ISBN 978-80-248-3787-1.

that corresponds to the reality. The result is the process model that is modeled from the "top" and the executions of the particular process should follow this model.

We have developed formal process modeling framework – Knowledge Support Framework for Software Processes. It includes modeling based on single process meta-model terminology defined in a formal way, utilization of explicit reusable knowledge profiles and intuitive visual modeling method based on diagrammatic language capable of software process modeling based on process patterns. In other words it offers complex framework for modeling software processes from the "top" and it is supported by the defined formal layer [4, 5].

The goal of this paper is to present our ideas and work that we have made in the area of connection between process mining that bring us the possibilities of the modeling from the "bottom" and the business process modeling that aim to model the process from the "top". The area of the process modeling is covered by our knowledge support framework that is naturally for all kind of processes but proved initially just for the software development [6] and healthcare processes [4] so far. We are also working on the implementation for all kind of business processes. In this paper, we are focused on software processes. However, our own framework bring us possibilities to adjust the methods and create one holonomic methodology that automatically supports modeling and improving of all kinds of business process from the top and also from the bottom.

The paper is organized as follows: Section 2 presents proposed approach of connection process mining and process modeling; and Section 3 presents the conclusion, benefits, published papers and intended future work.

2 Integration of Process mining to process modeling

The aim of this section is to introduce the core of this paper - connection of the process mining approach and the process modeling framework. This section describes introduction how is the process mining integrated to the Knowledge support framework and how is modeling supported from the top and from the bottom. The way of creating the framework, formalization of the process model, the integration of the process mining took some scientific research that we have done so far. In this area we have published several papers [2, 3, 4, 6, 7]. Idea of the Knowledge support framework for software processes was introduced in the paper [6]. Paper [4] discuss the possibilities of usage the framework in the area of clinical processes instead of the software processes and pronounce challenges and future work that has to be addressed. Paper [6] also described first basic ideas of connection of the framework with the process mining. In the paper [5] we have presented architecture of proposed framework for process modeling, possibilities of simulations, and we have also introduced the idea of the possible connection with process mining. This idea is developed in this paper.

The structure and important parts of the connection between the framework for process modeling and process mining are depictured in Fig. 1. We can see that figure is divided into the three parts – Knowledge support framework for software processes, Execution of the process, and Integration of the process mining.

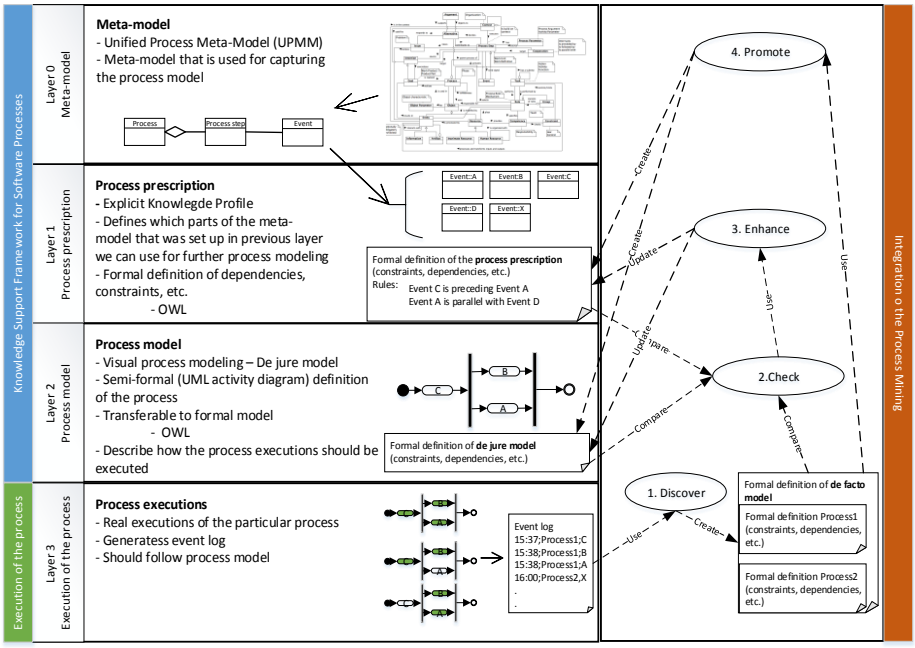

Fig. 1. Overview – Process mining and process modeling

2.1 Process modeling part

First part Knowledge support framework for software Processes aims to create the process model of the software process in particular organization. From simplified point of view it has three layers:

Layer 0 – meta-model layer

This part is focused on adjusting of the meta-model named Unified Process Meta-Model. There are various process meta-models available [6] however each had been designed to support different process aspects like context, goal (or product), activity, strategy, or automatization. Our meta-model – Unified Process Meta-Model, on the contrary, unifies all base terminology necessary for complex process capture and representation. The Unified Process Meta-Model is described in the paper [4, 5] – its compatibility with other meta-models opens possibilities like pattern-based visual process modeling and explicit knowledge profiles creation.
In this layer meta-model is adjusted according to organizational needs. Adjusting means that we do not have to use all the possibilities that meta-model supports but we can use only part of that model.

Layer 1 – Process prescription (Explicit Knowledge Profile)

Based on the selection of meta-model the process prescription is done here. The process prescription is developed and have e.g. defined constraints etc. For example we can prescribe that during the modeling phase we might use Event A and Event B, and define

some of many possible constraints that define how these events can be used – if in parallel or in sequence, etc. Constraints are written down in formalized way in OWL language.

Layer 2 – Process model (Visual Process modeling)

This layer is focused on visual process modeling, it means in our terminology creating the de jure model. The *de jure model* is normative, it means it specifies how things should be done. It is a prescription how the process should be handled. Typically it is a process model that is modeled from the top and used to configure a BPM system that forces people to work in a particular way. In our methodology the de jure model is assembled from the pieces that process prescription from the layer 1 provides to us. It has to follow the constraints of the prescription model and in case of need add new constraints.

We use UML Activity diagram as a tool for modeling - semiformal definition of the process. Thanks to the transferability of UML activity diagram to OWL we are able to write down process model in a formal definition too.

2.2 Process mining part

Second part of Fig. 1 is the Execution of the process. It represents execution of the process in the reality. Execution of the process is done by real people supported by information systems. During the execution lot of data are generated to event log.

Third part of figure represents integration of the process mining to the framework. There are four activities that are integrated for the usage in the framework:

1. Discover

This activity aims to discover the process from the event logs. **Fig. 1** depictures that in our case discover activity uses Event log of execution of the processes and create formal definition of de facto model. The *de facto model* is descriptive, it aims to capture reality not to steer or control reality. It is typically the discovered process model that is handled in the real business process execution. We use methods of the process mining for process model discovery [9] and we adjust the output of the methods to create formal definition that is written in the OWL language that we support in the framework. We had to create own method that automatically converts the process model to OWL that is our formal layer.

2. Check

This activity aims to compare the event log and de jure model. In our case it uses formal definition of the particular process cases and formal definition of de facto model and formal definition of the process prescription.

Method is comparing the formal definitions of the de jure model, process prescription and formal definitions of the particular process cases. We are able to automatically distinguish if the particular case follows the definitions and constraints of the de jure model. Definitions and constraints are written in OWL. If the particular

case break some definitions and constraints it can highlight this behavior and warn. The particular case can be then used for further investigation.

As it was mentioned we make comparisons on different levels:

- De facto and de jure level – this comparison aim to find the deviations between model of real process executions and the model that should be followed in the reality. If the models are identical it means that the process in the reality is executed in the way that we have modeled it. If not we can further analyze why not and how big is the deviation.
- De facto model and prescription model level – it compares de jure model with process prescription. It means if the execution of the process fits to main constraints in the prescription model at least. As it was mentioned above, if we find out that the de jure model fits to prescription model from organizational point of view we can say that the process followed in the reality is not that what was desired (de jure model), but at least it do not break important constraints of the structure that were designed in the level of process prescription during the process modeling. If the de jure model breaks also the prescription model we have found big deviation that we have to handle

3. Enhance

Enhance activity uses information gathered from the activities check or diagnose and updates prescription model or process model. This activity we propose for future automatization according to the information that we are able to gather from the formal layer.

4. Promote

Promote activity uses de facto model and creates de jure model and particular process prescription. This case can happen when the framework is used in the company that has not used the framework before and their process model is not done properly.

3 Conclusion

This paper introduced connection between process modeling that is presented by our framework and process mining that has possibilities to discover process model followed in the reality. All of that is supported by one formal layer that is common for process modeling and also process mining. We have set up approaches for several possible usages of this connection – discovery, check, enhance, and promote. In future work, would like to describe all possible usages of the approach, present case studies based on the real data, and also adjust the framework to support not just a software processes but also for all business processes.

Connection of the process modeling and process mining that is proposed in this paper is the basic of the methodology that we are working on. It will include process modeling, process mining, one common formal layer, and automatized methods. We would like to also integrate methods for process predictions [10, 11, 12, 13] that we

have developed in one our methodology. In future work we would also integrate process standards and process assessment [14] to the holonomic methodology. It is because process assessment covers part of the process execution where is process done without system and process mining cover parts of the process where process uses information system. When we will be able to connect these two kind of information in one formal methodology, we will have holonomic view of the process.

References

1. Ruth Sara Aguilar-Saven, "Business process modelling: Review and framework," International Journal of production economics, vol. 90, no. 2, pp. 129-149, 2004.
2. J. Czopik, M. A. Košinár, J. Štolfa a S. Štolfa, "Addition of static aspects to the intuitive mapping of UML activity diagram to CPN", Advances in Intelligent Systems and Computing ,vol. 334, pp. 77-86 ,2015
3. J. Czopik, M. A. Košinár, J. Štolfa a S. Štolfa, „Formalization of Software Process Using Intuitive Mapping of UML Activity Diagram to CPN", Advances in Intelligent Systems and Computing ,vol. 303, pp. 365-374, 2014
4. M. A. Kosinar, J. Czopik, J. Štolfa a M. Penhaker, „Knowledge Framework for Clinical Processes Architecture and Analysis," *13th International Symposium on Applied Machine Intelligence and Informatics (SAMI 2015), Herl'any, Slovakia*, 2015.
5. M. A. Kosinar, J. Czopik, J. Štolfa, "Formal Knowledge Framework for Software Processes Architecture", Frontiers in Artificial Intelligence and Applications, EJC 2015, 2015
6. M. A. Kosinar, J. Stolfa a S. Stolfa, „Knowledge support for software processes", *Frontiers in Artificial Intelligence and Applications,* vol. 272, pp. 205-223, 2014
7. J. Štolfa, S. Štolfa, J. Kožusznik a T. Moudrá, „Business process formal modeling in graphical ontology tool - Functional view," *Proceedings of the International Conference on Management of Emergent Digital EcoSystems, MEDES 2012*, pp. 187-188, 2012.
8. Wil MP Van Der Aalst and AJMM Weijters, "Process mining: a research agenda," Computers in industry, vol. 53, no. 3, pp. 231-244, 2004.
9. Wil Van Der Aalst, Ton Weijters, and Laura Maruster, "Workflow mining: Discovering process models from event logs," Knowledge and Data Engineering, IEEE Transactions on, vol. 16, no. 9, pp. 1128-1142, 2004.
10. J. Štolfa, S. Štolfa, P. Krömer, O. Koběrský, M. Kopka a V. Snášel, „Fuzzy Rules and SVM Approach to the Estimation of Use Case Parameters," *Innovations in Bio-inspired Computing and Applications, IBICA 2014*, Springer International Publishing, pp. 37-47, 2014.
11. J. Štolfa, O. Koběrský, P. Krömer, S. Štolfa, M. Kopka a V. Snášel, „Comparison of fuzzy rules and SVM approach to the value estimation of the use case parameters," *Proceedings of the 2013 Joint IFSA World Congress and NAFIPS Annual Meeting, IFSA/NAFIPS 2013*, pp.789-794, 2013.
12. J. Štolfa, O. Koberský, M. Kopka, P. Krömer, S. Štolfa, J. Kožusznik a V. Snášel, „Value estimation of the use case parameters using SOM and fuzzy rules," *Proceedings of the International Conference on Management of Emergent Digital EcoSystems, MEDES 2012*, pp. 166-173, 2012.
13. J. Štolfa, S. Štolfa, O. Koběrský, M. Kopka, J. Kožuszník a V. Snášel, „Methodology for estimating working time effort of the software project," *CEUR Workshop Proceedings*, vol. 837, pp. 25-37, 2012.
14. Mary Beth Chrissis, Mike Konrad, and Sandra Shrum, "CMMI for development: guidelines for process integration and product improvement," 2011.

Machine-Learning Supportive Methods for Software Effort Estimation

Radoslav Štrba

Department of Computer Science, FEECS,
VŠB – Technical University of Ostrava, 17. listopadu 15, 708 33 Ostrava – Poruba
radoslav.strba.st@vsb.cz

Abstract. Effort estimation is important task in software development process. This paper proposes new advanced methods for software process support in early phase of software development. In particular, these methods help improve software process development, using results of use case classification. Use cases are classified using artificial intelligence methods like feed-forward neural network or Naïve Bayes classifier.

Keywords: Software Process, Naïve-Bayes, Neural Network, Classification, Effort Estimation

1 Introduction

Main idea of this research is to support the estimation using machine-learning methods that are not so common in this. Our methods can help to project manager to estimate the project complexity and the risk of additional work for new projects based on the analysis of use cases. The method uses knowledge base of historical use cases and provides a decision support in the form of a probability given by estimation of extra work in the project. In nutshell, the guidance for support of effort estimation based on classification of use case scenarios is provided.

Use case scenarios are used in software requirements analysis for capturing and describing the functional requirements of a software system. Methods that can help to project managers automatically classify use case scenarios are presented. Use case scenarios are made during the first phase of software development, which is called elaboration phase.

Based on that classification, the estimations of selected parameters are made to support the manager's decision about the project in next phases. In our method, we used the Feed-forward Neural Network architecture with the Back-propagation training algorithm. Next technique used in for use case classification purpose is called Naïve Bayes Classifier.

© M. Krátký, J. Dvorský, P. Moravec (Eds.): WOFEX 2015, pp. 400–405.
VŠB – Technical University of Ostrava, FEECS, 2015, ISBN 978-80-248-3787-1.

2 Effort Estimation

Software estimation can be done at any stage within the requirements engineering process. However, performing estimation in the early stage, such as requirements elicitation means that the requirements of the software are not complete and more assumptions will need to be made in the estimation process. This could lead to poor results. There is need to find right stage within Requirements Engineering Process in which effort estimation can be done. [1]

Requirements engineering process consists of several activities. Manage the scope of the system is appropriate activity for effort estimation. The functional and nonfunctional requirements are collected use cases are prioritized so the system can be delivered on expected time and budget. [2,3]

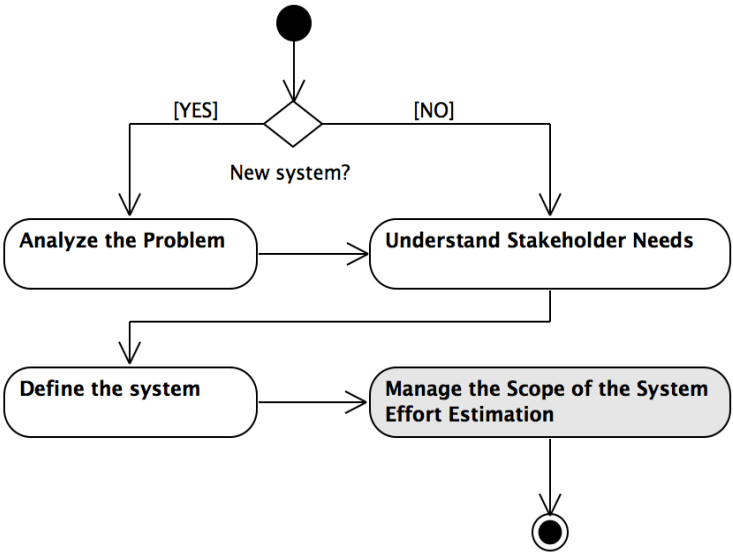

Fig. 1. Activity diagram of requirements engineering process.

3 Classification for Support of Effort Estimation

Classification methods can be used as supportive tool for effort estimation. Machine-learning methods help us to classify use case scenarios and predict risk factor of impropriate estimation of working time. We call working time like “extended work” parameter. Use case scenarios are used in the requirements, analysis and design stages in the software life cycle.

The use case model of the evaluated project includes a set of parameters of each use case. As parameterization method, we used existing approach detailed described in [4,5]. Basically we use three types of parameters: descriptive, structural and really evaluated parameters.

Descriptive parameters are evaluated from the description of the use case scenario. We use following descriptive parameters: *Overall difficulty* (represents number of words, rows, etc.). *RFC* is project ID.

Structural parameters are evaluated by the structural or relational property of the use case on given project. Set of structural parameters was defined as a result from the interview with several senior project managers. We use following structural parameters and values: *NSC, which means:* New, Standard and Change functionality of the system. The parameter *Concerned activities* means how many business processes are touched by the implementation of this use case. *Use case type* can be user or sub function. Next parameters are: *remote work*, *implementation remote*, *testing level*.

Evaluated parameters are evaluated backward after project end. We use following evaluated parameter in our experiment: *Extra work* means if there was some additional work then was expected for the use case scenario. This parameter obtain binary values Yes or No. More information about parameters and parameterization, that we used is described in following papers [4–6].

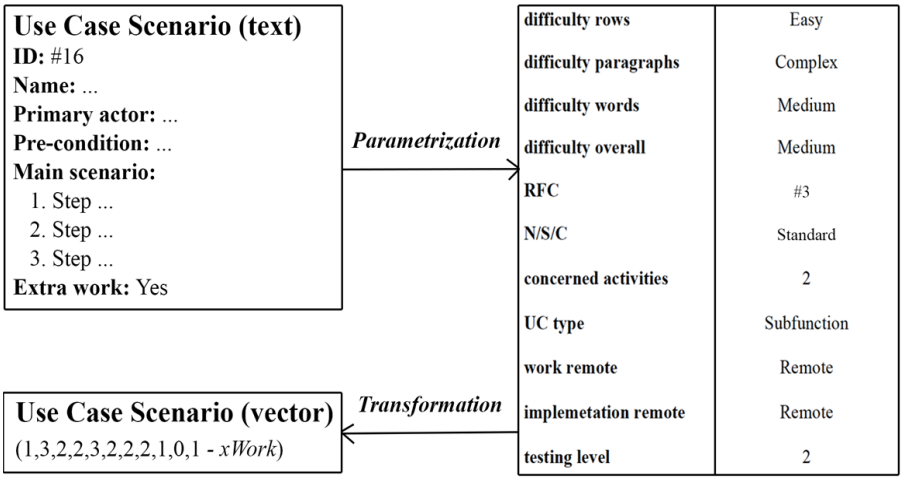

Fig. 2. Example of the parameterization and transformation of the Use Case Scenario.

4 Experiments

Naïve Bayes is a simple and very powerful classification method that should be using on our classification problem and it is also kind of supervised training. Next approach for Use Case classification is Neural Network. Most development of neural networks today is based upon manual design and configuration. A person who has knowledge about the specific application area specifies a network architecture, configuration and activation dynamics. This state of affairs is perhaps not surprising, given that the general space of possible neural networks is so large and complex that automatically searching for an optimal network architecture may in general be computationally intractable or at least impractical for complex applications [10], [11].

The whole process consists of five important activities. The first is Data Preprocessing, second is training, and third is testing type selection, which allows using selected vectors by project manager or all vectors from the next dataset for testing purpose. At the end of the process is activity called Evaluation.

4.1 Data Preprocessing

Whole use case training set consists of 1041 parameterized use cases. The value of some parameters is the same for all items, e.g. use case type, work remote and implementation remote. Actually they are same for whole dataset. That is the reason, why these parameters are not important, so they can be removed.

4.2 Train Classifier

Train the classifier means that we need to tell to classifier that the given features resulted in the given category (value of extended work parameter can be Yes or No). As is written above, the whole datasets consists of 1041 Use Cases from years 2008-2013. These items are divided into 6 datasets. Each dataset includes last 10 testing items.

4.3 Test Classifier Using Vectors from the Next Dataset

Finally, we tried to test neural network using all vectors from current and all vectors from next dataset. For example, the neural network is trained using use cases from year 2008 and is tested using use cases from year 2009. Table 2 shows results of testing Neural Network Classifier after training process. Table 1 shows results of testing Naive Bayes Classifier after training process.

5 Results

Use cases were divided into two categories. In the first category extra work on use case was needed. In this case *extra work* parameter obtains value 1. If extra work was not needed than parameter obtain value 0.

Table 2 shows results of testing process after training of Neural Network Classifier using 10 testing vectors selected by project manager from the next dataset as “testing accuracy” and all training vectors also from the next dataset as “training accuracy.”

Table 1 shows results of testing process after training of Naive Bayes Classifier using 10 testing vectors selected by project manager from the next dataset as “testing accuracy” and all training vectors also from the next dataset as “training accuracy.” [8]

Table 1. Results of Naïve Bayes Classifier

Training vectors from years	**Testing accuracy (all vectors** / 10 vectors) **from year:**
2008	2009 (102 vectors) **63,76%** / 70%
2008-2009	2010 (110 vectors) **66,71%** / 80%
2008-2010	2011 (110 vectors) **66,43%** / 90%
2008-2011	2012 (110 vectors) **66,60%** / 70%
2008-2012	2013 (109 vectors) **66,94%** / 70%

Results obtained from classification of Use Case datasets using Neural Network are showed in Table 2. Each *training cycle* parameter is complete neural network training process. Parameters *Acc1-Acc6* means testing accuracy value of the neural network. This accuracy is computed using six different training datasets (*Acc1 – Acc6*). The number of training items in each next dataset has increased, because training and testing items from previous dataset are added. Last 10 items of each dataset we are always using as testing items. The bold printed value is the highest value of accuracy of neural network trained using provided dataset.

For example, let us discuss the maximum precision neural network using second training dataset achieved in the first *training cycle.* This accuracy is achieved with 2744 *training iterations* and six *hidden neurons* and it is showed in column with name *Acc2* and value is 100 in Table 2. [7]

Table 2. Results of Neural Network

Training cycle	Iterations	Hidden neurons	Acc1	Acc2	Acc3	Acc4	Acc5	Acc6
1	8	12	**50**	60	80	60	**90**	60
2	64	11	50	60	80	60	80	60
3	216	10	50	70	80	80	80	60
4	512	9	30	80	70	90	60	**90**
5	1000	8	20	80	**100**	**100**	60	90
6	1728	7	20	80	100	100	70	90
7	2744	6	20	**100**	90	100	70	90
8	4096	5	20	100	90	100	70	90
9	5832	4	20	100	90	100	70	90
10	8000	3	20	100	90	100	70	90

As the main purpose of this experiment was just to prove the possibility of Neural Network and Naïve Bayes usage for our purposes we have performed simple experiments. Even those simple tests showed that the accuracy for the parameters prediction could be quite high even without any special adjustments and setting of our approach.

The main advantage of Naive Bayes Classifier is simplicity and good training time. Disadvantage of this approach is lower accuracy then for example neural network based classification.

Related publications

7. Štrba, R., Svatopluk. Š., Štolfa, J.: Finding an optimal Configuration of Feed-forward Neural Network; In Proceedings of the 25rd European-Japanese Conference on Information Modeling and Knowledge Bases; Editors: Yasushi Kiyoki,Takehiro Tokuda; 2015, Maribor, Slovenia

8. Štrba, R., Briš, R., Vondrák, I., Štolfa, S.: Application of Naïve Bayes in Classification of Use Cases; AECIA 2015 [accepted]

Other references.

1. Nassif AB, Capretz LF, Ho D. Estimating Software Effort Using an ANN Model Based on Use Case Points. 2012 11th Int. Conf. Mach. Learn. Appl. [Internet]. IEEE; 2012. p. 42–7. Available from: http://ieeexplore.ieee.org/lpdocs/epic03/wrapper.htm?arnumber=6406723

2. Gill NS, Sikka S. New complexity model for classes in object oriented system. ACM SIGSOFT Softw. Eng. Notes. 2010;35:1.

3. Nassif AB. Software Size and Effort Estimation from Use Case Diagrams Using Regression and Soft Computing Models. 2012.

4. Stolfa J, Kobersky O, Kromer P, Stolfa S, Kopka M, Snasel V. Comparison of fuzzy rules and SVM approach to the value estimation of the use case parameters. 2013 Jt. IFSA World Congr. NAFIPS Annu. Meet. [Internet]. IEEE; 2013. p. 789–94. Available from: http://ieeexplore.ieee.org/lpdocs/epic03/wrapper.htm?arnumber=6608501

5. Štolfa S, Štolfa J, Krömer P, Koběrský O, Kopka M, Snášel V. Fuzzy Rules and SVM Approach to the Estimation of Use Case Parameters. 2014. p. 37–47. Available from: http://link.springer.com/10.1007/978-3-319-01781-5_4

6. Štolfa J, Štolfa S, Koběrský O, Kopka M, Kožuszník J, Snášel V. Methodology for estimating working time effort of the software project. CEUR Workshop Proc. 2012. p. 25–37.

Memory Optimized Pheromone Structure for Max-Min Ant Systems

Martin Šurkovský

Department of Computer Science, FEECS,
VŠB – Technical University of Ostrava, 17. listopadu 15, 708 33 Ostrava – Poruba
martin.surkovsky@vsb.cz

Abstract. Ant Colony Optimization is a well-known meta-heuristic algorithm mainly determined for solving hard combinatorial optimization problems. The algorithm is inspired by the ants' behavior within a colony. A research group of which the author is a member is focused on parallel computing in massive parallel systems with distributed memory. The aim of the article is to propose an adjustment of Max-Min Ant System, so as it could be used in these parallel systems in the future. Generally, Ant Colony Optimization methods work with the information called pheromone. These pheromones are located on paths in a searched space, evolve during a computation, and help with the choosing of the next "best" step. Pheromone information is traditionally stored by means of a matrix. However, such an approach is very memory-demanding, especially in the case of large instances. Therefore, this article proposes an adjustment of the original method which does not use any matrix to store pheromone information. Instead, the desired information is assembled during a computation at a time when it is needed. The proposed solution was implemented in C++ and tested on large symmetrical instances of the Traveling Salesman Problem. The experiments have shown that this method enables results to be computed in a quality comparable to that achieved by a traditional approach while being faster and using only a portion of the original memory.

Keywords: Max-Min Ant System, memory optimized pheromone structures, distributed memory systems, C++

1 Introduction

This article presents a short version of the original article [2] published in the Neural Network World journal. For more detailed information the reader is referred to the original article.

Ant Colony Optimization (ACO) [3] represents a class of meta-heuristic algorithms for solving hard combinatorial problems. The algorithm is inspired by the ants' behavior within a colony. It has been used for various hard problems; as an example the Traveling Salesman Problem (TSP) can be named. TSP is a well-known NP-hard problem [4], thus it seems that there is no algorithm which would compute an optimal solution in a reasonable time. Nevertheless, there

© M. Krátký, J. Dvorský, P. Moravec (Eds.): WOFEX 2015, pp. 406–411.
VŠB – Technical University of Ostrava, FEECS, 2015, ISBN 978-80-248-3787-1.

are people who fairly often encounter such problems and try to compute at lest some suboptimal solution. For this reason, they often use some approximation or meta-heuristic algorithms.

The aim of this article is to present an adjusted version of an ACO algorithm which can be used for solving large problem instances on a supercomputer. There have been various attempts to adjust ACO algorithms for parallel/distributed systems [1]. Even though they address different issues like granularity or communication topology, the resulting implementations are still tested merely in relatively small systems with dozens of processors. Moreover, they frequently use shared memory systems.

Since a supercomputer is considered for running an ACO implementation, it is necessary to make some modifications of the standard implementation, so that such a computer could be efficiently utilized. The article is not about the invention of a new ACO variant with different guidelines, but rather about an adjustment to one of the existing algorithm – *Max-Min Ant System* (MMAS) – in a way that it uses memory more efficiently.

Although all variants of ACO algorithms differ from each other, most of them usually follow a basic guideline in each iteration: *construct ant solutions*, *(apply local search)*, *evaporate pheromones*, and *update pheromones*. The pheromone information is crucial to this sort of algorithms. The pheromone represents a piece of information which every ant stores on the paths of a searched space. All pheromones evolve during a computation and influence the decision-making process of choosing the next step of each ant. It can be said that the more pheromones there are on a specific path, the more ants are attracted to this path and it is more likely to be used. This most-used path then represents the best solution found by a colony. Conventionally a matrix – *pheromone matrix* (PM) – is used to store pheromone data. It then serves as a shared medium where artificial ants share their data. This attempt is an issue in the case of a supercomputer and large instances are considered. Firstly, supercomputers usually work with distributed memory, therefore there cannot be a large shared matrix. Secondly, a possible amount of memory which is needed to process large instances can be huge. For example, if we use the largest problem from TSPLIB[1] with 85900 cities, then the pheromone matrix will be the size of $85900 \times 85900 \times 8Bytes \approx 59GB$. For the purpose of illustration Anselm[2], a supercomputer we have used, consists of nodes with 64 GB of physical memory. Moreover, pheromone matrix should be shared among other processes.

This paper proposes a different approach which does not use a pheromone matrix. Instead, the data which is normally incorporated into the pheromone matrix is stored during a computation. Later, at a moment when the data is needed only some necessary parts are assembled. In this way the algorithm is able to emulate the original matrix while using only a portion of the original memory. Furthermore, because the stored data is relatively small, its distribution among computational nodes is easier.

[1] http://www.iwr.uni-heidelberg.de/groups/comopt/software/TSPLIB95
[2] https://www.docs.it4i.cz/anselm-cluster-documentation/compute-nodes

The proposed solution has been implemented in C++ and tested on symmetrical instances of TSP from TSPLIB. The results of experiments show that the new implementation of MMAS enables results to be computed in a quality comparable to standard implementations, while the time needed to reach such a solution is reduced.

Firstly, the Max-Min Ant System is introduced, including the discussion of reasons for choosing this algorithm. Then *Disassembled Pheromone Matrix* and *Sparse Pheromone Matrix* are described, the structures used in implemented solutions. This description is followed by their comparison. Finally, the ideas and results are summarized in a conclusion.

2 Max-Min Ant Systems

Max-Min Ant System [5] is one of the standard methods belonging to class of ACO algorithms. Although all variants differ from each other, they usually follow a basic guideline. This basic principle will be explained on a variant used for solving TSP problem. Most implementations work with a fixed number of artificial ants. Each of these ants constructs a tour between a given set of cities. The construction process is repeatedly performed in each iteration until termination conditions are met. At the beginning, each ant is placed into a random city. Then it constructs its tour through the unvisited cities. The decision which city will be visited next is influenced by a combination of heuristic information (e.g. distance between cities) and pheromone information. When each ant visits all the cities, the pheromone information is updated according to its tour. A way how to update pheromone information can be influenced by initial settings. Usually each ant puts a pheromone onto its path and then is chosen the ant currently holding the best solution and the pheromone on its tour is boosted. As can be seen, there may be many initial parameters that strongly influence the resulting speed of convergence and its quality.

The Max-Min Ant System algorithm was chosen to be adjusted because its properties are interesting for parallelization. These are as follows: (i) it does not modify the pheromone information during the tour construction, (ii) in each iteration there is only one ant modifying the pheromone matrix, (iii) minimum and maximum values are defined for pheromones. Last but not least, MMAS represents a successful algorithm which has been used for various problems.

To improve the results, some other methods are usually incorporated to the main algorithm, for example some local search strategies which can be helpful within a tour construction. Another mechanism that directly modifies the pheromone matrix is called *diversification*, a process where the pheromone matrix is reinitialized within a time period when no better solution has been found.

2.1 Operations with Pheromone Matrix

Because the pheromone matrix is the subject of modification, there is a description of the original matrix and operations performed on it. For this purpose the

pheromone matrix is called T in the rest of the text. It consists of N rows and N columns, where N is the number of cities. $\tau_{x,y}$ addresses an element on x-th row and y-th column. The values in matrix T are bounded by τ_{min} and τ_{max}. According to [5], these two values are set as follows: $\tau_{max} = 1/(\rho \cdot C^{best})$ and $\tau_{min} = \tau_{max}/(2 \cdot N)$, where C^{max} is the length of the best tour found so far and ρ is the parameter of evaporation. On the pheromone matrix T the following operations are performed:

Initalization and reinitalizaiton – at the beginning and after reinitialization all values in the pheromone matrix are set to τ_{max}.

Pheromone evaporation – during evaporation phase every value of the pheromone matrix is multiplied by $1 - \rho$.

Update pheromones – in each iteration only the best ant deposits its trail into the pheromone matrix. The pheromone τ is computed as $\tau = 1/C$, where C is the length of the current trail. If the ant goes from city x to city y in iteration i, then $\tau^i_{x,y} = \tau^{i-1}_{x,y} + \tau$.

3 Memory Optimized Structures

This section presents two different attempts at replacing the pheromone matrix by a less memory-demanding structure. The first structure – *Disassembled Pheromone Matrix* (DPM) – simulates the work with an original matrix while only storing the pheromone information from the visited trails. For an unvisited trail an approximated value is used, therefore DPM is not as precise as the original matrix. The second structure – *Sparse Pheromone Matrix* (SPM) – is inspired by the standard approach used for storing spare matrices.

3.1 Disassembled Pheromone Matrix

As mentioned above, DPM simulates work with the original pheromone matrix, but it is not as precise as the original one. The lack of precision is caused by the manipulation with pheromone values which have not been visited yet. For these values one approximated value, τ_{global}, is used.

$$\tau_{global} = \begin{cases} \tau_{max} \cdot (1-\rho)^i & \text{if } \tau_{max} \cdot (1-\rho)^i > \tau_{min} \\ \tau_{min} & \text{otherwise} \end{cases},$$

where i is an iteration.

An experiment ([2] section 3) which compared the disassembled pheromone matrix with the standard one, showed that the error (number of elements where they differ) is up to 5%.

Instead of incorporating the trails into the pheromone matrix, each ant remembers its trail. ACO algorithms produce this trail as a sequence of visited cities. This is, however, an inappropriate way to store them. It is desired to reach a target city from a given starting point quickly, which is why every trail uses two vectors. The first one says where to continue from a given city – *forward*

trail, while the other one shows the city from which it was reached – *backward trail*. Let us imagine a trail through the cities, as in figure 1. The backward and forward trail are shown on the right-hand side.

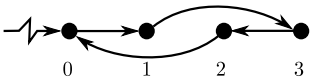

1	3	0	2	*Forward trail*
0	1	2	3	*Index*
2	0	3	1	*Backward trail*

Fig. 1. Illustration of forward and backward trail.

A method which accesses a pheromone located on an arc between cities x and y from this structure, returns both τ_{global} if there is no ant which has gone through this arc or τ_{global} increased by pheromones of all ants which have gone through it.

Several implementations using DPM structure have been made and tested. There is no global pheromone matrix where all additions of pheromones could be gradually stored. Instead, there is a queue of trails which are encountered. When a trail is dropped from the queue its pheromone addition is removed. The implementations differ in the way they utilize this queue. The first one uses a queue of a fixed size (FDPM); hence when a queue exceeds its size, the oldest trail is removed. The second implementation uses a dynamic size of queue (DDPM). In this case trails are removed from the queue if their deposit pheromone becomes "insignificant", i.e. its current deposit is smaller than some threshold, e.g. 1% of the original deposit. The last one, called *improved* DPM (IDPM), utilizes the fact that there can be two ant trails which are not able to boost the pheromone information above τ_{min} only by themselves. However, their combination can go beyond τ_{min}. In the case that the pheromone matrix is used, the deposit of such arcs is removed and τ_{min} is used instead. This is not true for the previous two versions. Nevertheless, this situation can be easily detected and such arcs can be removed.

3.2 Sparse Pheromone Matrix

This pheromone structure implements an idea similar to sparse matrices. There are only stored those values which differ from τ_{global}. While the previous structures only imprecisely simulate the pheromone matrix, SPM precisely represents all values from the original pheromone matrix. A comparison of the impact of all mentioned approaches on the convergence of the method may be seen in the chart bellow (figure 2). Of course, the chart shows a comparison on a specific example, but the results were similar in all performed tests.

4 Conclusion

The paper explored an idea whether or not it is really necessary to store pheromone information in a matrix. Using a matrix is the most common solution for ACO

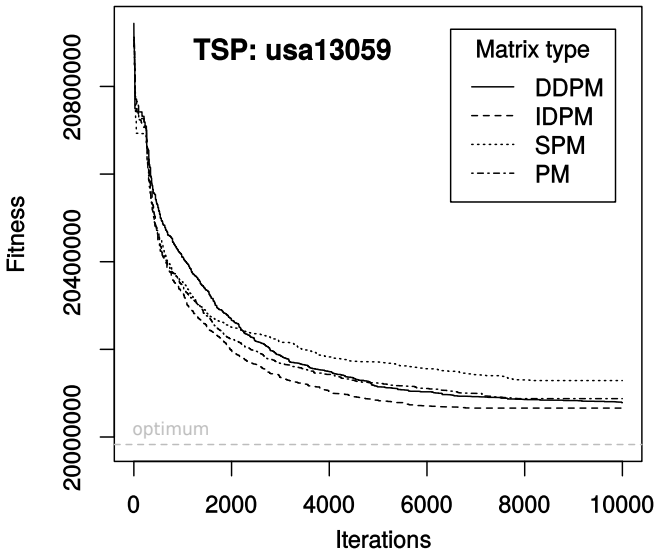

Fig. 2. Comparison of convergence of different pheromone matrix implementations.

algorithms. However, for large instances such a matrix can be huge and what is more, only a limited number of cells contain relevant data. This paper presents a different approach. In the case of MMAS, only ant trails and some additional data are stored. The information about a pheromone value is then composed at the only part where it is needed and at a time when it is needed.

As the experiments showed, the usage of such structures gives reasonable results while using significantly less memory. For instance with thousands of cities only dozens of trails need to be stored. Moreover, for larger instances the proposed solution becomes even faster.

Acknowledgment The work was supported by the student project SP2015/123.

References

1. Alba, E., Luque, G., Nesmachnow, S.: Parallel metaheuristics: recent advances and new trends. International Transactions in Operational Research 20(1), 1–48 (2013), http://dx.doi.org/10.1111/j.1475-3995.2012.00862.x
2. Běhálek, M., Šurkovský, M., Meca, O., Böhm, S.: Memory Optimized Pheromone Structure for Max-Min Ant Systems. Neural Network World 25(2), 161–174 (2015)
3. Dorigo, M., Stützle, T.: Ant Colony Optimization. Bradford Company, Scituate, MA, USA (2004)
4. Garey, M.R., Johnson, D.S.: Computers and Intractability; A Guide to the Theory of NP-Completeness. W. H. Freeman & Co., New York, NY, USA (1990)
5. Stützle, T., Hoos, H.H.: MAX–MIN Ant System. Future Generation Computer Systems 16(8), 889 – 914 (2000), http://www.sciencedirect.com/science/article/pii/S0167739X00000431

Parallelization of k-NN Problem on GPU to Speed up the Fruchterman-Reingold Graph Layout Algorithm

Vojtěch Uher

Department of Computer Science, FEECS,
VŠB – Technical University of Ostrava, 17. listopadu 15, 708 33 Ostrava – Poruba
vojtech.uher@vsb.cz

Abstract. Searching of the nearest neighbors (NN) in unordered point clouds (PC) is a well known task. This article describes a new parallel method which was tested on a graph layout algorithm. Graphs can visualize relationships between objects, but it is quite time consuming process. They are widely used in social network analysis, computer networks, and plenty other areas. This paper describes a novel variant of the Fruchterman-Reingold graph layout algorithm which is adapted to CUDA using our k-nearest neighbors (k-NN) approach based on space-filling curves and a new way of repulsive forces computation on GPU.

Keywords: k-NN, graph layouts, space-filling curves, nearest neighbors, Fruchterman-Reingold, graph visualization, GPU, CUDA

1 Background

A selected space-filling curve (SFC) is briefly described in this section. Also the Fruchterman-Reingold algorithm is mentioned.

1.1 Space-filling curves

Several variants of space-filling curves (SFCs) exist such as e.g. Peano, Z-order or Hilbert space-filling curve [3] [8] [2].

Practically, SFCs connect the points that are close to each other and thus transform the n-dimensional problem into one dimensional (1D). A common lack of these curves is that there are some space leaps between two points which belong to different octants (fig. 1). But a SFC can be very easily computed in parallel. A computation of only a single index for each point ($\Theta(N)$) is required. Point indices have to be sorted then, e.g. with parallel radix sort using CUDA. An example of Z-order SFC for which the Morton keys [9] of all points have to be computed can be seen in figure 1. A study of optimal properties of space-filling curves was presented by Xu in [12].

© M. Krátký, J. Dvorský, P. Moravec (Eds.): WOFEX 2015, pp. 412–417.
VŠB – Technical University of Ostrava, FEECS, 2015, ISBN 978-80-248-3787-1.

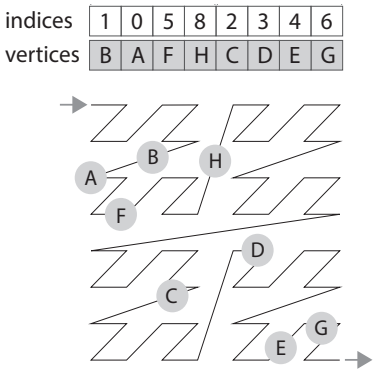

Fig. 1. 8 vertices (A, B, C, D, E, F, G, H) randomly placed and ordered by Z-order curve

1.2 Graph Layout and Fruchterman-Reingold

Let a graph $G \leftarrow (V, E)$ be a set of vertices V and edges E that connect those vertices. One of the algorithms for the graph layout is the Fruchterman-Reingold, which is part of the family of force-directed graph layout algorithms. Vertices connected by an edge attract each other. An ideal distance for each vertex is also defined. The vertices should be drawn near each other, but not too close. To lay out a graph, the vertices are replaced by steel ring and each edge with a spring mechanical system [4].

The algorithm basically consists of three independent parts. The computation of repulsive forces is the bottleneck of the whole algorithm.

1. Calculate repulsive forces ($\Theta(N^2)$).
2. Calculate attractive forces ($\Theta(E)$).
3. Iterate all vertices ($\Theta(N)$).

2 Our Approach

The aim of our research was to develop a variant of the Fruchterman-Reingold graph layout algorithm which can run fast on the GPU and provides similar results to the original algorithm. The whole computation is performed on GPU to avoid unnecessary memory transfers.

We present a new k-NN method for calculation of repulsive forces on GPU keeping the high visual quality. A memory structure based on oct-tree is used. The approximation of the nearest neighbors preferres the closer points of neighborhood.

2.1 Building the octant structure on GPU (CUDA)

Our method uses octants of Z-order curve, but a standard oct-tree [7] [1] is not built. An oct-tree is usually sparse, so there can be a huge number of empty

octants. The efficiency of passing the tree parallely on GPU is lower then. Our octant structure contains only unique ordered Morton-keys of existing octants of the lowest tree level and corresponding beginning indices of the octants in the sorted point cloud.

This process is described in the fig. 2 and consist of 3 parts:

1. *Finding of octant's beginnings in the point cloud:* The Z-order curve of point cloud has to be computed at first (sec. 1.1). The beginnings of octants are detected by parallel comparison of pairs of octcodes. The pairs differences are notified by number 1 flags in auxiliary array.
2. *Prefix sum of indices:* The beginning indices of octants were found in the 1st step. The indices of octcodes in the new structure are found out by computing of parallel prefix sum [10] at the beginnings of octants in auxiliary array. The order of points is thus preserved.
3. *Building the final structure:* The corresponding indices of unique structure codes are stored at the notified beginnings of octants (fig. 2). The final structure consists of two arrays: array of unique octants and array of beginning indices of octants in PC. The difference between two following octant indices is the number of points in the octant. The structure is cashed in the texture memory on GPU.

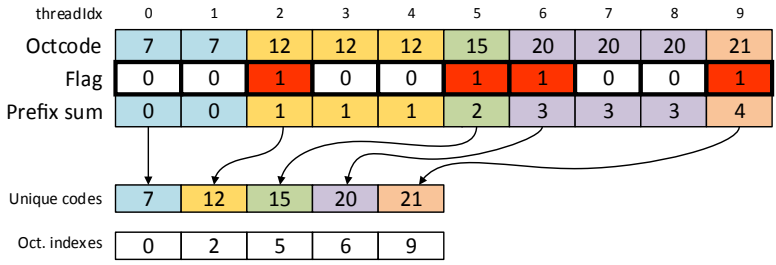

Fig. 2. Building octant structure

2.2 Nearest neighbors search

The described structure is used for searching k-NN in the space. A neighborhood of each point is solved by one block of threads and many neighborhoods are searched at once to get maximum occupancy of the GPU. The following steps are done for each point:

1. *Octant coordinates are computed.*
2. *Nearby octcodes hit by a radius of neighborhood are computed.* The query radius and sizes of octants are known in advance (fig. 3). According to known coordinates of actual octant, the surrounding octcodes are computed by

simple translating of coordinates along axises and by their re-hashing. An intersection between the query sphere and surrounding octants is checked. To make better approximation of k-NN, thread indexing from center to farther octants is used (2D case in fig. 3).

3. *Proposed octcodes are searched in the structure.* The Morton-keys are sorted in the structure, so it is simply possible to search a required octcode binary. Every thread does a binary search of one key. The found ones are stored in a shared memory.
4. *Found intervals of points are checked.* The intervals of octants stored in the shared memory are checked in parallel and the suitable points of these octants are stored to device memory.

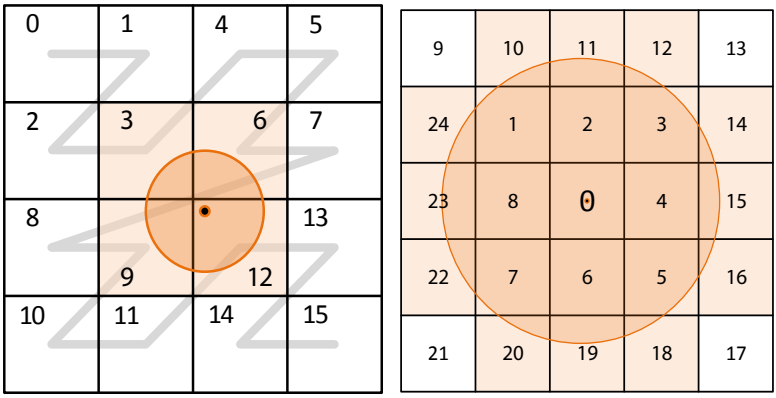

Fig. 3. Computing of nearby octants (left): Maximum number of hit octants is 9, only 4 of them (orange) are hit by radius of the point. **Indexing of octants (right):** The closer octants are preferred. Thread ids are assigned to octants as shown in the picture on the right. In 3D case the furthermost and the closest 2D blocks of surrounding octants are solved lineary. The rest is indexed like in 2D case.

2.3 Repulsive forces

The computation of the repulsive forces is the most time-consuming part of the Fruchterman-Reingold algorithm $\Theta(N^2)$. The forces that modify the positions of vertices can be neglected for all such vertex pairs where the vertices are far from each other. Focusing on the forces between close vertices only significantly reduces the computation time. Our proposed approach to speed up this part on GPU consists in a combination of the method described [5] and speed-up of the FR algorithm described in [6]. The main difference is that only the near points found and stored by our k-NN method in the device memory are used. All processes are done on GPU, so it is very fast.

3 Experiments

Reached graph layouts are shown in figure 4. A radius defines the sphere of neighborhood. It is set as a rate of bounding box size and its real value is recalculated in every iteration. Figure shows that the different radius rate affects the layout quality, but the radius rate about 0.2 seems to be good enough. The greater is the radius, the more nearby points are involved. Next experiments were focused on the performance. All the times mentioned in figure 5 are in milliseconds. Every test was run 10 times and the final computation times (including visualization) were averaged.

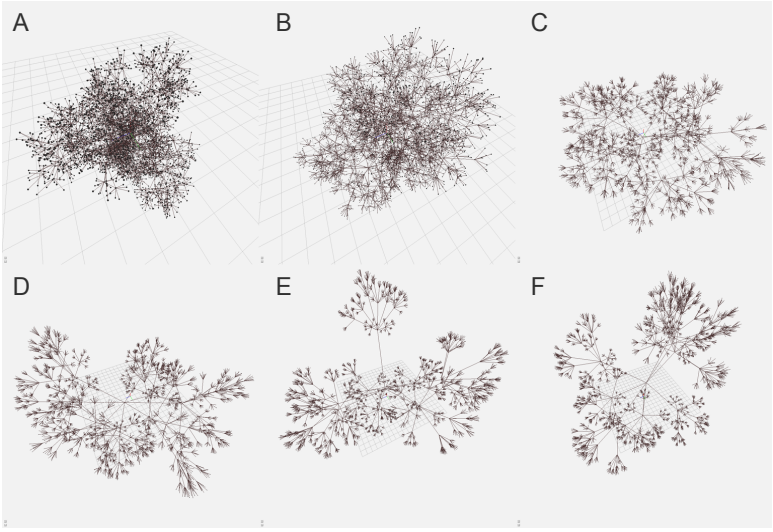

Fig. 4. Graph layouts with different settings of radius rate (A = 0.05, B = 0.1, C = 0.2, D = 0.3, E = 0.4, F = 0.5) after 200 iterations.

4 Conclusion

A novel approach of solving k-NN problem in unordered point clouds was described. The method was developed in parallel and optimized for GPU computing. It was tested on the improved Fruchterman-Reingold layout algorithm and the visual quality results and performance results were presented. Nice layout quality was reached in very short time. As compared with the original Fruchterman-ReingoldThis algorithm our method strongly reduces number of vertices involved in repuslive forces computation. The parallel processing on GPU allows one to visualize graph layouts on real time. This approach may be used in another applications dealing with k-NN problem. This article summarizes the results published in [11].

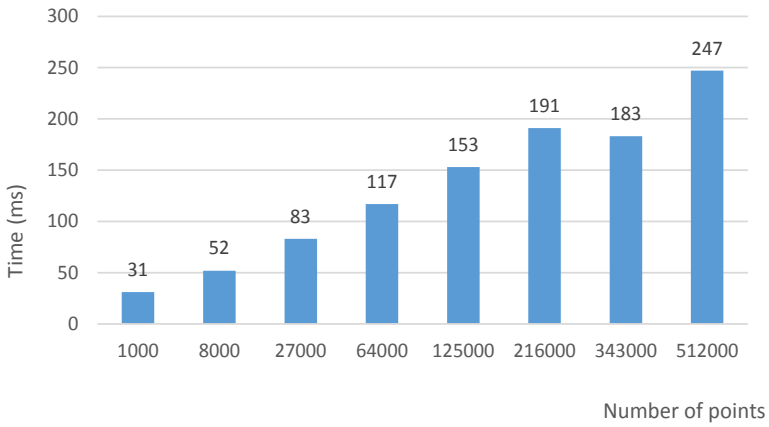

Fig. 5. Computation times in milliseconds for different sizes $|V|$

References

1. Jeroen Bédorf, Evghenii Gaburov, and Simon Portegies Zwart. A sparse octree gravitational n-body code that runs entirely on the gpu processor. *J. Comput. Phys.*, 231(7):2825–2839, April 2012.
2. Greg Breinholt and Christoph Schierz. Algorithm 781: Generating hilbert's space-filling curve by recursion. *ACM Trans. Math. Softw.*, 24(2):184–189, 1998.
3. Arthur R. Butz. Convergence with hilbert's space filling curve. *J. Comput. Syst. Sci.*, 3(2):128–146, 1969.
4. Thomas MJ Fruchterman and Edward M Reingold. Graph drawing by force-directed placement. *Software: Practice and experience*, 21(11):1129–1164, 1991.
5. Tomáš Ježowicz, Petr Gajdoš, Eliška Ochodková, and Václav Snášel. A new iterative approach for finding nearest neighbors using space-filling curves for fast graph visualization. In *SOCO*. Springer, 2014 (In Press).
6. Tomas Jezowicz, Milos Kudelka, Jan Platos, and Václav Snásel. Visualization of large graphs using gpu computing. In *INCoS*, pages 662–667, 2013.
7. Rensselaer Polytechnic Institute. Image Processing Laboratory and D.J.R. Meagher. *Octree Encoding: a New Technique for the Representation, Manipulation and Display of Arbitrary 3-D Objects by Computer*. 1980.
8. Warren M. Lam and Jerome M. Shapiro. A class of fast algorithms for the peano-hilbert space-filling curve. In *ICIP (1)*, pages 638–641, 1994.
9. G.M. Morton. *A Computer Oriented Geodetic Data Base and a New Technique in File Sequencing*. International Business Machines Company, 1966.
10. Shubhabrata Sengupta, Mark Harris, and Michael Garland. Efficient parallel scan algorithms for gpus. Technical report, 2008.
11. Uher V., Gajdoš P., and Ježowicz T. Solving nearest neighbors problem on gpu to speed up the fruchterman-reingold graph layout algorithm. In *Cybernetics (CYBCONF), 2015 2nd IEEE International Conference on*, June 2015.
12. Pan Xu and Srikanta Tirthapura. Optimality of clustering properties of space-filling curves. *ACM Trans. Database Syst.*, 39(2):10:1–10:27, May 2014.

Feature Preprocessing Methods For Machine Learning Algorithms

Tomas Vantuch

Department of Computer Science, FEECS,
VŠB – Technical University of Ostrava, 17. listopadu 15, 708 33 Ostrava – Poruba
tomas.vantuch@vsb.cz

Abstract. The increasing complexity of the issues that the nowadays data mining and modeling solvers are dealing with is strictly connected to the huge amount of variables in analyzed datasets. There are many problems that are arising with this phenomenon like decreasing precision of forecasting models, increasing computational time and lowering the ability of understanding of the inner dependencies. This paper is a summation of more approaches in building of the suitable dataset with purpose of the increase quality of the machine learning model.

Keywords: feature selection, feature extraction, grammatical programming, information theoretic criteria

1 Introduction

The tasks of machine learning bring often a tricky issue of handling the correct composition of the attributes that will hold the most relevant information for the observed model. The datasets, that the most solvers are dealing with, are in the raw states full of noisy, irrelevant or redundant data [1]. Ignoring of this circumstances leads to the lost of the accuracy of the prediction or classification models and increase of their learning-time.

There are more approaches for solving of this issue. In case of large amount of variables, there is easy and computationally fast to use the Ranking algorithm approach [12]. This method evaluates all of the variables by its intrinsic feature and it removes all of the variables with the lower rank values by different ways [5]. The most often used measures are the Mutual Information, the Information Gain, Correlation, etc. [10] This approach is able to select the most relevant subset of variables, but it is not able to remove the redundant information from the subset [7].

On the other hand, there are some more complex approaches that are performing the handling of both of the main requirements - the relevancy and the redundancy [13] of the variables. The main three categories of these complex algorithms are Filters, Wrappers and Embedded selectors. The Filters are the algorithms that compound the subset only by the intrinsic characteristic of its features without of use of any learning algorithm. The correctness of the subset is handled by heuristic merits like in Correlation-Based Feature Selection

© M. Krátký, J. Dvorský, P. Moravec (Eds.): WOFEX 2015, pp. 418–423.
VŠB – Technical University of Ostrava, FEECS, 2015, ISBN 978-80-248-3787-1.

(CBFS) [8], Consistency-Based Subset Evaluation (CBSE), etc. The wrappers are the algorithms based on the results of the learning algorithm, as the subset's evaluation. The algorithms of the group of the Embedded are considered as the work-flows where the resulted subset comes as a secondary output from the learning algorithm like in Decision Trees or Support Vector Machine.

The other very often used kind of approaches is the dimensionality reduction [17]. This method generates uncorrelated set of features that represents a linear or nonlinear combination (depends on chosen algorithm) of the dataset's variables. Some of the typical representative of this algorithms is the Principal Component Analysis [9] or Non Negative Matrix Factorization [3]. This approach is more likely to use in case when the predicted observation does not consist of the many variables, but it is defined by time set on other hardly structured data.

In case of larger time series data or other unstructured datasets, it could be used some kind of synthesis of the (non)linear feature by symbolic regression approach with properly defined fitness function [6] as it was used in some of the next proposed results.

2 Applications of proposed approaches

In this section it will be described a few real tasks which solving requires the application of this kind of algorithms to deal whit their datasets. The specific details of applied algorithms are not described in this paper, due to the limitation of pages, but they are described in referenced papers.

2.1 Feature selection for the task of forecasting

The first three introduced papers are dealing with the issue of forecasting of the Power Quality Parameters (PQP) in the Off-Grid systems [14, 4, 16]. This systems are defined as a unit supplied by electric energy only from the renewable energy source (RES). The stochastic character of the source (solar cell panel or wind turbine) does not support stability of the PQPs like frequency (freq), total harmonic distortion (Thdi, Thdu), etc. On the other hand the presence of the low short-circuit power brings the same issue (unstable PQPs) on the side of the demand (consumption) [11].

The complex management of the source's forecasting and the optimizer on the demand side can stabilize this model and make it safer for all of the connected appliances. This approach is described in the paper [14] where the Artificial Neural Network was applied as a forecasting model and for the feature selection, there was applied the correlation ranking approach. This experiment serves us as a baseline for later testing.

In the paper [16], there was applied another analysis of the connections between variables. In the first phase, it was applied the Correlation Based Feature Selection applied to remove redundant or irrelevant variables from the dataset, according to all of the predicted variables. The merit value was the fitness function for the genetic algorithm which was used as a search engine. From all of the

combinations of the variables, it was searched iteratively for the best combination according to the ratio of the relevancy (correlation of subset variables to the predicted variable) and redundancy (inter-correlation between variables) of the subsets variables. In the next phase the applied algorithms like Decision Tree (DT) and Grammatical Evolution (GE) was driven to create predictive rules for PQP on the chosen subset of variables.

In case of DT, there was used the $C4.5$ version of DT, which is able to deal with continuous variables. The model creates the complex conditions to categorize each observation by given input values. The modeling is driven by Information Gain (IG) criteria, which serves as a indication of the best splitting variable. The variables on the top of the resulted tree had the highest IG values and then we can assume that the entire predictive model is mostly depended on that variables.

The same approach was tried in case of GE. The given grammar (with ability to create the condition statements) and chosen variables was adjusted as an input values for the GE engine (ECJ implementation). As a result, there was obtained predictive conditions that consists of the variables values inside of the mathematical formulas.

The quality of the synthesized rules was compared by their MSE in both cases, the training and the testing. In most of the cases there was the presence of over-fitting. Each of the model was handling this issue by its own way and the future works will take it into account more seriously, because the difference between training and testing accuracy phases was in some cases very significant.

In the next paper [4] there was applied the different approach for the analysis of the same dataset. The dimensionality of the dataset was firstly reduced by Principal Component Analysis (PCA) to obtain significant features from all of the variables, so the previous length of the variable (14400 - ten days of one minute measurement) was decreased to its intrinsic dimension (the maximum likelihood estimation or the eigenvalues of the PCA can be applied for this task). The PCA [9] works by looking for the mapping matrix M. The mapping matrix M is orthogonal and is formed by principal components - eigenvectors of the covariance matrix cov(X), which are sorted according to their eigenvalues. The vectors with lower eigenvalues are truncated, so only the most significant features remain.

This dataset of 118 reduced variables were later used as an input into the Kohonen's Self-organizing map. The main principle of this algorithm is to reflect the similarities of the input observations into the wider two dimensional map. This is performed by excitation of the same neuron (winning neuron - competitive learning) for the similar kind of input. The result of the SOM algorithm is the 2D map, where by k-means clustering, we can distinguish all of the significant categories of the variables. This gives to us the another perspective for combining the variables for next forecasting models.

Future work: In case of the forecasting tasks, there was some attempts to apply the Granger Causality (GC) [2] for feature selection. This algorithm brings

more robust statistical analysis than any other previously used approach. The GC determines by adjusted stable VAR model if one variable is significantly helpful for prediction of the observed variable. As a secondary result, the number of past lags which were taken into account by VAR model could be helpful in the created machine learning model.

On the other hand, the issue of over-fitting has to be solved too. There are some approaches which are using the chained machine learning algorithms (ANN's, Random Forest Trees) in faith to stabilize that model. The other possibility of solving it is to obtain larger dataset which will contain more out-lied observations.

2.2 Feature synthesis for the classification

The different preprocessing method was applied in case of the experiment that evaluates the hidden patterns in partial discharges activity (PD). The PD's activity appears around places of ruptures or degradation of insulation system by fault on medium voltage overhead lines with covered conductors. This approach of classification of the PD patterns should be able to categorize the input signal to find out if there is some failure (native or unexpected) on the observed conductor.

In case of this experiment, the input signal was a continuous time set of a length of 400 000 real numbers. The important information for classification was mostly represented by less than 0.1% of the length of the time set, so none of the dimensionality reduction methods was reasonable to use.

In the article [15] there is described the attempt of creation of the non-linear polynomials, which input was the entire time set and they were very sensitive to that minority-represented areas of the time set. The results of that polynomial were able to distinguish the signals into defined groups.

For that task, there was applied Grammatical Evolution (ECJ's implementation) where the polynomial is created by the defined grammar. That grammar has to consist of the mathematical statements (sum, product, min, max) that are able to deal with time series data. The fitness function of the GE is not the MSE of the forecasting or classification as it is applied in the most times. Now there is a need to create the "splitting attribute", the polynomial that is able to generate significantly different output values for each of the known groups of the signals. For this purpose, all of the polynomial's output values and the class values of the signals are taken into fitness function and the Information Gain criteria is computed for comparing the candidates polynomials from GE.

This set of synthesized features creates entirely new dataset from the given data and gives us the opportunity to use a various of conventional models from machine learning like DT, Artificial Neural Networks, SVM, etc.

Disadvantage of this solution is the large computational time that is required, because the number of signals is today more than 20000, so the parallel computation has to be taken as required standard.

Future work: There are two remaining issue that needs to be solved in case of GE's feature extraction. The higher number of synthesized polynomials leads

sometimes the model to the higher accuracy. Some kind of boosting is an opportunity to use in the purpose of increasing accuracy and relevancy of the model.

The other issue comes with increasing number of signals. As we can imagine, most of the signals are trouble-free signals (more than 99%) and only very tiny rest of them are the signals of other classes. Such a dataset makes the applied neural network unable of a reasonable learning. It converges into bad behavior, when the ANN marks all of the signals as trouble-free and still gains more than 99% of accuracy. Deeper study on this issue is the open case.

3 Conclusions

The proposed experiments were dealing with larger datasets or unstructured data of larger format. The better understanding of the observed model was obtained by the deeper analysis of the variables (correlation, causalities, intrinsic criteria) and by describing of the connections between variables. These information bring the ability to create more suitable subsets for the machine learning purposes.

In all of the experiments, it was used some of the feature selection/extraction method and it brings some improvement in all of the application, for example the increase of accuracy, decrease of the learning-time, etc. Each of the applications works with the feature engineering task the different way, and it still remains a lot of other different approaches that can work with categorical, unstructured or sparse variables. These kinds of preprocessing depends on the type of the variables/data and on the task which for the dataset has to be created.

There are many high quality papers describing the experiments where the proper feature's preprocessing is equally important than the machine learning algorithm or its parameter's tuning.

Acknowledgment This paper was conducted within the framework of the project ENET CZ.1.05/2.1.00/03.0069, Students Grant Competition project reg. no. SP2015/142, SP2015/146, SP2015/170, SP2015/178, project LE13011 Creation of a PROGRES 3 Consortium Office to Support Cross-Border Cooperation (CZ.1.07/2.3.00/20.0075) and project TACR: TH01020426.

References

1. Almuallim, H., Dietterich, T.G.: Learning with many irrelevant features. In: In Proceedings of the Ninth National Conference on Artificial Intelligence. pp. 547–552. AAAI Press (1991)
2. Barnett, L., Seth, A.K.: The {MVGC} multivariate granger causality toolbox: A new approach to granger-causal inference. Journal of Neuroscience Methods 223(0), 50 – 68 (2014)
3. Buciu, I.: Non-negative matrix factorization, a new tool for feature extraction: Theory and applications

4. Burianek, T., Vantuch, T., Stuchly, J., Misak, S.: Off-grid parameters analysis method based on dimensionality reduction and self-organizing map. In: Matouek, R. (ed.) Mendel 2015, Advances in Intelligent Systems and Computing, vol. 378, pp. 235–244. Springer International Publishing (2015)
5. Gao, K., Khoshgoftaar, T.M., Wang, H., Seliya, N.: Choosing software metrics for defect prediction: an investigation on feature selection techniques. Software: Practice and Experience 41(5), 579–606 (2011), http://dx.doi.org/10.1002/spe.1043
6. Guo, L., Rivero, D., Dorado, J., Munteanu, C.R., Pazos, A.: Automatic feature extraction using genetic programming: An application to epileptic {EEG} classification. Expert Systems with Applications 38(8), 10425 – 10436 (2011)
7. Hall, M., Holmes, G.: Benchmarking attribute selection techniques for discrete class data mining. Knowledge and Data Engineering, IEEE Transactions on 15(6), 1437–1447 (Nov 2003)
8. Hall, M.A.: Correlation-based feature selection for discrete and numeric class machine learning. In: Proceedings of the Seventeenth International Conference on Machine Learning. pp. 359–366. ICML '00, Morgan Kaufmann Publishers Inc., San Francisco, CA, USA (2000)
9. Jolliffe, I.: Principal component analysis. Springer series in statistics, Springer-Verlang (1986), https://books.google.cz/books?id=cN5UAAAAYAAJ
10. MacKay, D.J.C.: Information Theory, Inference & Learning Algorithms. Cambridge University Press, New York, NY, USA (2002)
11. Matallanas, E., Castillo-Cagigal, M., Gutirrez, A., Monasterio-Huelin, F., Caamao-Martn, E., Masa, D., Jimnez-Leube, J.: Neural network controller for active demand-side management with {PV} energy in the residential sector. Applied Energy 91(1), 90 – 97 (2012)
12. Rathore, S.S., Gupta, A.: A comparative study of feature-ranking and feature-subset selection techniques for improved fault prediction. In: Proceedings of the 7th India Software Engineering Conference. pp. 7:1–7:10. ISEC '14, ACM, New York, NY, USA (2014), http://doi.acm.org/10.1145/2590748.2590755
13. Saeys, Y., Inza, I.n., Larrañaga, P.: A review of feature selection techniques in bioinformatics. Bioinformatics 23(19), 2507–2517 (Sep 2007)
14. Stuchly, J., Misak, S., Vantuch, T., Burianek, T.: A power quality forecasting model as an integrate part of active demand side management using artificial intelligence technique - multilayer neural network with backpropagation learning algorithm. In: Environment and Electrical Engineering (EEEIC), 2015 IEEE 15th International Conference on. pp. 611–616 (June 2015)
15. Vantuch, T., Burianek, T., Misak, S.: A novel method for detection of covered conductor faults by pd-pattern evaluation. In: Abraham, A., Jiang, X.H., Snel, V., Pan, J.S. (eds.) Intelligent Data Analysis and Applications, Advances in Intelligent Systems and Computing, vol. 370, pp. 133–142. Springer International Publishing (2015)
16. Vantuch, T., Stuchly, J., Misak, S., Burianek, T.: Data mining application on complex dataset from the off-grid systems. In: Matouek, R. (ed.) Mendel 2015, Advances in Intelligent Systems and Computing, vol. 378, pp. 63–75. Springer International Publishing (2015)
17. Ye, J.: Dimension Reduction Algorithms in Data Mining, with Applications. University of Minnesota, 2005. Major: Computer science. (2005)

Advances in Context Transformations

Michal Vašinek

Department of Computer Science, FEECS,
VŠB – Technical University of Ostrava, 17. listopadu 15, 708 33 Ostrava – Poruba
michal.vasinek@vsb.cz

Abstract. Context transformation theory is a novel approach to data transformations for data compression introduced recently. The former concept of transformation was based on the exchange of two different digrams beginning with the same symbol. The exchange was based on the simple assumption, that if the probability of the second symbol of the first digram is larger than the probability of the second symbol of the second digram and the first digram has zero frequency, then the exchange leads to a shorter resulted entropy coding. In the recent paper, we presented a theorem that describes exact decrease of information during the transformation process and using this knowledge, we were able to form a novel type of transformation called Generalized Context Transformation. Due to the limited computational efficiency we also explored possible parallelization of the transformation process.

Keywords: data compression, context transformation, entropy reduction, information theory

1 Introduction

Data compression is a field of computational science where researchers try to develop algorithms, that given input data of some length n_0, they encode data to output of length $n_1 < n_0$, if possible. There are two major approaches in data compression: the so called offline and online compression. Meanwhile in the first approach, we make a one pass through the whole data first and try to collect some statistical information that is later, in the next pass, used to establish a more efficient representation of data. For instance Huffman or Arithmetic coding are representants of this approach. In the second approach, statistics about data are collected and immediately used to form a better coding and only one pass through data is needed. The most famous online algorithms are Lempel Ziv dictionary coding or Prediction by Partial Matching(PPM).

Context transformations(CT) are intended to be used with offline compression algorithms. They are used to preprocess data and leave them in the form that can be more efficiently compressed using the entropy coding algorithms. There are other famous transformation techniques, two the most important transformations are Burrows-Wheeler Transformation and MoveToFront transformation. Context transformations were proposed in [2] and [3], and later revised and enhanced in [4] and parallelized in [5].

© M. Krátký, J. Dvorský, P. Moravec (Eds.): WOFEX 2015, pp. 424–429.
VŠB – Technical University of Ostrava, FEECS, 2015, ISBN 978-80-248-3787-1.

The rest of the paper is organized as follows. Section 2 contains description of the proposed Context(CT) and Generalized context transformations(GCT). Section 3 provides and explains a theorem about entropy reduction. Section 4 describes the ability of transformations to work in parallel. Section 5 contains brief comparison of results attained by CT and GCT approaches and also provides a summary of the speedup due to the parallelization. Last Section 6 concludes the paper and discusses achieved results.

2 Context Transformations

The context transformation is a method that takes two digrams, the digram $\alpha\beta$ that is present in the input message and the digram $\alpha\gamma$ that is not present in the input message. Context transformation then replaces all occurences of $\alpha\beta$ for $\alpha\gamma$. The symbol α is called a context symbol and it is present in both digrams.

Definition 1. *Context transformation(CT) is a mapping* $CT(\alpha\beta \rightarrow \alpha\gamma, w) : \Sigma^n \rightarrow \Sigma^n$, Σ *is the alphabet of the input message* w *and* n *is the length of the input message, that replaces all digrams* $\alpha\beta$ *for digram* $\alpha\gamma$, *where* $p(\alpha, \gamma) = 0$ *and* $\beta \neq \gamma$.

We consider also the transformation of the form $\beta\alpha \rightarrow \gamma\alpha$, such transformation would correspond to the same transformation like in Definition 1, if we perform replacement on a mirror message. There is one rule that we must care about and it is that such transformation must be applied on the input message from right to left, respectively from left to right in the case of $\beta\alpha \rightarrow \gamma\alpha$. This rule ensures, that for each context transformation an inverse transformation that transforms the new message back to the input message exists. The proof of this rule can be found in [2].

In paper [4], we introduced a new type of transformation - generalized context transformation. In this case both digrams can be present in the message. Generalized context transformation can be applied from left as well as from right, its inverse transformation has the same form, but is applied in the opposite direction. Context transformations are a subset of generalized context transformations.

Definition 2. *Generalized context transformation(GCT) is a mapping* $GCT(\alpha\beta \leftrightarrow \alpha\gamma, w) : \Sigma^n \rightarrow \Sigma^n$, Σ *is the alphabet of the input message* w *and* n *is the length of the input message, that exchanges all digrams* $\alpha\beta$ *for digram* $\alpha\gamma$ *and vice-versa.*

The main difference between a context and a generalized context transformation is that we can swap any digram for any digram, hence we are no more restricted on cases when one of digrams is not present in a message. Examples of transformations are presented in Figure 1.

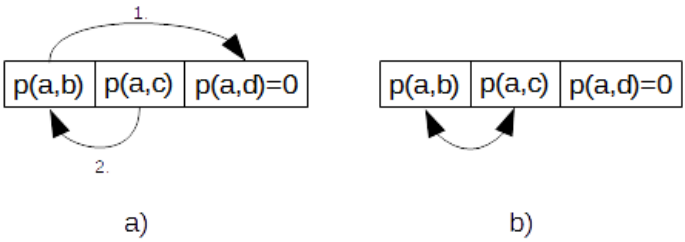

Fig. 1. Examples of two different types of transformations, $p(b) > p(c) > p(d)$, $p(a,c) > p(a,b)$, $p(b,c) > p(a,b)$: a) Sequence of context transformations $ab \rightarrow ad, ac \rightarrow ab$ and b) Generalized context transformation $ab \leftrightarrow ac$

3 Entropy Reduction Theorem

We use transformations to reduce uncertainty in data, this uncertainty is measured by Shannon's entropy[1] defined in equation (1). When we use a term entropy in this paper, we always mean the Shannon's entropy of alphabet's probability distribution.

$$H(X) = -\sum_{x \in \Sigma} p(x) \log p(x) \tag{1}$$

When $GCT(\alpha\beta \leftrightarrow \alpha\gamma, w)$ is applied on the input w, some probability flow Δp between the two letters β and γ will happen. Suppose that $p_0(x)$ is the probability of letter x before the transformation is performed and $p_1(x)$ after the transformation is performed.

The flow differs in two cases, let's consider the transformation $GCT(\alpha\beta \leftrightarrow \alpha\gamma, w)$ where $\alpha \neq \beta \neq \gamma$, then the resulted flow between the two letters β and γ is equal to $\Delta p = |p(\alpha,\beta) - p(\alpha,\gamma)|$. Corresponding probabilities after transformation are:

$$p_1(\beta) = p_0(\beta) - p_0(\alpha,\beta) + p_0(\alpha,\gamma) \tag{2}$$

and

$$p_1(\gamma) = p_0(\gamma) - p_0(\alpha,\gamma) + p_0(\alpha,\beta) \tag{3}$$

In the second case when the transformation $GCT(\alpha\alpha \leftrightarrow \alpha\beta, w)$ is considered, then the flow will not depend only on the probabilities of digrams, but we also must compute all n-grams of the form $\alpha\beta^m$, because such string would transform to $\alpha^m\beta$ and this change cannot be derived using only digrams distribution. In the algorithm design we approximate the second case using the first one, because to count all mentioned n-grams would not be computationally efficient.

No other letter has its probability changed, so the change in entropy is taken only between these two letters. Let H_0 is the entropy before the transformation is applied and let H_1 is the entropy after the transformation is applied, then we can express the change of entropy ΔH as:

$$\Delta H = H_1 - H_0 \tag{4}$$

If we use the fact that only two letters have their probability changed then we can rewrite the equation (4) into the detailed form of equation (5) that is used to evaluate transformations:

$$\Delta H = \sum_{x \in \{\beta\gamma\}} p_0(x) \log(p_0(x)) - \sum_{x \in \{\beta\gamma\}} p_1(x) \log(p_1(x)) \tag{5}$$

If ΔH is negative then the transformation reduces entropy of the message. The entropy reduction is precisely described in the following theorem.

Theorem 1. *Suppose the generalized context transformation* $GCT(\alpha\beta \leftrightarrow \alpha\gamma)$. *Let* $p_0(\beta)$ *and* $p_0(\gamma)$ *are probabilities of letters before the transformation is applied and let* $p_{0,max} = max\{p_0(\beta), p_0(\gamma)\}$. *After the transformation, the associated probabilities are* $p_1(\beta)$, $p_1(\gamma)$ *and* $p_{1,max} = max\{p_1(\beta), p_1(\gamma)\}$. *If* $p_{1,max} > p_{0,max}$ *then the generalized context transformation* T *reduces entropy.*

The proof of theorem (1) is based on properties of entropy when only two letters from alphabet Σ are considered. Let $p(\beta) + p(\gamma) = c$, where $c \leq 1$, c is invariant, it does not change during the transformation. We can express one of these probabilities using the other one, for example let $p(\gamma) = c - p(\beta)$, this allows us to express the entropy function as a function of only one variable. A few examples of such functions are shown in Figure 2. The maximum value of the function is located in the value $c/2$ and it has two minimums at 0 and at c.

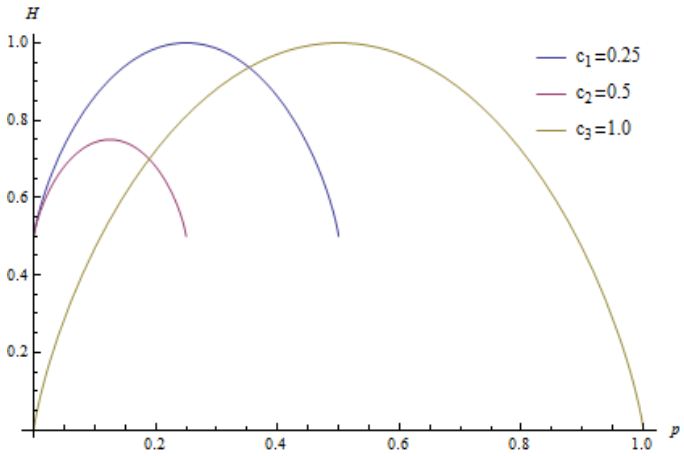

Fig. 2. The entropy of two letters with different $c_i \in \{0.25, 0.5, 1.0\}$.

Proof. Since the entropy function for two different letters is defined on the interval $\langle 0; c\rangle$ and it is concave with maximum at $c/2$ and minimum at 0 and c, then $p_{0,max}$ has to be located on the interval $p_{0,max} \in \langle c/2; c\rangle$, but on that particular interval the higher the maximum is the lower the entropy is, so if we increase the maximum(or we can say increase the absolute value of difference $|p_\beta - p_\alpha|$), then the entropy will decrease.

4 Parallel transformations

In [5] we made an observation that for several groups of transformations, the transformed data are of the same form no matter of the order in which they were applied. Such transformations can be applied simultaneously.

Before we show how to work with parallel transformations, we introduce two sets, an abstract set D_i and set K_i, that will be later used to present a lemma about parallel transformations:

Definition 3. *Let D_i be a set of all unique digrams that are modified(created or destroyed) by transformation $T_i(\alpha\beta \leftrightarrow \alpha\gamma)$ and let the set K_i be a set of all transformation digrams $K_i = \{\alpha\beta, \alpha\gamma\}$.*

The set D_i contains digrams $\alpha\beta$, $\alpha\gamma$ and all digrams of type βX and γX, where $X \in \Sigma$. Suppose two sets D_1 and D_2 and let $D_1 \cap D_2 \neq \emptyset$, these two sets share at least one common digram d, suppose that $d \in K_1 \cup K_2$, it means that transformations T_1 and T_2 will interfere on this particular digram i.e. when transformation T_1 modifies digram $\alpha\beta$ on $\alpha\gamma$ then the second transformation won't be able to modify digram $\alpha\beta$ as it would do in the case when there is no other transformation T_1. From the above reasoning we form a lemma about parallel transformations:

Lemma 1. *Two transformations T_1 and T_2 can be run in parallel if:*

$$D_1 \cap D_2 = \emptyset \tag{6}$$

For the proof of the Lemma 1 see [5], in the mentioned paper there are also described some other properties of the set of parallel transformations, for instance, the maximum size of the set of parallel transformations is $M = \lfloor \frac{|\Sigma|}{2} \rfloor$.

5 Results and Discussion

GCT significantly increases efficiency of entropy reduction. Table 1 provides overview of attained results over Calgary corpus. When parallel transformations are applied, we can speedup the process of digrams exchange almost linearly with the number of available processes with only a little increase of entropy in comparison with serial algorithms.

Table 1. Entropy and mutual information comparison for CT and GCT algorithms - Calgary Corpus.

File	H_0	I_0	H-I	H_{ct}	H_{gct}	I_1
bib	5.201	1.836	3.365	4,45	4.152	0.184
book1	4.527	0.943	3.584	4,43	3.945	0.069
news	5.189	1.097	4.092	4.75	4.480	0.089
obj1	5.948	2.484	3.464	—	5.070	1.127
obj2	6.260	2.390	3.870	—	4.846	0.247
paper1	4.983	1.337	3.646	4.52	4.197	0.218
paper2	4.601	1.079	3.522	4.18	3.981	0.162
pic	1.210	0.386	0.824	—	1.074	0.201
progl	4.770	1.558	3.212	4.10	3.823	0.164
progp	4.868	1.681	3.187	4.14	3.862	0.251
trans	5.532	2.177	3.355	—	4.216	0.210

6 Conclusion and future works

In the present paper, we summarized main improvements in the theory of context transformations, that allowed us to significantly improve entropy reduction, meanwhile parallel version of algorithm successfuly improved speed of application of individual transformations. The main focus of a future work will be to describe a theory that governs transformations of higher order contexts.

Generalized context transformation and entropy reduction theorem were introduced at Data Compression Conference(core: A*) 2015 in Salt Lake City, USA. The parallel version of algorithms were later introduced at Dateso workshop taken in Czech Republic.

7 Acknowledgment

This work was supported by the SGS in VSB - Technical University of Ostrava, Czech Republic, under the grant No. SP2015/146.

References

1. Shannon, Claude E., *A mathematical theory of communication* Bell System Technical Journal, vol. 27, pp. 379-423 and 623-656, 1948.
2. Vašinek, Michal, *Kontextové mapy a jejich aplikace* Master Thesis, VŠB - Technical University of Ostrava, 2013
3. Vašinek, Michal and Platoš, Jan, *Entropy reduction using context transformations* Data Compression Conference(DCC), pp. 431-431, 2014
4. Vašinek, Michal and Platoš, Jan, *Generalized Context Transformations - Enhanced Entropy Reduction* Data Compression Conference(DCC), pp. 474-474, 2015
5. Vašinek, Michal and Platoš, Jan, *Parallel Approach to Context Transformations* Proceedings of the Dateso 2015 Annual International Workshop on Databases, Texts, Specifications and Objects, pp. 40-51, 2015

Evolution Algorithms and Cryptography Based on Chaotic Systems

Filip Zatloukal

Department of Computer Science, FEECS,
VŠB – Technical University of Ostrava, 17. listopadu 15, 708 33 Ostrava – Poruba
filip.zatloukal@vsb.cz

Abstract. Systems based on deterministic chaos exhibits very different deviations, if even small changes are made in initial conditions. This feature can be very interesting on cryptography field. On the other hand, evolutionary algorithms are robust in searching and solving complex optimization problems. It's possible to use them in cryptography also.

This contribution gives comprehensive overview of methods used in cryptography based systems and shows experiment, how successful evolutionary algorithms can be in decryption of messages encrypted by chaotic systems.

Keywords: deterministic chaos, chaos cryptography, evolutionary algorithms

1 Cryptography Based on Chaotic Systems

Cryptographic methods can be dividing to symmetric and asymmetric. Symmetric cryptography use single key to both encryption and decryption, asymmetric use public key to encryption and private key to decryption. These asymmetric methods are based on problems of computational complexity theory. The core of the methods is complexity of mathematic problems, which are impossible to be solved in polynomial time.

Chaotic systems are based on complex rules of the chaotic environment, which can produce many pseudo-random values. Values can be used in different way to encrypt/decrypt messages, images or other content.

1.1 Non-linear dynamic systems

Dynamic system is the system, where changes are dependent on time. Dynamic systems can be deterministic or stochastic. Because process of ciphering transform plain text to cipher text and when is needed, it must be transformed back to plain text, there must exist known and exact decrypting way. If the process has been made in stochastic system, it would be possible to describe it only by statistical methods. That's the reason, why document focus on deterministic systems - because it's possible to describe actual and previous state of the systems. Deterministic state is based on previous state in every situation.

© M. Krátký, J. Dvorský, P. Moravec (Eds.): WOFEX 2015, pp. 430–435.
VŠB – Technical University of Ostrava, FEECS, 2015, ISBN 978-80-248-3787-1.

A nonlinear system is a system whose time evolution equations are nonlinear; this is, the dynamical variables describing the properties of the system appear in the equations in a nonlinear form [1].

1.2 Chaos theory and deterministic chaos

Chaotic behavior can be observed in nature, biology, economy, societies, etc. Chaotic systems have important characteristic: they are able to produce various complex data and patterns. If they are converted to mathematical values, they can generate a large number of various data.

Deterministic chaos isn't random phenomenon, but it's feature of even simply system, without random built-in mechanism, to behave highly unpredictably and messy. If all initial conditions are repeated in further observation, behavior of system will be exact same.

To use chaos system in cryptography, these conditions must be met [2]:

- Chaotic system must be deterministic nonlinear dynamical system
- Chaotic system must be highly sensitive on initial conditions. Even small change in one state of the input variable can result in large differences in later stat - this is also known as "butterfly effect" (author E. N. Lorenz).
- Topological transitivity
- Density of periodic orbits

1.3 Chaos based encryption techniques

CATEGORY	METHOD	DESCRIPTION	
Analog cryptosystems	Additive chaos masking	A chaotic signal is added to the message.	
	Chaotic shift keying	A digital message signal switches among different chaotic systems to be added to the message.	
	Chaotic modulation	A message signal is used to change the parameters or the phase space of the chaotic transmitter.	
	Chaotic control	A message signal is ciphered in a classical way and used to perturbate the chaotic system.	
Digital cryptosystems	Stream ciphers	Chaotic PRNG	A chaotic signal generates a pseudo-random sequence (keystream) to XORed the message.
		Chaotic inverse system approach	A message signal is added to the output of the chaotic signal, which has been feeded by the ciphered message signal in

			previous instants.
	Block ciphers	Backwards iterative	A block of a clear message is ciphered using of inverse chaotic systems.
		Forwards iterative	A block of ciphered message is obtained by pseudo-random permutations obtained from a chaotic system.
		S-Boxes	An S-Box is created from the chaotic system. There can be dynamic or static S-Boxes.
	Miscellaneous	Searching based chaotic ciphers	A table of characters is generated from a based chaotic chaotic system. The table is used to cipher the characters of the message text.
		Cell. Automata	The chaotic system is a Cellular Automata.

Table 1. Techniques used in cryptography based on deterministic chaos [3].

1.4 Chaotic maps

Chaotic maps are representation of dynamical systems, that show chaotic behavior. Maps can be parameterized by a discrete or a continuous time.

Lorenz system.

Lorenz system [4] is 3D dynamic deterministic system derivate from atmospheric flows. Mathematically it's defined by the three ordinary differential equations known as the Lorenz equations:

$$\begin{aligned} \frac{dx}{dt} &= \sigma(y - x) \\ \frac{dy}{dt} &= x(\rho - z) - y \\ \frac{dz}{dt} &= xy - \beta z \end{aligned} \tag{1}$$

σ is defined as Prandtl number, ρ is defined as Rayleigh number, β is geometric factor, t represents the time and x, y, z demonstrate actual system state.

Clifford attractors.

Attractor can be defined in both 2D and 3D:

$$\begin{aligned} x_{n+1} &= sin(ay_n) + ccos(ax_n) \\ y_{n+1} &= sin(bx_n) + dcos(by_n) \end{aligned} \tag{2}$$

$$\begin{aligned} x_{n+1} &= sin(ay_n) + ccos(ax_n) \\ y_{n+1} &= sin(bx_n) + dcos(by_n) \\ z_{n+1} &= sin(ey_n) + fcos(ez_n) \end{aligned} \tag{3}$$

a, b, c, d, e, f are variables that define each attractor.

Others.

Baker Map, Horseshoe Map, Cat Map and others defines transform operations and they can be used to image transformation and encryption. There are many more maps, but it's out of the article scope.

1.5 Chaos based cryptography in practice

Chaos cryptography realized in analog circuits are mainly based on synchronization technique, chaos cryptography in digital circuits doesn't dependent on synchronization.

Chaos synchronization technique.

The drive subsystem is used to generate a chaotic signal to which the plain message is added, the resulting signal will be sent to the receiver. On the receiver side the signal is used as input for the response subsystem, and the output of this subsystem is subtracted from the received signal. The result will be the decrypted message. [5]

Encryption.

There are many methods of encryption (mixing models, encryption key generation from chaos schema, transformation by chaotic map, …) - specific encryption algorithm depend on selected method (see Table 1. where methods are described).

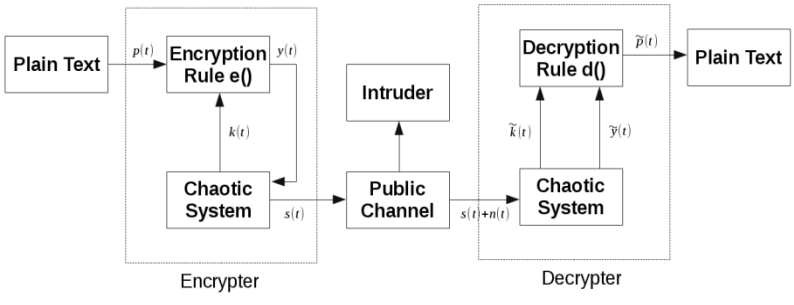

Fig. 1. Block diagram of the chaotic cryptosystem [5].

Experiment of decrypting by evolutionary algorithms will be shown in the last chapter. Process of encryption is based on Clifford attractor described by following schema:

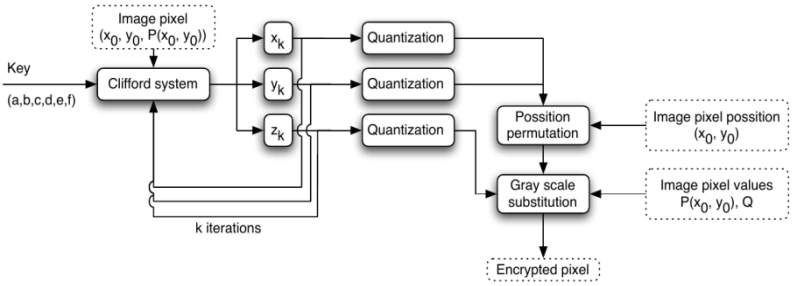

Fig. 2. Process of encryption based on Clifford attractor [6].

2 Evolutionary algorithms

Opposed to deterministic chaos, evolution algorithms work with stochastic searching (belongs to heuristics algorithms). They work with population, which is modified and improve their attributes. An evolutionary algorithm prefers genotypes with the highest "fitness" ranking obtained in many generations.

2.1 Decrypting by evolutionary algorithms

Chapter shows experiment and results of decrypting image by evolution algorithms. Image has been encrypted by Clifford attractor. Aim of the experiment was to check, whether evolutionary algorithms are able to identify "key" (control parameter) of chaotic system, which was used to encrypt information.

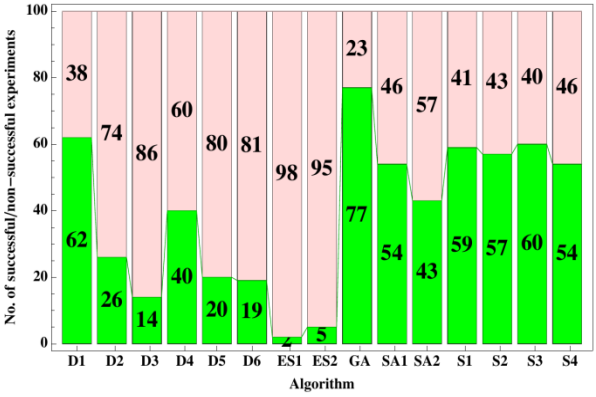

Fig. 3. No. of successful/no-successful decryption from total 100 experiments based on 15 versions of EA [6].

These algorithms were used to find key: differential evolution, self-organizing migrating algorithm, genetic algorithm, simulated annealing and evolutionary strategies in total of 15 versions [6].

It's very important to mention, that two very strong simplifications has been used:

- Only one parameter (of total 6) has been estimated
- By restriction of testing computer - numerical precision has been reduced

3 Conclusion

Due to simplifications, searching made by evolutionary algorithms has been restricted to tiny region. Results shows, that an evolutionary algorithms are able to be used on cryptography field and exhibit good results, but it's still impossible to decrypt messages encrypted by strong chaos based system by present computing capacity.

4 Future work

Research will continue with different maps, evolutionary algorithms, variables, hardware and others. Mixing with steganography methods will be tested also.

References

1. Hilborn, Robert C.: Chaos and Nonlinear Dynamics: An Introduction for Scientists and Engineers. New York: Oxford University Press, 1994.
2. Devaney, Robert L.: An Introduction to Chaotic Dynamical Systems. 2nd ed. Boulder, Colo.: Westview Press, 2003.
3. Pellicer-Lostao C., López-Ruiz R.: Notions of Chaotic Cryptography: Sketch of a Chaos Based Cryptosystem. INTECH Open Access Publisher, 2012.
4. Lorenz, Edward N.: Deterministic Nonperiodic Flow, Journal of Atmospheric Sciences, vol. 20, Issue 2, pp.130-148.
5. Tao Yang, Wu C.W., Chua L.O.: Cryptography based on chaotic systems, IEEE, 2002.
6. Zelinka I., Celikovský S., Richter H., Chen G.: Evolutionary Algorithms and Chaotic Systems. Berlin: Springer-Verlag, 2010.

Path Integral Monte Carlo Methods

Rajko Ćosić

Department of Applied Mathematics, FEECS,
VŠB – Technical University of Ostrava, 17. listopadu 15, 708 33 Ostrava – Poruba
rajko.cosic@vsb.cz

Abstract. Main topic of the present paper is path-integral Monte Carlo method applied on charged helium clusters. In the first section the motivation is briefly discussed. The second section briefly describes the core of the path integral Monte Carlo approach, the famous quantum to classical mapping. The implementation is mentioned in the third section and the results of the calculations are discussed in the fourth section. The last section sums up the work which is planned to be done in the future, either computational and programming goals.

Keywords: quantum systems, path-integral Monte Carlo, charged helium clusters

1 Motivation

In the scope of atoms and molecules there are effects which cause that the behaviour of some systems of particles can't be properly described by classical physics. In such cases we need to use quantum mechanical description. Clusters of helium or other rare-gas atoms which are studied within our group exhibit such quantum behaviour. Understanding of behaviour of these quantum systems is very important for further study of cold plasma (which is a very popular topic for its various applications in medicine [1]), behaviour of other particles (where the helium clusters are often used as the inert environment [2]) and many other phenomena.

2 Methodology

In this section we briefly introduce the famous quantum to classical system mapping which is the main idea of the path integral Monte Carlo (PIMC) method. This mapping was introduced in [3].

To describe the quantum system one needs the so-called *state sum*. This state sum is defined as

$$Z = \mathrm{Tr}\left(\mathrm{e}^{-\frac{\hat{H}}{k_B T}}\right), \tag{1}$$

where k_B is the Boltzmann constant, T is the temperature and self-adjoint operator $\hat{H} : X \to X$ is so-called *Hamiltonian operator*.

© M. Krátký, J. Dvorský, P. Moravec (Eds.): WOFEX 2015, pp. 436–441.
VŠB – Technical University of Ostrava, FEECS, 2015, ISBN 978-80-248-3787-1.

Although $X = L^2$ is separable infinite dimensional space and the matrix representation of $\hat{H}$ exists, it is not possible to do the eigendecomposition of the operator which is needed to get the desired trace. The main idea of the quantum to classical system mapping is to exploit the fact that Hamiltonian operator can be split into two parts

$$\hat{H} = \hat{T} + \hat{V}, \tag{2}$$

where $\hat{T}$ is the kinetic part of the Hamiltonian operator and $\hat{V}$ is its potential part. Then the *primitive approximation* says that for $\tau \in \mathbb{R}^+$ close to zero following approximation holds

$$\mathrm{e}^{-\tau\left(\hat{T}+\hat{V}\right)} \approx \mathrm{e}^{-\tau\hat{T}} \cdot \mathrm{e}^{-\tau\hat{V}}. \tag{3}$$

Let us for convenience denote $\frac{1}{k_B T}$ by β. The problem is that β is generally not close to zero. Here, the *Trotter formula* [4] is needed:

$$\mathrm{e}^{-\beta\left(\hat{T}+\hat{V}\right)} = \lim_{M\to\infty} \left(\mathrm{e}^{-\tau\hat{T}} \cdot \mathrm{e}^{-\tau\hat{V}}\right)^M, \tag{4}$$

where $\tau = \beta/M$ is positive and close to zero. By switching to position space representation we get

$$Z = \int \mathrm{d}R \rho\left(R, R, \beta\right), \tag{5}$$

where $\rho\left(R, R, \beta\right) = \left\langle R \left| \mathrm{e}^{-\beta\hat{H}} \right| R \right\rangle$ is so-called *density matrix*. By using the Trotter formula along with the unity decomposition on the density matrix and then approximating the kinetic and potential parts separately we get (for periodic boundary conditions on a cube) [1]

$$Z = \int \mathrm{d}R_1 \cdots \mathrm{d}R_M \, (4\pi\lambda\tau)^{-\frac{3NM}{2}} \cdot \mathrm{e}^{-\sum_{m=1}^{M}\left[\frac{(R_{m-1}-R_m)^2}{4\lambda\tau}+\tau V(R_m)\right]}. \tag{6}$$

Note that it follows from (5) that $R_0 = R_M$ must hold. This corresponds to replacing each quantum particle by the closed chain of classical particles (which are referred as *beads* or *time slices*). The beads within the chain interact via an effective potential representing the kinetic part of the energy and the adjacent time slices of different particles interact via the potential part.

3 Implementation

The many dimensional integral of (6) is computed via Monte Carlo method with *Metropolis sampling* [5], [6] . The implementation and also bottlenecks of this approach were discussed in [7]. The potential used for our calculations

[1] In the equation the constant $\frac{\hbar^2}{2m}$, where $\hbar$ is reduced Planck constant and m is the mass of the particle, is denoted by λ to follow notation stated in [3] and to avoid confusion since the letter m is used in text as sumation index.

of ionized helium clusters is based on *diatomics in molecules* (DIM) [8], [9] and is parallelized via MPI (scalability is shown and briefly discussed in the next section). There have also been implemented new features such as various boundary conditions, initial beads configurations, codes for further data analysis and many others. New methods are being developed for better convergence such as parallel-tempering method [10], [11] .

4 Calculations

The calculations were done for small charged helium clusters (He_n^+, $n \leq 10$) with the aim of computing their photoabsorption spectra. The PIMC calculations are used to compute either mean energies of the cluster and to generate the configurations of the particles. This ensemble of configurations can be later used to compute various properties of the cluster by averaging the property (e.g. energy or transition moment) over whole ensemble.

In Figure 1 one can see the mean energies of He_4^+ at temperature $T = 5$ K. Let us note that for one bead the energy level is exactly the same as it would be for classical Monte Carlo calculation at given temperature (for comparison the red solid line corresponds to the classical ground state). As the number of beads increases the energy grows which means that the quantum effects are no longer neglected. For sufficient number of beads the energy will exceed the zero vibrations level (red dotted line) and converges to the exact quantum energy of the cluster.

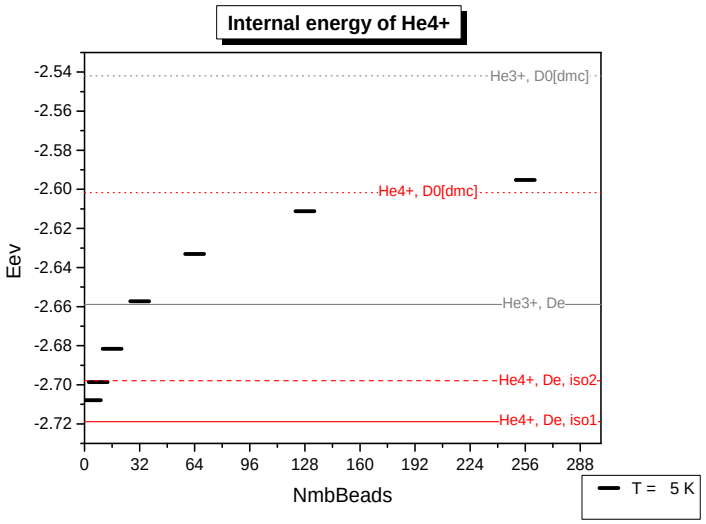

Fig. 1. The dependency of mean energy of He_4^+ on the number of beads.

For good description of the experimental data there is needed to keep system at temperature at which the energy is below the so-called *dissociation energy*. If the energy is higher the cluster will tend to split into smaller parts. In Figure 1 one can see that this is satisfied for temperature $T = 5$ K. The larger the cluster the smaller is the gap between the zero vibrations energy and the dissociation energy so the temperature has to be very low. This is very bad combination since the size of the cluster increases the computational costs but also for low temperatures a big amount of beads have to be used which also greatly influences the computational costs. For that reason some computations shown in Figure 2 were left immediately after the extrapolated energies exceeded the dissocaiation limit although they were not well converged. The dissociation gap of this cluster is between the red dashed line and the lowest grey dotted line in the picture. Now the cluster is being simulated at $T = 5$ K and $T = 2$ K.

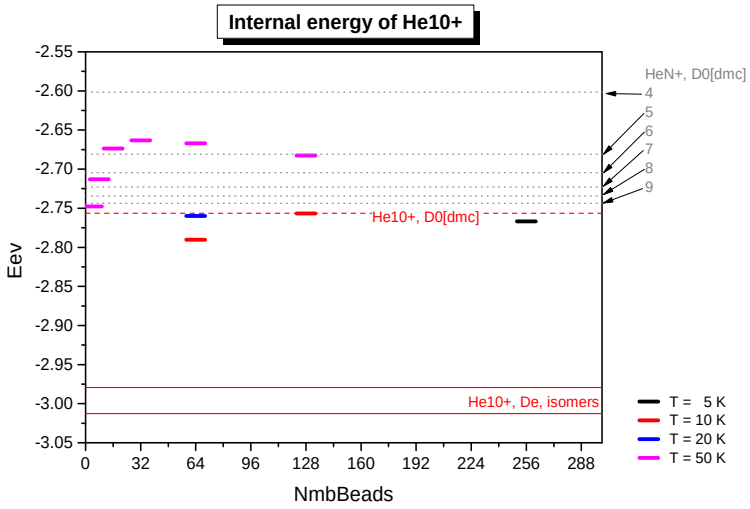

Fig. 2. The dependency of mean energy of He_{10}^{+} on the number of beads.

The scalability of PIMC method is very problematic topic since the Metropolis algorithm doesn't allow us to parallelize the sampling. The way to parallelize the PIMC computations is to exploit the independence of the time-slices and compute the potential part of energy in parallel. Figure 3 shows the scalability of He_4^+ cluster with 512 beads. The scalability is good up to 128 processors which means that each processor computes the energy of four time slices. The computational cost of DIM (which is $\mathcal{O}\left(n^3\right)$, where n is a number of particles) implies that for larger clusters the amount of work done for one time slice will be bigger and thus the parallelization will be more efficient. In Figure 4 one can see that the scalability of He_{10}^{+} is slightly better than that for He_4^+.

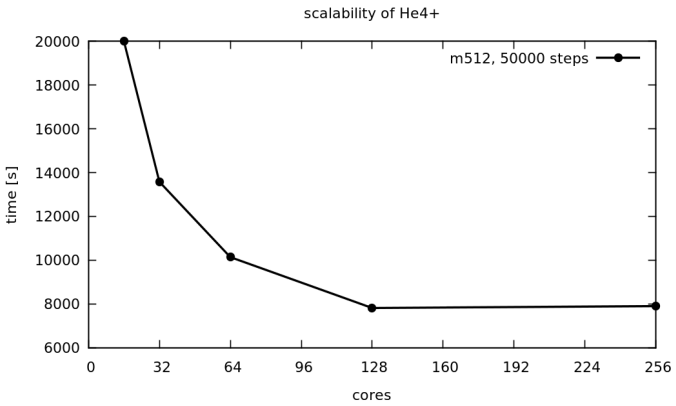

Fig. 3. The scalability of He_4^+ with 512 beads.

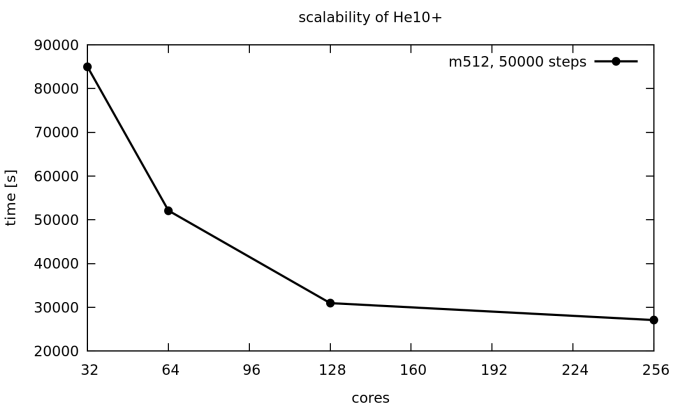

Fig. 4. The scalability of He_{10}^+ with 512 beads.

5 Outlooks

New features which are to be implemented include parallel-tempering method which will allow us to use multi-layered parallelism and to do calculations on different temperature levels at once. Moreover the swapping between these levels will improve convergence. The work on parallel-tempering routines has already begun and the preliminary version for simplified PIMC routines using pairwise Lennard-Jones potential is available. Other routines which we will focus on are routines for number-of-beads analysis, statistical analysis and better errorbar estimates.

The computational part includes the computations of photoabsorption spectra of charged helium clusters, ionisation potentials of helium clusters and simulations of the snowball structures in charged helium clusters and in helium clusters with ionic impurities.

References

1. Plewa, J., M., Yousfi, M., Frongia, C.: Low-temperature plasma-induced antiproliferative effects on multi-cellular tumor spheroids. New J. Phys. 16, (2014)
2. Yang, S., Ellis, A., M.: Helium droplets: a chemistry perspective. Chem. Soc. Rev. 42, p. 472, (2013)
3. Ceperley, D. M.: Path integrals in the theory of condensed helium. Rev. Mod. Phys. 67, (1995)
4. Trotter, H. F.: On the product of semi-groups of operators. Proc. Am. Math. Soc. 10, p. 545 (1959)
5. Metropolis, N., Rosenbluth, A., Rosenbluth, M., Teller, A., Teller, E.: Equation of state calculations by fast machines. J. Chem. Phys. 21, p. 1087, (1953)
6. Lewerenz, M.: Monte Carlo Methods: Overview and Basics. Quantum Simulations of Complex Many-Body Systems: From Theory to Algorithms, Lecture Notes, John von Neumann Institute for Computing, Julich, NIC Series, Vol. 10, ISBN 3-00-009057-6, p. 1, (2002)
7. Ćosić, R.: Mapping of a quantum system of particles onto a classical system of cyclic polymers. WOFEX 2014, p. 466, ISBN 978-80-248-3458-0, (2014)
8. Knowles, P. J., Murrell, J. M., Hodge, E., J.: An n-valued representation of He-n(+) potentials. Mol. Phys. 85, p. 243, (1995)
9. Knowles, P. J., Murrell, J. M.: The structures and stabilities of helium cluster ions. Mol. Phys. 87, p. 827, (1996)
10. Swendsen, R. H., Wang, J. S.: Replica Monte Carlo Simulation of Spin-Glasses. Phys. Rev. Lett. 57, p. 2607, (1986)
11. Geyer, C. J.: Markov-chain Monte-Carlo maximum-likelihood. in Computing Science and Statistics Proceedings of the 23rd Symposium on the Interface, American Statistical Association, p. 156, New York (1991)

Advances in fluid flow in porous medium

Martin Hasal

Department of Applied Mathematics, FEECS,
VŠB – Technical University of Ostrava, 17. listopadu 15, 708 33 Ostrava – Poruba
martin.hasal@vsb.cz

Abstract. This article summarizes the state of the art of recent research in fluid flow in porous medium. The first part of the paper aims at novel techniques in preconditioning of the saddle point system, which arises from the Stokes–Brinkman equation using the mixed finite element method. The second part describes the techniques of a posteriori error estimate for the Stokes–Brinkman model.
The third part of the article is devoted to the simulation of real experiment of bentonite behaviour in rock massive. This experiment focuses on unsaturated fluid flow in bentonite and in rock massive with respect to mechanical processes in bentonite and surrounding rock massive.

Keywords: Fluid flow, porous medium, Stokes–Brinkman equation, bentonite.

1 Introduction to Stokes–Brinkman model

The Stokes–Brinkman model simulates saturated fluid flow in porous medium with respect to cavities and fractures [14]. The Stokes–Brinkman model (1) is a single differential equation, which combines the Stokes and the Darcy's equation [14] and [4]. In this model, there can be various viscosity ν, effective visosity ν^* and K^{-1} hydraulic conductivity (we compute with $k_{ii} = \text{const.}, \forall i = 1 \dots N$ - homogeneous domain, $N = 2$). The Stokes–Brinkman model is coupled with mass conservation (incompressibility) equation (2). This coupling simulates the saturated fluid flow in porous medium with respect to fractures and cavities. It can be used in simulation of fluid flow in rocks, bio-porous matherials, soils etc. The coupled Stokes–Brinkman model is

$$\nu K^{-1}\mathbf{v} + \nabla p - \nu^* \Delta \mathbf{v} = \mathbf{f} \qquad \text{in } \Omega, \tag{1}$$

$$\nabla \cdot \mathbf{v} = 0 \qquad \text{in } \Omega, \tag{2}$$

where Ω is two-dimensional domain, together with boundary conditions on $\partial\Omega = \partial\Omega_D \cup \partial\Omega_N$ defined as

$$\mathbf{u} = \mathbf{w} \quad \text{on} \quad \partial\Omega_D, \quad \frac{\partial \mathbf{u}}{\partial n} - \mathbf{n}p = \mathbf{s} \quad \text{on} \quad \partial\Omega_N, \tag{3}$$

where $\mathbf{n}$ is the outward-pointing normal to the boundary, and $\partial\mathbf{u}/\partial n$ denotes the directional derivative in the normal direction.

© M. Krátký, J. Dvorský, P. Moravec (Eds.): WOFEX 2015, pp. 442–447.
VŠB – Technical University of Ostrava, FEECS, 2015, ISBN 978-80-248-3787-1.

2 Solving and preconditioning of saddle point system arising from Stoke–Brinkamn equation

We find that the discrete formulation (1) and (2) can be expressed as a system of linear equations

$$\begin{bmatrix} A & B^T \\ B & 0 \end{bmatrix} \begin{bmatrix} \mathbf{u} \\ \mathbf{p} \end{bmatrix} = \begin{bmatrix} \mathbf{f} \\ \mathbf{g} \end{bmatrix}. \tag{4}$$

The entries and process of creation are described at [13] and [2]. The SPD matrix $A \in \mathbb{R}^{n_u \times n_u}$ is sum of the mass and stiffness matrix. Matrix A is highly ill-conditioned and moreover it contains a jumps in coefficient of hydraulic conductivity, hence it causes slowing of iterative solvers. Matrix $B \in \mathbb{R}^{n_u \times m_p}$ is the divergence matrix. Main task it to find vectors $\mathbf{u} \in \mathbb{R}^{n_u}$ a $\mathbf{p} \in \mathbb{R}^{m_p}$ which creates **mixed finite element solution**.

This system can be solved by GMRES method [13]. The GMRES method is a iterative method and it needs a good preconditioner. There exists several methods how to preconditioning this saddle point system (4). Article [1] sugests some preconditioners for system (4), for example the first one is the HSS preconditioner. The HSS method one makes use of a Hermitian and skewsymmetric splitting of $\mathcal{A}$ for more details see [3],

$$\mathcal{A} = \mathcal{H} + \mathcal{S}$$

where $\mathcal{H} = \begin{bmatrix} A & 0 \\ 0 & 0 \end{bmatrix}$, $\mathcal{S} = \begin{bmatrix} 0 & B^T \\ -B & 0 \end{bmatrix}$.

Next type of preconditioning is a modified block triangular matrix preconditioners. Block type preconditioning for the saddle point matrix $\mathcal{A}$ can be constructed as an approximate version of the factorization

$$\mathcal{A} = \begin{bmatrix} A & B^T \\ -B & 0 \end{bmatrix} = \begin{bmatrix} A & 0 \\ -B & S \end{bmatrix} \begin{bmatrix} I & A^{-1}B^T \\ 0 & I \end{bmatrix},$$

where it is assumed that A is nonsingular and B has full rank, $S = S_A = BA^{-1}B^T$ is the Schur complement. Articles [2] and [1] also compares approximation of the inverse of block A, because computation A^{-1} as difficult as solve the original problem. For example it takes approximations D of inverse A were used. The list of used approximations inverse D is:

1. $D = \operatorname{diag}\left(A^{-1}\right)$ the approximative inverse which takes only the inverse of diagonal of original matrix A.
2. $D = D_{as} = \sum_E A_E^{-1}$, where $E = E_e \subset \Omega \subset \mathbb{R}^N$ is a union of all Taylor-Hood $(\mathbf{Q}_2 - \mathbf{Q}_1)$ elements $t \in \mathcal{T}_h$ such that $\partial t \cap \partial e$ has positive $d-1$ dimensional measure, A_E are the finite element matrices for E with zero Dirichlet conditions on $\partial E \backslash \partial \Omega$. D_{as} is therefore an additive Schwarz type approximation of A^{-1}.
3. D can be also constructed as SPD sparse approximate inverse $D = D_{ainv} = LL^T$ using the technique of Kolotilina-Yeremin, see e.g. [15]. The sparsity pattern is taken to be equal to sparsity pattern of A.

4. $D = D_{el} = \sum_e R_e^T A_e^{-1} R_e$ where $e \in \mathcal{T}_h$ and A_e is a regularized finite element matrix (regularization by $h^2 I_e$ is used for $e \in \Omega_S$.

Next type of the preconditioner is the augmented matrix type preconditioners. There are two versions of this method. Both are based on the augmented pivot block matrix, $A_W = A + B^T W^{-1} B$, in particular on $A_r = A + r B^T W^{-1} B$ when W is replaced by $\frac{1}{r} W$ and on various choices of W. The preconditioner of such type is

$$\mathcal{P} = \begin{bmatrix} A_r & \zeta B^T \\ 0 & W_r \end{bmatrix}, \quad W_r = \frac{1}{r} BDB^T. \tag{5}$$

Moreover, the system $A_r = A + r B^T (BDB^T)^{-1} B$ is solved by inner GMRES iterations with inner preconditioner $Q \sim A_r^{-1}$ based on projection,

$$Q = D - \frac{r}{r+1} B^T (BDB^T)^{-1} B \tag{6}$$

$Q = D - \frac{r}{r+1} B^T (BDB^T)^{-1} B$. The application of Q requires to solve systems with $W = BDB^T$.

Article [1] deals with preconditioner

$$\mathcal{P} = \begin{bmatrix} A & B^T \\ B & -\alpha I_* \end{bmatrix}, \tag{7}$$

where α is coefficient and I_* is the some form of the diagonal matrix. This preconditioner leads to solving SPD system $(\alpha A + B^T I_*^{-1} B)^{-1}$ ans suggest to use the method of approximative inverse for this system. Both articles citeone and citetwo contain numerical examples with example, which contains jumps in coefficients.

3 A posteriori error estimates for the steady StokesBrinkman equation in 2D

There were provided work at a posteriori error estimates for Stokes–Brinkman problem. For example in article [5] was derived theorem of a posteriori error estimate for Stokes–Brinkman problem

Theorem 1. *Let Ω be a polygon in R^2. Let $\mathcal{T}_h$ be a family of regular triangulations of Ω. Let $\{\boldsymbol{v}_h, p_h\}$ be the Hood-Taylor approximation of the solution $\{\boldsymbol{v}, p\}$ of the Stokes–Brinkman problem. Then the error $\{\boldsymbol{e}_v, e_p\}$ satisfies the following a posteriori estimate*

$$\begin{aligned} \|\mathbf{e}_v\|_1 + \|e_p\|_0 \;\le\; 2\, C_P\, C_I\, C_R \sum_{K \in \mathcal{T}_h} \Big\{ & h_K \|\mathbf{R}_1\{\mathbf{v}_h, p_h\}\|_{0,K} + \\ & + \|R_2\{\mathbf{v}_h, p_h\}\|_{0,K} + h_K^{\frac{1}{2}} \sum_{l \in \partial K} \left\| \frac{1}{2} \nu \frac{\partial \mathbf{v}_h}{\partial \mathbf{n}} - p_h \mathbf{n}_l \right\|_{0,l} \Big\} . \end{aligned} \tag{8}$$

where C_P, C_I, C_R are positive constants and $\boldsymbol{R}_1$ and $\boldsymbol{R}_2$ are the residuals from (1) and (2); and $\boldsymbol{e}_v = \boldsymbol{v} - \boldsymbol{v}_h$, $e_p = p - p_h$ where $\{\boldsymbol{v}, p\}$ is the exact solution

of weak formulation of Stokes–Brinkman equation, $\{\boldsymbol{v}_h, p_h\}$ *is the approximate solution.*

Article [6] introduced the the method of computation of a posteri error for the Stokes– Brinkman problem with numerical examples. This method can discover singularities caused by fluid flow near boundary edges and also from porous media structure.

4 Modelling of the SEALEX Experiment

In the context of radioactive waste geological disposal facilities, a key issue is related to the technical feasibility of the tunnel and shaft seals with respect to their safety functions and their expected performance level. This issue is investigated by IRSN via in situ experiments performed at representative scale, especially focused on quantifying the long-term hydraulic performance. These experiments, which are part of the SEALEX project, constitute the test case which is the object of Task A.

The generic layout of the in situ experiments (Fig. 1) consists of several components inserted in a horizontal large diameter borehole excavated in the Tournemire argillite:

1. The swelling clay core (MX80 bentonite based) is sandwiched between two porous plates (e.g. sintered steel filter or porous ceramic);
2. The upstream plate is in direct contact with host-rock while the downstream one is retained by a confining system (referred to as a confining plug) maintaining a constant volume condition;
3. A temporary venting system enhances air evacuation from the initial macrovoids (radial clearance, axial clearance, etc.) during flooding of the system;
4. Water tightness of the interface between the rock and the confining plug is achieved by a packer like device, which prevents water leaks during the whole test duration.

Regarding the test operational phases, water is first pumped into the injection chambers by means of injection lines connected to the injection chambers, which slowly saturates the clay core. At a first stage, it induces a swelling of the clay core, which closes the inner voids of the system (technological voids) and reduces the overall permeability. Then once the voids are filled, a swelling pressure develops due to the constant volume condition, which further reduces permeability. The results and methods of modelling are described at [7] and [10].

5 Conclusion

This article summarized the work provided in area of fluid flow in porous medium which was partly done by author. In section 1 were provided some information about Stokes–Brinkman equation. Section 2 shows how to solve this equation with jumps in coefficient with appropriate preconditioner. Section 3 briefly describes a posteriori error estimates. Last section 4 shows modelling of advanced experiment in nuclear waste disposal.

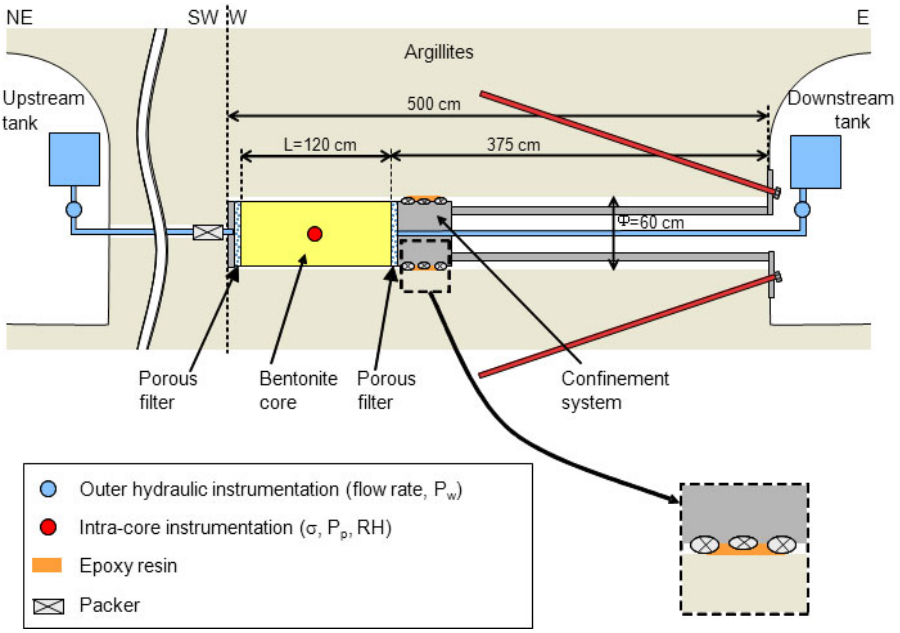

Fig. 1. Layout of the SEALEX in situ experiment

Acknowledgements This work was supported by the European Regional Development Fund in the IT4Innovations Centre of Excellence project (CZ.1.05/1.1.00/02.0070). This work is partially supported by the Science and Research Fund 2014 of the Moravia-Silesian Region, Czech Republic. SGS VŠB-TUO Grant No. SP2015/100 funded by VŠB - Technical University of Ostrava, 17. listopadu 15/2172, 708 33 Ostrava - Poruba, the Czech Republic.
Authors would like to express their special thanks to Prof. RNDr. Radim Blaheta, CSc. and Prof. RNDr. Pavel Burda, CSc. for their valuable suggestions and comments.

References - Author's publications 1-12

1. Axelsson, O., Blaheta, R., Hasal, M., *A comparison of preconditioning methods for saddle point problems with an application for porous media flow problems*, LNSC article - send.
2. Hasal, M., *Two level preconditioner of Steady StokesBrinkman Equation with Jumps in Coefficients*, ICNAAM 2015 - accepted.
3. Blaheta, R., Hasal, M., *Numerical solution of Stokes– Brinkman equation with mixed finite elements and HSS preconditioner*, SNA 15, Ostrava, 2015.
4. R. Blaheta, M. Hasal, S. Domesova, M. Beres, *RT1-code: A mixed $RT_0 - P_0$ Raviart-Thomas finite element implementation* , Report Institute of Geonics AS CR, Department IT4Innovations, software, 2014.
5. P. Burda, and M. Hasal, *An a posteriori error estimate for the Stokes-Brinkman problem in a polygonal domain*, Programs and Algorithms of Numerical Mathematics, Institute of Mathematics AS CR, 2015, pp. 3240.

6. M. Hasal, P. Burda, *Application of A Posteriori Error Estimates for the Steady StokesBrinkman Equation in 2D*, ICNAAM 2015 - accepted.
7. R. Blaheta, M. Hasal, Z.Michalec *Hydromechanical modelling with application in sealing for underground waste deposition*, ICNAAM 2014, Rhodes, Greece.
8. A.Millard, N. Mokni, J.D. Barnichon, K. Thatcher, A.Bond, A. Fraser-Harris, C. Mc Dermott, R. Blaheta, Z. Michalec, M. Hasal, T.S. Nguyen, O.Nasir, R. Fedors, *Comparative modelling of laboratory experiments for the hydromechanical behaviour of a compacted bentonite-sand mixture*, - in preparation.
9. A.Millard, N. Mokni, J.D. Barnichon, K. Thatcher, A. Bond, R. Blaheta, Z. Michalec, M. Hasal, T.S. Nguyen, O. Nasir, H. Yi, O. Kolditz, *Comparative modelling approaches of hydro-mechanical processes in sealing experiments at the-Tournemire URL*, - in preparation.
10. R. Blaheta, M. Hasal, Z.Michalec *Modelling hydro-mechanical processes for bentonite based sealing in rocks*, EUROCK 2015, - accepted.
11. M. Hasal, L. Pospisil, J. Nowakova, *Barzilai-Borwein Method in Graph Drawing Algorithm Based on Kamada-Kawai Algorithm*, ICNAAM 2015, - accepted.
12. L. Pospisil, M. Hasal, J. Nowakova, J.Platos, *Computation of Kamada-Kawai Algorithm Using Barzilai-Borwein Method*, INCOS 2015, - accepted.
13. ELMAN, H. C. - SILVESTER, D. J. - WATHEN, A. J. *Finite elements and fast iterative solvers: with applications in incompressible fluid dynamics*. Numerical Mathematics and Scientific Computation, Oxford University Press, New York, 1994.
14. P. POPOV, Y. EFENDIEV, G. QIN, *Multiscale Modeling and Simulations of Flows in Naturally Fractured Karst Reservoirs*, Global Science Preprint.
15. Axelsson, Owe, *Iterative solution methods*, Cambridge University Press, 1966.

Author's talks

Without conferences which were listed above.

1. O. Axelsson, R. Blaheta, M. Hasal, *A Comparison of Three Preconditioners for the Solution of Saddle Point Problems*, LSSC 2015, 08-12 June 2015,Sozopol, Bulgaria.
2. O. Axelsson, R. Blaheta, M. Hasal, T. Luber, *Preconditioners for Mixed FEM Solution of Stationary and Nonstationary Problems* , LSSC 2015, 08-12 June 2015,Sozopol, Bulgaria.
3. O. Axelsson, R. Blaheta, M. Hasal, Z.Michalec, *Preconditioning methods for flow around porous media*, High performance and computing 2015, 25-28 May 2015, Hotel Soláň, Czech republic.
4. R. Blaheta, M. Hasal, Z.Michalec, *DECOVALEX 2015 - Task A - Step3 - actual results*, 7^{th} Workshop & Steering Committee Meeting, 13-16 April 2015,Brno, Czech republic.
5. R. Blaheta, M. Hasal, Z.Michalec, *Modelling coupled Hydro-Mechanical processes*, 3^{rd} Annual conference of IT4Innovations, 21 October 2014,Ostrava, Czech republic.
6. R. Blaheta, M. Hasal, Z.Michalec, *Modelling coupled Hydro-Mechanical processes*, 6^{th} Workshop & Steering Committee Meeting, 10-13 November 2014, London, United Kingdom.

Risk of postoperative complications after surgeries: Laparoscopic versus open surgery

Pavel Jahoda[1], Radim Briš[1], Michal Běloch[1], and Lubomír Martínek[2]

[1]Department of Applied Mathematics, FEECS,
VŠB – Technical University of Ostrava, 17. listopadu 15, 708 33 Ostrava – Poruba
[2]University Hospital Ostrava, 17. listopadu 1790, 708 52, Ostrava-Poruba, Czech Republic {pavel.jahoda, radim.bris, michal.beloch}@vsb.cz, lubomir.martinek@fnspo.cz

Abstract. If colorectal cancer requires surgical intervention, it is performed in either laparoscopic or open way. It is desirable to choose best method for each patient. We first consider POSSUM model to estimate probabilities of occurring complications. Model is found not accurate enough so the logistic regression is used to find new parameters of POSSUM model. This new model is not accurate enough as well. Decision is made to decompose POSSUM model to its 18 core variables and try to find the ones statistically significant enough. By the means of logistic regression we isolate variables providing us the most information and base new model on them. Qualities of this model are further discussed and simple formula is provided to decide on optimal operation technique while minimizing the risk of post-operation complications.

Keywords: colorectal cancer, logistic regression, POSSUM model

1. Introduction

1.1 History of the problem

The first laparoscopic rectum resection is attributed to Patrick Leahy in November 1990, done for a carcinoma of the proximal third of rectum [1]. However, the development of the laparoscopic surgery of rectum carcinoma was markedly protracted by two facts.

© M. Krátký, J. Dvorský, P. Moravec (Eds.): WOFEX 2015, pp. 448–453.
VŠB – Technical University of Ostrava, FEECS, 2015, ISBN 978-80-248-3787-1.

The first from the above mentioned facts was the stagnation of the laparoscopic surgery of rectum in the beginning of 1990s, by reason of the anxiety about metastases appearance in ports and about the insufficient radicalism of the laparoscopic approach in colorectal malignities treatment. However, these fears abated over time.

The second fact, limiting the expansion of the laparoscopic surgery of rectum carcinoma practically even nowadays, is the demanding nature of these operations [2].

Nevertheless, with the development of advanced laparoscopic techniques and with further experience, the technical feasibility of the laparoscopic surgery of rectum has finally stopped being doubted. The attention has been increasingly focused on the short-term and long-term evaluation of laparoscopic and open surgery methods.

There has not been an agreement whether to operate the rectal carcinoma laparoscopic or open way. There are arguments equally in favour and disfavour of the use of the laparoscopic method.

Braga et al.[3] published a study comparing short-term results and costs of laparoscopic and open surgeries of rectum. This paper acknowledges a more favourable progression by patients operated the laparoscopic way.

Meta-analysis of Gao et al. [4] determines statistically significantly lower morbidity in a sample operated the laparoscopic way.

Aziz et al. [5] published a meta-analysis of short-term and long-term results comparing the laparoscopic and open surgery of patients with rectum carcinoma. They did not find any significant difference between the two groups with different operational techniques, although in the subgroup of abdominoperineal amputations there was a significantly lower occurrence of precocious infectious complications without any variance in the occurrence of these complications for the perineum wounds in the sample with the laparoscopic approach.

The study of Zhou et al. [6] proves a significantly higher morbidity of the open approach in comparison with the laparoscopic approach.

In the prospective randomized study of Ng et al. [7] comparing the laparoscopic and open amputation of rectum only, the laparoscopic approach proved the morbidity of 45.1% and the open approach proved the morbidity of 52.1%, without any significant variance.

The authors of the above mentioned studies described advantages and disadvantages of both methods. The published analyses tried to find an answer to the question, which of the methods has better results regarding the whole population. We believe in slightly different approach. We are not trying to find the best methodology in general, but rather decide on the best methodology for each patient individually. If we are able to cure the individuals better, it will show itself in the treatment results of the whole population. This approach is absolutely in compliance with the current trend in medicine, which is the individual care of a patient, the medical care "made-to-measure".

2. Creating a new model for diagnosis C20

2.1 Model generation

The failure of the above mentioned models to suitably predict postoperative complications has led us to creation of a new model using new explanatory variables. At first, we focused on the group of patients with diagnosis C20. From the total number of patients with diagnosis C20, 67 were operated using open method and 92 using laparoscopic method. With the help of statistical software STATGRAPHICS Plus 5.0, we selected from the range of 18 variables, available for each patient,[1] only the statistically significant ones (likehood ratio test, linear multi-variant discriminant analysis, χ^2 - tests of fit) as explanatory variables, requiring as high p-value as possible determined by tests of fit.

For group of patients operated laparoscopic way we isolated variables White Blood Cell – Leucocytes (L) and the Operative Severity (S) as statistically significant enough. For the group containing patients operated open way we considered variables Cardiac Signs (C) and Operative Severity (S) as statistically significant. Focusing only on these variables, we gained simple, yet very accurate (see Tables 1 and 2) models Os – POSSUM^2(l) for laparoscopic surgeries and Os – POSSUM^2(o) for open surgeries.

[1] age, cardiac signs, respiratory signs, systolic blood pressure, pulse, Glasgow coma scale, hemoglobin, white blood cell, urea, sodium, potassium, ECG, operative severity, multiple procedures, total blood loss, peritoneal soiling, cancer, mode of surgery

$$\text{Os} - \text{POSSUM}^2(l)\text{: } \Phi(\text{L,S}) = -9{,}57078 + 3{,}04722\text{L} + 0{,}89256\text{S} \quad (1)$$

$$\text{Os} - \text{POSSUM}^2\text{ (o): } \Phi(\text{C,S}) = -2{,}07602 + 0{,}46788\text{C} + 0{,}17504\text{S} \quad (2)$$

Logit interval	Number of patients	Number of complications	Predicted number of complications
$\langle -\infty; -2{,}953)$	25	1	0,790
$\langle -2{,}953; -1{,}691)$	7	1	1,089
$\langle -1{,}691; 0{,}617)$	30	19	19,233
$\langle 0{,}617, \infty)$	4	4	3,900
Total	66	25	25,012
χ^2 Goodness of fit test	$\chi^2_{OBS} = 0{,}177$	*p-value* = 0,915	

Table 1. Complications after laparoscopic surgeries predicted by the model *Os – POSSUM* ^{2}(*l*)

Logit interval	Number of patients	Number of complications	Predicted number of complications
$\langle -\infty; -0{,}908)$	25	7	6,628
$\langle -0{,}908; -0{,}440)$	20	8	7,277
$\langle -0{,}440; -0{,}208)$	13	6	5,827
$\langle -0{,}208; 0{,}260)$	19	10	10,728
$\langle 0{,}260; \infty)$	14	10	10,540
Total	91	41	41
χ^2 Goodness of fit test	$\chi^2_{OBS} = 0{,}376$	*p-value* = 0,945	

Table 2. Complications after open surgeries predicted by the model *Os – POSSUM* ^{2}(*o*)

3. Selecting optimal operational technique using the model

3.1 Choosing the optimal technique

Using the models Os – POSSUM^2(l) and Os – POSSUM^2(o), it is possible to choose an optimal operational technique for a particular patient to minimize the risk of postoperative complications. With respect to measured values of variables L, C, S, we can estimate when the probability of postoperative complications is higher after the open surgery than after the laparoscopic surgery and vice-versa. That is not difficult.

Let us denote the probability of complications after the laparoscopic surgery as π_l (L,S) (it is dependent on the values of the variables White Blood Cell – Leucocytes and the Operative Severity), and the probability of complications after the open surgery as π_o (C,S) (this depends on the values of variables Cardiac signs and the Operative Severity). We want to know for which values of L, C, S we can fulfil the following inequality:

$$\pi_l (L,S) < \pi_o (C,S) \tag{3}$$

The inequality (3) is equivalent with inequality:

$$\Phi_l (L,S) < \Phi_o (C,S) \tag{4}$$

In conjunction with relations (1) and (2), the inequality (4) holds if and only if:

$$7{,}49476 + 0{,}46788C - 3{,}04722L - 0{,}71552S > 0 \tag{5}$$

It is obvious that increasing values of Cardiac signs lead us to use of the laparoscopic method, whereas increasing values of Leucocytes and Operative severity speak on the behalf of open surgery.

References

1. Balantyne, G.H. Minimally invasive surgery for diseases of the colon and rectum: the legacy of an ancient tradition. In Jager, R.M., Wexner, S. Laparoscopic colectomy, Churchill and Livingstone, New York, 1995, p. 13-23.
2. Dulucq, J.L., P. Wintringer, C. Stabalini, & A. Mahajna. Laparoscopic rectal resection with anal sphincter preservation for rectal cancer. *Surg. Endosc.*, 2005, 19, p. 1468–1474.
3. Braga, M., M. Frasson, A. Vignali, W. Zuliani, G. Capretti, & V. Di Carlo (2007). Laparoscopic resection in rectal cancer patients: outcome and cost-benefit analysis. *Dis. Colon Rectum*, 464–471.
4. Gao, F., Y.F. Cao, & L.S. Chen (2006). Meta-analysis of short term outcomes after laparoscopic resection for rectal cancer. *Int. J. Colorectal. Dis.*, 652–656.
5. Aziz, O., V. Constantinides, & P.P. Tekkis (2006). Laparoscopic versus open surgery for rectal cancer: a metaanalysis. *Ann. Surg. Oncol.*, 413–424.
6. Zhou, Z., M. Hu, Y. Li, W. Lei, Y. Yu, Z. Cheng, L. Li, Y. Shu, & T. Wang (2004). Laparoscopic versus open total mesorectal excision with anal sphincter preservation for low rectal cancer. *Surg. Endosc.*, 1211–1215.
7. Ng, S.S., K.L. Leung, J.F. Lee, R.Y. Yiu, J.C. Li, A.Y. Teoh, & W.W. Leung (2008). Laparoscopic-assisted versus open abdominoperineal resection for low rectal cancer.: a prospective randomized study. *Ann. Surg. Oncol.*, 2418–2425.

Reconstruction of the human bones from CT images and their visualization

Milan Jaroš

Department of Applied Mathematics, FEECS,
VŠB – Technical University of Ostrava, 17. listopadu 15, 708 33 Ostrava – Poruba
IT4Innovation, VŠB – Technical University of Ostrava, 17. listopadu 15, 708 33 Ostrava – Poruba
milan.jaros@vsb.cz

Abstract. In this paper we introduce a workflow, which allows a creating 3D model of the human bones from CT images using Gaussian filter, K-means, Screened Poisson surface reconstruction and Laplacian smoothing method.

Keywords: Computed tomography · DICOM · Hounsfield Units · Gaussian blur · K-means · Poisson Surface Reconstruction · Laplacian smoothing

1 Introduction

Computed tomography (CT) is one of the particular areas of medicine which uses X-rays to create an image of human body in sequential slices. With development of this technique new directions in diagnostic medicine were found [Hsieh,Kak]. The 3D model created from CT images can be uploaded to the spine assists guidance system to create a pre-operational blueprint.

2 Data

The first step of our workflow is to obtain the measurement data stored in the DICOM format. DICOM (Digital Imaging and Communications in Medicine) is a standard for storing, displaying and distributing medical data obtained from CT, MRI or ultrasound.

In this paper we deal with medical data obtained from CT. The images from CT are stored as axial slices of a patient. The data contain images at mutual axial distance of 0.6 mm. This gives a good ability for future 3D model reconstruction. There is a problem with a noise, which is reduced by 3D Gaussian filter using the Gaussian smoothing operator.

The Gaussian smoothing operator is a convolution operator that is used to blur images to remove a noise. In this sense it is similar to the mean filter, but a different kernel is used.

The kernel is defined by formula

$$Y(t) = K(t)X(t) = \int K(t-s)X(s)ds, K(t) = \frac{1}{\sqrt{2\pi}} e^{\frac{t^2}{2}}, \tag{1}$$

© M. Krátký, J. Dvorský, P. Moravec (Eds.): WOFEX 2015, pp. 454–459.
VŠB – Technical University of Ostrava, FEECS, 2015, ISBN 978-80-248-3787-1.

where $K(t)$ is 1D Gaussian kernel, X is input signal and Y represents output signal.

Let $t = t_1, \ldots, t_n \in \mathbb{R}^n$. The Gaussian kernel for the n-dimensional space is defined by

$$K(t) = K(t_1)K(t_2)\ldots K(t_n), \tag{2}$$

in our case $n = 3$.

2.1 Hounsfield Units

Next step is to convert the original values of the pixel intensities from CT to Hounsfield Units (HU). To convert from the normal units to HU we use a linear transformation of the data, so

$$hu = pixelvalue * slope + intercept. \tag{3}$$

Values in Equation (3) are stored in the DICOM files. The tags are generally called the Rescale Slope and Rescale Intercept and usually have values 1 and -1024, respectively after converting to HU we can define the tissue type based on typical HU values. For example, the air has -1000 HU, the water has 0 HU, the liver has value from +40 to +60 HU and the bones have typically +700 HU or greater.

The last step before segmentation by k-means algorithm is the transformation of the image data. Usually the image segmentation is performed on 2D image. Here we need to segment all consecutive images in a series as one 3D image. To do this transformation from all the data has to be stored into one image vector. It means that intensity value of each pixel in an image and each image in a series are taken and are inserted into one image vector.

3 K-means clustering method

K-means clustering is method originated in signal processing and is often used in data mining [MacQueen]. Generally this method can be employed in different areas including image processing, where it can be used as image segmentation method based on clustering. This method divides n pixels into k clusters. K-means algorithm classifies pixels in an image into k number of clusters according to some similarity feature like gray level, intensity of pixels or distance of pixel intensities from centroid pixel intensity [Sonka,Dass]. An example of a 2D image segmentation is depicted in Figure 1.

This algorithm minimize the function

$$J = \sum_{j=1}^{k} \sum_{i=1}^{n} \left\| x_i^{(j)} - c_j \right\|^2, \tag{4}$$

Fig. 1. The image segmentation by k-means method (left), the flood algorithm (middle) and the founded boundaries (right).

where $\left\| x_i^{(j)} - c_j \right\|^2$ is a distance between the point $x_i^{(j)}$ and centroid c_j of the j-th segment.

The parallelization of this method by using Intel Xeon Phi was introduced in our paper [Pareng15].

4 Surface reconstruction

After recognition the individual segments we can proceed to the reconstruction of the surface. Each boundary of a segment is represented by a set of pixels, which is obtained using the flood algorithm [Flood], that determines the area connected to a given node in a multi-dimensional array. The segmented region is used as input for the 3D reconstruction using Poisson method as shown in Figure 1.

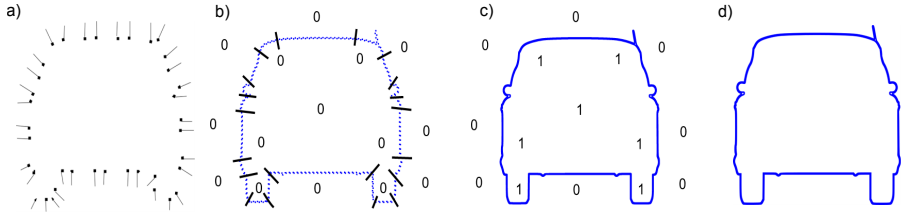

Fig. 2. The basic procedure consists of four steps: a) computation of normals $\boldsymbol{V}$, b) computation of gradient $\nabla\chi_M$, c) computation of indicator function χ_M, d) extraction of isosurface ∂M

Screened Poisson Reconstruction Surface method [Kazhdan] is not sensitive to noise, because it uses the whole set of points at once. The basic procedure consists of four steps: computation of normals $\boldsymbol{V}$, computation of gradient $\nabla\chi_M$, computation of indicator function χ_M, extraction of isosurface ∂M - see Figure 2.

The Poisson reconstruction needs the normal $n_i = (n_x, n_y, n_z)$ in each point of the boundary. The enumeration of this normal we can see on Figure 3.

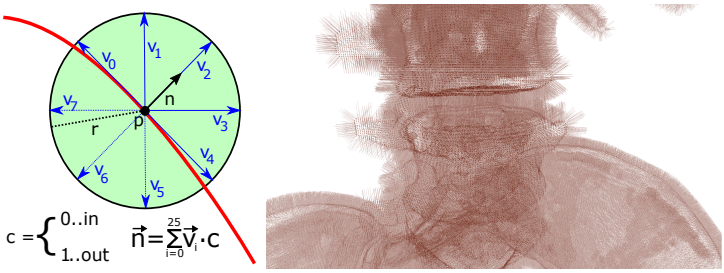

Fig. 3. The enumeration of the normal $n_i = (n_x, n_y, n_z)$ from 26× vectors v_i in each point of the boundary (left) and the results of the normals (right).

4.1 Laplacian smoothing

In the next step we use Laplacian smoothing to smooth a polygonal mesh - see Figure 4. The Laplacian algorithm [Vollmer] replaces the coordinates p_i of vertex i with the average of the coordinates of the adjacent vertices

$$p_i = \frac{1}{N} \sum_{j=1}^{N} q_{ij}, \tag{5}$$

where N is the number of adjacent vertices to node i and p_i are the new coordinates for node i.

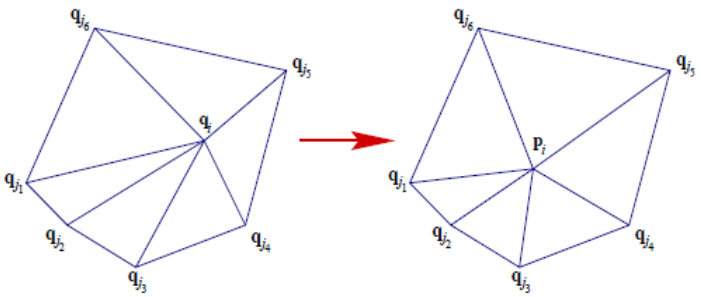

Fig. 4. Laplacian smoothing.

5 Conclusion

The resulting 3D model of the bones is shown in Figure 5. We can export the mesh to external software like Blender [Warsaw15] and generate a realistic picture - see Figure 5. The presented workflow can generate 3D model of any part of a human body from CT images, example: liver, brain, eye, lung, stomach.

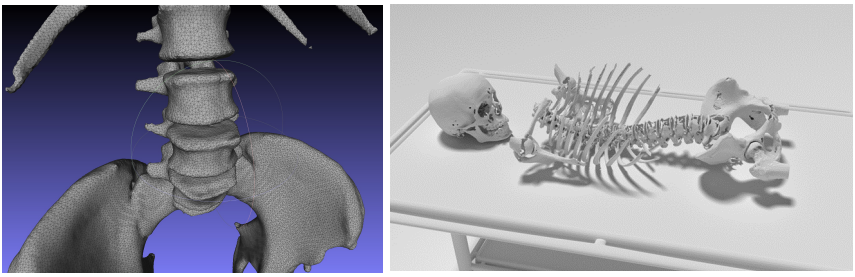

Fig. 5. The resulting 3D model of the bones.

6 Future work

We need to replace the Gaussian filter with better one (ex: BM3D filter), because this method removes all details from the original image. Our goal is to prepare an application, which can create a 3D model in real-time [Venice15]. To accelerate all these methods we develop the parallel version of the code.

Acknowledgment

This research has been elaborated in the framework of the support of VSB-TU Ostrava under the grant SGS SP2015/189. The work was also supported by the European Regional Development Fund in the IT4Innovations Centre of Excellence project (CZ.1.05/1.1.00/02.0070) and the Project of major infrastructures for research, development and innovation of Ministry of Education, Youth and Sports with reg. num. LM2011033.

References

[Pareng15] P. Strakos, M. Jaros, T. Karasek, L. Riha, M. Jarosova, T. Kozubek, P. Vavra, T. Jonszta *Parallelization of the Image Segmentation Algorithm for Intel Xeon Phi with Application in Medical Imaging*, in P. Iványi, B.H.V. Topping, (Editors), Proceedings of the Fourth International Conference on Parallel, Distributed, Grid and Cloud Computing for Engineering, Civil-Comp Press, Stirlingshire, UK, Paper 7, 2015. doi:10.4203/ccp.107.7.

[Venice15] P. Strakos, M. Jaros, T. Karasek, T. Kozubek, P. Vavra, T. Jonszta *Advanced image processing methods for automatic liver segmentation*, in B. A. Schrefler, E. Onate, M. Papadrakakis, (Editors), Proceedings of the VI International Conference on Coupled Problems in Science and Engineering, CIMNE, Barcelona, Spain, 2015, ISBN: 978-84-943928-3-2.

[Warsaw15] M. Jaros, L. Riha, T. Karasek, P. Strakos, A. Vasatova, M. Jarosova, T. Kozubek *Acceleration of Blender Cycles Path-Tracing Engine using Intel Many Integrated Core Architecture*, Proceedings of the 14th International Conference on Computer Information Systems and Industrial Management Applications, Warsaw, Poland, 2015.

[Kazhdan] Michael Kazhdan, Matthew Bolitho, Hugues Hoppe *Poisson Surface Reconstruction*. 2006.

[MacQueen] MacQueen J. B. *Some Methods for classification and Analysis of Multivariate Observations*. Proceedings of 5th Berkeley Symposium on Mathematical Statistics and Probability 1. University of California Press. pp. 281–297. MR 0214227. Zbl 0214.46201. Retrieved 2009-04-07. 1967.

[Hsieh] J. Hsieh *Computed Tomography: Principles, Design, Artifacts, and Recent Advances*, SPIE, 2002.

[Kak] A.C. Kak, M. Slaney *Principles of Computerized Tomographic Imaging*, SIAM, 2001.

[Sonka] M. Sonka, V. Hlavac, R. Boyle *Image Processing, Analysis and Machine Vision*, Thomson, 2006.

[Dass] R. Dass, Priyanka, S. Devi *Image Segmentation Techniques*, "IJECT", 3, 2230-7109, 2012.

[Vollmer] J. Vollmer *Improved Laplacian Smoothing of Noisy Surface Meshes*. 1999.

[Flood] Flood fill *http://en.wikipedia.org/wiki/Flood_fill*, 2015.

Towards parallel FEM data generation for PermonFLLOP FETI implementation

Pavla Jirůtková and Alexandros Markopoulos

Department of Applied Mathematics, FEECS,
VŠB – Technical University of Ostrava, 17. listopadu 15, 708 33 Ostrava – Poruba
{pavla.jirutkova, alexandros.markopoulos}@vsb.cz

Abstract. We describe domain decomposition method Total FETI. A special attention is paid to the kernel detection and to the description of our new heuristic approach. The first experiments and easy example are presented here. Finally, the basic information about Finite Element Method (FEM) generic libraries with two representatives (the libMesh and the FEniCS) is introduced.

1 Introduction

The FETI domain decomposition methods are ranked among efficient algorithms for a massively parallel solution of many problems of a computational mechanics. These methods are based on a divide and conquer principle. It means the original problem solved on a large domain is partitioned into a number of smaller problems defined on nonoverlapping subdomains. These subdomain problems can be solved in parallel and continuity of their solutions across interfaces is enforced via Lagrange multipliers.

In Total FETI, all subdomain stiffness matrices are singular and they have a-priori known kernels. The matrix whose columns are basis vectors of these kernels can be assembled directly from the coordinates. However this is possible only for specific academic problems and for problems with 'nice' partitioning, not for generally utilization - for example for discontinuous subdomains or for nonlinear problems. In these cases the kernel has to be generated numerically. In this paper we introduce our new approach to the kernel detection, which is still in development.

For overall efficiency a parallel FEM data generation is needed, especially for large and complicated geometries of computational bodies. The libMesh library was used for that in my diploma thesis [1], but there were some limitations. Now we focus on FEniCS software and we want to make an interface to the PermonFLLOP package [2] (a part of PERMON toolbox [3]).

2 Total FETI method

The TFETI (Total Finite Element Tearing and Interconnecting) method described by Dostál, Horák and Kučera in [4] is a variant of the FETI method

© M. Krátký, J. Dvorský, P. Moravec (Eds.): WOFEX 2015, pp. 460–465.
VŠB – Technical University of Ostrava, FEECS, 2015, ISBN 978-80-248-3787-1.

introduced by Farhat and Roux [5] in the early nineties of the last century. In both cases the domain Ω is decomposed into N non-overlapping subdomains $\Omega_i \subset \Omega$, $i = 1, \ldots, N$. The new gluing conditions are introduced on the interface between the subdomains and on the Dirichlet boundaries in TFETI method to enforce continuity of the displacements.

Let us consider the linear elasticity problem transformed using Finite Element Method (FEM) to the problem of solving system of linear equations written in form $K_g u_g = f_g$, where K_g is a global stiffness matrix and f_g is a global load vector. For all subdomains Ω_i, $i = 1, \ldots, N$ we assemble local stiffness matrices K_i and local load vectors f_i. Now we can introduce the minimization problem with constraints, so called energy formulation:

$$\min_u \frac{1}{2} u^\top K u - f^\top u \text{ subject to } Bu = c.$$

The matrix $K = diag(K_1, \ldots, K_N)$ is symmetric positive semidefinite block-diagonal singular stiffness matrix of order n, $f = (f_1, \ldots, f_N)^\top$ is a load vector of order n, $u = (u_1, \ldots, u_N)^\top$ is a solution vector of order n. The condition $Bu = c$ presents a continuity constraint, so that the matrix $B = (B_1, \ldots, B_N)$, also called the jump operator, denotes a full rank sparse constraint matrix $m \times n$ and c denotes a constraint vector of order m. These enforce the continuity of the displacements across the interface and the prescribed displacements on the Dirichlet boundary.

By introducing Lagrange multipliers λ enforcing all the constraints and the Dirichlet boundary conditions, we obtain so called dual formulation of our problem

$$\begin{cases} Ku + B^\top \lambda = f, \\ Bu = c \end{cases} \tag{1}$$

Let us gather a basis of $KerK$, i.e. the subdomains rigid body modes, in a block-diagonal matrix $R \in \mathbb{R}^{n \times l}$ (for $l = n - rank(K)$). Then the solution is given by

$$u = K^+(f - B^\top \lambda) + R\alpha, \tag{2}$$

where K^+ is a generalized inverse of K satisfying $KK^+K = K$. Now we introduce following notation:

$$F := BK^+B^\top, \;\; G := -R^\top B^\top, \;\; d := BK^+f - c, \;\; e := -R^\top f$$

and by eliminating the primal variable u in (1) we obtain

$$\begin{cases} F\lambda + G^\top \alpha = d, \\ G\lambda = e. \end{cases} \tag{3}$$

For elimination of the variable α in (3) a projector onto the $KerG$ as $P = P^\top = I - G^\top (GG^\top)^{-1} G$ is introduced. Applying P to the first equation in (3) leads to

$$PF\lambda = Pd. \tag{4}$$

In order to arrange (4) and $G\lambda = e$ as one equation on the vector space $Ker\, G$ we split the variable λ into $\lambda_{Im\, G^\top} \in Im\, G^\top$ and $\lambda_{Ker\, G} \in Ker\, G$ as $\lambda = \lambda_{Im\, G^\top} + \lambda_{Ker\, G}$. The $\lambda_{Im\, G^\top}$ can be identified easily as

$$\lambda_{Im\, G^\top} = G^\top (GG^\top)^{-1} e$$

and $\lambda_{Ker\, G}$ is computed with a conjugate gradient method from the following equation

$$PF\lambda_{Ker\, G} = P\left(d - F\lambda_{Im\, G^\top}\right).$$

Finally, if λ is known, the second unknown variable α is given by

$$\alpha = (GG^\top)^{-1} G(d - F\lambda).$$

For more information about TFETI see also [6], [7], [1].

3 Factorization and kernel detection of K

How we mentioned in the previous section, the stiffness matrix K is a symmetric positive semidefinite singular matrix. It stems from the fact that the body, which is represented by the matrix K, is not fixed yet in the space (Dirichlet boundary condition isn't applied in the matrix K). Literally it means, the body can move without elastic deformations, just like rigid body. In 3D space each body can make 6 rigid-body movements (3 rotations and 3 translations).

Because of singularity of the matrix K the generalized inverse K^+ has to be used in (2). It will cause, during the factorization (LU, LDL, Cholesky), several zero pivots will appear [8]. Total number of those zero pivots corresponds to the defect of the matrix K_i, $i = 1, \ldots, N$. The detection of zero pivots can be very difficult procedure highly depending on the solved problem (big jumps in material coefficients, irregular shape of borders between subdomains, ...). Together with rounding errors it can be very ambitious or even impossible.

In this paper we propose a heuristic technique. We try to find appropriate index sets s and r to permute original stiffness matrix K by permutation matrix Q and get the decomposition

$$QKQ^T = \begin{pmatrix} K_{r,r} & K_{r,s} \\ K_{s,r} & K_{s,s} \end{pmatrix},$$

which defines the Schur complement in the form

$$S = K_{s,s} - K_{s,r} K_{r,r}^{-1} K_{r,s}. \tag{5}$$

Let denote the set s as singular and set r as nonsingular, according to this notation the matrix $K_{r,r}$ will be non-singular and invertible matrix. The choice of sets is based on random number generator and the quality ('required properties') is handled by the dimensions of those sets. In other words we make a random

choice of the fixing nodes (every node with 3 degrees of freedom) and look at the number of bad choices (nodes lying on the same line) depending on a number of body partitions and on a number of the fixing nodes, see Table 1. The aim is to get a relatively small set s because the Schur complement (5) will be analyzed by algorithm for dense matrices.

Assume, the sets s and r are already well-chosen. The kernel of K can be derived from homogeneous system $KR = O$ itemized according to those sets

$$\begin{aligned} K_{r,r}R_r + K_{r,s}R_s &= O_r, \\ K_{s,r}R_r + K_{s,s}R_s &= O_s. \end{aligned} \tag{6}$$

From the first equation in (6) we derive $R_r = -K_{r,r}^{-1}K_{r,s}R_s$ to eliminate R_r in the second equation of (6). After that we obtain $SR_s = O$. Initial problem, the kernel detection of symmetric stiffness matrix K, was reduced to the kernel detection of the symmetric Schur complement S.

Num of partitions	**Bad cases from 100 exp.**	
in each direction	3 fix. nodes	4 fix. nodes
$2 \times 2 \times 2$	2	0
$3 \times 3 \times 3$	2	0
$4 \times 4 \times 4$	1	0
$5 \times 5 \times 5$	0	0
$6 \times 6 \times 6$	0	0
$\vdots$	$\vdots$	$\vdots$
$11 \times 11 \times 11$	0	0
$12 \times 12 \times 12$	0	0

Table 1. Numbers of bad random choices of the fixing nodes for various cube partitions.

Example

Let us consider the cube partitioned to $2 \times 2 \times 2$ elements, see Figure 1. We choose 3 nodes (9 degrees of freedom) randomly, so that these nodes haven't to lie on the same line. First we compute all possibilities, how choose 3 nodes from 3^3 nodes in the whole cube:

$$C_3(27) = \frac{27!}{3!\,24!} = 2925.$$

Now we look at all bad posibilities, i.e. selections with 3 nodes lying on one line. The example of bad choice is shown in Figure 2. We can see there are 24 lines and 12 diagonals on the surface of the cube and 3 lines and 8 diagonals inside the cube. Thus we obtain 47 bad posibilities. It remains to compute the probability of a bad choice as

$$P(BAD) = \frac{47}{2925} \doteq 0,0161 = 1,61\%.$$

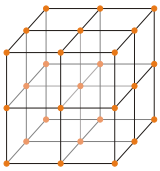

Fig. 1. The cube $2 \times 2 \times 2$.

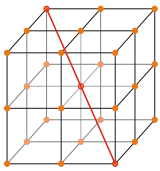

Fig. 2. The example of bad choice of fixing nodes - nodes lie on the diagonal line.

4 Generic FEM libraries

Today's exist many finite element generic softwares for the numerical simulation of partial differential equations (PDEs). However only a small number of these are well documented open-source softwares and support massive parallel computations at the same time [9]. In this section we introduce two of them, which we have used for our research.

4.1 LibMesh

The `libMesh` is an open-source software library in C++ [10] developed originally at The University of Texas at Austin in the CFDLab in March 2002. The `libMesh` library is a preprocessing tool for the numerical mesh-based simulation of PDEs on serial and parallel platforms, using the FEM. The library supports discretization of 1D, 2D and 3D steady and transient problems using various element types. The library hides parallel communication from the user, so basic MPI calls are not necessary in most applications. The `libMesh` provides interfaces to high performance existing software, such as PETSc, LASPack or SLEPc, whenever possible. More information about libMesh library is presented in [11].

The results of numerical experiments in my diploma thesis [1] showed us that the mesh generator in `libMesh` is limited by store size, the library is not scalable for the default `SerialMesh` and the `ParallelMesh` is currently still in development and so not applicable for massive parallel computations.

4.2 FEniCS

The FEniCS Project [12] is a collaborative project developed by researchers from a number of research institutes from the whole world and set out in 2003. Similar as libMesh library, the FEniCS is an open-source tool for automated, efficient solving PDEs by finite element methods, which can be programmed both in C++ and Python. Now the project consists of following components: the problem-solving environment DOLFIN, the form compiler FFC, the finite element tabulator FIAT, the just-in-time compiler Instant, the code generation interface UFC, the form language UFL and other additional components and applications. The FEniCS is a user-friendly tool, so the parallel communication

via MPI calls is hidden from the user as well as others programming difficulties. This means that the user can focus on specifications of mathematical problems and solve PDEs with FEniCS very easily. For more information look at [13].

5 Conclusion

We described the Total FETI method as an efficient method for massively parallel computations. The problem of kernel detection was introduced and our new approach was shown and illustrated on example. In the end we discussed some FEM data generation softwares.

References

[1] P. Jirůtková, Parallel input data generation in FETI methods.

[2] A. Vašatová, M. Čermák, V. Hapla in *Parallel Processing and Applied Mathematics 2015, 11th International Conference, PPAM 2015, Krakow, Poland, September 6-9, 2015. Revised Selected Papers*, **accepted 2015**.

[3] V. Hapla et al., PERMON (Parallel, Efficient, Robust, Modular, Object-oriented, Numerical) Web Pages, 2015, `http://industry.it4i.cz/en/products/permon/`.

[4] Z. Dostál, D. Horák, R. Kučera, *Communications in Numerical Methods in Engineering* **2006**, *22*, 1155–1162.

[5] C. Farhat, F.-X. Roux, *SIAM Journal on Sci. and Stat. Computing* **1992**, *13*, `http://dx.doi.org/10.1137/0913020`, 379–396.

[6] T. Kozubek, V. Vondrák, M. Menšík, D. Horák, Z. Dostál, V. Hapla, P. Kabelíková, M. Čermák, *Advances in Engineering Software* **2013**, *60-61*, 14–22.

[7] M. Čermák, V. Hapla, D. Horák, M. Merta, A. Markopoulos, *Advances in Engineering Software* **2015**, *84*, 48–54.

[8] T. Brzobohatý, Z. Dostál, T. Kozubek, P. Kovář, A. Markopoulos, *International Journal for Numerical Methods in Engineering* **2011**, *88*, 493–509.

[9] T. Heister, M. Kronbichler, W. Bangerth in *Recent Advances in the Message Passing Interface*, Springer Berlin Heidelberg, **2010**, pp. 122–131.

[10] B. S. Kirk et al., libMesh Web Pages, 2015, `http://libmesh.sourceforge.net`.

[11] B. S. Kirk, J. W. Peterson, R. H. Stogner, G. F. Carey, *Engineering with Computers* **2006**, *22*, `http://dx.doi.org/10.1007/s00366-006-0049-3`, 237–254.

[12] FEniCS Project - a collection of free software with an extensive list of features for automated, efficient solution of differential equations, 2015, `http://fenicsproject.org/` (visited on 2015).

[13] A. Logg, K.-A. Mardal, G. N. Wells, et al., *Automated Solution of Differential Equations by the Finite Element Method*, Springer, **2012**.

Optimization Techniques for Finding Approximations of Perfect Difference Sets

Michal Kravčenko

Department of Applied Mathematics, FEECS,
VŠB – Technical University of Ostrava, 17. listopadu 15, 708 33 Ostrava – Poruba
michal.kravcenko@vsb.cz

Abstract. The paper describes a possible approach to finding approximations of perfect difference sets. Those approximated sets can then be used, for example, to optimize a workload distribution of parallel matrix-vector multiplication in numerical solvers. The notion of perfect difference sets will be presented together with a new possible approach on how to obtain their approximations. Experimental results of the new technique will be presented in the form of a comparison to the previously used techniques.

Keywords: perfect difference sets, almost perfect difference sets, matrix-vector multiplication, parallelism, optimization, cyclic graph decomposition.

1 Introduction

Perfect Difference Sets are widely used in many areas, for example in error correcting codes. We, however, are also able to use them to optimize parallel implementation of matrix-vector multiplication. First, let us introduce the notion of perfect difference sets.

Definition 1. *Perfect Difference Sets*

Let $PDS_n = \{a_0, a_1, ..., a_k\}$ *be a set of residues with respect to an integer* n. PDS_n *is said to be a perfect difference set iff* $\forall x \in \{1, 2, ..., n-1\}$ *there exists exactly one pair of indices* $i, j \in \{0, 1, ..., k\}$ *such that* $(a_i - a_j)(mod\ n) = x$.

In [2] and [3] we described a method of parallel matrix-vector multiplication optimization based on complete graph decomposition into cyclic components. That is, we found a such sub-graph $H = (V \subseteq \{0, 1, ..., n-1\}, E)$ of K_n which we would rotate $n-1$ times, after which the set of those rotations would cover each edge of K_n exactly once. The connection between H and PDS_n is that H admitted to an edge weight function d such that $\forall u, v \in E(H) : d(u, v) = \min\{\{u - v, n - u + v\}(\mod n)\}$ and contained such set of vertices that $\forall x \in \{1, 2, ..., \frac{n}{2}\}, \exists!\{u, v\} : d(u, v) = x$.

© M. Krátký, J. Dvorský, P. Moravec (Eds.): WOFEX 2015, pp. 466–471.
VŠB – Technical University of Ostrava, FEECS, 2015, ISBN 978-80-248-3787-1.

It can be observed that to find such H we can use PDS_n as a set of its vertices, that's is $H = (PDS_n, E)$. Figure 1 explains the connection visually. You can see a dark green component H of K_7, where the vertices of H form a PDS_7.

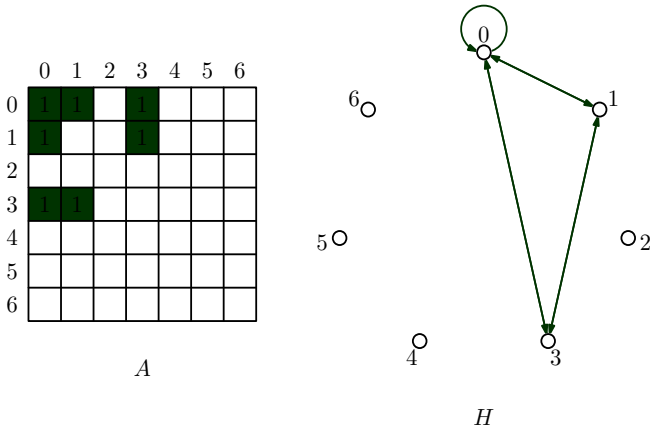

Fig. 1. Visual aid to help understand the connection between perfect difference sets and cyclic graph decomposition. The graph H on the right is a triangle sub-graph of K_7 on vertices $\{0, 1, 3\}$ which is also a PDS_7. On the left there is a corresponding adjacency matrix of H.

J. Singer showed in [1] that a necessary condition for PDS_n to exist is that $n = k^2 + k + 1$ and a sufficient condition is that such k is a power of a prime. Thus we know that for n in this form we are able to find an optimal solution, see [3].

Now that we know we can use perfect difference sets to solve our optimization problem, we can move onto more general value range of n and almost perfect difference sets.

Definition 2. *Almost Perfect Difference Sets*

Let $APDS_{k,n} = \{a_0, a_1, ..., a_k\}$ *be a set of residues with respect to an integer* n. *We will say that* $APDS_{k,n}$ *is a difference set iff* $\forall x \in \{1, 2, ..., n-1\}, \exists i, j \in \{0, 1, ..., k\} : (a_i - a_j)(mod\ n) = x$.

The difference between almost perfect difference sets and perfect difference sets is that in $APDS_{k,n}$, there can be more than one pair of indices i, j whose dif-

ference equals x. Naturally, our aim is to find a such $APDS_{k,n}$ which minimizes those redundant pairs.

Nevertheless, $APDS_{k,n}$ can also be used to induce a cyclic K_n decomposition, since in [2] we showed we are able to reduce the multiplicities in $E(H)$, as can be seen in figure 2.

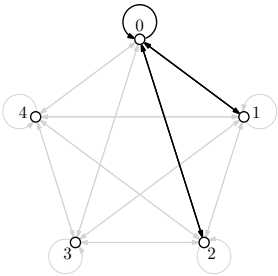

Fig. 2. This figure shows a cyclic sub-graph on 3 vertices, but not containing all the edges induced by those vertices on K_5.

2 Finding Approximations of Perfect Difference Sets

To find an optimal $APDS_{k,n}$, that is to find $APDS_{k,n}$ such that k is minimal, is for general n a difficult combinatorial task. Due to the fact that this optimization problem can be reduced to binary programming problem, it is difficult to postulate an objective function which could be used in meta-heuristic algorithms. While those meta-heuristic algorithms provided us with $\frac{3}{2}$-approximations (unproven, experimental results, see [2]) thus far, it is difficult to improve our results using those algorithms without restricting ourselves to simply investing more time in the computations.

Our new idea suitable for approximating $APDS_{k,n}$ for general cases of n is based on pruning the search tree of the algorithm in [2] using a particular set of initial partial solutions. We will denote those partial solutions by M.
Consider $n = k^2 + k + 1$ (k is a power of a prime) and a PDS_n. Now for any $M \subseteq PDS_n$ it is true that $\forall x \in \{1, 2, ..., n-1\}$ there exists at most one pair $u, v \in M$ such that $(u-v)(\text{mod } n) = x$. Furthermore lets denote the set of all such modular differences by $D(M)$, so that $D_n(M) := \{(u - v) \mod n : u, v \in M\}$.

Lemma 1. *Consider a set $M \subseteq PDS_n$ with the additional property that $\max\{|u - v| : u, v \in M\} \leq \frac{n}{2}$. Then $\forall m \geq n : |D_n(M)| = |D_m(M)|$.*

We enforced this property on M because otherwise we wouldn't be able to ensure that using M as a partial solution for problems of larger size than n would provide

us with sufficiently dense initial solutions, where by density we mean the ratio $\frac{|D_n(M)|}{|M|}$. We also assume that initial solutions of higher density will lead to final solutions of higher average density.

The important property of a such set M is that the number of differences it induces does not change with increasing m. Since it is difficult to find sufficiently dense such sets from scratch, we can use the following application of lemma 1 to find $APDS_{k,m}$:

1. We choose the highest $n < m$ such that $n = k^2 + k + 1$, where k is a power of a prime.
2. We find an arbitrary $PDS_{k+1}(\mod n)$ and in it we find a subset M of maximal cardinality with the property $\max\{|u - v| : u, v \in M\} \leq \frac{n}{2}$. M will be used as an initial solution of $APDS_{k,n}$.
3. We run the existing meta-heuristic algorithm 1 finding $APDS_{k,n}$, however the initial state of each solution will be M instead of an empty set. The algorithm 1 will then try to find a minimal $S \subseteq \{1, 2, ..., m-1\}$ such that $APDS_{k,n} = M \cup S$.

Algorithm 1 Find $APDS_{k,n}$

$iR = M$ (the initial set of vertices in H)
$c = 2$ (says we will look to expand iR on vertices v such that $v \geq c$)
D (the set of edge lengths in H induced by M)
$APDS_{k,n}$ (the final solution)
$k \in \{1, 2, \ldots, n\}$ (determines the breadth of the search for R)
$APDS_{k,n} = F(iR, c, D, \{0, 1, \ldots, n-1\}, k, n)$ with F below

procedure F(iR, c, D, R, k, n)
    if $D = \{0, 1, \ldots, \lceil \frac{n-1}{2} \rceil\}$ **then**
        if $|R| > |iR|$ **then**
            $R = iR$
        end if
        return R
    end if
    $C = \{v \in \text{argmax}\{|D \cup \{d(w, u, n) : u \in iR\}|, \forall w \in \{c, \ldots, n-1\}\}\}$
    $C_k \subseteq C$ such that C_k contains at most k lowest elements from C
    for all $m \in C_k$ **do**
        $mR = F(iR \cup \{m\}, m+1, D \cup \{d(m, u, N) : u \in iR\}, R, k, n)$
        if $|R| > |mR|$ **then**
            $R = mR$
        end if
    end for
    return R
end procedure

3 Experiments & Results

We implemented the described ideas and conducted experiments for $n \in \{7, 8, ..., 769\}$. As generators of the approximations, we used sets M described in the previous section. Figure 3 shows k, the overall number of elements in $APDS_{k,n}$ using the new method and the old method.

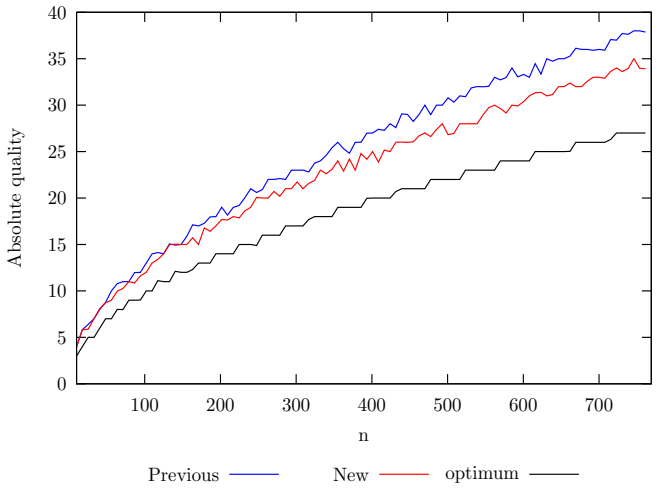

Fig. 3. The number of elements of $APDS_{k,n}$ obtained without using a generator (blue), with using a generator (red) and the lower bound (black). The lower is the red line compared to the blue line, the better the new method is.

As can be seen, the relative reduction in the number of used integers in $APDS_{k,n}$ seems to converge towards 10%.

4 Conclusion

We have presented a combinatorial optimization problem whose properties make it generally difficult to solve optimally or close to optimally. We offered a new approach on how to tackle this optimization problem using a preset generators which showed about 10% reduction in the factor we would like to minimize. To continue, we will inspect properties of those generators and conduct further experiments.

The first chapter introduced the notion of (almost) perfect difference sets and a connection to our previous work. The second chapter described the cumbersome nature of optimization techniques trying to approximate perfect difference

sets and offered an improvement on how to obtain those approximations. The algorithm was not described in detail, but the idea how to easily improve existing algorithms was presented.

The third chapter presented results of our experiments. The new optimization technique was compared to previously used one and showed 10% reduction in the size of approximated sets over the previously used technique.

References

1. Singer, J.; *A theorem in finite projective geometry and some applications to number theory,* Trans. Amer. Math. Soc., 43 (1938), pp. 377 - 385.

2. Kravčenko, M.; *Parallel Matrix-vector Multiplication, its Memory Requirements and Optimizations,* WOFEX 2014 12th annual workshop, pp. 496 - 501. ISBN 978-80-248-3458-0.

3. D. Lukáš, P. Kovář, T. Kovářová, and M. Merta; *A Parallel Fast Boundary Element Method Using Cyclic Graph Decompositions*, Numerical Algorithms (IF 1.128), accepted.

Optimization Out-degree in Planar and Simple Graphs

Matěj Krbeček, Michal Kravčenko, and Adam Silber

Department of Applied Mathematics, FEECS,
VŠB – Technical University of Ostrava, 17. listopadu 15, 708 33 Ostrava – Poruba
matej.krbecek@vsb.cz

Abstract. In this paper we address the problem of optimization of out-degree in planar and simple graphs. By "optimization" we understand the maximum out-degree will minimal.
First, we show how use this theory in praxis, further, we define basic notions, we explain a linear algorithm for planar graphs and a polynomial algorithm for simple graphs. In the last part of this paper we give a basic description of our heuristic algorithm, which we are now working on.

Key words: optimize, out-degree, planar graphs, simple graphs, polynomial algorithm, linear algorithm, heuristic algorithm.

1 Introduction

Suppose, we have some area Ω (Figure 1) and in this plane we try to solve a given math problem, by a supercomputer.

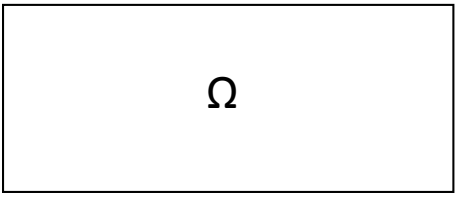

Fig. 1. Area Ω.

We do it the following way. We divide the region Ω (for example using triangulation) into sub-areas $\Omega_1, \Omega_2, \ldots, \Omega_n$, which satisfy the following conditions:

© M. Krátký, J. Dvorský, P. Moravec (Eds.): WOFEX 2015, pp. 472–477.
VŠB – Technical University of Ostrava, FEECS, 2015, ISBN 978-80-248-3787-1.

- $\bigcup_{i=1}^{n} \Omega_i = \Omega$,
- $\forall i, j : i \neq j : \Omega_i \bigcap \Omega_j = 0$,

where $i, j \in \{1, 2, \ldots, n\}$. This is shown in Figure 2.

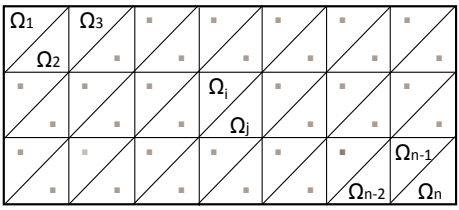

Fig. 2. The division of the area of omega Ω into sub-areas Ω_i.

Each sub-area will be processed on exactly one core of a supercomputer. This way we guarantee, that every sub-area will be processed. Because we want to solve our problem on the whole area Ω, we must process also the boundary of adjacent areas. Therefore, we must assign each border to some area, i.e for each boundary we must decide, on which core it will be processed. We want to do this assignment, so that no core will process too many boundaries.

The assignment of boundaries we want to optimize so, that the computing power is evenly divided, i.e each core will have assigned minimum number of boundaries. We can do it the following way.

First, we construct graph G of a given mesh. We divide the area of Ω into sub-areas Ω_i (Figure 2). Each sub-area will be represented by one vertex of a graph G, therefore $V(G) = \{v_1, v_2, \cdots, v_n\}$, where $v_1 = \Omega_1 \wedge v_2 = \Omega_2 \wedge \cdots \wedge v_n = \Omega_n$. Each boundary between areas will be represented by an edge, therefore $E(G) = \{e_1, e_2, \ldots, e_m\}$, where $e_i = (v_i v_j)$ and Ω_i is adjacent to Ω_j. The planar graph which was constructed this way is in Figure 3.

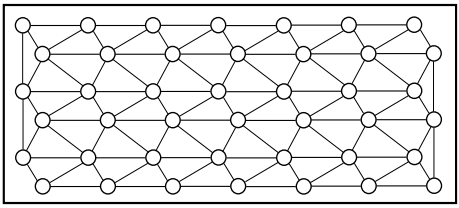

Fig. 3. Graf G.

If necessary consider mesh of a solid, we can proceed in the same way, but the final graph will not be planar. It will be a simple graph. Now we have graph, which shows adjacent regions. Next, we assign each boundary to some region by orienting the corresponding edge. If the edge is oriented from the vertex, then this edge belongs to this vertex (this core will processed this boundary).

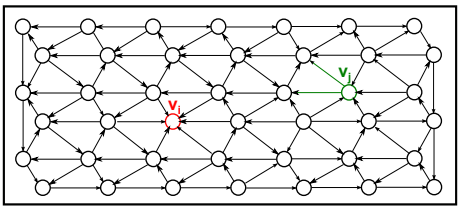

Fig. 4. Graph G with orientation of edges.

We can see on the Figure 4, that vertex v_i has no out-edge, while vertex v_j has two out-edges. Now we present an algorithm that optimizes the out-degree of planar graph [1].

2 Planar graphs

First we must define the so-called d-bounded orientation.

Definition 1. *[1] Let G be a planar graph $G = (V, E)$, let ω be it's a orientation. We say that ω is d-bounded if the condition is met:*

$$\forall v \in V(G) : deg^+_\omega(v) \leq d,$$

where $deg^+_\omega(v)$ is out-degree of vertex v.

If d is minimum, we have the optimum orientation. If we have a planar graph, then $d \leq 3$ [1] and we say ω is 3-bounded . The question is how to construct a 3-bound orientation? Now we show the main idea of construction, see [1].

We begin by defining a small vertex and a reducible vertex.

Definition 2. *A vertex $v \in V$ is small if $deg(v) \leq 18$, otherwise it is large.*

This degree of a small vertex was obtained in the proof of the existence of a reducible vertex in planar graphs. We don't present this proof here, it give in [1].

Definition 3. *[1] A vertex $v \in V$ is reducible if it satisfies one of the following conditions:*

1. *$deg(v) \leq 3$,*

2. *$deg(v) = 4$ and v has at least 2 small neighbors.*
3. *$deg(v) = 5$ and v has at least 4 small neighbors.*

In every planar graph there is at least one reducible vertex [1]. The idea of the algorithm is very simple, we find a reducible vertex and according it's the degree, we make the appropriate reduction. We continue while it is possible to reduce a graph. Then we start to return reduced edges back to the graph and orientate, them. This algorithm has two parts. First part is to reduce and the second is extension (returning the edge and orientation). The process of reduction depends on the degree of a reducible vertex. Hence we describe only the reduction of a reducible vertex with degree $deg(v) = 4$ (for $deg(v) \leq 3$ the reduction is very simple, and for $deg(v) = 5$ the reduce it more difficult, reader can see [1]).

Case $\underline{deg(v) = 4}$

– **Reduction**: Find a vertex $t_v \in N(v)$ such that $|N(t_v) \cap N(v)| \leq 2$. Remove v, and add an edge (t_v, x) for some $x \in N(v) \setminus N(t_v)$. See Figure 5.

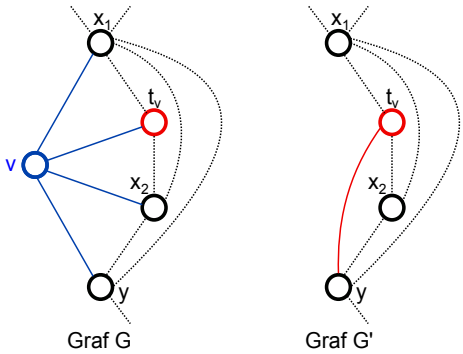

Fig. 5. Reducing a reducible vertex with degree 4.

– **Extension:** Add $v \to G$. Suppose that $\omega(t_v, x) = t_v \to x$ (the other case is symmetric). Set $\omega(t_v, v) := t_v \to v$. For all $s \in N(v) \setminus t_v$, set $\omega(s, v) := v \to s$. See Figure 6.

The next theorem tells us how fast is this algorithm .

Lemma 1. *If v is a reducible vertex, then the reduction of v and orientation ω can be made in time $O(1)$.*

Proof of this lemma is in [1]. Now we look at a case when we have a simple graph.

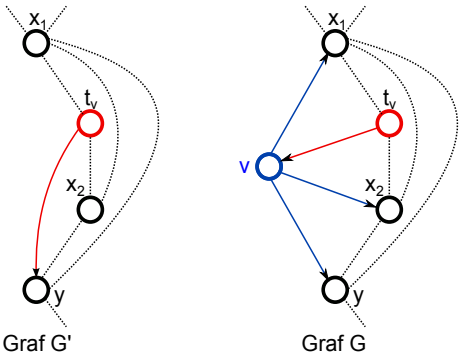

Fig. 6. Extension a reducible vertex with degree 4.

3 Simple graphs

If the mesh is of mathematical body instead of a planar model, then after the process described in the first chapter of this paper, we get a simple graph. How to optimize out-degree in a general simple graph?

In [2] an algorithm for trees with $O(n)$ complexity is described. The main idea of this algorithm is the following. We orient all edges toward a root chosen arbitrarily, which can be obviously achieved in linear time, using breadth-first search.

In [2] the algorithm "augmenting path" with $O(m^{3/2})$ speed is also described (m is the number of edges in the graph). This algorithm is more comprehensive, therefore we will give only a simple description. Input to this algorithm is a simple oriented graph $G(V, E, \omega)$. The orientation ω may be constructed arbitrarily. All we have to do is to find a "augmenting path" and reverse it. It is an oriented path in the graph, which has an initial vertex of out-degree by two greater than end-vertex (Figure 7). If you reverse the direction of this path, then the out-degree of end-vertex increases and the out-degree of start-vertex decreases. We will repeat this procedure, as long as the graph includes a "augmenting path".

We are working on a heuristic algorithm for general graphs, here we describe only the basic idea of this algorithm. This algorithm consists of three parts:

1. pre-orienting,
2. heuristic algorithm,
3. algorithm of "augmenting path".

The first part (pre-orienting) will orient edges from vertices, which have a degree smaller than our a predetermined minimum value. This value will probably be equal to half the average degree. In the second part heuristic algorithm selects the sequence of edges to be oriented depending on three conditions. These

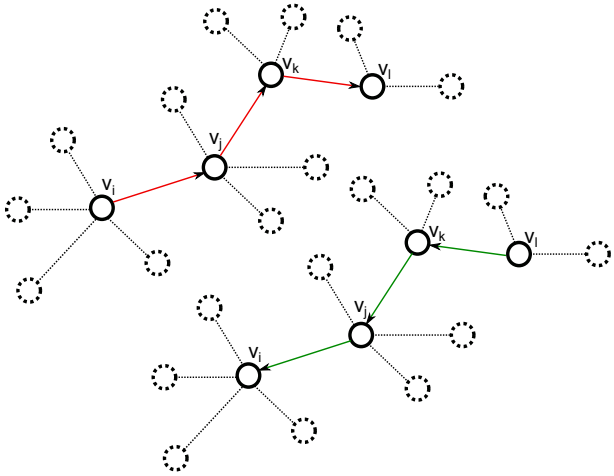

Fig. 7. "Augmenting path"(red path) and its reverse (green path).

three conditions are as follows. In each iteration we distinguish a current degree. Among vertices we choose the vertices, which have the smallest out-degree. If there are more such vertices, then select the one, which has smallest current degree and we orientate the edge from this vertex to his neighbor, which has biggest current degree among the neighbors.

Finally, if the optimum out-degree is not obtained for all vertices in graph G, then we will use the third part (algorithm of augmenting path). The last part is to use a known algorithm, described in article [2], but because we have a well preoriented graph, we believe that this last part will be faster than described in article [2].

We continue to work on this algorithm. Our goal give an algorithm, which will give an optimum out-degree. If it is not possible for every simple graph, then we want to identify a set for which it will be possible. Of course we want to make our algorithm as fastest as possible.

4 References

1. M. Chrobák, D. Eppstein. Planar orentations with Low Out-degree and Compaction of Adjacency Matrices, 1989, Theoretical Computer Science archive Volume 86 Issue 2.
2. Y. Asahiro, E. Miyano, H. Ono, K, Zenmyo. Graph Orientation Algorithms to Minimize the Maximum Outdegree, 2006, In Proc. Twelfth Computing: The Australasian Theory Symposium (CATS2006), Hobart, Australia.

Boundary Element Based Vertex Solver for Polygonal Subdomains

Lukáš Malý

Department of Applied Mathematics, FEECS,
VŠB – Technical University of Ostrava, 17. listopadu 15, 708 33 Ostrava – Poruba
lukas.maly@vsb.cz

Abstract. We present a parallel solver based on primal domain decomposition for two-dimensional elliptic partial differential equations with highly varying material coefficients. While the standard theory has been developed only for triangular or quadrilateral subdomains, where harmonic base functions are available, the practical mesh-partitioners generate complex polygonal subdomains. We aim at bridging this gap. Being inspired by [3] we generalized the method originally proposed and analyzed in [1], so that the coarse solver can treat rather general polygonal subdomains. To this goal we employ boundary element discretizations of Steklov-Poincare operators on subdomains.
Our method enjoys the parallel scalability $O((1+\log\frac{H}{h})^2\cdot\frac{n}{N})$, where h, H, n, and N denote the fine discretization parameter, coarse discretization parameter, number of DOFs, and number of processes, respectively. This is documented with numerical results. In [5] we give details of the standard analysis.
To reach maximal efficiency of presented parallel preconditioner we implemented an algorithm from the family of graph theory, stated in [2], which ensures a quasi optimal computational balance between computational processes.

1 Introduction

We consider a model problem, the Poisson equation with the homogeneous Dirichlet boundary conditions

$$\begin{aligned} -\operatorname{div}(\rho(x)\nabla u(x)) &= f(x), \quad && x\in\Omega \\ u(x) &= 0, && x\in\partial\Omega, \end{aligned}$$

where $\Omega\subset\mathbb{R}^2$ is a bounded polygonal domain, $f\in L^2(\Omega)$, and $\rho\in L^\infty(\Omega)$ is a piecewise constant positive material function.

When looking for the solution $u\in H^1_0(\Omega)$ and using classical variational framework, we obtain the weak formulation

$$\int_\Omega \rho(x)\nabla u(x)\nabla v(x)\,\mathrm{d}x = \int_\Omega fv\,\mathrm{d}x \quad \forall v\in H^1_0(\Omega).$$

Next we will solve the problem using the domain decomposition approach.

© M. Krátký, J. Dvorský, P. Moravec (Eds.): WOFEX 2015, pp. 478–483.
VŠB – Technical University of Ostrava, FEECS, 2015, ISBN 978-80-248-3787-1.

2 Primal Domain Decomposition

The domain Ω is decomposed into N nonoverlapping open, generally polygonal, subdomains Ω_i such that $\overline{\Omega} = \bigcup_{i=1}^{N} \overline{\Omega_i}$. The decomposition aligns with the jumps of the material function so that $\rho(x) = \rho_i > 0$ for x in Ω_i. We denote by $\Gamma := \bigcup_{i=1}^{M} \overline{E_i}$, the skeleton of the decomposition, where E_i is the interior of an edge apart from $\partial\Omega$.

For academic and test purpose, the decompositions depicted in Figure 1a) and 1b), i.e. the trivial triangular or quadrilateral subdomains, are commonly used. However, more relevant decomposition, which one can meet in real applications, is shown in Figure 1c). This decomposition was created by automatic mesh-partitioning generator metis [4].

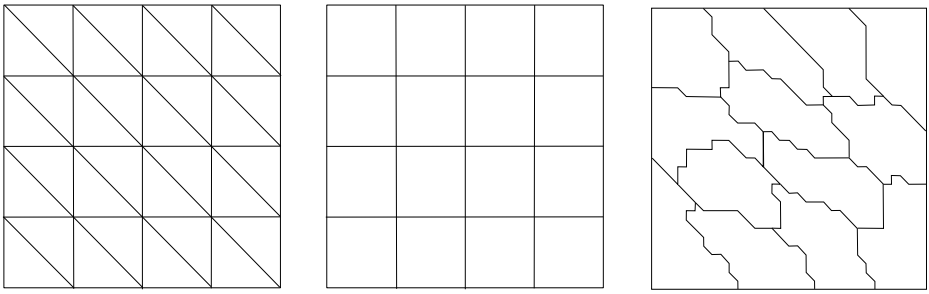

Fig. 1. Decompositions of square domain into: a) triangular subdomains, b) quadrilateral subdomains, c) general polygonal subdomains (by metis).

The related weak formulation after the decomposition reads

$$\text{find } u \in H_0^1(\Omega) : \sum_{i=1}^{N} \rho_i \int_{\Omega_i} \nabla u(x) \nabla v(x)\, \mathrm{d}x = \int_{\Omega} f(x) v(x)\, \mathrm{d}x \quad \forall v \in H_0^1(\Omega)$$

and is discretized by the classical conforming finite element method. This leads to the linear system

$$Au = b.$$

Primal domain decomposition method rely on re-sorting the linear system into parts related to subdomains interior nodes, denoted by index I, and parts related to skeleton nodes, denoted by Γ, which either belong to an edge E, or they are subdomain vertices V. This translate the linear system into the following form,

$$\begin{pmatrix} A^{II} & A^{I\Gamma} \\ A^{\Gamma I} & A^{\Gamma\Gamma} \end{pmatrix} \begin{pmatrix} u^I \\ u^\Gamma \end{pmatrix} = \begin{pmatrix} b^I \\ b^\Gamma \end{pmatrix},$$

where $I = (I_1, \ldots, I_N)$ and $\Gamma = (E, V)$ with $E = (E_1, \ldots, E_M)$ and $V = (V_1, \ldots, V_L)$. The discrete decomposition contains N subdomains, M edges and L vertices, excluding edges and vertices lying on $\partial\Omega$.

3 Schur Complement Method

To solve above system we use Schur complement method, also called a particular-solution approach, which consists of following three steps.

1. Find particular solution on subdomain interiors: $A_i^{II} v_i^I = b_i^I$.
2. Eliminate the interior unknowns on the subdomains and solve the system for skeleton unknowns: $Su^\Gamma = b^\Gamma - \sum_{i=1}^N A_i^{\Gamma I} v_i^I$, where S denotes the Schur complemet
$$S := A^{\Gamma\Gamma} - \sum_{i=1}^N A_i^{\Gamma I} \left(A_i^{II}\right)^{-1} A_i^{I\Gamma}.$$
3. Find the solution for homogenious problem with prescribed Dirichlet boundary conditions on subdomains: $A_i^{II} w_i^I = -A_i^{I\Gamma} u^\Gamma$, and set $u_i^I := v_i^I + w_i^I$.

This approach brings a few advantages. The first and the third step are independent for each subdomain, thus they can be done in parallel. In the second step, the left hand side, containing Schur complement, is a discrete version of the Steklov-Poincaré operator (Dirichlet to Neumann mapping) that allows the boundary element method [7] to be involved here.

The second step is a global operation that causes communication and is a bottleneck in domain decomposition methods. To overcome this bounds, we will introduce a suitable parallel preconditioning for Schur complement system.

4 Vertex-based preconditioner

In this section we introduce a preconditioner $\widehat{S}$ for Schur complemet matrix S. First of all we re-order the Schur complement system according to unknowns in individual edges and vertices, so we get the Schur complement matrix in the form
$$S = \begin{pmatrix} S^{EE} & S^{EV} \\ S^{VE} & S^{VV} \end{pmatrix},$$
where again $E = (E_1, \ldots, E_M)$ and $V = (V_1, \ldots, V_L)$.

Next define matrix $(R^E)^T$, a linear interpolation from vertices V into interior nodes of an associated edges E. Applying the linear interpolation on Schur complement leads to form
$$\begin{pmatrix} I & 0 \\ R^E & I \end{pmatrix} \begin{pmatrix} S^{EE} & S^{EV} \\ S^{VE} & S^{VV} \end{pmatrix} \begin{pmatrix} I & (R^E)^T \\ 0 & I \end{pmatrix} = \begin{pmatrix} S^{EE} & \widetilde{S}^{EV} \\ \widetilde{S}^{VE} & \widetilde{S}^{VV} \end{pmatrix},$$
where the block EE stays untouched, the off-diagonal blocks EV and VE are affected, and the block VV now becomes the problem matrix on the coarse mesh, given by the decomposition. We denote $A^H := \widetilde{S}^{VV}$.

The primal, so-called vertex-based preconditioner is constructed by neglecting $\widetilde{S}^{EV}$, $\widetilde{S}^{VE}$, and by omitting the off-diagonal blocks in S^{EE}, i.e.

$$\widehat{S} = \begin{pmatrix} I & 0 \\ -R^E & I \end{pmatrix} \begin{pmatrix} \overline{S}^{EE} & 0 \\ 0 & A^H \end{pmatrix} \begin{pmatrix} I & -(R^E)^T \\ 0 & I \end{pmatrix}.$$

Solving the model problem using preconditioned conjugate gradient method, an action of $\widehat{S}^{-1}$ is required. Because of the form of $\overline{S}^{EE}$, for the inverse holds

$$\widehat{S}^{-1} = \sum_{i=1}^{M} \begin{pmatrix} I \\ 0 \end{pmatrix} \left(S_{i,i}^{EE}\right)^{-1} (I, 0) + \begin{pmatrix} (R^E)^T \\ I \end{pmatrix} \left(A^H\right)^{-1} \left(R^E, I\right).$$

This form comprises solution to a global system with the coarse matrix A^H and solution to M local edge problems with matrices $S_{i,i}^{EE}$, which are local Schur complements related to the problems where two domains are connected via the edge E_i.

5 Implementation Details

Let us overview procedure of the algorithm. The implementation is highly parallel from the very beginning. To solve the model problem the algorithm starts with a mesh, that gives a definition for the domain. In applications, the mesh is decomposed into parts according to a material function. At the beginning, the mesh is further decomposed into demanded number of subdomains by automatic mesh partitioner - metis. This is done on an initial, relatively coarse, triangular mesh. After that, each process works only with its own part of mesh, which is refined onto demanded level. The global compound mesh stays conforming all the time. On the individual meshes, the boundaries are found and communicated to find out individual neighbours, thus the coarse mesh can be created.

Local matrices and vectors are assembled, including Steklov-Poincaré matrices, which serve for assembling of the global coarse matrix A^H, and are constructed using boundary element method [7]. The Schur complement matrices needed for the preconditioner are computed from the local system matrices A_i (on fine mesh) and are communicated over edges between connected subdomains, thus only one from a pair of processes will solve the problem over the common edge during an iteration process.

Finally, when everything is setted, the standard parallel conjugate gradient method with introduced parallel preconditioner is used to solve the problem.

6 Graph Theory

From the form of preconditioner inverse, stated in section 4, derives that one has to solve the edge-local problem over a pair of subdomains connected via an edge. This operation induces a communication between processes. They need to

add local contributions of edge Schur complement and one process from the pair has to solve the edge problem and share its results.

To optimize this stage of the algorithm, one has to distribute individual edges to processors/subdomains in a such way, that they will computationally balanced. Here, the graph theory comes into role. When construct dual graph to the mesh decomposition, problem of edge distribution corresponds to edge orientation in that graph. Since we are dealing only with 2-dimensional decomposition, the dual graph need to be a planar graph. For planar graphs there exist an orientation of graph edges in such a way, that for each vertex there are maximal 3 edges oriented outward. This is called 3-bounded orientation, for the theory and algorithms see [2]. Back to the original problem, the existence of a 3-bounded orientation in planar graphs ensures that all processes will solve at most 3 edge problems.

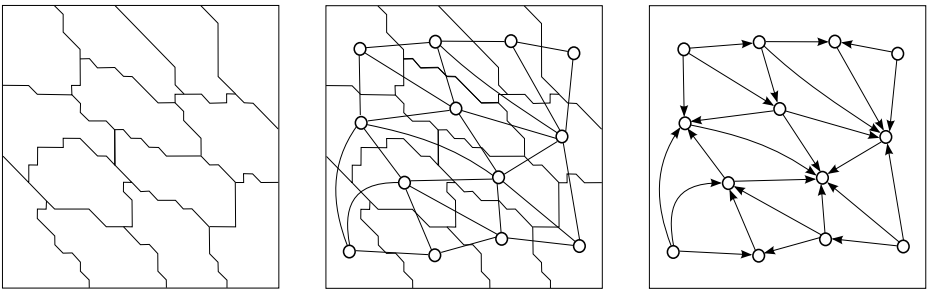

Fig. 2. a) Domain decomposition, b) respective dual graph (adjacency graph), c) oriented graph using the 3-bounded orientation algorithm.

In the Figure 2 there are depicted an original mesh decomposition and the respective dual graph. In Figure 2c) is shown a 3-bounded orientation computed by implemented algorithm according to [2]. The result does not have to be an optimal solution. However, the algorithm always finds a 3-bounded orientation. Also the pictured situation is not optimally balanced since there is a vertex which has all edges oriented inward and six vertices having 3 outward edges. By way of contrast, when the graph will be oriented based on subdomain id number, there still will be vertices lack of outward edges against the vertex with the highest id, which will have 5 of them.

7 Numerical Results

We tested the method for varied types of decompositions starting with triangular and quadrilateral subdomains, which do not require special approach to construct the coarse matrix. We also tested with L-shape subdomains and finally with general polygonal subdomains obtained by automatic mesh partitioner

metis. All the results were sufficient and confirmed the theory proposed in [5, 6]. Also problems with highly varying material coefficients across the subdomains give stable numbers of iterations. For all kind of tests we observed scalability $O((1+\log \frac{H}{h})^2 \cdot \frac{n}{N})$, where h, H, n, and N denote the fine discretization parameter, coarse discretization parameter, number of DOFs, and number of processes, respectively.

Numerical results were computed on Anselm, the supercomputer at IT4Innovations National Supercomputing Center, VSB-Technical University of Ostrava. Using this supercomputer we were able to test the algorithm for up to 2048 processors where the biggest problem has 17 millions DOFs in total and 2 hundred of thousands DOFs on boundary.

Acknowledgements

Together with the colleagues a joint paper [5] giving the theory in details for 2-dimensional primal domain decomposition has been published in the impacted Appliacations of Mathematics. Talks presented the numerical results have already been given by the author at

- the SPOMECH workshop held in Ostrava on 13/11/2013,
- the Modelling conference held in Rožnov pod Radhoštěm on 6/6/2014.

Another talk has been presented by author's supervisor Dalibor Lukáš at

- the conference DD22 held in Lugano on 16/9/2013.

The author was supported by Moravian-Silesian region under the grant 02669/2014/RRC.

References

1. Bramble, J.H., Pasciak, J.E., Schatz, A.H.: The construction of preconditioners for elliptic problems by substructuring, in Mathematics of Computation 47(175), pp. 103–134, 1986.
2. Chrobák, M., Eppstein, D.: Planar orientation with Low Out-Degree and Compaction of Adjacency Matrices, in Theoretical Computer Science, vol. 86, pp. 243–266, 1991.
3. Hofreither, C., Langer, U., Pechstein, C.: Analysis of a non-standard finite element method based on boundary integral operators, in Electronic Transactions on Numerical Analysis, pp. 413–436, 2010.
4. Karypis, G., Kumar, V.: A Fast and Highly Quality Multilevel Scheme for Partitioning Irregular Graphs, in SIAM Journal on Scientific Computing, Vol. 20, No. 1, pp. 359–392, 1999.
5. Lukáš, D., Bouchala, J., Vodstrčil, P., Malý L.: 2-Dimensional Primal Domain Decomposition Theory in Detail, in Applications of Mathematics, vol. 60, issue 3, pp. 265–283, 2015.
6. Toselli A., Widlund, O.: Domain Decomposition Methods - Algorithms and Theory, volume 34 of Springer Series in Computational Mathematics, 2005.
7. Steinbach, O., Rjasanow, S.: The Fast Solution of Boundary Integral Equations, in Springer, 2007.

Acceleration of the boundary element method

Michal Merta

Department of Applied Mathematics, FEECS,
VŠB – Technical University of Ostrava, 17. listopadu 15, 708 33 Ostrava – Poruba
michal.merta@vsb.cz

Abstract. This paper summarizes results achieved in the field of efficient parallel implementation of the boundary element method. The main focus is given on the description of a vectorization of computational kernels and their offload to Intel Xeon Phi coprocessors. Results of several basic numerical experiments are presented.

1 Introduction

The boundary element method (BEM) is generally less popular than its counterparts, such as the finite element method, mainly because of its higher demands from the implementation point of view, stemming from its quadratic complexity and necessity for nontrivial numerical quadrature. Its application to solution of large scale engineering problems is therefore a challenging task requiring combination of efficient implementation of main computational kernels, usage of matrix sparsification techniques (such as the adaptive cross approximation or the fast multipole method [1, 12, 13]) to reduce complexity to almost linear, and shared and distributed memory parallelization. Yet, since the method reduces problem to a boundary of a computational domain, it is a suitable choice for a certain set of problems, such as sound scattering on unbounded domains or shape optimization problems.

In [4, 5, 7] we presented a new approach for distribution of boundary element system matrices among computational nodes based on the cyclic graph decompositions. In [16, 9, 6] a distributed memory parallelization of the Galerkin boundary element method for the time dependent wave equation was described. In this work we focus on the acceleration of BEM using explicit vectorization and offload of computation to the Intel Xeon Phi coprocessors, which is in more details described in [10, 11].

An adaptation of scientific codes for the upcoming many core architectures is becoming increasingly important. Large number of current most powerful supercomputers, including the cluster Salomon at IT4Innovations NSC, are equipped with the Intel Xeon Phi coprocessors (MIC). The current generation of coprocessors offers up to 61 cores running on up to 1.2 GHz with four hyperthreads per core, 512-bit vector registers, and 350 GB/s memory bandwidth. A theoretical peak performance of the card is over one TFLOP/s of double precision floating point instructions and its employment can lead to a significant reduction of the computational time.

© M. Krátký, J. Dvorský, P. Moravec (Eds.): WOFEX 2015, pp. 484–489.
VŠB – Technical University of Ostrava, FEECS, 2015, ISBN 978-80-248-3787-1.

2 Discretization of the boundary integral operators

Let us only consider BEM for a solution of the Laplace equation in what follows. Similar techniques can be applied to solution of the Helmholtz or Lamé equations. See [15] for more details. Let $\{\tau_i\}_{i=1}^{N}$ be a triangulation of the boundary Γ of a computational domain Ω. We are concerned with an efficient assembly of the system matrices

$$V_h[k,l] := \frac{1}{4\pi}\int_{\tau_k}\int_{\tau_l}\frac{1}{\|x-y\|}\mathrm{d}s_y \tag{1}$$

and

$$K_h[k,l] := \frac{1}{4\pi}\int_{\tau_k}\int_{\Gamma}\frac{(x-y,n(y))}{\|x-y\|^3}\varphi_j(y)\mathrm{d}s_y \tag{2}$$

arising from the Galerkin discretization of the boundary integral equation

$$\frac{1}{4\pi}\int_{\Gamma}\frac{1}{\|x-y\|}t(y)\mathrm{d}s_y = \frac{1}{2}g(x) + \frac{1}{4\pi}\int_{\Gamma}\frac{(x-y,n(y))}{\|x-y\|^3}g(y)\mathrm{d}s_y \quad \text{for } x\in\Gamma,$$

$t \in H^{-1/2}(\Gamma)$.

To treat the singularities occuring in (1) and (2) during a numerical integration one can employ either a semi-analytic approach presented in [15] or fully numerical approach from [14]. Either way leads to a significantly more complicated code than in the case of a classical Gaussian quadrature, including numerous conditional expressions and evaluation of transcendental functions. This limits the possibilities of current compilers for automatic loop vectorization and leads to an inefficient utilization of available computational resources.

3 Explicit vectorization of computational kernels

In [10] we have provided a detailed description of application of the Vc library [3] to vectorization of the boundary element computation in our software package BEM4I [8]. The Vc library provides a high level object-oriented C++ interface to SIMD instruction set extensions, mainly SSE and AVX, thus allowing us to relatively easily modify current code to support vector computation. Since the AVX instruction set provides 256-bit vector registers, concurrent operations on eight single precision or four double precision operands are possible (see Fig. 1).

The vectorized code was tested on assembly of system matrices for the Helmholtz equation. Using vectorized version of the code we were able to achieve speed-up up to 1.81 (3.98) for semi-analytic assembly using double (single) precision arithmetics and SSE instruction set. The times of fully numerical assembly when employing AVX instructions are provided in Fig. 2.

The importance of the vectorization is even more apparent when accelerating a code using the MIC coprocessor, since the major part of its computational power stems from its 512-bit SIMD registers. This topic is briefly described in the following section.

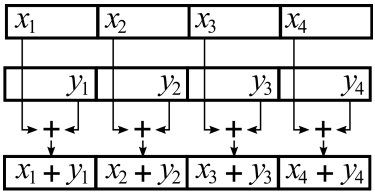

Fig. 1. Concurrent sum using SIMD instructions.

4 Offload of the computation to Intel Xeon Phi

The Intel Xeon Phi coprocessor offers several ways how to accelerate scientific code. In native mode the whole application is compiled for MIC and runs directly on the coprocessor. However, the main limitation in this case is the amount of available memory on the card (currently 8 or 16 GB). A user can also benefit from automatic offload of some MKL routines to MIC.

In our work we focus on the compiler-assisted offload model. In this case a user decides which parts of the code will be offloaded to the coprocessor using Intel's `#pragma offload target(mic)` pragmas. Inside of the offloaded code classical OpenMP pragmas can be used to distribute computation among coprocessor's 60 physical (240 logical) cores. The main bottleneck in this case is data transfer between the host and the coprocessor, as well as a dynamic memory allocation on the coprocessor.

In [11] we provide more details concerning the offload of computation of the boundary element system matrices for the Laplace equation. We offload a part of the computation of a system matrix to the coprocessor while the host processor continues the assembly of its part (see Fig. 3). When the computation on MIC is finished, the data are transfered to the host. Finally, the data from the coprocessor and the host are combined and the computation of the system matrix is complete.

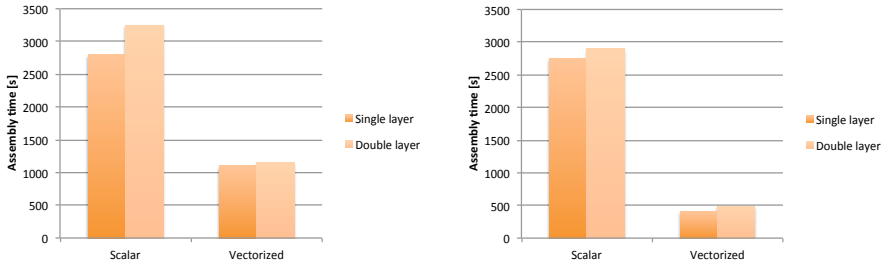

Fig. 2. Effect of vectorization on assembly of Helmholtz system matrices using fully numerical quadrature (AVX).

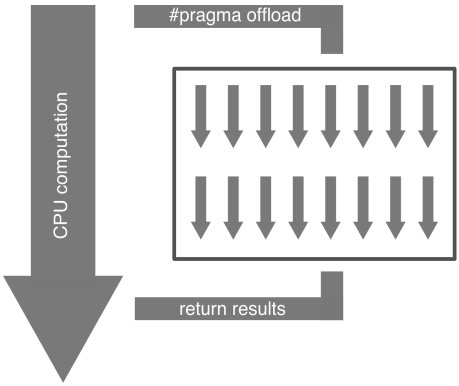

Fig. 3. Offload of computation to the coprocessor.

Times of assembly of the single layer matrix for the Laplace equation in double precision arithmetic are depicted in Fig. 4. Using the MIC acceleration we were able to achieve a speedup of 1.7. The main bottleneck is the data transfer from the coprocessor to host contributing more than 40 % to the total computational time.

5 Conclusion

We have presented an overview of our current research in the field of acceleration of the boundary element method using explicit vectorization and the Intel Xeon Phi coprocessors. The future work includes, e.g., the applications of MICs to accelerate the computation of system matrices for the Helmholtz or Lamé equations, or employment of the coprocessors to accelerate the adaptive cross approximation method.

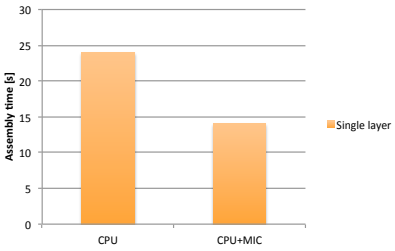

Fig. 4. Assembly times with/without acceleration on MIC.

Author's Publications

The author's results in the field of the boundary element method are listed in publications [2, 4, 9–11, 16].

Awards

The author has been awarded the 2015 Joseph Fourier Prize by Bull, s.r.o. / ATOS IT Solutions and Services, s.r.o. and the Embassy of France in Prague.

Acknowledgements

This work was supported by the IT4Innovations Centre of Excellence project (CZ.1.05/1.1.00/02.0070), funded by the European Regional Development Fund and the national budget of the Czech Republic via the Research and Development for Innovations Operational Programme, as well as Czech Ministry of Education, Youth and Sports via the project Large Research, Development and Innovations Infrastructures (LM2011033).

The author acknowledges the support of VŠB-Technical University of Ostrava under the grants SGS SP2015/100 and SGS SP2015/160.

Development of the BEM4I library is a joint work with Jan Zapletal.

References

1. Bebendorf, M., Rjasanow, S. *Adaptive low-rank approximation of collocation matrices*. Computing 70, 2003.
2. Čermák, M., Merta, M., Zapletal, J. A Novel Boundary Element Library with Applications. In Simos, TE and Tsitouras, C. *Proceedings of the international conference of numerical analysis and applied mathematics 2014 (ICNAAM-2014)*. AIP Conference Proceedings 1648, 2015.
3. Kretz, M., Lindenstruth, V. *Vc: A C++ library for explicit vectorization*. Software: Practice and Experience 42, 2012.
4. Lukáš, D., Kovář, P., Kovářová, T., Merta, M.: *A parallel fast boundary element method using cyclic graph decompositions*. Numerical Algorithms. In print (2015). DOI: 10.1007/s11075-015-9974-9.
5. Merta, M. Parallel implementation of fast boundary element method. In Krátký, M., Dvorský, J., Moravec, P. *WOFEX 2013*. 2013, pp. 363–368.
6. Merta, M. Parallel solution of time dependent wave equation. In Krátký, M., Dvorský, J., Moravec, P. *WOFEX 2014*. 2014, pp. 508–513.
7. Merta, M., Lukáš, D.: Parallel implementation of fast boundary element method. In: *Seminar on Numerical Analysis*, Institute of Geonics AS CR, Ostrava, 2013, pp. 90–92.
8. Merta, M., Zapletal, J.: *BEM4I*. `http://industry.it4i.cz/en/products/bem4i/`.
9. Merta, M., Zapletal, J. Library of Parallel BEM Based Solvers for Solution of the Time-Dependent Wave Equation. In Ivanyi, P.; Topping, B. H. V. *Proceedings of the Fourth International Conference on Parallel, Distributed, Grid and Cloud Computing for Engineering*. Stirlingshire, 2015.

10. Merta, M., Zapletal, J. *Acceleration of boundary element method by explicit vectorization*. Advances in Engineering Software 86, 2015, pp. 70–79.
11. Merta, M., Zapletal, J., Jaroš, J. *Many Core Acceleration of the Boundary Element Method*. Lecture Notes in Computer Science. Submitted (2015).
12. Of, G. Fast multipole methods and applications. In Schanz, M., Steinbach, O. *Boundary Element Analysis*. Lecture Notes in Applied and Computational Mechanics 29, 2007.
13. Rokhlin, V. *Rapid solution of integral equations of classical potential theory*. Journal of Computational Physics 60, 1985.
14. Sauter, S., Schwab, C. *Boundary Element Methods*. Springer, 2010.
15. Steinbach, O., Rjasanow, S. *The Fast Solution of Boundary Integral Equations*. Springer, 2007.
16. Veit, A., Merta, M., Zapletal, J., Lukáš, D. *Efficient solution of time-domain boundary integral equations arising in sound-hard scattering*. International Journal for Numerical Methods in Engineering. Submitted (2015).

Use of the ALNS Algorithm for Solving the Probabilistic Time-Dependent Vehicle Routing Problem

Tomáš Režnar

Department of Applied Mathematics, FEECS,
VŠB – Technical University of Ostrava, 17. listopadu 15, 708 33 Ostrava – Poruba
tomas.reznar@vsb.cz

Abstract. This paper describes modification of the Adaptive Large Neighborhood Search algorithm (ALNS) for solving Probabilistic Time-Dependent Vehicle Routing Problem (PTDVRP). The PTDVRP is focused on logistic situations dealing with vehicle fleets with limited load capacity and a set of customer requirements served by these fleets with the minimum overall time of delivery for the whole request. Particular demands may be restricted by a defined time window and may have a set of probabilities of the delivery time fulfillment. The delivery time between customers or between a customer and a depot is dependent on the traveling distance, time of arrival and probability of the arrival time fulfillment for load delivery through each particular vehicle route.

Keywords: Vehicle Routing, Time-Dependent Vehicle Problem, Probability of Arrival, Adaptive Large Neighborhood Search Algorithm

1 Introduction

Vehicle Routing Problem (VRP) was first defined fifty years ago. The VRP is aimed at minimizing transportation costs, transportation time, pollution emissions and others. There are many VRP variants and formulations. Recently, the formulation of the VRP has been widened because various problems arose. The paper proposes a novel variant of VRP.

Among others, Tasa et al. [9] work with the VRP with Time-Dependent and Stochastic Travel Times. They achieved minimum arrival times and they counted the total transportation costs and service costs. The authors of [11] proposed a transportation route so that a delivery service time window can be in the middle of the normal probability distribution; it is medium-probable the vehicle visits the client there. Dynamic Vehicle Routing Problem with fuzzy time windows (DVRPFTW) was presented in [3] so that the overall size of depots, the total arrival time and the waiting time can be minimized. In paper [4], the authors optimized the departure time of every vehicle in order to minimize the duty time of each driver and fulfill driving hours regulations. The authors of [5] minimized customer waiting time, the total driving distance, covered dynamic information

© M. Krátký, J. Dvorský, P. Moravec (Eds.): WOFEX 2015, pp. 490–497.
VŠB – Technical University of Ostrava, FEECS, 2015, ISBN 978-80-248-3787-1.

both random demand and dynamic network, and they maximized the number of customers they attend to serve. Time dependent vehicle routing problem with hard time windows was used in [2] to minimize the overall time of transportation and distance from a depot. The authors also maximized the number of customers served. In paper [10], the authors introduced load-dependent VRP which considers simultaneous pick-ups and deliveries. In paper [1], the Vehicle Routing Problems with Time Windows-Probabilistic model has been developed taking an uncertainty of transportation time into account. However, the model was time-independent.

In paper [6] we proposed the PTDVRP. The PTDVRP is time-dependent vehicle routing problem, which allows defining a probability of arrival in designed time for each one customer request. Adaptive large neighborhood search algorithm, solving the vehicle routing problem with time windows, was introduced in [7]. This paper describes modification of the ALNS algorithm to solve PTDVRP.

2 Formulation of the PTDVRP

The PTDVRP is problem of serving all customers in minimal total travel times of all vehicle routes. Location, capacity demand, service time window and probability of arrival in designed time is given for each customer. Maximal capacity for each vehicle is given. Each vehicle starts and ends in the same depot. Travel times between all locations (customer locations and depot location) are given. Each travel time is dependent on time interval of vehicle departure and on requested probability of arrival in time. Each customer must be served with the requested probability or higher in designed time. On Figure 1 is example of travel time probability between two locations within a time interval of vehicle departure.

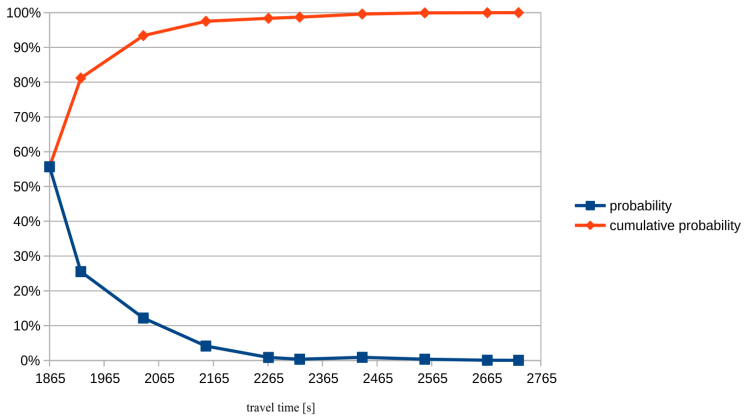

Fig. 1. Travel Time Probability and Cumulative Probability between Two Customer Locations for the PTDVRP

Mathematical formulation follows. A weighted directed multigraph $G'(V', E', w')$ is given. V' is set of nodes. E' is set of arcs. w' is step function, which assigns weight to each arc.

Node 1 represents depot, starting node for each vehicle route. Nodes $\{2, \ldots, n\}$ represent locations of customers. Nodes $\{n+1, \ldots, n+|K|\}$ represent ending nodes for each vehicle route (each vehicle ends in distinct node). K is set of all vehicles.

Weight of each arc represents travel time between two nodes in specific time interval and with specific probability that travel time will be less or equal to the weight. Set of arcs is defined as $E' = \{(i,j)_p^m : i, j \in V', p \in P, m \in M\}$, where M is set of distinct time intervals and P is set of available probabilities. From node i to node j exactly $|M| \cdot |P|$ arcs exist.

s_i is a given service duration at node $i \in V'$. T^m is upper bound for time interval $m \in M$. L_i and U_i are the earliest and the latest given arrival time at node $i \in V'$. a_i is a given probability of arrival in designed time at node $i \in V'$. d_i is a given customer demand at node $i \in V'$, b_k is a given capacity (or maximum load) of vehicle $k \in K$. B is a large number.

x_{ij}^{mp} is binary variable, if arc $(i,j)_p^m$ is traversed by any vehicle, then $x_{ij}^{mp} = 1$, otherwise $x_{ij}^{mp} = 0$. Variable t_i represents vehicle departure time from node $i \in V'$. Variable y_i is probability of arrival to node $i \in V'$ in designed time. Variable l_i represents vehicle load (in some unit, for example pieces or weight) at node $i \in V'$. For depot: $y_1 = 1$, $l_1 = 0$ and t_1 is given departure time of the all vehicles from the depot.

Objective function (1) minimizes total route times, where t_{n+k} is arrival time to the last node of the route. Constraints (2) and (3) ensure that each customer is served exactly once (exactly one inbound and one outbound traversed arc exist for each customer location). Constraint (4) allows vehicles to traverse directly from the start node to the end node. Constraint (5) computes the departure time at node j.

Constraint (6) ensures that appropriate arc for departure time t_i is chosen. Constraint (7) ensures that arrival time $t_i - s_i$ at node i is between the earliest (L_i) and the latest (U_i) given arrival time at node i. Constraint (8) ensures a probability of arrival in designed time for customer locations and a probability of return in designed time to the depot. Constraint (9) ensures that the arc with probability of arrival in design time is chosen high enough based on the probability of arrival at the antecedent node. Constraints (10) and (11) ensure that capacity of each vehicle is not exceeded. More detail description can be found in paper [6].

$$\min \sum_{k=1}^{|K|} t_{n+k} \tag{1}$$

subject to

$$\forall j \in \{2,\ldots,n+|K|\} : \sum_{\substack{i=1 \\ i\neq j}}^{n} \sum_{m\in M} \sum_{p\in P} x_{i\,j}^{m\,p} = 1 \tag{2}$$

$$\forall i \in \{2,\ldots,n\} : \sum_{\substack{j=2 \\ j\neq i}}^{n+|K|} \sum_{m\in M} \sum_{p\in P} x_{i\,j}^{m\,p} = 1 \tag{3}$$

$$\sum_{j=2}^{n+|K|} \sum_{m\in M} \sum_{p\in P} x_{1\,j}^{m\,p} = |K| \tag{4}$$

$$\forall i \in \{1,\ldots,n\}, \forall j \in \{2,\ldots,n+|K|\}, \forall m \in M, \forall p \in P :$$
$$i \neq j \implies t_j - t_i - B x_{i\,j}^{m\,p} \geq w'((i,j)_p^m) + s_j - B \tag{5}$$

$$\forall i \in \{1,\ldots,n\}, \forall j \in \{2,\ldots,n+|K|\}, \forall m \in M, \forall p \in P :$$
$$i \neq j \implies t_i + B x_{i\,j}^{m\,p} \leq T^m + B \wedge t_i - T^{m-1} x_{i\,j}^{m\,p} \geq 0 \tag{6}$$

$$\forall i \in \{1,\ldots,n+|K|\} : L_i \leq t_i - s_i \leq U_i \tag{7}$$

$$\forall i \in \{2,\ldots,n\} : y_i \geq a_i \wedge \forall i \in \{n+1,\ldots,n+|K|\} : y_i \geq a_1 \tag{8}$$

$$\forall i \in \{1,\ldots,n\}, \forall j \in \{2,\ldots,n+|K|\} :$$
$$i \neq j \implies y_i \cdot \Big(\sum_{m\in M} \sum_{p\in P} x_{j\,i}^{m\,p} \cdot p\Big) - B \sum_{m\in M} \sum_{p\in P} x_{i\,j}^{m\,p} \geq y_j - B \tag{9}$$

$$\forall i \in \{1,\ldots,n\}, \forall j \in \{2,\ldots,n+|K|\} : i \neq j \implies l_j - l_i - B \sum_{m\in M} \sum_{p\in P} x_{i\,j}^{m\,p} \geq d_j - B \tag{10}$$

$$\forall k \in \{1,\ldots,|K|\} : l_{n+k} \leq b_k \tag{11}$$

Problem Example

Following example shows an optimal solution dependency on order of nodes and probabilities of traversed arcs. Only one vehicle is available. The vehicle has capacity big enough to serve all the customers. Two customer requests are given. Both requests have zero service time duration, zero capacity demand, the earliest arrival time is zero and the latest arrival time is a big number (that means, customers may be served any time). Travel times between both customers and the depot and between the customers are time-independent and are dependent

only on the requested probabilities of arrival in designed time. The travel times are given for probabilities $0.5, 0.75$ and 1.0 and are 5, 6 and 10 minutes.

Customer locations are marked as node number 2 and 3. The depot is node 1. Given requested probabilities of arrival in designed time are 0.5 at nodes 1 and 2 and 1.0 at node 3.

In order to find an optimal solution, we need to examine two possible orders of nodes in the vehicle route. Figure 2 shows those possible orders. In both cases, the route starts at depot (node 1) and then continues in order as green or red arrows show (green and red route).

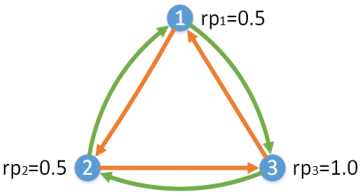

Fig. 2. Possible order of visiting nodes by single vehicle.

For each route 3^3 cases must be examined (3 nodes and between each two nodes 3 arcs exist in each direction). Each weight of arc between nodes represents travel time between those nodes. Each arc is associated with the probability of travel time (between locations represented by the adjacent nodes of the arc) less or equal to weight of the arc. Not all cases satisfy the problem constraints. Important cases are presented in Table 1. The table shows selected probability of the arcs and resulted driving times in different route variants. Probability of arrival to each node in a route is dependent on all arcs traversed by the vehicle before the vehicle visits the node and must be greater or equal to the given requested probability of the arrival in designed time to the node.

Main difference between the red and the green route is that in the red route is the node with lower given probability visited before the node with higher given probability of arrival in designed time. It leads to the selection of the arcs with higher given probabilities (which have longer travel times) to the first two nodes of the red route meanwhile in the green route, where the node with higher given probability is visited before nodes with lower given probabilities.

3 Solution Using ALNS Algorithm

The ALNS algorithm based on [7] and [8] was implemented and used for following experiment. The ALNS algorithm was chosen for its good extensibility and expected scalability. The ALNS algorithm is shown in Algorithm 1. The algorithm first finds an initial solution and then repeatedly changes current solution in order to find the optimal solution until an ending condition is met (in the example, the ending condition is predefined number of cycles). In line 6 are

Table 1. Feasible Solutions

Route color	**Arc probability**			**Driving time**
Red	**1 - 2**	**2 - 3**	**3 - 1**	
#1	1	1	0.5	25 s
Green	**1 - 3**	**3 - 2**	**2 - 1**	
#1	1	1	0.5	25 s
#2	1	0.5	1	25 s
#3	1	0.75	0.75	**22 s**

one ruin and one recreate methods from all available ruin and recreate methods selected. Ruin method removes some customers from the solution. Recreate method tries to insert all the removed customers back into the solution in better order. Ruin and recreate methods combination is adaptively selected based on its historical success (combination which found accepted solution more often has higher probability to be selected).

Ruin methods for solving the example are radial, axial and random ruin. Radial ruin removes predefined number of customer locations nearest to a random center location from a solution. Axial ruin removes string of customer locations from each vehicle route and random ruin randomly removes predefined number of customer locations.

Recreate method used for solving the example is greedy heuristic which tries to insert removed customer location to the all positions of the each vehicle route. From all the tried positions, position with the minimal cost change of the solution is selected and removed customer location is inserted into that position. During solution recreation must be followed given probabilities of arrival in designed time to customer locations. The recreate method randomly chooses travel time from travel times with high enough probability. This is repeated until all removed customer location are reinserted back to the solution.

In line 11 of the algorithm accept method decides whether current changed solution will become new current solution for next cycle of the algorithm. For solving the example the accept method which accepts every better solution was used.

Numerical Experiment

The following experiment compares travel times of the PTDVRP solutions to the TDVRP solutions. Data sets described below were solved as the PTDVRP (respecting given probabilities of arrival) and then as the TDVRP (ignoring given probabilities of arrival and using average travel times between customer locations).

Three experimental data sets were created[1]. The data sets differ in the number of customers. The first set has 10, the second set 50 and the third set 100 defined customers. Each customer was described by random location, random

[1] All sets are available at http://dataanalysis.vsb.cz/Collections/Ptdvrp

Algorithm 1 ALNS

```
1: best solution s_best := find a initial solution
2: next solution s_next := s_best
3: repeat
4:     temporary solution s_tmp := s_next
5:     (ruinMethod, recreateMethod) := select from all ruin and recreate methods
6:     ruinMethod(s_tmp)
7:     recreateMethod(s_tmp)
8:     if cost(s_tmp) < cost(s_best) then
9:         s_best := s_tmp
10:    end if
11:    if accept(s_tmp, s_next) then
12:        s_next := s_tmp
13:    end if
14: until ending condition is met
```

capacity demand, random time window for vehicle arrival and random probability of designed time arrival. Each customer has service time 300 seconds. All the sets have the same 25 vehicles available. Travel times between the nodes were generated on the basis of random customer locations, time interval and probability of arrival in designed time.

The solutions of testing sets were searched with the ALNS algorithm in 9000 cycles in each run. Table 2 shows travel times of the found solutions of the experimental data sets. Each set was run 20 times.

Table 2. Travel Times of the Found Solutions for Testing Sets

Number of Customers	Used Vehicles		Travel Time [hours]	
	PTDVRP	TDVRP	PTDVRP	TDVRP
10	3.2	1	36.4	19.2
50	15.7	3	167.0	37.0
100	24.5	6	297.1	74.4

Travel times of the TDVRP solutions are lower. It is expected result caused by higher travel times used by the PTDVRP. The PTDVRP uses travel times between customer locations based on requested probabilities of arrival in designed time. The TDVRP uses average travel times between the customer locations. Figure 1 shows an example of travel times between two customer locations for the PTDVRP. In the case of Figure 1, the PTDVRP would count with proper travel time in range from 1865 s to 2667 s, while the TDVRP would always count with 1925 s (which is average of the travel time function on figure 1) in contrast.

4 Conclusion

In this paper the ALNS algorithm was described. The ALNS algorithm was modified in order to solve the PTDVRP. In the experimental part of this paper the ALNS algorithm was used to solve the experimental testing data sets. The experimental data sets were solved as the PTDVRP and the TDVRP. Travel times of routes of the PTDVRP feasible solutions are higher than travel times of routes of the TDVRP feasible solutions, however the PTDVRP allows to ensure the probability of arrival in designed time to customer locations. In our future work we will concentrate on comparisons of the different algorithms for solving the PTDVRP.

References

1. Ando, N., and Taniguchi, E. Travel time reliability in vehicle routing and scheduling with time windows. *Netw Spat Econ 6* (2006), 293–311.
2. Figliozzi, M. A. The time dependent vehicle routing problem with time windows: Benchmark problems, an efficient solution algorithm, and solution characteristics. *Transportation Research Part E: Logistics and Transportation Review 48*, 3 (2012), 616–636.
3. Ghannadpour, S. F., Noori, S., Tavakkoli-Moghaddam, R., and Ghoseiri, K. A multi-objective dynamic vehicle routing problem with fuzzy time windows: Model, solution and application. *Applied Soft Computing 14, Part C* (2014), 504–527.
4. Kok, A., Hans, E., Schutten, J., and Zijm, W. A dynamic programming heuristic for vehicle routing with time-dependent travel times and required breaks. *Flexible Services and Manufacturing Journal 22*, 1-2 (2010), 83–108.
5. Qiuyun, W., Wenbao, J., and Gang, Z. A novel model and algorithm for solving dynamic vehicle routing problem on goods distribution. *Journal of Applied Sciences 13*, 22 (2013), 5410–5415.
6. Režnar, T., Martinovič, J., Slaninová, K., and Grakova, E. Probabilistic time-dependent vehicle routing problem. *Accepted to the 13th International Symposium on Operations Research, SOR'15* (2015).
7. Ropke, S., and Pisinger, D. An adaptive large neighborhood search heuristic for the pickup and delivery problem with time windows. *Transportation science 40*, 4 (2006), 455–472.
8. Schrimpf, G., Schneider, J., Stamm-Wilbrandt, H., and Dueck, G. Record breaking optimization results using the ruin and recreate principle. *Journal of Computational Physics 159*, 2 (2000), 139–171.
9. Tasa, D., Dellaert, N., van Woensel, T., and de Kok, T. The time-dependent vehicle routing problem with soft time windows and stochastic travel times. *Transportation Research Part C: Emerging Technologies 48* (2014), 66–83.
10. Zachariadis, E. E., Tarantilis, C. D., and Kiranoudis, C. T. The load-dependent vehicle routing problem and its pick-up and delivery extension. *Transportation Research Part B: Methodological 71*, C (2015), 158–181.
11. Zhang, J., Lam, W., and Chen, B. A stochastic vehicle routing problem with travel time uncertainty: Trade-off between cost and customer service. *Networks and Spatial Economics 13* (2013), 471–496.

Short-term electricity spot prices prediction using Neural Networks and hybrid ARIMA-NN model

Robert Skopal

Department of Applied Mathematics, FEECS,
VŠB – Technical University of Ostrava, 17. listopadu 15, 708 33 Ostrava – Poruba
robert.skopal@vsb.cz

Abstract. Even though the electricity HPFC (Hourly Price Forward Curve) is still surprisingly under-researched the prediction of electricity prices is highly important in order to keep power plants profitable or in order to optimize the electricity purchases based on future customers demand. In this work two methods to model and predict HPFC based on neural networks will be proposed and compared to more common time series approach - specifically ARIMA model. In the first method the neural network is applied to model the price at desired time as a function of some past observations and also to capture the seasonal character of the data. The second method uses hybrid model which consist of an ARIMA model combined with neural network. The ARIMA is used to capture linear patterns in the data. Then the neural network is used to model remaining non-linear residuals. In this case the whole process is done on deseasonalized data set. Both methods provide more accurate predictions than standard time series approach (in this case ARIMA model) and results clearly state that the neural network approach is a valid alternative for forecasting (not just) economic time series.

1 Introduction

Nowadays when electricity is no longer sold just by public companies with fixed tariffs electricity traders relies more and more on energy exchanges where prices are formed on day-ahead or intra day spot markets [7]. Prices on the spot markets are generally changed each hour of the day and show extreme movements. Since electricity is non-storable commodity movement of these prices increases risk for both producers and retailers. Modelling and predicting these prices is therefore highly important for example in area of risk management in order to estimate risk measures or assessing utilization and profitability of power plants.

One of the most widely used time series approaches for modeling and predicting economic time series is Box-Jenkins Auto Regressive Integrated Moving Average model (ARIMA) [1], [7]. Although this approach is quite flexible in order to represent different types of time series it's major limitation is the pre-assumed linear form of the model. Therefore only linear correlations can be captured by this models which could not be always enough in complex problems [8]. As an

© M. Krátký, J. Dvorský, P. Moravec (Eds.): WOFEX 2015, pp. 498–503.
VŠB – Technical University of Ostrava, FEECS, 2015, ISBN 978-80-248-3787-1.

alternative the regime-shifting models approach described in [3] could be also considered.

In this work another two alternative methods based on neural networks will be presented. Neural networks are well known as a universal modeling tool and can be used in variety of fields [2], [5], [6].

In first method the standalone neural network is applied to model output price at desired hour as a function of n past observations. Since spot prices show significant seasonality in different scales [7] the neural network is also trained to capture these cycles.

In practice it's difficult to determine whether the time series consist only of linear patterns or also significant non-linear correlations thus it's difficult to say which method should be used. Both ARIMA and neural network models achieved success in their own linear or non-linear domains. However none of them actually proofed to be a universal model that is suitable in all situations [8]. For this reason the second proposed method is hybrid ARIMA-NN model. By combining these two methods one can increase chance to capture different patterns in the data and improve prediction accuracy.

2 Methodology

2.1 Prediction using neural network

Main idea behind neural networks approach is to predict the price one time step (in this case one hour) ahead, i.e. to compute value $\hat{x}_{t+1}$ by using some function of n past observations, i.e. $x_t, x_{t-1}, \ldots, x_{t-n+1}$. At this point we could consider simple feed-forward neural network [6] and use past observations to predict future price while using same concept for teaching the network. Yet this idea isn't enough to provide sufficient electricity price prediction accuracy.

One of the main electricity prices property is seasonality in different scales [7] therefore one can take advantage of one of the key points of neural networks in time series modeling which is the pattern recognition [2]. As already been established n past observations will be provided in order to predict future price $\hat{x}_{t+1}$. Way to capture seasonal patterns is to add information about predicted day, i.e. *Monday, Tuesday,..., Sunday* (which is coded as $1, \ldots, 7$ respectively in implementation) and the predicted hour, i.e. $1, \ldots, 24$. Taking seasonal character of the data into account the final architecture of the network can be proposed. Considering n past observations plus information about hour and the day there is $n + 2$ neurons in input layer and one neuron in output layer for the predicted value. In this work the feed forward network with one hidden layer is being used [6]. Generally the number of neurons in hidden layer is still big unknown in this field and is usually determined empirically based on current problem. Additional information's about designing the neural networks in general can be found in [5].

In order to teach the network the back-propagation algorithm [6] is used. Moreover the sliding window of fixed size over the input time series formed by

historical spot prices is employed and the back-propagation is applied at every time step.

Final network architecture is shown at Fig. 1, where x_t denotes the price at time t, then $x_{t-1}, \ldots, x_{t-n}$ represents past observations and x_t^{Day}, x_t^{Hour} denotes day and hour of the observed price x_t.

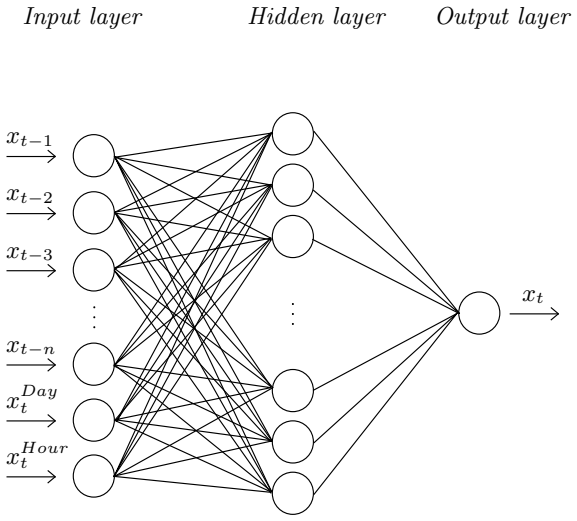

Fig. 1. Network architecture.

Whole learning process is realized by moving the window over the learning data set and applying back-propagation algorithm at every time step.

The sliding window concept that was proposed in order to teach the network will also be used for prediction. It's already been established that we are interested in one-step ahead prediction. Let's consider learning data set of length N. In order to predict next future value $\hat{x}_{N+1}$ last n observations from learning data set (i.e. $x_N,\ x_{N-1}, \ldots,\ x_{N-n+1}$) has to be provided to the network plus hour and day of the predicted price.

Generally any future value $\hat{x}_{N+s}$ can be predicted simply by repeating one-step ahead predictions. For example if one is interested in two steps ahead prediction (i.e. $\hat{x}_{N+2}$) the network input is formed by last observations $x_N,\ x_{N-1}, \ldots,\ x_{N-n+2}$ from learning data set, first already predicted value $\hat{x}_{N+1}$ plus information about hour and the day of the predicted value, i.e. $\hat{x}_{N+2}^{Hour}$ and $\hat{x}_{N+2}^{Day}$.

2.2 Prediction using hybrid ARIMA-NN model

One of the most common approaches used in time series modeling is Box-Jenkins methodology and it's typical representative - ARIMA model [1]. The fact about

ARIMA model which could be considered as disadvantage in certain situations is pre-assumed linearity of the model. This assumption sometimes makes ARIMA incapable of capturing all important correlations within the time series.

Let's consider the electricity spot prices time series in the form $X_t = L_t + R_t$, where L_t denotes linear component of the series and R_t the non-linear residuum. First the ARIMA is applied to model the linear part L_t which leaves the residual part defined as $R_t = X_t - L_t$ to contain only the non-linear patterns.

Now the very same methodology as proposed in chapter 2.1 is used to model remaining residuals R_t using the neural network. Predicted value $\hat{x}_{N+s}$ is then computed as $\hat{X}_{N+s} = \hat{L}_{N+s} + \hat{R}_{N+s}$, where $\hat{L}_{N+s}$ denotes linear component of the predicted value computed by the ARIMA model prediction [1] and $\hat{R}_{N+s}$ predicted non-linear component forecast by neural network one-step ahead prediction(s) from chapter 2.1.

3 Experiments

3.1 Learning and testing data set

Czech electricity spot prices from January 1st, 2011 to August 31, 2014 will be used as a learning data set. In order to validate the prediction the testing data set is represented by first two days of October 2014, i.e 48 time steps ahead prediction will be performed to demonstrate effectiveness of all mentioned methods.

3.2 Results

In all experiments sliding window of width 25 was used with 40 neurons in the hidden layer. Window width was in this study chosen based on information's given by Auto Correlation Function (ACF) [1] and knowledge of the problem, i.e. observed daily and weekly cycles. Another approach for window size estimation could be for example False Nearest Neighbour Method or the Singular Value Analysis proposed in [4]. Parameters of an ARIMA model has been chosen partially based on [7] and empirical study.

Table 1 show how all mentioned methods performed at 48 hours ahead prediction. Note that one of the used models is ARIMA (which is used as standalone model but also in hybrid methodology) with order $(5, 0, 1)$. Without the integrated part ARIMA becomes in fact so called ARMA model [1].

Results clearly state that in this case (i.e. electricity spot price prediction) the neural network alone achieved the most accurate prediction. Based on the MFE results the conclusion can be made that meanwhile all models using Box-Jenkins methodology (ARIMA and hybrid models) tend to under-forecast the predicted price the neural network prediction is just very slightly overpriced compared to Box-Jenkins. This implies that the network was able to capture all patterns in the data much better than linear Box-Jenkins methodology models and even the hybrid model. As expected the hybrid model performed quite better that stand alone ARIMA models.

	Order	*MAPE [%]*	*MAD*	*MFE*
ARIMA	(5,0,1)	11.41	5.08	3.76
ARIMA-NN	(5,0,1)	10.91	4.83	3.72
ARIMA	(5,1,1)	9.17	4.13	2.35
ARIMA-NN	(5,1,1)	8.71	3.84	2.25
NN		4.2	1.91	-0.69

Table 1. Prediction accuracy

Fact that neural network performed better than proposed hybrid model suggests that after removing seasonal patterns by decomposition proposed in [7] and linear correlations by ARIMA the non-linear part couldn't be modeled as precisely as in the case of stand alone neural network.

4 Conclusion

The research of Hourly Price Forward Curve showed to be highly important in energy exchange market and therefore variety of approaches to model and predict electricity prices has been studied.

In this work two neural network approaches to model and predict these prices were proposed and compared to Box-Jenkins ARIMA model. Results clearly showed that the neural network predictor was able to provide much higher prediction accuracy compared to ARIMA model and in this case also hybrid ARIMA-NN model and therefore proofed to be valid alternative for short-term energy spot prices prediction.

5 Acknowledgments

This work was supported by the internal grant agency of VSB Technical University of Ostrava, Czech Republic, under the projects no. SP2015/114 "HPC Usage for Analysis of Uncertain Time Series" and no. SP2015/84 "Stochastic modeling".

Results of this paper were published on the International Conference on Information and Digital Technologies 2015 in Žilina.

References

1. Ch. Chatfield, *The Analysis of Time Series, An Introduction*, CRC Press LLC (2004)

2. J. Faraway and Ch. Chatfield, *Time Series Forecasting with neural Networks: the comparative study using the airline data*,
Appl. Statis. (1998) 47, Part 2, pp. 231-250

3. S. Fleten, F. Paraschiv, and M. Schurle, *Spot-forward model for electricity price*,
Working Papers On Finance no. 2013/11 (2013)

4. R. Frank, N. Davey, and S. Hunt, *Time Series Prediction and Neural Networks*,
Journal of Intelligent and Robotic Systems 31, pp.91-103 (2001)

5. I. Kaastra and M. Boyd, *Designing a neural network for forecasting financial and economic time series*,
Neurocomputing 10 (1996), pp. 215-236

6. D. Kriesel, *A Brief Introduction to Neural Networks*,
www.dkriesel.com (2005)

7. D. Keles, Massimo Genose, Dominik Mst and Wolf Fichtner, *Comparison of extended mean-reversion and time series models for electricity spot price simulation considering negative prices*,
Energy Economics 34 (2012), pp. 1012-1032

8. P. Zhang, *Time series forecasting using a hybrid ARIMA and Neural network model*,
Neurocomputing 50 (2003), pp. 159-175

Probabilistic Time-Dependent Travel Time Computation using Monte Carlo Simulation

Radek Tomis

Department of Applied Mathematics, FEECS,
VŠB – Technical University of Ostrava, 17. listopadu 15, 708 33 Ostrava – Poruba
radek.tomis@vsb.cz

Abstract. This paper presents the experimental evaluation of probabilistic time-dependent travel time computation. The Monte Carlo simulation is used for the computation of travel times and their probabilities. The simulation is utilizing traffic data regarding incidents on roads to compute the probability distribution of travel times on a selected path. Traffic data has the information about an optimal speed, a traffic incident speed and a probability of a traffic incident to occur. The exact tree computation algorithm is used for the comparison of the simulation.

Keywords: probabilistic time-dependent route planning, Monte Carlo simulation, speed profiles, uncertainty, traffic incidents

1 Introduction

Finding the fastest path in the road network is a common task for navigation services. The efficient route planning can lower travel time and therefore lower travel costs for drivers. Some navigation services are using traffic data on road networks to compute more accurate paths. However, most navigation services use only averages of historic travel times on roads for computation of the paths, even though this is not sufficient in many cases. Some roads can be for example congested at the time of rush hours, which leads to larger delays, or there can be traffic incidents on the roads.

A departure time highly affects route planning in the real road network. The fastest path is actually a time-dependent shortest path [9] in a graph with variable travel times used as edge weights. Travel times on the edges are usually computed as historic averages [10], even though this is not sufficient sometimes [3, 5].

The main disadvantage of time-dependent route planning is that it does not take accidental events into account. There can be irregular but recurrent traffic congestions at some roads and navigation services should consider it in the computation of the path and offer alternative routes [7]. Even though the probability of the traffic congestion can be very low, the delay in the case the congestion happens can be very long. Therefore, we have to consider uncertain traffic events and their probabilities in the computation of the path [8, 13].

© M. Krátký, J. Dvorský, P. Moravec (Eds.): WOFEX 2015, pp. 504–509.
VŠB – Technical University of Ostrava, FEECS, 2015, ISBN 978-80-248-3787-1.

Traffic incidents and congestions cause uncertainty in travel times. There are existing algorithms [6, 2, 1, 11], which try to find a solution for time-dependent shortest path problem in uncertain networks. However, these algorithms are very time demanding even with very small road networks. Therefore, we proposed a new approach to route planning with uncertainty [12] based on the computation of probabilistic travel times.

In this paper, the Monte Carlo simulation is used for the computation of probabilistic travel times for given path. The simulation randomly selects the state of the traffic on individual road segments using historic traffic data and then computes the travel time at the end of the path. The simulation has to be performed repeatedly to obtain the result in the form of the probability function of travel time. The accuracy of the result is dependent on the number of simulation iterations. The description of the simulation is at section 2. Section 3 presents experiments and the description of traffic data.

2 Monte Carlo Simulation for Probabilistic Travel Time Computation

The focus of this paper is about the computation of travel times and their probabilities on the selected path. Let $G = \{V, E\}$ be a directed graph created from a road network, where vertices represent intersections and edges represent roads. Our selected path starts at a vertex u and ends at a vertex v, let's denote this path $P = \{u = v_0, e_0, v_1, e_1, \ldots, v_{n-1}, e_{n-1}, v_n = v\}$. The result is the probability function of travel time for selected departure time t_d.

The exact computation can be done using all possible combinations of speed profiles, which means travel times and their probabilities grow as a tree with root node represented by u, leaf nodes represented by v and each path between u and v represent one specific combination of speed profiles. The example of such travel time tree is presented in Fig. 1.

The tree can be very large and there can be any number of nodes in between u and v. The exact number depends on a quantity of speed profiles and also on the departure time, because our tree can be additionally forked between two neighbour nodes if travel time at the end of belonging edge would exceed the specific time boundaries of the current speed profile. Therefore the time complexity is the main issue with this approach.

Monte Carlo simulation is another approach to obtain the result. The algorithm is simulating traversal of the tree from u to v by randomly selecting speed profiles on the sequence of edges $e_0, e_1, \ldots, e_{n-1}$ and computing travel time of the path. The simulation is repeated for a specified number of samples and then the probability function is created from computed travel times. See Algorithm 1 for pseudo code of our algorithm. The result does not have to be exact, because there is a random factor, however the accuracy should improve with greater number of samples.

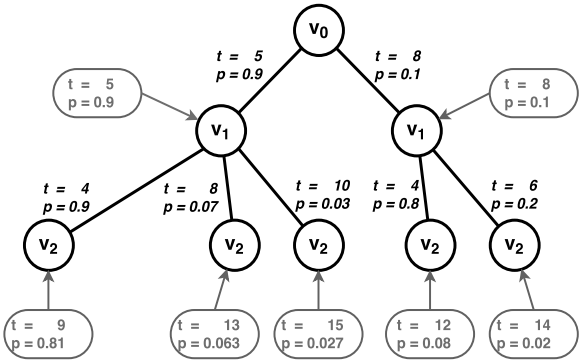

Fig. 1. Example of the specific travel time tree

Algorithm 1 Monte Carlo simulation for probabilistic travel time computation for given array of edges, departure time and number of samples

```
1: procedure MonteCarloSimulation(edges, t_d, samples)
2:     for all samples do
3:         t = t_d
4:         for e in edges do
5:             r = generate random number between 0 and 1
6:             t = ComputeTravelTime(e, t, r)        ▷ speed profile is selected by r
7:         end for
8:         add travel time t to result
9:     end for
10: end procedure
```

3 Experiment

The experimental results of our algorithm are presented in this section. We use the road network created from Traffic Message Channel (TMC) segments in the Czech republic, because it covers the backbone of the real road network.

We are using speed profiles computed from traffic data obtained due to online traffic monitoring system viaRODOS [4]. The experimental set of data was extracted from two months (October and November 2014) with traffic work on the highway D1. Speed profiles contain sets of pairs of data in 15 minutes interval for each day of the week and each measured place. The first pair contains average speed from values equal or higher than 50 percent of LoS (Level-of-Service - the measured speed divided by the normal free flow speed) and probability of the occurrence of this state. The second pair is computed by the similar way, but from the values under 50 percent of LoS. The values with reliability equal to 0 were excluded from the speed profiles computation. You can see probability intensity computed from values under 50 percent LoS (traffic problems) in the Fig. 2.

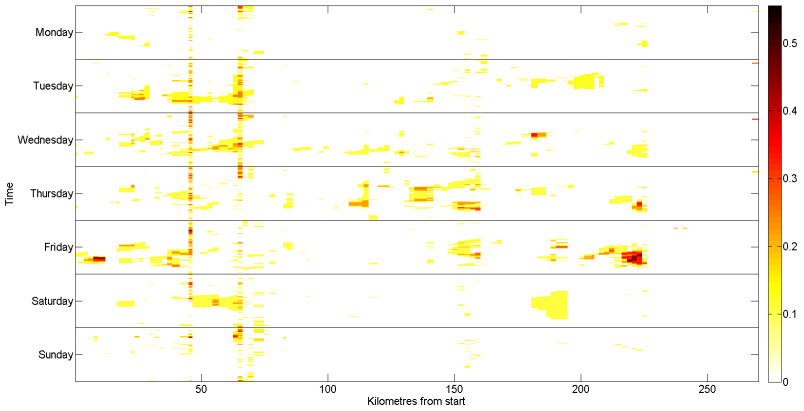

Fig. 2. Probability Intensity for values $< 50\%$ LoS

The path from Praha to Brno along the highway D1 was chosen for experiment. The whole path is composed of 84 road segments (edges). The departure time was set at 2 pm on Wednesday, because there are many traffic incidents on the highway D1 at that time. Fig. 3 shows the exact probability function for specified settings. Table 1 shows the comparison of computation time of Monte Carlo simulation with the exact tree computation algorithm for different number of road segments. We can see, that the computation time of the exact algorithm is increasing rapidly with greater number of road segments, while the time for Monte Carlo simulation is increasing in linear fashion.

Table 1. Comparison of computation times

		Computation Time [s]				
		Exact	Monte Carlo Samples			
			10^3	10^4	10^5	10^6
Number of Segments	40	0.700	0.027	0.205	2.050	19.969
	50	7.700	0.031	0.244	2.445	24.651
	60	122.000	0.037	0.301	2.905	28.918
	70	667.000	0.038	0.352	3.510	34.139
	80	4849.000	0.040	0.383	3.837	38.250

The accuracy of the simulation compared to the exact algorithm is in Fig. 4. Each mean absolute error of travel time was computed for 100 Monte Carlo simulations with specified number of samples. There are always two different lines for each number of road segments (first number in the legend). The first

line is computed for expected values (EX) and the second for standard deviations (Std). As expected, the accuracy is higher with greater number of samples.

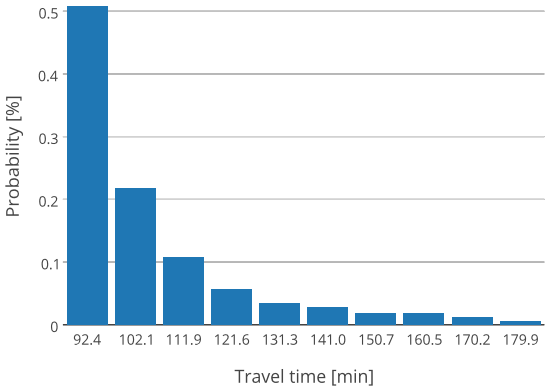

Fig. 3. Probability function of travel time

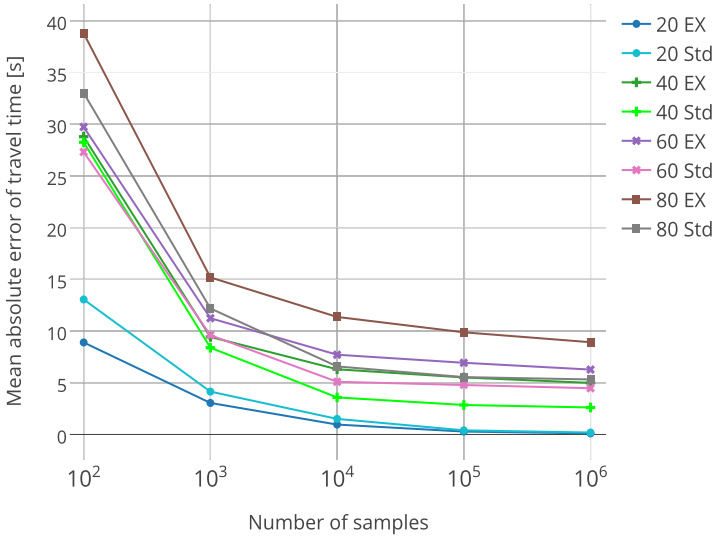

Fig. 4. Mean absolute error of Monte Carlo simulation travel times for different number of segments

4 Conclusion

The Monte Carlo simulation for computation of probabilistic travel times on the selected path was presented in this paper. The simulation proved to be a suitable substitute for the exact computation. While the computation time of the exact computation is increasing very steeply, the computation time of Monte Carlo simulation is increasing in linear fashion. This allows to compute results for a greater number of road segments, which would be almost impossible for the exact computation. The accuracy of results of Monte Carlo simulation depends on the number of samples and it is relatively precise, even with lower numbers of samples.

References

1. B. Chen, W. Lam, A. Sumalee, Q. Li, H. Shao, and Z. Fang. Finding reliable shortest paths in road networks under uncertainty. *Networks and Spatial Economics*, 13(2):123–148, 2013.
2. B. Y. Chen, W. H. K. Lam, A. Sumalee, Q. Li, and M. L. Tam. Reliable shortest path problems in stochastic time-dependent networks. *Journal of Intelligent Transportation Systems*, 18(2):177–189, 2014.
3. Y. Fan, R. Kalaba, and I. Moore, J.E. Arriving on time. *Journal of Optimization Theory and Applications*, 127(3):497–513, 2005.
4. D. Fedorčák, T. Kocyan, M. Hájek, D. Szturcová, and J. Martinovič. viaRODOS: Monitoring and visualisation of current traffic situation on highways. In *Computer Information Systems and Industrial Management*, volume 8838 of *Lecture Notes in Computer Science*, pages 290–300. Springer Berlin Heidelberg, 2014.
5. A. Hofleitner, R. Herring, P. Abbeel, and A. Bayen. Learning the dynamics of arterial traffic from probe data using a dynamic bayesian network. *Intelligent Transportation Systems, IEEE Transactions on*, 13(4):1679–1693, Dec 2012.
6. M. Hua and J. Pei. Probabilistic path queries in road networks: traffic uncertainty aware path selection. In *Proceedings of the 13th International Conference on Extending Database Technology*, pages 347–358. ACM, 2010.
7. E. Miller-hooks. Adaptive least-expected time paths in stochastic, time-varying transportation and data networks. *Networks*, pages 35–52, 2000.
8. E. Nikolova, M. Brand, and D. R. Karger. Optimal route planning under uncertainty. In *ICAPS*, volume 6, pages 131–141, 2006.
9. A. Orda and R. Rom. Shortest-path and minimum-delay algorithms in networks with time-dependent edge-length. *J. ACM*, 37(3):607–625, July 1990.
10. J. Rice and E. Van Zwet. A simple and effective method for predicting travel times on freeways. *Intelligent Transportation Systems*, 5(3):200–207, 2004.
11. S. Sun, Z. Duan, S. Sun, and D. Yang. How to find the optimal paths in stochastic time-dependent transportation networks? In *Intelligent Transportation Systems, 2014 IEEE 17th International Conference on*, pages 2348–2353. IEEE, 2014.
12. R. Tomis, J. Martinovič, L. Rapant, K. Slaninová, and I. Vondrák. Time-dependent route planning for the highways in the czech republic. In *Computer Information Systems and Industrial Management - 14th International Conference, CISIM*, 2015.
13. B. Yang, C. Guo, C. S. Jensen, M. Kaul, and S. Shang. Multi-cost optimal route planning under time-varying uncertainty. In *Proceedings of the 30th International Conference on Data Engineering (ICDE), Chicago, IL, USA*, 2014.

Parallel Inverse Modelling in Rainfall-Runoff Simulations

Radim Vavřík

IT4Innovations National Supercomputing Center,
Department of Applied Mathematics, FEECS,
VŠB – Technical University of Ostrava, 17. listopadu 15, 708 33 Ostrava – Poruba
radim.vavrik@vsb.cz

Abstract. Rainfall-runoff simulations are an integral part of a decision support in flood warning processes. Rainfall-runoff models are based on many parameters, which can be affected by inaccuracy. It is possible to gain more accurate results of simulations by performing calibration of models. Calibration of a model is formally an inverse problem and an aim is to estimate values of input parameters which provide the best possible simulation results. Since calibration consists of a large number of rainfall-runoff simulations, it is a very computational extensive process. For an efficient decision making process it is necessary to provide accurate results as fast as possible. For such a case it is very appropriate to use scalable algorithms in a high performance environment offering a sufficient amount of computational resources. In this paper, the main components of parallel rainfall-runoff inverse modelling are described.

Keywords: inverse modelling, rainfall-runoff model, rainfall-runoff calibration, high performance computing, parallelization

1 Introduction

Floods are a very significant cause of extensive losses of lives and damages to property. Therefore it is very important to predict potential flood events reliably and provide relevant data and recommendations to authorities responsible for a flood alert issuance. For this task a flood prediction and monitoring system named Floreon$^+$ is developed by our research team.

As an essential component of the system, rainfall-runoff models describe a transformation process of precipitation fallen in a given catchment area into surface runoff. Rainfall-runoff simulations are then capable to answer how much streamflow occurs in a river in response to a given amount of rainfall.

For development and testing purposes we use mainly our in-house rainfall-runoff model called Math1D. It is a numerical semi-distributed rainfall-runoff model dividing a catchment (basin) into sub-basins and consisting of other parameterisable units, e.g. river channels, or hydrometeorologic gauges.

Since every sub-basin and river channel are described by a set of parameters which values may not be accurate for each simulated rainfall-runoff event, it is

© M. Krátký, J. Dvorský, P. Moravec (Eds.): WOFEX 2015, pp. 510–515.
VŠB – Technical University of Ostrava, FEECS, 2015, ISBN 978-80-248-3787-1.

necessary to refine these values to get more precise and valuable results. This process is called calibration of a rainfall-runoff model and will be explained in section 2. In section 3, used HPC environment is briefly introduced. Section 4 presents individual calibration components and experimental results. Finally, in section 5 conclusions about presented work are summarized and plans for a future work are outlined.

2 Rainfall-Runoff Model Calibration and Inverse Modelling

In general, calibration means adjustment of model parameters to a set of observed values of the system or to trusted reference model parameters. When the estimated parameters are causal factors, we consider such a task as an inverse problem. This allows us to estimate actual parameters that we cannot directly observe.

In the case of a rainfall-runoff model, we compare real discharge volumes supplied by measurement gauges with simulated ones. The goal is to find the set of model parameters for which the simulation provides the output values as near as possible to the measured ones; in other words, to achieve the simulation with the lowest possible error. To evaluate an error size, we can use commonly used error estimators. Several of them will be introduced in following sections.

It is possible to calibrate model parameters for a given rainfall-runoff event manually, but for a fast and periodic calibration execution it is necessary to automate the task. From the foregoing follows that the calibration process can be formulated as a constrained minimization problem:

$$f(\boldsymbol{x}) \rightarrow min \quad \text{subject to} \quad \boldsymbol{x} \in \{l_i \leq x_i \leq u_i, i = 1, ..., n\},$$

where f is the objective function measuring simulation error and $\boldsymbol{x}$ is the vector of the calibrated parameters, in our case Runoff Curve Number, Manning's Roughness Coefficient and Initial Abstraction. Constraints of the minimization problem are formed by lower (l) and upper (u) physical limits of the particular parameter type. The total number of calibrated parameters is determined by a size of a simulated catchment, in case of semi-distributed models by a number of catchment sub-basins.

We can define the general calibration algorithm as follows:

1. Set initial parameter values.
2. Run simulation.
3. Evaluate objective function.
4. Check simulation error. If termination condition is satisfied then stop.
5. Perform minimization step.
6. Update parameters with new values.
7. Continue in step 2.

3 HPC environment

The most of the development, testing and experiments presented in this paper were performed on the IT4Innovations Supercomputer Center cluster named Anselm. Each of 180 non-accelerated nodes of the cluster is an x86-64 computer equipped with two 8-core Intel Sandy Bridge E5-2665 2.4 GHz processors and 64 GB RAM. The nodes are interconnected by a fully non-blocking fat-tree InfiniBand network (3600 MB/s).

4 Automatic Calibration Components

Calibration Strategies. The three strategies of the calibration process were designed and implemented [2]. Local gradient-based Line search method was implemented as a minimization algorithm. The strategies differ in the partitioning of the catchment structure and in the form of parallelization.

1. In the first strategy, whole catchment is calibrated for each measurement gauge separately. Each such separate calibration process uses measured data from the assigned gauge as the reference for minimization of the objective function. One MPI process is linked to one calibration process which produces separate set of calibrated parameters. The advantage of this strategy is its simple parallel implementation. As the main disadvantage we identified excessive computation costs for the gauges that are not located at the outlet of the basin. Calibration of these gauges is done even for their downstream part that does not influence the simulation results. The principle of the 1^{st} implementation strategy is shown in figure 1a.
2. The second strategy performs calibration of the whole catchment only for the outlet gauge. This leads to one set of calibrated parameters while measured data from other gauges are not used. An objective function gradient evaluation is distributed among all assigned MPI processes which significantly improve the scalability. This scalability is limited by a number of sub-basins in the catchment. The principle of the 2^{nd} implementation strategy is shown in figure 1b.
3. The third strategy takes into account the hierarchy of the catchment which is partitioned according the measurement gauges. Only upstreams of the gauges are calibrated, starting from ones that are the nearest to the river springs. Such intermediate results are reused for downstream gauges calibrations. The parallelization strategy is the same as in the 2^{nd} strategy, but downstream gauges have to wait for the upstream ones. The advantage is that all measurement gauges data are used. The principle of the 3^{rd} implementation strategy is shown in figure 1c.

The calibration was executed with the same input data and the same termination condition but with different numbers of assigned MPI processes to test scalability. Above that, the Math1D model performance was tested using various number of OpenMP threads. In the table 1, the execution times are presented.

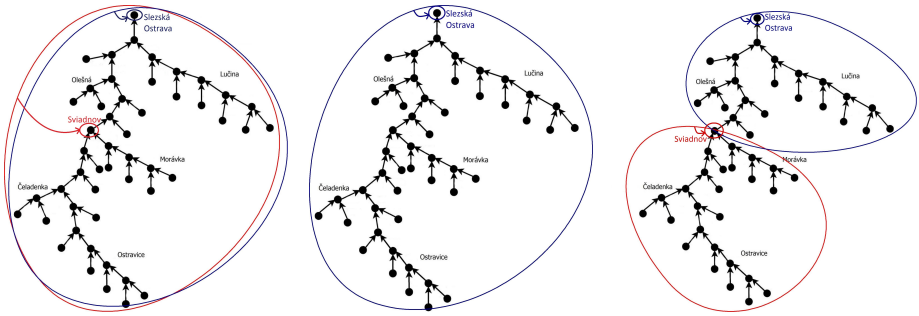

Fig. 1: Schematic simulation diagrams for the 1^{st} strategy (a), 2^{nd} strategy (b) and 3^{rd} strategy (c).

Table 1: Experimental execution times for different configurations of MPI processes and OpenMP threads.

Processes	Threads	1^{st} Strategy	2^{nd} Strategy	3^{rd} Strategy
1	1	22 min 42.96 s	16 min 15.76 s	11 min 31.49 s
1	2	16 min 10.10 s	12 min 22.59 s	8 min 12.37 s
1	4	11 min 10.03 s	8 min 33.29 s	5 min 39.49 s
1	8	10 min 22.68 s	7 min 46.77 s	5 min 21.06 s
2	1	17 min 53.18 s	8 min 43.43 s	6 min 44.50 s
2	2	12 min 15.33 s	5 min 56.74 s	4 min 48.59 s
2	4	9 min 12.37 s	4 min 12.10 s	3 min 20.21 s
2	8	7 min 48.05 s	4 min 33.36 s	3 min 5.22 s
4	8	-	3 min 25.91 s	1 min 33.19 s
8	8	-	1 min 45.87 s	48.56 s
16	8	-	1 min 6.70 s	47.06 s

Optimization Methods. In a calibration process, optimization methods with different characteristics can be used. Our aim was to compare several commonly used global and local optimization methods and identify which are the most effective [1]. It means to provide the best improvement of the rainfall-runoff simulation error against the original simulation performed with uncalibrated parameters in an acceptable time frame.

Experiments were performed using a programming language and computing environment MathWorks MATLAB R2013a. We tested these optimization methods:

- Local: Line search, Interior point
- Global: Pattern search, Global search, Multi-start Interior point, Genetic algorithm

To evaluate precision we used six different metrics – combinations of norms. Parameters were calibrated for each measurement gauge separately, which means a separate objective function evaluation and thus an intermediate error computation using one of the following three norms:

– Adapted Nash-Sutcliffe model efficiency coefficient:

$$err_i^A = \frac{\sum_{t=1}^{T} \left(Q_o(t) - Q_m(t)\right)^2}{\sum_{t=1}^{T} \left(Q_o(t) - \overline{Q_o}\right)^2};$$

– Normed peak error:

$$err_i^B = \frac{|Q_o(t_p) - Q_m(t_p)|}{Q_o(t_p)}, \text{ where } t_p = \underset{t \in \langle 0,T \rangle}{\arg\max} \left(Q_o(t)\right);$$

– Normed volume error:

$$err_i^C = \frac{\sum_{t=1}^{T} |Q_o(t) - Q_m(t)|}{\sum_{t=1}^{T} |Q_o(t)|},$$

where $Q_o(t)$ stands for the observed discharge at the time t, $Q_m(t)$ the modelled discharge at the time t and $\overline{Q_o}$ denotes the mean of observed discharges.

The total error is then computed by L^2-norm and L^∞-norm using intermediate errors err^X obtained during individual partial calibrations:

$$\left\|err^X\right\|_2 = \sqrt{\sum_{i=1}^{N} \left|err_i^X\right|^2}, \qquad \left\|err^X\right\|_\infty = \max_{i \in \{1,\ldots,N\}} err_i^X,$$

where N is the number of measurement gauges.

Example results of the method comparison for the Nash-Sutcliffe coefficient and L^2-norm can be seen in the table 2.

Table 2: Statistical results for improvement of $\left\|err^A\right\|_2$.

	mean	median	std
Local methods			
Linesearch	0.811	0.855	0.183
Interior point	0.852	0.864	0.099
Global methods			
Pattern search	0.892	0.907	0.080
Global search	0.802	0.840	0.159
Multistart	0.677	0.769	0.304
Genetic alg.	0.768	0.772	0.132

Implementation and Deployment of Optimization Methods. Based on the previous results and calibration components knowledge, local Line search and global Multi-start optimization methods were chosen for the next exploitation due to their good efficiency and suitability for massive parallelization [3].

Both methods were implemented in the C++ programming language using a hybrid parallelization model to fully utilize allocated computational resources of an HPC cluster. The Line search method using a single-node multi-threaded parallelization provides fast calibration of model parameters pregenerated and distributed by the Multi-start method to a given number of computation nodes.

This calibration module was integrated to the new parametrization and execution HPC framework which is an important component of the Floreon$^+$ flood prediction system.

5 Conclusion and Future Work

In this paper, the process of rainfall-runoff models automatic calibration was explained and individual components of calibration and their exploitation were introduced.

First, calibration strategies design and the experimental implementation were presented. This brought outline of the strategies behavior. Then, several local and global optimization methods were compared by their effectivity and suitability for parallelization. The Line search and Multi-start methods were chosen, implemented and integrated into the HPC framework of the Floreon$^+$ system.

Our future work will focus on testing and improvement of the optimization methods implementation, enabling other rainfall-runoff models and connecting actual outputs to e.g. hydrodynamic models.

Acknowledgement

This work was supported by the European Regional Development Fund in the IT4Innovations Centre of Excellence project (CZ.1.05/1.1.00/02.0070), by the project of major infrastructures for research, development and innovation of Ministry of Education, Youth and Sports with reg. num. LM2011033 and by the SGS project SP2015/171 - Flood and pollution modeling.

References

1. Theuer, M., Vavrik, R., Vondrak, V., Kuchar, S., Sir, B., Portero, A.: Efficient methods of automatic calibration for rainfall-runoff modelling in the Floreon+ system. Neural Network World. September 2014. (Submitted)
2. Vavrik, R., Theuer, M., Golasowski, M., Kuchar, S., Podhoranyi, M., Vondrak, V.: Automatic Calibration of Rainfall-Runoff Models and its Parallelization Strategies. ICNAAM'2014. September 2014, Rhodes, Greece.
3. Vondrak, V., Kuchar, S., Golasowski, M., Vavrik, R., Martinovic, J.: Scalable algorithms for inverse and uncertainty modelling in hydrology. CC2015. 1-4 September 2015, Prague, Czech Republic. (Accepted)

Boundary element based evaluation of homogenized coefficients in conductivity

Jan Zapletal

Department of Applied Mathematics, FEECS,
VŠB – Technical University of Ostrava, 17. listopadu 15, 708 33 Ostrava – Poruba
jan.zapletal@vsb.cz

Abstract. We present a boundary element method for the auxiliary problem arising in homogenization of conductive composite media. Similarly as the well-studied volume approach, the problem is only stated in a periodic cell. However, contrary to the finite element discretization only the boundary of the cell and the inclusion has to be discretized. To solve the auxiliary problem we propose a Steklov-Poincaré formulation, present convergence results for the effective coefficients and validate the theoretical findings by numerical experiments. The presented work is a summary of the joint paper [3].

1 Introduction

We consider periodic composite materials with piecewise constant material coefficients. The homogenization framework is based on the well-established theory presented in, e.g., [1, 2, 5, 9]. The composite bounded Lipschitz domain $\Omega \subset \mathbb{R}^3$ consists of two phases arranged in a periodic pattern, see Figure 1.1. By $Y := (0,1)^3$, $Y = \overline{Y_1} \cup Y_2$ we denote the periodic cell with the inclusion represented by a Lipschitz domain $Y_1 \subset Y$, $\operatorname{dist}(\partial Y_1, \partial Y) > 0$. We further denote $\Gamma := \partial Y$, $\Gamma_1 := \partial Y_1$, $\Gamma_2 := \partial Y_2$.

The homogeneous Dirichlet problem for the steady-state heat transfer in Ω is described by the elliptic boundary value problem to find $u^\varepsilon \in H_0^1(\Omega)$ satisfying

$$\int_\Omega a^\varepsilon(\boldsymbol{y}) \langle \nabla u^\varepsilon(\boldsymbol{y}), \nabla v(\boldsymbol{y}) \rangle \,\mathrm{d}\boldsymbol{y} = \int_\Omega f(\boldsymbol{y}) v(\boldsymbol{y}) \,\mathrm{d}\boldsymbol{y} \quad \forall v \in H_0^1(\Omega) \tag{1.1}$$

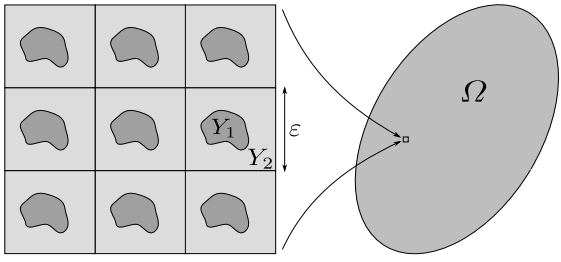

Fig. 1.1. Material with highly oscillating coefficients.

© M. Krátký, J. Dvorský, P. Moravec (Eds.): WOFEX 2015, pp. 516–521.
VŠB – Technical University of Ostrava, FEECS, 2015, ISBN 978-80-248-3787-1.

with $f \in L^2(\Omega)$. By $\varepsilon > 0$ we denote the scaling parameter and $a^\varepsilon(\boldsymbol{y}) := a(\boldsymbol{y}/\varepsilon)$ represents the piecewise constant material function with

$$a(\boldsymbol{y}) := \begin{cases} a_1 & \text{for } \boldsymbol{y} \in Y_1, \\ a_2 & \text{for } \boldsymbol{y} \in Y_2 \end{cases}$$

extended to $\mathbb{R}^3$ by periodic translations of Y. For $\varepsilon \to 0_+$ it is known [1, 2, 5, 9] that for the unique weak solutions to (1.1) it holds

$$u^\varepsilon \rightharpoonup u^0 \text{ in } H_0^1(\Omega)$$

with $u^0 \in H_0^1(\Omega)$ denoting the unique solution to the homogenized problem

$$\int_\Omega \langle \mathsf{Q}\nabla u^0(\boldsymbol{y}), \nabla v(\boldsymbol{y})\rangle \,\mathrm{d}\boldsymbol{y} = \int_\Omega f(\boldsymbol{y}) v(\boldsymbol{y}) \,\mathrm{d}\boldsymbol{y} \quad \forall v \in H_0^1(\Omega).$$

The effective coefficient matrix Q is given by the formula

$$\mathsf{Q}[i,j] = \delta_{ij} \int_Y a(\boldsymbol{y}) \,\mathrm{d}\boldsymbol{y} - \int_Y a(\boldsymbol{y}) \frac{\partial w^j}{\partial y_i}(\boldsymbol{y}) \,\mathrm{d}\boldsymbol{y}$$

with $w^j \in H^1_{\mathrm{per}}(Y)$, $j \in \{1,2,3\}$, solving the cell problems

$$\int_Y a(\boldsymbol{y}) \langle \nabla w^j(\boldsymbol{y}), \nabla \varphi(\boldsymbol{y})\rangle \,\mathrm{d}\boldsymbol{y} = \int_Y a(\boldsymbol{y}) \frac{\partial \varphi}{\partial y_j}(\boldsymbol{y}) \,\mathrm{d}\boldsymbol{y} \quad \forall \varphi \in H^1_{\mathrm{per}}(Y). \tag{1.2}$$

By $H^1_{\mathrm{per}}(Y)$ we denote the subspace of $H^1(Y)$ containing functions with equal traces on the opposite sides of the reference cell Y. Note that the solutions to (1.2) are uniquely defined up to an additive constant. This can be fixed, e.g., by setting

$$\int_{\Gamma_2} w^j(\boldsymbol{y}) \,\mathrm{d}\boldsymbol{s}_{\boldsymbol{y}} = 0. \tag{1.3}$$

2 Boundary integral formulation

In this section we derive the boundary integral formulation as presented in [3].

Using the Gauss theorem, the evaluation of the effective coefficients can be reduced to the boundary of the inclusion,

$$\mathsf{Q}[i,j] = \delta_{ij} a_2 + (a_1 - a_2) \int_{\Gamma_1} (\delta_{ij} y_i - \gamma_1^0 w^j(\boldsymbol{y})) \, n_i^1(\boldsymbol{y}) \,\mathrm{d}\boldsymbol{s}_{\boldsymbol{y}}, \tag{2.1}$$

with γ_1^0, $\boldsymbol{n}^1$ denoting the Dirichlet trace operator and the unit exterior normal vector to Γ_1, respectively. Similarly, we denote by γ^0, γ_2^0, $\boldsymbol{n}$, $\boldsymbol{n}^2$ the Dirichlet traces and normal vectors to Γ and Γ_2, respectively. Note that due to $\Gamma_2 = \Gamma_1 \cup \Gamma$ the Γ_2-trace can be decomposed as $\gamma_2^0 w = (\gamma_1^0 w, \gamma^0 w)$.

Due to $\varphi \in H^1_{\mathrm{per}}(Y)$ the right-hand side of the auxiliary problem (1.2) can be rewritten as

$$\int_Y a(\boldsymbol{y}) \frac{\partial \varphi}{\partial y_j}(\boldsymbol{y}) \,\mathrm{d}\boldsymbol{y} = (a_1 - a_2) \int_{\Gamma_1} \gamma_1^0 \varphi(\boldsymbol{y})\, n_j^1(\boldsymbol{y}) \,\mathrm{d}\boldsymbol{s}_{\boldsymbol{y}}. \tag{2.2}$$

From (1.2) it also follows that $-\Delta w^j = 0$ in Y_1 and Y_2 in the weak sense and thus we have

$$\int_Y a(\boldsymbol{y}) \langle \nabla w^j(\boldsymbol{y}), \nabla \varphi(\boldsymbol{y}) \rangle \,\mathrm{d}\boldsymbol{y} = a_1 \langle S_1(\gamma_1^0 w^j), \gamma_1^0 \varphi \rangle_{\Gamma_1} + a_2 \langle S_2(\gamma_2^0 w^j), \gamma_2^0 \varphi \rangle_{\Gamma_2} \tag{2.3}$$

for all $\varphi \in H^1_{\mathrm{per}}(Y)$ with the Steklov-Poincaré operators

$$S_i \colon H^{1/2}(\Gamma_i) \to H^{-1/2}(\Gamma_i)$$

realized, e.g., by the boundary integral operators [8, 6, 7] as

$$S_i := D_i + (1/2 I_i + K_i^*)\, V_i^{-1}\, (1/2 I_i + K_i)$$

with V_i, K_i, K_i^*, D_i denoting the single-layer, double-layer, adjoint double-layer, and hypersingular boundary integral operators, respectively. By I_i we denote the identity operators, and $\langle \cdot, \cdot \rangle_{\Gamma_i}$ represents the duality pairing between $H^{-1/2}(\Gamma_i)$ and $H^{1/2}(\Gamma_i)$. Combining (1.2), (2.2), and (2.3) we finally obtain the boundary integral formulation to find $(\gamma_1^0 w^j, \gamma^0 w^j) \in H^{1/2}(\Gamma_1) \times H^{1/2}_{\mathrm{per}}(\Gamma)$,

$$\begin{aligned} a_1 \langle S_1(\gamma_1^0 w^j), \varphi_1 \rangle_{\Gamma_1} + a_2 \langle S_2(\gamma_1^0 w^j, \gamma^0 w^j), (\varphi_1, \varphi) \rangle_{\Gamma_2} \\ = (a_1 - a_2) \int_{\Gamma_1} \varphi_1(\boldsymbol{y})\, n_j^1(\boldsymbol{y}) \,\mathrm{d}\boldsymbol{s}_{\boldsymbol{y}} \end{aligned} \tag{2.4}$$

for all $(\varphi_1, \varphi) \in H^{1/2}(\Gamma_1) \times H^{1/2}_{\mathrm{per}}(\Gamma)$. By $H^{1/2}_{\mathrm{per}}(\Gamma)$ we denote the trace space of $H^1_{\mathrm{per}}(Y)$.

The Galerkin discretization of S_i reads

$$\mathsf{S}_i := \mathsf{D}_i + (1/2 \mathsf{M}_i + \mathsf{K}_i)^{\mathsf{T}}\, \mathsf{V}_i^{-1}\, (1/2 \mathsf{M}_i + \mathsf{K}_i)$$

with

$$\begin{aligned} (\mathsf{V}_i)_{jk} &:= \langle \psi_{i,j}, V_i \psi_{i,k} \rangle_{\Gamma_i}, & (\mathsf{K}_i)_{jk} &:= \langle \psi_{i,j}, K_i \varphi_{i,k} \rangle_{\Gamma_i}, \\ (\mathsf{D}_i)_{jk} &:= \langle D_i \varphi_{i,k}, \varphi_{i,j} \rangle_{\Gamma_i}, & (\mathsf{M}_i)_{jk} &:= \langle \psi_{i,j}, \varphi_{i,k} \rangle_{\Gamma_i}, \end{aligned}$$

and $\psi_{2,\bullet} = (\psi_{1,\bullet}, \psi_\bullet)$, $\varphi_{2,\bullet} = (\varphi_{1,\bullet}, \varphi_\bullet)$ denoting the piecewise constant and continuous piecewise linear ansatz and test functions, respectively. We seek the discretized solution in the form

$$(\gamma_1^0 w^j)_h := \sum_{k=1}^{N_1} w_{1,k}^j \varphi_{1,k}, \quad (\gamma^0 w^j)_h := \sum_{k=1}^{N} w_k^j \varphi_k.$$

Table 1. Convergence table for 3D experiments.

E	e^h_{sphere}	eoc	e^h_{cube}	eoc	e^h_{fichera}	eoc
192	$1.01 \cdot 10^{-1}$	–	$5.15 \cdot 10^{-2}$	–	$1.02 \cdot 10^{-1}$	–
768	$2.66 \cdot 10^{-2}$	3.80	$1.91 \cdot 10^{-2}$	2.69	$2.77 \cdot 10^{-2}$	3.70
3072	$6.44 \cdot 10^{-3}$	4.13	$6.37 \cdot 10^{-3}$	3.00	$8.48 \cdot 10^{-3}$	3.27
12288	$1.30 \cdot 10^{-3}$	4.95	$1.69 \cdot 10^{-3}$	3.77	$2.16 \cdot 10^{-3}$	3.93

Regularization of S_2 due to (1.3),

$$\widetilde{\mathsf{S}}_2 := \mathsf{S}_2 + \boldsymbol{c}\boldsymbol{c}^{\mathsf{T}},\ c_j := \langle \varphi_{2,j}, 1 \rangle_{\Gamma_2},$$

and the decomposition of $\widetilde{\mathsf{S}}_2$ with respect to $\Gamma_2 = \Gamma_1 \cup \Gamma$ leads to the system of linear equations

$$\begin{bmatrix} a_1\mathsf{S}_1 + a_2\widetilde{\mathsf{S}}_2^{\Gamma_1\Gamma_1} & a_2\widetilde{\mathsf{S}}_2^{\Gamma_1\Gamma}\,\mathsf{P} \\ a_2\mathsf{P}^{\mathsf{T}}\,\widetilde{\mathsf{S}}_2^{\Gamma\Gamma_1} & a_2\mathsf{P}^{\mathsf{T}}\,\widetilde{\mathsf{S}}_2^{\Gamma\Gamma}\,\mathsf{P} \end{bmatrix} \begin{bmatrix} \boldsymbol{w}_1^j \\ \widehat{\boldsymbol{w}}^j \end{bmatrix} = \begin{bmatrix} \boldsymbol{b}_1^j \\ \boldsymbol{0} \end{bmatrix}$$

with P ensuring the periodicity of $\boldsymbol{w}^j$, $\boldsymbol{w}^j = \mathsf{P}\widehat{\boldsymbol{w}}^j$, and

$$(\boldsymbol{b}_1^j)_k := (a_1 - a_2) \int_{\Gamma_1} \varphi_{1,k}(\boldsymbol{y}) n_j^1(\boldsymbol{y})\, \mathrm{d}\boldsymbol{s}_{\boldsymbol{y}}.$$

Finally, the approximated coefficient matrix Q_h is computed as in (2.1) by substituting w^j by w_h^j.

In [3] the convergence of the above presented method is studied. It can be shown that for regular solutions to (2.4), including the condition

$$(w_1^j, w^j) \in H^\beta(\Gamma_1) \times H^\beta_{\text{per}}(\Gamma)$$

for $\beta \in (1, 2]$, it holds

$$\max_{i,j} |\mathsf{Q}_h[i,j] - \mathsf{Q}[i,j]| \leq c h^{2\beta - 1}, \tag{2.5}$$

where h denotes the discretization parameter, see [3] for details.

3 Numerical experiments

In this section we present numerical experiments to validate the above described boundary element technique for the computation of effective coefficients. We consider three different inclusions, namely a sphere, a cube, and a rotated Fichera corner (see Figure 3.1a) placed in the centre of the cell $Y = (0, 1)^3$. The material parameters are chosen as $a_1 := 1$, $a_2 := 10$. Because the analytical solutions $\mathsf{Q}_\bullet$ are not known, we consider the matrices computed on the finest discretization

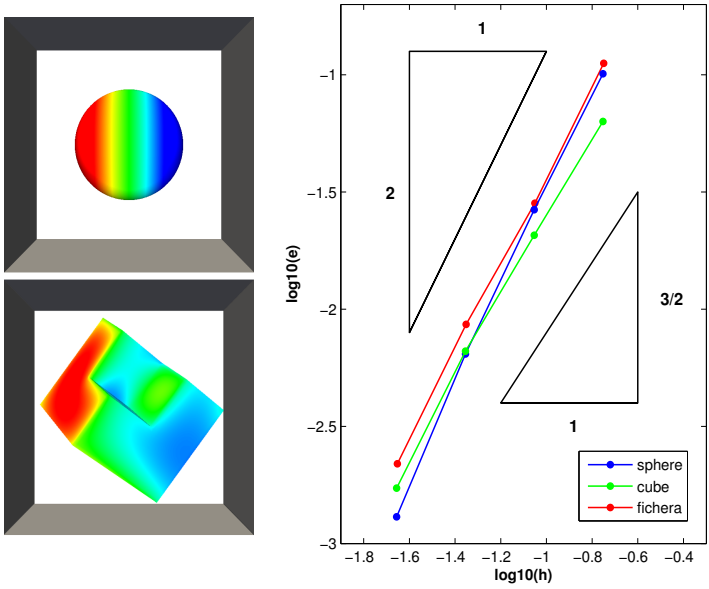

(a) Different inclusions. (b) 3D.

Fig. 3.1. Convergence graphs for 2D and 3D experiments.

level exact and evaluate the estimated order of convergence accordingly. The finest level matrices for the respective inclusions read

$$\mathsf{Q}_{\text{sphere}} = \operatorname{diag}(9.1819, 9.1819, 9.1819),$$
$$\mathsf{Q}_{\text{cube}} = \operatorname{diag}(8.3998, 8.3998, 8.3998),$$
$$\mathsf{Q}_{\text{fichera}} = \begin{bmatrix} 8.4830 & -0.0182 & -0.0791 \\ -0.0182 & 8.5758 & -0.0170 \\ -0.0791 & -0.0170 & 8.5381 \end{bmatrix}.$$

Results of the experiments are summarized in Table 1, where we denote by E the number of elements on Γ (and choose similar discretization parameter for the inclusion), by $e_\bullet^h$ we denote the error in the maximum norm (2.5) with respect to the finest approximation. The estimated order of convergence eoc $:= e_\bullet^h / e_\bullet^{h/2}$ roughly ranges between $2^{3/2} \approx 2.83$ ($\beta \approx 5/4$) and $2^2 = 4$ ($\beta \approx 3/2$) consistently with the theory. The convergence results are also depicted in Figure 3.1b.

Acknowledgements

The theoretical part of the presented boundary element method for homogenization has been done jointly with D. Lukáš, J. Bouchala, and M. Theuer and

the resulting paper [3] has been submitted to Jimp. Except for the 3D numerical results presented here, it includes 2D experiments performed in a MATLAB code.

The 3D numerical experiments have been implemented in the C++ library BEM4I, which is an cooperation with M. Merta at the National Supercomputing Centre IT4Innovations. In its current state, BEM4I supports boundary element solvers for the 3D Laplace, Helmholtz, Lamé, and wave equations. Results achieved by utilizing the library have been recently presented at

- Modelling 2014, Rožnov pod Radhoštěm, Czech Republic,
- ENGOPT 2014, Lisboa, Portugal,
- Söllerhaus Workshop on Fast BEM 2014, Kleinwalsertal, Austria,
- CMAM 2014, Strobl, Austria,
- ICNAAM 2014, Rhodes, Greece,
- SNA 2015, Ostrava, Czech Republic,
- EASC 2015, Edinburgh, United Kingdom,
- HPCSE 2015, Soláň, Czech Republic,
- IFIP 2015, Sophia Antipolis, France,

and published in [3, 4, 10] with more publications under review or in preparation.

References

1. Allaire, G. Homogenization and two-scale convergence. *SIAM J. Math. Anal. 23*, 6 (Nov. 1992), 1482–1518.
2. Cioranescu, D., and Donato, P. *An Introduction to Homogenization.* Oxford lecture series in mathematics and its applications. Oxford University Press, 1999.
3. Lukáš, D., Bouchala, J., Theuer, M., and Zapletal, J. The boundary element method for homogenization. *Numerische Mathematik* (submitted).
4. Merta, M., and Zapletal, J. Acceleration of boundary element method by explicit vectorization. *Advances in Engineering Software 86* (2015), 70–79.
5. Papanicolau, G., Bensoussan, A., and Lions, J. *Asymptotic Analysis for Periodic Structures.* Studies in Mathematics and its Applications. Elsevier Science, 1978.
6. Rjasanow, S., and Steinbach, O. *The Fast Solution of Boundary Integral Equations.* Mathematical and Analytical Techniques with Applications to Engineering. Springer, 2007.
7. Sauter, S., and Schwab, C. *Boundary Element Methods.* Springer Series in Computational Mathematics. Springer, 2010.
8. Steinbach, O. *Numerical Approximation Methods for Elliptic Boundary Value Problems: Finite and Boundary Elements.* Texts in applied mathematics. Springer, 2008.
9. Tartar, L. *The General Theory of Homogenization: A Personalized Introduction.* Lecture Notes of the Unione Matematica Italiana. Springer, 2009.
10. Čermák, M., Merta, M., and Zapletal, J. A novel boundary element library with applications. In *Proceedings of ICNAAM 2014* (2015), T. Simos and C. Tsitouras, Eds., vol. 1648 of *AIP Conference Proceedings.*

Different Metods of Optical Fibers for Use in Interferometric Arrangements

Jakub Cubik

Department of Telecommunications, FEECS,
VŠB – Technical University of Ostrava, 17. listopadu 15, 708 33 Ostrava – Poruba
jakub.cubik@vsb.cz

Abstract. Nowadays, the interferometric sensors belong to the one of the most accurate, thanks to its great sensitivity. Due to these features and the ability to measure phenomena such as temperature, strain, level, flow, vibration, stress, etc. This article was focused on composition of fiber-optic interferometer, especially Michelson type. Michelson was performed by two arms, where one suitable for measurement and second serving as reference. When light comes through interferometer, in ideal case, phase of light was shifted in measure arm and second arm was unchanged. When phases recombining at the end of the sensor interference, which was generate by the interferometer, are proportional to the measured value.
Issue of these applications was laying and fixation of fibers in real environment. It was different in approach for measure and reference arm. Cannot be accessed in a uniform way. Reference arm have to be separate from measurand, but second arm was strictly affected. These fixations (isolation) may be an unlimited amount. This paper was targeted in conventional construction methods of installation. Such as aluminum tube, flexible PVC tube, double sided tape, steel clinch, PVC strip, PVC strip filled by silicon and superglue.

Keywords: Michelson, Interferometer, Optical, Fibers, Methods, Vibration,

1 Introduction

The possibility to guide light through reflection, first demonstrated in 1840, resulted in much progress in the field of fiber optics. Nowadays, it is common the use of light for high-speed data transmission in backbone networks and slowly approaching a state where everyone will have optical fiber reaching up to the living space (so called FTTH fiber-to-the-home). With the development of fiber optics for data transmission another field of interest was developing simultaneously. The field of fiber optic sensors did not experience such a rapid rise, but now there is a great interest in this area. Interest in optical sensors is primarily due to the possibility to measure with high sensitivity over a long distance and also the fact that the optical fiber is a dielectric.

© M. Krátký, J. Dvorský, P. Moravec (Eds.): WOFEX 2015, pp. 522–527.
VŠB – Technical University of Ostrava, FEECS, 2015, ISBN 978-80-248-3787-1.

Optical fiber sensors are generally divided into two groups. The intensity sensor evaluates the change in light intensity depending on the measured variable, while the phase sensor evaluates the phase change of the light beam. The intensity sensors are usually used for evaluating displacements or other physical phenomena affecting the fiber. Phase sensors also called interferometers are using phase change of light in one part of the measuring system (measure arm), compared with unchanged phase in reference part (reference arm). By comparing these phase differences, variable acting on the fiber can be measured with extreme precision. These sensors are more accurate than intensity sensors, but at the cost of a higher price and therefore are mainly used for complex applications requiring accuracy and dynamic range [1].

Many different types of interferometers, including Fabry-Perot, Sagnac, Michelson, Mach-Zehnder has been introduced. This article uses a Michelson-type interferometer.

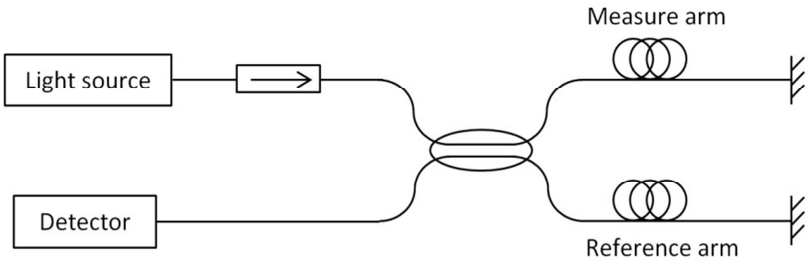

Fig. 1. Basic scheme of Michelson interferometer

In the case of Michelson interferometer the light source, which is protected against back reflection by using isolator, is divided between two arms terminated by mirrors. One arm acts as a measure arm and is directly exposed to the measurand, while the second arm act as a reference experiencing constant environment without being affected by the measured value. Division of the light and its merging occurs at the same coupler. The signal is further propagated to the optical detector, where it is converted into electric current corresponding to the measurand. Visibility of interference depends on relative intensity of measuring and reference beam, their relative state of polarization and their mutual coherence. In optimal case, relative intensity and state of polarization are equal and the difference of optical path length between measure and reference arms is lower than coherence length of source light [2].

This publication relies on previous research performed by our research team [3,4,5] and on the article [6] Interferometric sensor based on the polarization-maintaining fibers in particular.

Other possible applications that use interferometry are known. These experiments, however, are based on different principles, use other components or focus on the measurement of other phenomena. For example, in the article In-Fiber Quasi-Michelson Interferometer for Liquid Level Measurement with a Core-Cladding Modes-Fiber End-Face Mirror was a quasi-Michelson interferometer used to measure liquid level. The article A Single-Mode Fiber Sensor Based on Core-Offset Inter-

Modal Interferometer discusses the use of conventional single-mode fiber and a very small portion of the multi-mode fiber.

In the reference [7] Fiber Bragg Grating Vibration Sensor with DFB laser diode, bragg grating is used as a sensing element. This fiber optical sensor is a possible alternative to the interference sensor, but exhibits lower sensitivity to the measured phenomenon.

2 Experimental setup

As mentioned above, the article deals with the use of fiber optic Michelson interferometer as a sensor of the impact of different objects on different surfaces. The entire diagram is composed of polarization-maintaining components to achieve higher sensitivity. As the radiation source DFB laser with a wavelength of 1550nm and a spectral line width of 0.03 nm was used. The operating point of the laser was kept by Thorlabs temperature and current controller. The diode is pigtailed with PM fiber terminated by inappropriately keyed FC/APC connector. Inappropriately keyed connector is compensated by the polarizer at the output of the laser. The suitability of this solution was verified by measuring the polarization and visualization on the Poincaré sphere. Due to the absence of the polarization-maintaining coupler 2x2 was replaced by circulator, which also serves as isolator. Further, the light is brought into the 1x2 coupler, which distributes the light beam into two arms equally. The arms were formed by 2 m long polarization-maintaining fibers terminated with mirrors. This fiber optic mirror reflects incoming light directly back, with very low optical loss. Reflected light recombines in the coupler gets on InGaAs photodetector through the circulator, where it is converted into the electrical signal. The electrical signal is further processed as shown in Figure 3. The picture 2 depicts the final measurement setup for this experiment.

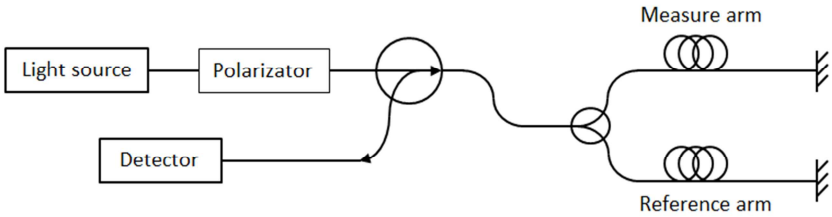

Fig. 2. Real configuration of Michelson interferometer

An electrical signal was fed to the LC high–pass filter with a cutoff frequency at 8 Hz via 50 Ω coaxial cable in order to suppress DC component. After that was fed into a measuring card NI USB–6210 with sampling rate up to 250 kS/s. The card was capturing voltage on analogue input using the application written in LabView development suite. The application also performs a discrete Fourier transformation so the voltage was transferred into the frequency domain. Hanning window function was used in our case.

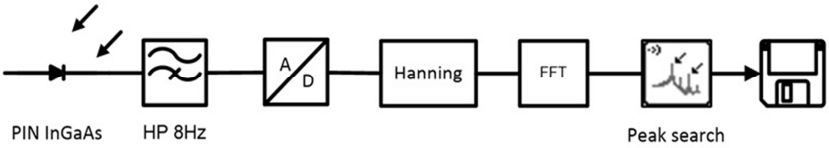

Fig. 3. Schematic diagram of electrical signal processing.

The reference arm was placed in the polystyrene box during the whole measurement. The measure arm was directly exposed to the measured phenomenon and was placed on the different surfaces, where selected objects had fallen. The first case was a concrete floor covered with linoleum the second was a pane of glass was inserted in a metal frame, which was shielded from external influences by means of rubber. The last measured surface was wooden board placed on a metal frame, from which was also shielded using the rubber.

The test measurement was performed with loudspeaker located one meter above the measure arm and it was powered by signal generator Hameg HMF2550. The rectangular signal with frequency of 200 Hz and with 50% duty cycle was used. Frequency spectrum from this measurement can be found in Figure 4.

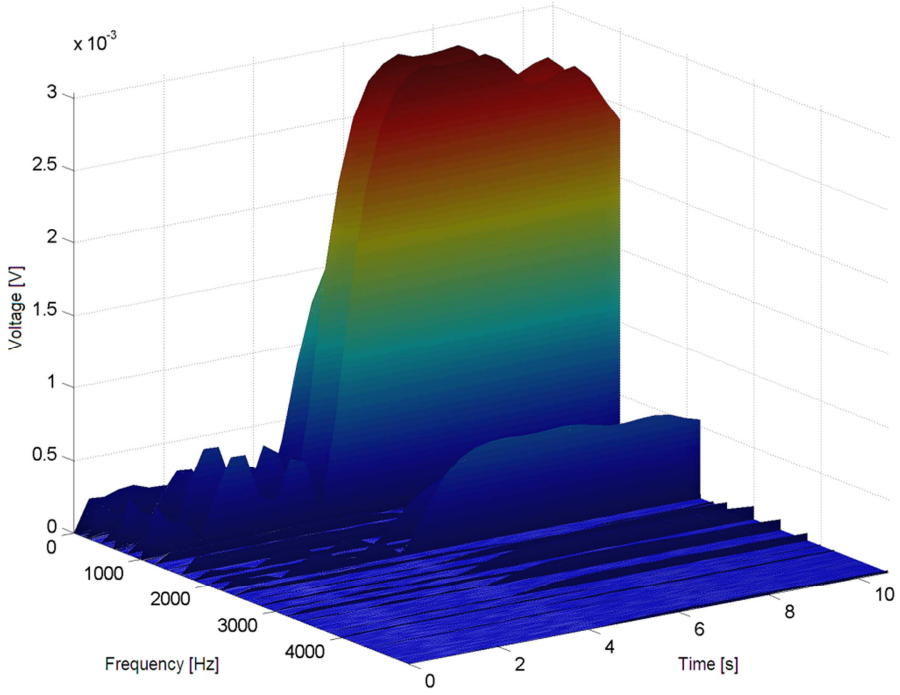

Fig. 4. Reference measurement on 200Hz

The measuring arm on all three surfaces was influenced with three selected objects by impingement on the surface from a height of one meter. These four objects were a tennis ball weighing 56g and diameter of 63mm, plasticine ball with a diameter of 3 cm, table-tennis ball weighing 2g and diameter of 37,5mm and weight of 20 grams and the last object was a steel ball with a diameter of 8 mm and weight of 2g. Each measurement was repeated 10 times for statistical reasons. Results of measurements and evaluation are shown below.

3 Results and discussion

As mentioned above, the first measurement was verification of test setup by an acoustic signal from the speaker. This measurement showed that the measuring set was able to measure a large frequency range. Thanks to the low-pass filter frequencies below 10Hz were excluded from the measurement. Figure 5 shows the spectrum of the 10 attempts in case of impact of steel ball on the pane of glass. The x-axis is frequency in Hertz and the y-axis is plotted the voltage in volts. The x-axis represents the frequency in Hertz and the y-axis voltage in Volts. For better interpretation of the data are then converted to voltage level in decibel Volts. In tables 1-3 medians of voltage level and frequency for 10 repeated measurements can be found. Values were transferred to the tables to 3 decimal places. For each case the standard deviation is further calculated. Tables with results are situated in annex, in case of compliance with requirement.

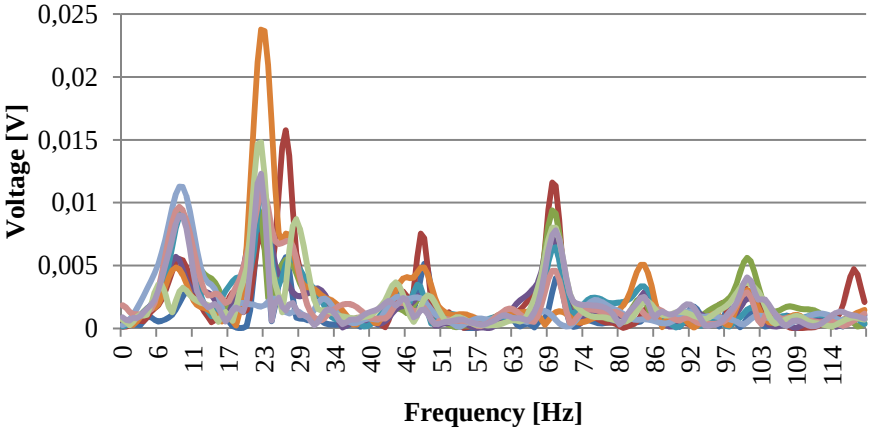

Fig. 2. The measured spectra at the time of impact of steel ball on the pane of glass.

4 Conclusion

Measurements published in this article points out the dependence of frequency spectra of various objects impacting on surface. It can be stated that interferometric measurements, fiber optic Michelson interferometer in particular, are very sensitive

and has wide frequency range of the measurement. The advantage was scheme with polarization-maintaining fibers. This improvement over the use of conventional fibers had a valuable contribution to the sensitivity of the apparatus. This measurement should prove the recognisability of individual objects, through comparing their frequency spectra in time. In the near future it will be necessary to better stabilize the amplitude of each frequency leading to a lower standard deviation. The aim is to build a measurement set, which would be able to measure virtually constant amplitude and frequency spectrum on repeated measurements. Due to this fact, a variety of objects could be detected using a software application.

References

1. Krohn, D., [Fiber optic sensors: fundamentals and applications], Instrument Society of America, Research Triangle Park, NC (1992).
2. López-Higuera, J.M. [Handbook of Optical Fibre Sensing Technology], J.Wiley and Sons, New York, 227-245 (2002).
3. Cubik, J., Kepak, S., Doricak, J., Vasinek, V., Jaros, J., Liner, A., Papes, M., and Fajkus, M., "The Usability Analysis of Different Standard Single-Mode Optical Fibers and its Installation Methods for the Interferometric Measurements." Advances in Electrical and Electronic Engineering 11 (6): 535-542 (2013).
4. Vasinek, V., Cubik, J., Kepak, S., Doricak, J., Latal, J., and Koudelka, P., "Mach-zehnder interferometer for movement monitoring," Paper presented at the Proceedings of SPIE - the International Society for Optical Engineering, Vol. 8370, 83700R (2012).
5. Kepak, S., Cubik, J., Doricak, J., Vasinek, V., Siska, P., Líner, A., and Papes, M., "The arms arrangement influence on the sensitivity of Mach–Zehnder fiber optic interferometer, " Proceedings of SPIE - The International Society for Optical Engineering Vol. 8697, 877415-877415-8. DOI: 10.1117/12.2017305.
6. Cubik, J., Kepak, S., Doricak, J., Vasinek, V., Líner, A., and Papes, M., "Interferometric sensor based on the polarization-maintaining fibers," Paper presented at the Proceedings of Czech-Polish-Slovak Optical Conference, (2012).
7. Siska, P., Brozovic, M., Cubik, J., Kepak, S., Vitasek, J., Koudelka, P., Latal, J., and Vasinek, V., "Fiber Bragg Grating vibration sensor with DFB laser diode," Proceedings of SPIE - The International Society for Optical Engineering Vol. 8697, 86971P-86971P-9. DOI: 10.1117/12.2010467

Research of Ageing of Attenuation Parameters of Optical Coupler

Lukas Bednarek

Department of Telecommunications, FEECS,
VŠB – Technical University of Ostrava, 17. listopadu 15, 708 33 Ostrava – Poruba
lukas.bednarek@vsb.cz

Abstract. Ageing of optical components is a very topical issue nowadays. Mainly, multiple increase of powers in WDM systems caused accelerate research in this area. This article deals by the optical coupler 1:2 with split ratio 50/50 specifically. Research is focused on the attenuation parameters mainly. The measurement was performed at the wavelengths 1310 nm and 1550 nm. To accelerate of the ageing of the optical coupler were used gamma radiation from ^{60}Co, which emit two gamma-rays with energies 1.17 MeV and 1.33 MeV. Three series of the irradiation were performed until later and the coupler received a total dose of the radiation 34.32 kGy.

1 Introduction

Due to rapid an increase powers and the number of channels in WDM systems, there is increasing need to examine the ageing of optical components. In this article, I deal by attenuation or power parameters of the optical coupler 1:2 with split ratio 50/50 specifically. The examined parameters are insertion losses of the individual branches, precise split ratio, total losses, homogeneity of the losses and directionality (crosstalk attenuation). Measurements were made at the wavelengths 1310 nm and 1550 nm. This coupler passed by three series of the irradiation with magnitudes of received doses 5 kGy, 20.15 kGy and 34.32 kGy. The first part of the article is focused on describe of the optical coupler. Methods of measurement and calculation parameters are shown in the next chapter. Finally, the measurement results of the optical coupler are summarized.

2 Optical coupler

The optical coupler is a passive element which serves to merge of the optical powers from several optical fibers. Conversely, the optical splitter is used for distribution of the powers to several optical fibers. Coupler and splitter can be the one component, the difference is only in the direction of transmitting or receiving of the optical power.

© M. Krátký, J. Dvorský, P. Moravec (Eds.): WOFEX 2015, pp. 528–533.
VŠB – Technical University of Ostrava, FEECS, 2015, ISBN 978-80-248-3787-1.

Optical couplers are classified according of several criteria. The basic division is on singlemode and multimode. Singlemode couplers can be divided on power-split couplers and WDM couplers. WDM couplers are capable split or merge certain wavelengths of the light. The most commonly used couplers or splitters are power-split couplers, which divides powers according of the split ratio between the output fibers. Variants of these type couplers are 1:2 with split ratios 50:50 to 1:99 in various combinations. Then 1:4, where split ratio is approximately 25:25:25:25. The coupler 1:8, where split ratio is the same between all fibers. The couplers 1:16 and 1:32, where are a large insertion losses, therefore these couplers are used in large passive networks only.

Split or merge proceeds in the merge (fused) region. The principle is simple, in this region occurs the zoom of the cores of fibers, thereby changing the diameter of the cores by pulling out of the fibers. Consequently, the normalized frequency is changed. MFD alias mode field diameter interferes to adjacent fibers, therefore powers begin divide. This proceeds in the coupling area (coupling region). For control of the split ratios of the couplers 1:2 are used different distance of the cores of fibers, diameters of the cores and wavelengths of the light. This can work at the couplers 1:4 also, but here mostly uniform split ratios are used.

3 Description of the individual parameters

3.1 Insertion loss

The insertion losses are losses in the individual trace, i.e. from the input to the individual outputs. These losses may be different for individual outputs due to different split ratios. They are given in dB for each output separately. The equation 1 displays the mathematical expression.

$$IL_{12} = -10 \log \frac{P_2}{P_1} \tag{1}$$

Where IL_{12} is insertion loss in dB for the trace from input to output 2, P_1 is the input power in W and P_2 is the output power at the output 2 in W.

3.2 Split ratio

The split ratio expresses the distribution of power to all output fibers. It is expressed in % for each output separately and logically the sum of all the split ratios must be 100 %. The most commonly used split ratio is 50:50 for coupler 1:2, but usable combinations are 30:70 and 10:90 also. Uniformly distributed split ratios are used mainly for couplers with multiple outputs. It should be noted that the split ratios are never absolutely exact, for example, coupler carries the designation of split ratio 50:50, and in fact we can measure small variations in this ratio. This is due to the production, each coupler is different, and we cannot make two absolutely identical couplers. The equation 2 shows the calculation.

$$SR = \frac{P_2}{P_2+P_3}100 \quad (2)$$

Where SR is the split ratio in %, P_2 is the output power at the output 2 in W and P_3 is the output power at the output 3 in W.

3.3 Total losses

Total losses alias residual attenuation are losses of power in itself coupler. Values are given in dB after the calculation of the measured powers. Ideally, these losses should be zero, but this is not possible in practice. The calculation is described by equation 3.

$$TL = -10\log\frac{\sum P_j}{P_1} \quad (3)$$

Where TL are the total losses in dB, P_1 is the input power in W and Σ Pj is the sum of output powers in W.

3.4 Homogeneity of the losses

Homogeneity of the losses is the difference between the maximum insertion loss at any output of the coupler and minimal insertion loss at any output of the same coupler. This means that calculation is simple for the coupler 1:2, but for the couplers with a plurality of output is first necessary determine the maximum and minimum insertion losses. It is expressed in dB, and should be minimized. Equation 4 indicates the calculation.

$$\mathrm{HL} = \mathrm{IL}_{\max} - \mathrm{IL}_{\min} \quad (4)$$

Where HL is the homogeneity of losses in dB, IL_{max} is a maximum insertion loss in dB, IL_{min} is minimal insertion loss in dB.

3.5 Directionality

Directionality alias attenuation of crosstalk expresses attenuation between two adjacent inputs or outputs. It is expressed in dB and directionality is needed be the greatest, because coupler did not work properly at low crosstalk attenuation, instead of the distribution of power from the input side to the output side, there is a partial radiated of power at the input side of the coupler, and thus to increase of residual and insertion losses. The calculation is in equation 5.

$$D = -10\log\frac{P_{23}}{P_1} \quad (5)$$

Where D is the directionality in dB, P_1 is the input power in W a P_{23} is the output power in W, however measured with a source connected to the output 2 and the detector at the output 3.

4 The method of measurement of powers of optical coupler

The optical couplers have different connectors than laser and power meter, therefore it is necessary to perform measurements in two stages. First, it is needed measured input power and the individual output powers of the output fibers subsequently. All measurement is not particularly challenging because it is the readout of data from the power meter only and the subsequent recalculation of all powers on the above parameters. Therefore, the first phase is the measurement of the power that enters to the coupler from the laser. Scheme of this measurement is shown in Figure 1.

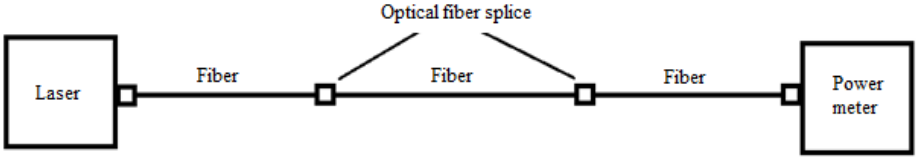

Fig. 1. Scheme of the measurement of the input power

This scheme of measurement of power is chosen deliberately, because measured input power contains attenuation of two optical fiber splice and the connectors of the individual components, thereby we eliminates possible distortion of measured and calculated values.

The second phase is almost identical scheme, only the middle fiber is replaced by the measured coupler. This coupler is connected to the laser by the input fiber and power meter is successively connected to the individual output fibers.

5 Results

The graph of insertion losses is shown in Figure 2 for the wavelength 1310 nm. Abbreviation AI means measurement with time interval after the end of irradiation. Abbreviation DI is measurement immediately after removal from irradiation facility. Insertion loss was 3.45 dB and 3.5 dB for branch 1 and branch 2 before irradiation. All insertion losses were increased after first irradiation. The second irradiation decreased insertion loss for measurement after the end of irradiation. Conversely, insertion losses increased for measured immediately after irradiation. After the third irradiation, the insertion losses were 3.03 dB and 3.29 dB for the given measurement branches after the end of irradiation. Values were 4.05 dB and 3.65 dB for measurement during irradiation.

Figure 3 shows a graph of insertion losses for the wavelength 1550 nm. Insertion losses were 3.28 dB and 3.43 dB for the given branches before irradiation. The course of the insertion losses is similar as in the case of the wavelength 1310 nm. After the third irradiation, the values were 3.17 dB and 3.19 dB for the given branches when measurement after the end of irradiation. In the case of measurement during irradiation, values were 3.95 dB and 3.66 dB.

Split ratios were 51/49 and 50/50 for the given wavelengths before irradiation. The first irradiation changed split ratio at the wavelength 1310 nm on 52/48. The split ratio was changed at the wavelength 1550 nm on the value 52/48 by the second irradiation. The third irradiation changed split ratio on the values 51/49 and 50/50 for the given wavelengths.

The total losses were 1.14 dB and 0.97 dB for the given wavelengths before irradiation. The first irradiation improved total losses on both wavelengths. The values were 0.89 dB and 0.65 dB. The second dose of radiation improved the values of this parameter again. Calculated values were 0.42 dB and 0.26 dB. Last irradiation showed the best results of the total losses. Calculated values were 0.14 dB and 0.17 dB for the given wavelengths.

The values of homogeneity of the losses were 0.1 dB and 0.07 dB for the wavelengths 1310 nm and 1550 nm before irradiation. The first irradiation worsened homogeneity of the losses on values 0.31 dB and 0.08 dB for the given wavelengths. Also, the second irradiation had worse values of homogeneity of the losses and it 0.4 dB and 0.33 dB. The last irradiation improved this parameter on values 0.26 dB and 0.08 dB.

The last examined parameter was crosstalk attenuation. This parameter had values 57 dB and 54 dB for the wavelengths 1310 nm and 1550 nm before irradiation. First irradiation slightly improved values on 58 dB and 56 dB. The second irradiation worsened this parameter to the value 52 dB at the wavelength 1310 nm. The third irradiation changed values of directionalities on 55 dB and 58 dB for the given wavelengths.

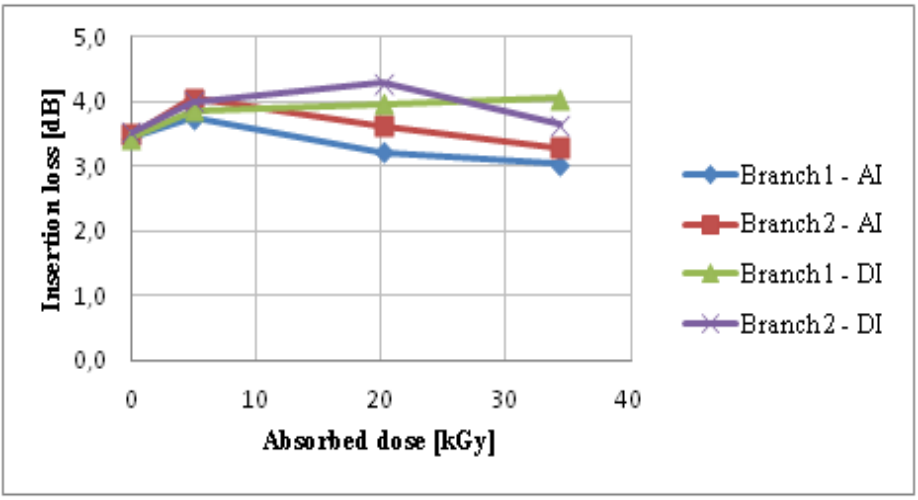

Fig. 2. Insertion losses during irradiation (DI) and after the end of irradiation (AI) for the wavelength 1310 nm

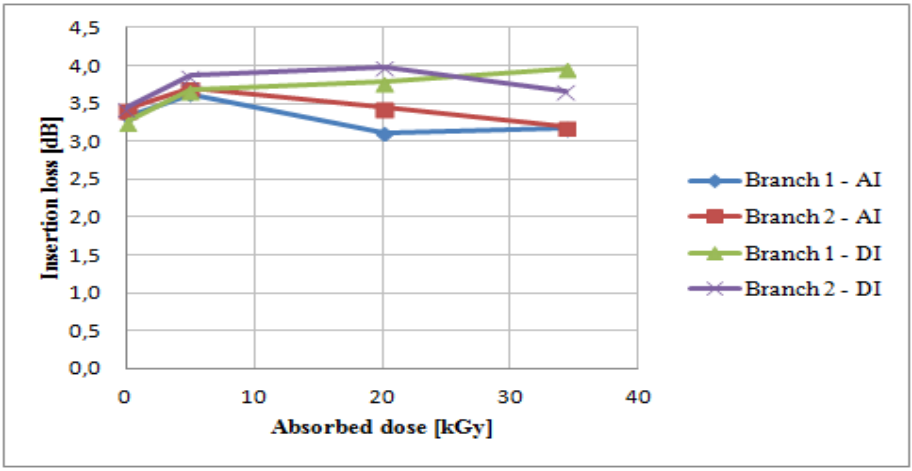

Fig. 3. Insertion losses during irradiation (DI) and after the end of irradiation (AI) for the wavelength 1550 nm

6 Conclusion

The paper dealt by the power parameters of the optical coupler. The first part described the principle of the optical coupler and then it followed example calculation of individual parameters. The last section summarized the results of this research.

The results show, that the effect of gamma radiation on the optical coupler is not what is expected. It was assumed that the parameters will worsen, however, this did not occur. Therefore, it is necessary to perform a further series of irradiation with higher doses of gamma radiation.

However research of ageing of optical components will not be carried out only using gamma rays, but to accelerate this process will be used high optical powers and thermal stress.

7 References

1. Bednarek L., Marcinka O., Perecar F., Papes M., Hajek L., Nedoma J., Vasinek V., *The ageing process of optical couplers by gamma irradiation*, published at the conference Photonic Fiber and Crystal Devices: Advances in Materials and Innovations in Device Applications IX, San Diego (USA), August 2015

2. Vasinek V., Hajek L., Bednarek L., Vanderka A., Hlavinka T., Marcinka O., *Influence of gamma radiation on optical fibers and devices*, published at the conference International Conference on Photonics Solutions, Hua Hin (Thailand), July 2015
3. Vasinek V., Siska P., Bednarek L., Latal J., Koudelka P., Marcinka O., *Ageing of fiber optical devices* In: Next-Generation Optical Communication: Components, Sub-Systems, and Systems IV, 2015, DOI: 10.1117/12.2087165.

Deformation measurement with Bragg gratings and analysis of multiplexing techniques for quasi-distributed measurement

Marcel Fajkus

Department of Telecommunications, FEECS,
VŠB – Technical University of Ostrava, 17. listopadu 15, 708 33 Ostrava – Poruba
marcel.fajkus@vsb.cz

Abstract. I am acted on department of telecommunications under prof. RNDr. Vladimir Vašinek CSc. in fourth year of doctoral studies. In my studies I am interested in optical sensors based on Fiber Bragg Gratings.
In cooperate with Faculty of Civil Engineering we realized measurement of deformation of cement fiber composite with standard resistive strain gauge, Fiber Bragg Gratings and DSTS (Distributed Sensor of Temperature and Strain). Special cement fiber composite provide greater flexibility and then we could apply higher deformation. We demonstrate the applicability of FBG and DSTS sensors in civil engineering.

I spend 20 days of internship in Ankara University in Turkey, in Electrical and Electronics Engineering Department by Assoc. Prof. Isa Navruz. We have devoted to design of the optical sensor. Mainly I worked on my theses on the theme Quasi-distributed sensors based on Fiber Bragg Gratings.

Furthermore I am interested in wireless networks too. I measured quality of speech, realized in my own wireless network which is created by software project OpenBTS and universal software controlled transceiver.

1 Measurement of deformation cement sample with FBG

Colleagues from faculty of civil engineering proposed special cement fiber composite which is more flexible as standard cement composite. This special composite is resistant to cracking and breaking. We made experimental beam with dimensions 165x12x10 cm with two steel rebbars to prevent the rapid fracture of the sample during measurement. In this sample we placed two FBGs with central wavelength 1549.538 nm and 1555.138 nm. One FBG with secondary polyamide protection was placed into composite direct and second FBG at first was inserted into plastic tube with internal dimension 0.3 mm and length 183.9 mm and then it was inserted into beam. Next we used resistive strain gauge for reference measurement.

Loading of the beam was continuous and very slowly. In the Fig. 1 blue line shows recorded progress of deformation by resistive strain gauge. Red resp. green line shows measurement of deformation by FBG resp. FBG in plastic tube. It can be seen that the course of deformation has the same tendency at the all sensors but strain to strain gauges

© M. Krátký, J. Dvorský, P. Moravec (Eds.): WOFEX 2015, pp. 534–539.
VŠB – Technical University of Ostrava, FEECS, 2015, ISBN 978-80-248-3787-1.

are approximately double then values on FBG for each the step. This could be due to differences in the voltage waveform in a region close to the reinforcing rod and the surface of the concrete beam. A difference in the values of individual FBG sensors is most likely due to the use of a protective tube on one fiber.

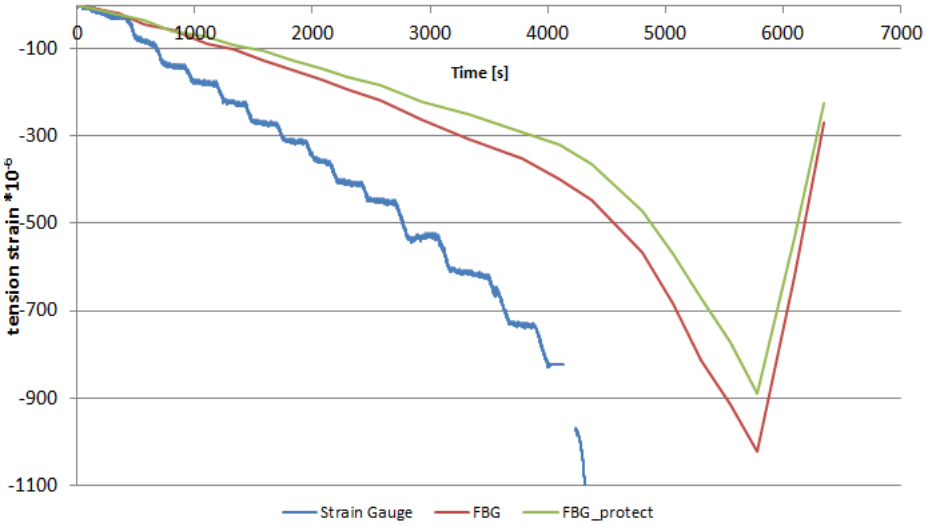

Fig. 1. Deflections in thirds and half of the beam and the corresponding load force

FBGs reach high sensitivity for measurement very small deformation and very high strength which is higher as by standard resistive strain gauge. [1]

2 Measurement of deformation cement sample with DSTS

We used single mode optical fiber with secondary protection for measurement deformation with DSTS system. Optical fiber embedded to cement beam was divided into eight sections (Fig. 2). In the each section was optical fiber with length 1 m. Between sections was ring of optical fiber long 133.7 cm.

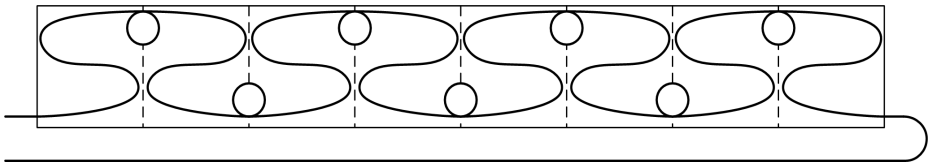

Fig. 2. Deployment of the single-mode optical fiber in the sample

Fig. 3 show results of measurement. Lines represent strain of beam for three various values of applied deformation. In sample was created 8 measuring loops. The figure shows that the greater deformation arise in the middle of beam and the smaller on the margins. [2]

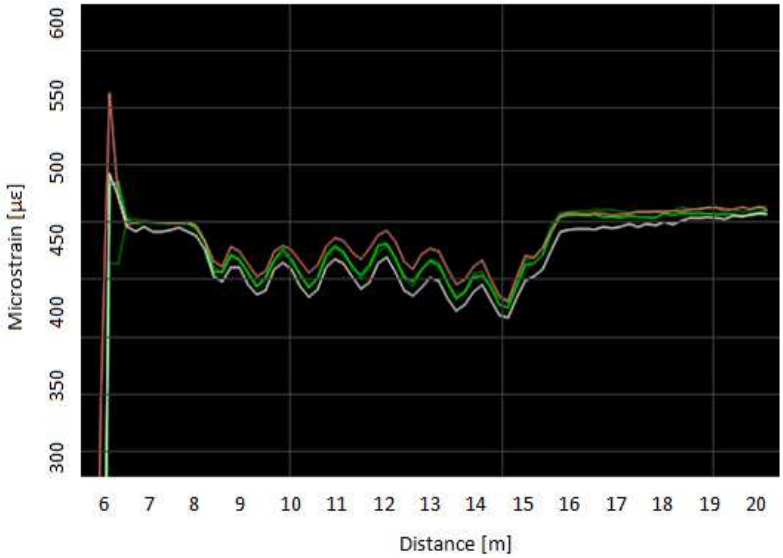

Fig. 3. Measured shifts of microstrain in 8 sensory loops

DSTS system measure Brillouin Frequency shift. This frequency depends on acted temperature and deformation. Actually, I have worked on measurement deformation with DSTS system. I have glued optical fiber on metallic surface with dimensions 1100x1100x3 mm. I created various configurations (Fig. 4). I bended this surface with optical fiber and I measured deformation with DSTS. Various configurations shows various sensitivity on bending of surface. I am going to analyze measurement dates and I am going to search how longitudinal and transverse deformation act to glued optical fiber and how deformation act on circle and arc etc.

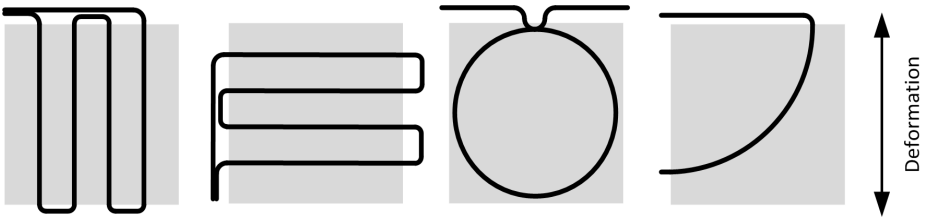

Fig. 4. Configuration of optical fiber for measurement deformation with DSTS system

3 Internship in Turkey

I spend 20 days of internship in Ankara University in Turkey, in Electrical and Electronics Engineering Department by Assoc. Prof. Isa Navruz since 26.3.2015 to 14.4.2015. We simulated optical sensors in software environment OptiBPM by OptiWave. Mainly, I worked on my theses on the theme Quasi-distributed sensors based on Fiber Bragg Gratings. Time (TDM) or wavelength (WDM) multiplexing technique is

used for quasi-distributed measurement with FBGs. WDM is the simplest technique how to place on one optical fiber more FBGs. Each FBG has a different central wavelength. In optical spectral analyzer are individual peaks separated in frequency domain. Shift of wavelength present information about measurement value. TDM is based on the finite speed of light. Into evaluation part come individual pulses from FBGs and these pulses are separated in time domain. Spectral part of these pulses gives information about measurement value as temperature or deformation.

We determined the procedure for design WDM and calculation of the maximum number of FBGs in the optical fiber. This maximum number depends on spectral width of source of light and spectral width of individual FBGs, measuring range and type of measured value. For TDM we analyzed effect of time condition, attenuation, crosstalk and chromatic dispersion.

Crosstalk is created by multiple reflections between Bragg gratings. Reflected pulses from various FBGs arrive to evaluation part in the same time. Size of crosstalk depends on reflectivity of FBG and number of FBGs in optical fiber. In Fig. 5 is comparing reflected power and crosstalk of first order for reflectivity FBGs -20, -30 and -40 dB. For correct measurement is important that the size of reflected power must be greater than crosstalk. [3]

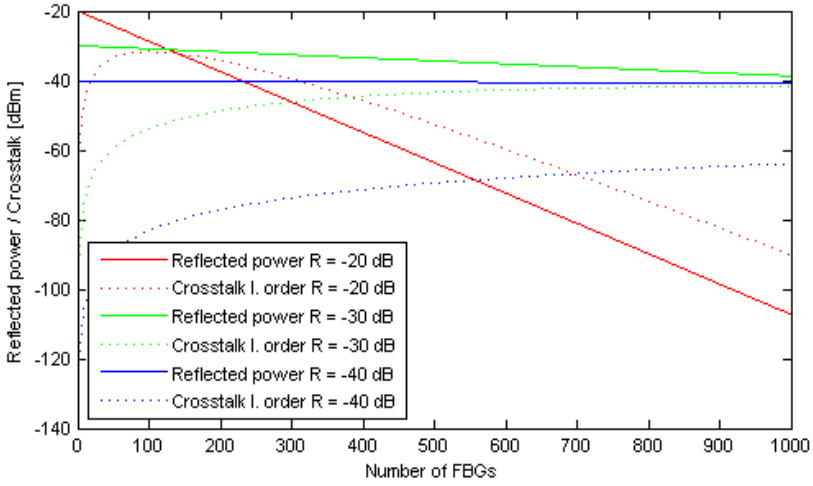

Fig. 5. A comparison of reflected power (Pi) and first order crosstalk (Ci) at various values of reflectivity

4 Quality of speech measurement

With my colleague Martin Mikulec we implemented our own GSM network based on open source project OpenBTS and universal software controller transceiver USRP N210. Scheme of measurement is in Fig. 6. Asterisk PBX playback is used as a mobile terminal. This terminal ensures answering the call and playing original sound sample. OpenBTS provides SW control of transceiver and creates GSM network. SIMENA is

equipment which emulates network parameters as bandwidth, packet loss, delay and jitter. In the right side is Asterisk PBX record which records degraded sounds sample.

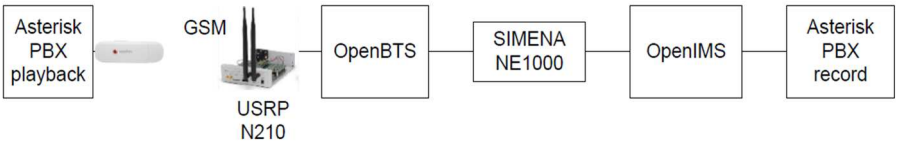

Fig. 6. Scheme of measurement

On this platform we made many measurements in dependent on

- various values of parameters: bandwidth, packet loss, delay and jitter,
- number of active calls (1, 2 and 3 calls),
- to use of cipher (AES-256). [4]

Next, we measured effect of transcoding on degrade speech quality. We were interested in codecs GSM, µlaw and G.729. [5]

5 Matlab server

I have developed Matlab server for our Department of telecommunications. At first phase we will provide it only for our department. Later we will offer Matlab server other departments and faculties in VŠB – TU Ostrava. Matlab server provides sharing of knowledges or informations, mathematical calculations and simulations between students or educators. It is possible to use matlab applications in teaching by students who do not have Matlab or by students who do not work with Matlab.

Matlab server enables to run through web browser programs written in Matlab. The advantage is that user does not have to on your computer matlab installed. This concept is based on toolboxes Matlab Builder JA and Matlab Compiler. This toolboxes generate from matlab program JAVA components. This component is possible run in application server. Application server work as web server. Application server receives parameters from user, runs JAVA components and results send back to user.

In Fig. 7 is web user interface of Matlab Server. In the left part is hierarchy of applications in Matlab server. In the right part is form for input parameters and calculated results.

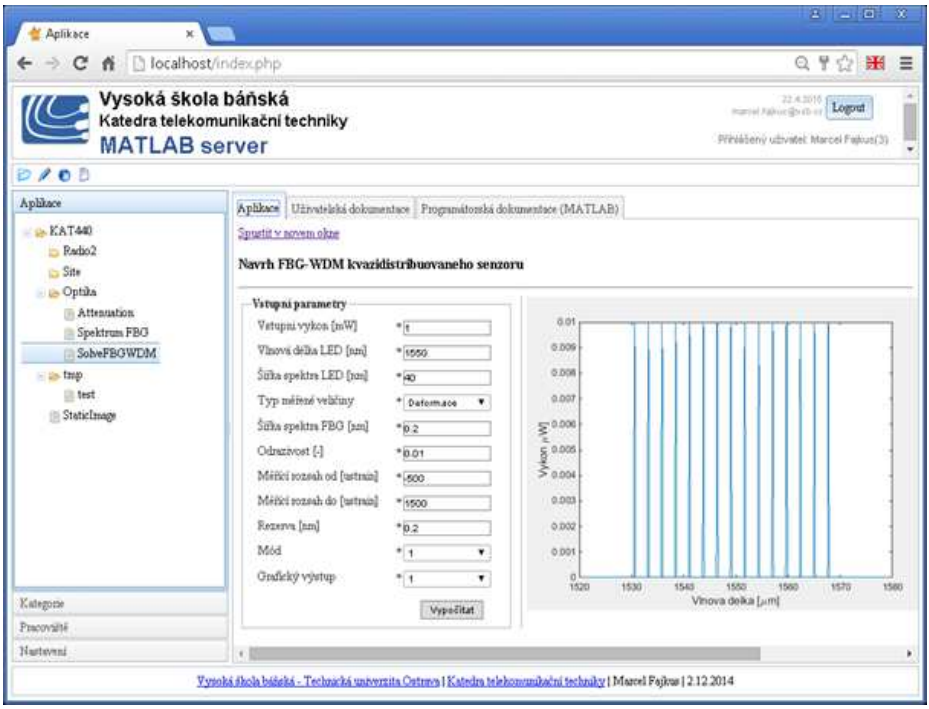

Fig. 7. User interface of the Matlab server

6 References

1. Hurta, J., Fajkus, M., Mec, P., “Application of FBG in the experimental measurements of deformation elements of cement composites“
2. Papes, M., Jaros, J., Fajkus, M., Hurta, J., Liner, A., Hruby, D.,Kajnar, T., Vasinek, V., “Concrete Deflection Measurement Using Fiber Optic Distributed Strain System“
3. Fajkus, M., Kepak, S., Davidson, A., Siska, P., Cubik, J., Vasinek, V., “Capacity of wavelength and time division multiplexing for quasi-distributed measurement using Fiber Bragg Gratings“
4. Mikulec, M., Voznak, M., Fajkus, M., Partila, P., Tovarek, J., Chmelikova, Z., “Building GSM Network in Extreme Conditions“
5. Mikulec, M., Fajkus, M., Voznak, M., “Multiple transcoding impact on speech quality in ideal network conditions“

Software Tool for Prediction and Implementation of QoS in IP Based Networks

Jaroslav Frnda

Department of Telecommunications, FEECS,
VŠB – Technical University of Ostrava, 17. listopadu 15, 708 33 Ostrava – Poruba
jaroslav.frnda@vsb.cz

Abstract. The main contribution of this paper is to describe the application able to predict the quality of Triple play services in the network. Prediction mathematical model is based on results obtained from many performed testing scenarios. Due to the cooperation with Huawei CZ we could verify our results on two the most common network infrastructure vendors (Cisco and Huawei). Based on the proposed model, speech or video quality is calculated with regard to policies applied for packet processing by routers and to the level of total network utilization. The application can not only predict QoS parameters, but also generate the source code of particular QoS policy setting according to the user interaction and apply the policy to the routers in the network. This simulating model implemented in SW tool enables networkers to predict objective QoS parameters of triple play services and to help them in network design.

Keywords: Application, Codecs, E-Model, Policies, QoS, Triple Play, Video, Voice

1 Introduction

Network convergence that took place during the early 90's of the 20th century brought the new network concept based on IP called NGN (Next Generation Network). This concept allowed the transfer of formerly separate services (voice, video and data) by one common network infrastructure. However, this transition had to deal with some difficulties because packet networks based on IP protocol had not been designed to transfer delay-sensitive traffic. The difficulties appeared especially at the transfer of voice. Packet network has to use supplementary mechanisms securing the quality of service during the transmission over the network, able to provide a high-quality interactive communication similar to standard fixed lines (PSTN).

QoS policies used for prioritization of time-sensitive data streams on routers seems to be a one of the techniques for securing at least minimal QoS level in a packet network. The second important factor is network monitoring. Constant network performance monitoring and intervening as needed, keep the impact of network

© M. Krátký, J. Dvorský, P. Moravec (Eds.): WOFEX 2015, pp. 540–545.
VŠB – Technical University of Ostrava, FEECS, 2015, ISBN 978-80-248-3787-1.

behavior on the acceptable level. Therefore, the purpose of the application described in this paper is to provide an effective monitoring tool capable of predicting qualitative QoS parameters according to network status. The application aims to be an alternative to expensive monitoring tools, as well as a helpful tool for designing the network infra-structure and implementation of QoS policies on selected routers.

2 State of the Art

Last decade brought growing interest in multimedia services transfer through packet networks based on IP protocol. Nowadays, voice and video service as a component of Triple play make a significant part of total data sended via the network. Voice as the most sensitive service to an overall network status, depends on many QoS parameters. Particularly, jitter and packet loss have an important impact on voice quality [2], [4]. To achieve the satisfactory voice quality, the network architecture must be designed by using representative congestion management techniques. Congestion management features allow to control congestion by determining the order in which packets are sent out an interface based on priorities assigned to those packets. In order to implement methods for packet classification and prioritization, it is necessary to monitor the QoS parameters by means network measurements. Evaluation of voice service according to the network behavior is based on the simplified version of calculation model based on recommendation ITU-T G.107 (also known as E-model) [6]. This model allows to evaluate the quality of speech, adjusting the model to be suitable especially for packet networks.

But, on the other hand, the video has become the major part of all data traffic sent via IP networks. In general, a video service is a one-way service (except e.g. video calls), so network delay is not such an important factor as in voice service. Analysis of video quality concentrates on the resistance of video codecs to packet loss in the network, which causes artifacts in the video.

Because the inclination to NGN concept is huge, that is why monitoring of impacts on QoS efficiency and evaluation is highly important and necessary in order to secure the competitiveness of any multimedia services provider.

3 Methodology

Nowadays, practically, computer networks are not built only on a homogeneous infrastructure, but they use heterogeneous devices. Due to the cooperation with Huawei we could use network items from both vendors Cisco and Huawei.

Implementation of the computational model was carried out in programming language C#.

3.1 Measured parameters

E-model, defined by Recommendation G.107 by ITU-T [6], was used as an objective evaluation method for voice service. This recommendation also includes a set of recommended values that enable to simplify the calculation. Regarding of QoS in IP networks, transmission bandwidth, packet loss, network delay and variation in latency (jitter) are key parameters [5]. These parameters can be express in two factors used for R-factor calculation, namely in I_D and $I_{E\text{-}EFF.}$ The first parameter I_D represents impairments caused by echo (Echo-cancellation has been solved in ITU-T G.168 recommendation) and by the too long transfer delay. In generally, the factor $I_{E\text{-}EFF}$ represents impairment caused by low bit-rate codecs and actual packet loss ratio of the network. The typical score range of R-factor is from 50 (bad) to 100 (excellent). By keeping all the default values during the calculation, the R-factor reaches a final value of 93.35 [6]. In order to meet user's expectations, the value of 70 or more is needed [6].

The aim of the video measurement was to simulate the effect of packet loss for the video formats MPEG-2 and MPEG-4, to determine the impact on the resulting image using objective methods for measuring the quality of the video. As an objective evaluation method was selected the most common used metric SSIM (Structural Similarity Index) of scale 0-1, where 1 means two identical video sequences.

4 Results

The network topology consists of at first two Huawei routers, than two Cisco routers of about the same performance, four VoIP clients, two Video clients, FTP client and server. In order to simulate voice and video traffic, IxChariot tool from Ixia company was used. QoS policies were implemented on both routers. The level of network utilization was at first 0%, then 50, 75 and 100%.

Due to the limited space of this paper, I presented here some interesting results. As it was mentioned above, simplified E-model consist of two factors influences the final score of R-factor. Figure 1 shows our results of the packet loss impairment factor $I_{E\text{-}EFF}$ on voice codecs G.711 and G.711 with PLC, G.729 and AMR. The results of measurements were proceeded into regressive equations.

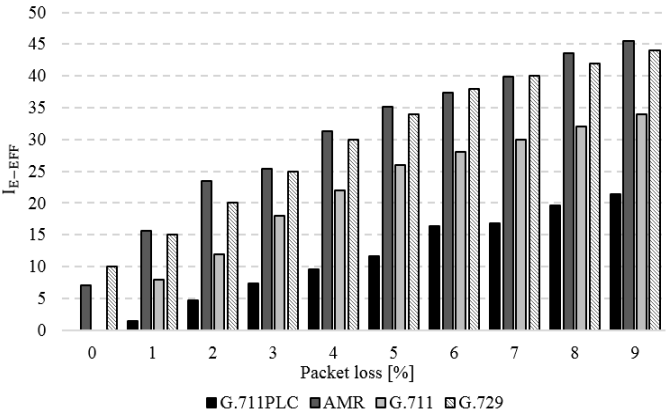

Fig.1. $I_{E\text{-}EFF}$ factor for voice codecs

To evaluate the quality of the video it was used the method SSIM. SSIM correlates better with the perception of the human eye than other objective metrics [3]. We evaluated this method by using MSU VQM Tools. As a first step, we created a stream in the VLC Player. As for the video content, streaming process RTP/UDP/IP method with MPEG2 (TS) and H.264 (MP4) was used. We captured the broadcast stream on the local computer interface using VLC Player. This video was saved and tagged as the original video. We set the packet loss to 1% on the interface using Netem and then repeated the whole measurement. Then we repeated this step for packet loss in increments of 1%, 2%, ..., 10%. For a better illustration, Figure 2 demonstrates the video quality results for full HD resolution.

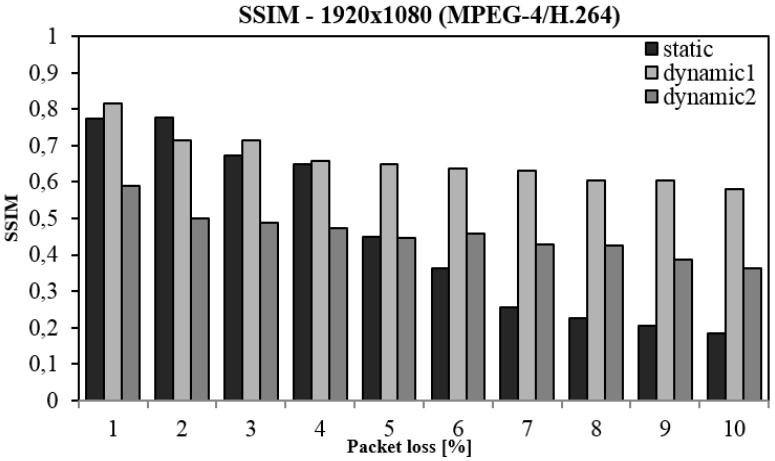

Fig. 2 SSIM results for MPEG-4

All movies were measured in a resolution of 720 x 576 (PAL), 1280 x 720 (HD) and 1920 x 1080 (Full HD). Static video was represented by TV news (slow motion), the first dynamic video by a NASA space shuttle launch and the third video with the highest bitrate (70 Mbps in full HD) was an open source animation movie for testing

purposes called Big Buck Bunny. All measured results led to the creation of video quality prediction model. Our goal was to find regressive equations with the highest R-squared factor. These regression equations have been calculated by statistical program Statgraphics and they have exponential character.

5 Application

For the first implementation, we have chosen the conventional method using the CLI via SSH protocol since the Huawei routers used in this project does not support NETCONF protocol, even if the manufacturer documentation declares it [1]. Currently, besides the mentioned implementation, the application is prepared to support editing configuration on remote devices. Application provides these functions:

- Calculation of MOS and the R-factor, based on prediction of total delay, Jitter buffer, selected packet loss and network utilization.
- Calculation of SSIM for video with regard to selected packet loss in the network
- Creation of configuration file with selected parameters of QoS policy and apply then on the router via SSH.

Following parameters are possible to set for the purposes of application settings the specification:

- Bandwidth uplink and downlink at end-user.
- Number of routers, their configured policies and utilization.
- Distance between communicating points.
- Type of video sequence and its resolution.

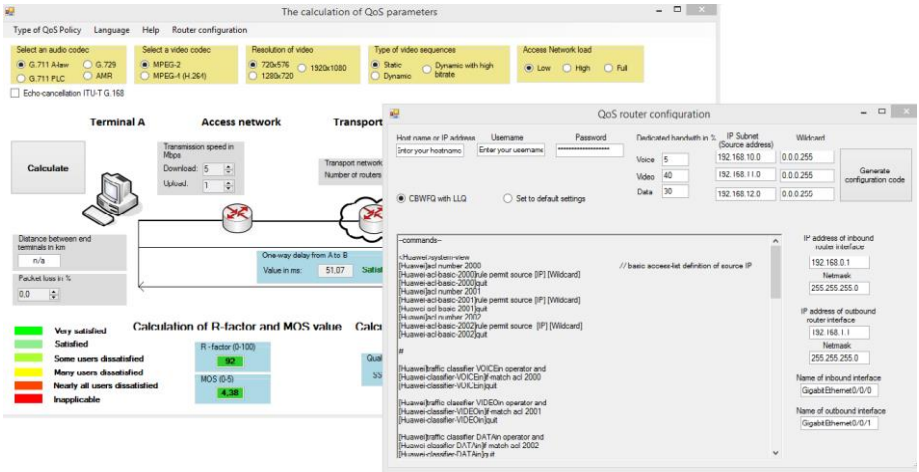

Fig. 3. Graphic interface of application

6 Conclusion

The main purpose of the paper was to present the software tool able to predict the final quality of service. Keeping the user´s satisfactory on the high level should by a one of goals for each service providers. Our application can served as a monitoring tool for computing an objective QoS parameters of Triple play services in IP network. In order to develop our SW application, it was necessary to create real computer network and apply appropriate QoS policies. Based on many measurements we obtained appropriate values, which were used for our mathematical prediction model. The application also allows to generate the configuration of selected QoS policy and saves time during the implementation of QoS techniques on routers in the network. This SW tool is one of the outputs of cooperation with Huawei CZ and it serves as proof that our research is interesting for the commercial sector.

Acknowledgements

This work was supported by the internal grant of Faculty of Electrical Engineering and Computer Science SGS No. SP2015/82.

Recent publications

1. J. Frnda, M. Voznak, M. Hlozak, J. Slachta, J. Lin, *Application Tool for Prediction and Implementation of QoS in IP Based Network*, In SPRINGER Advances in Intelligent Systems and Computing AISC, Volume 370, 2015, pp. 143-154.
2. J. Frnda, M. Voznak, L. Sevcik, P. Fazio, *Prediction Model of Triple play services for QoS Assessment in IP Based Networks*, In Journal of Networks, Vol. 10, No. 4, pp. 232-239, April 2015.
3. J. Frnda, M. Voznak, L. Sevcik, *Impact of packet loss and delay variation on the quality of real-time video streaming*, In SPRINGER Telecommunication Systems, 17 April 2015.
4. J. Frnda, M. Voznak, L. Sevcik, "*Network Performance QoS Prediction*," In SPRINGER Advances in Intelligent Systems and Computing AISC, Volume 297, 2014, pp. 165-174.
5. L. Sevcik, K. Tomala, J. Frnda, M. Voznak, "*QoS of Triple Play Services in LTE Networks*," In SPRINGER Advances in Intelligent Systems and Computing AISC, Volume 298, 2014, pp. 25-33.

Other references

6. ITU-T G.107 – Recommendation G.107 of the International Telecommunication Union: *The E-model: a computational model for use in transmission planning*, ITU-T, 2014.

Determination of Empirical Equations for the FSO with Respect to Meteorological Measurements

Lukas Hajek

Department of Telecommunications, FEECS,
VŠB – Technical University of Ostrava, 17. listopadu 15, 708 33 Ostrava – Poruba
lukas.hajek@vsb.cz

Abstract. The atmosphere is unstable and unpredictable environment, where are continual changes of the air refractive index. These changes cause fluctuation of optical power at the receiver site. The prediction of behavior of the atmosphere and effect of this behavior on the FSO link is very complicated or even impossible. Aim of this article is focused on statistical analysis of measured level signal RSSI of the FSO link and atmospheric properties measured by hydro-meteorological station. For measured data the statistical analysis tools were used. Next part of article is focused on determination of the linear regression model to calculate level of RSSI depending on the atmospheric properties. Two empirical equations are result for day and night time. These equations describe behavior of signal RSSI in 30 days interval. Finally, comparison of the obtained mathematical model with real measured data of RSSI was introduced for one week before and one week after the analyzed time interval.

Keywords: FSO, turbulence, atmosphere, RSSI, statistical analysis, linear regression

1 Introduction

The Free Space Optics (FSO) technology is one of alternative communication technologies which uses the atmosphere as a medium for data transmission in short range. Universally, whatever atmospheric effect more or less disturbs this kind of communication. Wind turbulences, sudden or slow temperature variations, air density, atmospheric pressure, humidity etc. create small as well as large air locks with differences of refractive indices or dissipation centers. These air locks, also called cells, cause change of optical beam direction and scintillation of optical intensity in the receiver's detector. Hence it is necessary these wireless systems should have mechanisms for reduction of atmospheric effects thereby disturbances of communications should be minimalized.

If it was possible to predict the atmosphere behavior by a mathematical model these FSO systems would be more improved. The prediction of the atmosphere behavior would also determine whether the used FSO system is enough effective or it could help to choose the suitable FSO link before its installation. This could reduce purchase costs

© M. Krátký, J. Dvorský, P. Moravec (Eds.): WOFEX 2015, pp. 546–552.
VŠB – Technical University of Ostrava, FEECS, 2015, ISBN 978-80-248-3787-1.

and operating costs. Chaotic changes of atmospheric parameters give off whatever predictions of atmospheric behavior in short period. If the data files are enough wide it will be possible to forecast the behavior outside the analyzed period with certain accuracy by the help of the statistics.

2 Description of analyzed area

The ninth month of year 2012 was chosen for analysis. This month was chosen with regard to compact measured data of FSO link and meteorological station. The FSO link is placed in area which was then analyzed, see Fig. 1. The one head of FSO link is placed on the main building of our University, the other head is placed on the observatory tower. The distance between them is 1.47 km. The type of heads creating the FSO link is MRV-TS-5000/G. Their basic technical parameters are in Table 1.

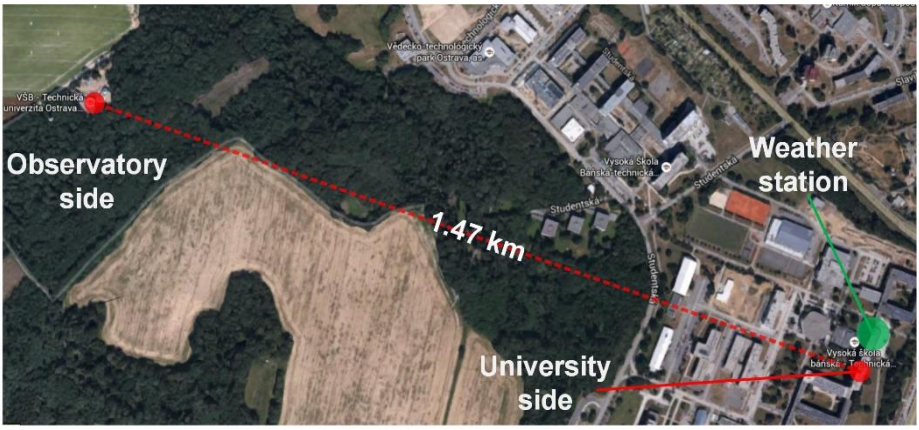

Fig. 1. The bird's eye view on analyzed area. Red cash line is the FSO link MRV-TS-5000/G. The green circle highlights the placement of meteorological station Davis Vintage Pro 2.

Both heads record the RSSI values in interval two minutes. The memory of heads is limited for saving maximal 14 days record of the RSSI. The meteorological station Davis Vintage Pro 2 was used for measurement of atmosphere conditions. This station records each minute the average values of wind speed ($m \cdot s^{-1}$), solar radiation ($W \cdot m^{-2}$), dew point (˚C), temperature (˚C), air pressure (hPa) and humidity (%).

Table 1. Parameters of analyzed area, FSO link and meteorological station.

Parameters of analyzed area			
Transmitter		Receiver	
Light source	3 x Lasers	Detector	APD
Wavelength	830-860 nm	Field of view	2 mrad
Total Output power	120 mW	Sensitivity	-33 dBm
Beam divergence	2 mrad	Lens Diameter	20 cm
Lens diameter	6 cm		
Analyzed area			
Length of optical path	1.47 km		
Altitude	31 m		

3 Results

We chose the September 2012 for analysis of measured data, i.e. 1st-30th. According to the statistical analysis of this month we compared measured RSSI and modeled RSSI, which was described by empirical equation. This comparison was done for two weeks, the first week from 25th to 31st August 2012 and the other week from 1st to 7th October 2012. Before the analysis of September we analyzed only one day when the changes of the atmosphere were very weak.

3.1 Analysis of day 23rd September 2012

The multifactor analysis needs dependent and independent variables. The dependent variable was chosen RSSI value, the independent (or control) variables were wind speed (Ws), dew point (Dp), humidity (H), air pressure (P), solar radiation (Sr) and temperature (T). The analysis of measured data showed that is a significant difference between data obtained in night and in day. Figure 2 shows difference between the measured value RSSI, the calculated value RSSI according to the total regression model (Eq. 1) and the value calculated from the model compounded of equations for night and for day (Eq. 2 and Eq. 3).

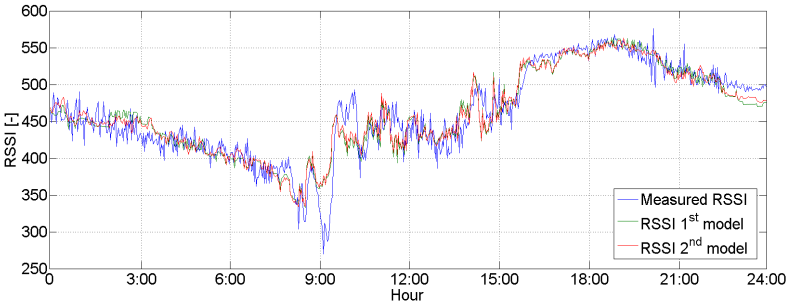

Fig. 2. Comparison of measured RSSI, model with complete regression analysis and model with regression analysis divided into day and night on 23rd September 2012.

$$RSSI = 2646.31 + 102.547 \cdot Dp - 24.4895 \cdot H + 0.07937 \cdot P - 0.1692 \cdot Sr - 96.4828 \cdot T + 0.9184 \cdot Ws \quad (1)$$

$$RSSI_{Day} = 2896.17 + 118.462 \cdot Dp - 27.5231 \cdot H + 0.1123 \cdot P - 0.1499 \cdot Sr - 111.407 \cdot T + 5.1305 \cdot Ws \quad (2)$$

$$RSSI_{Night} = 2259.01 + 75.4635 \cdot Dp - 17.7451 \cdot H - 0.1898 \cdot P - 65.9369 \cdot T - 6.3086 \cdot Ws \quad (3)$$

3.2 Ana1ysis of period 1st to 30th September 2012

For data analysis in period 1st to 30th September 2012, an averaging of separate values of all variables was done and further an hour averages of separate values were calculated. By the help of the final equation (Eq. 4 and Eq. 5) the values RSSI for day and night were calculated. Figure 3 shows a comparison of the measured RSSI and the modeled RSSI. The biggest deviations appeared in the period from 10th to 15th September. These deviations could be caused by dissipation effects which were not included to the analysis.

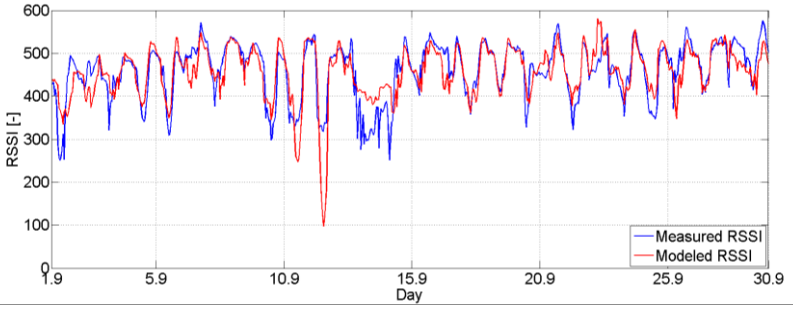

Fig. 3. Comparison of the measured RSSI and model with regression analysis for period 1st to 30th September 2012.

$$RSSI_{Day} = 3175.96 + 124.293 \cdot Dp - 28.9379 \cdot H - 0.2181 \cdot Sr + 0.04454 \cdot P - 123.1 \cdot T + 5.816 \cdot Ws \quad (4)$$

$$RSSI_{Night} = 1900.19 + 65.5546 \cdot \mathrm{Dp} - 15.3901 \cdot \mathrm{H} - 61.1284 \cdot \mathrm{T} - 3.7562 \cdot \mathrm{Ws} \quad (5)$$

3.3 Comparison of model with week 25th to 31st August 2012 and week 1st to 7th October 2012

Thereinafter displayed graphs (fig. 5 and 6) show comparison of the measured and the modeled RSSI. These curves show very good conformity and they vary very small from real measurement.

The mutual linear regression of measured and calculated RSSI according to Eq. 4 and Eq. 5 shows that the conformity was 76.37% in week 25th to 31st August 2012 and 65.07% in week 1st to 7th October 2012.

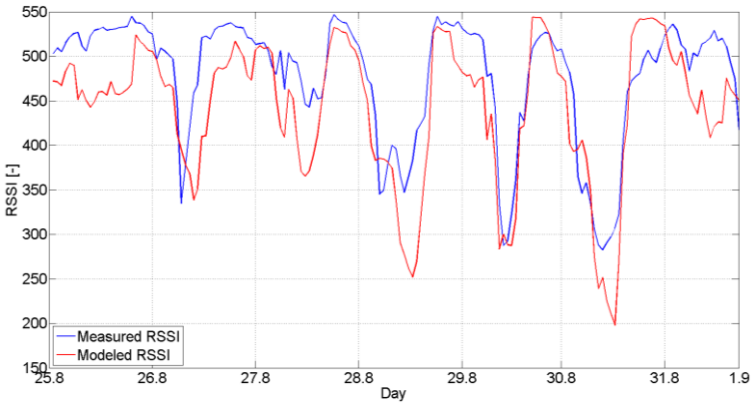

Fig. 4. Comparison of the RSSI from 25th to 31st August 2012.

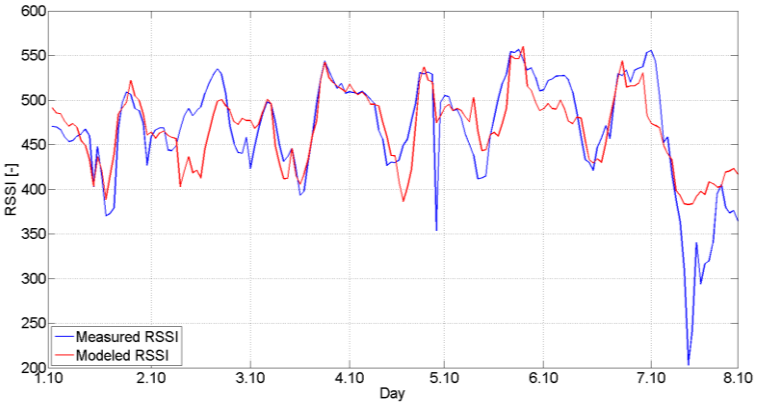

Fig. 5. Comparison of the RSSI from 1st to 7th October 2012.

4 Conclusion

The results in this article describe percentage conformity or the ability of obtained empirical equations to describe certain volume of measured data. If the regression analysis is done only for one day then the percentage ability of this model is logically high. The analysis of 23rd September 2012 reached the accuracy around 88.8 %. Further it has been found that there is a difference between the analysis of the whole data file and the analysis of two separate data files which contain value for day hours and night hours. The difference of evaluated results was 0.14 % for day hours and 4.4 % for night hours. The average value of difference of both models (model for the whole day and model for day and night) was around 2.27 %. The main part of this article was focused on analysis of longer time period. The data file covering the September 2012 was chosen for the analysis. By the help of the regression analysis we obtained two linear equations describing a curve of RSSI in dependence on atmospheric behavior in given area. The accuracy of this model is around 67.29 %. By the help of obtained empirical equations the measured and modeled RSSI values are graphically and statistically compared for a week before and after analyzed month. For a week in period 25th to 31st August the conformity of measured and modeled RSSI values was 76.37 %, the conformity was 65.07 % in period 1st to 7th October. In the future we want to develop the idea of this article in several directions. We would like to add other sensors for visibility measurement, total rainfall etc. These parameters will be included to the analysis which becomes considerably more accurate. The other direction will be testing of other than linear regression models which could more precisely describe the measured data but these models will be more complicated. The automatic data collection was created recently which automatically correlates and saves data from FSO head and from meteorological station. We would also like to analyze longer time periods together with correlation of days, weeks and months in different years.

Acknowledgement

The research described in this article could be carried out thanks to the active support of the Ministry of Education of the Czech Republic within the projects no. SP2015/130, SP2015/182. This article was supported by projects Technology Agency of the Czech Republic TA03020439 and TA04021263. The research has been partially supported by the Ministry of Education, Youth and Sports of the Czech Re-public through grant project no. CZ.1.07/2.3.00/20.0217 within the frame of the operation programme Education for competitiveness _nanced by the European Structural Funds and from the state budget of the Czech Republic.

5 References

1. Devore, J. L., [Probability and Statistics for Engineering and the Sciences], Brooks/Cole, Boston, 469-593 (2010)
2. Arockia Bazil Raj and A., Arputhia Vijaya Selvi, J., "Comparison ofdifferent models for ground-level atmospheric attenuation prediction with new models according to local wather data for FSO applications" Journal of Optical Communications, 181-186 (2015).
3. Nadeem, F. and Leitgeb, E., "Dense maritime fog attenuation prediction from measured visibility data," Radioengineering, 223-227 (2010).
4. Brazda, V., Fisher, O., Pek, V., Pesice, P. and Schejbal, V., "Meteorological measurement of atmospheric turbulence and FSO link attenuation – Preliminary results," EuCAP 2014, 1046-1048 (2014).
5. Dror, I., "Accurate method for prediction of atmospheric transmission according to weather," Optical Engineering, 2548-2555 (1996).
6. Andrews, L. C. and Ronald, L. P., [Laser beam propagation trough random media], SPIE Optical Engineering Press, Belingham, 1-775 (2005).
7. Dordova, L. and Wilfert, O., "Volume of atmospheric turbulences evaluation on the basis of the turbulent area quantification," 14th Conference on Microwave Techniques, 1-4 (2008).

Research of Ageing of Optical Fibers and Development of Optical Sensor

Tomáš Hlavinka

Department of Telecommunications, FEECS,
VŠB – Technical University of Ostrava, 17. listopadu 15, 708 33 Ostrava – Poruba
tomas.hlavinka@vsb.cz

Abstract. Article summarizes activities during the second year of the author´s doctoral study at the Department of Telecommunications in the field of Communication technology. For the most part this article summarized activities associated with the ageing of optical fibers and related research projects in this field and a list of publications in which the author participated over the academic year 2014/2015.

Keywords: ageing of optical fibers, distributed optical sensor

1 Introduction

I am studying second year of doctoral study programme in the field of Communication technology at Faculty of Electrical Engineering and Computer Science at the Technical University of Ostrava. This year I dealt with the ageing of optical fibers for the most part, although my specialisation is in the field of optical fiber sensors. One of my activities were the periodic measurements of parameters of optical cable polygon constructed on the roof of the building "N" in the University complex. The main goal of this measurements is to determine the level of the impact of external atmospheric influences on ageing of optical fibers and its transmission properties. Another research in the field of ageing of optical fibers was conducted in cooperation with the ÚJV Řež. There was a series of measurements of parameters of optical fibers, which have been exposed to high temperatures and dangerous radiation. From the field of optical sensor I dealt with constructing a distributed optical temperature sensor for experimental measurements over the next year. Furthermore, I participated in a practical measurements of vibrations using by an optical interferometer in the Prague subway. All these activities are described below.

© M. Krátký, J. Dvorský, P. Moravec (Eds.): WOFEX 2015, pp. 553–558.
VŠB – Technical University of Ostrava, FEECS, 2015, ISBN 978-80-248-3787-1.

2 Activities in the field of ageing of optical fibers

2.1 Measuring the interaction of weather conditions on the transmission parameters of the optical fibers

I participated in the construction of cable polygon for measuring the interaction of weather conditions on the transmission parameters of the optical fibers. The polygon is located on the roof of the N building and it is composed of two circuits with lengths of 23 and 25 kilometres (Figure 1). The fiber optic cables are composed of 48 and 72 fibers with the parameter 9/125μm of the ITU-T G.652 standard. Since the beginning of this year, on this polygon were made a periodical series of measurements on four paths 11 km, 11 km, 9 km and 14 km and it was examined how the transmission parameters varies during the year. For this measurement were used these methods: insertion loss by 1C method, analysis of the attenuation fiber in its full length by OTDR method, chromatic and polarization dispersion, temperature changing by DSTS system.

Fig. 1. Placement of the cable polygon on the roof of the N building.

2.2 Measurement of aging of optical fibers in cooperation with the ÚJV Řež

At the beginning of the year we got the opportunity to participate in the research of optical fibers under an extreme stress. ÚVJ Řež has the equipment and facilities that we could use. In this measurement were used the optical fibers which were exposed to thermal and radiation stress. First, it had to make required length of paths from a particular type 62.5/125μm 24-core fiber optical cable. Subsequently, these cables were placed into a two furnace in ÚVJ Řež. The temperature in the first furnace was gradually set up to value of 105°C and in the second furnace was set to a constant temperature value of 92°C. For this measurement were used these methods: insertion loss by 1C method, analysis of the attenuation fiber in its full length by OTDR method, brillouin frequency shift by DSTS system, temperature changing by DTS system and numerical aperture. This measurements were taken from March to June. Then the cables were move from the furnaces into the radiation laboratory where were continuously measured insertion loss by 1C method, analysis of the attenuation fiber in its full length by OTDR method two times during the day and numerical aperture before and after the measurement. This measurements were taken than the total value of radiation was 100 Gy. After that was realized the last measurement of relaxation of irradiated fiber then the attenuation of irradiated fiber reached a stable value [5].

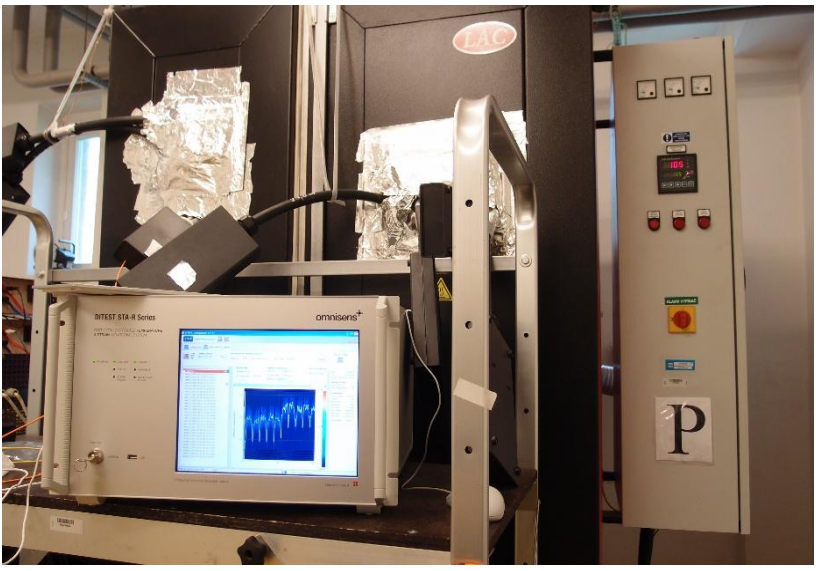

Fig. 2. Measurement of brillouin frequency shift by DSTS system during thermal stress.

3 Activities in the field of optical sensors

3.1 Measurement of vibrations in Prague subway

In June this year I participated in the measurement of vibrations and the results would help to solve the problem with GSM coverage in the Prague subway. Currently, only subway station has GSM coverage. For this measurement were used own constructed optical interferometers. Measurements were carried out in four different subway stations, when each station was measured for 24 hours. The first interferometer was installed at the beginning of each platform station. The second interferometer was installed at a different distance in the range from 300 to 1000 m. After that was tested functionality of the sensors by passing service train. Measurements were carried out in three cycles, in the morning peak time, in the afternoon peak time and in off the peak time. [1]

Fig. 3. Interferometers for measurement of vibrations

3.2 Optical Distributed Temperature Sensor

I am currently working on a fiber optical distributed temperature sensor, which will be used to detecting and rendering of temperature distribution in space. The sensor consists 324 meanders from 1.3 km of optical fiber, which form matrix 18x18 from the created meanders of total dimension 1x1 m. For measuring of temperature is used the DTS system and the resulting values of temperature are plotted in 2D or 3D graph using the script created in software Matlab. [1]

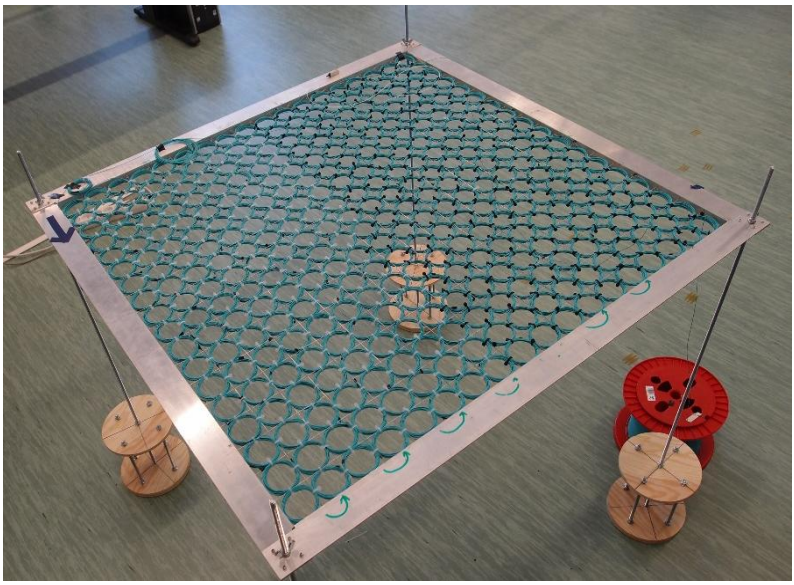

Fig. 4. Optical Distributed Temperature Sensor.

4 Publications

As co-author, I participated in the following publications in last year. Possibility of computer simulation of modulation formats for real environment conditions of free space optics [2], RFoG deployment into the next-generation networks [3], Real measurements and evaluation of the influence of atmospheric phenomena, combined with modulation format for fso [4] and Influence of gamma radiation on optical fibers and devices [5].

5 Conclusion

In this year I dealt with issue of the ageing of optical fiber, which is very important in guaranteeing the specific parameters of a certain type of optical fiber when exposed to stress in a particular environment. Currently, I prepare experimental measurements for created optical distributed temperature sensor that can be used especially to examine the effect of temperature on the optical beam for use free space optic and other upcoming applications. This article presents an annual review of activities over the year.

References

1. Eric Udd, William B. Spillman, Jr.:“Fiber Optic Sensors: An Introduction for Engineers and Scientists, 2nd Edition”, ISBN: 978-0-470-12684-4, August 2011

2. Hajek L., Hlavinka T., Vanderka A., Latal J.:“Possibility of Computer Simulation of Modulation Formats for Real Environment Conditions of Free Space Optics” WOFEX 2014 conferention, pp. 596–603., 2014, ISBN 978-80-248-3458-0, September 2014

3. Šiška P., Hlavinka T., Koudelka P., Látal J., Vitásek J., Hájek L., Pobořil R.:“RFoG deployment into the next-generation networks”. Proceedings of SPIE - The International Society for Optical Engineering. Volume 9388, SPIE, 2015, pages 1-10, 978-1-62841-478-3

4. Latal J., Hajek L., Vanderka A., Hlavinka T., Vitasek J., Koudelka P., Jargus J., Hejduk S., Vasinek V.:“Real measurements and evaluation of the influence of atmospheric phenomena, combined with modulation format for fso”, published at the 3rd international conference on Advances in Electronic and Photonic Technologies, Strbske pleso (Slovakia), June 2015

5. Vasinek V., Hajek L., Bednarek L., Vanderka A., Hlavinka T., Marcinka O.:“Influence of gamma radiation on optical fibers and devices”, published at the International Conference on Photonics Solutions, Hua Hin (Thailand), July 2015

Effective planning and analysis of Huawei and Cisco routers for MPLS network design using fast reroute protection

Martin Hlozak and Jaroslav Zdralek

Department of Telecommunications, FEECS,
VŠB – Technical University of Ostrava, 17. listopadu 15, 708 33 Ostrava – Poruba
{martin.hlozak, jaroslav.zdralek}@vsb.cz

Abstract. This paper deals with a description of the MPLS Traffic Engineering technology behavior on two heterogeneous, but nowadays the most commonly used network vendors Cisco and Huawei. Compatibility and functionality between network devices Huawei and Cisco were verified by testing the appropriate network topology. In this topology, we mainly focused on MPLS TE Fast Reroute (FRR) protection. After successful validation, compatibility and functionality between the routers of the network topology was verified. Using Fast Reroute protection it will be possible to use this MPLS TE application in a real network.

Keywords. Cisco, Fast Reroute, Huawei, MPLS, Router

1 Introduction

Since 1999, the draft of Multiprotocol Label Switching (MPLS) has become the IETF [1] [2] standard and internet service providers started to use this concept for IP/MPLS transmission over older ATM technology. In this paper, we focus on application of MPLS called MPLS Traffic Engineering. MPLS TE can be understood as "effective planning utilization" [3]. Instead of the normal routing of IP packets, MPLS TE routes traffic according to the source IP addresses. This application can choose the most appropriate links according to the speed of individual lines, delay, delay variability and can also react automatically to the change of these parameters [3] [4]. This paper is focused on the most used function of MPLS TE called Fast Reroute. Fast Reroute can be used in case of a link or node failure in the MPLS network. Both vendors Huawei and Cisco supports MPLS TE, but each vendor can use a different function model. The main motivation of this paper is to bring complex view on usage and cooperation between routers of two different vendors using Fast Reroute protection.

2 MPLS Technology

Multiprotocol Label Switching (MPLS) is a backbone technology, which uses labels attached to the packets for their transmission. Packets are not transmitted based on the destination IP addresses but according to the MPLS labels. The protocol allows most packets to be forwarded at the Layer 2 (switching) rather than at the Layer 3 (routing). The term “Multiprotocol” means that it can transport various protocols on Layer 3

© M. Krátký, J. Dvorský, P. Moravec (Eds.): WOFEX 2015, pp. 559–564.
VŠB – Technical University of Ostrava, FEECS, 2015, ISBN 978-80-248-3787-1.

such as IPv4, IPv6, IPX and protocols of Layer 2, e.g. Ethernet, HDLC, Frame-Relay, or ATM [6].

As shown in Fig.1, source A sends packet to the router CE1. CE1 handles the packet according to its routing table in a standard way. According to the destination IP address of each packet, the ingress router (PE1) inserts a label in front of the IP header at the edge of the backbone network. All the subsequent routers ignore the IP headers and perform the packet forwarding based on the labels in front of them. This MPLS label determines path which is used for the routing of a particular packet. Paths, through MPLS network are called LSPs [6], [7].

Each label has its local importance and every MPLS backbone router processes the packet based on the MPLS label. Finally, the egress router (PE2) removes the label and forwards the original IP packet toward its final destination.

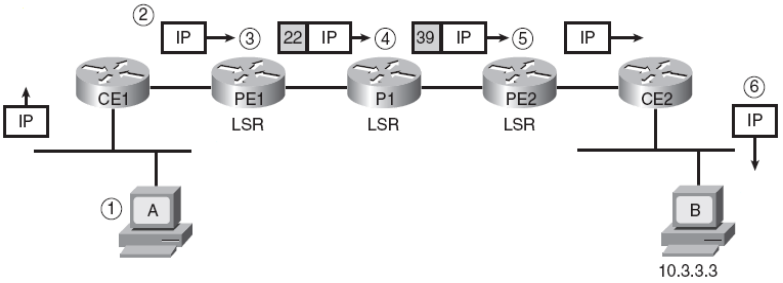

Fig.1. Packet forwarding via MPLS network [5].

3 Methodology

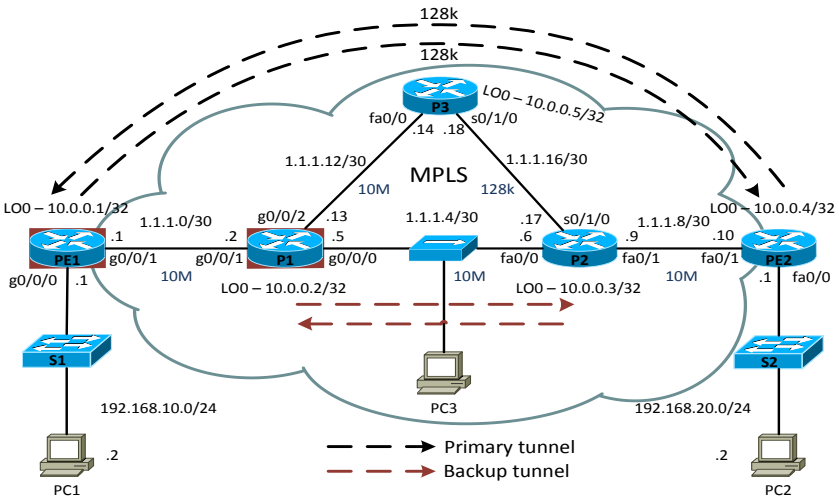

Fig. 2. MPLS TE topology

As depicted in Fig. 2, the basic MPLS topology consists of two Huawei routers – the first one AR3200 and the second one AR2200 (marked in the red frame) and two Cisco 2800 Series routers. The first goal was to verify MPLS functionality and interoperability among these above mentioned routers.

3.1 Configuration of MPLS TE on Huawei Routers

At first, it is necessary to configure MPLS TE technology and then turn on signalling protocol RSVP-TE using *mpls rsvp-te*. In case of a link or node failure we configure *mpls rsvp-te hello*. It is also necessary to enable modified SPF algorithm called CSPF which excludes. Using CSPF algorithm, the ingress MPLS router do not use these lines, which not satisfying the requirements of the data flow.

It is also necessary to explicitly turn on RSVP-TE for each MPLS physical interface. The part of the configuration is setting of the maximum bit rate of line, which can be reserved. This bit rate cannot exceed the bit rate of a physical interface. The last command *mpls te bandwidth bc0 10000* defines maximum total bandwidth for class type 0. In this case, the maximum bit rate of a physical interface is used.

In order to LSR routers could exchange information about set parameters such as maximum bit rate of the line, it is necessary to configure support for a special type of message OSPF LSA 10 for OSPF area. Then this type of message is used for CSPF algorithm. By the command *opaque-capability enable,* we allow propagation of LSA 10 messages. Next command *enable traffic-adjustment advertise* includes static LSP tunnels into SPF calculation and to the routing table.

At first, it is necessary to define an explicit path for the primary line through the MPLS network via routers PE1-P1-P3-P2-PE2 using *next hop 1.1.1.2, 1.1.1.14, 1.1.1.17, 1.1.1.17, 1.1.1.10, 10.0.0.4* command. Each next hop is defined by the IP address of the LSR router.

MPLS TE technology includes configuration of MPLS tunnel connections. As a tunnel source, a loopback interface is defined by *IP address unnumbered interface LoopBack0* command. Last next hop IP address of an explicit path must match the destination of the tunnel. In our case, 10.0.0.4 is used. Identification of the MPLS tunnel is made by *mpls te tunnel-id 1* command. Priority is set by the command *mpls te priority 0* where zero indicates the highest priority. A part of the configuration must be *mpls te record-route label* which records the links during the initiation of the tunnel.

Bit rate 128 kbit/s is assigned to the MPLS tunnel using *mpls te bandwidth ct0 128* command. It is necessary to define an explicit path. During the failover of the primary line, command *mpls te fast-reroute bandwidth* guarantees switching to the backup line with a keeping bit rate of the primary line. By *mpls te igp shortcut* command, tunnel becomes a virtual tunnel line, which will be inserted into the IP routing table. To ensure the tunnel connection precedence over the traditional calculation by OSPF routing protocol, we define an absolute metric for this tunnel using *mpls te igp metric absolute 1* command.

In next step, the router P1 is configured. Backup explicit path is defined between routers P1 and P2. This backup tunnel will be used when the primary path PE1-P1-P3-P2-PE2 fails. The function of the backup exit node has a destination router P2

which uses 10.0.0.3 address. This tunnel interface becomes a backup link using *mpls te bypass-tunnel* command. Last command protects the interface GigabitEthernet0/0/2, in case of failure of the router P3 or link between P1 and P3.

4 Results

After the configuration, it is time to verify the correct functionality of the MPLS TE technology.

4.1 Configuration of Verification of MPLS TE Technology

Fig. 3 shows LFIB table with MPLS labels and also a created primary MPLS TE tunnel. The entry point of the tunnel is the PE1 router with IP address 10.0.0.1, which corresponds to the configured IP address on the loopback interface. Exit point is the router PE2, which is identified by IP address 10.0.0.4. Likewise, we can see establishment of the primary tunnel PE2_t0 to the IP address 10.0.0.4. Each one-way tunnel route has its own identification (LSPID) and assigned MPLS label.

```
[PE1]display mpls lsp
------------------------------------------------------------------------------
                LSP Information: RSVP LSP
------------------------------------------------------------------------------
FEC                 In/Out Label  In/Out IF                      Vrf Name
10.0.0.1/32         3/NULL        GE0/0/1/-
10.0.0.4/32         NULL/1077     -/GE0/0/1
------------------------------------------------------------------------------
                LSP Information: LDP LSP
------------------------------------------------------------------------------
FEC                 In/Out Label  In/Out IF                      Vrf Name
10.0.0.2/32         NULL/3        -/GE0/0/1
10.0.0.2/32         1024/3        -/GE0/0/1
10.0.0.5/32         NULL/1074     -/GE0/0/1
10.0.0.5/32         1076/1074     -/GE0/0/1
1.1.1.4/30          NULL/3        -/GE0/0/1
1.1.1.4/30          1041/3        -/GE0/0/1
10.0.0.1/32         3/NULL        -/-
1.1.1.0/30          3/NULL        -/-
192.168.10.0/24     3/NULL        -/-
10.0.0.4/32         1072/NULL     -/-
192.168.20.0/24     1073/NULL     -/-
1.1.1.16/30         NULL/1075     -/GE0/0/1
1.1.1.16/30         1077/1075     -/GE0/0/1
1.1.1.12/30         NULL/3        -/GE0/0/1
1.1.1.12/30         1078/3        -/GE0/0/1
```

Fig. 3. LFIB table of router PE1.

As it can be seen in Fig. 4, the transmission rate of 128 kbit/s is reserved throughout the LSP routers PE1-P1-P3-P2-PE2. The same transmission rate is reserved for the tunnel line PE2-P2-P3-P1-PE1 as well.

```
[PE1]display mpls te link-administration admission-control
LspID                       In/Out IF                   S/H Prio CT BW(kbps)
10.0.0.1:1:13               --- / GE0/0/1               0 /0     0  128
10.0.0.4:-:164              GE0/0/1 / ---               0 /0     0  128
```

Fig. 4. Reserved transmission rates of MPLS tunnels.

Fig. 5 shows the established primary tunnels, which pass through the router P1, but also established backup tunnels. The entry point of the backup tunnel is the IP address

10.0.0.2 and the exit point is the router P2, which is identified by the IP address 10.0.0.3. Likewise, we see the backup tunnel (P2_t0), which was defined on the router P2.

```
[P1]display mpls te tunnel lsr-role all
------------------------------------------------------------------------------
Ingress LsrId     Destination      LSPID   In/Out Label     R  Tunnel-name
------------------------------------------------------------------------------
10.0.0.3          10.0.0.2         31      3/--             E  P2_t0
10.0.0.4          10.0.0.1         164     1076/3           T  PE2_t0
10.0.0.1          10.0.0.4         13      1077/28          T  Tunnel0/0/0
10.0.0.2          10.0.0.3         3       --/0             I  Tunnel0/0/0
```

Fig. 5. Primary and backup MPLS TE tunnels established on the router P1.

4.2 Verification of MPLS TE Fast Reroute

```
root@pcn312h:~# ping 192.168.20.2
PING 192.168.20.2 (192.168.20.2) 56(84) bytes of data.
64 bytes from 192.168.20.2: icmp_req=1 ttl=62 time=13.0 ms
64 bytes from 192.168.20.2: icmp_req=2 ttl=62 time=12.9 ms
64 bytes from 192.168.20.2: icmp_req=3 ttl=62 time=12.9 ms
64 bytes from 192.168.20.2: icmp_req=9 ttl=60 time=0.913 ms
64 bytes from 192.168.20.2: icmp_req=10 ttl=60 time=0.747 ms
64 bytes from 192.168.20.2: icmp_req=11 ttl=60 time=0.738 ms
64 bytes from 192.168.20.2: icmp_req=12 ttl=60 time=0.720 ms
64 bytes from 192.168.20.2: icmp_req=13 ttl=60 time=0.721 ms
^C
--- 192.168.20.2 ping statistics ---
13 packets transmitted, 8 received, 38% packet loss, time 12041ms
rtt min/avg/max/mdev = 0.720/5.355/13.098/5.924 ms
```

Fig. 6. Rerouting of ICMP traffic to the backup tunnel from PC1 to PC2.

Now is the time to verify the functionality of Fast Reroute on the Huawei site. An Ethernet link between routers P1 and P3 was disconnected. Every single second was sent an ICMP message from PC1 to PC2. Because 5 ICMP messages were lost, the reconvergence time of Fast Reroute was just 5 seconds, which can be seen in Fig. 6.

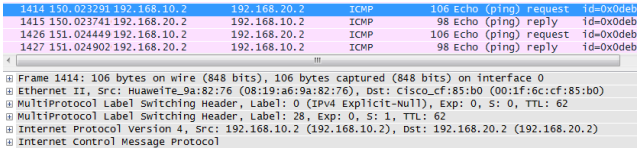

Fig. 7. ICMP traffic between routers P1 and P2.

As depicted in Fig. 7, the primary tunnel line used inner MPLS label 28, there is still maintained as inner label. Value "zero" is used as the outer MPLS label. This Explicit NULL label signals to the receiving router P2 to remove the outer MPLS label.

```
root@pcn312h:~# ping 192.168.20.2
PING 192.168.20.2 (192.168.20.2) 56(84) bytes of data.
64 bytes from 192.168.20.2: icmp_req=1 ttl=62 time=13.0 ms
64 bytes from 192.168.20.2: icmp_req=2 ttl=62 time=12.9 ms
64 bytes from 192.168.20.2: icmp_req=3 ttl=62 time=12.9 ms
64 bytes from 192.168.20.2: icmp_req=19 ttl=60 time=0.932 ms
64 bytes from 192.168.20.2: icmp_req=20 ttl=60 time=0.728 ms
64 bytes from 192.168.20.2: icmp_req=21 ttl=60 time=0.738 ms
64 bytes from 192.168.20.2: icmp req=22 ttl=60 time=0.712 ms
^C
--- 192.168.20.2 ping statistics ---
22 packets transmitted, 7 received, 68% packet loss, time 21041ms
rtt min/avg/max/mdev = 0.712/5.924/13.013/5.128 ms
```

Fig. 8. Rerouting of ICMP traffic without using Fast Reroute.

As depicted in Fig. 8, the reconvergence time of the OSPF protocol was also measured without the function of Fast Reroute. The measured time was 15 seconds.

5. Conclusion

The goal of this paper was to test a network scenario of interoperability between different vendor's network devices for MPLS TE technology using the Fast Reroute function. Our goal was to verify the compatibility and functionality between the Cisco and Huawei devices. Although MPLS technology is standardized by RFC, some of our practical experience showed us problems in interoperability between different vendors within various RFC standardized technologies. The basic MPLS configuration was without any problems. The appropriate IP prefixes were successfully exchanged. LIB and LFIB tables were filled up. The big disadvantage of Huawei routers during the MPLS TE configuration is necessity to have the appropriate license. After the license activation, the MPLS TE technology worked properly and the primary and backup MPLS tunnels were established. Without using the technology MPLS TE, the OSPF reconvergence lasted about 15 seconds, after disconnecting Ethernet cable. Due to function Fast Reroute of MPLS TE, the reconvergence lasted only 5 seconds between routers P1 and P3, which is 1/3 of convergence time within OSPF protocol. When using Fast Reroute, the convergence lasted only 2 seconds after disconnecting serial link between routers P2 and P3. It is 1/8 of convergence time within OSPF protocol. If more routers were added to the network topology, it would lead to a longer convergence time of OSPF but the reconvergence time within Fast Reroute would remain unchanged.

Because nowadays the fast convergence is very critical, this paper showed that the ISPs can use these heterogeneous network routers together with Fast Reroute technology, which can greatly reduce the convergence time.

References

1. K. I. Park, "QoS in Packet Networks," *SPRINGER The Kluwer International Series in Engineering and Computer Science,* vol. 779, pp. 213-231, 2005.
2. IETF (2001). *RFC 3031: Multiprotocol Label Switching Architecture* [online]. Available: https://www.ietf.org/rfc/rfc3031.txt
3. A. Ghanwani, B. Jamoussi, D. Fedyk, P. Ashwood-Smith, L. LI, N. Feldman, "Traffic engineering standards in IP-networks using MPLS," *IEEE Communications Magazine*, vol. 37, pp. 49 – 53, 2002.
4. B. Dekeris, L. Narbutaite, "Traffic control mechanism within MPLS networks," *IEEE Information Technology Interfaces,* pp. 603 – 608, 2004.
5. Y. Kang, J. Lee, "The implementation of the premium services for MPLS IP VPNs," in *IEEE Advanced Communication Technology*, *ICACT 2005*, 2005, pp. 1107 - 1110.
6. M. Conte, "Multiprotocol Label Switching," *SPRINGER Broadband Networks and Services*, vol. 3, pp. 55-62, 2003.
7. M. A. Rahman, A. H. Kabir, K. A. M. Lutfukkah, M. Z. Hassan, M. R. Amin, "Performance analysis and the study of the behavior of MPLS protocols," in *IEEE Computer and Communication Engineering*, 2008, pp. 226 – 229.

Measurement of masonry moisture with distributed temperature system

David Hrubý

Department of Telecommunications, FEECS,
VŠB – Technical University of Ostrava, 17. listopadu 15, 708 33 Ostrava – Poruba
david.hruby@vsb.cz

Abstract. This article describes my activities in second year at the Faculty of Electrical Engineering and Computer Science.It description my dissertation work, publication activities work on projects and next activity for department of Telecommunications.

1 Dissertation work

The head of my dissertation is prof. RNDr. Vladimír Vašinek, CSc. My work deals with the measurement of masonry moisture with distributed temperature system. For the realization of this measurement, it was necessary to build a brick wall (Fig. 1). In the production of this wall optical fiber was inserted between layers. This wall was built in stainless steel tub (with a valve for draining water) and placed on a mobile cart with a capacity higher than 500 kg. The final dimensions of the wall were 106 x 96 x 30 cm.Then the entire measurement is carried out in a laboratory where we are able to regulate the temperature stability and prevent air flow. All this to prevent influencing of the measurement results.

Fig. 1. Measuring wall.

© M. Krátký, J. Dvorský, P. Moravec (Eds.): WOFEX 2015, pp. 565–569.
VŠB – Technical University of Ostrava, FEECS, 2015, ISBN 978-80-248-3787-1.

The first experimental measurements lasted about a month and a half. The objectives of this measurement was to determine the effect of moisture on the temperature inside the wall and whether it is even possible to use optical fiber to capture these changes. The measurements were carried out in two phases. In the first phase, the wall was immersed in water. All measurement lasted about two weeks. During this period was measured a change in temperature between the layers of bricks. The measurement was carried to saturation, ie the moment when the wall has no moisture adopted. In the second phase, was launched a bath and examined the drying wall. Both of these phases are shown in Figures 2 and 3.

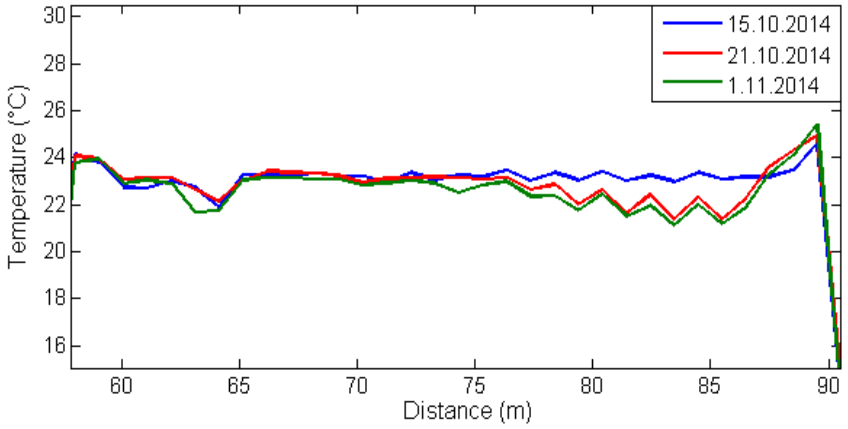

Fig. 2. A change in temperature with increasing humidity wall.

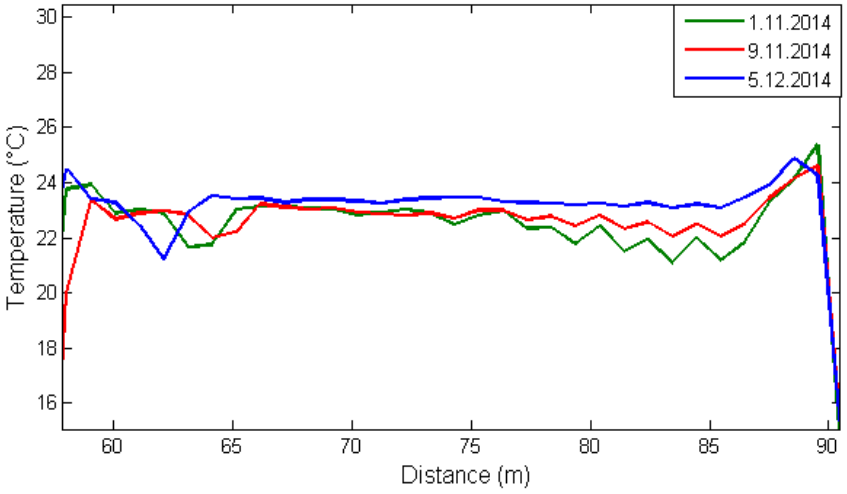

Fig. 3. Changing temperatures in the drying wall.

Currently, this measurement will be repeated. For this measurement will no longer be measured only temperature but also humidity individual layers of the wall. For these purposes, a wall has been drilled several holes into which they will be placed brick samples. These samples will be weighted at regular intervals and they will be calculated specific humidity value. This way we will be able temperature difference inside wall assign specific humidity. Preparation of this wall we can see on Figure 4.

Fig. 4. Preparation wall.

2 Publications during academic year

2.1 Measurement of insulation layers using DTS system

This article deals with the measurement of temperature transmission over various insulation layers using the DTS system. One of the problems of temperature transmission is that most of the sensors cannot measure the entire temperature profile but only allows a point measurement. This problem is solved by DTS systems with optical fibers.

2.2 Measurement of the temperature distribution inside the power cable using distributed temperature system

This article deals with the temperature distribution measurement inside the power cables using distributed temperature system. Nowadays, the power cables are manufactured to fulfill the following condition - the highest allowable temperature of the cable during normal operation and the maximum allowable temperature at short circuit conditions cannot exceed the condition of the maximum allowable internal temperature. The distribution of the electric current through the conductor leads to the increase of the amplitude of electrons in the crystal lattice of the cables material. The consequence of this phenomenon is the increase of friction and the increase of collisions between particles inside the material, which causes the temperature increase of the carrying elements. The temperature increase is unwanted phenomena, because it is causing losses. In extreme cases, the long-term overload leads to the cable damaging or fire.

2.3 Study of the effect of temperature on the optical connectors

High requirements in terms of purity, quality, mechanical design and method of grinding are placed on the optical connectors. Connectors are mostly exhibited to the negative effects, such as temperature, humidity, dusty environments, etc. The effects of temperature on the optical fiber are already known and well described. However, the way in which the temperature change has effect on different types of connectors is not yet well understood and validated. Therefore it was necessary to find the answers within this article to the questions whether a change in temperature has the effect on the connector return loss and if so how big.

All papers was presented at the conference Photonics, Devices, and Systems VI Prague registered in a recognized Scopus, WOS and IEEE and published in January 2015.

3 Cooperation on projects

As part of my studies, I was actively involved in solving four projects, namely:

1. TA ČR - Intelligent modules for lighting and communication
2. TA ČR - Safety of optical transport networks and the development of opt. parts for electric power and electrical appliances
3. Project Excom
4. Project PROSEED TG0101013

4 Other activities for the department

In the winter semester, I was actively involved in ensure the teaching with the sub-ject ZEL (Groundwork Electronics). In the summer semester, I taught courses TS (Tele-communication Networks). My Other activities were stocktaking on building N, CPIT and FEI and and on revisions of electrical devices for building FEI.

5 References

1. HRUBY, D., Aplikace optovláknových DTS systémů ve stavebnictví, Ostrava, 2013. pp. 43 Avaible at: https://dspace.vsb.cz/bitstream/handle/10084/98538/HRU285_FEI_N2647_2601T013_2013.pdf?sequence=1

2. LONG, D. *The Raman effect: a unified treatment of the theory of Raman scattering by molecules.* New York: Wiley, c2002, xxiv, 597 p. ISBN 0471490288-.

3. BALL, David W. *Theory of Raman Spectroscopy. Spectroscopy* [online]. 2001, roč. 11, č. 16, 28 - 30 [cit. 2013-05-04]. ISSN 0887-6703. Availbe at: http://www.spectroscopyonline.com/spectroscopy/data/articlestandard//spectroscopy/452001 /1017/article.pdf

4. KOUDELKA, P., J. LÁTAL, J. VITÁSEK, P. ŠIŠKA, J. HURTA, A. LÍNER a M. PÁPEŠ. *Implementation of Optical Meanders of the Optical-Fiber DTS System Based on Raman Stimulated Scattering into the Building Processes* [online]. 2012 [cit. 2013-05-01]. ISSN 1804-3119. Avaible at: http://advances.utc.sk/index.php/AEEE/article/view/643

Measurement of attenuation of PDMS fiber

Jan Jargus

Department of Telecommunications, FEECS,
VŠB – Technical University of Ostrava, 17. listopadu 15, 708 33 Ostrava – Poruba
jan.jargus.st@vsb.cz

Abstract. The importance and use of silicone materials currently grows. These materials have many of excellent physical and chemical properties due to which find application in many industries. Various optical components are produced from these materials and the production of polydimethylsiloxane (PDMS) fiber is developed too. Also, our team is starting to deal with this issue. This article is focused on the description of the initial measurements of attenuation PDMS fiber performed at our department.

1 Introduction

As already mentioned, the silicone materials have use for various industrial applications. The main applications include the production of LEDs, production of solar panels, heat dissipation, electronics, automotive, aviation, cosmonautics, etc [1]. We started to produce own short PDMS optical fibers in our laboratories of optics but this proces is still in its infancy. When we produced our first pieces of PDMS fibers the requirement for measurement of their optical properties have appeared. At first, we focused on measuring of the attenuation of PDMS fiber and then we want to measure their other optical properties. The first part of the article is focused on familiarization with the problems of measuring the attenuation PDMS fiber and the methods of measuring of the attenuation are proposed. The equipment for measuring is shown in the next chapter and then experimental measurements are presented. Finally, the results of measurements of attenuation of PDMS fiber are summarized.

2 Problems and methods of measurement of attenuation of PDMS fiber

PDMS fibers that we produce in our laboratories have considerable attenuation, and we can produce only short fibers yet. Thus the problem appeared how to measure the attenuation of these PDMS fibers? During the initial tentative measurements I have found that due to the large attenuation PDMS fiber I measured the ambient light instead of light radiating from the fiber. So I came to the conclusion that It is necessary to darkle measurement probe against ambient light. Measurements were performed

© M. Krátký, J. Dvorský, P. Moravec (Eds.): WOFEX 2015, pp. 570–575.
VŠB – Technical University of Ostrava, FEECS, 2015, ISBN 978-80-248-3787-1.

in the optical laboratory N311, which is not obscured specially. It is probable, that if the measurement is performed in a dark room, then the results will be much better, but the requirement for the best possible obscuring of the measuring probe would remain

We can see scheme of the measurement of the attenuation of PDMS fiber in the figure 1.

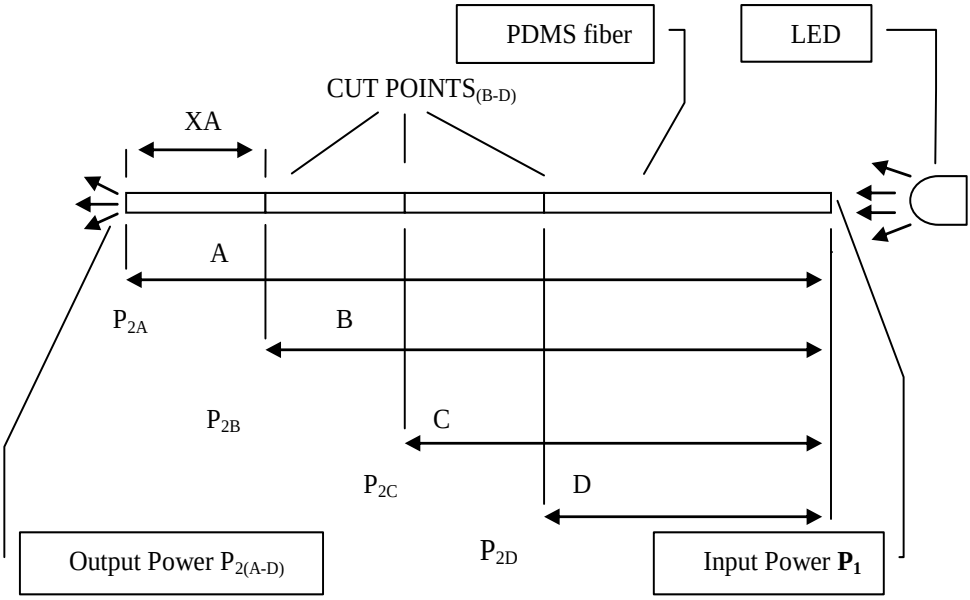

Fig. 1. Scheme of the measurement of the attenuation of PDMS fiber

The measuring of the input power P_1 coupled into the fiber is very technically difficult, so it is easier, when we measure the output power P_2 radiating from the fiber. But how to determine P_1, which is coupled to the fiber? It is necessary to derive a relationship in which a variable output intensity can determine the intensity of the input. So I decided to shorten fiber gradually and to measure the optical intensity radiating from the abbreviated fibers and try to determine both the input power coupled into the fiber and subsequently attenuation of PDMS fiber.

The attenuation is defined by the equation 1.

$$u = 10\ log \frac{P_1}{P_2} \tag{1}$$

Obviously, the equations 2 and 3 are true.

$$u_A = 10\ log \frac{P_1}{P_{2A}} \tag{2}$$

$$u_B = 10\ log \frac{P_1}{P_{2B}} \tag{3}$$

Assuming that the fiber is homogeneous over its entire length, we get the equation 4.

$$u_A = u_B . \frac{A}{B} \tag{4}$$

We can easily find out length A and B. Further we can measure P_{2A} and P_{2B} and then using equations (2) - (4) we can calculate P_1.

$$10\ log\frac{P_1}{P_{2A}} = (10\ log\frac{P_1}{P_{2B}}).\frac{A}{B} \tag{5}$$

Equation 6 follows from the rules of logarithmic calculations.

$$log\frac{P_1}{P_{2A}} = log(\frac{P_1}{P_{2B}})^{\frac{A}{B}} \tag{6}$$

We can remove the logarithm and we get the equation 7.

$$\frac{P_1}{P_{2A}} = (\frac{P_1}{P_{2B}})^{\frac{A}{B}} \tag{7}$$

Further we obtain the equation 8.

$$P_1^{\frac{A}{B}-1} = \frac{(P_{2B})^{\frac{A}{B}}}{P_{2A}} \tag{8}$$

And if we put e.g. k = A /B-1 we can use the exponent 1 / k for whole equation 8 and we obtain equation 9.

$$P_1 = \left[\frac{(P_{2B})^{\frac{A}{B}}}{P_{2A}}\right]^{1/k} \tag{9}$$

The results from equation 9 then we can inserted into the equations 2 and 3 and we get the attenuation for a given length of fiber.

However, this procedure is complicated unnecessarily. Because we want to detect a fiber attenuation per unit length especially (in our case dB / cm), so we can calculate attenuation of fiber between the end of the fiber A and the individual cut points of fiber (B, C, D). We can measure value P_{2A} for the length of the fiber A and then we can shorten the fiber to length B and further we can measure the value P_{2B}. From these values, then we can easily find the value of attenuation in dB / cm. We will assume that P_{2B} is input power and P_{2A} is output power which is passing through the fiber length of XA in this case, where XA = A – B. So we can write equation 10.

$$u_{XA} = 10\ log\frac{P_{2B}}{P_{2A}} \tag{10}$$

Then the attenuation per unit length of fiber is given by the equation 11.

$$u_{jXA} = (10\ log\frac{P_{2B}}{P_{2A}})/XA \tag{11}$$

When the value XA is length in units cm, then the attenuation per unit length of fiber is in units dB / cm. In a similar way we can measure in cut points C and D [2].

3 The equipment for measuring

Our PDMS fiber had a diameter 1 mm. The radiation power emitted from PDMS fibers was measured using Thorlabs PM100USB power and energy meter with the measuring probe S120VC (200 – 1100 nm, 50 mW). LED was used as a light source. DC regulated power supply Manson NP-9625 was used for the LED as a stabilized power supply and voltage 3,9V has been applied. The current through the LED was controlled by multimeter HM 8112-3 and its amperage was set to value 45,65 mA. The spectrum of the LED was measured using a spectrometer Ocean Optics USB 4000 and we can see it in the figure 2. Maximum radiated power was at a wavelength of 470nm.

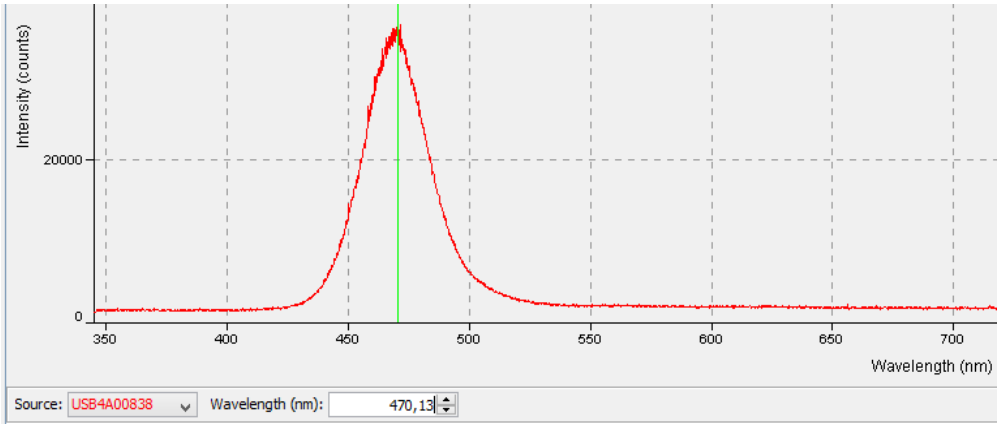

Fig. 2**.** The spectrum of the LED

We can see whole equipment for measuring in fig. 3 and some details in fig. 4 and 5.

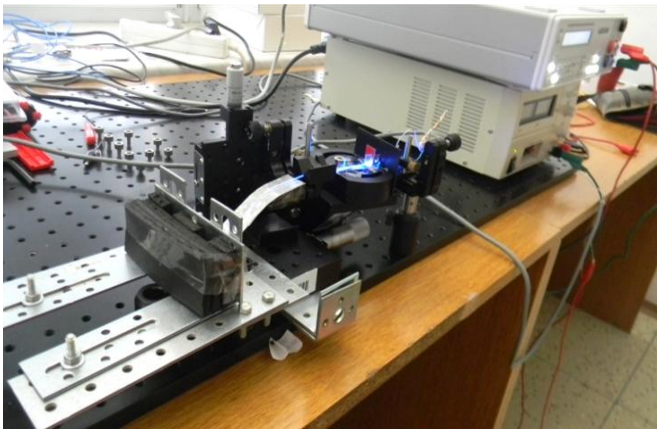

Fig. 3. The equipment for measuring

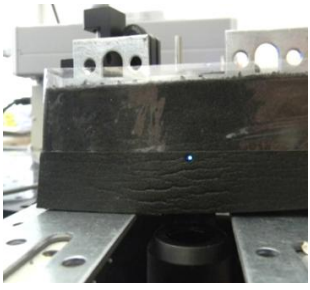

Fig. 4. Blackout material with the hole for PDMS fiber

Fig. 5. Blackout material with the measuring probe

4 The experimental measuring

Four series of measurements were carried out for length of fiber A = 30 cm, B = 27 cm, C = 24,5 cm and D = 22 cm. Fifty individual measurements were carried out in each series. Measurement results can be seen in table 1.

P2A [W] for A = 30 cm				P2B [W] for B = 27 cm				P2C [W] for C = 24,5 cm				P2D [W] for D = 22 cm			
1.	2,10E-08	26.	1,74E-08	1.	7,15E-08	26.	7,08E-08	1.	1,38E-07	26.	1,52E-07	1.	3,88E-07	26.	3,98E-07
2.	7,17E-09	27.	1,74E-08	2.	6,47E-08	27.	4,97E-08	2.	1,29E-07	27.	1,38E-07	2.	3,95E-07	27.	3,90E-07
3.	1,62E-08	28.	1,66E-08	3.	5,43E-08	28.	6,96E-08	3.	1,60E-07	28.	1,57E-07	3.	3,78E-07	28.	3,95E-07
4.	2,43E-08	29.	5,82E-09	4.	7,17E-08	29.	4,45E-08	4.	1,60E-07	29.	1,30E-07	4.	3,94E-07	29.	3,96E-07
5.	2,40E-08	30.	8,91E-09	5.	6,60E-08	30.	7,56E-08	5.	1,30E-07	30.	1,60E-07	5.	3,88E-07	30.	3,85E-07
6.	4,00E-09	31.	1,69E-08	6.	4,63E-08	31.	4,56E-08	6.	1,41E-07	31.	1,31E-07	6.	3,91E-07	31.	4,01E-07
7.	1,51E-08	32.	1,62E-08	7.	7,64E-08	32.	7,62E-08	7.	1,54E-07	32.	1,60E-07	7.	3,98E-07	32.	3,83E-07
8.	2,16E-08	33.	8,05E-09	8.	4,45E-08	33.	4,50E-08	8.	1,34E-07	33.	1,43E-07	8.	3,78E-07	33.	4,01E-07
9.	1,94E-08	34.	3,42E-09	9.	7,57E-08	34.	7,57E-08	9.	1,61E-07	34.	1,45E-07	9.	4,02E-07	34.	3,80E-07
10.	1,40E-08	35.	1,11E-08	10.	4,50E-08	35.	4,64E-08	10.	1,34E-07	35.	1,54E-07	10.	3,76E-07	35.	4,09E-07
11.	2,20E-08	36.	1,68E-08	11.	7,58E-08	36.	6,89E-08	11.	1,48E-07	36.	1,33E-07	11.	4,06E-07	36.	3,78E-07
12.	2,08E-08	37.	4,93E-09	12.	4,69E-08	37.	6,29E-08	12.	1,44E-07	37.	1,61E-07	12.	3,76E-07	37.	4,07E-07
13.	1,82E-08	38.	6,57E-09	13.	6,93E-08	38.	6,75E-08	13.	1,37E-07	38.	1,33E-07	13.	4,04E-07	38.	3,78E-07
14.	1,03E-08	39.	2,12E-08	14.	5,46E-08	39.	5,07E-08	14.	1,58E-07	39.	1,60E-07	14.	3,77E-07	39.	4,05E-07
15.	2,01E-08	40.	1,81E-08	15.	5,98E-08	40.	6,37E-08	15.	1,30E-07	40.	1,34E-07	15.	4,04E-07	40.	3,85E-07
16.	1,87E-08	41.	3,57E-09	16.	6,84E-08	41.	6,72E-08	16.	1,61E-07	41.	1,54E-07	16.	3,77E-07	41.	4,07E-07
17.	1,90E-08	42.	1,20E-08	17.	5,15E-08	42.	5,30E-08	17.	1,55E-07	42.	1,46E-07	17.	4,06E-07	42.	3,85E-07
18.	7,55E-09	43.	1,65E-08	18.	6,83E-08	43.	6,96E-08	18.	1,33E-07	43.	1,38E-07	18.	3,82E-07	43.	3,96E-07
19.	3,59E-09	44.	5,63E-09	19.	5,85E-08	44.	4,68E-08	19.	1,61E-07	44.	1,55E-07	19.	4,02E-07	44.	3,97E-07
20.	1,15E-08	45.	1,95E-08	20.	6,08E-08	45.	7,36E-08	20.	1,33E-07	45.	1,41E-07	20.	3,84E-07	45.	3,86E-07
21.	1,71E-08	46.	2,24E-08	21.	6,00E-08	46.	4,51E-08	21.	1,50E-07	46.	1,55E-07	21.	3,77E-07	46.	4,00E-07
22.	1,88E-08	47.	8,25E-09	22.	5,87E-08	47.	7,47E-08	22.	1,40E-07	47.	1,31E-07	22.	4,03E-07	47.	3,97E-07
23.	1,33E-08	48.	1,24E-08	23.	5,39E-08	48.	4,54E-08	23.	1,54E-07	48.	1,60E-07	23.	3,81E-07	48.	3,87E-07
24.	1,21E-08	49.	1,83E-08	24.	6,67E-08	49.	7,34E-08	24.	1,44E-07	49.	1,37E-07	24.	4,05E-07	49.	3,97E-07
25.	1,82E-08	50.	1,69E-08	25.	5,72E-08	50.	5,07E-08	25.	1,36E-07	50.	1,54E-07	25.	3,82E-07	50.	4,01E-07

Table 1. The measured values of P_{2A}, P_{2B}, P_{2C} and P_{2D}.

The average values of P_{2A}, P_{2B}, P_{2C} and P_{2D} can be calculated simply from table 1. And if we put XA = A – B; XB = B – C and XC = C – D, then we can calculated the attenuation per unit length of fiber using equation 10 and 11. The results of calculations can be seen in the table 2.

The average value [W]	The length of fiber [cm]	The attenuation for length of fiber equal XA, XB and XC [dB]	The length XA, XB and XC [cm]	The calculated fiber attenuation per unit length [dB / cm]
P2A = 1,45E-8	A = 30	Uxa = 6,23	XA = 3	Ujxa = 2,08
P2B = 6,08E-8	B = 27	Uxb = 3,80	XB = 2,5	Ujxb = 1,52
P2C = 1,46E-7	C = 24,5	Uxc = 4,29	XC = 2,5	Ujxc = 1,72
P2D = 3,92E-7	D = 22			

Table 2. The table of the resulting measurements and calculations.

5 Conclusion

This article dealt with attenuation of PDMS fiber primarily. Great use of silicone materials was mentioned in the beginning. Then problems and methods of measurement of attenuation of PDMS fiber have been described. The description of the equipment for measuring followed further. The results of measurements and calculations are content of the next chapter.

The variance of the results for calculated fiber attenuation per unit length was influenced by several factors. Output power P_{2A} is too weak for the length of the fiber A = 30 cm, because P_{2A} is approaching the size of the noise in this case. Our production of PDMS fiber has some imperfections, and this fiber may be inhomogeneous. Measurement has not been carried out in a dark room, and therefore the value of the input power P_1 is not the same when measuring the output power P_{2A}, $P_{2B,}$ P_{2C} and P_{2D}. Further, input power P_1 fluctuated over time and finally output sectional areas were not homogenous after shortening the fibers. Despite these imperfections measurements, we can estimate that the average fiber attenuation per unit length is about 1,6 dB / cm in this case, if we do not count the value U_{jxa} = 2,08 dB / cm.

However, research in this area will continue, because we want to measure not only the fiber attenuation but also other optical properties of PDMS fibers.

Acknowledgement

The research described in this article could be carried out thanks to the active support of the Ministry of Education of the Czech Republic within the projects no. SP2015/130, SP2015/182. This article was supported by projects Technology Agency of the Czech Republic TA03020439 and TA04021263. The research has been partially supported by the Ministry of Education, Youth and Sports of the Czech Republic through grant project no. CZ.1.07/2.3.00/20.0217 within the frame of the operation programme "Education for Competitiveness" financed by the European Structural Funds and from the state budget of the Czech Republic.

References

1. NORRIS, A., J. DEGROOT, F. NISHIDA, U. PERNISZ, N. KUSHIBIKI a T. OGAWA. Silicone Materials for Optical Applications. *DOW Corning* [online]. 2003 [cit. 2015-08-07]. Dostupné z: http://www.dowcorning.com.cn/zh_CN/content/publishedlit/75-1007-01_single.pdf

2. Ghatak,A.K., Thyagarajan,K.: *Introduction to fiber optics*. Cambridge University Press, 1.vydání, 1998, ISBN 0-521-577853

Temperature measurement inside metallic cables using distributed temperature system

Jakub Jaros

Department of Telecommunications, FEECS,
VŠB – Technical University of Ostrava, 17. listopadu 15, 708 33 Ostrava – Poruba
jakub.jaros@vsb.cz

Abstract. Nowadays, metallic cables are produced so as to avoid the maximum allowable temperature of the cable by the normal operation and the maximum allowable temperature for short-circuit the exceeding the maximum allowable internal temperature. The temperature increase is an unwanted phenomena causing losses in the cable and its abrasion. Long-term overload can lead to damaging of the cable or to the risk of fire in extreme cases. In our work, we present the temperature distribution measurement inside the metallic cables using distributed temperature system. Within the cooperation with manufacturer of the metallic cables, optical fibers were implemented into these cables. The cables are double coated and the fibers are allocated between these coatings and also in the centre of the cable. Thus we are able to measure the temperature inside the cable and also on the surface temperature along the whole cable length with spatial resolution 1 m during the cable heating. This measurement method can be also used for short-circuit prediction and detection, because this phenomena is always accompanied with temperature increase. Distributed temperature systems are already successfully implemented in temperature measurements in industry environment, such as construction, sewer systems, caliducts etc. The main advantage of these systems is electromagnetic resistance, low application price and the possibility of monitoring several kilometers long distances.

Keywords: Optical-Fiber DTS, temperature, power cable

1 Introduction

Based on results of our previous experiments, we were approached by Kabex Company. They were interested in temperature measurement inside power cables along its whole length in real time. This power cable was supposed to be further loaded with electric current. Passing of the electric current through the conductor leads to the increase of the electrons amplitude of the crystal lattice of the current path material. This phenomena leads is the increase of the friction and collisions inside the material. With increasing frictions and collisions of the particles increases also the temperature of current-carrying components. The overheating of the cable is unwanted

© M. Krátký, J. Dvorský, P. Moravec (Eds.): WOFEX 2015, pp. 576–581.
VŠB – Technical University of Ostrava, FEECS, 2015, ISBN 978-80-248-3787-1.

phenomena, because of the increasing losses inside the cable. Excessive overheating can damage the cable and cause fire. After initial testing measurements, it was decided that a special cable will be fabricated, which will contain a tube with optical fibers. Specifically, multimode optical fibers have been chosen, and as a measuring device was chosen distributed temperature system based on stimulated Raman scattering. This system can measure the ambient temperature along the optical fiber with spatial resolution about 1 m.

2 Experiment Description

The experiment was carried out at the Department of Electric Power VSB-Technical University Ostrava. The measuring system consisted of heavy current three-phase voltage source, DTS device from Sensornet Company and current clamp meter.

Fig. 1. Experimental workplace

Thanks to our collaboration with Kabex Company a special heavy current cable with six copper wires with a diameter of 3 mm (Fig. 2). The center of the cable was formed by plastic tube with multimode optical fibers. These were used for temperature measurements inside the cable. The aim of our experiment was to determine the temperatures inside the cable during over loading with heavy current. The total cable length was 110 m.

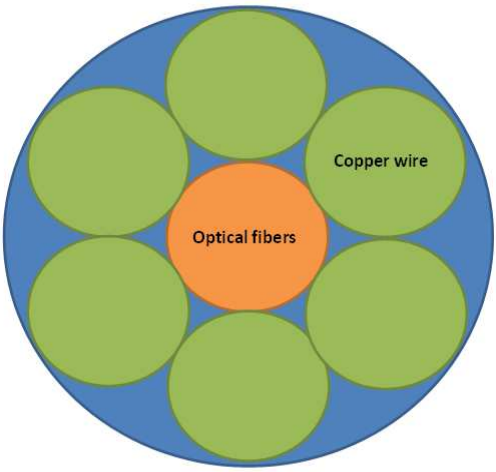

Fig. 2. Power cable

The initial measurement was performed at the cable which was rolled and the radius about 1 m. This part represented the cable reserve, because rolled cables are characterized with higher overheating, especially, at the cable parts inside the swab due to the insufficient heat dissipation. Two types of wiring, first one two-phase and the second one three-phase with supply voltage about 16 V. For each phase a pair of cables was used with a short circuit at the end of the route. The assumption was that the three-phase connection will overheat the cable faster.
The second part of the measurement was carried out on stretched cable. Here, much better heat dissipation was assumed. Therefore, much lower cable overheating was expected and it should be homogeneous along the whole cable length. A three-phase connection with supply voltage of 16 V was used.

3 Measurement Description

The laboratory temperature was constant and about 20 °C. The cable was placed into this laboratory in advanced, so that the temperature of the whole cable has been constant and the measurement should be not affected by external influences. Individual measurements were carried out on different days, so the cable temperature had sufficient time to saddle up at the original value of the laboratory.

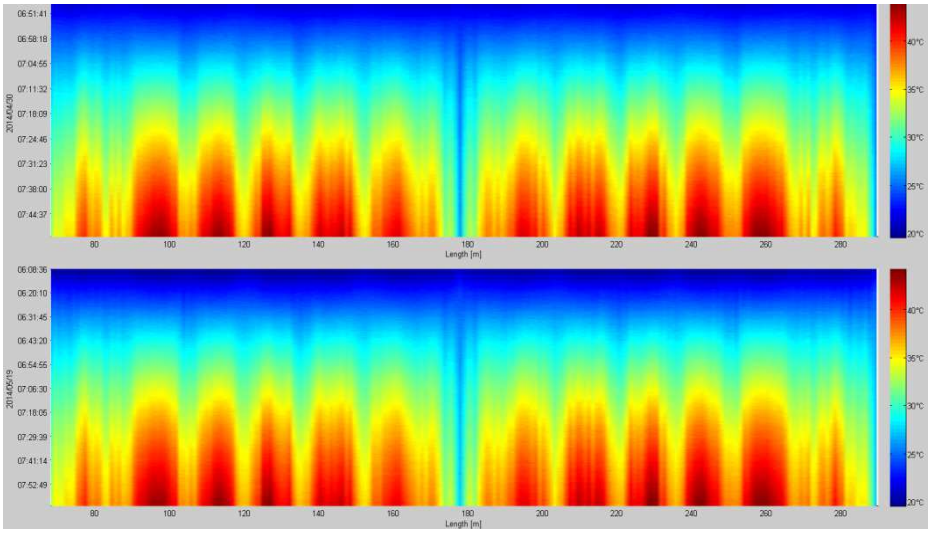

Fig. 3. Graph of the measured values – three-phase and two-phase

In the Fig. 3 can be seen the comparison of the two-phase and three-phase measurements. The two-phase system can be seen slower overheating, as expected. First 68 m of the route consists from the ballast and connecting fiber. From 68 m to 178 m takes place the temperature measurement from the source. Here, at the length of 178 m are the fibers welded and from this distance to the distance of 298 m takes the place the temperature measurement from the opposite direction. These results are presented in the graph. It can be seen, that the temperature distribution is uneven, as was expected by the rolled cable. The inner parts of the swab were overheated much faster, than the external parts, which were cooled by the ambient environment. The final temperature was set up to 50 °C. By this temperature, the measurement was terminated. The measured currents were 22 A for three-phase settings and 11 A for two-phase settings.

In the Fig. 4 are shown the results of the stretched cable measurement. A three-phase setting was set for higher heating efficiency. The supply voltage was 16 V and the measured current was 21 A. From the measured values can be clearly seen, that the stretched cable was heated less. After a certain time, the temperature increased from 20 °C to 33 °C. It can be seen, that at distance of 122 m there was a bigger overheating caused by a environment influence.

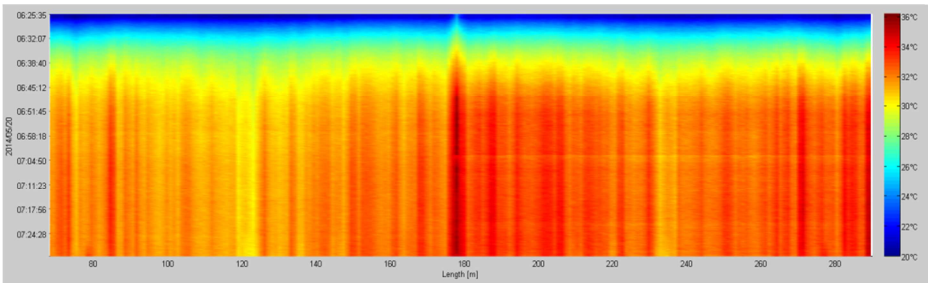

Fig. 4. Graph of the measured values - unwound

4 Conclusion

The aim of our experiment was to investigate the functionality of the optical fiber embedded in the heavy current cables and verify the temperature measurement while overloading these cables. The measurement proved the high measurement accuracy of this method. With this method, it is possible to measure the inner temperature inside the heavy current cables along their whole length, with spatial resolution 1 m and detect various anomalies. The future work of these experiments will be focused on mechanical loading of these power cables.

5 References

[1] Koudelka, P., Latal, J., Vitasek, J., Hurta, J., Siska, P., Liner, A. and Papes, M., "Implementation of Optical Meanders of the Optical-Fiber DTS System Based on Raman Stimulated Scattering into the Building Processes," Advances in Electrical and Electronic Engineering 10 (3), 187-194 (2012).

[2] Long, D., "The Raman Effect: A Unifield Treatment of the Theory of Raman Scattering by Molecules", John Willey & Sons, (2002).

[3] Koudelka, P., Petrujova, B., Latal, J., Hanacek, F., Siska, P., Skapa, J. and Vasinek, V., "Optical fiber distributed sensing system applied in cement concrete commixture research," Radioengineering 19 (1), 172-177 (2010).

[4] Rogers, A., "Distributed optical-fibre sensing, " Measurement Science and Technology 10(8), (1999).

[5] Jaskelainen, M., "Distributed Temperature Sensing (DTS) in Geothermal Energy Applications," Spectroscopy (9), (2009).

[6] Koudelka, P., Liner, A., Papes, M., Latal, J., Vasinek, V., Hurta, J., Vinkler, T. and Siska, P., "New Sophisticated Analysis Method of Crystallizer Temperature Profile Utilizing Optical Fiber DTS Based on the Stimulated Raman Scattering," Advances in Electrical and Electronic Engineering 10 (2), 106-114 (2012).

[7] Korenko, B., Jasenek, J, Cervenova, J and Hlavac, M. “Optical Fiber Sensor with Distributed Parameters Based on Optical Fiber Reflectometry,” Advances in Electrical and Electronic Engineering. 9 (1), 48-55 (2011).

[8] Liner, A, M. Papes, J. Jaros, J. Cubik, S. Kepak, P. Smira, A. Nasswettrova and J. Gabriel. “Implementation of Optical Meanders in the Temperature Measurement of the Extermination of Basidiomycete Serpula Lacrymans Using Microwave Heating,“ Advances in Electrical and Electronic Engineering. 11 (6), 535 – 542 (2013).

[9] Papes, M, Liner, A, Koudelka, P, Siska, P, Cubik, J, Kepak, S, Jaros, J, Vasinek, V. “Detection and localization of building insulation faults using optical-fiber DTS system“, Proc. Optical Sensors 2013.

[10] Sokol, V, Vajtr, J, Hoffmann, K. "Vizualizace elektomagnetickeho pole," http://vizualizace.elmag.org (2003),
[11] Lopez-Higuera, J.M., [Handbook of Optical Fibre Sensing Technology], John Wiley & Sons, (2002)
[12] Wu, Z.-J., Zhang, B.-M., Wang, D.-F., Du, S.-Y. "Application of fibre optic sensors in civil structures," Harbin Gongye Daxue Xuebao/Journal of Harbin Institute of Technology, 33 (4), 469-474 (2001).
[13] Inaudi, D. "Application of Fibre optic Sensors to Structural monitoring," Proc. of SPIE 4763, 31-38 (2003).
[14] Rogers, A.,"Distributed optical-fibre sensing," Measurement Science and Technology, 10 (8), 75-99 (1999).

Study of the incidence of external influences on various types of optical connections

Tomáš Kajnar

Department of Telecommunications, FEECS,
VŠB – Technical University of Ostrava, 17. listopadu 15, 708 33 Ostrava – Poruba
tomas.kajnar@vsb.cz

Abstract. This article describes my incidence of my second year at the Faculty of Electrical Engineering and Computer Science. It description my dissertation work, work on projects, publication activities and next activity for department of Telecommunications.

1 Dissertation work

The head of my dissertation is prof. RNDr. Vladimír Vašinek, CSc. My work deal with the influence of external factors on various types optical connections. Has work tie follows on diploma work. The work deals with the long-term effects of temperature, humidity, water and other influences on optical connections. The most important parameters for monitoring the insertion loss and return loss, which arises mainly on optical connectors and mechanical couplings. Particular scheme measurement is shown Figure 1. and 2.

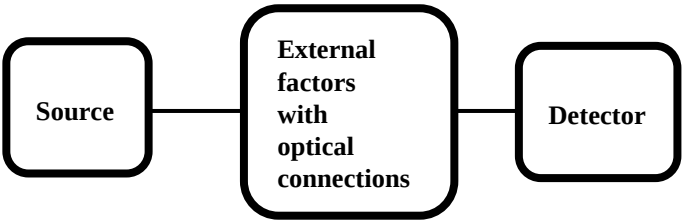

Fig. 1. The wiring diagram for the measurement of insertion loss

© M. Krátký, J. Dvorský, P. Moravec (Eds.): WOFEX 2015, pp. 582–587.
VŠB – Technical University of Ostrava, FEECS, 2015, ISBN 978-80-248-3787-1.

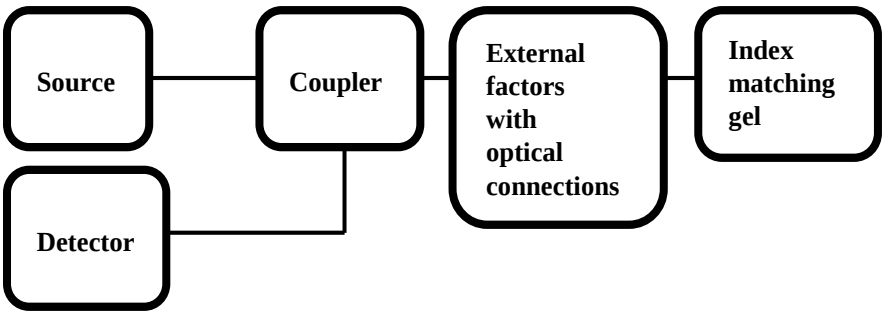

Fig. 2. The wiring diagram for the measurement of return loss

At measuring short - term temperature influence on optical fibre connector type SC, FC and E2000 with ferrule PC and APC was ascertained, that the return loss is dependent on the temperature and his dependence is for every type connector other and so, that the don't agree with parameters specified by the manufacturer. Changes loss is also dependent on the wavelength. Measurement was carried out at the wavelengths for single mode fiber at 1310 nm and 1550 nm. Evaluation was carried out followed by regression analysis and analysis of variance, as shown in Figure 3. and 4.

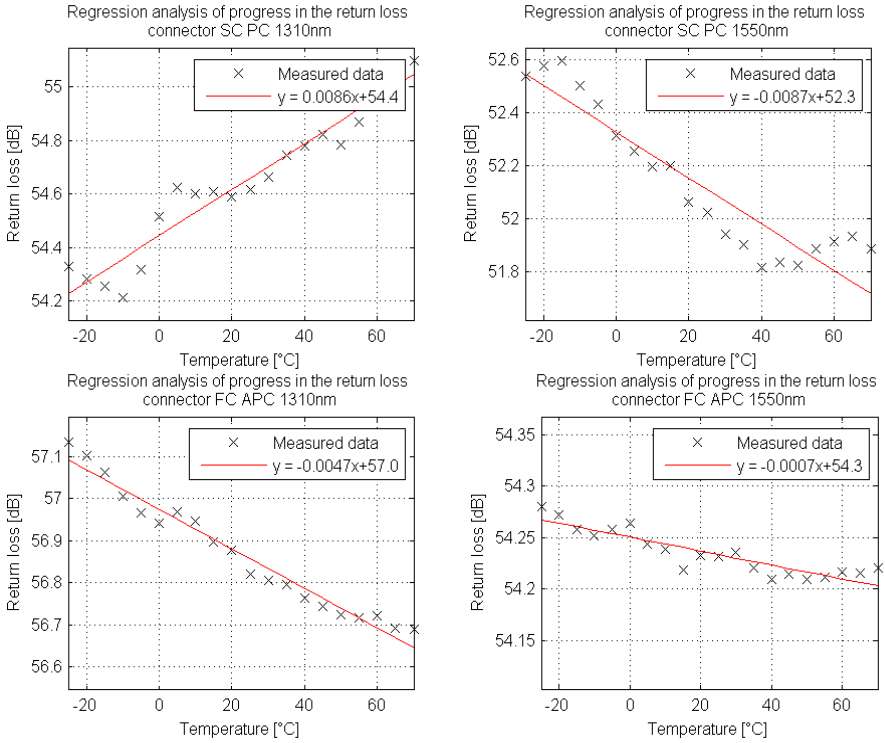

Fig. 3. The regression line for SC and FC connector

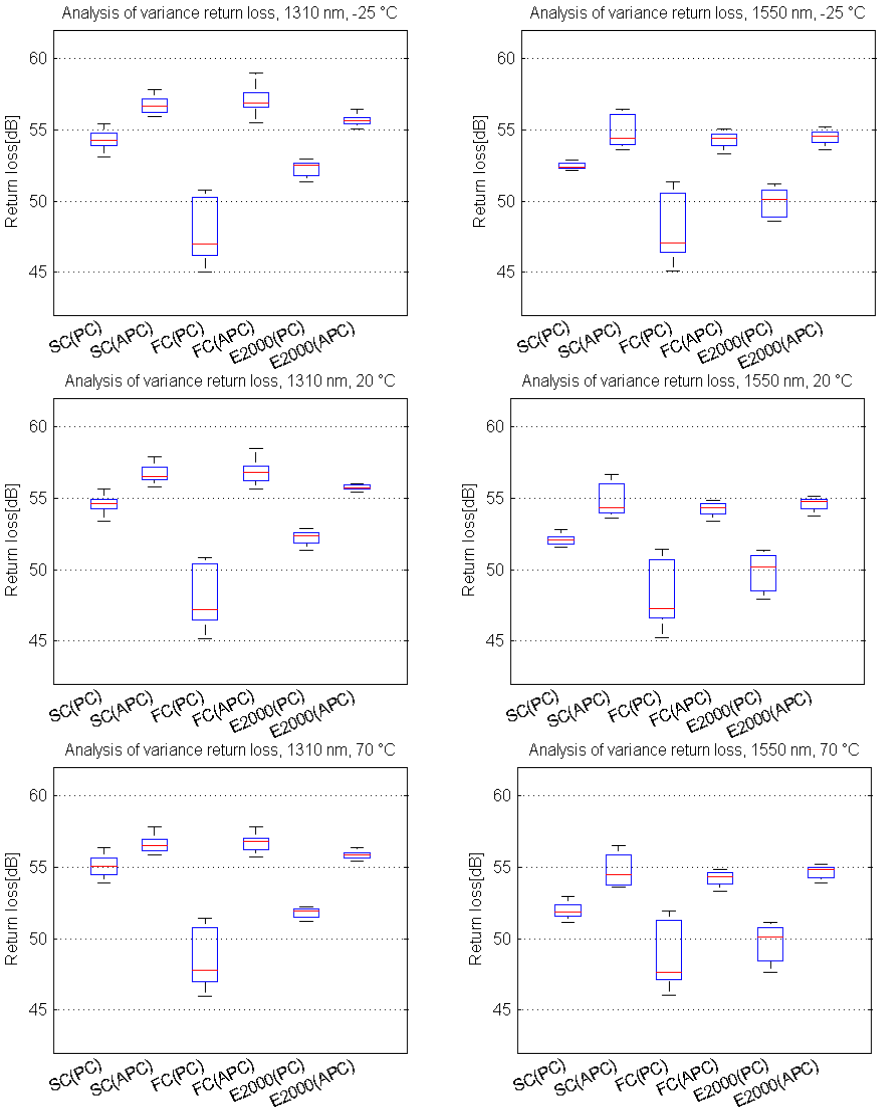

Fig. 4. Analysis of Variance of the measured data

Within statistical analysis was confirmed that the APC ferrule has a larger return loss than the PC ferrule for all types of studied optical connectors. APC ferrule has on average 4.67 dB larger return loss than PC ferrule. The analysis of variance confirmed the significant impact of ferrule on the optical connector return loss. Groups of connectors which had approximately same return loss were identified. The largest group consists of four connectors: FC (APC) on 1550 nm, E2000 (APC) on 1550 nm, SC (PC) on 1310 nm and SC (APC) on 1550 nm. Furthermore, it was found that the used wavelength also affects the return loss. Larger return loss is achieved using the

wavelength of 1310 nm, but this property was not confirmed for FC (APC) connector. It was found that the most dependent return loss on temperature exhibits SC (PC) connector at both of the measured wavelengths with the fact that with increasing temperature the return loss increases too. Conversely, the smallest temperature dependence exhibit E2000 (APC) and SC (APC) connectors. SC (APC) and FC (APC) connectors are suitable, if maximum return loss is required. In addition, if the application will require a minimal temperature dependence the best choice is the SC (APC) connector both at the wavelength of 1310 nm and 1550 nm.

2 Publications during academic year

2.1 Study of the Effect of Temperature on the Optical Connectors

The paper deal with temperature influence on return loss on optical fibre connector and is based on measurements, which took place on diploma work and will used also in dissertation work. The paper was presented at the conference Photonics, Devices, and Systems VI Prague registered in a recognized Scopus, WOS and IEEE and published in January 2015.

2.2 Measurement of Insulation Layers Using DTS System

Article deals with the measurement of temperature transmission over various insulation layers using the DTS system. The paper was presented at the conference Photonics, Devices, and Systems VI Prague registered in a recognized Scopus, WOS and IEEE and published in January 2015.

2.3 Measurement of the temperature distribution inside the power cables using distributed temperature system

The paper deal with temperature measurement by the help of DTS system rising on power cable at transit electric field. The paper was presented at the conference Photonics, Devices, and Systems VI Prague registered in a recognized Scopus, WOS and IEEE and published in January 2015.

2.4 Fiber-optic interferometer for traffic monitoring

Share in patent application, find and build patent search, patent administered originality checking and compiling an application for a patent filing. The invention have to do with fiber - optic sensor that be instrumental to street traffic monitoring and to analysis traffic passing vehicles, their identification and categorization behind usage interferometry.

2.5 Fiber-optic interferometer for the security of space assets

Share in patent application, find and build patent search, patent administered originality checking and compiling an application for a patent filing. The invention solves the security of enclosed spaces from unwanted entries, it is the "invisible" touch sensor.

3 Cooperation on projects

As part of my studies, I was actively involved in solving four projects, namely:

1. TA ČR - Intelligent modules for lighting and communication
2. TA ČR - Safety of optical transport networks and the development of opt. parts for electric power and electrical appliances
3. Studenstká grantová soutěž SP2015/130
4. Project GUARDSENSE

Below these projects belongs to cooperation in the design, build and measuring with next members, such as:

- Preparation of fiber for measuring ageing in Řež

  Preparation of fiber and welding optical fiber pigtail on fiber for measuring influence radiation on aging fibers in nuclear research institute in Řež.

- Preparation of fiber for measuring on power cable

  Preparation of fiber and welding optical fiber pigtail placed in power cable company Kabex for temperature measuring generated by passage of electrical energy.

- Preparation of fiber and measuring ageing fiber influence to external conditions on the roof building N

  Preparation of the fibers, their installation and measurement of various parameters affecting aging fibers by external influences

- Measuring mechanical and acoustic vibration in the metro DP Praha a.s.

  Installation, supervision and measuring mechanical and acoustic vibration generated when passing metro trains at various places in tunnels and underground station.

4 Other activities for the department

In the winter semester, I was actively involved in ensure the teaching with the subject PSaM (Communication Systems and Media). In the summer semester, I taught courses TS (Telecommunication Networks). Further I'm involve on stocktaking on building N, CPIT and FEI and on revisions of electrical devices for building FEI.

5 References

1. KAJNAR, Tomáš. Studium působení vnějších vlivů na optické konektory. Ostrava, 2013. pp. 53. Avaible at: https://dspace.vsb.cz/bitstream/handle/10084/98613/KAJ050_FEI_N2647_2601T013_2013.pdf?sequence=1. Diploma thesis. VSB-Technical university of Ostrava.
2. KAJNAR, Tomas, Jan LATAL, Marcel FAJKUS, David HRUBY, Stanislav KEPAK a Vladimir VASINEK. Study of the effect of temperature on the optical connectors. In: *Photonics, Devices, and Systems VI* [online]. 2015 [cit. 2015-08-24]. DOI: 10.1117/12.2070326.
3. HRUBY, David, Tomas KAJNAR, Petr KOUDELKA, Jan LATAL, Jan HURTA, Stanislav KEPAK, Jakub JAROS a Vladimir VASINEK. Measurement of insulation layers using DTS system. In: *Photonics, Devices, and Systems VI*[online]. 2015 [cit. 2015-08-24]. DOI: 10.1117/12.2073555.
4. JAROS, Jakub, Andrej LINER, Martin PAPES, Vladimir VASINEK, Veleslav MACH, David HRUBY, Tomas KAJNAR a Frantisek PERECAR. Measurement of the temperature distribution inside the power cable using distributed temperature system. In: *Photonics, Devices, and Systems VI* [online]. 2015 [cit. 2015-08-24]. DOI: 10.1117/12.2070412.

Software Design of LEDs for Visible Light Communication

Andrej Liner

Department of Telecommunications, FEECS,
VŠB – Technical University of Ostrava, 17. listopadu 15, 708 33 Ostrava – Poruba
andrej.liner@vsb.cz

Abstract. This article describes wireless optical data networks using visible spectra of optical radiation with a focus on interior areas with direct line of sight LOS (line-of-sight). This type of network represents progressively evolving area of information technologies. Development of lighting technologies based on white power LED was the impulse for wireless optical data networks based on visible spectra of optical radiation development. Its basic advantage is the flexibility of users. Users do not have to stay on one place during the data sharing anymore. Wireless optical data networks represent an alternative solution for metallic and fiber networks. This paper deals with the software simulation of homogeneous distribution of optical irradiation in dark room model, carrying out in LightTools software. First, in previous simulations, the optical source composed from 9 SMD LEDs was designed. In various simulations, various numbers and distributions of LEDs were used. These were placed at the ceiling of a dark room. At last, the results of optical irradiation homogeneity are compared.

Keywords: Homogenous distribution, LighTools software, simulation, SMD LED.

1 Introduction

In the beginning, the optical wireless link is described. This optical wireless link operates in visible spectra of optical radiation (380–780 nm). Next, the visible light communication (VLC) system operation principle is described, which allows line of sight (LOS) transmission and also non-LOS transmission between the transmitter and receiver. VLC transmitter consists of two main parts. From the control circuit and LEDs. The transmission medium is air. VLC receiver consists of receiving optical elements as photodiode, optical filter and others. VLC systems are sensitive to the sun and other types of radiation. White power LEDs are mostly used as a source.

2 Optical Wireless Communication

The basic types of link involve the direct line of sight (LOS) and the non-direct line of sight (non-LOS), the direct non-LOS and the non-direct non-LOS. Whether the link is direct or none direct depends on whether the transmitter is in the direction of the receiver. In the case of LOS or non-LOS it depends on whether there is an obstacle

© M. Krátký, J. Dvorský, P. Moravec (Eds.): WOFEX 2015, pp. 588–593.
VŠB – Technical University of Ostrava, FEECS, 2015, ISBN 978-80-248-3787-1.

between the transmitter and receiver during the communication. In VLC system, it is very important non direct LOS due to the illumination of the environment, which could be aimed or direct. LOS system transfers the signal within one direction without any obstacles from the transmitter to the receiver. The area without any obstacles between transmitter and receiver is a condition. If this condition is not followed, there is a decrease of signal quality. The size of the zone without obstacles depends on operating frequency and the distance from the transmitter to the receiver. The non-LOS system, unlike the LOS system, uses reflections from the elements in space and does not transmit a signal within one direct route, so it is also known as diffusion system. These systems operate regardless to obstacles or persons in the space. The disadvantage of this system is their reduced transmission capacity due to the complexity of the signal path.

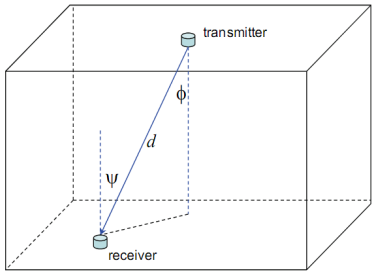

Fig. 1. Indoor, non direct LOS VLC link geometry.

In Fig. 1 is a simplified geometry in indoor area. This is non direct LOS link with the transmitter mounted on the ceiling and the receiver on the floor.

Received optical power is calculated in Eq. (1):

$$P = P_t \cdot \frac{m+1}{2\pi d^2} \cdot \cos^m(\phi) \cdot T_S(\psi) \cdot g(\psi) \cdot \cos(\psi), \quad 0 \leq \psi \leq \Psi_C, \tag{1}$$

where P_t is transmitted power of LEDs, ϕ is radiation angle to the axis perpendicular to the surface of the transmitter; ψ is angle of incidence to the axis perpendicular to the surface of receiver, d is the distance between LEDs and the detector surface. $T_S(\psi)$ is the transmission filter. $g(\psi)$ is the gain of concentrator. Ψ_C is the field of view concentrator, with a half angle is the half power. m is the serie of Lambert sources and its given by the half angle of transmitter $\phi_{1/2}$ as:

$$m = \frac{-\ln 2}{\ln(\phi_{1/2})}, \tag{2}$$

where $m = 1$ in case of $\phi_{1/2} = 60^\circ$ (Lambert transmitter). According to the axial symmetry of the Fig. 1 $\phi = \psi$. In front of the photodetector can be used optical filter and concentrator.

3 The Simulation in LIGHTOOLS Software

LightTools software allows an elegant system of modeling with full optical accuracy and precision. Its unique design and analytical capabilities combined with ease use allow lighting design according to predetermined specifications. Design and simulation is carried out by inserting the individual components directly into 3D models. These components may have variable size, position and orientation. Rays monitoring gives us a description of the optical behavior of the proposed system. This program is also able to calculate the total intensity distribution of light in the created object.

For the experiment was designed room in the LightTools program, which has the same parameters as our real dark room (shown in figure 2). In the simulation room was placed the photodetector at 75 cm above the floor level as is high of work table.

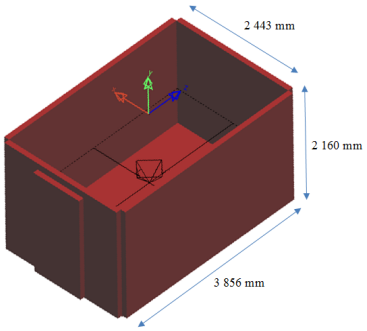

Fig. 2. The model of dark room.

4 The Appropriate LED Selection

Currently, the market offers many types of LED. The leading manufacturers of semiconductor light sources are Lumileds, Nichia, Cree and Osram Opto Semiconductors. After researching several manufacturers LED from Osram Opto Semiconductor were selected. This company deals with lighting systems and light since 1906. Two categories were selected and that were Advanced Power TOPLED and Advanced Power TOPLED PLUS (Fig. 3). These two categories provide excellent performance. Due to the low thermal resistance have very high output lighting. These LEDs are used in the automotive industry, such as in the interior as well as exterior. It is also used for indoor and outdoor lighting of buildings and for illuminated advertising and various decorations. Also serve as a backlight displays.

They have several advantages:

- high power,
- available in big color scale,
- long lifetime up to 50 000 hours,
- a wide range of brightness and high luminous intensity.

Fig. 3. Advanced Power TOPLED and Advanced Power TOPLED PLUS.

4.1 The Design of LED Panel Shape

The basic mathematical forms were considered at the beginning, from which could be designed LED panel (LED matrix) of the nine LEDs. Following shapes were experimentally created. The first one was a square of size 3x3 diodes, as shown in Figure 4.

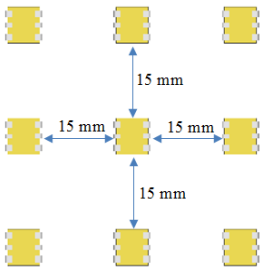

Fig. 4. LED panel with a square shape.

The second was the trapezoid shape, where the LEDs are arranged in the two planes in a row, see Figure 5.

Fig. 5. LED panel with a trapezoid shape.

The third arrangement is the octagon, where eight diodes are on the perimeter and one diode is in the middle, this layout can be seen in Figure 6.

The fourth and final shape, which has been proposed is the inverse Y (Figure 7).

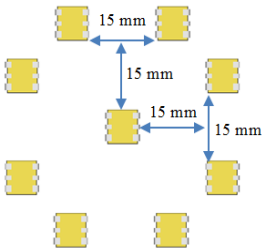

Fig. 6. LED panel with a octagon shape.

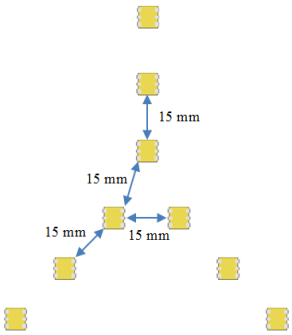

Fig. 7. LED panel with a inverse Y shape.

5 Simulation and Result

The simulations were carried out in the LighTools software. As a basis for the simulation was necessary to establish the model of the dark room first, this is shown in Figure 2. This model is based on real measured values. The inner walls of the dark room are lined with a light no reflective material. In the room there are no obstacles. Therefore, the proposal was based on the assumption that the light is not reflected in the room and therefore no reflectance value from the elements was defined.

In all designs have been used 9 LEDs of both categories (Advanced Power TOPLED and Advanced Power TOPLED PLUS) and all six types of these categories. The LED panel was placed in the middle of ceiling of model dark room. The distance was gradually adjusted between the diodes. I started with the shape ”square” and the distance between diodes was 0.5 cm. Until distance of 10 cm, the step was 0.5 cm. From 10 cm up to 30 cm the step was 1 cm. With this distribution of LEDs, only small changes in optical power distribution were observed, this can be seen in Figure 8. Best distribution of optical power is at a distance of 0.5 cm with a value $8.8780372 \cdot 10^{-8}$ W/mm^2. The largest decrease was recorded at the maximum LED spacing, which is 30 cm and its value is $8.0515258 \cdot 10^{-8}$ W/mm^2. In next simulations were used the distances of 1.5 cm, 10 cm and 30 cm for all shapes of LED panels.

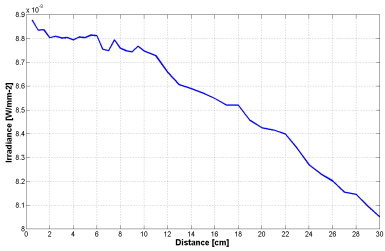

Fig. 8. Dependence of irradiance on the distance between LEDs in panel in square shape.

References

1. Liner, A., M. Papes, J. Jaros, F. Perecar, L. Hajek, J. Latal, P. Koudelka a V. Vasinek. "Software Design of SMD LEDs for Homogeneous Distribution of Irradiation in the Model of Dark Room", "Advances in Electrical and Electronic Engineering", 12(6), 622–630, (2014).
2. Liner, A., F. Perecar, J. Jaros, M. Papes, P. Koudelka, J. Latal, J. Cubik a V. Vasinek. "Features and range of the FSO by use of the OFDM and QAM modulation in different atmospheric conditions", "Wireless Sensing, Localization, and Processing IX", Baltimore, (2014).
3. Liner, A., M. Papes, J. Jaros, P. Koudelka, J. Latal, J. Vitasek, L. Hajek a V. Vasinek. "Software design of optical link for indoor wireless optical communication network used LEDs as source visible light communication", "Broadband Access Communication Technologies IX", San Francisco, SPIE, (2015).
4. Liner, A., M. Papes, J. Vitasek, P. Koudelka, J. Latal, J. Cubik a V. Vasinek. "The optical power distribution in a dark room", "18th Czech-Polish-Slovak Optical Conference on Wave and Quantum Aspects of Contemporary Optics", Ostravice, (2012).
5. Liner, A., M. Papes, J. Jaros, J. Cubik, S. Kekpak, P. Smira, A. Nasswettrova a J. Gabriel. "Implementation of Optical Meanders in the Temperature Measurement of the Extermination of Basidiomycete Serpula Lacrymans Using Microwave Heating", "Advances in Electrical and Electronic Engineering", 11(6), 528–534, (2013).

Calculation of the final key length for quantum key distribution using BB84 and B92 Protocol

Miralem Mehic and Miroslav Voznak

Department of Telecommunications, FEECS,
VŠB – Technical University of Ostrava, 17. listopadu 15, 708 33 Ostrava – Poruba
miralem.mehic.st@vsb.cz, voznak@ieee.org

Abstract. Quantum Key Distribution (QKD), often called in a more general context Quantum Cryptography, is a technology that uses the properties of quantum mechanical systems in combination with information theory to achieve unconditionally secure distribution of secret keys. BB84 and B92 are the oldest QKD protocols. These protocols consist of several phases in which initial key is significantly reduced: secret key exchange, extraction of the raw key (sifting), error rate estimation, key reconciliation and privacy amplification. In this article we explained the reduction of the initial key in each of QKD phases.

Keywords: BB84, B92, QKD, Quantum Key Distribution, Symmetric Cryptography

1 INTRODUCTION

Until recently, cryptography was the point where security engineering meets mathematics. Today, this definition is extended to include the principles of quantum physics. Quantum cryptography uses quantum physical principles to establish symmetrical binary keys between legitimate users that will use these keys to encrypt theirs communication data. Therefore, this technology can be better described as "Quantum Key Distribution" or just QKD.

The concept of quantum cryptography was originally proposed in 1960s by Stephen Wiesner, a student of Columbia University, and finally published in 1983 [1], thought its real development is recorded from 1984 when Charles Bennett (IBM) and Gilles Brassard (University of Montreal) presented BB84, the first QKD protocol [2]. Five years later they made a first practical demonstration of QKD by establishing secret key over 30cm through the air. This protocol is even today most widely used. Eight years later Bennet developed B92 [3] protocol that is simpler and faster than its predecessor.

BB84 and B92 are the oldest QKD protocols which consist of several post-QKD operations[1] in which initial key is significantly reduced. In this article, we analyzed

[1] Sifting, Error-rate estimation, Key reconciliation, Privacy amplification, Authentication

© M. Krátký, J. Dvorský, P. Moravec (Eds.): WOFEX 2015, pp. 594–599.
VŠB – Technical University of Ostrava, FEECS, 2015, ISBN 978-80-248-3787-1.

these phases and we compare BB84 and BB92 protocol on the basis of the length of the final key.

2 Secret key exchange

At the beginning of communication, the sender hereinafter named Alice and the recipient hereinafter named Bob must agree on the same alphabet. BB84 assumes that the polarization of photons is used as a carrier of information, so Alice defines a random key with a length Q and uses a randomly selected polarization from the alphabet as a carrier of the key. For example, for the bit value 1 she can choose either vertical (x=90°) or diagonal polarization (x=45°), and for the bit value 0 she can choose either horizontal polarization (x=0°) or opposite diagonal polarization (x=-45°). On the receiving side of the quantum channel, Bob chooses a randomly selected basis for detection. Since Bob does not know which basis Alice has used, and he uses a randomly selected basis, he will be able to reliably detect only 50% of the sent key.

In order to establish a secret key using B92 protocol, Alice and Bob can use only two non-orthogonal polarizations, each one coding for one bit-value. Alice sends modulated photons over the quantum channel to Bob. Since Bob has no information about the sequence which Alice used, he will use randomly basis in order to measure the incoming photons. If Bob chooses the correct basis, he will measure the incoming photon. If he chooses the wrong basis, he will not measure anything; a condition in quantum mechanics which is known as an erasure [4]. However, the probability that Bob will choose correct basis is approximately 25%. All subsequent steps are identical for BB84 and B92 protocol.

3 Extraction of a raw key – Sifting

After exchanging the key values via the quantum channel, all further communication is performed via the public channel. First, Bob informs Alice which polarization basis he has used for each received bit. Second, Alice responds when Bob uses the correct polarization basis and when he uses incompatible bases (these bits must be removed). It must be stressed that Bob only discloses information about the used basis, while the value of the measurement remains secret. After this step, Bob is certain of the sequence of the correct polarization he used for detection. However, we can conclude that the length Q of the raw key is significantly decreased. Bob reliably receives approximately 50% of the raw key. In the rest of this paper, B represents the length of Bob's reliably received key.

4 Error rate estimation

The purpose of error estimation is to determine the percentage of errors in the key after quantum transmission and sifting have occurred. Errors may occur because of a disturbance of the quantum channel, noise in the detectors or an optical misalignment

and other reasons. But errors may also occur due to eavesdropping by eavesdropper Eve. However, the threshold of bit error rate for optical channel without presence of Eve is known in forward so Alice and Bob must compare a small portion of their key in order to estimate the quantum bit error rate (QBER). If the error rate is higher than a given threshold, Alice and Bob revealed the presence of Eve and the key distribution process starts all over again.

If we mark n as the total length (Q) of the raw key then the number of bits k that will be used for the QBER estimation depends on the length of the sample block used for error rate estimation which is defined with a parameter we refer to as "level of security" $\hat{S}(k)$. In [5], two levels of security are defined: basic and advanced. Alice and Bob must select the desired level of security $\hat{S}(k)$, and use Equation (1) to calculate k.

However, Alice and Bob must delete the part of the key which they used for estimation of the error rate. It means that the raw key will be shortened even more. We use notation R to mark the length of the key after this phase.

$$\hat{S}(k) = \frac{-\sum_{k=1}^{n} \frac{k}{n} \log \frac{k}{n}}{n} \tag{1}$$

5 Key reconciliation

When Alice and Bob are sure that the key distributed via the quantum channel has a low error rate, they must find and correct or delete all errors in the rest of the key. This phase is known to be highly interactive and time-consuming, since the discussion about the location of errors in the key is performed through the public channel. The cascade protocol [6] is the most widely used reconciliation protocol due to its simplicity and efficiency. It is run iteratively in the given number of iterations where random permutation of the key is performed with the objective to evenly disperse errors throughout the key. Next, the permuted key is divided into equal blocks of k_i bits, and after each iteration permutations are performed again and the block size is doubled: $k_i = 2k_{i-1}$. For each block, Alice and Bob will exchange the results of the parity test and perform a binary search to find and correct errors. Instead of going through all the iterations continuously, the Cascade protocol investigates errors in pairs of iterations. The process is recursive.

However, the length of the initial block k_1 is a critical parameter, and should depend on the estimated error rate. An empirical result in [6] indicates that the optimal value of k_1 is 0.73/p, where p is the estimated error rate (QBER) [6]. The Cascade protocol is modified in [7], with the aim of reaching the theoretical limit for protocol efficiency. From these results, it is clear that four iterations are sufficient for a successful key reconciliation, as was suggested in the [6]. Since the initial block length depends on the estimated error rate, it is necessary to perform all the iterations. The

number of iterations i is increased to the value for which the length of block k_i can be used to split the raw key into two parts ($k_i < \frac{n}{2}$).

Now, let us go back to the parity check results. If the parity of a block disagrees between Alice and Bob, they perform a binary search on that block with the aim of identifying the single bit error. The binary search consists of dividing the block in half and comparing the parity check results for the divided block until the error is located. This means a maximum of $1 + \lceil \log_2 k_i \rceil$ parity bits are exchanged for each block with an error bit since $\lceil \log_2 k_i \rceil$ is the maximum number of times block k_i can be divided, and one parity bit is exchanged for blocks without errors. In order to minimize the amount of information gained by Eve, it is advisable to discard the last bit of each block and sub-block for which the parity bit was exchanged. Now if we define L_i as the maximum number of leaked bits, and k_i as the length of the block in the i[th] iteration, it is clear that:

$$L = \sum L_i = \sum_i \left(\frac{n}{k_i} + \sum_{\substack{errors \\ corrected}} \lceil \log_2 k_i \rceil \right) \tag{2}$$

where $k_i = 2k_{i-1}$, $k_i < \frac{n}{2}$ and n is the length of the initial key. Now it is clear that the number of leaked bits depends on the initial block size and error rate.

6 Privacy amplification

Alice and Bob finally have an identical key without errors, but since Eve may have gained significant knowledge of the key, Alice and Bob should strengthen their privacy. This is done by deleting some of the bits of the final key, so the raw key is shortened even more. The number of rejected bits during the privacy amplification process is defined in Equation (4) [8], where S is the number of bits that need to be discarded and n is the length of the key (B).

$$\frac{n \cdot 2^{-S}}{\log 2} < 1 \tag{4}$$

We mark the length of the final key after this phase as A. Now we can compare the length of the key in each previous step:

$$Q > B > R > F > A \tag{5}$$

Finally, this means that the raw key (Q) must be significantly longer than the key after being reduced in all phases explained above (A). The final key must be long enough to be used for the encryption and decryption of confidential data.

7 Calculations

To summarize, we present the formula for calculating the length of the raw/initial key (Q) from the length of the final key (A), error rate and parameter "level of security" $\hat{S}(k)$.

$$Q = 2 \cdot \left\lceil A + \frac{\log \left\lceil \frac{Q}{2} \right\rceil}{\log 2} + S\frac{Q}{2} + L \right\rceil \tag{6}$$

Where
S - percentage of raw key (Q) used for calculating QBER
L - number of bits leaked during the key reconciliation phase
A - length of the final key

Equation (6) is the Lambert W-function, also known as the Product Logarithm function, and it has two solutions in the real domain.

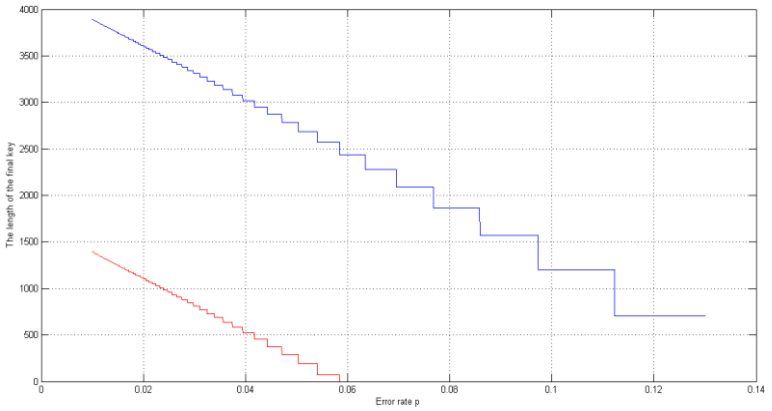

Fig. 1. Comparation of the length of the final key; red line – B92; blue line – BB84

8 Conclusion

In this article we present the Equation (6) which is used to calculate the length of the final key A based on the length of the raw key Q, error rate in quantum channel and on security parameter $\hat{S}$. From Equation (6), it is clear that the length of the final key increases with the parameter error rate (p) and the "level of security" $\hat{S}$. In [9] and [10] authors defined the upper bound for tolerated quantum bit error rate p_{max} of

12.9% for BB84 protocol. However, we showed empirically that this error rate for B92 protocol is not acceptable. For minimal value of parameter $\hat{S}_{min}$= 8.16% the maximal error rate is 5.84% as it is shown in Figure 1. This value is the direct consequence of twice smaller number of photons that Bob detects in relation to the BB84 protocol. Due to limitation of this document, Equation (6) does not contain calculation of authentication tag.

It is important to underline that parameter $\hat{S}$ defines the amount of key which is needed to estimate QBER in the channel. Also, it is worth noting that the influence of eavesdropping is not included in the Equation (6) since the entire QKD process will be repeated if the estimated QBER is higher than maximally tolerated QBER.

9 References

1. Wiesner, S.: Conjugate Coding. ACM Sigact News. 15, 78–88 (1983).
2. Bennett, C.H., Brassard, G.: Quantum Cryptography: Public Key Distribution and Coin Tossing. Proceedings of IEEE International Conference on Computers, Systems and Signal Processing. p. 8 (1984).
3. Bennett, C.H.: Quantum Cryptography Using Any Two Nonorthogonal States. Physical Review Letters. 68, 3121–3124 (1992).
4. Lomonaco, S.J.: A Quick Glance at Quantum Cryptography. Cryptologia. 23, 1–41 (1999).
5. Niemiec, M., Pach, A.R.: The Measure of Security in Quantum Cryptography. 2012 IEEE Global Communications Conference (GLOBECOM). 967–972 (2012).
6. Brassard, G., Louis, S.: Secret-Key Reconciliation by Public Discussion. Advances in Cryptology - EUROCRYPT93. 765, 410–423 (1994).
7. Sugimoto, T., Yamazaki, K.: A Study on Secret Key Reconciliation Protocol. IEICE Transactions on Fundamentals of Electronics, Communications and Computer Sciences. E83-A, (2000).
8. Niemiec, M.: Design , Construction and Verification of a High-Level Security Protocol Allowing to Apply the Quantum Cryptography in Communication Networks, http://winntbg.bg.agh.edu.pl/rozprawy2/10409/full10409.pdf, (2011).
9. Smith, G., Renes, J., Smolin, J.: Structured Codes Improve the Bennett-Brassard-84 Quantum Key Rate. Physical Review Letters. 100, 170502 (2008).
10. Kollmitzer, C., Pivk, M.: Applied Quantum Cryptography. Springer Science & Business Media (2010).

Convergence of OpenBTS and OpenIMS projects

Martin Mikulec and Miroslav Voznak

Department of Telecommunications, FEECS,
VŠB – Technical University of Ostrava, 17. listopadu 15, 708 33 Ostrava – Poruba
{martin.mikulec, miroslav.voznak}@vsb.cz

Abstract. The convergence between BTS station and the other networks is possible through IP network. The paper tries to define connection parameters to provide sufficient quality of voice service between GSM network and IP Multimedia Subsystem. The paper brings practical results of voice call quality measurement between users inside BTS station mobile network and users inside IP Multimedia Subsystem network. The Perceptual Evaluation of Speech Quality method is used to get final comparable results. The communication between BTS station and connected has to be secured against the interception from the third party.

Keywords: GSM, OpenBTS, IMS, PESQ

1 Introduction

OpenBTS project bridges two historically different worlds. The world of mobile network infrastructure, which is de facto closed and is based on pre-Internet protocols and architectural concepts, and the world of opened IP-based systems, which allows anyone witch IP connectivity to connect each other. The tested GSM infrastructure was built on Universal Software radio Peripheral (USRP N210) hardware [8] from Ettus Research ™ in combination with Daughterboard WBX. The performance parameters inside [2] and outside [3] our laboratory were observed. The next logical step was to interconnect the BTS station with the rest of the world. We chose OpenIMScore system as the VoIP provider to connect with the tested OpenBTS mobile network. The line between OpenBTS and OpenIMScore was degraded by Simena NE1000 Network Emulator. It allowed us to change network behavior between the systems and measure influence of different network parameters on the quality of voice calls and define that way the minimal requirements for the successful peering with VoIP provider through IP network.

The Perceptual Evaluation of Speech Quality (PESQ) algorithm computes the speech quality in Mean Opinion Score (MOS), which is five-degree scale developed by ITU-T. This objective intrusive method uses the original sound sample as it has entered the communication channel and compare it with the degraded signal at the output. The objective methods, in general, are trying to be as precise as possible to gain adequate MOS

© M. Krátký, J. Dvorský, P. Moravec (Eds.): WOFEX 2015, pp. 600–605.
VŠB – Technical University of Ostrava, FEECS, 2015, ISBN 978-80-248-3787-1.

value as it would be obtained by subjective methods with sufficient number of participants for adequate statistical analysis. The effectivity of this method lies in the automation of the whole measurement without any human intervention. We have developed that automatic measurement tool in our laboratory.

The measurement tool is based on open source software, and low-cost USB dongle modems connected with Asterisk PBX system. It allowed us to generate calls automatically and record the sounds samples for quality of speech evaluation.

2 Measurement

2.1 Measurement scheme

The Fig. 1 depicts the scheme of the measurement. It consists of several servers and components.

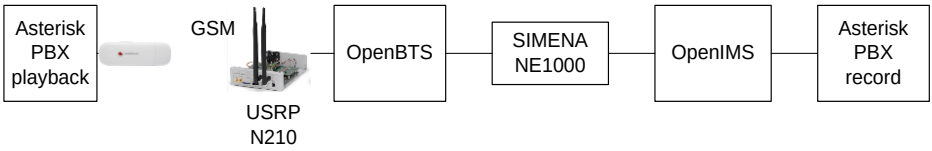

Fig. 1. Scheme of measurement

Asterisk PBX playback – server is used as the end mobile terminal. The GSM modem is connected with the Asterisk PBX and ensures answering the call and playback of original sound sample.

USRP N210 – Universal Software Radio Peripheral – device provides radio part of created GSM network [9]

OpenBTS – server provides software part of created GSM network. Asterisk PBX inside is used for routing calls and for peering with remote VoIP provider [10]

SIMENA NE1000 - network emulator influences network parameters such as bandwidth, packet loss, jitter and latency

OpenIMS – acts as VoIP provider for peering with OpenBTS system

Asterisk PBX record – server is used as SIP client to OpenIMS and ensures generating calls and record degraded sound sample. The PESQ algorithm is used for speech quality evaluations on that server.

2.2 OpenBTS with OpenIMScore interconnection

OpenBTS and OpenIMScore were connected through IP network using SIP trunk. The calls between the systems were generated by calling SIP URI sip:user@open-bts.home or sip:user@open-ims.home. Servers have to be defined in DNS records of the domain. Asterisk on OpenBTS server maps external SIP URIs to internal SIP URIs IMSI00101XXXXXXXXX@127.0.0.1:5062 and served by OpenBTS software and

USRP N210 hardware. OpenBTS stores user information in sqlite database, which can be shared with OpenIMScore system, which uses the same type of database to store user information.

2.3 Perceptual Evaluation of Speech Quality

According to the adequate results from the previous measurements, we have decided to use PESQ algorithm as the keystone of our measurement again. This method is standardized as ITU-T recommendation P.862. [4]. PESQ algorithm determines the quality of the speech according to the comparison of original signal x(t) with the degraded signal y(t) taken at the other end of the transmission chain. The results are evaluated in MOS-PESQ scale. This score has to be converted to more accurate scope for human subjective evaluation. Therefore, it is necessary to use complementary ITU-T P.862.1, which transfer the scale from MOS-PESQ to MOS-LQO. Scale MOS-LQO provides a range of values from 1 to 5. Conversation from MOS-PESQ to MOS-LQO is defined by equation 1.

$$y = 0{,}999 + \frac{4{,}999 - 0{,}999}{1 + e^{-1{,}4945x + 4{,}6607}} \tag{1}$$

Inverse score (MOS-PESQ) from LQO is shown in Equation 2.

$$x = \frac{4{,}6607 - \ln\left(\frac{4{,}999 - y}{y - 4{,}999}\right)}{1{,}4945} \tag{2}$$

3 Results

The measurement started by evaluation of speech quality in channel without any disturbing network conditions. The results were influenced only by transcoding between channels, which couldn't be removed from two reasons. USB modem is able to playback only SLIN codec, samples in 16 bit Signed Linear PCM format, which is natively transcoded to GSM and GSM codec is not typically used as the codec for VoIP provider interconnection. We have decided to use G711 u-law codec because it is considered as the mandatory codec for interconnection between VoIP providers.

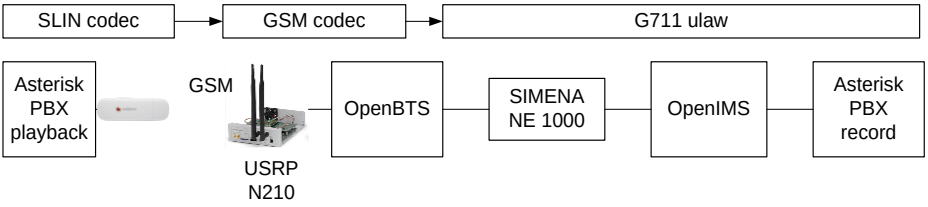

Fig. 2. Transcoding between communication channels

There are main three factors, which influence the final speech quality in our measurement. The first factor is G.711 codec used between the OpenBTS and OpenIMS systems. This codec defines required bandwidth or packet loss resistance between the systems. Theoretically, G.711 codec takes 85.6 kbit/s of bandwidth for one channel.

This rate was confirmed practically by measurement of the bandwidth influence on the speech quality. As the Fig. 4 depicts, insufficient bandwidth under approximately 90 kbit/s cause decreasing of the speech quality. We have considered four different scenarios of the measurement. The red u-law line presents quality of speech in MOS between OpenBTS and OpenIMS without GSM translation. The green u-law-aes256 line presents situation, when the SIP trunk is secured by Transport Layer Security protocol with AES256 cypher [5]. We can see higher requirements for bandwidth from ciphered channel, which requires more overhead for securing the channel.

The blue line depicts quality of speech between OpenBTS and OpenIMS with GSM translation, which occurs in the radio part. The bandwidth requirements are almost the same as the previous case, but with lower speech quality, due to the GSM codec translations. The securing the channel with AES256 cypher brings the similar result that the speech quality in the secured channel decreases earlier than in non-secured channel.

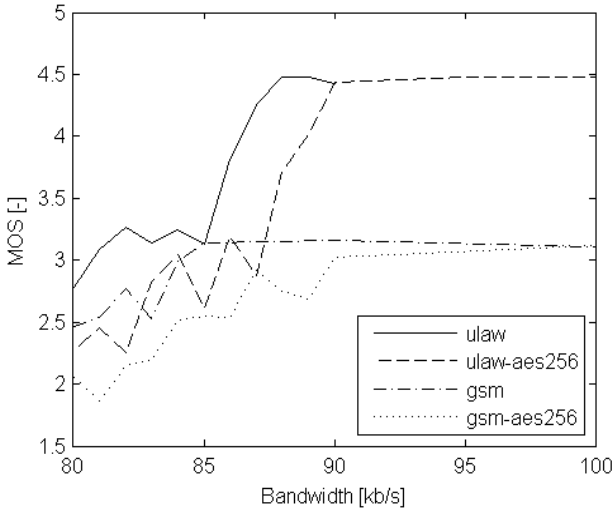

Fig. 3. Influence of bandwidth on speech quality for 1 call

As is shown in the Figure 5, in the case of 2 simultaneous calls, we had confirmed the theoretical prerequisites. The minimal bandwidth for one channel is close to 90 kbit/s. The securing of the communication channel does influence the bandwidth requirements, but with insignificant impact from the administrator point of view.

From that result, there are two aspects due to installation of OpenBTS system and connecting it with a VoIP provider. The bandwidth relies only on the G711 codec between OpenBTS and VoIP provider. GSM codec requires only 13 kbit/s + 21.6 kbit/s overhead bandwidth. According to that fact, GSM codec is not able to provide better speech quality than G711 codec and the overall speech quality depends on the GSM codec.

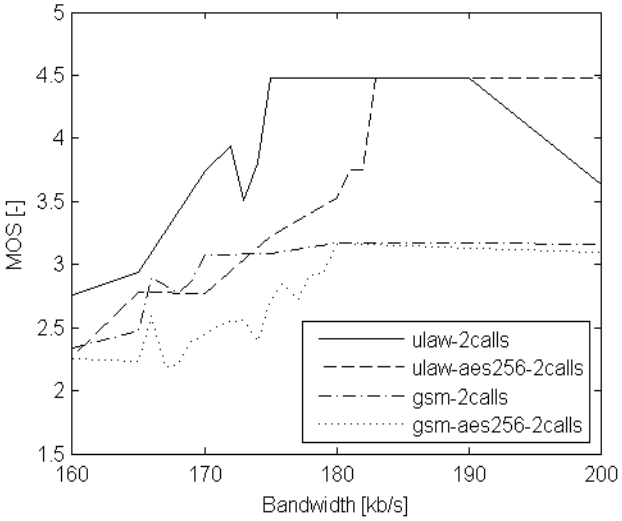

Fig. 4. Influence of bandwidth on speech quality for 2 calls

The next network parameter, which influence the quality of speech is packet loss. Every dropped packet will cause space in the voice call and decrease the quality of speech. We have measured all four scenarios as for the previous network parameter. The Figure 6 depicts the influence of packet loss on the speech quality after linear regression of the measured results.

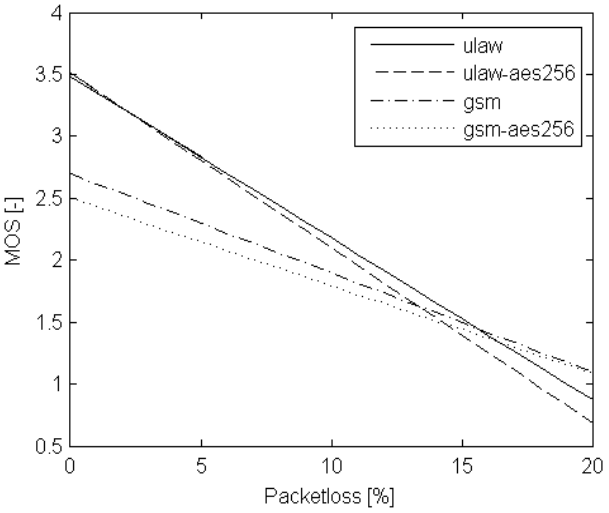

Fig. 5. Influence of packet loss on Speech Quality

The red and green lines present G711 u-law codec. The secured channel is more affected by packet loss. The same relation is presented for GSM codec. The both G711

and GSM codec's lines intersect near 15% of packet loss. According to our subjective sensation from the recorded samples, we can consider 15% of packet loss as the limit value for the sufficient voice quality in our measurement.

The next network parameters, which influence the quality of service are jitter and latency. According to the fact, that the both parameters cause only delay between original and degraded sound sample, we weren't able to evaluate the results by PESQ algorithm. PESQ algorithm as a first step perform time alignment of the original and degraded samples. The both samples then start at the same time, and maximum quality of service is evaluated from that samples.

From that perspective, we have used subjective method to evaluate an influence of jitter and latency on the quality of service. The test call was originated between mobile end terminal connected to the OpenBTS system and SIP client connected to the OpenIMScore system.

Our subjective results respond with ITU-T G.114 Recommendation, which recommends the end-to-end delay for VoIP service up to 150 ms. 300 ms and higher delay cause degradation of the speech quality and grow exponentially with growing delay.

4 Conclusion

The paper was aimed to build own GSM station based on the open source software and low-cost hardware. The built GSM station offers secured communication between the connected mobile terminates in a limited range of signal. The OpenBTS station can be deployed and put into operation in a few minutes in the required area. The connectivity with the outside the world can be provided by any IP-based connection such as mobile broadband, WLAN or satellite connection.

The paper defines required network parameters for the sufficient quality of voice service. The required parameters are 90 kbit/s of bandwidth for one channel. The standard voice calls contain one uplink and one downlink channel for one call. The maximum value of packet loss on the line was measured as 15%, and end-to-end delay is recommended under 150 ms.

Our plans for the future are to build more OpenBTS station in the area to increase coverage of the GSM signal from our mobile station and solve related issues with roaming, handover etc.

Fiber optic Mach-Zehnder interferometer with FBG for movement analysis

Jan Nedoma

Department of Telecommunications, FEECS,
VŠB – Technical University of Ostrava, 17. listopadu 15, 708 33 Ostrava – Poruba
jan.nedoma@vsb.cz

Abstract. Article summarizes the progress of the first year of the author's study of the field of Communication technology. The topic of dissertation thesis is the Fiber optic Mach-Zehnder interferometer with FBG for movement analysis. Article summarizes activities at the Department of Telecommunications during the academic year 2014/2015, research and development activities related to the theses and research projects.

Keywords: interferometer, optical fiber, sensing unit, thesis

1 Introduction

Allow me to introduce myself. My name is Jan Nedoma. I am studying full-time doctoral study at the Faculty of Electrical Engineering and Computer Science at the Technical University of Ostrava. My study programme is called Computer Science, Communication technology and Applied Mathematics and field of study is Communication Technology. Head of my dissertation thesis is professor Vladimir Vašinek. The theme of my thesis is entitled "Fiber optic Mach-Zehnder interferometer with FBG for movement analysis „ and as the title implies, focuses within optoelectronics and optical communications.

2 Activities related to the dissertation thesis

For the most part this theme follows the continuation of my thesis, and after entering the study and consultation with Professor full academic year I worked on data acquisition and analysis. With the help of my colleagues have during the winter and summer semester made a 14 full day external measurements focused on the analysis the movement of cars, trams but also trains. Particular scheme measurement is shown in Figure 1.

© M. Krátký, J. Dvorský, P. Moravec (Eds.): WOFEX 2015, pp. 606–611.
VŠB – Technical University of Ostrava, FEECS, 2015, ISBN 978-80-248-3787-1.

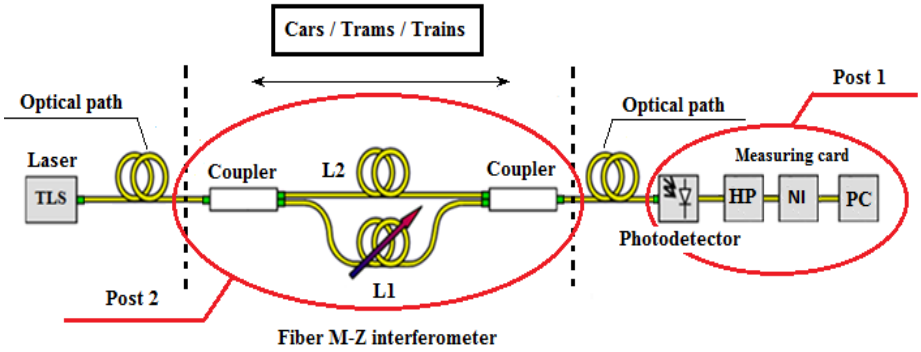

Fig. 1. Measurement scheme

Concerning the analyzes, I worked on processing of each waveform data from the photodetector in the form of frequency and amplitude analysis - amplitude and frequency depending on the time - Figure 2. These data also serve as a basis for further processing in determining the ability of the most accurate detection of individual traversed cars or trains using the MZ interferometer or ability distinction in terms of individual type vehicles - about cars the idea is detection according to a particular brand and model, in the detection of trains distinguish between kits.

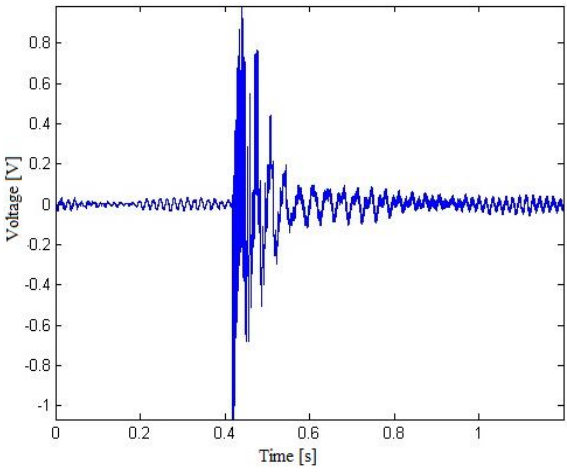

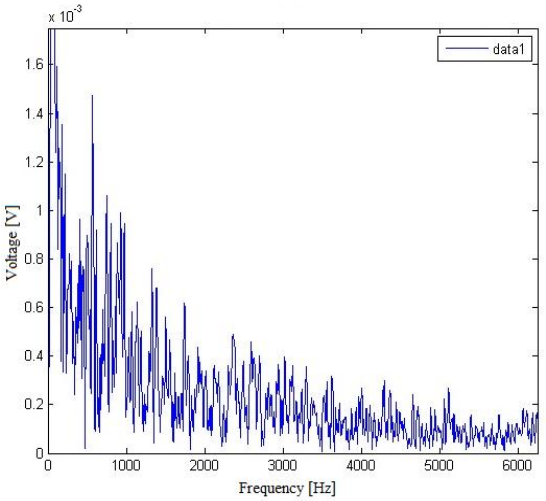

Fig. 2. Record movement

In the first case, detecting cars are now working with numbers that exceed the threshold of 65% successfully detected and about trains 95%. For the first show we have positive results, but need longer time horizon to get more data and modify the software itself for analysis of the data processed.

3 Projects

As part of my studies, I was actively involved in solving four projects, namely:

1. TA ČR - Intelligent modules for lighting and communication
2. TA ČR - Safety of optical transport networks and the development of opt. parts for electric power and electrical appliances
3. PRE SEED fund VŠB-Technical University of Ostrava - TA ČR GAMA PP1
4. Project GUARDSENSE

In project number 1 I conducted according to the assignment of laboratory measurements and individual evaluation of experiments, field measurements, I worked on the preparation of documents for publishing the results. I also dealt with the preparation of new types of experiments to verify the reproducibility of the measurement of MZ interferometer.

The project number 2 was my task to take part in the design layout of scientific research laboratories project and I participated in the research and development of fiber optic networks and systems, mostly in the form of measuring the impact of weather conditions on the transmission characteristics of optical cable / fiber, which are installed N building on the roof areas. Within a measurement polygon parameters are

measured attenuation, chromatic and polarization mode dispersion, changes in temperature over the length of testing circuits.

In project number 3 is my main task improvement sensing unit M-Z interferometer and implementation experimental tests in practice. Individual measurements correspond with the topic of my dissertation. Within the sensing unit, we arrived at the reduction both in terms of size or weight. There was also better arrangement the optical fibers both in terms of sensory or reference. The actual sensing unit was placed in a removable plastic cover with the appropriate interconnection systems. (Figure 3) Thanks to these adjustments was increase frequency range and increase sensitivity to vibration response. During the continuation of the project is due to findings gained in the construction and measurements made plans to re-raise the sensitivity and frequency range and through appropriate structural adjustments and reduction unit.

Fig. 3. Sensing unit

In project number 4 my task was to help design a prototype implementation of Security plastic windows against foreign intrusion based on fiber optic interferometer. As part of this task, I also conducted experimental measurement functionality and output characteristics of the assembled prototype - optimization solutions engagement, measurement frequency range prototype sensitivity to vibration sensing of the environment and the ability to detect speech. In October 2014 I was then involved in advocacy - functional prototype demonstration project in Prague. The idea of this solution is protected in the form the patent application.

Fig. 4. Window prototype

Furthermore, in the study, I actively participated in the external measuring vibration response of the train DP Metro Prague for T-Mobile. My task, together with colleagues there was the installation and uninstallation sensing unit, supervision when implemented types of measurements.

4 Publications

1x Publishing an original contribution in a foreign language at a conference registered in recognized databases (Scopus, WOS, IEEE) as co-author. Title of the article reads as „The ageing process of optical couplers by gamma irradiation“. Article will be published at a conference in San Diego in term 9 to13 august 2015.

1x Patent, utility model according to the percentage of participation, further to the doctoral thesis topic with a 20% share with the name “Fiber optic interferometer for the security of space assets” (using polarization-preserving fiber). Share of the work was based on the design of a prototype device, its verification and evaluation of measurement data. Another portion of my work consisted of processing the selected part of the patent application – to find and build patent search, patent administered originality checking and compiling an application for a patent filing. Date of filing - December 2014.

5 Pedagogic part

In the winter semester, I was actively involved in ensure the teaching with the subject ZEL (Groundwork Electronics). After an agreement with the course supervisor I led the lessons 6h per week throughout the semester. I also worked as supervision during exam tests. In the summer semester, I taught courses ÚDKT (Introduction to Communication Technologies) and OK II (Optical Communications II). In both cases, I led the complete teaching load exercise course - 4h per week. I also was a member

of two cathedral commissions and helped in the final state exams. As an opponent, I've evaluated a bachelor thesis. As a leading bachelor thesis I listed three topics.

6 Other activities at the Department of Telecommunications

I worked full-year presentation of the Department of Telecommunications. The proportion of work consisted mainly in the preparation and presentation of the presented subjects of the Department of Telecommunications Engineering at secondary schools, the building of FEI or open days. Furthermore, I was involved in preparing a presentation for the optical portion, preparation and presentation of the optical laboratory and putting my whole program.

Big analytics tools on cloud

Lukáš Orčík and Miroslav Voznak

Department of Telecommunications, FEECS,
VŠB – Technical University of Ostrava, 17. listopadu 15, 708 33 Ostrava – Poruba
{lukas.orcik.st, miroslav.voznak}@vsb.cz

Abstract. Nowadays for more complex data analysis you will need more than only high-performance desktop PC. Ideally, you need hundreds of gigabytes of RAM and fast disk arrays. Another option is to distribute the processing performance of a larger number of devices with lower performance. For efficient use of limited resources, workflow and data flow must be comprehensive manageable. It is the possibility to use Apache Hadoop as most affordable open source technology that uses distributed computing. Using other technologies that use Hadoop as a base can be a powerful analytic platform that offers a lot of tools for the analysis and data processing. Most of the tools that we can use is located on the cloud. Hadoop provides tools for acquiring, storing, processing, and visualizing data. My job is to prepare a platform that provides a uniform approach to data processing and analysis.This paper deals with describing technologies that I used for building the platform.

Keywords. Apache Hadoop, Apache Zookeeper, Apache Hbase, Apache Hive, Apache Sqoop, Apache Flume, Cloudera Impala, Apache oozie, Hue

1 Technology

As a core technology, I chose the Apache Hadoop. It is a framework that allows for distributed processing of large data sets across clusters of computers using simple programming models. Hadoop framework includes four main modules: Common Hadoop, Hadoop Distributed File System (HDFS), HadoopYARN and Hadoop MapReduce. Common is a utilities that creates support for other Hadoop module. It is a distributed file system that provides high-throughput access to application data. YARN is a framework for job scheduling and cluster resource management. MapReduce is a YARN-based system for parallel processing of large data sets. Next important modul is Hadoop Apache Zookeeper.It provides high performance coordinated process for distributed applications. Distributed system is not trivial problem. It is very prone to changing conditions, blocking, looping at different levels of the system. The Zookeeper is a powerful tool for the fast, scalable and reliable coordination of distributed applications. Another powerful tool is Apache HBase, which as such requires a zookeeper Hadoop project. HBase is used for incidental real-time access to reading and writing big data. It is a non-distributed relational database modeled after Google BigTable. It provides tables that have billions of rows and columns Millions. Another very useful module is Apache

© M. Krátký, J. Dvorský, P. Moravec (Eds.): WOFEX 2015, pp. 612–615.
VŠB – Technical University of Ostrava, FEECS, 2015, ISBN 978-80-248-3787-1.

Hive. It is data warehouse software facilitates querying and managing large datasets residing in distributed storage. Hive provides a mechanism to project structure onto this data and query the data using SQL-like language called HiveQL. For fast data processing it is preferable to use Cloudera Impala. This module is primarily designed for real-time applications. First we need to import them from various sources in order to work with data. For this purposes it is intended modules Apache Sqoop and Apache Flume. Sqoop is designed to transfer data between relational databases and the central store to move data using JDBC and ODBC adapters. It is primarily intended for the database such as MySQL, Postgres, Oracle. Flume is a distributed, reliable, and available service for efficiently collecting, aggregating, and moving large amounts of log data. It has a simple and flexible architecture based on streaming data flows. It is robust and fault tolerant with tunable reliability mechanisms and many failovers and recovery mechanisms. For the most efficient data processing is used by Apache PIG most suitable choice. Pig is a platform for analyzing large data sets that consists of a high-level language for expressing data analysis programs, coupled with infrastructure for evaluating these programs. The salient property of Pig programs is that their structure is amenable to substantial parallelization, which in turns enables them to handle very large data sets. Users write scripts in a high-level language called Pig Latin, which Pig translates into MapReduce jobs that run on a Hadoop cluster. Pig Latin supports a wide variety of data analysis and transformation functions, including join, sort, group, filter, and aggregate. Pig Latin can be extended using UDF (User Defined Functions) which the user can write in Java, Python, JavaScript , Ruby or Groovy and then call directly from the language. On the top of technology, Hadoop stands Hue. Hue is a graphical user interface to operate and develop applications for Apache Hadoop. Hue applications are collected into a desktop-style environment and delivered as a Web application, requiring no additional installation for individual users. All of these technologies help data analysts create complex information systems.

2 Install and develop

In the first stage, my task was to install and configure Hadoop technology on a local server. An appropriate allocation of cores, RAM and disk array for individual nodes determine total computing performance of the cluster. For the Hadoop installation and management used Cloudera distribution.

In the second stage, my task is developing Hadoop application. I'm developing the complex applications for data processing. In Figure 1, we can see the flow of data across modules. In the first step, we import data into the data store with using flume and sqoop. Typical sources of data are IDOS, RUIAN, ČSU, Open street map. In the second step, we select relevant data and store them in the required format. Next step is filtering, aggregation and processing data with using PIG, Hive, and Impala. Pig used for

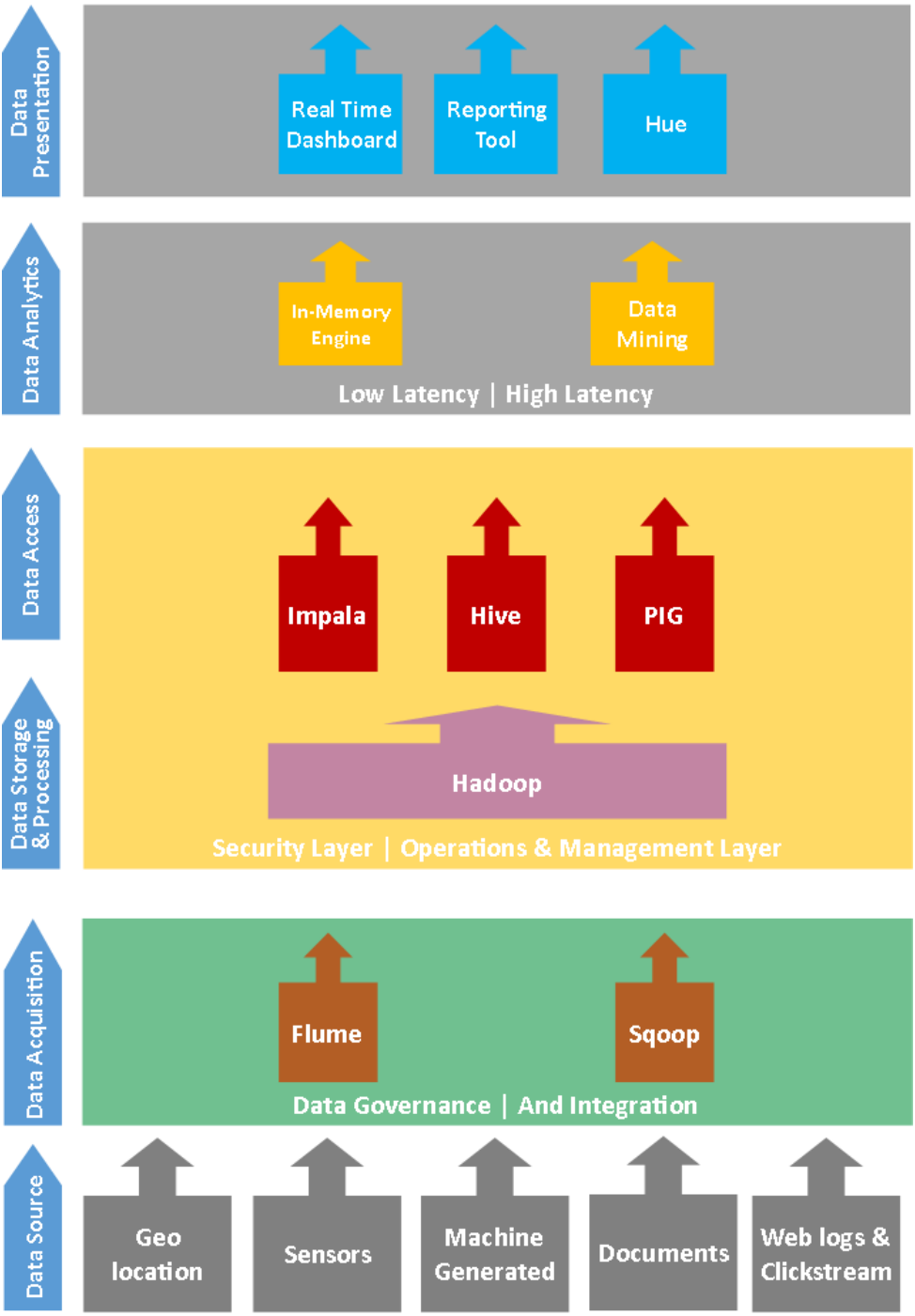

Fig.1. *Data Flow*

merging data sets and store them in the required format. Hive used for filtering large

volumes of data. And Impala for real time application. For final visualization, we can use internally and externally visualization tools. The main visualization tool is Hue. For advanced data, visualization are used external tools that are not part of Hadoop. Typically, external geo utilities and customer visualization tools.

Conclusion

Building analytical platforms and development of applications for data processing is activity on which I focused. This platform offers great opportunities in data processing. Data analysts have all the instruments placed in the cloud, so they can focus primarily on data analysis and not on thing concerning technology of data processing.

References

1. Hadoop. Apache™ Hadoop [online]. 2015 [cit. 2015-08-07]. Dostupné z: http://hadoop.apache.org
2. Flume. Apache™ Flume [online]. 2015 [cit. 2015-08-07]. Dostupné z: http://flume.apache.org
3. HBase. Apache™ HBase [online]. 2015 [cit. 2015-08-07]. Dostupné z: http://hbase.apache.org
4. Hive. Apache™ Hive [online]. 2015 [cit. 2015-08-07]. Dostupné z: http://hive.apache.org
5. Oozie. Apache™ Oozie [online]. 2015 [cit. 2015-08-07]. Dostupné z: http://oozie.apache.org
6. PIG. Apache™ PIG [online]. 2015 [cit. 2015-08-07]. Dostupné z: http://pig.apache.org
7. Sqoop. Apache™ Sqoop [online]. 2015 [cit. 2015-08-07]. Dostupné z: http://sqoop.apache.org
8. Zookeeper. Apache™ Zookeeper [online]. 2015 [cit. 2015-08-07]. Dostupné z: http://zookeeper.apache.org
9. Impala. Cloudera Impala [online]. 2015 [cit. 2015-08-07]. Dostupné z: http://www.cloudera.com/content/cloudera/en/products-and-services/cdh/impala.html
10. Hue. Hue [online]. 2015 [cit. 2015-08-07]. Dostupné z: http://cloudera.github.io/hue/docs-3.7.0/manual.html

Concrete Deflection Measurement Using Fiber Optic Distributed Strain System

Martin Papes

Department of Telecommunications, FEECS,
VŠB – Technical University of Ostrava, 17. listopadu 15, 708 33 Ostrava – Poruba
martin.papes@vsb.cz

Abstract. The monitoring of building structures deformations and testing of construction materials resilience are very important processes in the development and production of given materials and structures. Undesirable or excessive deformations of materials are phenomena which are unacceptable in construction, especially in supporting structures. These issues are currently monitored by electromechanical sensor in most cases. It is a classic technique when the sensor measures the material stress at the point of its installation. This paper deals with the concrete deflection measurement using fiber optic distributed strain system. This system uses optical fibre as a sensor and operates at the principle of measurement of Brillouin frequencies. The mechanical stress on the optical fiber causes shift of these frequencies. This change is subsequently converted to stress unit micro-strain. In our experiments, the optical fiber was embedded in concrete along its whole length. The advantage of this system is that the measurement is carrying out along the entire fiber length with spatial resolution around 50 cm, so it is possible continuously measure several thousands of points at the distance of several kilometers.

Keywords: Brillouin scattering, concrete, deflection, distributed strain system.

1 Introduction

Monitoring of building structures deformations and testing of construction materials by using Fiber Optic Distributed Strain System is a quiet new method in this field. Nowadays, most of these measurements or monitoring are carried out by using standard electromechanical sensors. This method has one main disadvantage and that is it measures the strain only at the point of its installation. Therefore, monitoring of long distances is costly because many sensors have to be installed. With a long term cooperation between the Department of Telecommunications and the Faculty of Civil Engineering was found the opportunity to take special measurements focused in this field, specifically concrete deflections measurement using a Fiber Optic Distributed Strain System. This system uses an optical fiber as a sensor, with spatial resolution 0.5 m, so it is possible to have 2000 measuring points at optical fiber with 1 km length. The optical fiber was embedded in cementitious composites and these were gradually loaded [1], [2], [3], [4], [5].

© M. Krátký, J. Dvorský, P. Moravec (Eds.): WOFEX 2015, pp. 616–619.
VŠB – Technical University of Ostrava, FEECS, 2015, ISBN 978-80-248-3787-1.

2 Experiment Descriptions

The dimensions of experimental elements were adapted to laboratory conditions and to laboratory equipment. The testing was performed on the beam with dimensions of 166.35 × 12 × 10 cm. This beam was manufactured from cement fibers composite reinforced with two steel bars to avoid fast fracture of the sample during the testing. Also, other samples were manufactured during concreting. These were determined at the compressive strength and Youngs modulus. The average compressive strength cubes specimens was 62.5 MPa with a static elastic modulus 34 GPa[3].

The aim of our experiment was to verify the functionality of method of concrete deflection measurement by using fiber optic strain system. The single mode optical fiber was embedded in the sample. The sample was divided into 8 sections. Each section was 20.8 cm long. The optical fiber was placed in the sample in the following way. On each section interface was a sensory ring, made of 133.17 cm of optical fiber. The sensory rings were interconnected with optical fiber with length of 1 m. Therefore, the fiber in each section was wrapped into the loop. The length of the optical fiber before the sample was 5 m and the fiber after the sample was long 45 m. Totally, there was 17.322 m of optical fiber embedded in the sample.

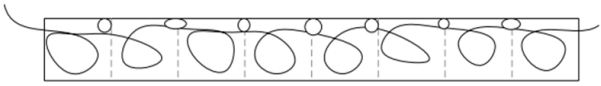

Fig. 1. Deployment of the single-mode optical fiber in the sample.

The testing of the sample was carried out on the tear device FP 10. This device is equipped also with a pressure sensor. The load was performed by deformation with an increment of 0.1 mm per minute. The whole measuring system can be seen in Fig. 2.

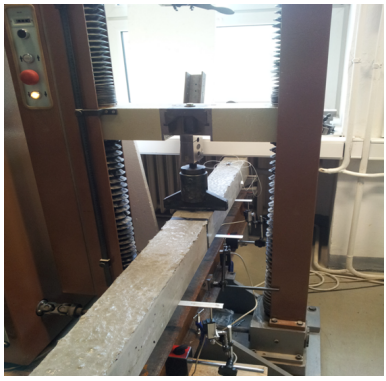

Fig. 2. Measuring system composed from FP 10 device, cementitious sample and optical fiber.

3 Experiment Results

Figure 3 presents the measured values along the measured route; it means the whole optical fiber embedded in the cementitious beam. Totally, 6 measurements were carried out with intervals of loading about 0.1 mm. The measured values are presented as shifts of Brillouin frequencies. Totally, it was created 8 measuring rings in the beam. From the measured results can be clearly seen, that the system recognized only 6 of them. The first and the last sensory rings are pooled, or affected by some external influences, because the optical fiber right in the front of the first ring and the fiber behind the last sensory ring is nor loaded, what is probably the main cause of measurement error.

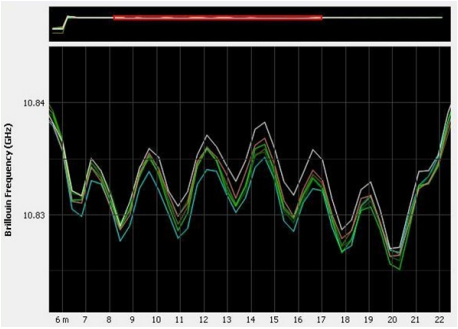

Fig. 3. Measured shifts of Brillouin frequencies in 6 sensory rings.

Figure 4 presents the same measurements results in microstrains. These results clearly present that the increase of concrete deflection causes the constant increase of microstrains values.

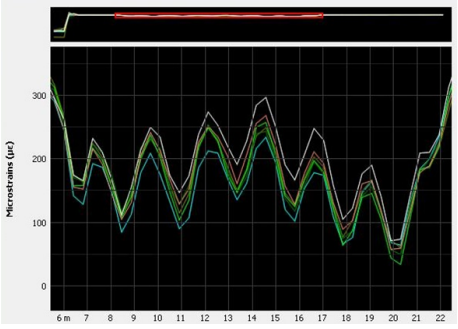

Fig. 4. Measured shifts of microstrains in 6 sensory rings.

4 Conclusions

The aim of this experiment was to determine the functionality of this not wide spread and quite unique method of concrete deflection measurements. For these measurements we used a fiber optic distributed strain system. Based on the measured results we can conclude that this unique technique and this system is applicable for this kind of application and it also introduce some major advantages, such as very high sensitivity, which can detect even a very small deflections in tenths of a millimeter. Very interesting is also the cost of this method, taking into account the spatial resolution of 0.5 m, the number of measuring points what can be created with an optical fiber and the distances which can be covered. The future measurements will be focused on similar trivial experiment using special optical fibers.

References

1. OMNISENS, User Manual DITEST STA-R - Fiber Optic Distributed Temperature and Strain Analyzer. Omnisens SA, 3 Rjond Bosson, CH-1110, Morges, Switzerland.
2. OMNISENS, User Manual DITEST Data Viewer. Omnisens SA, 3 Rjond Bosson, CH-1110, Morges, Switzerland.
3. Hurta, J., Fajkus, M., Mec, P., Application of FBG in the experimental measurements of deformation elements of cement composites.
4. Koudelka, P., Latal, J., Vitasek, J., Hurta, J., Siska, P., Liner, A., Papes, M., Implementation of Optical meanders of the Optical-fiber DTS system based on Raman stimulated scattering into the building processes, Advances in Electrical and Electronic Engineering 10(3), 187-193 (2012).
5. Hanacek, F., Latal, J., Siska, P., Vasinek, V., Koudelka, P., Skapa, J., Hurta, J., Fiber optic sensor for high temperatures, 2010 International Conference on Applied Electronics, (2010).

Stress Detection from Human Speech

Pavol Partila, Jaromir Tovarek, and Miroslav Voznak

Department of Telecommunications, FEECS,
VŠB – Technical University of Ostrava, 17. listopadu 15, 708 33 Ostrava – Poruba
{pavol.partila, jaromir.tovarek, miroslav.voznak}@vsb.cz

Abstract. This article discusses the stress recognition of human speech. Nowadays, the Speech Processing scientific teams is trying to extract secondary information from the voice. Secondary information can be age, gender, or in this case the emotional state of man. Knowledge of the emotional state of the speaker allows us to adapt human-computer conversation. Similarly, information about the increased stress of policeman, a soldier or firefighter will allow dispatching regulates the procedure of intervention. Results of this work compare methods for extracting the fundamental frequency. This parameter serves as input to the classifier, whose role is to recognize stress. The classifier is created by the self-organizing map (SOM). The aim was to compare different methods of extraction parameters and their significance for the SOM classifier.

Keywords: Classification, Features extraction, Human Speech, Speech processing.

1 Introduction

Secondary speech information is an important part of verbal communication. The way we pronounce a word carries a large amount of information. A different intona-tion of a spoken word changes the meaning. There are many words that mean some-thing totally different with a different intonation. The word "immediately?" pro-nounced with a rising intonation at the end of the word has a different meaning than "immediately!" with the intonation at the beginning of the word. The intonation is a word associated with the emotional state of the speaker.

There are many areas in which the information about the emotional state is needed. Nowadays, technological development puts more emphasis on the increased accuracy and simplicity of communication between man and computer. Modern applications use the speech for input-output interface increasingly. In this type of interaction two problems can occur, caused by the absence of information about the emotional state. The first one is an incorrect recognition of a word or a command from a person who is under stress. The machine recognizes human speech differently than a man with his hearing. The accuracy is affected by changes in the voice signal due to stress on the vocal tract. The second problem is that we feel the absence of emotional state in the machine speech of the loudspeaker. Classic applications such as Text-To-Speech combine parts of speech sounds that are truly correct, but ultimately this signal is without any emotion. Such speech acts on the man and is synthetically unreliable.

© M. Krátký, J. Dvorský, P. Moravec (Eds.): WOFEX 2015, pp. 620–625.
VŠB – Technical University of Ostrava, FEECS, 2015, ISBN 978-80-248-3787-1.

There are several physiological criteria such as for example heart rate, breathing changes and sweating, which enable determining the emotional state of a man. A number of speech signal parameters is used in speech processing. An imperfect human ear responds to parameters such as intensity, intonation, and speech rate. Fundamental frequency of speech, zero crossings rate, energy and cepstral coefficients are parameters which are used in digital speech processing. The following sections contain a description of signal processing methods , selection of the training sets and neural network classifier.

2 Pre-Processing

Speech signal is stochastic by nature. However, a speech signal has a number of characteristics that may be unwanted during processing. This chapter describes a process called pre-processing that is an important part of the digital speech signal processing. These few steps prepare the signal for subsequent extraction of signal parameters. The values of these parameters could be wrong without the pre-processing process. Figure 1 shows the pre-processing procedure.

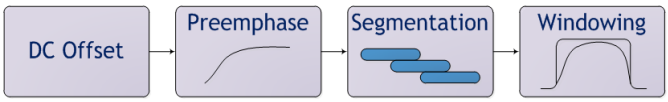

Fig. 1. Pre-Processing procedure

Train respectively testing is the key step of the system. The quality of the input data, the audio signal in this case, has a direct impact on the classification accuracy.

For this reason, it is used the Berlin database containing over 500 recordings of actors consists men and women. The database contains 10 sentences in the seven emotional states. This corpus of recordings is considered as a high-quality database, because it was created by professional actors in the sound studio.

As mentioned, the speech signal has to be modified by routine operations such as removing the DC component, pre-emphasis and segmentation stochastic signal into quasi-periodic frames.

3 Fundamental frequency of vocal cords

Age, gender, speech errors and emotional state of a man can be determined using this parameter. There are several methods in signal processing which enable estimating the fundamental frequency. Human speech consists of voiced and unvoiced speech sounds. The vocal cords are almost completely open in the creation of voiceless phonemes. The basic tone does not arise with opened vocal cords and therefore F_0 can be calculated only from the voiced parts. Each method to calculate F_0 has advantages and disadvantages. This article compars four methods and their use in a self-organizing feature map classifier.

3.1 Auto-correlation function

This simple method can be used where we have a full signal. The auto-correlation function is defined in Eq. (1).

$$R(m) = \sum_{n=m}^{N-1} s(n)\, s(n-m). \tag{1}$$

Lag k determined by the position of maxima. The fundamental frequency of vocal cords is calculated using Eq. (3).

$$k = argmax R(m). \tag{2}$$

$$F_0 = \frac{F_{sampling}}{k}. \tag{3}$$

3.2 Normalized cross-correlation function

The difference in energy shifted and original framework is settled by normalization:

$$NCCF(m) = \frac{\sum_{n=m}^{N-1} s(n)\, s(n-m)}{\sqrt{E_1 E_2}} \tag{4}$$

where E_1 is energy of original frame and E_2 is energy of shifted frame. Lag and F_0 are calculated. F_0 extraction is performed just as in the ACF (Eqs. 1 and 3).

3.3 Central clipping

Voiced and voiceless parts of the signal are separated with the threshold level. The speech signal constantly changes and thus it is not possible to to use a single threshold for the entire signal. The threshold is determined for each frame separately, using the equation bellow.

$$P(i) = \alpha min(MAX_{i-1}, MAX_{i+1}). \tag{5}$$

Peaks of neighboring frames *i-1* and *i+1* are established. The threshold level is determined as the lower value of the two. Constant α is set within the range 0.8 to 1. The original signal of frame i is weighted with threshold *P(i)*. Samples with a higher value are clipped and normalized to 1 and lower to 0.

3.4 Subharmonic-To-Harmonic Ratio

This method is developed in frequency domain. *A(f)* is short-term spectrum function. Suppose that f_0 is fundamental frequency. The sum of harmonic amplitude is defined below.

$$SH = \sum_{n-1}^{N} A(nf_0) \tag{6}$$

N is number of all harmonics which can be considered. If we consider the subharmonic frequency, that is the one half of f_0. The sum of subharmonic amplitude is described in Eq. (7). Subharmonic-to-harmonic ratio can be obtained by dividing SS and SH.

$$SS = \sum_{n-1}^{N} A\left[\left(n - \frac{1}{2}\right) f_0\right] \tag{7}$$

4 Self-Organizing Feature Map

The emotional state classifier is based on self-organizing maps (SOM). These maps represent a specific type of neural networks with uncontrolled competitive learning. There are generally two-dimensional maps of neurons. The learning process of SOM is uncontrolled which means that the input data do not need to know the output. In the process of learning, SOM themselves determine how to classify the inputs. At the beginning of learning, the weights of all the inputs of all neurons can be set randomly. Randomly selected input vectors are applied to neurons and then analyzed in order to find one which is most similar to input. This neuron is called the winner. The weights of neighboring neurons are adjusted according to the following rule.

$$w_{ij}(t+1) = w_{ij}(t) + \gamma(x_j(t) - w_{ij}(t)) \tag{8}$$

This equation describes the weight between neurons i and j for $t+1$ iteration and input $x_j(t)$. Next iteration means a new vector on input, finding new winner and changing weights between neurons again. After the learning process is completed, the map has a shape that represents the characters of input parameters. The aim of this article is to clarify the appropriate choice of parameters for the two-dimensional maps. They are two-dimensional because counting the change weights between neurons for more than 2D dimensions poses high demands on hardware. This should be taken into account as these days real-time speech processing is sought after in the entire telecommunications services sector.

5 Results

The system which was designed in software Matlab finally consists of three main blocks. These have been described above. Figure 2 shows the block diagram. The input speech signal is embedded into the system sequentially. Audio records of different emotional states were used as the speech signals.

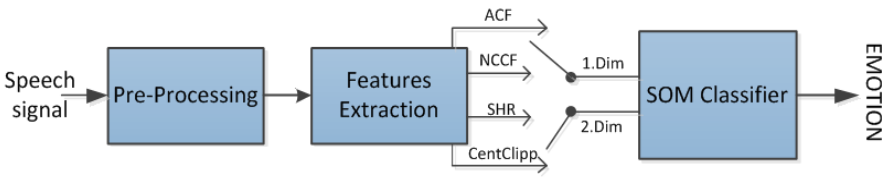

Fig. 2. Speech emotion recognition system

The first block algorithm performed the pre-processing operations. The next block is designed to extract the basic tone using the four above-mentioned methods. These parameters are input data for the neural network. The combination of the four methods ACF, NCCF, Clipping Central and SHR yielded pairs of inputs.

Table 1. Pairs of SOM Classifier Inputs

Input	ACF-NCCF	ACF-SHR	ACF-CClip	NCCF-SHR	NCCF-CClip	SHR-CClip
Resolution	Bad	Normal	Normal	**Worst**	Bad	**Best**

Mixed couples all calculation methods F_0 yielded different results. The worst decision was level classifier at NCCF versus SHR. The best classifier had a distinctive character input methods in SHR and Clipping Central, which was to be expected, because these two methods are less prone to adverse extract F_0 from unvoiced parts of the signal. Best and worst results are shown in Figure below.

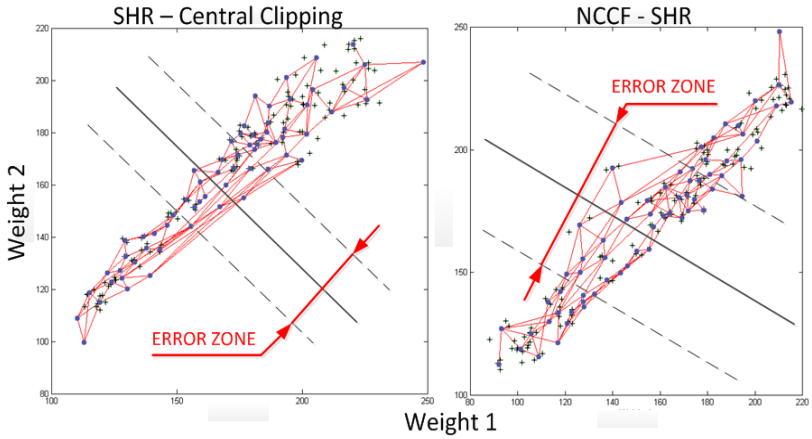

Fig. 3. Trained self-organizing maps with error zones.

6 Conclusion

This article focused on the distinctive character classifier. Using different methods for calculating the fundamental frequency of human voice can yield results of differ-ent accuracy. Therefore, it is recommended to apply at least two methods for calculating F_0. The second perspective is not appropriate to use high dimensional maps for the classification of emotional state. Such classifiers are hardware and time consuming. The problem of delay is unacceptable for telecommunications services and applications that require real-time access.

The block algorithm for pitch extraction is designed to calculate F_0 using four methods. Inputs for the two-dimensional neural network were created by combining these four methods. Subharmonic-To-Harmonic Ratio, and Central Clipping methods were considered more reliable than others.

It is interesting to note that the classifier has the highest error rate for combined SHR and NCCF. The SOM classifier has the lowest error rate, and thus the best re-

solving power between normal and stress emotional state, provided SHR and Central Clipping methods had been applied on its inputs. The aim of the article was to determine a suitable combination of the two methods to determine F_0 for classifying human emotional state.

References

1. Voznak, M., Rezac, F., Rozhon, J. Speech Quality Monitoring in Czech National Research Network. Advances in Electrical and Electronic Engineering. 2010, vol. 8, no. 5, pp. 114-117. ISSN 1804-3119
2. Partila, P., Voznak, M., Mikulec, M., Zdralek, J. Fundamental Frequency Extraction Method using Central Clipping and its Importance for the Classification of Emotional State. Advances in Electrical and Electronic Engineering. 2012, vol. 10, no. 4, pp. 270-275. ISSN 1804-3119.
3. Partila, P., Tovarek J., Frnda, J., Voznak, M., Penhaker, M.and Peterek, T. Emotional Impact on Neurological Characteristics and Human Speech. : 527. DOI: 10.1007/978-3-319-07773-4_52.

The Influence of Radiation Burden on Ageing Effects of Optical Fiber Coupler

Frantisek Perecar

Department of Telecommunications, FEECS,
VŠB – Technical University of Ostrava, 17. listopadu 15, 708 33 Ostrava – Poruba
frantisek.perecar@vsb.cz

Abstract. The paper discuss about accelerated ageing of optical fiber elements in their burdened with gamma radiation. The article focus on applied research and experimental development of resources for safety operation of optical networks since monitoring of ageing substantially contributes to its security. It addresses issues of accelerated ageing of optical fiber elements in their burdened with gamma radiation. How does radiation energy of gamma radiation influence optical network elements? This effect is explored just very little bit and is yet another unanswered question. In addition to the destruction of coating materials, gamma radiation has its effect on the internal structure of the optical fiber. It is necessary to specify the changes in the optical coupler and find out why these changes occur. This article contains experimental measurement of the impact of gamma radiation Cobalt-60 on the optical coupler of split performance ratio 50:50. Optical passive component were exposed to gradually increasing doses of 60Co. Measurements are focused on the overall distribution of the energy of LP01 mode in the core and cladding various branches of SM optical fiber coupler. Graphical and mathematical detect changes in the dissemination of energy coupler after single doses of gamma radiation are useful to understand the phenomenon of accelerated ageing elements of optical networks in environments with an increased incidence of radiation energy [1].

Keywords: coupler, gamma irradiation, Cobalt-60, ageing, energy propagation,

1 Introduction

Issue of accelerated aging of passive optical device can be viewed from several angles. Huge increase performance, increase the number of channels in a single fiber, high temperature, and tension, compression or dose of gamma radiation reduce expected life of optical passive components. The optical fiber is used for data communications, application for many sensitive applications in the form of optical fiber sensors. Optical fibers are non-electric, immune to radio-frequency interference and electromagnetic interference, have low weight and size and allow entry to the normally inaccessible areas. As optical sensors exhibit high accuracy of observed variables they can be linked to data communications systems [2]. We can capture most of the physi-

© M. Krátký, J. Dvorský, P. Moravec (Eds.): WOFEX 2015, pp. 626–631.
VŠB – Technical University of Ostrava, FEECS, 2015, ISBN 978-80-248-3787-1.

cal properties with optical fibers. Temperature, pressure, sound, position, rotation, light intensity, radiation, stress, electric field, MP, flow, liquid level, chemical analysis and vibration are just some of the phenomena that can be captured. Optical coupler as a passive optical element merges or divides the optical power into multiple optical fibers [3]. In our research we used SM performance-split couplers that distribute power according to the split ratio among all output fibers. The most frequently used splitting ratio couplers for 1:2 is 50:50. This article highlights the changes in the parameter of optical fiber coupler, namely parameter MFD, due to ^{60}Co gamma irradiation and is an introduction to a comprehensive solution of the issue. Optical passive components are potentially resistant against ionizing radiation and we try to find out what is happening in the various couplers increasing doses of radiation [7]. Is radioactivity destructing only cover materials or has it got an effect also on the inner cable structure leading to changing the transmission parameters of optical fibers? The coupler was irradiated doses of gamma radiation 5kGy, 20.15kGy and 34.32kGy gradually.

2 Irradiation optical couplers

The coupler irradiation was provided by gamma source in the irradiation shaft. Type of source of gamma irradiation was ^{60}Co that emits two gamma rays with energies of 1.17 MeV and 1.33MeV. Those energies are not sufficient to activate irradiated samples. The source total activity was approximately 2TBq and a dose rate depended on a sample position relative to the source [4].

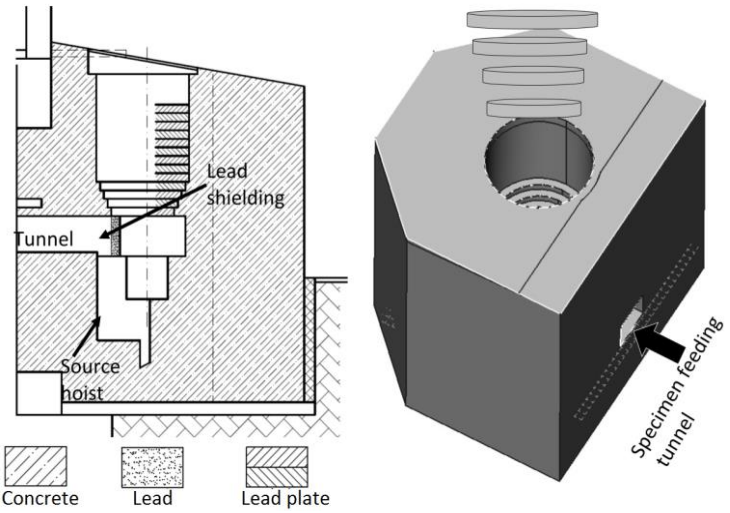

Fig. 1. The scheme of irradiation shaft at the Institute of Nuclear Research in Rez

Sample was mounted around the circumference of a polymeric cylinder to reach maximum homogeneity of irradiating. During irradiating the source was placed in the

cylinders centre. Three alanine pills were fixed to the cylinder in different height to measure absorbed doses. Average absorbed dose rate to a sample is 0.02kGy/hod. Temperature in the shaft is not stable and moved between 16-20°C. Sample total absorbed dose was 34.32kGy that can represent 60 years of operation metallic cables in containment of some nuclear power plants [5].

3 Experimental Measurement

For monitoring parameter and distribution of energy in each output optical fiber couplers use a scanning slit system applied to the profile of the optical beam (Optical Scanning Slit Beam Profiler) from Thorlabs. BP109-IR device covers band from 700nm to 1800nm. As detection material is used Indium Gallium Arsenide compound - InGaAs. It enables high-precision analysis of beam quality and captures the spatial distribution of energy. Foundation is mobile head, whose main component is a rotating drum with a photosensitive material intended solely to detect radiation in the infrared range. The device has an integrated Power Meter, which is not calibrated and can effectively suppress the noise level [6]. Scanning slit method is ideal for analysis of laser profiles, which shape of the beam is close to a Gaussian distribution. Software environment was covered by program Thorlabs Beam, which is freely downloadable package with driver and graphical user interface. Thorlabs Beam version 5.0 was used for the measurement. After calibration of the device, energy propagation was measured at a distance of 1 cm from scanning slit on our machine. Scan rate was set at 12000Hz and target resolution 2.5µm

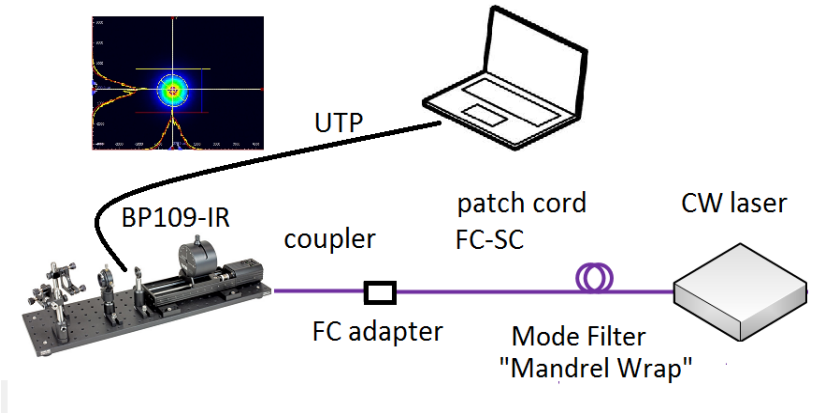

Fig. 2. Synoptic diagram visualization system for measuring an energy propagation of optical fiber coupler

The measurements were made on single-mode coupler with dividing ratio 50:50 manufactured by company Optokon. Coupler original conditions conditions after the first

irradiation conditions after the second irradiation and conditions after third irradiation finally were observed. The measurements were carried out at constant conditions (i.e. room temperature), in the absence of external variable weather conditions, at wavelengths 1303nm and 1553nm of CW laser. We used optical light source FLS-2100 manufactured by company EXFO. Output power was 1mW. We applied filter modes to restrict of wrong modes. Common mode filter was realized on patch cord FC-SC. Mode filter was the "mandrel wrap", where the fiber was snugly wrapped around a mandrel five times with mandrel diameter of 3.2 cm. This concept is filtering higher order modes.

4 Results

As it was already mentioned, parameter light intensity was measured at a distance of 1 cm from the detection device slot of BP109-IR. Parameter MFD was observed before irradiation coupler by gamma radiation and after the radiation dose 5kGy, 20.15kGy and 34.32kGy of gamma radiation. Average values of MFD are shown in Table 1. Laser was set on power 1mW. MFD was measured separately for the X-axis and the Y-axis. For the X axis, MFD variably changed in the range from 1800µm to 1950µm, at a wavelength of 1303nm. For a wavelength of 1553nm, the MFD is in the range from 1830µm to 2000µm. In both cases, for the wavelength of 1303nm and 1553nm, rate of MFD parameter decreases to a total dose of irradiation 34.32kGy coupler.

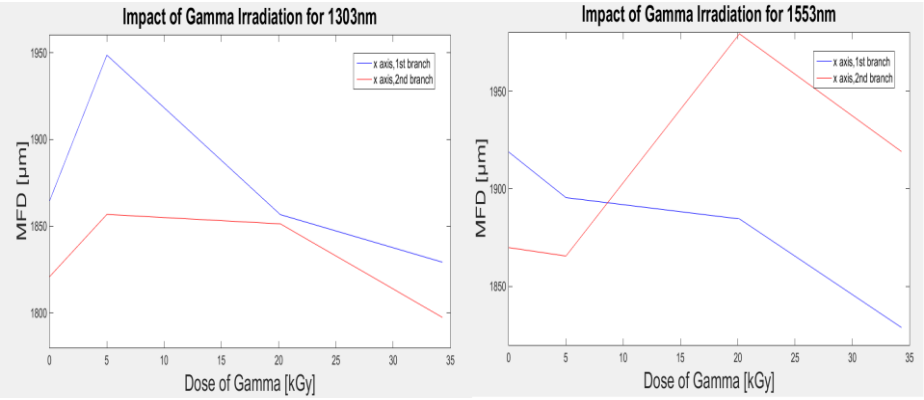

Fig. 3. Dependence MFD dose gamma radiation on X-axis, for wavelengths 1303nm and 1553nm

On Y-axis, MFD reached 1700-1850µm at wavelength 1303nm. For Wavelength 1553nm MFD ranged from 1750µm to 1950µm. The values of the MFD gamma radiation will not change linearly, MFD values decreased with increasing radiation dose. The values of the MFD gamma radiation will not change linearly, MFD values decreased with increasing radiation dose. It being understood that at a wavelength of

1553nm MFD reaching higher values for X-axis and Y-axis as the wavelength of 1303nm.

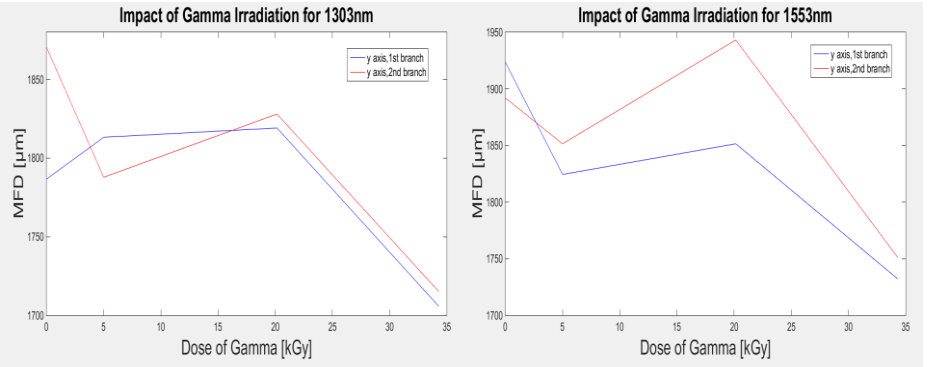

Fig. 4. Dependence MFD dose gamma radiation on Y-axis, for wavelengths 1303nm and 1553nm

λ [nm]	branch	axis	γ[kGy]\MFD			
			0	5	20.15	30.14
1303	1	x [µm]	1864.70	1948.63	1856.70	1829.26
		y [µm]	1786.68	1813,26	1819.15	1705.68
	2	x [µm]	1820.98	1856.82	1851.38	1797.42
		y [µm]	1870.41	1787.82	1828.01	1715.06
1553	1	x [µm]	1918.89	1895.53	1884.64	1828.94
		y [µm]	1923.46	1824.47	1849.54	1732.19
	2	x [µm]	1869.96	1865.63	1979.45	1919.05
		y [µm]	1892.04	1851.52	1943.19	1751.07

Table 1. : Average values of MFD for coupler with split ratio of 50:50

5 Summary

The goal of team of authors of this article was to determine whether gamma radiations are passive optical devices, couplers, in a way, which would cause accelerated aging. The aim was to determine the appropriateness of using optical network elements in areas with higher doses of gamma radiation without rapidly shortening its expected lifetime. This article is an introduction to research of changes that occur in the performance characteristics of the spread of energy in different SM optical fiber couplers

under effect of different doses of 60Co gamma radiation. Measurements were made in the software environment program Thorlabs Beam 5.0 on the device BP109-IR from Thorlabs. Parameter measurement was carried out in the laboratory campus VSB-TU Ostrava, while ^{60}Co irradiation was carried out in the Nuclear Research Institute in Rez – Czech Republic. Branch of coupler on which the measured parameter MFD was at a distance of 1cm from scanning slit of device BP109-IR. CW laser was set with an output power of 1mW and the wavelength of 1303nm and 1553nm. We applied filter modes to restrict of wrong modes. MFD parameter was measured in two axes X and Y. By comparing parameters MFD after irradiation doses of 5kGy, 20.15kGy and 34.32kGy to the original value before irradiation, for coupler with split ratio of performance 50:50 we can conclude that the MFD and FWHM parameters decreased to a total dose of irradiation 34.32kGy coupler in both cases for the wavelength of 1303nm and 1553nm. The values of parameters due to gamma irradiation burden will not change linearly, MFD values decreased with increasing radiation dose. This is demonstrated by graphs and tables. This article is an introduction to research changes in performance characteristics of the distribution of energy reserves in the optical fiber coupler. It is necessary to find out what is actually happening in the coupler, if there are changes and determine why it is happening.

References

1 Agrawal, G. P., [Fiber-Optical Communications Systems], 3rd ed. Wiley, New York (2002).

2 Chovan, J., Uherek, F., Kurinec, R., Satka, A., Pavlov, J., & Seyringer, D. (2011). Temperature Characterization of Passive Optical Components for WDM-PON FTTx. Advances in Electrical and Electronic Engineering, 9(3), 143 - 149.

3 Girard S, Laurent A, Pinsard E, Robin T, Cadier B, Boutillier M, Marcandella C, Boukenter A, Ouerdane Y. Radiation-hard erbium optical fiber and fiber amplifier for both low- and high-dose space missions. Opt Lett 2014;39(9):2541-4.

4 Friebele, E.J., Askins, C.G., Gingerich, M.E., Long, K.J. Optical fiber waveguides in radiation environments, II (1984) Nuclear Inst. and Methods in Physics Research, B, 1 (2-3), pp. 355-369.

5 Troska, J., Batten, J., Gill, K., Vasey, F. Radiation effects in commercial off-the-shelf single-mode optical fibres (1998) Proceedings of SPIE - The International Society for Optical Engineering, 3440, pp. 112-119. doi: 10.1117/12.326687

6 Kakuta, T., Shikama, T., Narui, M., Sagawa, T. Behavior of optical fibers under heavy irradiation (1998) Fusion Engineering and Design, 41 (1-4), pp. 201-205.

7 Sporea, D., Adelina Sporea and Constantin OPROIU. Comparative study on the degradation of UV optical fibers subjected to electron beam and gamma ray irradiation. Optical Fiber Technology. 2013, vol. 19, issue 6, s. 652-657. DOI: 10.1016/j.yofte.2013.10.005.

Hybrid WDM/TDM Topology Using the Fabry-Perot Laser

Radek Poboril

Department of Telecommunications, FEECS,
VŠB – Technical University of Ostrava, 17. listopadu 15, 708 33 Ostrava – Poruba
radek.poboril@gmail.com

Abstract. The aim of this article is to point out the possibility of solving problems related to a concept of a flexible hybrid optical access network. The entire topology design was realized using the OPTIWAVE development environment, in which particular test measurements were carried out as well. Therefore, in the following chapters, we will subsequently focus on individual parts of the proposed topology and will give reasons for their functions, whilst the last part of the article will consist of values measured in the topology and their overall evaluation.

Keywords: Hybrid PON network, WDM, TDM, WDM/TDM, Fabry-Perot laser, AWG, topology design, Optiwave.

1 Introduction

The motivation of passive optical network (PON) technology is to provide end-users with a cost-effective access mechanism that is interference-free and bandwidth-abundant. The general PON topology consists of single mode fibres linking the optical line terminal (OLT) and the optical network units (ONUs) with an optical distribution network (ODN). Based on this, TDMPON technology is already mature [1].

End users make use of Internet services such as HDTV, VOIP, gaming or video conference, and their demands for bandwidth exceeded 100 Mb·s-1 around 2012. In 2009 in Japan, the number of users connected via optical fibre exceeded 17 million. Copper lines and wireless access methods are not able to meet these requirements and that is why the attention is now turned to the use of optical fibres [2], [3].

Passive optical networks got their name because of the fact that they don't use powered devices in the outside infrastructures, the so-called active amplifiers or splitters and hubs, elements providing splitting of the light output power into branches. Instead of these active elements we can use passive splitters because they allow signal to be divided among many users.

© M. Krátký, J. Dvorský, P. Moravec (Eds.): WOFEX 2015, pp. 632–637.
VŠB – Technical University of Ostrava, FEECS, 2015, ISBN 978-80-248-3787-1.

Typically, the optical signal is divided among 16, 32, 64 or 128 users within the maximum distance of 10-20 km. A great advantage of the passive network over the active one is the fact it can be expanded relatively cheaply.

Time-division multiplexing and wavelength-division multiplexing belong among the most popular multiplex methods. The time-division multiplex method is used especially for short distances within metropolitan networks etc., while the wavelength-division multiplex one is used for long distances, such as for example backbone networks.

Each of these multiplex methods has its pros and cons. Time-division multiplex is able to serve only a small number of participants, with low speed, but for reasonable prices. On the other hand, wavelength-division multiplex can serve a high number of participants, but its price is much higher.

In light of these different properties, there is an effort to create a hybrid network that would have positive characteristics of both of these multiplexes and at the same time would meet the characteristics of the passive optical network [4], [5].

The Stanford University ACCESS (SUCCESS) initiative within the Photonics & Networking Research Laboratory encompasses multiple projects in access networks. One of these projects is the Hybrid TDM/WDM PON or SUCCESS-HPON [6].

2 Hybrid PON

Time division multiplexing (TDM) and wavelength-division multiplexing (WDM) technologies have their pros and cons and therefore, in order to obtain the best topology properties for signal transmission, combinations of these two multiplex methods are being developed. The disadvantages of TDM are the advantages of WDM. The time-division multiplex is not able to fully exploit the optical fibre possibilities, and the wavelength-division multiplex is quite expensive as for the implementation. Their unification brings about good transmission properties for favourable economic aspect of the project. As for remote operation between OLT and ONT, we use the WDM multiplex. It is then divided by the arrayed waveguide gratings (AWG) demultiplexer into individual wavelengths, which are then sent to the topology. A part of the network, which is behind the WDM demultiplexer, already uses the TDM multiplex. That is why the TDM demultiplexer is located as close as possible to the target area, which is served by the access network.

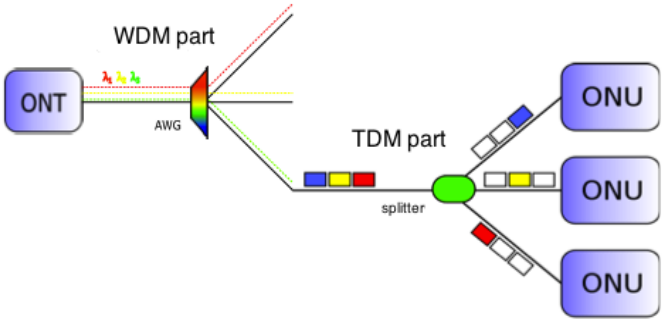

Fig. 1. Hybrid passive optical network.

3 A Topology Design in the Environment Optiwave

As for the transfer, our topology uses the L band and C band. The L band is used for downstream and the C band for upstream. Thanks to using dense wavelength-division multiplexing (DWDM) technology, we used 32 wavelengths with 100 GHz spacing in each band. The speed of each channel is 10 Gbit·s-1, the topology total transfer rate is thus 320 Gbit·s-1 bidirectionally on a single fibre (full duplex). Every wavelength is then multiplexed using TDM for two ONUs. The topology design is depicted in Fig. 4.

4 The Topology Evaluation

In this chapter, we are dealing with the precisely measured properties of the topology. Parameters tested are the following: the total path attenuation, the drop of the output power between the transmitter and the receiver, and the quality of the signal the basic properties of which are the Q factor, the bit error rate and the eye diagram.

The topology will be tested in downstream and upstream, with the path length 2, 5 and 10 km, and with the speed 10 Gbit·s-1 and 1 Gbit per channel. In the following chapters we will test the first channel of the downstream and the upstream.

4.1 Eye Diagram

The eye diagram shows the superposition of all mutually overlapping bits in the signal. The eye opening indicates the differentiability of the logic 1 from the logic 0. The more the eye is wide open, the greater the differentiability is, because of its better signal noise to ratio. Other eye-readable parameters are: jitter (delay fluctuation), intersymbol interference (ISI) and time length of rising or falling edge.

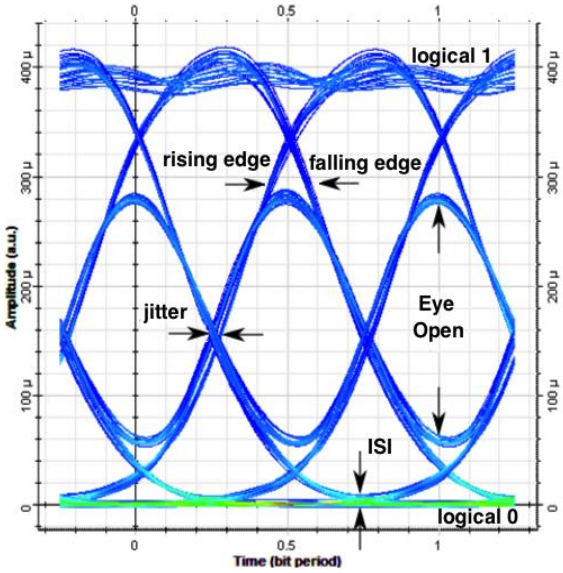

Fig. 2. Eye diagram description.

The following figures show the eye diagrams of the first channel at 10 Gbit·s-1 speed on the path length of 2, 5 and 10 km downstream.

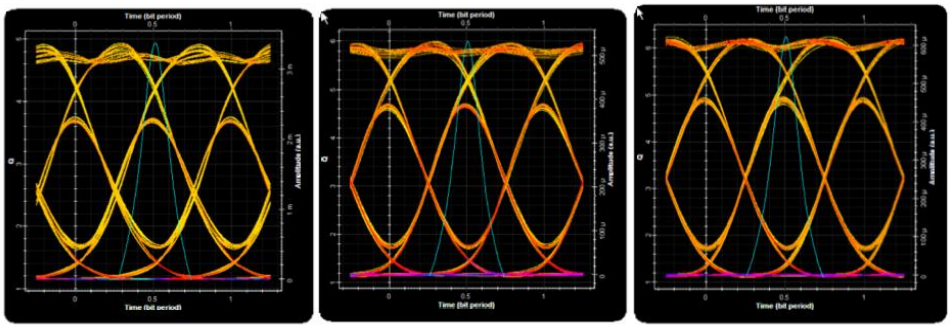

Fig. 3. Eye diagram showing the first channel of the topology with 10 Gbit·s-1 on fiber length of 10, 5 and 2 km (from left).

Parameters of the particular eye diagrams correspond with the measured values, which we have already mentioned in the previous parts of this chapter. It is clearly seen that the Q-factor is lower when the route length is 10 km than when it is 2 km. On the other hand, jitter is increased due to the effect of dispersion. Nevertheless, the measured parameters are still normal and a signal transmission would be realizable.

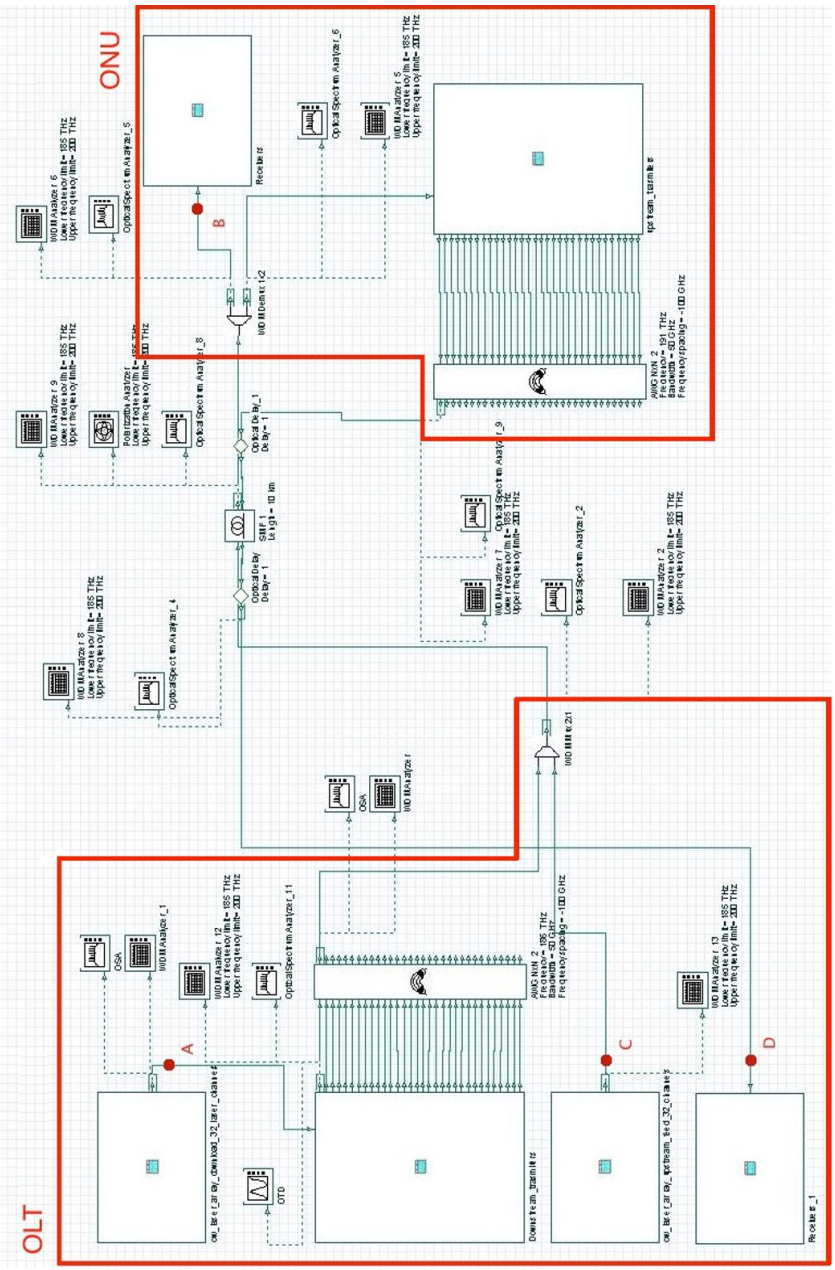

Fig. 4. Hybrid WDM/TDM topology.

5 Conclusion

Hybrid access networks are a very important solution that will be used profusely in the future thanks to its key properties such as large data transfer rate for a large number of participants for favourably low prices. This article describes one of the immense number of ways how to design a network. We used a tree architecture and modern components in dependence on wavelength such as FP lasers and AWG routers. All the simulations had the expected results. The bit rate of 320 Gbit·s-1 for 32 channels duplex is sufficient for the 10 km distance. At this transmission rate, the bit error rate ranged from 10^{-7} to 10^{-12}, which are satisfactory results. It follows that a hybrid WDM/TDM PON is a quality future proof solution offering a great potential.

References

[1] LIN, R. Next generation PON in emerging networks. In: OFC/NFOEC 2008 - 2008 Conference on Optical Fibre Communication/National Fibre Optic Engineers Conference, art. no. 4528701. IEEE, 2008. pp. 1-3, ISBN 978-1-55752-856-8.

[2] KIMURA, S. WDM/TDM-PON Technologies for Future Flexible Optical Access Networks, In: OptoeElectronics and Communications Conference (OECC), IEEE, 2010. pp. 14 – 15, ISBN 978-1-4244-6785-3.

[3] QIU, S.; HUANG, J.; GUO, X.; LUO, J, T.; ZHANG, Z, Z. A novel hybrid WDM/TDM optical passive network architecture. In Proceedings of SPIE - The International Society for Optical Engineering 6354 II, art. no. 63543K. IEEE, 2006. ISBN 978081946449-1. doi:10.1117/12.691062.

[4] AHSAN, Shamim; LEE, Seop, Man. Migration to the Next Generation Optical Access Networks Using Hybrid WDM/TDMPON, Journal of Networks, 2011, Vol. 6, No. 1, pp. 18-25. ISSN 1796-2056.

[5] LEE, S.; KIM, E.; LEE, Y.; LEE, S.; JUNG, D.; HWANG, S.; OH, Y.; PARK, J. A design of WDM/TDM-PON provisioning for future optical access network upgrade. IEICE TRANSACTIONS on Communications, 2007. Vol. E90-B, No. 9, pp. 2456-2463. ISSN 1745-1345.

[6] AN, F.-T.; GUTIERREZ, D.; KIM, K., S.; LEE, J., W.; KAZOVSKY, L., G. SUCCESS-HPON: A next-generation optical access architecture for smooth migration from TDM-PON to WDM-PON. 2005. IEEE Communications Magazine, Vol. 43, No. 11, pp. S40 - S47. ISSN 0163-6804.

Improvements of neural network SIP attack classifier

Jakub Šafařík

Department of Telecommunications, FEECS,
VŠB – Technical University of Ostrava, 17. listopadu 15, 708 33 Ostrava – Poruba
jakub.safarik@vsb.cz

Abstract. This article deals with improvements of an artificial intelligence Voice over IP attack classifier. Honeypot nodes collect attack information in various networks and upload them for classification to a centralized server. The server not only process attack data from honeypot nodes but also serves as a data store, node monitor, and web interface. The neural network classifier is the main part of the centralized server in honeypot network cloud. It classifies all attacks from nodes. The previous generation of neural network proves its abilities in attack recognition. But there were restriction blocking the further improvement. The changes described in article help lower the number of training cycles and significantly improve attack recognition capabilities. The new generation is now able to learn more complex training set with higher successfulness then previous neural network.

Keywords: MLP, Neural network, SIP, VoIP attack classification

1 Introduction

The main purpose of a honeypot is to simulate the real system and interact with anyone in the same way as the production system would. It watches the behavior of anyone who interacts with it [1]. Monitoring of VoIP infrastructure, IDS/IPS (Intrusion Detection/Prevention Systems) or honeypots application can detect these attacks and malicious activity in the network [2], [3], [4]. Some of these mechanisms can disrupt or mitigate certain types of attacks, but there is still much of remaining attacks, which can impact VoIP servers [5], [6].

The information about SIP attacks from a honeypot application brings a valuable source of network attacks. However analysis of data from these honeypots, especially in a large or divergent network, cause unwanted overhead for network administrators.

In order to collect and classify data from honeypots, I designed a centralized network of honeypot nodes.

The main part of distributed network concept is honeypot image, which contains already prepared and preconfigured honeypot application, operation system and other software needed. This single node communicates with a centralized server via a secured channel and periodically sends information about detected attacks to the aggregation server.

Server's main task is the collection of received data and their analysis. It also monitors nodes activity, authenticate nodes and data uploads. The server runs a web server for easy management and representation of classification results.

© M. Krátký, J. Dvorský, P. Moravec (Eds.): WOFEX 2015, pp. 638–641.
VŠB – Technical University of Ostrava, FEECS, 2015, ISBN 978-80-248-3787-1.

The classification engine is based on MLP neural network. The MLP is a feed forward neural network with 2 hidden layers. Its input layer has 10 neurons, hidden layers have 30 and 24 neurons, output layer contain 8 neurons for 8 output classes. The successfulness on the training set was higher than 95%, and practical testing shows good results. The detail description of this neural network contain one of previous paper by author [7], [8].

Running the MLP for real attacks shows some of its disadvantages, especially in real data successfulness comparison. This lead to the search of a new training set, better representing the real attack data. But the MLP was unable to learn this new training set properly.

2 MLP improvements

The MLP neural network mentioned before (called MLPv1) contained several flaws. These flaws affected various aspects of MLP like the speed of learning, the number of backpropagation iteration, successfulness, etc.

The main disadvantage of MLPv1 was problematic learning of items with the unsuccessful classification. These items were gathered from real data after successfulness comparison check. We include wrong classified items to a new training set. But MLPv1 was unable to learn this enhanced training set. The best rate of learning drop under 70%, which was unacceptable. Therefore, we implement new techniques enhancing capabilities of a neural network in the new version (MLPv2) [9], [10].

One of biggest improvements was normalization of input data. The normalization algorithm first searches the training set for maximum and minimum in each input parameter. Each item in the training set is normalized with linear function (Eq. 1) before feeding to the neural network. Same max and min values use neural network for real data normalization.

$$f_{norm}(x) = \left(2 * \frac{x-min}{max-min}\right) - 1 \tag{1}$$

Equation 1 changes all values in the training set to number in a range from -1 to 1. Real attack data contains higher or lower values than those set as minimum and maximum from the training set. Those values will be changed to numbers outside from range (-1; 1), but most of the items will be normalized properly. A sigmoid function is defined for all real inputs, so normalization of higher values than training maximum and vice versa is acceptable.

Another improvement brings backpropagation change. Instead of changing just weights (w) for each connection in the neural network, each neuron bias (b) is also adapted. The bias changes the inner potential for neuron activation. Equation 2 then computes the input of a single neuron (z^x) in MLPv2.

$$z^{x,l} = w^l a^{x,l-1} + b^l \tag{2}$$

Index l in equation 2 indicates a layer in the neural network. The input layer is the only one, which does not use bias and compute the output just with sigmoid function.

But even with normalization and bias modification, training of neural network could be slow. The slowdown is caused by computing the gradient of the cost function. Initial values for all neural network weights and biases are random values. So if the bias is, for instance, a high number, the neuron will give output even for low excitations from other neurons. The situation is also similar for connection weights.

The adaptation of this highly exposed neuron (from bias or connection weights) is slow, due to small adaptations in the network. The higher learning factor cannot solve this situation because the network will then learn only one item at the time. The backpropagation will significantly change previously learned values of weights and biases. This means that the network will forget previously learned classes.

This solve cross-entropy cost function (eq. 3), which adapts weights and biases depending on the actual error. The higher the error is, the higher the correction will be. So the most wrong neurons will learn quickly, and the almost correct neurons will make just slight adaptations. Using the cross-entropy cost function further decreases the number of backpropagation iteration.

$$C = -\frac{1}{n}\sum_x [y \ln a + (1-y)\ln(1-a)] \tag{3}$$

The training mechanism also changes a little. Instead of training the set in the same order over and over again, the new version shuffles all items in training set before each backpropagation algorithm. The network then adapts to the randomly chosen item and do not skip over items of single class in the same order.

The older version MLPv1 verify the level of training successfulness on the same training set. MLPv2 support verification of successfulness with the independent test set, which provides more accurate results for network training status. Independent set means that it does not contain any items from the training set.

All of improvements mentioned above significantly lower the number of backpropagation iteration. MLPv1 reinitiate whole backpropagation (randomize all weights) after 2 500 000 iteration. This feature prevents the network from local minimum stuck. The MLPv1 reinitiate backpropagation several times, especially with a complicated training set. The MLPv2 mechanism lowers the number of iteration from millions to thousands. The first generation was unable to learn items in enhanced training set with successfulness higher than 70% (and millions of backpropagation iterations). The MLPv2 can learn the enhanced training set in the average of 4000 backpropagation iterations with the successfulness of 96%. The inner structure of neural network remains the same as in MLPv1 – two hidden layers with 30 and 24 neurons.

The MLPv2 works with a various number of hidden layers. But our experiments confirmed the problem of vanishing gradient descent in deep neural networks. We achieve best successfulness results with neural networks containing just two hidden layers.

3 Conclusion

The MLP provides an accurate and reliable classifying mechanism for SIP attack classification. It enables us to detect various kind of attacks without the need to use memory

or computational consuming methods. To classify attack correctly, MLP need good representatives in the training set.

The training of the MLP is time and computational consuming process. But after training, classification is straightforward and quick, without any delays or complex computation. Each aggregated attack group is classified at the same speed, no matter which kind or how many SIP messages has an attacker used.

This paper contains the description of improvements for neural network classifying SIP attacks. These changes lead to a new version of the neural network with better attack recognition capabilities than its predecessor.

There are other mechanisms, which can improve classification capabilities of the neural network. Some of them will be implemented to MLPv2 before its final deployment. The future plan also contains testing of other artificial intelligence algorithms.

Single data store for attacks allows us to test new classification algorithms more quickly and with current SIP attacks. We can compare results between different algorithms or use them together to achieve higher accuracy of classification.

References

1. L. Spitzner, Honeypots: Tracking Hackers, Addison-Wesley Proffesional, 2002.
2. M. Collier, D. Endler, Hacking Exposed Unified Communications & VoIP Security Secrets and Solutions," McGraw-Hill Osborne Media, December 16, 2013, 560 p.
3. J. Tang, Y. Cheng, "Quick Detection of Steathy SIP Flooding Attacks in VoIP Networks," Communications (ICC), 2011 IEEE International Conference on, p. 1-5.
4. J. Gomez, C. Gil, N. Padilla, R. Banos, C. Jimenez, "Detection of a Snort-Based Hybrid Intrusion Detection System," Distributed Computing, Artificial Intelligence, Bioinformatics, Soft Computing, and Ambient Assisted Living, Lecture Notes in Computer Science Volume 5518, 2009, pp. 515-522.
5. M. Voznak, J. Safarik, F. Rezac, "Threat Prevention and Intrusion Detection in VoIP Infrastructures," International Journal of Mathematics and Computers in Simulation, Issue 1, Volume 7, 2013, pp.69-76.
6. J. Safarik, M. Voznak, F. Rezac, Security evaluation of multimedia systems, 28th Annual TERENA Networking Conference, TNC 2012, Reykjavik, May 2012, 10p., ISBN 978-90-77559-00-0. (SCOPUS)
7. M. Voznak, J. Safarik and J. Slachta, A Neural Network Based System for Classification of Attacks in IP Telephony, International Journal of Circuits, Systems and Signal Processing, Volume 8, 2014, pp. 368-375.
8. J. Safarik, M. Voznak, M. Mehic, P. Partila, M. Mikulec, "Neural network classifier of attacks in IP telephony," In Proc. SPIE. 9118, Independent Component Analyses, Compressive Sampling, Wavelets, Neural Net, Biosystems, and Nanoengineering XII, 91180X. Baltimore, Maryland, USA, May 22, 2014.
9. R. Rojas, Neural Networks, Springer-Verlag, 1996.
10. J. Heaton, Introduction to Neural Networks for JAVA, 2nd Edition", Heaton Research, 2008.

Impact of IPsec Network Security on Video Quality

Lukáš Ševčík and Miroslav Vozňák

Department of Telecommunications, FEECS,
VŠB – Technical University of Ostrava, 17. listopadu 15, 708 33 Ostrava – Poruba
{lukas.sevcik.st1, miroslav.voznak}@vsb.cz

Abstract. The paper deals with quality assessment of video transmission in IPsec environment and is focused on the most used codecs and encryption techniques. Two metrics have been used for the quality evaluation, the first one SSIM is a method based on measuring the similarity between two images, the second one VQM is based on simplified human spatial-temporal contrast sensitivity model. Model calculates distortion of a compressed video. In the second part of our measurement, we create network with IPsec tunnel.

Keywords: IP network, IPsec, packet loss, video quality, SSIM, VQM

1 Video quality evaluation

The aim of the measurement was to simulate the effect of packet loss and encryption for the video formats MPEG-2 and MPEG-4, to determine the impact on the resulting image using objective methods for measuring the quality of the video and comparing the results. We made measurements for one static and two dynamic videos of 25 seconds. All the movies were measured at a resolution of 1280 x 720 (HD) and 1920 x 1080 (Full HD). Static video was represented by TV news (slow motion), the first dynamic video by a NASA space shuttle launch and the third video with the highest bit rate (70 mbps in full HD) open source animation movie for testing purposes called Big Buck Bunny.

The process of measuring packet loss is shown in the Fig.1. Our testing scenarios reflect the situation that can actually happen in the network. Especially the mobile networks, capable of using IP architecture like UMTS and LTE, reach high values of packet loss [1]. For the purpose of settings of our scenarios, we used Linux tool called Netem. Netem is a network emulator in the linux kernel 2.6.7 and higher that reproduces network dynamics by delaying, dropping, duplicating or corrupting packets. Netem provides Network Emulation functionality for testing protocols by emulating the properties of wide area networks and the current version emulates variable delay, loss, duplication and re-ordering.

Fig. 1. Measurement procedure

© M. Krátký, J. Dvorský, P. Moravec (Eds.): WOFEX 2015, pp. 642–647.
VŠB – Technical University of Ostrava, FEECS, 2015, ISBN 978-80-248-3787-1.

In the second part of our measurement, we create network with IPsec tunnel. It uses ESP and AH header. We configured an authentication with share password (ISAKMP) and a hash function SHA (HMAC variant). As regards encryption standards, symmetric ciphers AES and 3DES were applid and the topology is depicted in in Fig. 2.

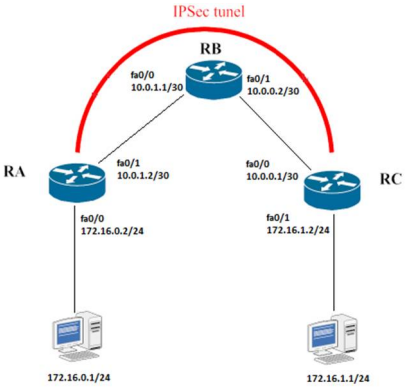

Fig. 2. Topology with IPsec technology

To evaluate the quality we adopted methods SSIM and VQM. SSIM correlates better with the perception of the human eye [2], [3]. Video records were assessed by using MSU VQM Tool. As a first step, we created a stream in the VLC Player. As for the video content, streaming process RTP/UDP/IP method with MPEG 2(TS) and H.264 (MP4) was used. The video stream was broadcasted on the local computer interface. We captured and saved the stream to the local disk by using another VLC Player. We saved this transfer video and tagged it as the original video. The process of evaluation is shown in the Fig.3.

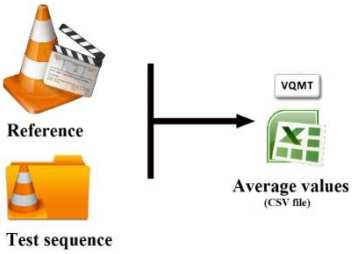

Fig. 3. Comparing tested sequence with original video

2 Packet loss settings using Netem

We set the packet loss to 1% on the interface using Netem and then repeated the whole measurement. Then we repeated this step for packet loss in increments of 1%, 2%, ..., 10%.

Add packet loss on interface

```
#tcqdisc add dev eth0 root netem loss 1%
```

Change packet loss on local interface

```
#tcqdisc change dev eth0 root netem loss 2%
```

This causes that 2 % (i.e. 2 out of 100) packets are randomly dropped. Videos for measurement were in these formats, so we did not set any additional transcoding by creating or capturing a stream.

3 Configuration of IPsec tunnel

We use OSPF protocol in our topology. The sooner is necessary to define ISAKMP policy. It is mean to define authentication and encryption of transmission data. This policy must be the same on both side of tunnel. Policy with higher number takes precedence, the other policies are standby.

Configuration of router RC is same. As next step we define a password. It is shared at both sides for mutual authentication. At the end of this command is necessary to provide IP address of second side of tunnel.

```
RA(config)#crypto isakmp key PASSWORD address 10.0.0.1
```

In order to create a tunnel, we have to specify a type of encapsulation. Optionally, we can specify the duration of the security association. These must be the same on both sides of tunnel.

```
RA(config)#crypto ipsec transform-set 50 esp-aes 256
esp-shahmac ah-sha-hmac
RA(cg-crypto-trans)#exit
RA(config)#crypto ipsec security-association lifetime
seconds 3600
```

The next step is setting, which packets will pass through the IPsec tunnel. This is determined by setting the range of source and destination IP addresses of the packets. Other packets will pass through the network unencrypted.

```
RA(config)#access-list 101 permit ip 172.16.0.0
0.0.0.255 172.16.1.0 0.0.0.255
```

4 Results

4.1 Packet loss

The results of the measurements verified our prediction that not only the type of video codec has a degradation impact on video quality. On the other hand, video resolution was not proven as a significant parameter of video robustness.

Performed experiments demonstrated that the video compression type is the most important factor affecting video quality. Compression rate of video codec H.264 (MPEG-4 Part 10) is higher, nevertheless its robustness against packet loss is lower

than the older MPEG-2. According to the results of the static video measurements, which are listed in Table 1, there is no significant difference between the resolutions used. We detected a slight decrease in higher resolution. During the static scene, where changes were very slow, mainly the P and B frames contained approximately the same information regardless of the resolution used [4].

The table 2 describes the results of the first tested dynamic video sequence. This sequence achieved worse results than the static video. Again, the differences between the used resolutions were small. All the GOP frames contain more information, so packet loss influences more the picture reconstruction. That is the reason why dynamic video is generally more sensitive to data loss [1], [3].

Table 1. VQM and SSIM results for first tested dynamic video

Packet loss [%]	1280x720				1920x1080			
	MPEG-2		MPEG-4		MPEG-2		MPEG-4	
	SSIM	VQM	SSIM	VQM	SSIM	VQM	SSIM	VQM
1	0.859	8.18	0.736	8.67	0.915	8.76	0.817	8.83
2	0.837	9.33	0.750	9.53	0.875	8.67	0.715	10.26
3	0.789	9.71	0.745	10.35	0.809	9.06	0.715	12.03
4	0.766	10.30	0.714	10.46	0.808	9.33	0.657	12.11
5	0.752	11.16	0.699	10.40	0.781	9.45	0.649	13.32
6	0.741	11.18	0.663	10.62	0.799	9.85	0.637	15.16
7	0.717	12.80	0.582	10.76	0.764	9.97	0.632	15.16
8	0.701	12.88	0.545	11.08	0.728	10.19	0.605	15.36
9	0.694	13.49	0.502	11.41	0.703	10.60	0.604	15.35
10	0.678	14.08	0.485	11.79	0.683	11.54	15.80	0.582

4.2 IPsec

The chosen codec has important impact on quality of video encrypted by using IPsec. The produced stream by H264 codec requires lower bandwith than MPEG2 codec, therefore the CPU of router executing encryption is less occupied in case of H264 than MPEG2 and moreover the load on network interfaces is lower if H264 is used. Results depicted in Fig. 4 and 5 confirm explanation mentioned above and meet our expectation. We can see assessment of video achieved in both objective methods - SSIM and VQM, results for MPEG2 are placed in the left part of picturesWe observed the most significant degradation in case of dynamic video 2 where differences between H264 and MPEG2 are greatest.

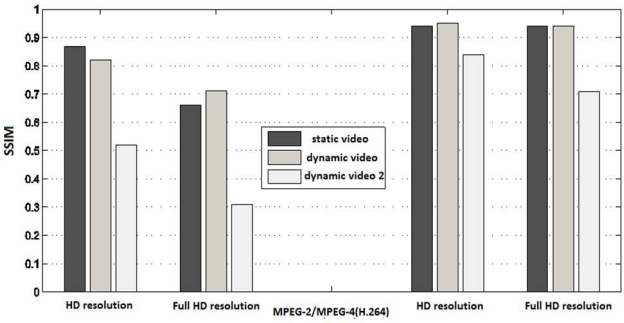

Fig. 4. Comparison of AES256 encryption

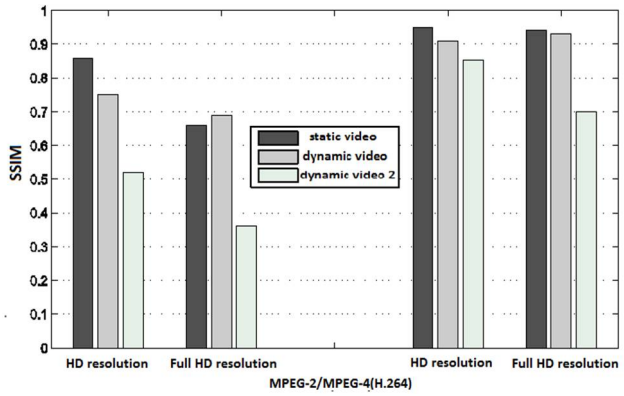

Fig. 5. Comparison of 3DES encryption

The figures 4 and 5 show differences in quality of transmission video between AES256 and 3DES. Whereas results of assessment by SSIM method are depicted in Fig. 4 and 5, results achieved by VQM method are listed in Tab. 4 for HD and in Tab. 5 for Full HD video.

The aim of this paper was compare impact of packet loss and encryption on video quality. Our results show that H264 codec achieves better results for encryption, but worse results for packet loss.

5 Conclusion

Security is a highly discussed topic nowadays, and protocols such as IPsec, VPN/SSL and SRTP are becoming more and more frequently used to secure the content of voice or video, so computational mathematical models should handle this new situation.

The aim of this work was to bring a detailed view of the performance of video streaming over an IP-based network. We compared quality of video with packet loss and encryption as well. The measured results demonstrated the relation between the video codec type and bitrate to the final video quality. It showed differences between

encryption ciphers and advantages of H246 in case of encryption.
Our future works in security will focus on impact of other cipher algorithms on quality of video and we will include technologies MPLS VPN and OpenVPN into our experiments.

In this paper I showed only part from configuration and results. In the last section I share link for our publications and there is possible see more information about our measurement and results.

6 References

[1] M.C. Chan, R. Ramjee, "TCP/IP Performance over 3G Wireless Links with Rate and Delay Variation," in SPRINGER. Wireless Networks, Volume 11, 2005, pp. 81-97, DOI 10.1007/s11276-004-4748-7

[2] H.M. Loke, P.E. Ong, W. Lin, Z. Lu, S. Yao, "Comparison of Video Quality Metrics on Multimedia Videos," in: IEEE International Conference on Image Processing, 2006. Atlanta: IEEE, 2006, pp. 457{460. ISBN 1-4244-0480-0. DOI: 10.1109/ICIP.2006.312492

[3] M. Uhrina, J. Hlubik, M. Vaculik, "Correlation Between Objective and Subjective Methods Used forVideo Quality Evaluation," in Journal Advances in Electrical and Electronic Engineering, Volume 11, Number 2, December 2013, ISSN: 1804-3119

[4] M. Uhrina, J. Hlubik, M. Vaculik, "Impact of Compression on the Video Quality," in Journal Advances in Electrical and Electronic Engineering, Volume 10, Number 4, December 2012, ISSN: 1804-3119

7 Our publications

J. Frnda, M. Voznak, L. Sevcik, Impact of packet loss and delay variation on the quality of real-time video streaming, In SPRINGER Telecommunication Systems , 17 April 2015, DOI 10.1007/s11235-015-0037-2 , pre-published, SCIE, IF=1.163 (2013)

L. Sevcik, D. Uhrin, J. Frnda, M. Voznak, H. Toral-Cruz, M. Mikulec, S. Jakovlev, Encryption for confidentiality of the network and influence of this to the quality of streaming video through network, In Proc. SPIE. 9497, Mobile Multimedia/Image Processing, Security, and Applications 2015,Baltimore, Maryland, USA. (May 21, 2015) doi: 10.1117/12.2177555 expecting WoS, SCOPUS, SJR=0.203 (2014)

L. Sevcik, J. Frnda, M. Voznak, Degrading effect analysis, packet loss and out of order data on various tips and video resolution, In Proceedings of the 2014 Networking and Electronic Commerce Research Conference, Trieste, Italy, ISBN 978-0-9820958-0-5, pp. 130-138.

J. Frnda, L. Sevcik, M. Uhrina, M. Voznak, Network Degradation Effects on Different Codec Types and Characteristics of Video Streaming, In Journal Advances in Electrical and Electronic Engineering, Vol. 12, Issue 4, 2014, pp. 377-383, ISSN 1336-1376 (SCOPUS, SJR=0.239 Q3)

L. Sevcik, M. Voznak, M. Prokes, P. Fazio, H. Total-Cruz, Study of security issues in GSM network and their practical demonstration, In Proceedings of the 2014 Networking and Electronic Commerce Research Conference, Trieste, Italy, ISBN 978-0-9820958-0-5, pp. 297-305.

Exploratory Analysis of Measurements Real-time Applications in Virtualized Environment

Jiri Slachta and Miroslav Voznak

Department of Telecommunications, FEECS,
VŠB – Technical University of Ostrava, 17. listopadu 15, 708 33 Ostrava – Poruba
jiri.slachta@vsb.cz

Abstract. This article deals with the exploratory analysis of the measurements of virtualization techniques in interactive delay-sensitive environment, particularly IP telephony. Virtualization, which was chiefly the prerogative of companies and the academic world in its early days, has gradually develop its platform to reach out to the ordinary users who can benefit from running virtual machines. The aim of this paper is to examine the impact of a virtual machine on real-time traffic, in our case IP telephony based on the SIP and the RTP, which are now the cornerstone of VoIP technology. This article also analyses the impact of memory size and the number of processor cores on the delay itself and its variance, thus allowing user to have full picture when deciding what virtualization tool to use and how to configure so it performs the best possible way.

Keywords: Asterisk, Benchmarking, Delay, Full virtualization, Jitter, KVM, Real-time applications, Virtualbox, VMware Player

1 Introduction

Nowadays virtualization presents a solution for increasing security and effectiveness and eases the infrastructure maintenance in corporate and academic environments. Moreover, virtualization spreads even to home PCs, which is in great contrast to what was common in the very beginning of this technology. The service providers' offers confirm this trend as they incorporate the virtual machine hosting as one of the key services they provide. This way the virtualization technology has found its path to many implementations in many areas including data centers, development studios and even households. There are three main advantages of the virtualization. First, it allows us to separate critical applications, which are considered problematic when running simultaneously. Second, the increased portability makes possible to transfer the virtualized system among physical devices with different software and even hardware architectures. And third, it prevents the need for frequent operating system configurations as the work can be performed on the copy of the virtualized operating system leaving the original one intact for further use. Apart of the advantages we also have to

© M. Krátký, J. Dvorský, P. Moravec (Eds.): WOFEX 2015, pp. 648–653.
VŠB – Technical University of Ostrava, FEECS, 2015, ISBN 978-80-248-3787-1.

think about the drawbacks of the technology, especially now when it is used more and more. The main disadvantage is an overhead generated by the virtualization tool. This overhead causes the virtual machines to be less effective and less performing than the physical devices with similar attributes. This overhead can have a negative impact especially on real-time applications, since it can cause long delays and increase the variance of delay between the individual packets [1], [2].

This paper's aim is to find out, how deep the impact of the different implementations of the virtualization technology is on the real-time traffic, which is represented by the IP telephony, since it is one of the most widely spread real-time technology. The influence of the number of processor cores and memory size is also to be analyzed [3].

2 Methodology and Testing Platform

The methodology used in this paper rely and uses the free full virtualization tools, the virtual machines of which will be run on a high performing hardware with a hardware assisted virtualization support [5], [6].

2.1 Measuring Platform Preparation

Because of the KVM needing the hardware assisted virtualization support it is necessary to use a computer equipped with a processor supporting Intel-VTx or AMD-V technology, which are two incarnations of the mentioned hardware assisted virtualization technology from both biggest x86 processor producers.

Testing topology consists of one computer, one 1Gbps switch and traffic generator Optixia XM2 with suitable modules. Hosting computer, where the virtual machines will be run, has two NICs, from which one is connected to a university network and the second is dedicated for the test segment of the network. Traffic generator is also connected to the university network so we are able to communicate with control software IxLoad, which apart of the test itself will perform data analysis as well.

2.2 Measured Parameters

Real-time network applications, to which the IP telephony belongs, depend on network parameters, which influence the transmission quality. The concepts used for traffic quality control in computer networks based on packet switching can be summarized with QoS (Quality of Service). The QoS is highly popular especially when transmitting voice and video over IP networks, where it is used for reserving a bandwidth or prioritizing the one traffic over others, so that the critical parameters including delay, its variation and the packet loss are not overstepped. Using the Optixia XM2 we are able to measure these parameters [2]:

– Interarrival Jitter – This parameter is measured using the RTP timestamps and represents mean difference of arrive time between consecutive packets compared to the same difference on the sending side.
– Delay Variation Jitter – This parameter represents a time between transmission and reception of the RTP packet.
– Post Dial Delay – This is the delay between sending the INVITE message and reception of the response from other endpoint. Media Delay – Time between the INVITE message dispatch and reception of first RTP packet.

2.3 Test Methodology

Test scenario remains the same for all the tests, while several parameters of the virtual machines are being changed including amount of RAM, number of processor cores and used virtualization tool. As the accepted values of the measured parameters we use those defined in the section 2.2. The end-to-end delay variation can be measured only between calling UA and the communication server because of the mentioned limitations. During the scenario traffic has a linearly increasing trend, however the utilization and delay increase is not linear at all. Asterisk PBX responds to an increasing load with the step increase after exceeding certain load threshold. When the hardware limit is reached Asterisk begins to refuse registrations and first unsuccessful calls appear.

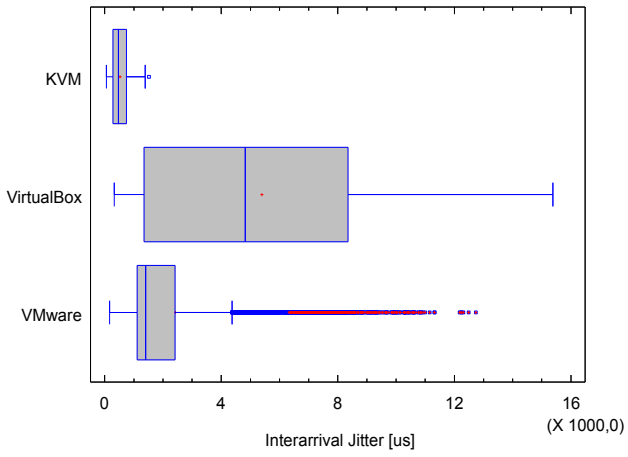

Fig. 1. Boxplot of Interarrival Jitter for all three virtualization tools.

3 Results

Data files were analyzed using the exploratory analysis of each individual parameter and then ANOVA test for verification of data independence and other required properties.

3.1 Classification using the Performance of Virtualization Tool

This classification describes the properties of the data with three variables, which represent individual virtualization tools. Fig. 1 depicts the box charts for the Interarrival Jitter. As we can see there are no extreme outlying observations for KVM and VirtualBox. The values range is very thin for KVM therefore variance analysis cannot be performed on this data. On the other hand, VirtualBox has very variant values of jitter. VMware has high number of outlying observations, therefore a mean value is also one of the outlying observations. This means that in most cases this virtualization tool performed well, hovever in some cases the values got unexpectedly high, which could have caused problems in voice quality in real environment.

Table 1. Exploratory analysis for Interarrival Jitter.

	Count	Average [μs]	Median [μs]	Coeff. of variation [%]	Minimum [μs]	Maximum [μs]	Range [μs]	Lower Quartile [μs]	Upper Quartile [μs]
KVM	4705	1109,35	982	53,91	96	7466	7370	621	1603
VirtualBox	4705	12672,4	11369	76,86	603	38016	37413	2553	18604
VMware	4705	5505,47	2896	99,04	349	34799	34450	2290	5066

3.2 Classification by the number of processor cores

This classification describes the properties of the data samples set up by the number of processor cores. The Interarrival Jitter has extremely outlying observations when measuring with two and three cores. When measuring with a single active processor core the values range highly and are evenly distributed, which can be learnt from the position of median and mean value. The case with two active processor cores already has outlying observations and its values are distributed mainly in the lower quartile. Three cores continue with this trend, which means the values are distributed in the thinner area and the number of outlying observations is the highest. Four cores have the values distributed in the thinnest area and just several outlying observations.

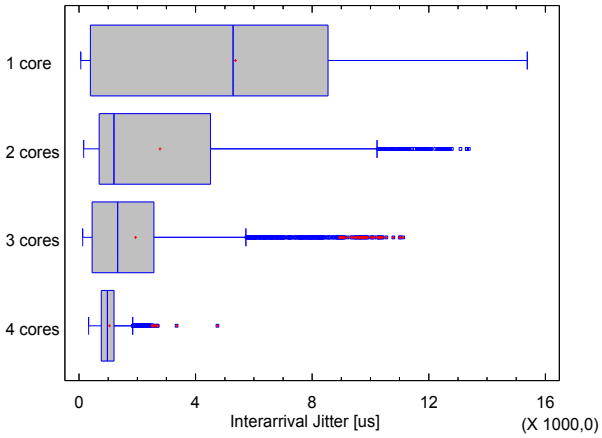

Fig. 2. Boxplot of Interarrival Jitter for different number of active processor cores.

3.3 Classification by Amount of RAM

The amount of RAM was set to 4 different values – 512 MB, 1GB, 2GB and 4GB – presenting an independent variable and the values of interarrival jitter present the depending variable. The Fig. 5 depicts the relation between these two sets of variables. The average values and the values distribution of the Interarrival Jitter were almost the same for all four cases. All the cases suffered from multitude of outlying observations as well. Because of this we can assume that the virtual machines are memory independent when speaking about the reasonable amounts of memory

4 Conclusion

During the measurement we paid attention not to exceed the limiting values of the delays and their variations as they are defined in the G.114 recommendation of the ITU-T and practical experience as well. Although the properties of the test did not allow for measuring data traffic between source and destination user agents because of the codec translation, it was possible to compare obtained values of communication between user agent and server providing the IP telephony services. We can find out from the exploratory analysis that the pre-test assumptions were correct regarding the virtualization tool performance. The lowest range of values of interarrival jitter is achieved with the use of KVM. Although the VMware product has the background of large and prosperous company, it did not perform well enough to beast its competitor KVM especially in the stability of results. From the real-time application point of view VirtualBox can be considered as the least effective and advantageous solution.

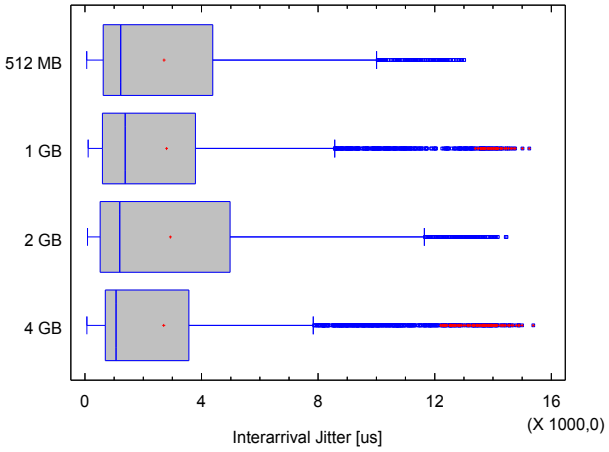

Fig. 3. Boxplot of Interarrival Jitter for different amounts of RAM.

References

1. R. Jain, S. Paul, "Network virtualization and software defined networking for cloud computing: A survey, " In IEEE Communications Magazine, 51 (11), art. no. 6658648, 2013, pp. 24-31.
2. A. Elenkov, "Virtualization of virtual measurement machines as component of distributed artificial intelligence system," in Proceedings of the 8th WSEAS international conference on Artificial intelligence, knowledge engineering and data bases, Cambridge, 2009, pp. 134-138.
3. M. Voznak, J. Slachta, F. Rezac, J. Rozhon, "Exploratory analysis of virtualization tools in delay-sensitive environment," In Komunikacie, 15 (2 A), 2013, pp. 150-154.
4. L. Lazic, S. Popovic, N. Mastorakis, "A simultaneous application of combinatorial testing and virtualization as a method for software testing," WSEAS Transactions on Information Science and Applications, Volume 6 Issue 11, November 2009, pp. 1802-1813.
5. L. Rizzo, G. Lettieri, V. Maffione, "Speeding up packet I/O in virtual machines," In ANCS 2013 - Proceedings of the 9th ACM/IEEE Symposium on Architectures for Networking and Communications Systems, art. no. 6665175, 2013, pp. 47-58.
6. O. Agesen, A. Garthwaite, J. Sheldon, P. Subrahmanyam, "The evolution of an x86 virtual machine monitor," In Operating Systems Review (ACM), 44 (4), 2010, pp. 3-18.

Railway Wireless Barrage State

Martin Tomis

Department of Telecommunications, FEECS,
VŠB – Technical University of Ostrava, 17. listopadu 15, 708 33 Ostrava – Poruba
martin.tomis@vsb.cz

Abstract. This article briefly introduces the basic operation of the newly developed device designed to increase the safety of railway level crossing called 'wireless barrage'. The improvement is based on the use of the direct radio connection with a train instead of cable connected pole barrage state. Train vehicle driver is continuously informed about the state of nearby level crossing safety devices.

Keywords: barrage, railway, RF modem, safety, WBS

1 Introduction

This article briefly describes the development of a prototype system for wireless communication between train vehicle and the level crossing safety devices (LCSD), where the status and safety information are being transmitted.

A fundamental part of the railway level crossing active warning alarm (red lights, barriers) should inform the driver of approaching train about the correct functioning of the LCSD. It responds correctly and in time to the approaching railway vehicle and ideally even on level crossing while there is no obstacle that could endanger the railway vehicle. Railway vehicle is passing the level crossing too fast, unable to stop, not even to slow down to avoid a collision.

Building of the pole barrage state (PBS) is presently the most appropriate solution, but expensive due to such a long cable, and often even technically impossible (Fig. 1).

Fig. 1. The current form of the PBS.

The intention of the proposed solution is to develop and produce a prototype device for wireless transmission of information about the state of the level crossing equipment directly to the approaching railway vehicle – see Fig. 2.

© M. Krátký, J. Dvorský, P. Moravec (Eds.): WOFEX 2015, pp. 654–659.
VŠB – Technical University of Ostrava, FEECS, 2015, ISBN 978-80-248-3787-1.

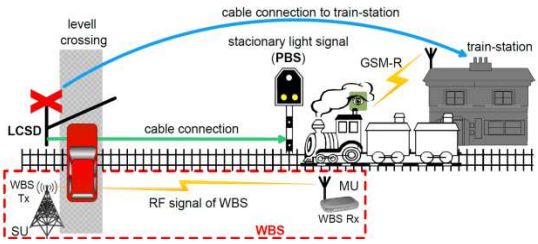

Fig. 2. Basic function of WBS.

The wireless transmission of information should comply with the following basic requirements [1]–[7]:

- reliable communication at medium distance (minimum 2 km) and in the difficult terrain (trees, buildings, profile, etc.),
- secured two-way communication with the ability to relay commands from the receiver unit to LCSD, such as an alarm (so-called warning on departure),
- the ability to transmit more status information (fault, warning, obstacle),
- the ability to connect GPS receivers for automatic selection of information, warnings and automatic recording of events into history log,
- the industrial design of basic parts and implementation of safety functions according to the requirements from [7] on the integrity of the security.

This system is mentioned abroad in a very vague way in the context of different ideas and concepts descriptions without a hint of practical solutions. The device is being developed at Trakce, a.s. in cooperation with the VSB-TU Ostrava as a part of the project TA02030946 ”Development of the Wireless Barrage Signal for Safety Transmission of the Railway Level Crossing State to the Rail Vehicle”. Due to the company’s know-how this article cannot disclose all of the designed device details.

2 Current state of barrage signal

Currently, there are three ways to alert the driver approaching the level crossing whose LCSD has some problems:

- The operator monitors the status of the level crossing tracks in the nearest railway station or the dispatcher that supervises on rail transport in the area. If the LCSD signals a problem, operator (or dispatcher by radio) informs the railway driver, before exiting from the station.
- The status of the level crossing is automatically forwarded to the automated railway safety system, which can warn the driver by using the railway signaling device (signal for speed reduction or stop drive) before the railway level crossing. This situation is possible only on railway-lines equipped with line security signaling and control system (auto-block, etc.). Level crossing, however, can be placed in the railway section so that the nearest signal that could warn the driver is very far away.

- The status of the level crossing is indicated to the driver directly using PBS. The disadvantage of this solution is a large distance between PBS and level crossing, which needs to be connected by cable. After passing PBS driver cannot be informed about the current level crossing state.

In the past, in The Czech Republic the system from TESLA.CZ was tested, but due to limited technological capabilities at that time (absence of encryption and analogue radio transmission), the system was not adopted in practice. Unfortunately, there are no longer references to this project.

3 Description of the WBS

The system consists of a base-stationary unit that is located near the level crossing control system device and from mobile moving units. These are placed on the railway traction units. There is also a wireless portable service terminal for monitoring and repairing purposes.

- The Stationary Unit (SU) receives information about the warning from the LCSD and transmits the information via radio to rail vehicles approaching the level crossing (Fig. 2). The stationary part consists of a control unit (CU), which cares for the safe collection and processing of data from the LCSD and from one up to four radio-frequency units (RFU). RFUs are located separately from the CU near the antennas.
- The Mobile Unit (MU) is placed on the traction device (locomotive), and passes the information transmitted by SU to the driver. (testing prototype Fig. 5).
- Coverage of the radio signal must be at least as long as the approaching distance of rail-road level crossing sections. That is usually 500 meters away both ways of rail-road, ideally 1 to 2 km on each side.

3.1 RF Unit

Analysis of suitable frequency band: For the verification of function of WBS, it was decided to use nonlicensed Industrial, Scientific and Medical (ISM) frequency band for the variety of RF modem modules commonly available. After the analysis of the available RF bands, the appropriate band ISM 869 MHz was selected, where there are 10 channels in the range of frequencies 869.400-869.650 MHz. The range in the Line-of-sight is approximately 4–8 km, in Non-Line-of-sight, it is approximately 0.1–1 km. Maximal channel usage time is 10 %. The advantages of this frequency band are higher maximum transmitted power (500mW EIRP) and less band-penetration than the 433 MHz. The disadvantage is the worse radio signal propagation than in 443 MHz bands [8]-[11].

RF modem selection: Under the analysis of the applicable modems and according to technical parameters, built-in functions and prices model Adeunis ARF868 was selected (Fig. 3).

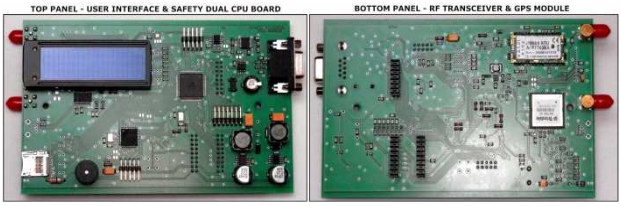

Fig. 3. Adeunis RF modem ARF868 implementation in the mobile part of the WBS.

The connection of the antenna and electromagnetic field shielding: The RF module with microprocessor and all TTL level circuits are placed in a metal box for maximum shielding from electromagnetic fields emitted by the external antenna.

Location and connection to the radio module on a printed circuit board: On the Printed Circuit Board (PCB) is in the corner positioned radio module, so that the pin for the connection of the antenna of the module was closest to the selected corner of printed circuit boards. The most important element with the highest priority in the design is a coaxial cable connection. The most important condition is the shortest route of the radio signal from the unshielded RF pin of radio module to the central wire of coaxial cable. Shielding should be designed as ground plane with the shortest possible connection between coaxial cable shielding and the GND pin nearest to the RF pin of RF module.

The connection of the radio part to the microprocessor: The WDS design provides two radio modules. The first is placed directly into the device (internal radio module). The second (optional), separated on the roof of the vehicle or building, connected to the RS485 interface (external/remote radio module).

3.2 CU and front-end unit

The design of the CU of SU and MU must respect the specifics of the railway environment not only in terms of mechanical design, but also about the interaction with the operator. The front-end interface must not unreasonably burden, in particular on a traction unit. The key is to ensure security of processing information. Therefore, the security critical tasks are performed in parallel.

The primary parts of the CU unit:

- The power supply in the range of 12/24 V DC, specifically in the range of 10.5 V to 32 V with the galvanic separation and insulation strength 4 kV is required.
- The outputs of the power supply for the radio unit designed for supplying external radio unit with insulation strength 1.5 kV to the internal circuits of the base unit and 4 kV to the circuits of the LCSD.
- Binary inputs for the connection of signals from the LCSD are working in the range of 10-32 V. The inputs are isolated from the internal circuits of the module with insulation strength 4 kV.
- The GPS module is used mainly for its automatic time synchronization necessary to record the history and possible correction of deviations of actual position data for MS in the selection of relevant SU within radio range.

Elements of the user interface on the module consist of the display for basic operating states information; basic diagnostics and configuration with 4 × 20 characters, then the keypad, LED indicators and audio alarms for critical events. The memory card slot is also available, intended for recording of the history of events and for transfer and backup of configuration.

4 Testing of the prototype

Laboratory testing: A prototype of the device consists of a mobile unit designed for portable temporary location on the traction vehicle and from the base unit that is connected to the LCSD, from which it obtains the information about the alert. The stress tests were carried out in laboratory conditions, where the multiple access on a shared medium was tested with a lot of different noise sources. WBS has passed all the tests with satisfactory results. Detailed results of the laboratory tests are property of the participating company and could not be published.

External testing: First outside testing took a place on Dec. 2014 in a real deployment, on the railway no. 314 (Otice u Opavy), on the LCSD no. 5.645 on the propulsion vehicle type no. M131. The important points are marked in the map (Fig. 4): (1) Approaching–sector in the direction of Slavkov, (2) Existing PBS in the direction Slavkov, (3) A repetition PBS in the direction Slavkov, (4) LCSD Otice u Opavy, (5) Existing PBS in the direction Opava, (6) Approaching–sector in the direction of Opava.

Fig. 4. Map of the testing LCSD Otice u Opavy and one part of the radio propagation model.

WBS RF signal propagation model was created in software RadioMobile to verify the coverage of the radio signal. The direction to Opava see (Fig. 4). The rainbow scale was set to follow the RF modem sensitivity. The red color indicates an excellent signal > -90 dBm. The result of simulation of signal propagation does not indicates problem with WBS signal in both directions, thus on the whole sector between point 1 and 6. The outside test in Dec. 2014 has confirmed the theoretical model presumption. The WBS signal was received up to 2.2 Km far from LCSD. The functionality of the transmission of information was verified and compared with the PBS.

Fig. 5. The Mobile Unit under the external tests.

5 Conclusion

At present stage of running project, the base and mobile unit of WBS were designed and constructed. The principle of the safe acquisition, evaluation and transmission of information through the radio channel was designed. The developed solution is presently the most appropriate one. In contrast to older PBS that uses such a long cables. The PBS may in many cases not be technically possible to realize.

Furthermore, the construction team performed first external test of the operation of the device in real conditions. The last work considers to finish the WBS prototype that could take under certification process for deployment on the railway in the future. The long-term stress-testing of WBS is also planned during the summer 2015.

Acknowledgements

This work was supported by the project TA02030946 'Development of the wireless barrage signal for safety transmission of the level crossing state to the rail vehicle' supported by Technology Agency of the Czech Republic and company Trakce, a.s. The main results of the development are published in TSP2015 Conference, Praha.

References

1. CSN EN 50159 Railway applications - Communication, signaling and processing systems - Safety-related communication in transmission systems., Czech Standard Institute Std., 2011.
2. CSN 34 2650 ed.2 – Railway signalling and interlocking equipment - Level crossing protection equipment., Czech Standard Institute Std., 2010.
3. CSN EN 60077 – Railway applications – Electric equipment for rolling stock – Part 1: General service conditions and general rules., Czech Standard Institute Std., 2003.
4. CSN EN 50125-3 – Railway applications – Environmental conditions for equipment – Part 3: Equipment for signalling and telecommunications., Czech Standard Institute Std., 2003.
5. CSN 34 2600 ed.2 – Railway applications - Railway Signalling Equipment., Czech Standard Institute Std., 2009.
6. Guidelines SZDC c. 34 – Guidelines for the commissioning of products that are part of the communication and safety equipment., Sprava zeleznicni dopravni cesty Std., 2012.
7. CSN EN 50126-1 Railway applications – The specification and demonstration of Reliability, Availability, Maintainability and Safety (RAMS)., Czech Standard Institute Std., 2001.
8. General Licence No. VO-R/10/05.2014-3 The use of radio frequencies and operation of short-range devices., Czech Telecommunication Office Std., 2014.
9. National Table of Frequency – Regulation 105-2010 sb 038-10., Czech Telecommunication Office Std., 2010.
10. Part of the Radio Spectrum Utilisation No. PV-P/10/08.2012-11 for the frequency band 470–960 MHz, Czech Telecommunication Office Std., 2012.
11. Government Regulation 426/2000 sbl. laying down technical requirements for radio equipment and telecommunications terminal equipment., Czech Telecommunication Office Std., 2000.

Impact of classification methods for speech stress recognition accuracy

Jaromir Tovarek and Miroslav Voznak

Department of Telecommunications, FEECS,
VŠB – Technical University of Ostrava, 17. listopadu 15, 708 33 Ostrava – Poruba
{jaromir.tovarek, miroslav.voznak}@vsb.cz

Abstract. Classification methods for recognition of stress are evaluated in this article. Nowadays, technological developments aimed at simplification of communication between man and computer. One current goal is estimated mood of the conversation. Given the many applications is voice control, research explores the stress detection accuracy of a person from his voice for different classification methods. Voice recordings were created by 10 actors. They recorded 10 assorted sentences each. Mel-frequency cepstral coefficients (MFCC) were extracted from the speech signal. These parameters represent the inputs for the three classifiers: Gaussian Mixture Model (GMM), k-Nearest Neighbours (k-NN) and Artificial Neural Network (ANN). The results are represented by the confusion matrix and ROC curve.

Keywords: Artificial neural network, GMM, KNN, Neutral, Speech, Stress

1 Introduction

As the title suggests, this article describes a system for classifying emotional state of human speech. Emotion is one of the characteristics of human which describes his mental condition affecting physiological changes in the human body. These changes are also reflected in the human speech. Information about the emotional state is requested in many fields. Statistical evaluation of customer satisfaction, his interest in the products is evaluated by affected emotional state. This information is a direct response to any stimulus. Information about the emotional state can be used for call centers and the military, police and fire dispatching.

These are just the first examples of utilizations for speech emotion recognition systems. It is obvious that the system will have great application in human-machine interaction. Therefore it is appropriate to identify a classification ability of different classifiers for different emotional states. [1]

2 Speech Emotion Recognition System

System design consists of several blocks, which it distributed to major functions. Input values for the training and testing to create database of audio signals. Block diagram of the system is shown in Figure 1

© M. Krátký, J. Dvorský, P. Moravec (Eds.): WOFEX 2015, pp. 660–665.
VŠB – Technical University of Ostrava, FEECS, 2015, ISBN 978-80-248-3787-1.

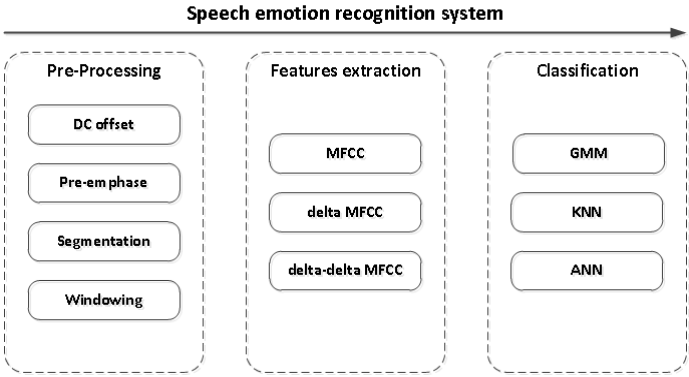

Fig. 1. Block diagram of Speech Emotion Recognition System (SERS). The system consists of .

Train respectively testing is the key step of the system. The quality of the input data, the audio signal in this case, has a direct impact on the classification accuracy. For this reason, it is used the Berlin database containing over 500 recordings of actors consists men and women. The database contains 10 sentences in the seven emotional states. This corpus of recordings is considered as a high-quality database, because it was created by professional actors in the sound studio. As mentioned, the speech signal has to be modified by routine operations such as removing the DC component, pre-emphasis and segmentation stochastic signal into quasi-periodic frames.

Speech recognition system is context-independent, that meaning take into account only signal parameters, not content informations. These parameters are the training and testing vectors for classifiers. The calculation parameters are represented by the Features Extraction block that extracts the Mel-Frequency Cepstral Coefficients (MFCC) and dynamic parameters (first and second derivative of MFCC). [1]

3 Classifiers

Individual research shows that cannot be said which classifier for emotion recognition is the best. Each classifier or their combination achieved some results accuracy, which depends on several factors. The success of classifier is directly dependent on the data. This is derived from the fact that the accuracy varies with the data character such as the quantity, density distribution of each class (emotions) and the language also. One classifier has different results with acted database, where the density of each emotion are equitable and different with real data from call centre where normal (calm) emotion state occupies 85 to 95 percent of all data. Appropriate choice of parameters has a considerable effect on the accuracy of these classifiers. The following subsections describe the used classification methods.

3.1 Gaussian Mixture Model

A Gaussian Mixture Model is a parametric probability density function represented as a weighted sum of Gaussian component densities. GMMs are commonly used as a para-

metric model of the probability distribution of continues measurements or features in biometric system, such as vocal tract, in speaker recognition systems as well. Probability distribution of the parameter vectors derived from human speech can be described using GMM.

$$p(o|\lambda^s) = \sum_{i=1}^{M^s} w_i^s \; p_i^s(o) \tag{1}$$

Where M is number of components for s class, w_i, $i=1, \ldots, M$ are weights of components complying condition that sum of all weights is 1, p means the probability density of the components represented by the mean value and covariance matrix C_i. Speaker model can be described mentioned mixture characterized by the equation below.

$$\lambda^s = \{w_i^s, \mu_i^s, C_i^s\}, \;\; i, ..., M^s \tag{2}$$

The criterion of maximum likelihood is found lambda parameters with maximum p probability density based on sequence parameters $O = o_1, o_2, \ldots o_n$ obtained from speech, seen below. [2]

$$\lambda^s = argmax \; p(o|\lambda^s) \tag{3}$$

3.2 K-Nearest Neighbour

In pattern recognition, the k-Nearest Neighbour algorithm (KNN) is a method for classifying objects based on the closest training examples in the feature space. kNN is a type of instance-based learning, or lazy learning where the function is only approximated locally and all computation is deferred until classification. The kNN algorithm is amongst the simplest of all machine learning algorithms: an object is classified by a majority vote of its neighbours, with the object being assigned to the class most common amongst its k nearest neighbours (k is a positive integer, typically small). If $k = 1$, then the object is simply assigned to the class of its nearest neighbour. The various distances between the vector x_s and x_t.

$$d_{st}^2 = (x_s - x_t)(x_s - x_t)' \tag{4}$$

The neighbourhood distance is calculated through Euclidean metric. Given an m-by-n data matrix X, which is treated as m (1-by-n) row vectors $x_1, x_2, \ldots, x_m$.

3.3 Artificial Neural Network

Our emotional state classification problem with high number of parameters can be considered as a pattern-recognition problem. In this case, it can be used two-layer feed-forward network. A two-layer feed-forward network, with sigmoid hidden and output neurons, can classify vectors arbitrarily well, given enough neurons in its hidden layer. The network is trained with scaled conjugate gradient (SCG) backpropagation.

Let's say that, MFCC and dynamic coefficients in this case, are the input vectors x_i where $i = 1, ..., d$. The first layer of network forms M linear combinations of these

inputs to give a set of intermediate activation variables $a_j^{(1)}$

$$a_j^{(1)} = \sum_{i=1}^{d} w_{ij}^{(1)} x_i + b_j^{(1)} \quad j = 1, \cdots, M, \tag{5}$$

with one variable $a_j^{(1)}$ associated with each hidden unit. Here $w_{ij}^{(1)}$ represents the elements of first-layer weight matrix and $b_j^{(1)}$ are the *bias* parameters associated with the hidden units.

SCG training implement mean squared error *E(w)* associated with gradient $\bigtriangledown E$ and avoids the line-search per learning iteration by using Levenberg-Marquardt approach in order to scale the step size. A weights in te network will be expressed in vector notation. [2]

$$w = \left(..., w_{ij}^{(1)}, w_{i+1j}^{(1)}, ..., w_{N_1 j}^{(1)} \theta_j^{(l+1)}, w_{ij+1}^{(1)}, w_{i+1j+1}^{(1)}, ... \right) \tag{6}$$

4 Results and Discussion

The following settings and features were used in the experiment:

- Input samples - Berlin database of emotional utterances.
  - 10 different sentences recorded by 10 different actors (both genders).
  - Over 530 samples consisting with 7 emotions: *anger, bored, disgust, fear, happiness, sadness, neutral*.

- Feature Extraction - computing of input vectors (speech parameters).
  - 13 Mel-frequency Cepstral Coefficients c_m=*[*c_m*(0), ..., *c_m*(12)]*.
  - Dynamic coefficients of MFCC - Δc_m and $\Delta^2 c_m$ (acceleration coefficients).

- Emotion Classification.
  - GMM - 64 mixture components.
  - K - Nearest Neighbours (set up 5 neighbours.)
  - Artificial Neural Network - Feed Forward Backpropagation.

4.1 Conclusion

This research was aimed at recognizing the stressed out person. It means recognizing deviations from the neutral state. This state is not defined in the Berlin database. Therefore, it was necessary to assemble a set of data, so-called ”stress cocktail” from defined emotional states. The stress of a person can be assembled from emotional states, other than neutral. Emotions Anger and Fear were used to compile the stress data set that because these emotional states are reflected most often when a person is exposed to stressful situations.

As before, the GMM, k-NN and the ANN were used to classify the stress versus neutral. Results for all three classifiers are shown in Fig. 2. The Receiver Operating Characteristic (ROC) is applied for better understanding the system. ROC curve is a tool for the evaluation and optimization of binary classification system (test), which

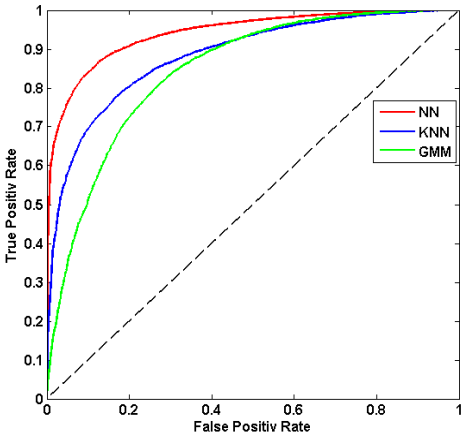

Fig. 2. Receiver Operating Characteristic of GMM, k-NN and ANN classifier for Neutral vs. Stress Recognizing.

Table 1. Confusion Matrix - description of cells.

Classifier			
Output classes	True Positive	False Positive	Positive Predictive Value
	False Negativ	True Negativ	Negative Predictive Value
	Senzitivity	Specificity	Precision
	Target classes		

Table 2. Confusion Matrix for ANN, k-NN and GMM classifiers and results for neutral vs. stress recognition.

	ANN			k-NN			GMM		
Neutral	7445 22.1%	1901 5.7%	79.7%	4919 14.6%	2209 6.6%	69.0%	6305 18.8%	3507 10.4%	63.3%
Stress	1684 5.0%	22587 67.2%	93.1%	4210 12.5%	22279 66.3%	84.1%	2824 8.4%	20981 62.4%	88.1%
	81,6%	92.2%	89.3%	53.9%	91.0%	80.9%	69.1%	85.7%	81.2%
	Neutral	Stress		Neutral	Stress		Neutral	Stress	

shows the relationship between the sensitivity and specificity of the test or the detector for all possible threshold values.

The graph shows that the classification accuracy for the detection of stress is comparable to the classification of different emotional states. ANN achieved the best results in this experiment. Confusion Matrix for all classifiers is shown in Table 2. Explanation of cells for this matrix is described in Table 1. The results of Table 2 are presented for clearer representation of ROC curves.

This experiment shows that these classification methods can be used on the recognition of emotional state. At the same time, the question arises, what emotional states will characterize stress. The answer will probably depend on which system would be applied.

References

1. Partila, P., Tovarek, J., Voznak, M., Safarik, J. Classification Methods Accuracy for Speech Emotion Recognition System. In: Springer Advances in Intelligent Systems and Computing AISC, Vol. 289, 2014, pp. 439–447, DOI: 10.1007/978-3-319-07401-6_44.
2. Partila, P., Tovarek, J., Frnda, J., Voznak, M., Penhaker, M., Peterek, T. Emotional Impact on Neurological Characteristics and Human Speech. In: Springer Advances in Intelligent Systems and Computing AISC, Volume 298, 2014, pp. 527–533, DOI: 10.1007/978-3-319-07773-4_52
3. Partila, P., Voznak, M., Peterek, T., Penhaker, M., Novak, V., Tovarek, J., Mehic, M., Vojtech, L. Impact of human emotions on physiological characteristics. In: Independent Component Analyses, Compressive Sampling, Wavelets, Neural Net, Biosystems, and Nanoengineering XII, 2014, DOI: 10.1117/12.2050679

Design and Creation of Czech Speech Emotional Database

Dominik Uhrin and Miroslav Voznak

Department of Telecommunications, FEECS,
VŠB – Technical University of Ostrava, 17. listopadu 15, 708 33 Ostrava – Poruba
{dominik.uhrin, miroslav.voznak}@vsb.cz

Abstract. The paper describes the creation of Czech speech emotional database. This database consists of short sounds records which is also called emotion samples. One part of the paper deals with implementation of special tool for subjective evaluation of database samples. The first step, in emotional database creation, was extraction of sound records from broadcasting of three radio and one television stations. All the recordings have been analyzed and short parts of records have been subjectively selected and cut out to be prepared for next step as database samples. In next step, all database samples were subjectively evaluated using our designed evaluation tool and results were analyzed. According to results of analysis, samples were rated how they are credible and reliable and how they represent different states of emotions. As the result of evaluation three separated emotional databases were created.

Keywords: Emotion, Emotion samples, Emotion state, Evaluation, Samples, Speech, Voice

1 Introduction

The speech is one of the most developed methods for information exchange between people. Therefore, in last few years, developers, scientists and companies are trying to make interaction between people and smart devices as natural as possible. Today smart devices offer voice and gesture control. This not only allow user to give orders to execute something, but also device have built-in sensors which are able to detect and record some parameters important not only for emotional and physical detection. Of course, option of emotional and physical state detection is still developing, but it can be achieved by use of emotional classifier. In our case we are using speech to detect emotional state of human. Speech offers whole range of information which can be extracted with high accuracy. This information is divided in primary and secondary and secondary ones characterize speaker and his actual state. From this information we can determine speaker age, gender, actual emotional state, speech deviations etc. [1]. Emotion is not only a part of secondary speech features but it is complex phenomenon which also includes experience. In general emotion can be defined as a change of psychological status which is triggered during achieving of some aim. In

© M. Krátký, J. Dvorský, P. Moravec (Eds.): WOFEX 2015, pp. 666–672.
VŠB – Technical University of Ostrava, FEECS, 2015, ISBN 978-80-248-3787-1.

dependence on success we can talk about positive or negative emotion. Information extraction from human speech and it analysis can be used in different fields. Agents in call centers are also paid in dependence how they behave during communication with customers. In government sectors like police, fire department and mainly military forces, create most emotional pressure on their employees. Abilities of a soldier, a police officer or a fireman to perform work depend on commands from dispatching. So using of system, system for emotional state recognition from human speech, makes it harder to change dispatching orders for a man in action. Also emotion recognition system can be used to analysis calls on emergency lines to determine emotion state of caller. Application security usually requires a use of speech as authorization key. For example, access can be denied to a person with authorization access because authorization part of the system recognized changes in speech and evaluate it as unauthorized key. So it is useful to use secondary speech information which can prevent from false authorized access. To create emotion recognition system emotional samples are needed to train it. Nowadays a lot of emotional recordings databases exist, but a significant number of databases are made on the basis of simulated emotions by actors not on real life emotions. To create this type of database is much easier compared to the real emotion database, which samples are manually cut out from sound records that contain real emotions as we did in our work. Actors are mostly pronouncing same sentences, it guarantees same context of recordings. These recordings are more efficient for training emotion classifier. Here are some most known and recent emotion recordings databases: Humane [2], Emotional Prosody Speech and Transcripts, Danish Emotional Speech Corpus, Berlin Emotional Speech Database [3], Serbian Emotional Speech Database [4].

2 Design and Implementation

2.1 Creation of Sample Database

First step in the creation of real emotion database, no simulated by actors, it was recorded few hours of two radio broadcastings. Some of the recordings have been available on the official webpage archive of third radio station and also some of the recordings of television broadcasting were downloaded from share video portal Youtube. Out of television broadcasting was cut only sound part for the creation of database samples. Parameters of database samples had to meet these conditions:

- sample has to have a duration from one to six seconds;
- sample should not contain environment noise;
- sample has to contain human speech in a form of few words or a full sentence;
- sample has to be uniquely named.

Name of database sample consists from three parameters. The first one is state of the emotion. It exists seven basic emotion states [5], [6]. Database samples have been made for four emotion states because for the rest of states it is difficult to find real emotion recordings or is hard to recognize it by using subjective methods (boredom,

disgust, fear). Second parameter is order number, third and the last one is gender of the speaker on sound recordings, see figure 1.
As an output format for database samples have been used waveform audio file with 16-bit PCM (Pulse Code Modulation) coding, mono channel and sample frequency at level of 16 kHz. These parameters are more than enough if it notes that source recordings of broadcasting was recorded to MPEG-2 Audio Layer III audio file with bitrate of 128 kbps. Some of the source recordings from which database samples have been obtained were recorded using VideoLAN Client media player. For editing and cutting of source recordings, software Audacity was used. By default, Audacity is unable to edit mp3 audio file, so LAME Encode library had to be installed.

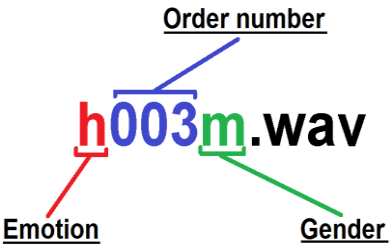

Fig. 1. Database sample name

2.2 Evaluation Tool

Next step in building of emotional database was creation of the tool for evaluation of database samples from which emotional database have been created after evaluation. As methods for evaluation of emotion samples, it was chosen subjective one. Subjective methods, in this meaning, represent using of people to evaluate small amount of samples. The webpage represents evaluation tool as a direct tool for evaluation connected with MySQL database for saving results of subjective evaluation. The webpage consists of four pages. First one is invitation page, it invite evaluating subject and giving it short instruction. Second page is evaluating page. It is the core of whole evaluating tool. It consists of html5 audio player for playing database sound samples and rollout menu for selection of state of emotion. Subject just play recording selected by algorithm and subsequently select emotion in rollout menu by it decision. Result is sent to and saved in MySQL database. The last two pages of the tool are final page to announce the end of the process of evaluation to subject and error page which is announcing to subject that something went wrong during the evaluation process. Beside webpage tool also consist from MySQL database. As it was mentioned above, database was used to save results of subjective evaluation. Database consists from two connected tables. These tables are shown in figure 2. First table is dedicated to information about individual emotional samples and contains four kinds of information. Number column represents how many times sample have been loaded to audio player. Emotion column represents the first letter from English expression of selected sample. Ref_id column represents a unique name for a sample. Second table

is dedicated to information about evaluation of sample and contains seven kinds of information. Meaning of first one, ref_id, is same as in table one. Origin column represents how many times have been selected same emotion by subject for sample as was originally selected by author during the process of creating database samples. Information from third to sixth column represent emotional state selected by subject during the process of evaluation. And finally the last column, counter, represents the total number of sample evaluation.

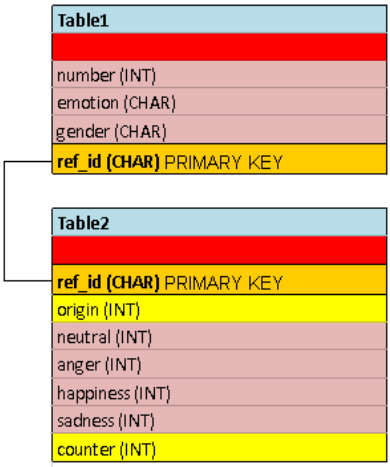

Fig. 2. MySQL database tables

For connecting webpage to the MySQL was used typical script mysql_connect($host, $login, $pass) and mysql_select_db($db_name, $connection_active). The webpage also logically contains scripts to perform queries by using mysql_query() with SELECT or UPDATE queries. It was also necessary to create a customs function for loading and saving data from or to the database named database_load(). Web page is also using POST and GET forms to obtained data from previous page loads. Also it were necessary to create custom functions generate_sample() and audio(). First function is used to generate the name of the sample that will be loaded to html5 audio player using second function audio(). Using htlm5 audio player is much easier. Flash or any other plugin do not have to be installed. All is part of web browser and it is using a lot less of computation performance. Custom functions were created for insertion of obtained data to database tables and it was also used function mysql_close() to close the connection with the database.

3 Results

The evaluation of database samples was made by subjects whose were represented by students in age range from 18 to 26 years. Selection rate of each emotion kind for random sample shows table 1. After sample evaluation, it was necessary to evaluate results of sample evaluation. For each sample from the database, it was necessary to

determine level of evaluation in percentage. Table 2 shows first 5 samples of database with percentage of veracity, state of emotion and a level of veracity.

Table 1. probability with what was emotion selected.

Emotion	*Probability for one sample (%)*
Neutral	33
Anger	25
Happiness	19
Sadness	23

After determining of veracity value, three levels of veracity were assigned to samples: low, medium, high. Low level has a range from 0 - 75, medium level range is from 75 – 90 and high level percentage range is from 90 up to 100. Three final emotion databases have been created on the basis of these three levels. Name of these emotion database samples was formed under conditions as it shows figure 1. During the creation process, database samples have been named under conditions as you can see in figure 1 and emotion state of these samples have been subjectively selected by author. But after the process of evaluation, emotion state of some emotion samples have been changed in dependence on the evaluation output. First database with high veracity of samples, with average veracity of 97,02 percent, is suitable for learning of neural emotion classifier. This classifier is developing Mr. Partila at our university [1],[7],[8]. Second database of samples with medium veracity and average veracity level of 81,61 percent is suitable for training of neural classifier and to verify it learning skills. And the last database of emotion samples with low level of veracity and average veracity level of 57,66 percent is formed by samples that contain mixed emotion. For this emotion database, it was hard to determine emotion state of samples. For better determining of emotion state more evaluations of samples has to be performed.

Table 2. veracity table for first five samples with emotion kind determined.

Evaluation veracity (%)	*Emotion kind*	*Level of veracity*
72,23	neutral	low
36,36	anger	low
45,45	neutral	low
80,00	happiness	medium
80,00	neutral	medium

Figure 3 shows a difference in count of individual levels of veracity within one emotion state. In the case of neutral emotion it is almost exponential increase. In the case of happiness and sadness it is almost linear increase. And in the case of anger it is approximately same number in all levels.

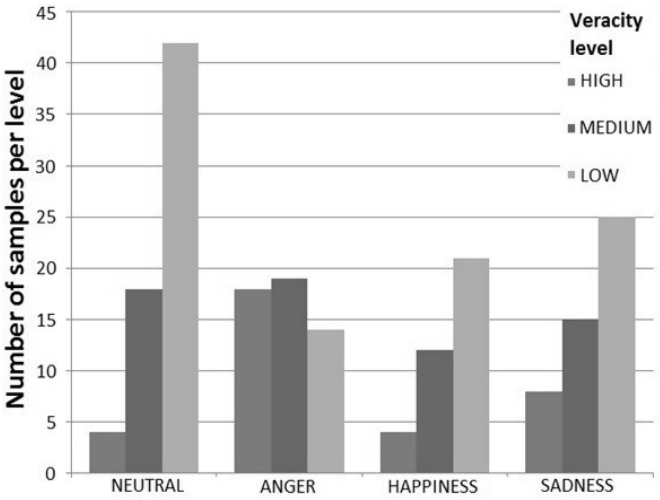

Fig. 3: Number of samples per emotion state and also per veracity level

4 Conclusion

The aim of this work was to create the emotion database of samples in a form of sound recordings so these recordings contain real emotions, not simulated. After long editing and cutting of source recordings, sample database with size about 200 samples was prepared for evaluation. During the process of sample creating there was a problem with background noise and also noise caused by quality of phone calls recordings. Next step was to create the tool for subjective evaluation of this sample database in purpose to create emotion database. The tool consists of the webpage connected with MySQL database. This MySQL database was used for saving results of the evaluation process and also for saving and loading of auxiliary variables. As a part of evaluation process, it was necessary to analyze results. On the basis of the analysis, three final emotion databases were created. The first two databases, with veracity level high and medium, are useable for learning and training of neural classifier. This classifier has been developing in our department since 2011 [1],[7],[8]. And last database with veracity level of low should be evaluated more times because it contains samples with mixed emotions or samples which are not understandable. The idea of all this was to create the basis for open database of real emotions in a way that any subject could access database and have an option to insert samples that will be evaluated. For a possible future development, the tool has to be modified for inserting samples with strictly defined parameters and the tool should be publically accessible. For further development automatic evaluation of samples is an option to be used instead of subjective evaluation. Automatic evaluation of samples will have a form of neural classifier [1],[7],[8] and also function of automatic sending of results of sample evaluation should be implemented.

5 References

1. P. Partila, M. Voznak, “Speech Emotions Recognition Using 2-D Neural Classifier”, Nostradamus 2013: Prediction, Modeling and Analysis of Complex Systems, Springer International Publishing, 2013, Pages 221-231.
2. D. Ververidis, C. Kotropoulos, “A review of emotional speech databases” , Proc. Panhellenic Conference on Informatics (PCI). 2003, Pages 560-574.
3. F. Burkhardt, A. Paeschke, M. Rolfes, W. Sendlmeier, B. Weiss, “A Database of German Emotional Speech”, Interspeech 2005 – Eurospeech, 9th European Conference on Speech Communication and Technology, September 2003, Pages. 1517–1520.
4. S.T. Jovičić, Z. Kašić, M. Đorđević, M. Rajković, "Serbian emotional speech database: design, processing and evaluation", 9th Conference Speech and Computer, SPECOM 2004, St. Petersburg, Russia, Pages 77–81.
5. M. Nakonecny (2000). *Human emotions* [Lidske emoce] (1st ed.). ISBN 80-200-0763-6
6. L. Cerny (2009). Emotional state recognition and classification based on speech signal analisis. [Rozpoznavani a klasifikace emocii na zaklade analyzy reci]. Available: https://dspace.vutbr.cz/bitstream/handle/11012/10673/DP_cerny_lukas.pdf
7. M. Voznak, P. Partila, M. Mehic, S. Jakovlev, “Recognizing Emotions from Human Speech Using 2-D Neural Classifier and Influence the Selection of Input Parameters on its Accuracy”, 21st Telecommunications Forum Telfor, art no. 6716272, November 2013, Pages 482-485.
8. P. Partila, M. Voznak, M. Mikulec, J. Zdralek, “Fundamental frequency extraction method using central clipping and its importance for the classification of emotional state”, Advances in Electrical and Electronic Engineering, Volume 10, Issue 4, 2012, Pages 270-275.

Simulation of Modulation Formats for FSO with Respect to Measurements of the Influence of Atmospheric Phenomena

Ales Vanderka

Department of Telecommunications, FEECS,
VŠB – Technical University of Ostrava, 17. listopadu 15, 708 33 Ostrava – Poruba
ales.vanderka@vsb.cz

Abstract. The influence of atmospheric environment is fundamental for Free-Space Optical link (FSO). The atmosphere can significantly degrade the communication quality of FSO up to so low received power/RSSI level that can lead to loss of communication. For this reason, authors used a professional weather station built on site of FSO link for measurement of real atmospheric phenomena, such as wind speed, temperature, relative air humidity, pressure and solar radiation. Random changing of these atmosphere parameters creates atmospheric turbulences, ab-sorption and dispersion centers. It is necessary to specify the value for structural parameter of refractive index C_n^2 because the need of the influence of atmosphere FSO.

Keywords: FSO, atmospherics, modulation format, PAMELA, eMOS, MOS.

1 Introduction

FSO system are used a long time for its advantages in terms of use of communication in the unlicensed band, high security level and simple and fast installation. FSO began to use extensively in the context of increasing transmission speed for last mile networks, there was needed a system with a higher capacity in comparison with conventional radio waves communication systems. Increase of the transmission speed and reliability of FSO link, is largely given by the type of modulation format, which is used for communication. The most commonly used modulation format is therefore modulation format OOK (On Off Keying) variants RZ (Return to Zero) and NRZ (Non-Return to Zero). Disadvantage, which greatly reduces deployment and utilization of FSO systems is then atmosphere used as a transmission environment.

An atmospheric environment is dynamic and chaotic transmission medium, where the refractive index of air is fluctuating during the day, especially at the turn of the day and night. Furthermore, the fluctuation of refractive index is related on wind velocity, roughness of the earth's surface, amount of solar radiation, rainfall, air pressure, density and composition of the air. The intensity of these fluctuation is described by structural parameter of the refractive index C_n^2. For the theoretical calculation of structural parameter of refractive index can be used basic mathematical models, ob-

© M. Krátký, J. Dvorský, P. Moravec (Eds.): WOFEX 2015, pp. 673–678.
VŠB – Technical University of Ostrava, FEECS, 2015, ISBN 978-80-248-3787-1.

tained from empirical study of the influence of the atmosphere on the structural parameter of the refractive index.

2 Description of the measurement area, the equipment used and the measurement values

The data was analyzed during the month of March 2015 (1st March 2015 – 15th March 2015). This days were chosen due to the completeness of the data and also due to the development of RSSI value in each days, because the RSSI value fluctuated approximately within the same range. It was considered that in this month there were very few dispersion centers, which would be appreciably showed on the RSSI diagram.

2.1 Description and measurement of the FSO

Measurement of the received signal strength indication (RSSI) was realized on the installed FSO in the premises of the VŠB – Technical University of Ostrava and on the observatory pylon of Johan Palisa. This is a professional optical link from the MRV type TS5000G. The total length of the optical path was 1,47 km and as a sources of light radiation were used three infrared lasers which works at λ = 830 – 860 nm, beam divergence was 2 mrad, total power of the optical head was 140 mW (2x40 mW and 1x60 mW). The beam width on the receiver side is 2,94 m. Transmitting lens diameter was 6 cm and receiving lens diameter was 20 cm. For detection of an optical signal has been used APD diode (sensitivity -33 dBm). The maximum bit rate of the FSO was 1,25 Gbitps. Azimuth defined by the manufacturer for optical link TS5000G is 107.26 °. The basic circuit diagram FSO is shown in Figure 1. Optical head for FSO link transmits periodically sequence of bits and measures value of the received signal strength indication RSSI. The RSSI is recorded in 60 seconds intervals.

3 Measurement of climatic effects

For measurement of meteorological data weather station Davis Vintage Pro2 was used. This weather station is installed in close proximity to the optical head for FSO on the roof of the main building of VŠB–Technical University of Ostrava. In addition to the values of wind speed, temperature, pressure, relative humidity and solar radiation station the weather station is also capable of measuring wind direction and rainfall. Separate data were read in minute interval in time period 1st April 2015 to 14th April 2015. During the measurement of climatic influences a sensor failure occurred in 10th and 11th day of measuring due to electric energy failure. The sensor measured a solar radiation. Due to this failure the days 10th April 2015 and 11th April 2015 were removed from subsequent calculations.

4 Calculation if structure parameter of the refractive index C_n^2

According to the theory the calculations of models PAMELA, MOS and eMOS were done. These calculations went from measured data which were obtained in period 1st to 14th April 2015. The final calculation is displayed in Fig.1, where the x-axis represents minutes of one day and y-axis shows values of the structure parameter of the refractive index C_n^2. The calculations of separate minutes are represented by grey crosses. For each minute 12 calculations were done in our cases and from these 12 values the arithmetic mean was calculated.

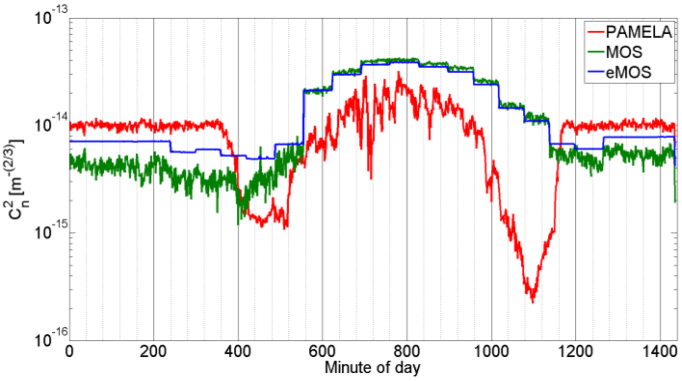

Fig. 1. Comparison of models PAMELA, MOS, eMOS.

5 Simulation of the influence of atmospheric phenoma for FSO in Optiwave system

For simulation of the influence of atmospheric conditions on the free space optical link was used Optiwave OptiSystem software ver. 11. To simulate the influence of atmospheric phenomena for the quality of communication were selected mostly used modulation formats RZ, NRZ and BPSK for FSO communication. Modulation formats affect important parameters such as bandwidth and energy efficiency, which affect overall system performance. The main goal of modulation formats is increase spectral/power efficiency and reduce sensitivity to fluctuation of received power.

Modulation of the optical beam is provided in optical area by Mach-Zhender modulator. Simulation is set to correspond to the real professional circuit, which is located between the campus building of the VSB-TU Ostrava and pylon at the Johan Palisa observatory.

During simulation were successively entered structural parameter values of the refractive index derived from calculation of the real measured data, when it was monitoring BER progress, eye diagram.

Figure 2 shows the simulation result for the dependence of the structural parameter of the refractive index at BER level. The structural parameter values of the refractive index are entered from 10^{-17} to 10^{-12} with logarithmic increase. In figure 2 is designated area from $2.21E^{-16}$ do $4.27E^{-14}$ that corresponding to the maximum and minimum value of the structural parameter of the refractive index calculated models. In this area is reflected the expected increase of BER that shows the logarithmic character of behavior. However, computational model presents particular and mistaken behavior in the area around $4E^{-14}$, when BER begins decline with increasing turbulence error rate. This behavior is contrary to the logical assumption and it can be considered as an error caused by an internal algorithm program.

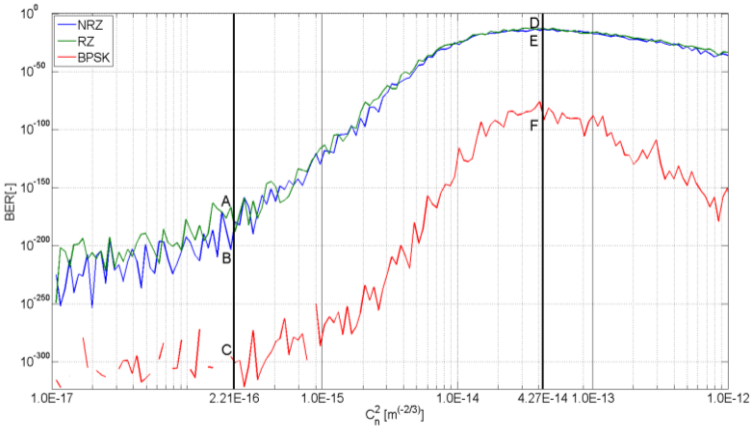

Fig. 2. Simulation of depending of structural parameter of refractive index on the BER parameter for modulation formats NRZ, RZ and BPSK.

In Figure 2 are shown the points of intersection of the individual charts with the limit values of the structural parameter of the refractive index. For these states were monitored state of the eye diagram. From the eye diagrams and the characteristics of the waveforms the most resistant modulation format is BPSK for the examined area. The other modulation formats RZ and NRZ exhibit small deviation. For NRZ and RZ modulation, with the limit values can be seen a clear increase in symbol errors ISI and eye closure. From simulated data of BPSK modulation format it can also be observed that the marked red curve of Q factor is unchanged at the minimum and maximum influence values of the structural parameter of refractive index. Transmission speed of optical head for the simulation was set to 1.25 Gbps, which corresponds to real value at the optical head MRV TS5000G.

Development of BER with regards to chosen type of modulation format and structural parameter of refractive index for models PAMELA, MOS and eMOS is showed in figures 3-5. Good results could by seen for modulation format BPSK from simulations and development of BER parameter. This behavior is not in the case of RZ or NRZ modulation format, for these modulations increasing of BER is more significant. In this case interruption of communication channel could occur because of higher values of BER.

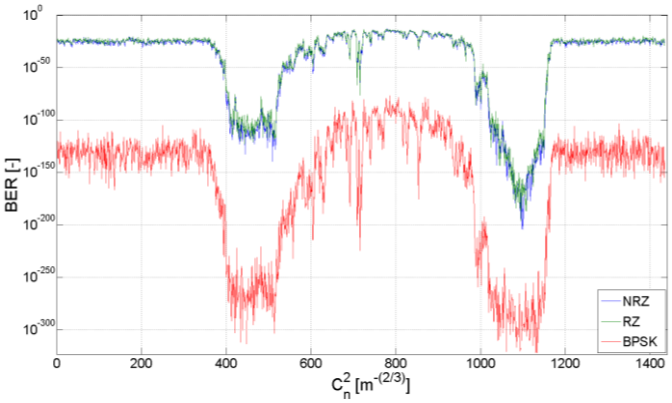

Fig. 3. BER simulation for structure parameter of refractive index computed by PAMELA.

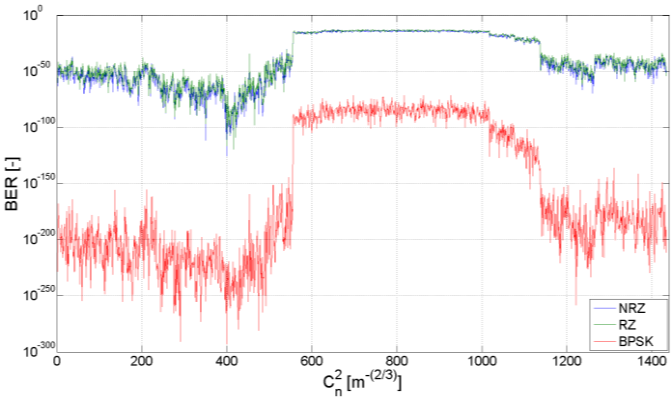

Fig. 4. BER simulation for structure parameter of refractive index computed by MOS.

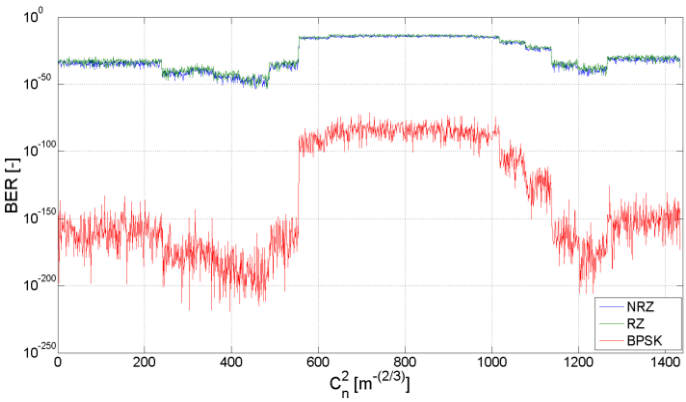

Fig. 5. BER simulation for structure parameter of refractive index computed by eMOS.

6 Conslusion

Within the article team of authors focused its attention to the area of atmospheric influence to Free-Space-Optics. Based on real measured values of atmospheric environment three models of structural parameter of refractive index (PAMELA, MOS and eMOS) were computed. Each model uses different principles for calculating the C_n^2 which is reflected especially during sunset and sunrise, when PAMELA model has the lowest level of turbulence compared to MOS and eMOS. These models were then correlated with BER for different modulation formats in our case RZ, NRZ, and BPSK. With regards to real atmospheric measurement, the BPSK modulation showed good resistant for communication in turbulent condition in comparison to RZ and NRZ modulation.

Acknowledgement

The research described in this article could be carried out thanks to the active support of the Ministry of Education of the Czech Republic within the projects no. SP2015/130, SP2015/182. This article was supported by projects Technology Agency of the Czech Republic TA03020439 and TA04021263. The research has been partially supported by the Ministry of Education, Youth and Sports of the Czech Republic through grant project no. CZ.1.07/2.3.00/20.0217 within the frame of the operation programme Education for competitiveness financed by the European Structural Funds and from the state budget of the Czech Republic.

7 References

1. MAJUMDAR, Arun K and Jennifer Crider RICKLIN. Free-space laser communications: principles and advances. New York, NY: Springer, c2008, x, 417 p. ISBN 9780387286778.
2. KOPEIKA, Norman S and Jennifer Crider RICKLIN. A system engineering approach to imaging: principles and advances. Bellingham, Wash.: SPIE Optical Engineering Press, c1998, xxi, 679 p. ISBN 08-194-2377-7.
3. BENDERSKY, S., N. S. Kopeika, and N. Blaunstein, "Atmospheric optical turbulence over land in middle east coastal environments: prediction modeling and measurements," Appl. Opt. 43, 4070-4079 (2004)
4. RAMIREZ-INIGUEZ, Roberto, Sevia M IDRUS and Ziran SUN. *Optical wireless communications: IR for wireless connectivity*. Boca Raton: CRC Press, c2008, xxxi, 344 p. ISBN 08-493-7209-7.
5. TUNICK, A. *C_n^2 model to calculate the micrometeorological influences on the refractive index structure parameter.* Environmental Modelling & Software: Elsevier Science, 2003, pp. 165-171. DOI: 10.1016/S1364-8152(02)00052-X
6. BLAUNSTEIN, N., S. Arnon, A. ZIELBERMAN and N. KOPEIKA. *Applied aspects of optical communication and LIDAR*. Boca Raton: CRC Press, 2009, pp. 262. ISBN 978-1-4200-9040-6. DOI: 10.1201/9781420090451-c3
7. JACOBSON, Z. M. *Fundamentals of atmospheric modeling.* New York: Cambridge University Press, 2005, pp. 813. ISBN 05-215-4865-9

Current progress in research of optical fibers ageing

Petr Závodný

Department of Telecommunications, FEECS,
VŠB – Technical University of Ostrava, 17. listopadu 15, 708 33 Ostrava – Poruba
petr.zavodny@vsb.cz

Abstract. This article presents current progress in research of optical fibers ageing. In first part will be described basic aspect of research focused on the ageing of the optical cable placed outside and exposed to common weather conditions. Next part describes another ageing process which includes impacts of radioactive environment on the optical cable.

Introduction

Fiber optic devices became very important part of telecommunication infrastructure since most copper wires were replaced by optical fibers. In present most of the back bone networks in entire world depends on high throughput and reliability of the optical fibers. The reliability now becomes more and more often discussed subject of optical networks as number and age of the optical network increases. Correct estimation of optical network reliability from long term viewpoint becoming more requested for designation of risks. In past most limiting factor for fast data transmission in optical networks was speed of the electronic devices an optical fiber was treated as quite stable and reliable medium with almost unlimited bandwidth. Most important attribute of optical fiber was attenuation, but now when high speed electronic circuits are widely available it is possible utilize high bandwidth of optical fibers and more attention is dedicated to the fine attributes of fibers like wavelength depended attenuation, chromatic and polarization dispersion. These fine attributes tend to be less stable in time and can be critical for correct functionality of high speed optical network [1-5]. This article describes some parts of research in which I'm personally participating.

1 Ageing of the optical cables

Goal of this research is observation changes transmission parameters of cabled optical fibers exposed to stress of the regular weather condition during long period of time.

1.1 Examined cables

For purpose of this research was build testing polygon consisting of two optical cables connected together. Both cables are regular ITUT single mode telecommunication

© M. Krátký, J. Dvorský, P. Moravec (Eds.): WOFEX 2015, pp. 679–683.
VŠB – Technical University of Ostrava, FEECS, 2015, ISBN 978-80-248-3787-1.

cables consisting of multiple fibers. Fibers cladding is protected by hard coating and all fiber strands are placed in lose tube filled by gel. Tubes are bundled in cable with outer polymer based protective cover. Individual fibers are connected together using fuse splices to form four optical paths marked A, B, C, D. Paths A and B are 11.5 km long, path C is 10 km long and path D is 16 km long.

1.2 Cable location and test conditions

Testing polygon is located on the roof of building and optical cables are exposed to all weather conditions (e.g. rain, sun, cold, wind) during year. This simulates stress condition for cables which are usually hanged in air. Both ends of the cables are covered and protected from stress conditions to prevent direct damage of the cable core. These ends contain fused splices and pigtails. Both ends each of the four optical paths are ended with SC APC connector placed in dry room inside building with stable temperature.
Cables were placed on the roof in winter 2014/2015 and after that it were leaved until February/March (due to bad weather) when preparing of cable started. Frist measurements were executed in March.

1.3 Measuring methodic

Measurement is currently still in pilot stage, in which we need to evaluate conditions and methodic of measurement and it's possible that final methodic will be different.
Cable parameters are measured in one week cycle. Monitored parameters include attenuation, chromatic and polarization dispersion, Brillouin frequency. Before beginning of measurement cycle each connector in measurement chain is cleaned and inspected by probe. Pictures from probe are saved and serve for monitoring of condition of the optical connector ferrule. Ferule of optical connectors seems to be one of the most critical parts of long term measurement because each measurement cycle involves many connecting and disconnecting of the optical fibers. At early beginning of the measurement several ferrules had been damaged probably by few grain of sand which stuck on one of the ferules.

Measurement of attenuation

Attenuation is measured in two ways using Optical time-domain reflectometer (OTDR) and standard source and power meter. Using of the OTDR is possible to measure attenuation profile along whole fiber length. Result of this measurement gives us global picture of fiber condition and serves for eventual fault location. Sample result of OTDR measurement is on figure (**Fig. 1**). Results of OTDR are evaluated on beginning of measurement to ensure that optical path is not damaged. Measurement is performed on the wavelength 1310 nm and 1550 nm in both directions (e.g. AB, BA). Used OTDR parameters are length of measurement 60 s and length of optical pulse 30 ns. Average measured attenuation is 0.46 dB/km.

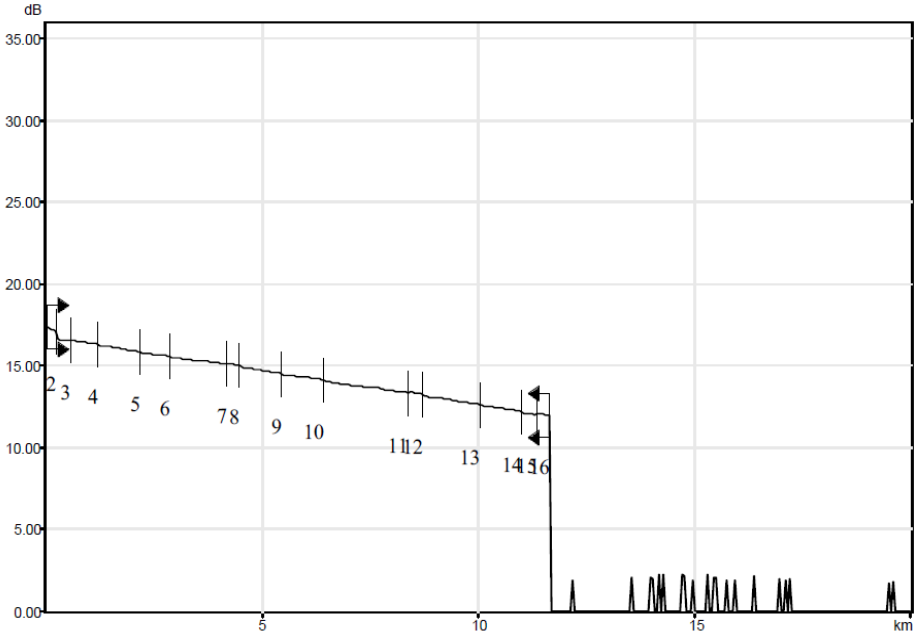

Fig. 1. Result of the OTDR measurement on 1310 nm direction AB.

Second way of attenuation measurement is using of direct method 1C. Schematic connection of measurement is on the figure (**Fig. 2**). This method uses three fibers to estimate reference level. After setting the reference level the measured fiber is connected in middle section. This method benefits from maintaining constant number of connectors during measurement and minimizes measurement error. Attenuation is measured in both direction of fiber.

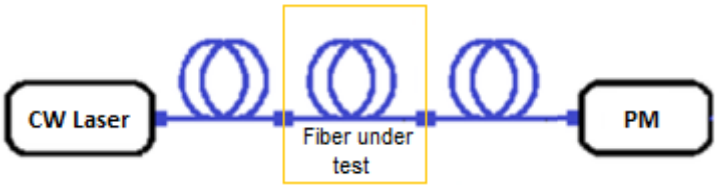

Fig. 2. Connection diagram for measurement of attenuation using method 1C.

Dispersion measurement

Reason for realization of dispersion measurements is that we expect a change in material of fiber causes change in dispersion, since dispersion is strongly related material properties of a fiber. For measuring of chromatic and polarization dispersions is

used inbox device based on EXFO FTB500 platform. This device contains specialized hardware modules and software to perform direct measurement of dispersion. Chromatic dispersion is measured in both directions of the fiber. Polarization dispersion is measured only in one direction. Connection diagram is described on figure **Fig. 3Fig. 1**.

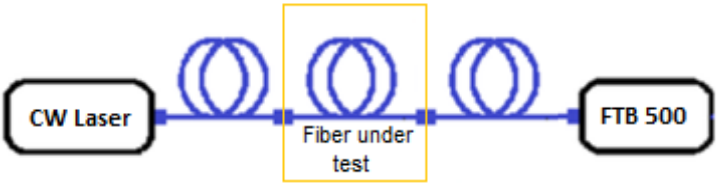

Fig. 3. Connection diagram for measurement of dispersion.

2 Measurement of numerical aperture of radiation aged optical fibers

This part of ageing research is focused on the observation of effect of invisible radioactive environment on the multimode optical fibers. Optical cables are exposed to the increased amount cobalt radiation. Parameters of the optical fibers are measured before, during and after radiation. This project includes measuring of several parameters of optical fibers like attenuations, Brillouin frequency and numerical aperture. My part in this project is creating of software for realization of automatized measurement of numerical aperture due lack of needed device.

2.1 Measuring device

For purpose of the numerical aperture measurement was constructed simple device assembled from rotation stage holding optical power detector and laser source at 850 nm. Rotation stage is motorized and controlled from PC, by custom made software written in LabVIEW. Measured fiber is fixed in holder in center of arc. Around perimeter of arc moves detector bounded to rotating stage. Detector is connected to optical power meter which is connected to the PC.

2.2 Measurement

Measuring software controls rotation stage to periodically perform step of defined starting size in unit of degrees. On each step is measured optical power and actual angular position of rotation stage. Software performs number of steps from user defined range of movement. Movement through set range is repeated several times in each iteration size of the moving step set to half, so number of iteration and starting size of step determines final measurement resolution. This way of measurement gives quick overall view on the shape of beam. Once all iterations are done measured data

are used to find maximal value of power and it's angle (θ_{max}). From maximal power is then calculated 5% power, which is used to find corresponding angle $\theta_{5\%}$. Difference between angle θ_{max} and $\theta_{5\%}$ gives size of the acceptance angle θ (from fiber axis) this angle used to calculate final numerical aperture NA:

$$NA = \sin(\theta)$$

3 Conclusion

Research of optical cable ageing is currently in pilot stage, in which we trying estimate critical parameters of fibers to be monitored. No dramatic changes in properties of optical fibers are expected since cable is exposed to normal operation conditions. There will be probably only small changes in some of the fiber properties. We need find out this changes and investigate if they correlate to the weather condition or are time depended. Further result will be presented in other papers soon as will be available. Measurement of numerical aperture is currently successfully tested and ready for measuring of radiated fibers.

References

1. Mark L. Lundergan; Bernd D. Zimmermann; Bill Waterman, „Mechanical and Optical Functionality Of Field Aged Optical Ground Wire Cable“ Corning Incorporated
2. Verification of Optical Fiber and Cable Reliability. Kevin Houser - Corning Incorporated. Shirley Chahanovich - Pirelli Cables and Systems North America.
3. Bakshi, B.; Rahman, L.; Mohs, G.; Vaa, M.; Patterson, W.W.; Cai, J. -X; Lucero, A.; Golovchenko, E. A.; Abbott, S.M., "Impact of fiber aging and cable repair in an installed 28-nm transatlantic 96 x 10 Gb/s DWDM system," Optical Fiber Communication Conference, 2005. Technical Digest. OFC/NFOEC , vol.1, no., pp.169,171, 6-11 March 2005
4. Krzysztof Borzycki, „Influence of temperature and aging on polarization mode dispersion of tight-buffered optical fibers and cables“ JTIT March 2005
5. Al-Ammar, E.; Karady, G.G.; Tuominen, M.W., "Impacts of the induced current on the aging of the ADSS fiber optic cables," Power Engineering Society General Meeting, 2006. IEEE , vol., no., pp.7 pp.,, 0-0 0

Optoelectronic sensoric elements made from polydimethylsiloxane

Ondřej Zbořil

Department of Telecommunications, FEECS,
VŠB – Technical University of Ostrava, 17. listopadu 15, 708 33 Ostrava – Poruba
ondrej.zboril@gmail.com

Abstract. This article describes the progress of the second year of the author's study of the field of Communication technology. Article summarizes author's activities at the Department of Telecommunications during the academic year 2014/2015, research and development activities, work on projects and other activities in which the author participated.

Keywords: fiber, interferometer, polydimethylsiloxane, siloxane

1 Introduction

I am studying full-time doctoral study at the Faculty of Electrical Engineering and Computer Science at the Technical University of Ostrava. My study programme is called Computer Science, Communication technology and Applied Mathematics and field of study is Communication Technology. My dissertation thesis is focused on sensing elements made from polydimethylsiloxane and my tutor is Professor Vašinek. This article summarizes the second year of study.

2 Dissertation work

My dissertation deals with sensoric elements made of siloxane. First it is necessary to handle the production of simple elements of siloxane and master these manufacturing processes. Elements of siloxane are analyzed and its properties are measured. Then is adjusted the mixture composition in order to adjust its properties, particularly the optical properties.

There were formed thin fibers from siloxane which were subjected to further testing. The fibers were subjected to mechanical stress, high temperatures in the sand molds dryer, low temperatures in the cryo chamber and last but not least, also measured optical parameters such as attenuation.

© M. Krátký, J. Dvorský, P. Moravec (Eds.): WOFEX 2015, pp. 684–688.
VŠB – Technical University of Ostrava, FEECS, 2015, ISBN 978-80-248-3787-1.

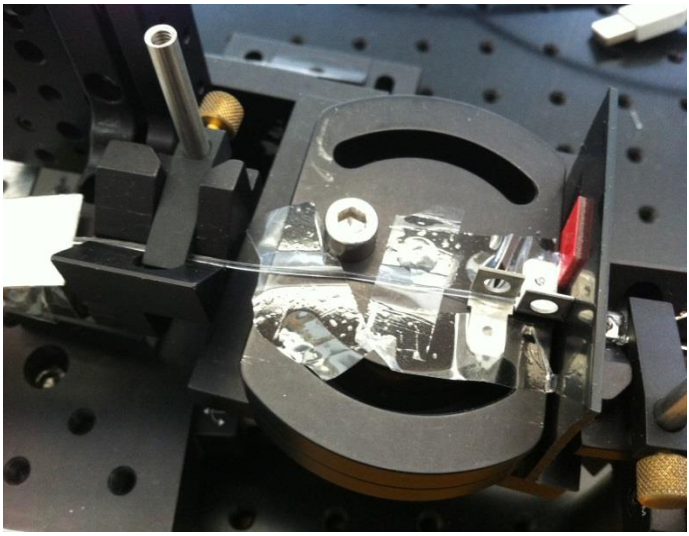

Fig. 1. Attenuation measurement

An experimental prism piece was formed from siloxane. I created design of the core box that will serve as a mold for the creation of other prisms.

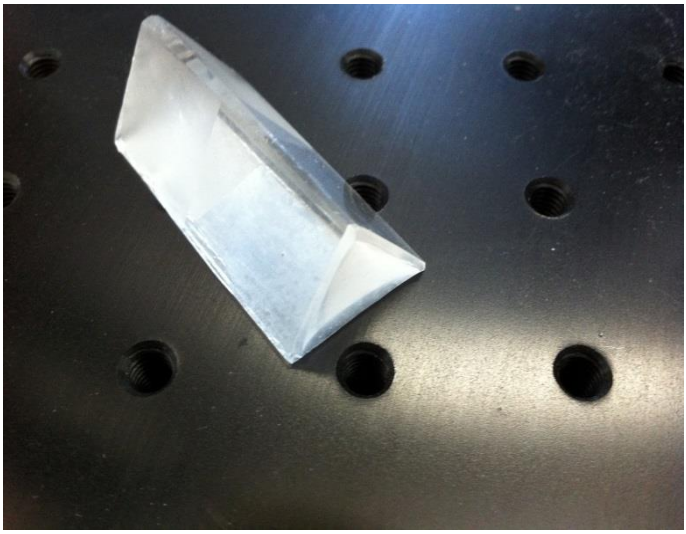

Fig. 2. Experimental prism piece

I am currently waiting for the mechanical shaker, through which i will achieve better homogeneity of the mixture in the preparation of siloxane. Then i can proceed with further process steps.

3 Cooperation on projects

I was actively involved in solving on two projects under the auspices of the Technology Agency of the Czech Republic. I also participated on project GUARDSENSE under the auspices of the Ministry of Interior.

- TA ČR - Intelligent modules for lighting and communication
- TA ČR - Safety of optical transport networks and the development of opt. parts for electric power and electrical appliances
- Project GUARDSENSE

Participation on these projects includes activities as designing, building and measuring, such as:

- Measuring mechanical and acoustic vibration for the security of space assets via fiber-optic interferometer

I participated in the production of a prototype measurement units built into a plastic window. The unit serves as the detector against external intrusion. The prototype functionality has been tested, also the frequency range and sensitivity. The results of this work has resulted in patent proceedings.

Fig. 3. Window prototype

- Measuring mechanical vibration for traffic monitoring via fiber-optic interferometer

Installation and measuring mechanical vibration generated when passing cars around.

- Preparation of fiber and measuring ageing fiber influence to external conditions on the roof building N

Installation of the fibers on the roof and measurement of various parameters affecting aging fibers by external influences.

4 Internship

I was an intern in HiLASE project under the auspices of the Institute of Physics (FZÚ AV ČR) for three months. I worked there on more tasks, but mainly I worked on construction and subsequent tuning of a fiber-less optical interferometer. In the final stage, I constructed and tuned micro shift of mirror placed in one arm of the interferometer. Minimum shift was measured by the size of tenths of micrometer.

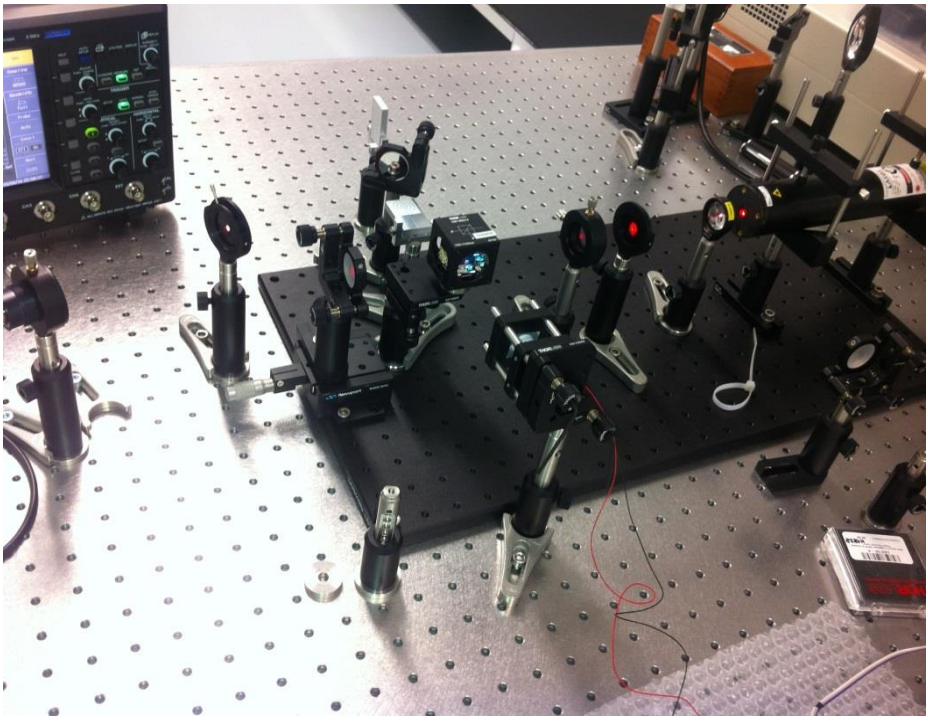

Fig. 4. fiber-less interferometer

5 Publications during academic year

As co-author, I participated in the creation of patent. This patent was the result of successful experiment of securing area using an optical fiber placed inside the plastic window. Patent is named "Fiber-optic interferometer for the security of space assets" and i have a share of 20% on it. I was involved in prototype design, measuring data and verifying its functionality. Furthermore, i was processing the part of the patent application.

6 Pedagogic part

In the winter semester, I was actively involved in ensure the practical tutorials in Communication Systems and Media (PSaM). I should have to teach Logical Circuits (LO) in the summer semester for the second year, but it was canceled because of my internship in HiLASE.

I was opponent for bachelor and diploma thesis. I also listed the two bachelor thesis and students has already signed on these topics. I was a clerk / registrar for final state examination for two days, same as last year.

7 Other activities at the Department of Telecommunications

I represented the Department of Telecommunications and the faculty at secondary schools or the building of faculty. I also participated in the open days in Šumperk and Ostrava. I was involved in preparing a presentation for the optical portion, preparation and presentation of the optical laboratory and putting whole program.

8 References

1. NORRIS, A., J. DEGROOT, F. NISHIDA, U. PERNISZ, N. KUSHIBIKI a T. OGAWA. *Silicone Materials for Optical Applications*. DOW Corning [online]. 2003. Available from: http://www.dowcorning.com.cn/zh_CN/content/publishedlit/75-1007-01_single.pdf

2. GHATAK,A., THYAGARAJAN,K.: *Introduction to fiber optics*. Cambridge University Press, 1998, ISBN 0-521-577853

3. MÉNDEZ, Alexis, T MORSE. *Specialty optical fibers handbook*. Oxford: Academic Press, 2007, xlii, 798 p.

Computer Application for Identification of the Geometry of Overhead Power Line Conductors

Michał Krawiec

Opole University of Technology, Faculty of Electrical Engineering, Automatic Control and Computer Science, Department of Power Plants and Measuring Systems, ul. Prószkowska 76, 45758 Opole, Poland
michalkrawiec2@gmail.com

Abstract. The article presents a real-time computer application for determination of overhead power lines catenary curve using computer vision. The application is implemented in National Instruments LabVIEW with the Vision module and in Microsoft .NET.

1 Introduction

Computer image processing is understood as carrying out a range of conversions and modifications for a specific purpose. The conversions improve the quality, enhance the components of the image, bring the image into a format which is convenient for saving and easy to recognize. Image recognition algorithms are described in detail in [2] and [5].

In the application presented herewith, image recognition methods are used to identify the geometry of overhead power line conductors. As described in [4], an increase in the demand for electric power in Poland will translate into overloading of the existing overhead power lines. As shown in [1], overhead power line spans may be described using catenary equations. Selected methods of span parameter determination are presented in [6].

2 Application architecture

The computer application for identification of the geometry of overhead power line conductors was implemented in NI LabVIEW and Microsoft .NET environments. The structure of the application is shown in fig. 1.

© M. Krátký, J. Dvorský, P. Moravec (Eds.): WOFEX 2015, pp. 689–693.
VŠB – Technical University of Ostrava, FEECS, 2015, ISBN 978-80-248-3787-1.

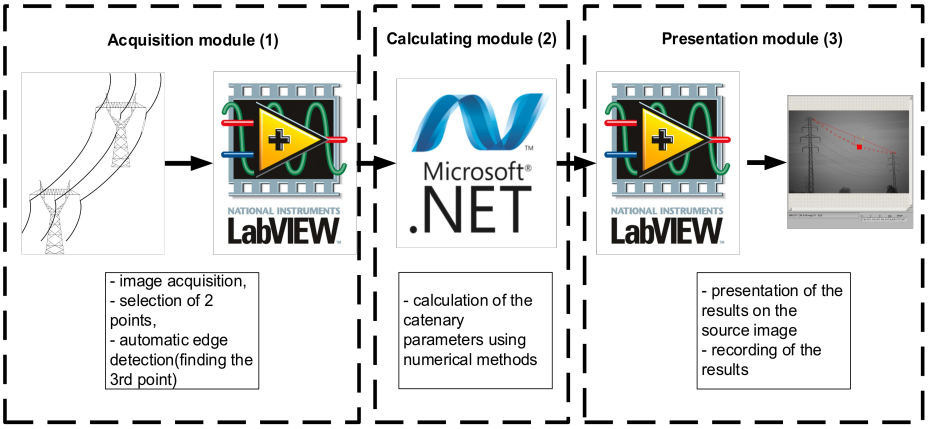

Fig. 1. Structure of the application for identification of catenary parameters

LabVIEW environment was selected from among other available solutions for several reasons. NI LabVIEW has well-developed tools for acquisition of data from external devices. It is possible to perform direct acquisition of images from a digital camera into the image processing application (module 1 acquisition). Numeric calculations are performed within the calculation module in .NET environment. The calculation module was written in the programming language c#. The third module is the presentation module. The results obtained are saved in a text file and displayed directly in the form of a digital image.

3 Acquisition module

In order to identify a catenary, the application uses the algorithm presented in [3], which generates curve equations based on 3 points in the coordinate system. The points clearly determine the catenary described with the determined equation. In the first application module, 3 points are selected which creates a catenary.

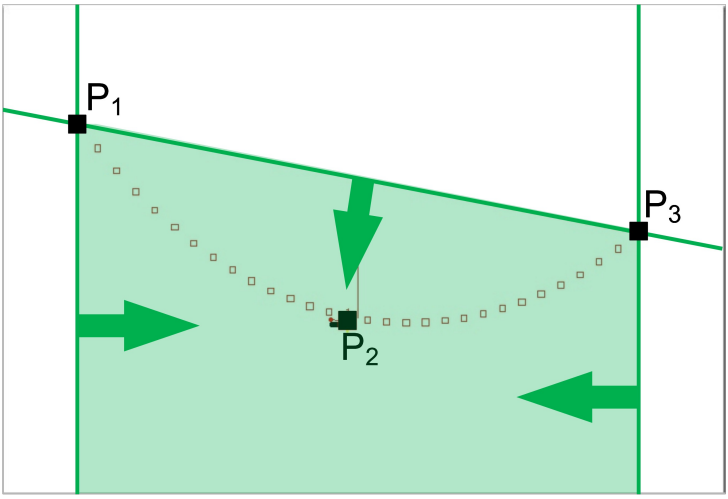

Fig. 2. Correct data input area

Point P1 and point P3 (Fig. 2) are indicated by the user as anchor points, which do not change their location during identification of subsequent images. They constitute end points of the catenary. Point P2 is generated by the program using automatic image recognition. The user inputs the ROI (Region of Interest), which the application browses for straight edges. ROI should be narrow enough to enable the application to recognize a fragment of the curve as a section very close to a straight section. From the determined straight edge of the electric power line fragment, the application registers one of the ends of the section as point P2. Point P2 is generated upon every performance of subsequent operating cycles of the application.

4 Presentation module

After conclusion of the operation of the calculation module, the application proceeds to displaying the results using NI LabVIEW environment. The digital image depicts two lines (Fig. 3). The line between points P1 and P2 constitutes chord of the catenary curve. The section between points S1 and S2 is the line which determines the catenary curve sag. For subsequent x coordinates, the results of the operation of the generated function are displayed with square markers. The application uses pixels as the length unit. Further works are to involve implementation of a module for converting pixels into actual length units. The application does not account for changes in length caused by the influence of the perspective either.

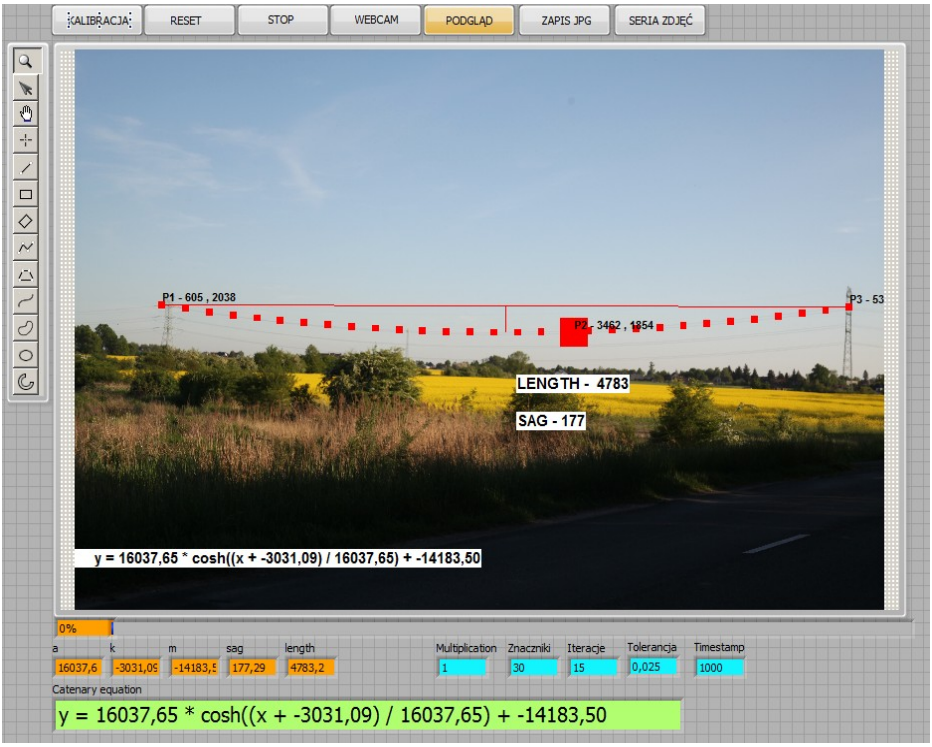

Fig. 3. Graphical user interface – view on the observed electric power line

As the result the application calculated output data (Table 1.) and an equation for the catenary curve. The values are given in pixel.

Table 1. Output data [pixel]

Parameter a	23098,37
Parameter k	-3494,70
Parameter m	-21253,92
Sag of the catenary curve	43,00
Length of the catenary curve	2820,97
Point S_1 współrzędna x	3036,00
Point S_1 współrzędna y	1892,00
Point S_2 współrzędna x	3036,00
Point S_2 współrzędna y	1849,00

$$y = 23098{,}37 * \cosh((x + -3494{,}70) / 23098{,}37) + -21253{,}92 \quad (1)$$

5 Summary

While using the presented application, satisfactory results of identification of the geometry of overhead power lines conductors were obtained. The algorithms used in the program are efficient enough to enable the application to operate in the online mode and process the graphical material obtained on an ongoing basis. The presented method enables online measurements of the electric power line cable sag. Benefits are to be expected from using this method to observe critical spans at the smallest distances from the ground surface, which pose a potential risk to safety of people and property.

References

1. CIGRE TB No 324 – Task Force B2.12.3, Sag-tension calculation methods for overhead lines, 2007
2. FOLEY J. D., VAN DAM A., FEINER ST. K., HUGHES J.F., Wprowadzenie do grafiki komputerowej, WNT, Warszawa, 1995
3. LANCE C., http://mathhelpforum.com/calculus/96398-catenary-cable-different-heights.html dostęp 25.11.2014
4. SIWY E., Metody i możliwości zwiększenia zdolności przesyłowych KSE z wykorzystaniem monitoringu linii napowietrznych, Elektroenergetyka, nr 4(6) 2010, Warszawa
5. TOMASZEWSKI M., KRAWIEC M., Wykrywanie obiektów liniowych na podstawie analizy obrazu z wykorzystaniem transformaty Hougha, Przegląd Elektrotechniczny 88, nr 10b/2012
6. ŻMUDA K., Elektroenergetyczne układy przesyłowe i rozdzielcze, Wydawnictwo Politechniki Śląskiej, Gliwice, 2012

KAPITAŁ LUDZKI
NARODOWA STRATEGIA SPÓJNOŚCI

POLITECHNIKA OPOLSKA

UNIA EUROPEJSKA
EUROPEJSKI
FUNDUSZ SPOŁECZNY

Michał Krawiec is a recipient of a Ph.D. scholarship under a project funded by the European Social Fund

Measurement of Partial Discharges with the Use of a High Voltage Testing System, Where PDS100 Analyser Was Used for Detection

Ireneusz Urbaniec

Opole University of Technology, Faculty of Electrical Engineering, Automatic Control and Computer Science, Institute of Electric Power and Renewable Energy, ul. Prószkowska 76, 45-758 Opole, Poland
ireneusz.urbaniec@gmail.com

Abstract. This article presents results of partial discharge (PD) measurements carried out in lab conditions with the use of the high voltage testing system, where the PDS100 Analyzer was used for detection.

The measuring instrument applied allows for detection of partial discharges (PD) using the scanning technique of radio frequencies (RFI) within a range (50 – 1000) MHz. Other technical parameters of PDS100 detector (Fig. 1) are as follows: accuracy ±100kHz, dimensions 225x310x70mm, weight 2.4 kg, operating temperature 0 - 50°C, IP64. These parameters allow to perform on-line PD testing at the running system during its normal operation. Therefore we classify this method to non-invasive PD measurement techniques [1, 2].

Fig. 1. PDS100 Detector

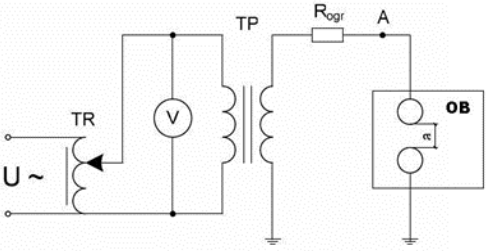

Fig. 2. A high voltage AC testing system

The lab test station was used to perform tests consisting of the following components: AC voltage source (U), control transformer (TR), test transformer (TP) and spark gap transmitter (OB measuring circuit) (Fig. 2).

Testing of the electromagnetic waves generated by PD was conducted for the following spark gaps:

– sphere to sphere (Fig. 3),
– multipoint to point (Fig. 4),
– multipoint to plane (Fig. 5).

© M. Krátký, J. Dvorský, P. Moravec (Eds.): WOFEX 2015, pp. 694–697.
VŠB – Technical University of Ostrava, FEECS, 2015, ISBN 978-80-248-3787-1.

Fig. 3. Spark gap transmitter - sphere to sphere

Fig. 4. Spark gap transmitter: multipoint to point

Fig. 5. Spark gap transmitter - multipoint to plane

A view of a test station and applied test transformer are presented in Fig. 6, 7.

Fig. 6. Measuring station

Fig. 7. Transformer

In result of measurements of electromagnetic waves generated by PD for each type of spark gap transmitters i.e. sphere to sphere (distance between spheres: 2 cm), multipoint to point (distance between multi point and point: 5 cm) and multipoint - plane (distance between multipoint and plane: 5 cm) the frequency curves were obtained, presented in Fig. 8, 9 and 10.

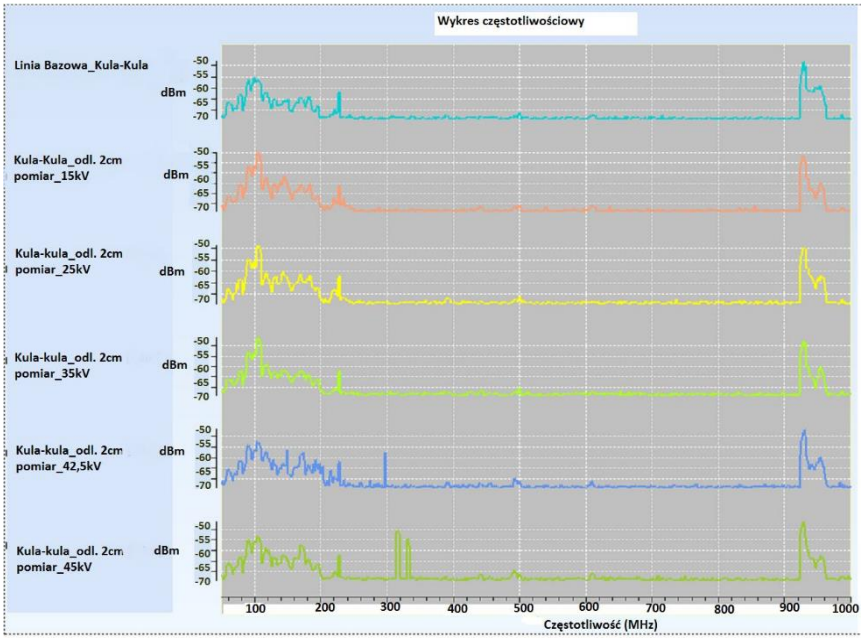

Fig. 8. Test system - sphere to sphere spark gap transmitter, distance between spheres: 2 cm, for measurements at voltages 0V, 15kV, 25kV, 35kV, 42,5kV, 45kV

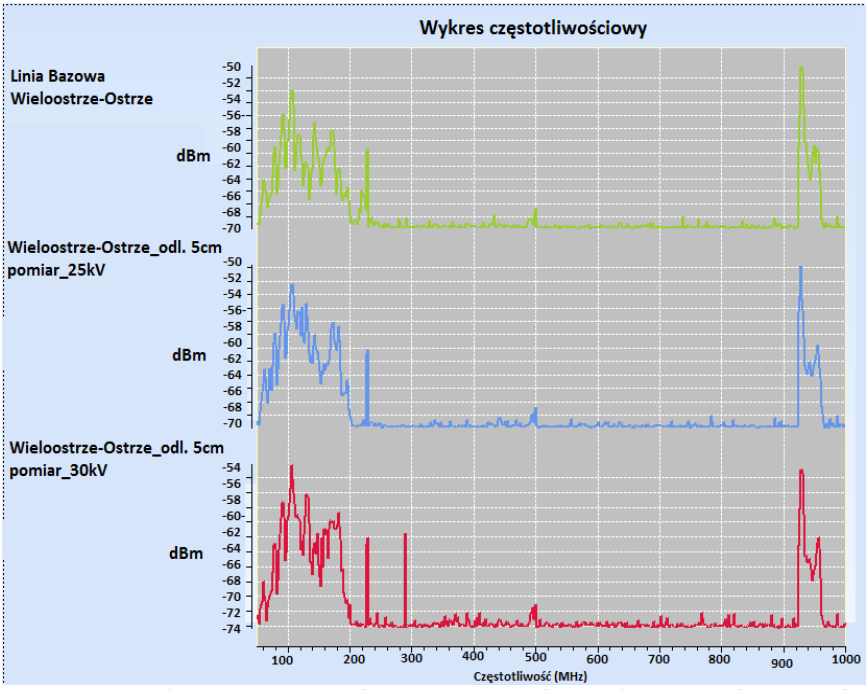

Fig. 9. Test set - multipoint to point spark gap transmitter, distance between multipoint and point: 5 cm, for measurements at voltages 0V, 25kV, 30kV

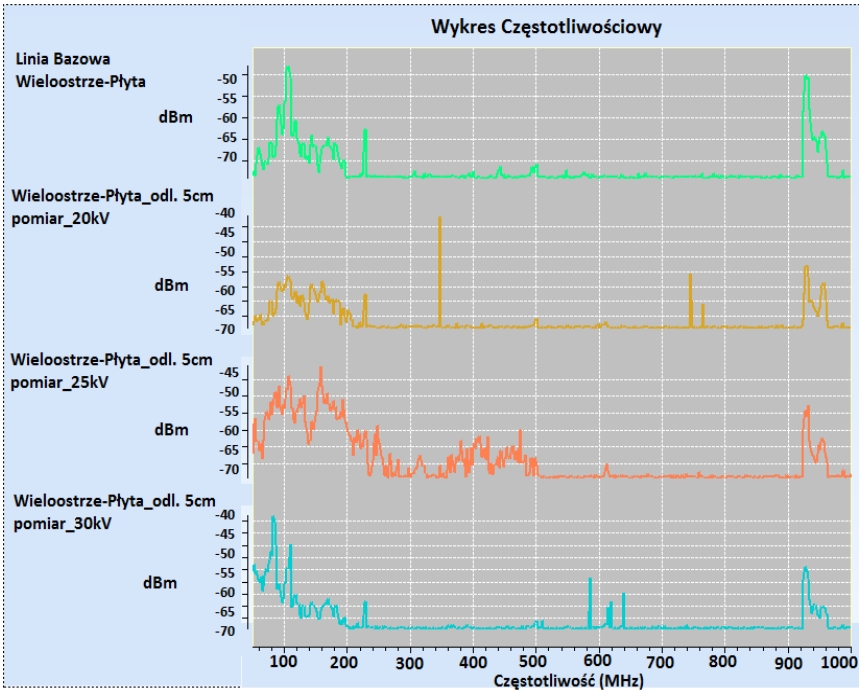

Fig. 10. Test set - multipoint to plane spark gap transmitter, distance between multi-point and plane: 5 cm, for measurements at voltages 0V, 20kV, 25kV, 30kV

Based on measurements results obtained it can be stated, that accuracy of the PDS100 device used for detection is sufficient and that the measuring method applied is an effective tool to measure electromagnetic waves generated by PDS.

Observations made demonstrate that with application of that method used during testing, the occurrence of characteristic frequencies may be observed for individual configurations of the spark gap transmitter, where the amplitude of the signal measured increases together with the voltage rise compared to a so-called "baseline" (characteristics measured at 0V in the given measuring circuit).

REFERENCES

1. A. NESBITT, B.G. STEWART, S.G. MCMEEKIN, S. CONNER, J.C. GAMIO: HV Substation Surveillance Using RFI: Isolator Fault Detection And Characterisation, School of Engineering and Computing, Glasgow Caledonian University, Glasgow, UK. 2010.
2. DOBLE TRANSINOR AS: PDS100 Partial Discharge Surveyor – User's Manual. Norway.

KAPITAŁ LUDZKI
NARODOWA STRATEGIA SPÓJNOŚCI
UNIA EUROPEJSKA
EUROPEJSKI
FUNDUSZ SPOŁECZNY

Projekt współfinansowany ze środków Europejskiego Funduszu Społecznego
Post-graduate scholarship - investment in research personnel of Opole province II

Author Index

Baleja, Richard, 67
Baresova, Katerina, 145
Bednarek, Lukas, 528
Běloch, Michal, 448
Bielik, Marian, 256
Borski, Martin, 151
Bos, Petr, 1
Briš, Radim, 448
Buček, Petr, 261
Burianek, Tomas, 266

Cigánek, Jiří, 6
Cubik, Jakub, 522
Czopik, Jan, 277

Čerbák, Michal, 272
Ćosić, Rajko, 436

Dong, Chau Si Thien, 90, 127

Fabian, Tomas, 382
Fajkus, Marcel, 534
Feberová, Karolína, 283
Friedrischková, Kristýna, 175
Frnda, Jaroslav, 540
Fulneček, Jan, 12

Golasowski, Martin, 289
Goňo, Radomír, 36, 43
Gruss, Martin, 18

Hajek, Lukas, 546
Hajovsky, Jiri, 96
Hasal, Martin, 442
Hendrych, Jakub, 295
Hlavica, Jakub, 181
Hlavinka, Tomáš, 553
Hlozak, Martin, 559
Holuša, Michael, 301
Holý, Branislav, 307
Horák, Bohumil, 175, 234
Houdek, Vít, 24
Hrabal, Josef, 313
Hrabuška, Radek, 187
Hrubý, David, 565

Chlebis, Petr, 102

Jahoda, Pavel, 448
Janoušek, Jan, 319
Janša, Jiří, 30
Jargus, Jan, 570
Jaros, Jakub, 576
Jaroš, Milan, 454
Ježowicz, Tomáš, 326
Jirůtková, Pavla, 460

Kajnar, Tomáš, 582
Kašpar, Adam, 332
Kelnar, Michal, 193
Kojecký, Lumír, 337
Koutný, Martin, 36
Kral, Martin, 43
Kravčenko, Michal, 466, 472
Krawiec, Michał, 689
Krbeček, Matěj, 472
Kroczek, Lukáš, 343
Krohova, Jana, 199, 246
Kubicek, Jan, 204
Kunčický, Radim, 295

Liner, Andrej, 588
Lukáš, Petr, 348

Malý, Lukáš, 478
Marcincin, Oliver, 49
Markopoulos, Alexandros, 460
Martínek, Lubomír, 448
Meca, Ondřej, 354
Meca, Roman, 360
Mehic, Miralem, 594
Merta, Michal, 484
Michalikova, Marketa, 181, 216
Mikolajek, Martin, 210
Mikulec, Martin, 600
Minařík, Daniel, 18
Mozdřeň, Tomáš, 55
Mročková, Agáta, 222
Mrovec, Tomas, 102

Nedoma, Jan, 606
Ney, Michal, 61
Novák, Tomáš, 1, 67
Novosád, Ladislav, 72
Nowaková, Jana, 228

Ondrejka, Adam, 365

Ondruš, Jakub, 370
Orčík, Lukáš, 612
Otevřel, Vít, 234
Otýpka, Jan, 108

Papes, Martin, 616
Partila, Pavol, 620
Perecar, Frantisek, 626
Peter, Lukas, 240
Peterek, Tomas, 246
Petrtýl, Ondřej, 114
Pieš, Martin, 222
Plaček, Jiří, 78
Poboril, Radek, 632
Pokorný, Miroslav, 222, 228
Prauzek, Michal, 181
Prokeš, Martin, 376

Režnar, Tomáš, 490

Sampathila, Niranjana, 187
Sevcik, Jiri, 388
Silber, Adam, 472
Skanderova, Lenka, 382
Skopal, Robert, 498
Slachta, Jiri, 648
Slanina, Zdeněk, 234
Slíva, Ladislav, 120
Smondrk, Maros, 199, 246
Sokanský, Karel, 1, 67
Stolfa, Jakub, 277, 394
Stolfa, Svatopluk, 277

Šafařík, Jakub, 638
Ševčík, Lukáš, 642
Špaček, Michal, 84
Špička, Jiří, 157
Štrba, Radoslav, 400
Šulák, Radek, 163
Šumpich, Jan, 1
Šurkovský, Martin, 406

Takáč, Jiří, 169
Tomis, Martin, 654
Tomis, Radek, 504
Tovarek, Jaromir, 620, 660
Tran, Thinh Cong, 127

Uher, Vojtěch, 412
Uhrin, Dominik, 666
Urbaniec, Ireneusz, 694

Vala, David, 175, 250
Vanderka, Ales, 673
Vantuch, Tomas, 418
Vašinek, Michal, 424
Vavřík, Radim, 510
Verner, Tomáš, 133
Vo, Hau Huu, 127, 139
Vondrák, Ivo, 277
Voznak, Miroslav, 594, 600, 612, 620, 642, 648, 660, 666

Zapletal, Jan, 516
Zatloukal, Filip, 430
Závodný, Petr, 679
Zbořil, Ondřej, 684
Zdralek, Jaroslav, 559

Editors:	Michal Krátký, Jiří Dvorský, Pavel Moravec Dept. of Computer Science VŠB – Technical University of Ostrava
Title:	WOFEX 2015
Place, year, edition:	Ostrava, 2015, 1st
Page count:	719
Edit:	VŠB – Technical University of Ostrava, 17. listopadu 15, 708 33 Ostrava-Poruba Czech Republic
Impression:	200

Not for sale.

ISBN 978-80-248-3787-1